inam
Institute of Advanced Materials
UJI Castelló

UNIVERSITAT
JAUME·I

Development of Advanced Materials Based on Polymeric Ionic Liquids Formulated for Additive Manufacturing

Sara Miralles Comins

April 2023

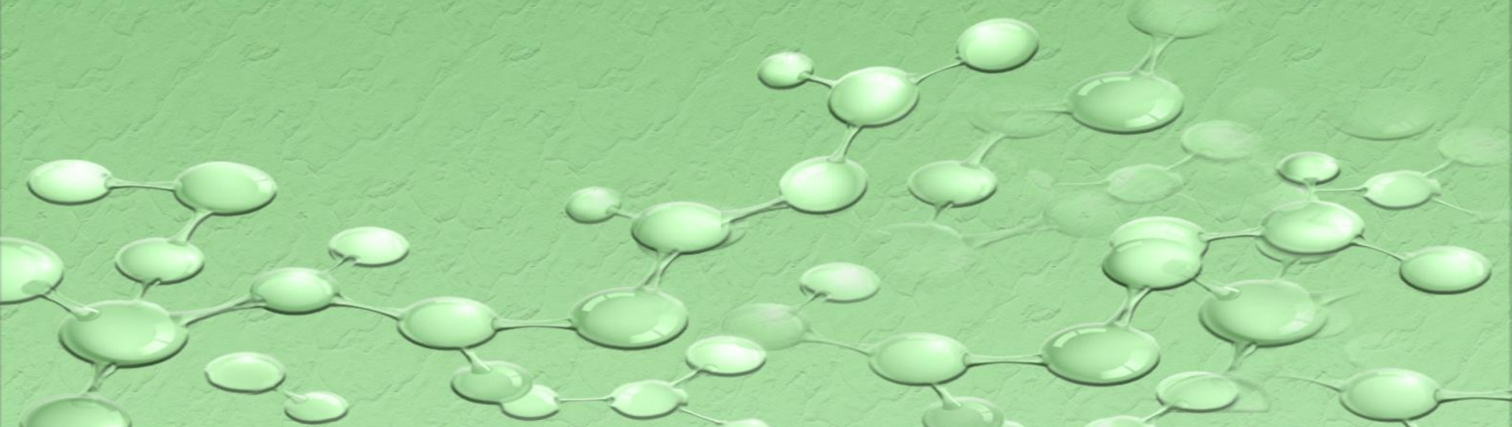

UNIVERSITAT
JAUME•I

Programa de Doctorat en Ciències

Escola de Doctorat de la Universitat Jaume I

Development of Advanced Materials Based on Polymeric Ionic Liquids Formulated for Additive Manufacturing

Memòria presentada per Sara Miralles Comins per a optar al grau de doctora per la Universitat Jaume I

Doctoranda

SARA|
MIRALLES
|COMINS

Firmado
digitalmente por
SARA|MIRALLES|
COMINS
Fecha: 2023.04.13
13:28:15 +02'00'

Sara Miralles Comins

Directors

VICTOR|
SANS|
SANGORR
IN

Firmado
digitalmente por
VICTOR|SANS|
SANGORRIN
Fecha: 2023.04.13
16:46:17 +02'00'

Dr. Víctor Sans Sangorrín

SIXTO|
GIMENE
Z|JULIA

Firmado digitalmente por
SIXTO|GIMENEZ|JULIA
Nombre de reconocimiento
(DN): cn=SIXTO|GIMENEZ|
JULIA,
serialNumber=34804561H,
givenName=SIXTO,
sn=GIMENEZ JULIA,
ou=CIUDADANOS, o=ACCV,
c=ES
Fecha: 2023.04.13 17:02:54
+02'00'

Prof. Sixto Giménez Juliá

Castelló, abril 2023

Funding Sources

Aquesta tesi s'ha realitzat gràcies a la concessió d'una beca predoctoral de la Generalitat Valenciana (ACIF/2020/338), i una beca per a estades predoctorals fora de la Comunitat Valenciana (05TUI/2020/125811) que em van permetre fer una estada curta del 15/09/2022 al 20/12/2022 en el Departament de Ciència Aplicada i Tecnologia (DISAT) en el *Politecnico di Torino*, sota la supervisió del professor Candido Fabrizio Pirri.

Així mateix, agraeixo a la Generalitat Valenciana (CIDEGENT 2018/036) el finançament d'un any d'investigació doctoral i d'algunes despeses extraordinàries en cursos i congressos.

Finalment, agraeixo a la Universitat Jaume I el finançament d'algunes activitats de formació mitjançant les convocatòries d'ajudes per a activitats formatives de doctorat.

Acknowledgements

Ha sigut tot un plaer per a mi haver pogut realitzar aquesta tesi acompanyada d’una gent tan increïble. M’agradaria donar les gràcies tant a aquelles persones que ja estaven presents abans de començar aquesta etapa com a totes aquelles que he anat coneixent durant els anys de doctorat. Sense elles aquesta tesi no haguera sigut possible.

La possibilitat d’haver format part de l’Institut de Materials Avançats (INAM) ha estat tot un privilegi. En especial agraeixo al meu supervisor l’oportunitat que em va donar al confiar en mi per iniciar el seu grup d’investigació. Moltíssimes gràcies Víctor per tot el suport, consells i l’ajuda que m’has proporcionat durant aquesta etapa d’aprenentatge. El grup, inicialment format per mi i per Víctor, no va tardar en créixer. A poc a poc s’ha anat formant un grup excepcional i ha estat tota una sort poder treballar amb tots ells. Per suposat, el grup continua creixent i continua arribant gent genial amb els quals m’hagués agradat haver coincidit abans. D’ahí que el nom extraoficial del nostre grup siga els *MASPro*. M’agradaria donar les gràcies en particular a Marci, que va arribar un poc tard però encara així ha estat la persona que més m’ha ajudat i guiat en aquesta etapa.

A més, com que he tingut el plaer de col·laborar amb diferents grups de l’INAM, he pogut conèixer molta gent meravellosa tant en l’àmbit de treball com fora. Però bé, no tota la gent genial forma part de l’INAM, algunes amistats naixen simplement per compartir *pasillo*. Espere que aquestes amistats es mantinguin força temps encara que ja no ens veiem tant.

Per suposat, no em puc oblidar de tota la gent increïble que vaig conèixer durant la meua estada en Turin. Va ser tot un plaer tenir a Ignazio i a Annalisa com a supervisors. A part, els companys que vaig tindre van ser immillorables, tant per treballar com per conèixer Itàlia.

Finalment, voldria donar les gràcies als meus pares per estar sempre ahí. També he d’agrair a la meua família i als amics la seua paciència i el suport que m’han donat. Per ajudar-me a desconnectar sempre que ho he necessitat! I de manera especial, vull agrair a Pascual que sempre confiés en mi i haja estat present en tot moment, orgullós sempre de cada cosa que faig. Això ha estat el motor de seguir endavant. Estic molt agraïda de tenir-te al meu costat.

Moltíssimes gràcies a tots vosaltres per fer que aquesta etapa hagi estat increïble!!

Index

Abstract

This PhD thesis, entitled "*Development of Advanced Materials Based on Polymeric Ionic Liquids Formulated for Additive Manufacturing*", has been written with a traditional structure and contains six chapters. The initial chapter is the introduction to the thesis, followed by three chapters that provide the main research performed, as well as the results obtained, and ends with two final chapters (general conclusions and annex) and the literature.

The thesis focuses on the design, development and characterisation of 3D printable materials based on polymeric ionic liquids, which are studied and evaluated in several applications, including antibacterial and photodegradation of pollutants.

Additive manufacturing, commonly known as 3D printing, is a revolutionary set of technologies with many benefits compared to conventional fabrication techniques. The design and production flexibility of this technology in conjunction with its capability to transfer advanced properties of nanostructured materials across scales, opens up new opportunities to design cost-effective smart materials for next-generation devices in practically all fields of application. Nevertheless, 3D printing is critically limited by the availability of resins designed for additive processes. Moreover, smart molecular systems are frequently incapable of being integrated into 3D printable formulations, limiting the printability of functional devices. Therefore, innovation in advanced materials specially formulated for additive manufacturing is of great interest.

In this regard, polymeric ionic liquids (PILs) are ideal matrices to stabilise molecular and nanostructured materials as a result of their ionic and supramolecular interactions. PILs are high-molecular-mass compounds that combine attractive IL properties (wide electrochemical windows, chemical and thermal stability, low vapor pressure, non-flammability and non-volatility) with polymer features (i.e., mechanical robustness, durability, low toxicity, rapid manipulation). In addition, these polymers can be formulated to be printed by 3D techniques. For that reason, PIL-based formulations are really desirable for designing biomedical, optoelectronic, electrochemical, redox and photoactive devices among others.

Within this context, this PhD thesis has demonstrated the outstanding ability of PILs to stabilise different active materials, including perovskite nanocrystals, metallic nanoparticles, conductive polymers and ionic liquids. Firstly, a variety of monomeric ionic liquids were synthesised and characterised by spectroscopy and spectrometry techniques (^{1}H NMR, ^{13}C NMR, elemental analysis, ESI-MS, FT-IR and TGA-DSC). These polymerisable molecules were mixed with a cross-linker, a photoinitiator and different functional materials in order to obtain novel 3D printable formulations that were photopolymerised after exposure to UV light. The resulting advanced PILs with tailor-made geometries were characterised by different techniques (FT-IR, RAMAN, TGA-DSC, UV-Vis, optical microscopy and SEM etc).

In **Chapter 2**, several PIL formulations were functionalised with metallic precursors to obtain antimicrobial materials. Their capacity to generate and stabilise nanoparticles was studied. The 3D-printed devices presented antimicrobial activity against different bacteria and fungi. Moreover, the printing parameters of a broad family of polymers were optimised in order to improve the print performance. Afterwards, the biocompatibility of the resulting prints was analysed. The monomeric ionic liquid and the photoinitiator play an important role in enhancing the biocompatibility of the samples. Finally, the resultant non-toxic and antimicrobial formulations were employed for 3D-printing a medical demonstrator at high resolution.

In **Chapter 3**, the synergistic potential of encapsulating caesium perovskites into PILs was demonstrated, generating optical devices. Different formulations were tested to achieve the optimal embedding matrix. The stability of the nanocrystals after the suitable encapsulation was enhanced, showing better light, moisture, water and thermal stability compared to pure perovskite nanocrystals. A variety of perovskites were evaluated, including lead and lead-free nanocrystals. Furthermore, the formulations were successfully 3D-printed in tailored geometries. Solid photocatalysts capable to degrade an organic dye (methyl red) were prepared by combining the well-known photocatalyst activity of the perovskites with the adsorbent properties of PILs.

In **Chapter 4**, conductive fillers were added into the PIL formulations in order to reduce the resistance of the materials and obtain conductive devices. Mainly, it was investigated the influence of adding conductive polymers (PEDOT) varying the order and form of addition.

The introduction of homogeneous ionic liquids at different concentrations into the systems was also studied for enhancing the conductivity of the materials. Additionally, these systems were capable to stabilise and encapsulate successfully perovskite nanocrystals, reaching optoelectronic properties. Lastly, PIL-based materials were functionalised with metallic salts as another approach to increase the conductivity of polymers.

In summary, a big variety of formulations have been prepared and successfully photopolymerised. By varying the monomeric ionic liquid, the cross-linker, the active materials and the digital images, precise 3D objects with specific polymeric properties were achieved. Subsequently, the different materials were employed in various applications, depending on their respective characteristics.

As a result of the work presented in this thesis, several papers were published in high impact journals and there is another one in progress. The publications include a book chapter, a review and two articles:

Miralles-Comins, S.; Alvarez, E.; Lozano, P.; Sans, V., 9 Exothermic advanced manufacturing techniques in reactor engineering: 3D printing applications in flow chemistry. **2021**, 259-276.

Miralles-Comins, S.; Zanatta, M.; Sans, V., Advanced Formulations Based on Poly(ionic liquid) Materials for Additive Manufacturing. *Polymers* **2022,** *14* (23), 5121.

Wales, D. J.; **Miralles-Comins, S.**; Franco-Castillo, I.; Cameron, J. M.; Cao, Q.; Karjalainen, E.; Alves Fernandes, J.; Newton, G. N.; Mitchell, S. G.; Sans, V., Decoupling manufacturing from application in additive manufactured antimicrobial materials. *Biomaterials science* **2021,** *9* (16), 5397-5406.

Miralles-Comins, S.; Zanatta, M.; Gualdrón-Reyes, A. F.; Rodriguez-Pereira, J.; Mora-Seró, I.; Sans, V., Polymeric ionic liquid-based formulations for the fabrication of highly stable perovskite nanocrystal composites for photocatalytic applications. *Nanoscale* **2023**, *15*, 4962-4971.

Resum

Aquesta tesi doctoral, titulada "*Development of Advanced Materials Based on Polymeric Ionic Liquids Formulated for Additive Manufacturing*", ha estat redactada amb una estructura tradicional i conté sis capítols. El capítol inicial és la introducció a la tesi, seguit de tres capítols que descriuen les principals investigacions realitzades, així com els resultats obtinguts, i finalitza amb dos capítols finals (conclusions generals i l'annex) seguits de la literatura.

La tesi es centra en el disseny, desenvolupament i caracterització de materials imprimibles en 3D basats en líquids iònics polimèrics, el quals es van estudiar i avaluar en diverses aplicacions, incloent la fotodegradació de contaminants i aplicacions antibacterianes.

La fabricació additiva, coneguda comunament com a impressió 3D, és un conjunt revolucionari de tecnologies amb molts avantatges en comparació amb les tècniques de fabricació convencionals. La flexibilitat de disseny i producció d'aquesta tecnologia, juntament amb la seva capacitat per transferir propietats avançades de materials nanoestructurats a través de les escales (de nano a macro), obre noves oportunitats per dissenyar materials intel·ligents per a dispositius de nova generació en pràcticament tots els camps d'aplicació. No obstant això, la impressió 3D està molt limitada per la disponibilitat de resines dissenyades per a processos additius. A més, els sistemes moleculars intel·ligents sovint són incapaços d'integrar-se en formulacions imprimibles en 3D, limitant la imprimibilitat dels dispositius funcionals. Per tant, la innovació en materials avançats especialment formulats per a la fabricació additiva és de gran interès.

En aquest sentit, els líquids iònics polimèrics (PILs) són matrius ideals per estabilitzar materials moleculars i nanoestructurats com a resultat de les seves interaccions iòniques i supramoleculars. Els PILs són compostos d'alta massa molecular que combinen propietats atractives dels líquids iònics (ampli rang electroquímic, estabilitat química i tèrmica, baixa pressió de vapor, no inflamabilitat i no volatilitat) amb característiques del polímer (és a dir, robustesa mecànica, durabilitat, baixa toxicitat, ràpida manipulació). A més, aquests polímers es poden formular per ser impresos mitjançant tècniques 3D. Per aquest motiu,

les formulacions basades en PILs són realment desitjables per dissenyar dispositius biomèdics, optoelectrònics, electroquímics, redox i fotoactius, entre d'altres.

En aquest context, aquesta tesi doctoral ha demostrat l'extraordinària capacitat dels PILs per estabilitzar diferents materials actius, incloent nanocristalls de perovskita, nanopartícules metàl·liques, polímers conductors i líquids iònics. En primer lloc, es van sintetitzar i caracteritzar una varietat de líquids iònics monomèrics mitjançant tècniques d'espectroscòpia i espectrometria (^{1}H RMN, ^{13}C RMN, anàlisi elemental, ESI-MS, FT-IR i TGA-DSC). Aquestes molècules polimeritzables es van barrejar amb un reticulant, un fotoiniciador i diferents materials funcionals per obtenir noves formulacions imprimibles en 3D que es van fotopolimeritzar després de l'exposició a la llum UV. Els PILs resultants amb propietats avançades i geometries fetes a mida es van caracteritzar per diferents tècniques (FT-IR, RAMAN, TGA-DSC, UV-Vis, microscòpia òptica i SEM, etc.).

En el **Capítol 2**, es van funcionalitzar diverses formulacions basades en PIL amb precursors metàl·lics per obtenir materials antimicrobians. Es va estudiar la seva capacitat per generar i estabilitzar nanopartícules. Els dispositius impresos en 3D presentaven activitat antimicrobiana contra diferents bacteris i fongs. A més, es van optimitzar els paràmetres d'impressió d'una àmplia família de polímers per tal de millorar la resolució d'impressió. Posteriorment, es va analitzar la biocompatibilitat de les impressions resultants. Tant el líquid iònic monomèric com el fotoiniciador van tindre un paper important en la millora de la biocompatibilitat de les mostres. Finalment, les formulacions no tòxiques i antimicrobianes resultants es van utilitzar per imprimir en 3D un demostrador mèdic a alta resolució.

En el **Capítol 3**, es va demostrar el potencial sinèrgic d'encapsular perovskites de cesi en PILs, generant dispositius òptics. Es van provar diferents formulacions per aconseguir la matriu d'incrustació òptima. L'estabilitat dels nanocristalls després de l'encapsulació adequada va augmentar considerablement, mostrant una millor estabilitat front a la llum, humitat, aigua i temperatura en comparació amb els nanocristalls purs de perovskita. Es van avaluar una varietat de perovskites, incloent perovskites sense plom. A més, les formulacions es van imprimir amb èxit en 3D en geometries personalitzades. Es van preparar fotocatalitzadors sòlids capaços de degradar un colorant orgànic (vermell de metil) combinant la coneguda activitat fotocatalitzadora de les perovskites amb les propietats adsorbents dels PILs.

Per últim, en el **Capítol 4**, es van afegir additius conductors a les formulacions basades en PILs per tal de reduir la resistència dels materials i obtenir dispositius conductors. Principalment, es va investigar la influència de l'addició de polímers conductors (PEDOT) variant l'ordre i la forma d'addicionar-lo. També es va estudiar la introducció de líquids iònics homogenis a diferents concentracions en els sistemes per tal de millorar la conductivitat dels materials. A més, aquests sistemes van ser capaços d'estabilitzar i encapsular amb èxit nanocristalls de perovskita, aconseguint propietats optoelectròniques. Finalment, els materials basats en PILs es van funcionalitzar amb sals metàl·liques com un altre enfocament per augmentar la conductivitat dels polímers.

En resum, una gran varietat de formulacions s'han preparat i fotopolimeritzat amb èxit. Variant el líquid iònic monomèric, el reticulant, els materials actius i les imatges digitals, es van aconseguir objectes 3D precisos amb propietats polimèriques específiques. Posteriorment, els diferents materials es van emprar en diverses aplicacions, en funció de les seves respectives característiques.

Acronyms

^{13}C NMR	Carbon-13 nuclear magnetic resonance
^{1}H NMR	Hydrogen-1 nuclear magnetic resonance
3DP	Three-dimensional printing
A. niger (AN)	*Aspergillus niger*
AcrEMA.BF$_4$	[2-(acryloyloxy)ethyl]trimethyl-ammonium tetrafluoroborate
AcrEMA.Cl	[2-(acryloyloxy)ethyl]trimethyl-ammonium chloride
AcrEMA.I	[2-(acryloyloxy)ethyl]trimethyl-ammonium iodide
AcrEMA.N(CN)$_2$	[2-(acryloyloxy)ethyl]trimethyl-ammonium dicyanamide
$AgNO_3$	Silver nitrate
AgNPs	Silver nanoparticles
$AgSbF_6$	Silver hexafluoroantimonate
AM	Additive manufacturing
APS	Ammonium persulfate
B. subtilis (BS)	*Bacillus subtilis*
BA	Butyl acrylate
BAPO	Phenylbis(2,4,6-trimethylbenzoyl)phosphine oxide
BDA	1,4-butanediol diacrylate
BMI.Br	1-butyl-3-methylimidazolium bromide
BVI.Br	1-butyl-3-vinylimidazolium bromide
BVI.I	1-butyl-3-vinylimidazolium iodide
BVI.N(CN)$_2$	1-butyl-3-vinylimidazolium dicyanamide
C. cladosporioides	*Cladosporium cladosporioides*
Ch.Cl	Choline chloride
$CsPbX_3$	Caesium lead halide nanocrystals (X = Cl, Br, I and combinations)
$Cu(NO_3)_2\cdot 3H_2O$	Copper dinitrate trihydrate
CV	Cyclic voltammetry
DCM	Dichloromethane
DMI.Br	1-dodecane-3-methylimidazolium bromide
DPAP	2,2-dimethoxy-2-phenylacetophenone
DSC	Differential scanning calorimetry
DTG	Derivative thermogravimetry
E. coli (EC)	*Escherichia coli*
EDOT	3,4-ethylenedioxythiophene
ESI-MS	Electrospray ionization mass spectrometry
EtOH	Ethanol
FT-IR	Fourier-transform infrared spectroscopy
HMPP	2-hydroxy-2-methylpropiophenone
HVI.Br	1-(3-hydroxypropyl)-3-vinylimidazolium bromide

IL1	1-butyl-3-methylimidazolium bis(trifluoromethane)sulfonimide
IL2	1-dodecyl-3-methylimidazolium bis(trifluoromethane)sulfonimide
IL3	Choline bis(trifluoromethane)sulfonimide
IPA	Isopropanol
IS	Impedance spectroscopy
JIS	Japanese Industrial Standard
KI	Potassium iodide
MACl	Methylammonium chloride
MAI	Methylammonium iodide
MeOH	Methanol
mIL	Monomeric ionic liquid
mIL1 (BVI.NTf$_2$)	1-butyl-3-vinylimidazolium bis(trifluoromethane)sulfonimide
mIL2 (HVI.NTf$_2$)	1-(3-hydroxypropyl)-3-vinylimidazolium bis(trifluoromethane)sulfonimide
mIL3 (AcrEMA.NTf$_2$)	[2-(acryloyloxy)ethyl]trimethyl-ammonium bis(trifluoromethane)sulfonimide
MR	Methyl red
NaCl	Sodium chloride
NCs	Nanocrystals
nm	Nanometres
NPs	Nanoparticles
OLED	Organic light emitting diode
PEDOT	Poly(3,4-ethylenedioxythiophene)
PEGDA	Poly(ethyleneglycol) diacrylate
PEGDA 250	Poly(ethyleneglycol) diacrylate, Mn = 250 g/mol
PEGDA 575	Poly(ethyleneglycol) diacrylate, Mn = 575 g/mol
PEGDA 700	Poly(ethyleneglycol) diacrylate, Mn = 700 g/mol
PI	Photoinitiator
PILs	Polymeric ionic liquids
PL	Photoluminescence
PLQY	Photoluminescence quantum yield
PNCs	Perovskite nanocrystals
SEM	Scanning electron microscopy
S. epidermidis	*Staphylococcus epidermidis*
TEM	Transmission electron microscopy
Tg	Transition glass temperature
TGA	Thermogravimetric analysis
THF	Tetrahydrofuran
T_{onset}	Thermal decomposition temperature
TPO	Diphenyl(2,4,6-trimethylbenzoyl)phosphine oxide
UV-Vis	Ultraviolet visible
VIm	Vinyl imidazolium
WP	Washing protocol

Compound Chart

Monomeric Ionic Liquids

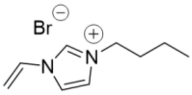
BVI.Br

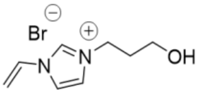
HVI.Br

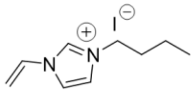
BVI.I

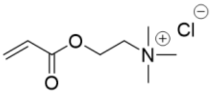
AcrEMA.Cl

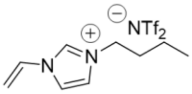
BVI.NTf$_2$ (mIL1)

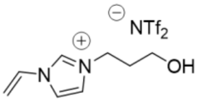
HVI.NTf$_2$ (mIL2)

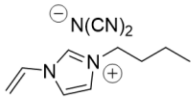
BVI.N(CN)$_2$

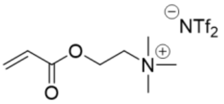
AcrEMA.NTf$_2$ (mIL3)

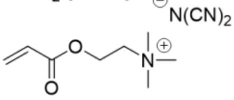
AcrEMA.N(CN)$_2$

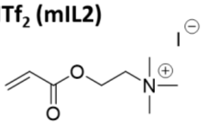
AcrEMA.I

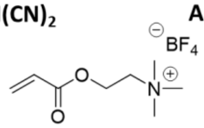
AcrEMA.BF$_4$

Cross-linkers

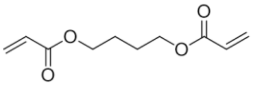
BDA

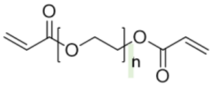
PEGDA

Photoinitiators

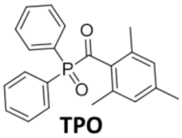
TPO

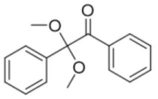
DPAP

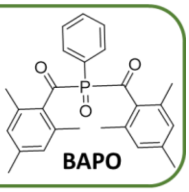
BAPO

Ionic Liquids

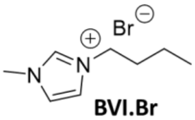
BVI.Br

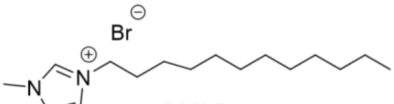
DMI.Br

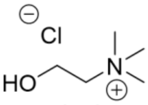
Ch.Cl

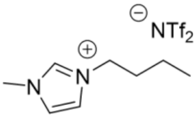
BVI.NTf$_2$ (IL1)

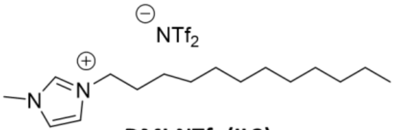
DMI.NTf$_2$ (IL2)

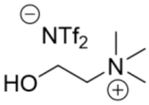
Ch.NTf$_2$ (IL3)

Additives

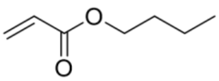
BA

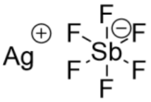
AgSbF$_6$

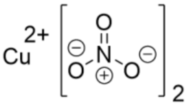
Cu(NO$_3$)$_2$

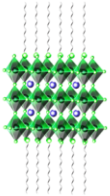
PNCs

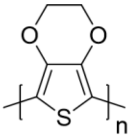
PEDOT

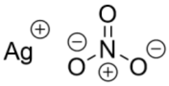
AgNO$_3$

General Nomenclature for Formulations

PILX: mILX (80 mol%) + BDA (20 mol%) + TPO (1 wt%)

Ag@PIL1: PIL1 + $AgSbF_6$ (1 wt%)

PILX.1: mILX (60 mol%) + PEGDA 575 (40 mol%) + TPO (1 wt%)

PILX.2: mILX (80 mol%) + PEGDA 575 (20 mol%) + TPO (1 wt%)

PILX.3: mILX (90 mol%) + PEGDA 575 (10 mol%) + TPO (1 wt%)

PILX.4: mILX (100 mol%) + PEGDA 575 (0 mol%) + TPO (1 wt%)

PILX.5: mILX (80 mol%) + PEGDA 250 (20 mol%) + TPO (1 wt%)

PILX.6: mILX (80 mol%) + PEGDA 700 (20 mol%) + TPO (1 wt%)

Ag@PILX.2: PILX.2 + $AgSbF_6$ (1 wt%)

Cu@PILX.2: PILX.2 + $Cu(NO_3)_2{\cdot}3H_2O$ (2 wt%)

PIL3a: mIL3 (100 mol%) + BDA (0 mol%) + TPO (1 wt%)

PIL3b: mIL3 (95 mol%) + BDA (5 mol%) + TPO (1 wt%)

PIL3c: mIL3 (90 mol%) + BDA (5 mol%) + BA (5 mol%) + TPO (1 wt%)

PIL3d: mIL3 (80 mol%) + BDA (5 mol%) + BA (15 mol%) + TPO (1 wt%)

PIL3h: mIL3 (0 mol%) + BDA (5 mol%) + BA (95 mol%) + TPO (1 wt%)

PIL3x@PS: PIL3x + $CsPbBr_3$ (2 wt%)

E_xPIL: EDOT (x mol%) + PIL formulation

P_xPIL: PEDOT (x wt%) + PIL formulation

E/P_xILX$_y$PIL: EDOT or PEDOT (x %) + ILX (y mol%) + PIL formulation

P_xPIL3b@PS: PEDOT (x %) + PIL3b + $CsPbBr_3$ (2 wt%)

ILX$_y$PIL3b: ILX (y mol%) + PIL3b

ILX$_y$PIL3b@PS: ILX$_y$PIL3b + $CsPbBr_3$ (2 wt%)

Ag_xPIL: $AgNO_3$ (x wt%) + PIL formulation

Cu_xPIL: $Cu(NO_3)_2{\cdot}3H_2O$ (x wt%) + PIL formulation

Where X = 1, 2 or 3 depending on the mIL used (mIL1, mIL2 or mIL3, respectively)

Chapter 1:

Introduction

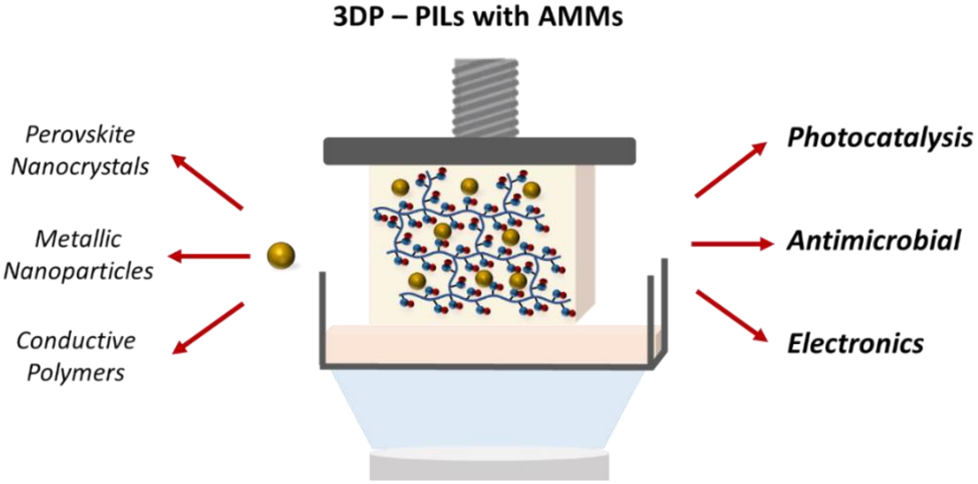

1.1 3D Printing Overview

The recent growth of additive manufacturing techniques, also known as three-dimensional (3D) printing, is attributed to several advantages including rapid translation of fundamental molecular properties, fabrication of complex geometries with high precision and resolution, unprecedent flexibility in design, waste minimisation and personal customisation which enables the fine control of structural features.[1] Furthermore, it enables distributed production as opposed to logistically complex production lines with conventional production methods, reducing costs and increasing the flexibility and sustainability of the process. Whereas traditional fabrication techniques have limitations in controlling the geometry and architecture of macroscopic components without compromising the performance, 3DP techniques are an efficient strategy to engineer well-controlled functional materials across the scales (from nano to macroscale) with an accurate control over geometry (dimension, porosity and morphology) and structure. Moreover, 3DP expands the boundaries of materials science and provides an exciting opportunity for interdisciplinary research as it allows the incorporation of multiple nano-materials in the same printing process to obtain multi-functional devices.

The main feature of AM is to design an object by adding material in a layer-by-layer mechanism until the model is completed. The first step is to generate the data from a three-dimensional Computer-Aided Design (3D CAD) software, in a simple machine avoiding complicate production chains or process planning. Then, the digital CAD model is translated into computer readable formats as an STL file (an industry-standard stereo-lithography format) which slices cross-sections into codes that allow the machine to build the object before printing. This is a fast, reliable and facile way to design prototypes and devices, and additionally, this 3D CAD files can be easily shared and modified with large on-line databases of design shared under creative commons licenses.[2]

Additive manufacturing is a booming area. According to Smithers Group - a provider of strategic market research reports -, billions of dollars are invested in the 3DP market and an annual growth is expected until 2027, potentially reaching $55.8 billion.[3] Additionally, a quantitative life cycle analysis (LCA) data shows that the AM process has lower environmental impact compared to other existing manufacturing technologies as 3DP produces no wastes or emissions. It is estimated that the implementation of printing processes might low the carbon dioxide emission intensities by about 5 % by 2025. Furthermore, the additive nature of this technique minimizes the amount of material employed, reduces the energy required and the resource demanded.[4]

In the last years, AM techniques have been vastly researched and are increasingly finding industrial applications as part of Industry 4.0 initiatives.[5] The development of formulations tailored specifically for AM which can add advanced functionality to the parts fabricated is a promising avenue. Manufacturing materials with advanced properties specifically designed for 3D printing is highly desirable for a variety of applications like household goods, renewable energy, personalised healthcare, automotive components, soft robotics, medical devices or tissue engineering. The loop between design, manufacture and application can be rapidly closed with additive manufacturing. Hence, the unique properties of molecular and nanostructured materials can be directly transferred to macroscopic functional devices. The possibility of integrating functional molecules into 3D printable materials, while simultaneously controlling the geometry, is a great contribution that will accelerate the development of novel devices with complex 3D geometries.[6] However, the range of available materials, resins and inks available for AM is limited, thus hindering the development of the field.

In this regard, polymeric macromolecules have received increased attention for printing smart materials due to the wide variety of materials, the versatility for novel chemistries, and the ability to tune chemical composition and architecture.[7] For instance, stimuli-responsive polymers (*i. e.*, materials that respond to external stimuli from its environment in a reproducible, reliable, specific, and useful way)[8] have been widely employed to pave the way for 4D printing.[9] Hydrogels are being evaluated as potential materials since they are excellent candidates for biomedical applications given their biocompatibility.[10] Further emerging polymers with vastly varied chemical structure and properties have been developed for 3DP, including covalent organic frameworks (COFs),[11] polypeptides,[12] ionogels,[13] and many more.[14] Recently, polymeric ionic liquids (PILs) have gained prominence as intelligent materials[15] capable of responding to temperature,[16] light,[17] solvents,[18] pH[19] and CO_2.[20] Ionic liquids (ILs) and polymeric analogues are a fascinating field of research due to the possibility of controlling the macroscopic properties by changing the formulation (cation/anion).[21] These polymers can be especially designed to be printed by 3D techniques allowing to design and manufacture high-resolution multi-material devices essential to the development of future technologies.[22] The countless combinations cation-anion (it is theoretically feasible to generate 10^{18} distinct ILs) possess unique physicochemical properties that can be tuned easily without sacrificing 3D printability and resolution.[23] Moreover, PILs are ideal materials to stabilise molecular and nanostructured materials due to their ionic and supramolecular interactions. The development of printable PILs is an expanding area, although it is still in its infancy.

1.1.1 Types of 3D Printing Technologies

The first rapid prototyping system "Stereolithography Apparatus" (SLA) was patented by Charles Hull in 1986.[24] Since then, many different types of AM techniques have been developed and commercialised. Depending on the form of the starting material and the way the materials are deposited and assembled in the additive fashion, 3DP techniques can be divided into seven categories, opening new pathways for creating devices with outstanding performance at fine resolutions.[25] These techniques cover a broad range of scales from micro- to macroscale devices and materials available. The seven characteristic techniques are: vat photopolymerisation, powder bed fusion, material extrusion, material jetting, binder jetting, direct energy deposition and sheet lamination (*Table 1*). All of them have been widely studied in several literature reviews,[26] in which the materials, benefits, drawbacks and main application areas of each printing method are specified. According to the technique employed, the parts may be post-processed to improve the strength or surface quality. This section provides a brief overview about the state-of-the-art of the different AM technology. In our work we have mainly focus on vat polymerisation further explained in the following section.

Vat polymerisation includes stereolithography (SLA) and digital light processing (DLP) techniques. The printing process produce macroscopic solids from liquids by the selective photopolymerisation of monomers with UV light. Each photopolymer layer is cured with UV light producing fully cured models that can be handled and used immediately, without post-curing. These AM technologies can create high-resolution objects, but the process is rather slow, quite expensive and the range of printable materials is very limited.[26a]

Similarly, **powder bed fusion** (PBF) also presents a fine resolution and high quality of printing, but it is also a slow process with high cost. PBF consists in thin layers of very fine powders, which are spread and closely packed on a platform, and then the powder in each layer is consolidated by heating with a laser or an electron beam over the photopolymer surface. PBF does not require support structures as the parts are supported by unfused powder in the build area.[1] As a post-processing step, the material can be heated to improve physical and mechanical properties, although it can lead to shrinkage of parts. The laser-based AM technology include two methods, selective laser sintering (SLS) and selective laser melting (SLM). Both have similar process formation of the layers, but the sintering process of SLS do not fully melt the powder and additionally, SLS can be used for a variety of polymers, metals and alloy powders while selective laser melting (SLM) can only be used for certain metals.[27] Electron beam melting (EBM) is another PBF method where materials are placed under vacuum and fused together by direct heating using a high-powder electron beam as source of energy reaching superior accuracy.[26c]

On the contrary, **material extrusion** methods are low cost, high speed and simple processes. Fused fabrication filament (FFF) is an AM technique based on the extrusion of a thermoplastic polymer. The resin is heated at the nozzle to reach a semi-liquid state and then extruded on the platform. Parts can be built with single or multiple materials with the option of a dual extruder nozzle on some platforms. The problematics of FFF are the poor mechanical properties, the layer-by-layer appearance, low quality (resolution between 0.2 and 0.05 mm), and the limited number of thermoplastic materials. Another kind of extrusion method is direct ink writing (DIW). DIW extrudes a paste through a thin needle allowing the processing of relatively dense and viscous materials compared to other AM techniques. It can print the electrode with a high active material loading and with much less clogging risk.[28]

In **material jetting** (MJ), a print head, similar to a standard inkjet printer head, is used to dispense materials in a continuous or drop on demand approach onto a platform. Droplets are released on demand due to the pressure change in the nozzle by thermal or piezoelectric actuators. The latter permits the use of a wider range of materials. Commercial MJ devices allow a layer resolution of micron size layer resolution,[29] and multiple nozzles can be used in order to incorporate multiple materials in a single build. As a post processing step, the pieces can be cured under UV light to enhance their physical properties. However, it still faces some challenges related to the limited solvent resistance of the materials.[1, 26a]

Inkjet printing is one of the main methods for printing complex and advanced ceramics, consisting in pumping and depositing the stable ceramic suspensions in the form of droplets via the injection nozzle onto the substrate. This is a fast and efficient method able to print complex structures with high resolution and flexibility in design. While direct writing needs the ink to be high viscosity, i.e., non-Newtonian paste with shear-thinning behaviour, inkjet printing requires low viscosity Newtonian liquid-like ink. Another similar technology to inkjet printing is called contour crafting which is widely used for large building structures. This method is capable of extruding concrete paste or soil by using larger nozzles and high pressure.[28]

Binder jetting (BJ) is similar to powder bed fusion method since parts are built up from layers of powder but they are consolidated with binder agent jetted on demand from a nozzle head. BJ methods pose similar advantages in terms of resolution. Nevertheless, when the powder is fused with a binder, the porosity is generally higher compared to laser because it can print denser parts.[1, 26a]

Direct energy deposition (DED) is very used for engineering high-performance super-alloys. DED also uses a source of energy (laser or electron beam) which melts a small region of the substrate and the feedstock material simultaneously. The melted material is then deposited and fused into the melted substrate and solidified after movement of the laser beam. The main difference between DED and SLM methods is that in DED no powder bed is used and the feedstock is melted before deposition in a layer-by-layer fashion similar to FFF but employing a higher amount of energy for melting the metals. It has low accuracy and quality just as FDM and can be used for printing large envelopes due to its high speed.[1, 26a]

The last method is **sheet lamination** where sheets of material are bonded together using an adhesive or welding and laser cut. A common methodology is laminated object manufacturing (LOM), a roll-to-roll based process used in various industries such as paper manufacturing, foundry industries, electronics and smart structures. LOM consists in layer-by-layer cutting and lamination of sheets or rolls of materials and results in a reduction of tooling cost and manufacturing time, becoming in one of the best methods for big structures. But, it is not recommended for complex shapes because of its inferior surface quality and resolution.[28]

Table 1. *Overview of AM classification.[28]*

Process principle	***AM Technology***	***Materials***	***Features***
Vat Photopolymerisation (VP)	Stereolithography (SLA) Dynamic Light Processing (DLP) Continuous Liquid Interface Production (CLIP)	Photopolymer Ceramic	High resolution Slow process High cost
Powder Bed Fusion (PBF)	Selective Laser Sintering (SLS) Selective Laser Melting (SLM) Electron Beam Melting (EBM)	Metal Polymer Ceramic	High resolution Slow process High cost
Material Extrusion	Fused Filament Fabrication (FFF) Direct Ink Writing (DIW)	Polymer Ceramic Biomaterials	Low resolution Fast process Low cost
Material Jetting (MJ)	Ink-jetting Thermojet Polyjet	Photopolymer Wax	High resolution Fast process
Binder Jetting (BJ)	Ink-jetting	Metal Polymer Ceramic	High resolution Slow process High cost
Direct Energy Deposition (DED)	Direct Metal Deposition (DMD) Laser Deposition Laser Consolidation	Metal Powder Wire	Low resolution Fast process Low cost
Sheet Lamination (SL)	Ultrasonic Consolidation Laminated Object Manufacturing (LOM)	Hybrids Metallic Ceramic	Low resolution Fast process Low cost

Over the last years, different methods like Inkjet[29] or FFF,[30] have been employed for 3D manufacturing PIL materials, however vat polymerisation has become the preferred technique for printing PILs. Both, DLP,[4, 31] and SLA[32] methods have been widely used in this area, for this reason VP techniques will be reviewed in more detail.

1.1.2 Vat Polymerisation Techniques

The vat polymerisation method is so-called because it is carried out in a vat containing a liquid photopolymer which is selectively irradiated by UV light. The principle of this technology is based on the chemical reaction known as photopolymerisation. This process takes place when liquid light sensitive inks, composed of linear and cross-linking monomers, photoinitiator, additives and fillers are polymerised or cured upon light irradiation. The photoinitiator's role is to generate reactive species (radicals or ions) by absorbing incident light.[33] The reactive species when interacting with the reactive groups of the monomer initiate a set of reactions in the resin, normally by a chain growth mechanism to form polymeric chains. As the reaction proceeds, the system's molecular weight increases, and so does the degree of branching if the formulation contains cross-linkers. Depending on the type and the number of reactive groups in the monomers/oligomers involved, different macromolecular structures can be synthesised: linear, branched, or cross-linked.[34]

During the 3DP process, the object is built on a platform that moves up and down while a light source strongly enough irradiates each layer in order to activate the photopolymerisation reaction. This step is repeated layer by layer by immersing the polymer parts into the liquid monomer each time. Therefore, it is critical that the solid parts are insoluble in the liquid resin. For that reason, it is necessary to use some percentage of a cross-linking polymer to reach the gel point of the material and to obtain an insoluble polymeric material with physical and chemical properties completely different from those of the starting material.[35] The printing does not require complex machine configurations and supporting structural materials, and the final macroscopic models are solids that can be used immediately. However, a post-printing treatment is usually employed to remove the excess of uncured resins, and also photo-curing or heating to improve the mechanical properties.[36]

This technology was developed in the 1980's, being the first patented additive manufacturing system. However, in recent years, the interest in this methodology is growing both in the industrial and research fields. Photopolymerisation techniques are gaining importance due to the flexibility in the development of starting printable materials that can be used, opening a broad range of choices. Furthermore, complex-shaped and customised structures can be produced quite quickly (depending on the size) with excellent printing resolution.[33] This trend is reflected in the increasing number of scientific articles involving vat polymerisation along the last decade (*Figure 1*).

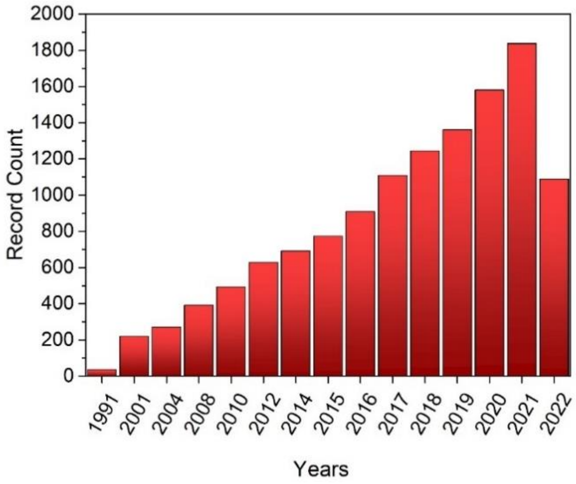

Figure 1. *Publications on Vat Polymerisation in the last 3 decades. Data from Web of Science database.*

In vat polymerisation there are two different processes of fabrication, where the building platform moves downwards or upwards during the printing process, represented in *Figure 2*. In the former, the layers are photopolymerised on the vat surface as the platform moves downward toward the bottom of the platform so the piece is fully submersed in the photopolymer resin during the build. In this case, the light source is on the top of the vat. On the contrary, in the upward configuration, the printed piece is held above the vat of resin and, fixed in the platform, moves upward. The UV light is projected from underneath the optically clear vat window. The latter is more advantageous, since it requires less resin because it is not necessary to cover the entire structure, it is independent of the bath size and the printable layer is not in contact with the atmosphere, reducing oxygen inhibition.

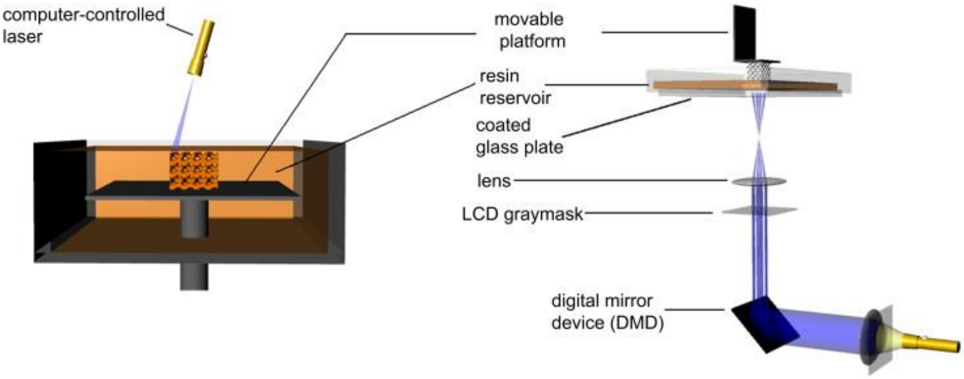

Figure 2. *(Left) A lowering platform system with scanning laser, and (right) a upward set-up with digital light projection. Reproduced from reference [37] with permission.*

Stereolithography (SLA), Digital Light Processing (DLP) and Continuous Liquid Interface Production (CLIP) methods are common VP techniques, summarised in *Scheme 1*.

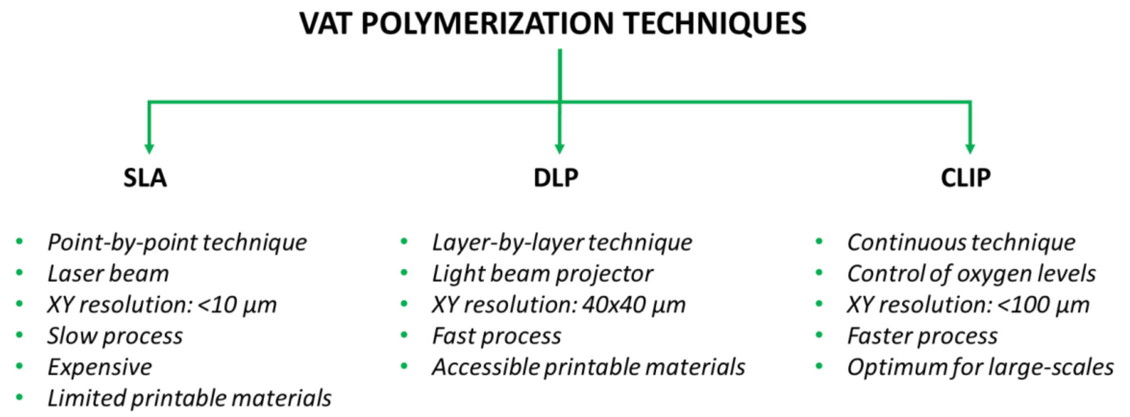

Scheme 1. *Main characteristics of the different Vat Polymerisation methodologies.*

a) Stereolithography (SLA):

SLA is a well-established AM technology since it was one of the earliest methods implemented. This technique has a laser beam which draws the customised design on the photopolymer surface and selectively cures point-by-point the liquid resin contained in the vat (X-Y plane). SLA machines can be configured either in the classical bottom-up approach where the platform is below the resin surface or the top-down where the building support is above the vat.[37] Due to several disadvantages of bottom-up methodology, including the extensive cleaning process normally required, top-down systems are gaining more and more prominence.

SLA is mostly used to create high-quality objects since it can achieve features <10 µm at a fine resolution, however it is slower than other AM techniques, quite expensive, and the range of printable materials is very limited.[1] A derivate of SLA technology is the micro-stereolithography 3D printing (µ-SLA) which can achieve 5 µm as a minimum feature size.[38] For that reason it is used to create very small size parts such as microcomponents, micromechanisms and microfabricated devices. Masked Stereolithography (MSLA) is another type of technique where a mask is used to protect certain areas of the layer during the curing process. This allows for finer and more detailed layers to be created in the final piece. MSLA is known for its high precision and resolution.[39]

b) Digital Light Processing (DLP):

This technique involves the irradiation of an entire layer simultaneously using a light beam projector. The substitution of the laser by a beam allows to build parts much quicker than SLA.[27] Although laser technology presents higher printing resolutions with finer results in terms of surface finishing,[33] commercial DLP technology is able to reach a layer thickness of down to 1 µm and resolutions as small as 40x40 µm.[40] In optimised research set-ups, features of 18x20 µm for 3D serpentine flow channels were reported using a custom digital light processor stereolithographic (DLP-SLA) 3D printer and a custom resin.[41]

c) Continuous Liquid Interface Production (CLIP):

An innovative variation of DLP-3D printing is the CLIP method, which uses a projector that works in continuous instead of layer-by-layer by controlling oxygen levels throughout an oxygen-permeable membrane. This thin oxygen layer inhibits free-radical polymerisation only at the interface between the polymer film and the transparent window preventing the constructed film from adhering to the vat bottom. The printing speed increases dramatically being the fastest VP technique, but the accuracy is not as high as by DLP, with feature resolutions of less than 100 µm.[42] Large-scale structures can be produced with the CLIP approach.[43]

There are other types of photopolymer-based 3D printers that have been developed in recent years, however to date they have not experienced the impact that SLA or DLP-3D printing has had.[44] One of them is Two-Photon Polymerisation (2PP) processes which is similar to Stereolithography as it uses lasers to scan a photopolymer, but in this method the photoinitiator absorbs two photons simultaneously.[45] Additionally, the laser point can be moved in the x-y-z-directions to polymerise the resin being possible to use high viscosity photopolymers and create complex geometries without supporting structures.[46] However, 2PP has several drawbacks that make the technique unpopular: the dimensions of the objects are limited (no more than 1 mm in height), the printing speed is very low, it requires expensive equipment to generate the pulsed NIR laser beam and needs high energy to cure the material. Another alternative is a novel volumetric 3D printing system known as CAL (Computed Axial Lithography) which is based on computed tomography (CT) scans technique to generate a hologram.[47] The hologram is created by simultaneously projecting multiple 2D images that propagate through the resin from different angles as the vat container rotates, generating a 3D image with sufficient energy for light curing. This technique can polymerise very high viscous resins (up to about 90 000 cP) that are difficult to achieve with other techniques such as DLP or SLA, but there are some major issues related to poor surface definition and the slow printing speed of manufacturing that make the technique uncommon.[48]

Photopolymers

The photopolymer is the liquid precursor of the polymer and it can be polymerised by several methods, although light-induced polymerisation offers remarkable advantages. It delivers rapid polymerisation rates, room temperature treatments, low energy requirements, the use of solvent-free formulations, broad range of wavelengths (from X-rays to NIR) to activate the photopolymerisation,[49] and high dimensional accuracy as the photopolymerisation can be controlled by managing the light settings during the process. Despite all these positive qualities, the main benefit of photopolymers is that the resin can be tailored to meet precise requirements.[1] The combination of the appropriate elements (monomers, active materials, photoinitiators and additives) must be fine-tuned to achieve the specific properties (*e.g.*, chemical, mechanical, optical, etc.) and the desired resolution.[36, 44] In conclusion, the photopolymer can be custom-prepared by combining chemical and reactive compounds (both liquid and powder) to meet the intended application (*Figure 3*).[33] Some recent studies show great progresses employing self-assembling molecular systems with stimuli-responsive behaviour to specific external stimuli, providing new functionalities to the additively manufactured objects.[50] The type and degree of stimulus response of smart polymers can be regulated through precise synthetic design or via incorporation of additives.[9]

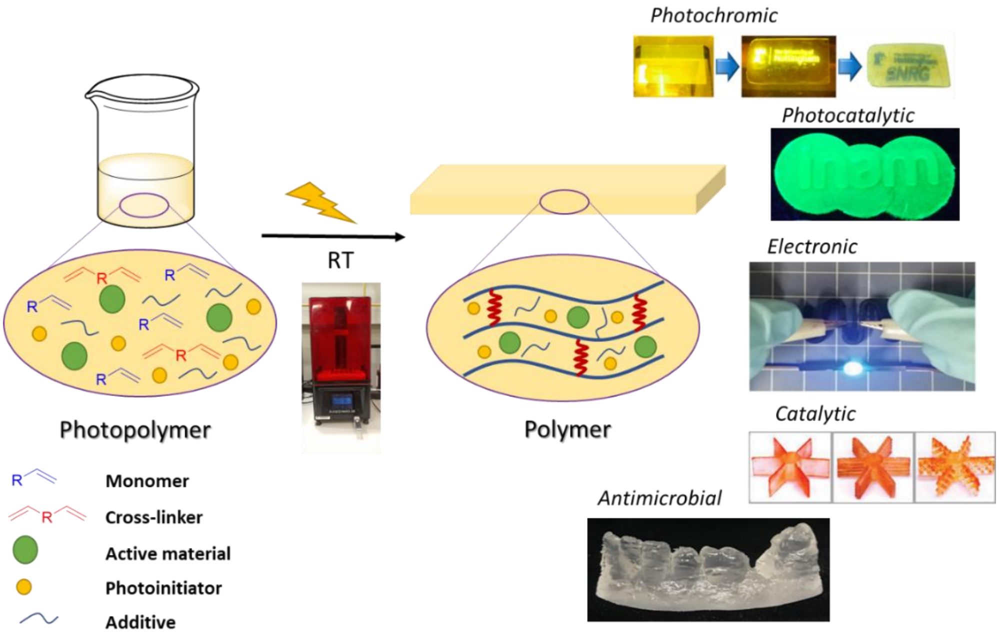

Figure 3. *Representation of the Vat Photopolymerisation process and some demonstrated applications. Adapted from references: 23a, 31a, 51.*

Photopolymers are widely used in vat polymerisation. Other AM techniques like Inkjet, MultiJet, or some binder jetting methods can also use photopolymers, however, these methods cannot be considered among the VP techniques, as they build objects by selectively adding resin along with the support from a jetting head or tiny nozzles.

The photopolymers for 3D printing are usually composed by:

- **Monomers and oligomers**: liquid compounds that have reactive groups necessary to create the polymeric network. The backbone of these materials defines the final physical and mechanical properties of the cured part. These reactive species are mainly based on free-radically polymerisable resins characterised by having unsaturated C=C double bonds, more frequently (meth)acrylate functionalities since they present high reactivity upon light irradiation and well-established mechanisms of reactions. Many (meth)acrylate-based substances compatible with vat polymerisation techniques are already commercially available.[52] Not only acrylates, but also other functionalities can also be employed, such as unsaturated polyester, vinyl, vinyl ether, or thiol-ene/yne systems.[53] Among them, 1,6-hexanediol diacrylate (HDDA), polyethylene glycol diacrylate (PEGDA), bisphenol A ethoxylate diacrylate (BEDA), trimethylolpropane triacrylate (TMPTA) and butyl acrylates (BA) are some of the most used in light-based 3DP. It may happen that unreacted monomers are trapped while the polymerisation is going on and consequently, the conversion of the system will be lower than 100 %.[54] In those cases, the isolated species that remain active may eventually react with another reactive species (like oxygen) by diffusing the polymeric network. This may be the cause of aging or other changes in the mechanical and chemical properties of the cured material.

- **Photoinitiators**: chemical compounds that absorb the incident light, generating active species or radicals capable of initiating the polymerisation process through the reaction with the double bonds of the monomers.[33, 55] Currently, several chemical compounds act as photoinitiators and can operate in different wavelengths of the electromagnetic spectrum, from UV and visible to NIR.[56] The choice of the right photoinitiator is essential for the fabrication of objects; it determines the reaction efficiency and photopolymerisation rates, which directly influence printing resolution and accuracy.[33] That is the reason why these compounds have been widely investigated in the literature.[57] Although most of them are commercial, there is still a scientific interest to develop more efficient photoinitiators.[58] In general, the absorption spectrum of the photoinitiator selected must match the emission light from the printer's light source to obtain an efficient photopolymerisation.

- **Additives**: some additives can be used to tailor the printable material features or add specific properties to both the liquid formulation and the printed part.[31b, 59] The most commonly used additives are reactive diluents, dyes or colorants and fillers. The reactive diluent is added mainly to adjust the viscosity of the photopolymer in order to reach the range suitable for the vat polymerisation technique, as well as to improve the compatibility between the other resin components.[60] This substance can also be a monomeric species and, in that case, it will participate in the polymerisation process by forming part of the polymer backbone after the curing stage.[61] The choice of the appropriate reactive diluent depends on the required characteristics (such as the affinity with the photopolymer components, the final physical properties of the cured material, the formulation's processability, the volatility of the substance's,…).[60]

Dyes are mainly added to control the penetration of the light during 3D printing (Z-axis) and to enhance the printing accuracy (XY plane).[62] These compounds are usually based on organic or organometallic molecules and the selection of the appropriate one will be determined mainly by the light source of the 3D printer. The dye is incorporated in low concentrations, but if it is too low the final printing resolution may be poor. Conversely, high concentrations of dye can affect the efficacy of the photoinitiator.[41] It is therefore important to find the balance of the dye with the other components of the photopolymer. In the last few years, some functional dyes have been developed. Functional dyes are of great interest because they can improve print resolution while conferring specific characteristics to the printed object.[63] Another element frequently added to the photopolymer formulations are active materials used to develop high-performance polymer composites. These compounds are mostly composed of organic, inorganic, or metallic compounds, such as graphene, carbon nanotubes, metal powders, composite polymers.[1, 30, 64] A precursor can also be added to obtain exceptional composites. For example, a silver salt can be reduced in a photopolymer to form silver nanoparticles after the printing process generating a functional polymer.[31b, 65] These elements are incorporated to manufacture structures with enhanced properties like mechanical strength, thermal resistance, and electrical conductivity.[66]

Summarizing, photopolymer composition is a key factor in obtaining reliable 3D-printed structures.[36, 44] Furthermore, both the digital design (3D CAD model) and the printing parameters must be properly optimised considering the photopolymer composition in order to obtain high-resolved printings.[67]

1.1.3 Applications of 3D Printing

3D printing is capable to build objects with specific shapes and sizes, making the manufacturing possibilities limitless. Most companies can benefit from these advantages, being possible to focus more directly on the customer preferences. As a result, this technology has revolutionised the industry scenario, searching for new ways of fabrication, opening up new horizons. On the other hand, it does not need expensive tooling and long production lines as is the case with conventional production methods. The whole process, therefore, is cheaper (at low production volumes), safer, more environmentally friendly and much faster. In its early years, 3D printing was primarily used to create prototypes, but as

Wohlers' report points out,[3] this trend has changed, and 3DP can now be found in a wide range of fields, including biomedicine, aerospace, automotive, construction, food processing, education, and even art and jewellery, to name a few.

One of the main fields where AM technologies are seeing tremendous growth is **biomedicine**.[68] Implants, prosthetics, synthetic tissues, and organs all need the development of sophisticated models.[69] Moreover, the models must be tailored to the needs of the patients.[70] All of this can be accomplished without difficulty thanks to 3D printing's design freedom and it can also be used to customise the dosage forms and release profiles of drugs.[71] And, CAD models can be easily exchanged between scientists and doctors.[72] For all these reasons, great effort is being done in the preparation of printable biomaterials with high biocompatibility.[36] In recent years, bioprinting has grown in popularity.[73] The main difference between bio-fabrication and standard AM techniques is that in the former, cells are introduced into the biomaterial to make bio-inks.[74]

Healthcare and cosmetics have also benefited from this technology. In 2021, L’Oréal announced its partnership with the multinational printing company HP. With the capacity to tailor the pucks, L'Oréal was able to rapidly design and scale large quantities of customizable pucks during the Covid-19 epidemic. The cosmetics giant was able transfer, fill, and label products with greater agility, resulting in a 33 % cost reduction and a 66 % improvement in time savings.[75]

HP’s Metal Jet 3D printing platform has also found application in other fields with partners like GKN and Volkswagen. **Automotive** is an industry that needs lightweight and resistant materials.

Figure 4. *A printed part from a Volkswagen car using HP Metal Jet technology. Photo via HP, from reference [75]. Retrieved 20 November 2022.*

In this respect, 3DP has an important role to play, especially for luxury vehicles with customised parts.[76] The 3D-printed parts obtained by HP Metal Jet technology weighed almost half of conventional components and have passed crash certification (*Figure 4*).[75] In addition, the idea of keeping models digitally rather than physically is not only efficient, but also saves money on manufacturing and storage.[77]

Similarly, **aerospace industry** is another of the key domains where AM technologies are gaining traction. This field, like the preceding one, employs sophisticated and functional structures that can be easily developed using AM.[67] Besides, this industry relies mainly on pricy advanced materials, such as titanium, nickel or ultra-high temperature ceramics, which are difficult to fabricate using traditional processes.[78] In contrast, with AM techniques these materials can be easily processed, reducing material wastes from 95 % to 10 %.[79] Another factor of great relevance in the aircraft sector is to obtain lightweight, high-strength parts.[80] NASA's Aeronautics Research Institute is exploring lightweight, temperature-resistant materials to develop a non-metallic gas turbine engine by 3D printing.[81] The use of this technology with ultra-high temperature ceramics (like ZrB2, ZrC, TiC and others) is becoming a major research topic.[82]

The implementation of AM in the **construction industry** has been another revolutionary breakthrough. The application of this fabrication technique in construction is still in its early stages of development, but the potential that it has shown in the last few years makes it a very promising area.[83] The construction sector consumes a high percentage of environmental impact resources, an issue that could be solved with 3DP. However, the most exciting thing about this approach is that AM can be used in hard-to-reach areas with geometric complexities and hollow structures and, even on the moon.[84] We can already find several low-cost homes manufactured by 3DP spread all over the world. This technology may be the best method to respond to the global housing crisis, since it can swiftly increase supply without compromising quality, beauty, or sustainability. The BOD2, Vulcan or Crane WASP are some of the 3D construction printers developed in this regard by COBOD, ICON and WASP companies respectively (*Figure 5*). The goal is to create a more robust and long-lasting dwelling compared to conventional constructed homes, while also being quicker, cheaper and more ecological.[85] For instance, in 2021, the Italian building firm, WASP, 3D-printed an eco-habitat constructed entirely from biomaterials, such as on-site soil, straw chopped rice, rice husk and hydraulic lime.[86]

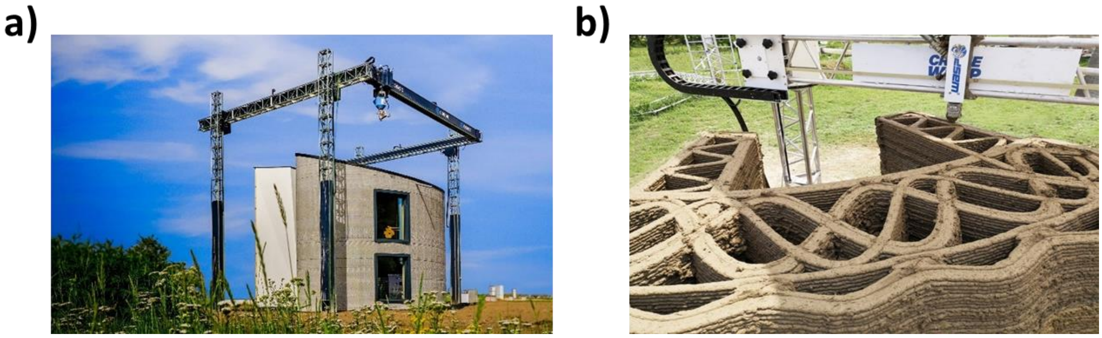

Figure 5. ***a)*** *BOD2 printer from COBOD's company;* ***b)*** *Crane Wasp printer from WASP's company. Photos via COBOD's webpage (https://cobod.com/products/) and Crane Wasp webpage (https://www.3dwasp.com/en/3d-printing-architecture/). Retrieved 27 January 2023.*

Another interesting area where AM is beginning to be used is in **food processing**. Again, the design versatility of this system makes it possible to print bespoke structures with eatable ingredients such as sugar, chocolate or gelatine.[87] Chefs and food designers can benefit from this technology, but also dieticians and nutritionists, as it is possible to tailor foods to each individual according to their physical and caloric needs.[88] However, in order to get components with the appropriate shape and qualities, it is critical to properly tailor the physico-chemical properties of the ink prior to printing. Solvent characteristics, like density, boiling point, solubility, viscosity, specific gravity and surface tension, are particularly significant parameter for obtaining successful printings.[89] With the right conditions and parameters, a wide variety of materials can be printed, increasing the number of edible foods on the market.[90]

3DP is not only popular in industry, but it is also gaining ground in fields like **education**. More and more schools are adding AM techniques into their courses. 3D printing makes it straightforward to transform basic graphics on a page into tangible, three-dimensional objects. 3D printers are now often seen in classrooms and even in public libraries. This technology may be extremely beneficial to graphic design students, biology students, who can generate cross-sections of human body organs; or chemistry students, who can make 3D models of molecules and chemical compounds.

The world of **jewellery** and **art** has found an unexpected use of this technology as well. Using 3D printing materials such as gold, or platinum, jewellery may be considerably more distinctive with sophisticated patterns that are not achievable with traditional production, at a cheaper cost. This technology is also being used in the realm of art. Banksy, the famous British graffiti artist, has begun to use powder binding 3DP. Likewise, the Prado Museum organised a 3D exhibition of paintings by well-known artists to enable visually impaired people to appreciate works that were previously unavailable to them. Another implementation of 3DP is in museums, where it can be used to reproduce figures of missing objects by printing their original shape. An example of this kind of simulation can be found at the Egyptian museum in Turin, where various 3D-printed amulets and jewels of Kha and Merit were exhibited, shown in *Figure 6*. Previous X-ray images of their bodies revealed for the first time the presence of these objects adorning their bodies. After that, it was possible to represent the form of the jewels with very accurate drawings and developing the digital models that were used for the manufacture of the 3D models.

Figure 6. *3D models of Kha and Merit amulets exposed at the Egyptian museum in Turin.*

It is important to point out that 3DP has also an important potential in designing materials, rather than simply designing geometries. Herein, a team of researchers led by the City University of Hong Kong used digital manufacturing to create a novel titanium-based alloy that is super-strong, extremely ductile, and super-light.[91] This research might open the door for a new paradigm in material development. Another exciting aspect of AM technology is its capacity to recycle materials and incorporate them as 3D resin. The serious impact that plastics have on our environment can be mitigated if it is possible to reuse them. *Abax Innovation Technologies* in collaboration with the Polytechnic University of Madrid are pioneers in this discipline, repurposing old plastic materials like plastic bottles. For example, a research group at the University of Bristol has succeeded in converting surgical masks into printing material by heating and pressing the masks, transforming them into a tough sheet that is ground into fine grains of polypropylene.[92] This is an excellent tool for finding new applications to trash (*Figure 7*). Currently, only universities are researching in this topic, but it is a tremendous business opportunity for the future since it is a strategy to partially solve the ecological disaster caused by plastics.

Figure 7. *Processing surgical masks for transforming them into 3D printing materials. Photos Credits: University of Bristol, from reference [92]. Retrieved 27 January 2023.*

These are just few of the countless ways in which 3D printing technologies are impacting our world today. Because of the immense promise of this technology, significant study and investment is being made in it, and as a result, technological improvements in this sector are advancing by leaps and bounds. A growing number of industries and disciplines are introducing 3DP into their manufacturing processes, such as textiles, baby diapers, footwear and electronic applications.[93] As shown above, the main intrinsic property of AM that makes it empowering is its flexibility both in geometric design and in the preparation of the printable material. This leads to more customised and, in general, more sustainable results. In the near future, 3DP could monopolise production processes, but it is necessary to improve this technology, making it more automated, accurate and speedy. At the same time, novel materials are constantly required to produce functional parts for all kind of applications.[94] Materials are essential to achieve the desired characteristics and properties in order to obtain functional devices.

1.1.4 Challenges in 3D Printing

Undoubtedly, 3D printing is a powerful technology able to revolutionise the industrial processes from electronic devices to biomaterials. The freedom of design and fabrication that AM offers is leading to the emergence of exciting fields, like 4D printing.[95] 4DP will have tremendous potential, foreseeing advancements in existing manufacturing methods as well as the emergence of new ones in the coming decade.[96] Nevertheless, despite all those amazing features, there are still some challenges that would require further research and technological development to adopt ubiquitously this manufacturing methodology in multiple areas.[97]

One of the main drawbacks is related with the final appearance and mechanical properties of the printed part. For example, the intrinsic porosity between the subsequent layers in some 3D techniques can be very high, reducing the mechanical performance of the printed device. Another common problem is the anisotropic behaviour that is caused by the layer-by-layer printing nature. The microstructure of the material, as well as the mechanical behaviour inside each layer can be different compared to that of at the boundaries between layers. The printing direction can also affect the mechanical behaviour of nanocomposites. Not only the internal properties can be affected, but also the device aesthetics will be influenced by the layer-by-layer appearance. Moreover, it can diverge from design to execution because transferring CAD models into a 3D-printer often results in inaccuracies and defects, particularly in curves surfaces. The generation of supporting materials easy to remove after printing, and slicing the part into sufficient layers, as well as post-processing the printed objects are possible solutions to eliminate all these defects.[1]

Another important challenge is the optimisation of printable smart materials to fabricate entire smart systems. Most of the AM processes can only manufacture one or two components of the device but not the full device. Thus, a one-step printing process of a whole system is a promising route to develop fully-integrated usable devices.[25] However, there is a significant constraint in present technology that makes it hard to build these sophisticated structures.[25] The combination of different AM techniques can be another way to overcome this issue, using inks.[98] Likewise, in terms of design and manufacturing, it would be quite beneficial to combine emerging 3DP processes with traditional techniques.

Further, there is still a big limitation of materials suitable for 3DP. The development of printable inks is crucial to improve the production process and pattern definition. The materials and their qualities are important not only for the final application, but also for the manufacturing process. For example, in vat polymerisation, not all the photoactive monomers can be properly photopolymerised under the printing conditions. A typical problem that emerges while preparing a photosensitive mixture is the low affinity of the components used, which has a direct influence on the printed formulation's homogeneity if they are not effectively integrated.[99] For instance, most resins are non-polar reagents, while other components, like dyes, have a different polarity.[100] Mixing those components directly might cause solvation problems that creates light scattering or reflection during the 3D printing step due to the dye's aggregation. Thus, inhomogeneous baselines will lead to low resolutions and inaccurate printings, which could negatively affect the final application.[101] Using a suitable reactive diluent (compatible with the polymeric matrix) as an intermediate reagent can be a way to boost the dye solubility in the monomer. This issue can be also found when adding some nanostructured active materials in order to enhance specific characteristics of the printed objects.[102] The addition of such materials can change the matrix properties, including the transparency[103] or viscosity[104] what may affect the resolution of the printed parts. Similarly, the incident light that activates the polymerisation reaction can be modified by the additive since it can also absorb part of the light.[105] Therefore, it is important to find a balance between nanomaterials' amount and photopolymer printability in order to design printed parts with the appropriate form and qualities at high resolution.[106] In some cases, a promising solution to avoid printing constraints without compromising the quantity of active material added to the resin formulation may be to functionalise the active materials to increase their compatibility with the rest of the resin formulation, thus favouring solubility, dispersibility and stability.[104, 107]

Overall, there is a need to explore and broaden the availability of functional printable materials or, alternatively, materials capable of stabilising and properly integrating smart agents in homogeneous and compatible formulations. The encapsulation of smart materials is essential for protecting them against extreme environments, for example providing electrical insulation or thermal dissipation.[108] Polymeric materials can be used to design robust structures able to resist against natural hazards, with longer lifetimes.[109] Their facility for printing, avoiding typical problems found when printing metallic or ceramic films (i.e., fragility, clogging, sintering, low control on particle sizes…), offers significant benefits.[6a, 110]

Within this context, ionic liquids and analogous polymeric species are gaining popularity for manufacturing novel materials due to their ability to encapsulate and stabilise functional fillers. In addition, ILs and PILs present some unique properties, like their extended ion-conductivity and enhanced charge stability, as well as a limitless tunability by changing the corresponding ions, that make them promising candidates for developing next-generation 3D-printed complexes.[22] Polymeric resins and ceramics are mainly electrically insulating, while some metals may be chemically unstable, requiring long post-treatments that might not be compatible with all components in the formulation.[25] Normally, conductive materials are manufactured by conventional methods using conductive composites which are expensive, require extra energy and often lead to composite leaching. Printable ILs materials are opening new opportunities in material design, as well as, broadening applications for 3D printing technologies. A wide variety of advanced molecular materials (AMMs) such as perovskites nanocrystals (PNCs), polyoxometalates (POMs) or metallic nanoparticles (NPs), carbon-based materials and conductive fillers have been embedded into PILs to enhance the performance of the printed devices in different applications (*Figure 8*). In a short period, these materials have had a significant impact across various areas of AM (*e.g.*, photoactive, antimicrobial, catalysts, electronics, robotics and bio-applications).[22, 30, 31b, 51b, 111]

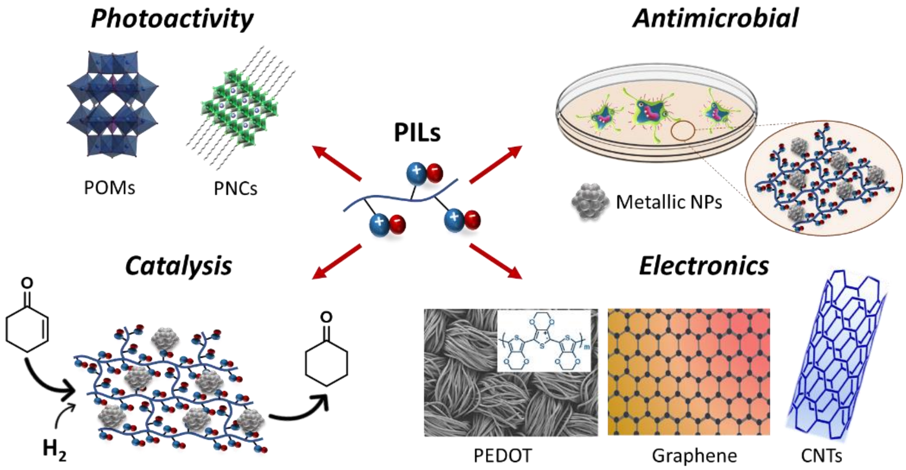

Figure 8. *Common applications of 3D printable PILs capable to stabilise active materials. (PEDOT: Adapted from Du et al.[112] (under CC BY-NC-SA 4.0 license)).*

1.2 Polymeric Ionic Liquids

1.2.1 Properties of Ionic Liquids

Ionic liquids are organic molten salts in which the ions are poorly coordinated and the salts melt below 100 ^oC, or even at room temperature. The first IL, ethanol ammonium nitrate, was reported in 1888[113] but, it was few decades ago when the vast potential of these compounds was noticed. The renewed interest in them is due to their unique characteristics: chemical and thermal stability, high viscosity, wide electrochemical windows, low vapor pressure, specific solvating ability, good tuneable solubility, wide solid to liquids range and high ionic conductivity. The number of publications related to ILs has been increasing sharply every year for the last two decades, indicating their relevance.[114]

Initially, these materials were mainly used as solvents for organic synthesis and catalysis since they were more desirable than conventional volatile solvents.[115] Indeed, due to its low flammability, negligible vapor pressure, low melting point and non-volatility properties, ILs were considered as “green solvents”,[116] although some concerns about its toxicity have appeared.[117] But, still these ionic compounds can contribute to make chemical production and usage more sustainable.[118] In addition, they could create a biphasic system, having the catalyst solubilised while the products were insoluble in the IL,[119] a feature that have also been widely used in analytical chemistry for separation procedures.[120] Progressively, the uses of ILs have broaden, being used in CO_2 capture and separation systems,[121] in electrocatalysis,[122] in pharmaceutical industries[123] and even in space technology.[124] In particular, these chemicals have shown a lot of promise in the development of green catalytic technologies.[125] ILs can play the role of solvent in the catalytic reactions, since they are able to dissolve a wide range of organometallic and inorganic compounds. Furthermore, the ionic behaviour of these materials can stabilise the catalytic species and the intermediates.[126] Even more, the ILs itself have been the catalysts in a variety of reactions, from biodiesel production to CO_2 conversion.[127] In some studies, ILs acted as both a solvent and a catalyst simultaneously.[128]

Likewise, they are extensively used in electrochemical applications as their charge density is much higher than that of a traditional salt solution.[129] Electrolytes based on ILs offer some benefits over aqueous and organic electrolytes making them attractive for use in flexible and stretchable energy storage systems,[130] high temperature supercapacitors,[131] lithium-ion batteries,[132] and electrochemical CO_2 reductions.[133] Doping IL into polymers is another process that has recently been investigated, yielding significant changes in both conductivity and overall mechanical properties.[134] Pure polymer electrolytes generally have a limited ionic conductivity, thus adding an ionic molecule can be really favourable.[135] The addition of ILs can benefit not only neutral polymers, but also conductive polymers.[136]

Despite ILs are very popular in both the academic community and industry due to their well-known advantages,[137] some downsides have been highlighted. The main problematics in using ILs are related with the processing difficulties. For example, in catalysis or as a solvent the employment of ionic moieties can complicate the purification procedure of the product and it is almost impossible to recycle them. Moreover, ILs cannot be used in fixed bed reactors, which, along with certain toxicity concerns, are critical challenges to overcome for future scale-up. Additionally, these compounds are liquids which means that they can liquify and leach over time. One first approach to overcome all these disadvantages was to use supported ionic liquid phases (SILPs) prepared by immobilising the ILs onto solid supports.[138] In many cases the performances improved since the properties of ILs were transferred to the solid support, and simultaneously, working with a solid material offered additional benefits.[138c, 139] Further methods have been developed to prepare IL-based polymers like in situ polymerisation of neutral vinyl monomers with non-polymerisable ILs or directly polymerising an ionic monomer of IL structure.[140] A variety of polymeric IL systems such as polycation-type ILs,[140d] polyanion-type ILs,[141] copolymer,[140b] and poly(zwitterion)[140d] have been reported (*Figure 9*).

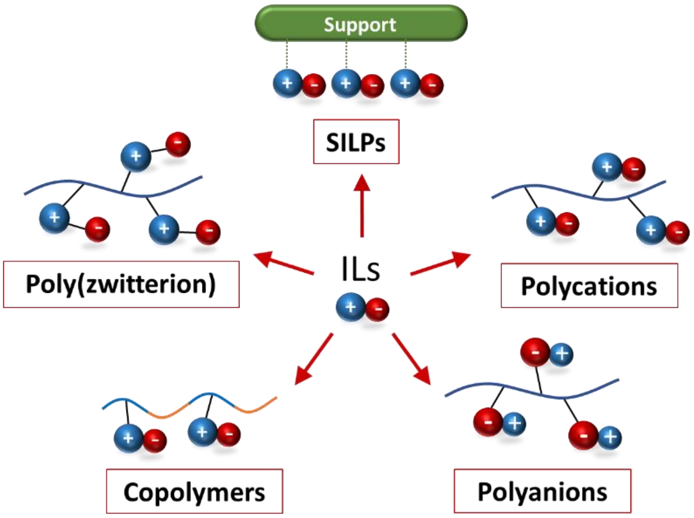

Figure 9. *Schematic representation of the variety of polymeric materials produced from ILs.*

1.2.2 Properties of Polymeric Ionic Liquids

Polymeric ionic liquids/poly(ionic liquids) (PILs) are the union of multiple anionic or cationic monomers forming a polymer backbone with its counterion species bonded to it. These high-molecular-mass compounds combine attractive IL properties with polymer properties (i.e., particularly durability, low toxicity, potential for facile construction of highly multifunctional systems combined with easy polymer processing). In other words, during the development of PILs it is possible to preserve the specific features of ILs and improve other ones taking advantage of the polymer nature including mechanical robustness, thermal stability, hydrophilicity, rapid manipulation via classical polymer processing methods, optimum assembly and stabilisation properties.[142] Another unique feature of PILs is that the properties of the polymers can be controlled by changing the corresponding ions. Depending on the ion pairs it is possible to vary the polymer's solubility, fusibility, hydrophilicity, ionic conductivity, molecular mass, glass transition temperature, heat resistance and thermal stability in a wide range. Main PILs are nitrogen-based polycationic type, namely imidazolium, pyridine, pyridinium, quaternary ammonium, cholinium, although phosphorous-containing cationic PILs are gaining popularity (*Figure 10*a). While ILs only can undergo structural variation by ion metathesis or cation/ anion exchange, PILs can be modified by selecting cations, anions, side chains and functionalities. Even using the same ionic species and the same number of monomers, different PILs can be built only changing the architecture: linear, hyperbranched or star-shaped polymers, getting an unlimited library of species (*Figure 10*b).[143] Homopolymerisation is an important route to prepare PILs however, other types of polymers can be added covalently to the PIL to form PIL block copolymers.

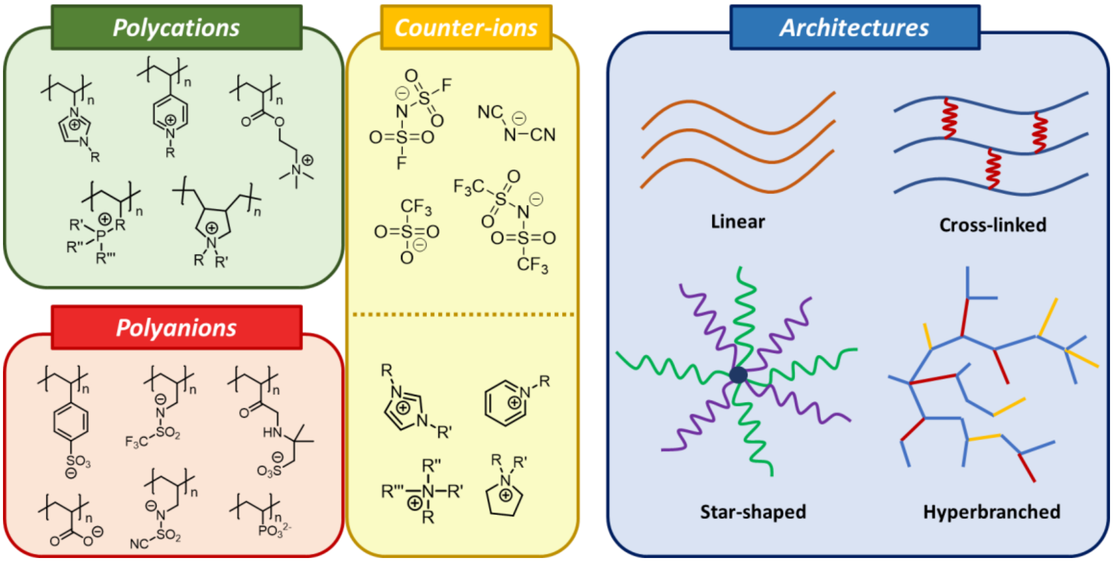

Figure 10. ***a)*** *Most common structures of polycations, polyanions and counter-anions of PILs;* ***b)*** *Different polymeric architectures.*

In a first approach, PILs were considered for improving the properties of ILs. However, the tailorable physicochemical properties of PILs have provided the basis for further design of smart materials, implementing this new class of polyelectrolytes in fields from material science and chemistry to medicine; with applications related with energy and environment, analytical chemistry, electrochemistry, biotechnology, bioelectronics, catalysis or surface science among others. Thus, these multifunctional polymers have been recognised as a separate class from ILs and extensive work have been done in this direction.[23b, 143-144]

Solid electrolytes are very desirable in many electrochemical devices in order to avoid leakage issues and, additionally, they can improve some electrochemical properties, like energy density, rate capability and cycling stability. In this regard, PILs are often less fragile and less hygroscopic than traditional polyelectrolytes. And what's more, electrochromic devices and actuators using PIL-based electrolytes have better performance, cyclability, speed, and long-term stability.[21a, 145] The ionic polymers are both permanent and strong polyelectrolytes owing to the ILs species' solvent-independent ionisation state. The unique dielectric properties of PILs makes them potentially useful not only as polymer electrolytes, but also as sorbents, and dispersing agents.[146] Several groups have investigated PIL-based electrolyte membranes for use in alkaline fuel-cell operation where the anion exchange membrane acts as an electrolyte to transport anions from cathode to anode and is one of the key components of alkaline fuel cells.[147] It is also remarkable the use of PILs as binders for electrodes and/or electrolytes in the design of solid-state supercapacitors.[148] The addition of PILs into graphene electrodes, for instance, improve the contact between the conductive carbon and the liquid electrolyte, facilitating the diffusion of ions into the electrode and increasing the specific capacity of the supercapacitor by 130 %.[149] Moreover, the addition of PIL improved the cyclability of the supercapacitor, keeping the specific capacitance almost inalterable after multiple cycles.

In addition, PILs are ideal materials to stabilise and solubilise molecular and nanostructured materials as a result of their ionic and supramolecular interactions, hence these polymeric compounds are extensively used for stabilising smart materials.[150] In the fabrication of composite materials by light based 3DP techniques, it is crucial to avoid phase separations to avoid the presence of turbidity that will undesirably scatter light and thus reduce the printed resolution. Generally speaking, ionic polymers are able to distribute homogeneously a broad range of additives in their matrices, thus minimising these problems. For example, some reports demonstrate the excellent capabilities of PILs to immobilise and stabilise metal nanoparticles acting as active catalysts in heterogeneous catalytic reactions.[151] The nanoparticles can even be synthesised and immobilised simultaneously, forming the nanoparticles in situ during the polymerisation process.[152] This approach is not limited to metallic nanoparticles, as a broad range of nanoparticles,[153] macrostructures such as polymers,[154] carbon-based materials[155] or enzymes[156] have been successfully stabilised or immobilised by PILs. A wide variety of functional materials including porosity-switchable membranes and coatings,[157] thermally responsive compounds,[158] biosensors,[159] flexible sensors[160] or reversible systems switching hydrophobicity/hydrophilicity by exchanging the anion[157] and the cation[161] have been explored.

Nevertheless, it is worth to remember that PILs have one of the charges polymerised, becoming a single-ion conductor. Therefore, the conductivity of neat PILs described in the literature up to now is usually low and still insufficient for practical use due to the reduction of the ion mobility. Another factor that has a direct influence in the conductivity is the increasement of the glass transition temperature after polymerising. Several times, it has been found that the ionic conductivity values of PILs are at least two magnitudes lower than the corresponding IL monomer unit.[138c] Accordingly, the conductivity of PILs need to be improved by doping with other materials like ILs, metallic nanoparticles, conductive polymers, AMMs, etc., taking advantage of the good stabilisation properties of PILs. The preparation of mixtures of ILs with PILs as electrolytes has been explored for different applications.[148, 162] Into this context, different ILs and PILs have been combined successfully without observing segregation into two phases due to the similarity in the chemical structure. The completely compatible formulations have been used, for instance, as polymer electrolytes, enhancing their performance and conductivity compared to conventional polyelectrolytes,[163] improving the device lifetimes,[164] the solar cell efficiency,[165] and the electromechanical performance of the actuators.[166] By mixing IL and PIL in different ratios the electrolyte can be tailor-made. The ionic conductivity varies significatively (from 10^{-5} S/cm to 10^{-2} S/cm) after increasing IL content. Also, the physical appearance of the polymer electrolytes change from a transparent solid film (100 % PIL) to a very viscous and sticky gel (low PIL/IL ratio) with intermediate states where the polymer electrolytes are usually rubbery and transparent.[21a, 164]

Another matter to be considered when using PILs and ILs, is that the properties of these materials can vary a lot just by changing the ions. This is helpful for designing customised PILs. However, in order to meet the specific requirements, it is necessary to have a clear understanding of how chemical differences affect the final features. Depending on the chosen PIL, important properties like thermal stability can vary from 150 to >400 ^{o}C,[21a, 167] measured as the onset for thermal degradation by TGA, and its electrochemical window from 2.5 to 5.0 V.[168] Solubility is another clear evidence of the variations across PILs. For instance, poly(1-vinyl-3-alkyl-imidazolium) with bromide anions is soluble in water as a conventional polyelectrolyte and, after substituting the halide anion by tetrafluoroborate or hexafluorophosphate the polymer become soluble in methanol and polar aprotic solvents, but not in water anymore. Then, changing the counter-anion by fluorinated bis(trifluoromethanesulfonamide) anion or an hydrophobic anion, the polymer become soluble in non-polar solvents.[21b] It is therefore essential to know all the characteristics of each PIL or IL before using them.

Thus, to get the most from PILs, it is important to combine PILs with advanced materials to produce composites. The ionic nature of PILs ensures their outstanding compatibility with other composites since the active ions across the polymer chains can promote interactions with other reagents.[150a] The hybrid materials obtained after those unions highlight for having an enhanced performance like increased conductivity, thermal stability, antimicrobial activity or optical properties.[149] Moreover, PILs can be manufactured by 3D methods, what makes them promising candidates for developing next-generation devices. For all these reasons, 3D printable PIL composites are an exciting and potential research field.

1.2.3 Combination of Ionic Polymers with Advanced Materials

Some required features, including higher stability, flexibility, durability, catalytic activity and a lower cost are crucial for new types of multifunctional devices used in medical, electronic or environmental field. Herein, smart materials such as nanomaterials or carbon-based materials are promising alternatives to meet these requirements since they can improve mechanical and electrical properties of polymer matrices. Over the past 20 years, a tremendous expansion in the development of nanostructured composite systems has emerged and been employed in a wide range of applications.[169]

As previously mentioned, PILs' ionic character assures their excellent compatibility with other composites.[150a] Consequently, PILs are good stabilizers and effectively improve the solubility of nanoparticles and polymers. That is why PIL nanocomposites are an important and potential research field. Carbon nanotubes (CNTs), graphene, graphite and different metal nanoparticles have been incorporated in poly(ionic liquid)s to form nanocomposites.[151, 155]

On the other hand, combinations of conductive polymers with PILs have attracted much interest as well. Conductive polymer dispersions need non-acidic and non-aqueous stabilizers to avoid some issues found in implementation, such as leakage, agglomeration and solvation.[164, 170] Into this context, new classes of non-volatile organic solvents with hydrophobic nature, like PILs, have been studied, combining all beneficial properties of ILs with those of classical polyelectrolytes. Polyaniline (PANI), polypyrrole (PPy) and poly(3,4-ethylenedioxythiophene) (PEDOT) organic dispersions have been prepared using PILs as stabilizers, having the ionic species covalently bonded to a polymer backbone. This synthetic method takes advantage of the solubility change of the cationic PIL after anion exchange. Hydrophobic PEDOT/PIL dispersions have been successfully tested by several groups as alternative materials for electrochemical applications due to its organic nature, its large electrochemical window and thermal stability (up to 300 ºC).[21a, 143, 154b] For instance, a fluorescent organic light emitting diode (OLED) device was fabricated using PEDOT with an imidazole PIL as a hole-injection layer (*Figure 11*). In comparison with a control device using a conventional PEDOT based material, the device with PEDOT:PIL was found to achieve a significant improvement in terms of device lifetime.[171]

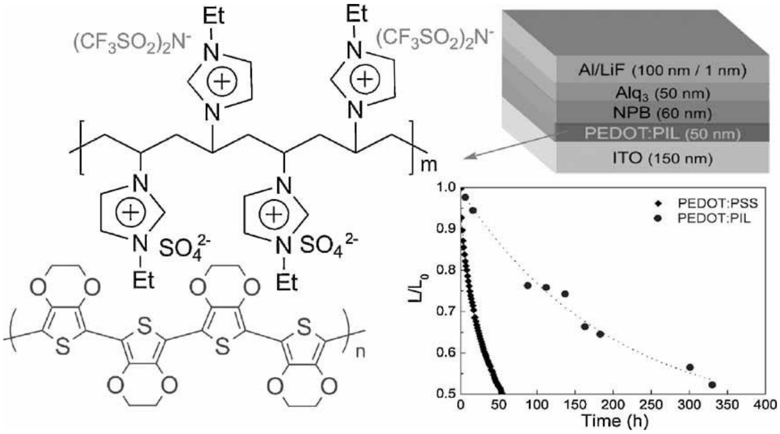

Figure 11. *Structure of the fluorescent OLED device including the chemical structures of PEDOT:PIL and the luminance decay of PEDOT:PSS and PEDOT:PIL devices as a function of time. Reproduced from reference [171b] with permission.*

Similarly, in dye-sensitised solar cells (DSSC), liquid electrolytes have been widely used,[172] however a single-ion conductive gel polymer electrolyte is highly desirable to avoid limitations in the long-term operation and practical use due to leakage and evaporation.

The possibility of using a PIL as all-in-one oxidising agent and polymeric stabilizer for the preparation of PEDOT aqueous dispersions is another exciting area of research.

Poly(dimethyldiallylammonium) with $S_2O_8^{2-}$ oxidising counter-anion has been used to obtain PEDOT dispersions in a conventional acrylic polymer latex. The addition of EDOT monomer into an aqueous solution of the PIL with the persulfate oxidant counter-anion resulted in the formation of a stable PEDOT blue dispersion due to oxidative polymerisation of the EDOT monomer. All in all, the poly(ionic liquid) showed oxidising and stabilising properties.[173]

As well, it has been demonstrated that there is an enhancement of the electrical properties when CNT-based composites are prepared in a conductive polymeric matrix. In order to avoid the segregation of CNTs and conducting polymers due to the limited miscibility among them, a third component such as poly(ionic liquids) have been introduced. There are very few attempts combining CNT-PEDOT complex with a PIL, although it has been established that CNT and PEDOT integration is possible by interfacial engineering using PIL. As a result, fine dispersions of CNTs in conducting polymer matrices are achieved. It was found that the negative charges of PILs stabilise PEDOT positive charges, promoting the binding of PEDOT chains with CNT-PIL via electrostatic interactions. And the complexes can be prepared in organic or aqueous solutions by modifying the PIL's structure.[154c, 174]

Another example showing good results after mixing PILs with conductive polymers and an extra active material is a hybrid of PEDOT-PIL-modified Fe_3O_4. This composite was used successfully as detection channel material for a chemiresistive sensor to detect VOC vapours. In this case, the resulting hybrid sensor displayed lower noise and greater sensitivity than its PEDOT-PIL-only homologue. As with the carbon composites, PIL was used as the polymerisation template for the oxidative polymerisation of EDOT, providing an efficient linkage of PEDOT to the surface of the metal nanoparticles. Furthermore, the use of PILs prevented the aggregation of Fe_3O_4 nanoparticles as well as acted as stabilizer of the nanoparticles.[175] Likewise, by mixing hydrophobic PEDOT:PIL with an elastomeric polymer, it is possible to obtain stretchable conductive materials useful for preparing flexible sensors and actuators with multiple applications.[176]

1.2.4 PILs in 3D Printing

Nowadays, the development of polymers especially designed to be printed by 3D techniques is of huge interest. And, at the same time, in both academic research and industry, there is a need to create polymeric systems with controlled precision in architecture, domain size, functionality, polarity, solubility and reactivity. Into this context, PILs combine the tuneable properties of the ILs with polymeric features, becoming an invaluable material for AM.

In 2014, the first study using printable ionic polymers was reported. 4-vinylbenzyl trioctyl phosphonium bis(trifluoromethanesulfonate)imide mixed with diacrylates were photopolymerised by mask projection micro-stereolithography with low UV light intensity and high digital resolution. The IL monomers were polymerised during the printing process together with other comonomers, in the presence of a cross-linker and a photoinitiator. The resulting electro-active membranes showed high thermal stability, optical clarity and ion-conductivity.[32a] In that example, the IL monomers were viscous, hence that formulation was not proper for all printing techniques. A totally different strategy was proposed for an inkjet method, generating a variety of low viscosity printable polycationic materials with finely tuned mechanical, thermal and superficial properties. In this paper, copolymers based on butyl acrylate and vinyl imidazole were crosslinked with divinylbenzene at different concentrations of the components in order to find the suitable composition to be 3D printed by inkjet. The post-polymerisation and modification of the polymer allowed to improve the mechanical properties of the printed parts (*Figure 12*).[29]

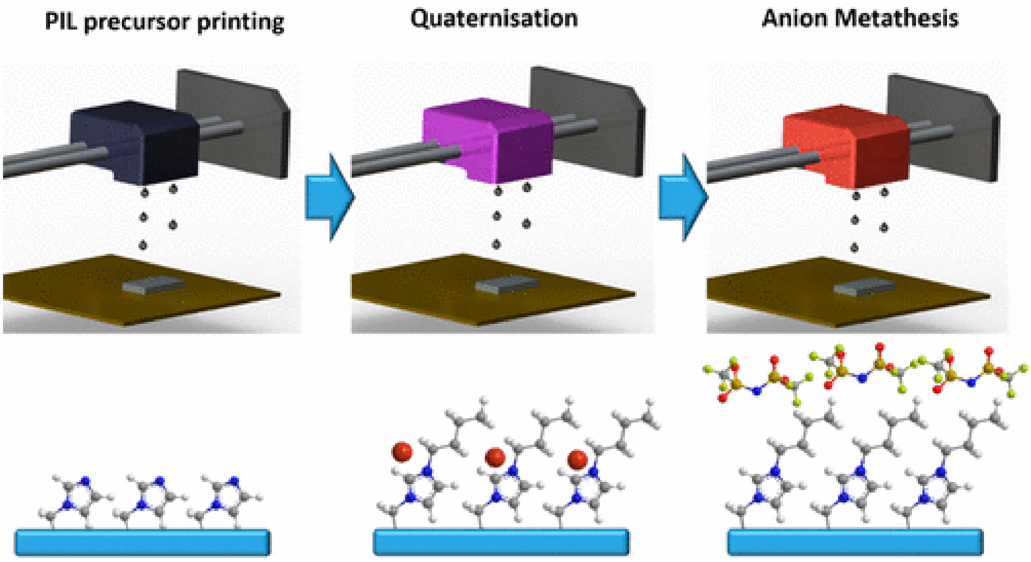

Figure 12. *Schematic representation of the method proposed to inkjet print polyionic films (PILs). Reprint adapted with permission from reference [29]. Copyright 2018 American Chemical Society.*

Our group has demonstrated for the first time the possibility to successfully design functional advanced multi-materials and devices based on PILs with embedded hybrid organic-inorganic polyoxometalates (POMs). This work exemplified how the unique photo/redox properties of nanostructured POMs could be translated into a macroscopic material by DLP as shown in Figure 13. Smart materials containing imidazolium-based PILs and photochromic POMs were designed allowing fine-tuning of the overall properties of the 3D printed material. The rich redox properties of the POMs were transferred to obtain geometrically complex photoactive devices with reversible photochromism. These advanced properties can be useful in different potential applications such as reversible information storage and temporal reduction/oxidation of pre-formed printed devices.[31a]

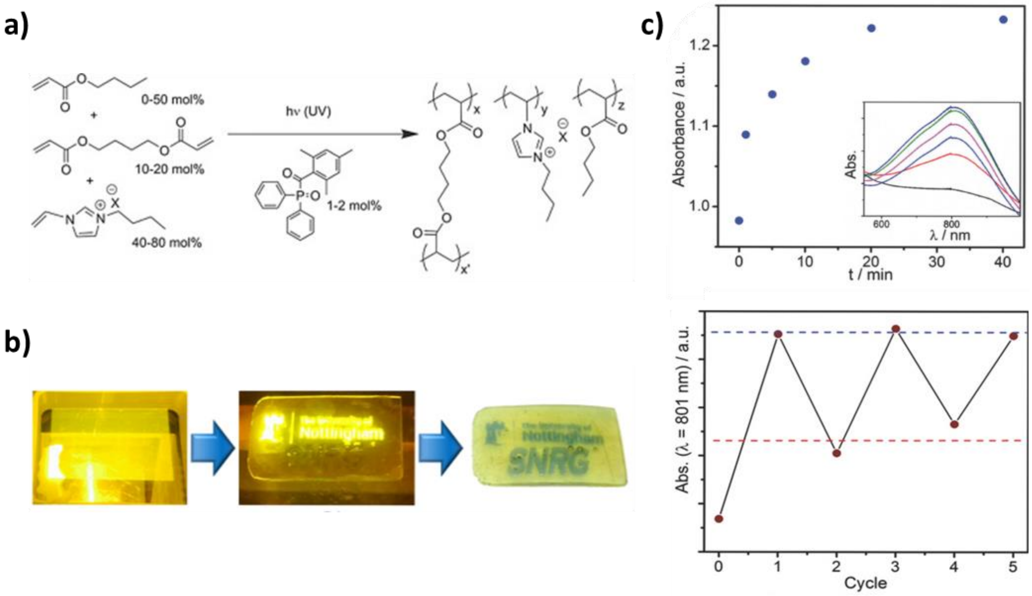

Figure 13. ***a)*** *Compositions of the PIL-based 3D printing formulation capable to stabilise the POMs (C_{10}POM@[BVIM][NTf$_2$]) that were introduced before the printing process;* ***b)*** *Controlled topological and temporal photoreduction of the POM material with visible light to encode information;* ***c)*** *(Up) Increase in absorption at λmax = 801 nm due to photoreduction of the encapsulated POMs upon exposure to the project light over time, with the corresponding UV–vis spectra inset; (Down) Absorbance intensity at λmax = 801 nm upon cycles of photoreduction (encoding) and oxidation (erasure). Adapted from reference [31a] with permission.*

Similarly, recent works demonstrate that PILs are ideal materials to stabilise perovskite nanocrystals (PNCs). Xia *et al*. has recently published a report showing the advantages of protecting hybrid perovskites from decomposition in humid environments with in situ IL polymerisation. The sensitivity to moisture during the cell fabrication was effectively reduced, improving quality and long-term stability.[177] Nevertheless, PNCs are not commonly added as additives into 3D printing materials because of their instability. Therefore, combinations based on PILs can represent a great chance for designing photoactive 3D printed devices for photocatalysis, optoelectronic, conductive, electrochemical and redox applications among others.

On the other hand, the use of PILs for antimicrobial applications has expanded considerably.[178] Li *et al*. 3D printed a tooth model with high precision by DLP using cholinium-based photopolymerisable ILs with antibacterial properties (*Figure 14*).[51a]

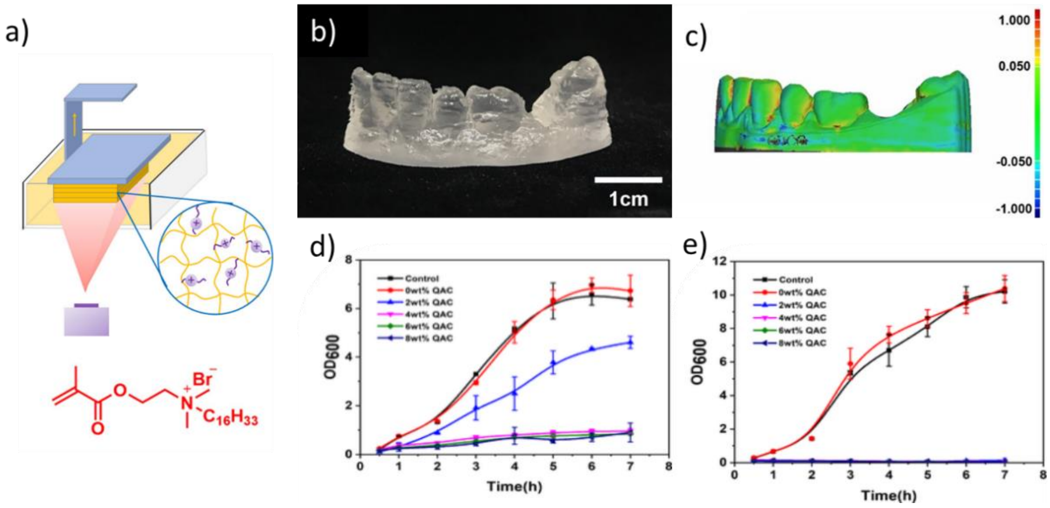

Figure 14. ***a)*** *Schematic representation of the 3D printing process and the monomeric IL involved for preparing the photosensitive resin;* ***b)*** *Picture of the dental model made by DLP 3DP;* ***c)*** *Picture of the corresponding scan data;* ***d)*** *Growth curves of E. coli using PIL formulation with different contents of the antibacterial agent;* ***e)*** *Growth curves of Staphylococcus aureus using PIL formulation with different contents of the antibacterial agent. Adapted from reference [51a] with permission.*

The antibacterial resins are essential in the biomedical field. Furthermore, additive manufacturing contributes to the research and development of biomaterials for prototyping complex and customised structures with patient-specific necessities.[179] Bioprinting has become mainstream and, ILs and PILs have a great potential in this area owing to their tailorable biocompatibility and antimicrobial properties.[180] Into this context, PIL-based bio-inks formulated for 3D printing have been prepared for applications in tissue-engineering (*Figure 15*).[111a]

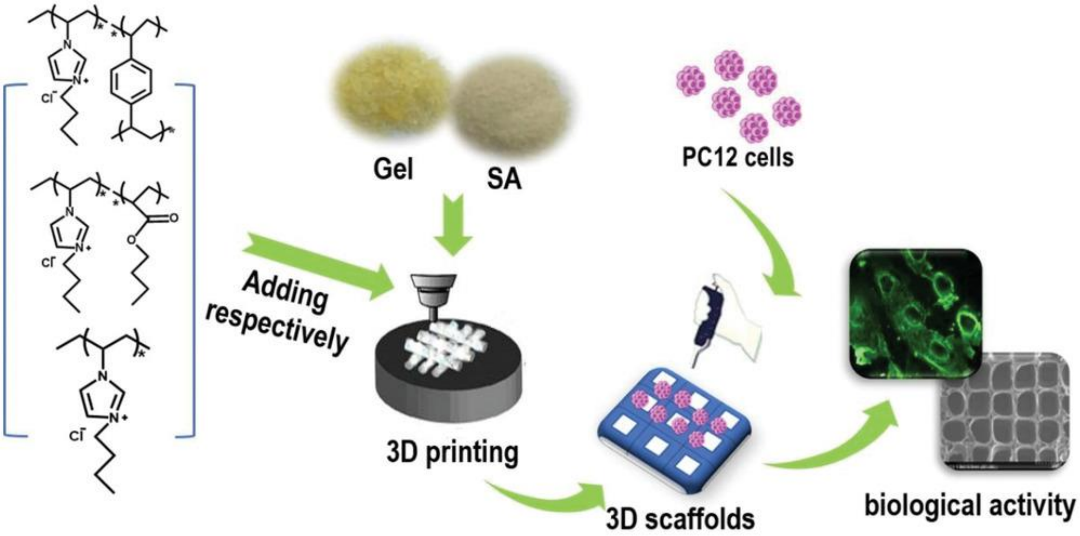

Figure 15. *Schematic diagram including the synthesis of PILs, the 3D printing process and the detection of biological activity. Reproduced from reference [111a] with permission.*

Additionally, the flexibility to modify the physicochemical properties of these compounds solve most of the issues found in drugs delivery systems like low bioavailability and drug insolubility.[181]

In catalysis, the use of 3DP is becoming attractive as well. The combination of digital control over the geometry, function and chemical composition of this technique is having a significant potential for preparing reactors and structured catalysts.[182] For instance, 3D-printed magnetic stirrers have been successfully designed and implemented for catalysing chemical reactions.[183] Once the reaction is over, the stirrer can be removed from the reaction media, washed and reused without further purification steps. Also, a 3DP catalytic device based in Cu/Al_2O_3 showed high catalytic efficacy and good recyclability in different Ullmann reactions.[184] Most work in this area focus on improving mass transfer through geometry optimisation. The use of PILs can help in this regard. Wu *et al.* constructed an agitating impeller (AI), shown in *Figure 16*, with prismatic structure combining 3DP and PILs, and demonstrated that mass transfer, catalyst activity and recovery were enhanced when using printable PILs loaded with palladium ions. Imidazolium ILs with acrylate groups were synthesised and modified on the surface of the impeller by photopolymerisation using SLA.[51b]

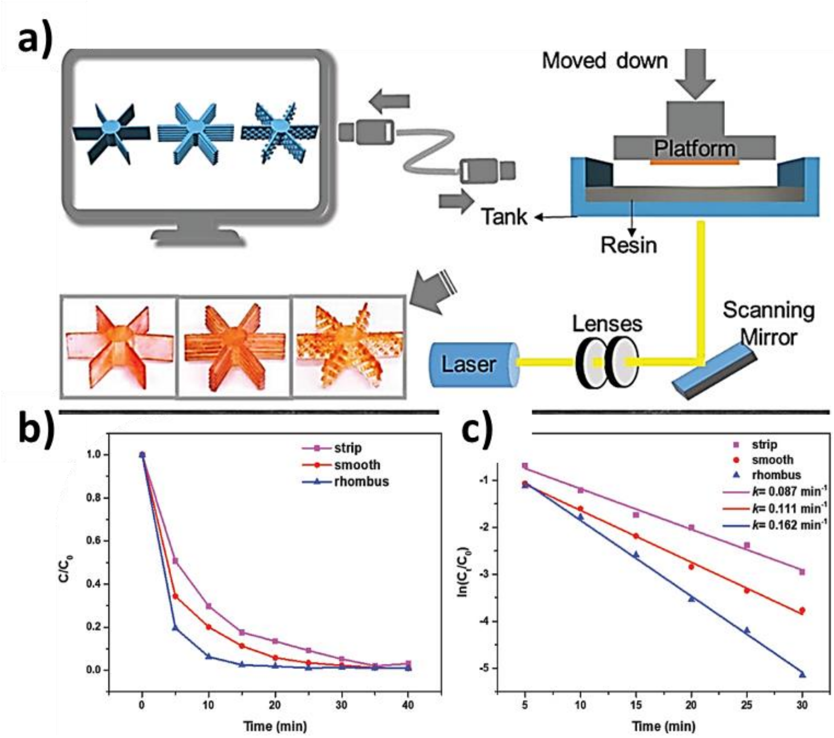

Figure 16. ***a)*** *Schematic illustration of the agitating impeller preparation from the digital CAD model using SLA 3DP technology;* ***b)*** *Degradation curves of 4-nitrophenol (4-NP) catalysed and stirred by three types of Al-Pd respectively;* ***c)*** *Plot of ln(C_t/C_0) versus time spectra for the reduction of 4-NP, showing a linear relationship. Adapted from reference [51b] with permission.*

In a different example, a cellulose-based catalyst was prepared by AM using cellulose dissolved in a quaternary-ammonium-based IL. The freedom in design of this manufacturing technique allowed to build-up thin and homogeneous films of different shapes, types and designs. As a result, the final catalytic printed parts were implemented in specific reactors for dye removal from wastewater.[185]

Furthermore, microfluidic reactors can be fully 3D-printed with internal flow channels and high surface quality.[186] The possibility of printing a reactor with a catalytic material properly supported in the channels can be very beneficial for catalysing reactions. Herein, our group has reported different 3D printed column architectures using SILPs that were successfully implemented for the catalysis of CO_2 cycloaddition to epoxide. The formulations were based on the polymerisation of glycidyl methacrylate with dimethacrylate as crosslinker, whit further functionalisation with imidazolium-based ILs (*Figure 17*a). The catalytic column was used in a continuous-flow process of cyclic carbonate preparation from CO_2 and epoxide (*Figure 17*b). The AM generated catalytic reactors with higher catalytic activity than similar sized packed bed reactors. The catalytic activity and stability of the reactor were kept over 300 hours without loss of activity.[187]

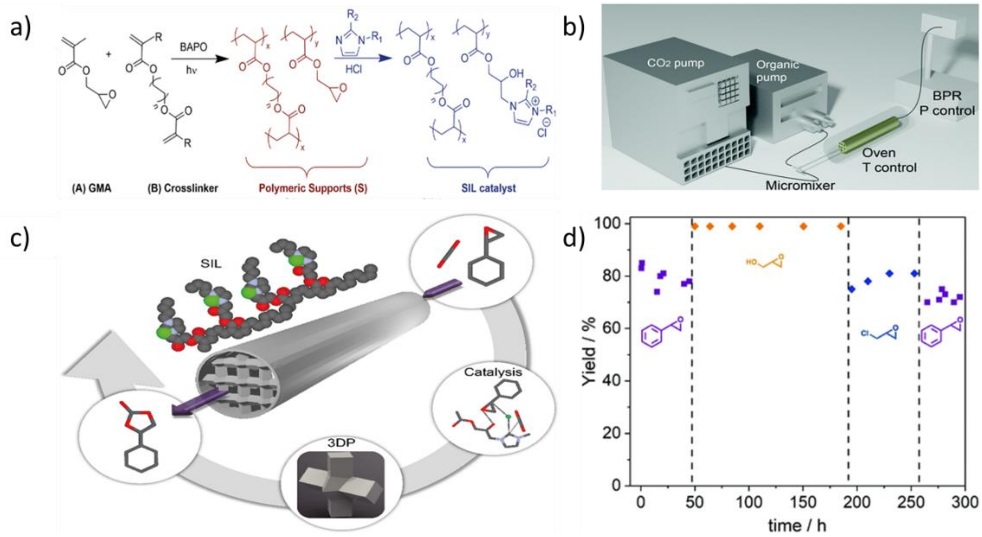

Figure 17. ***a)*** *Preparation of SILPs;* ***b)*** *Continuous flow set-up;* ***c)*** *Application of 3DP catalytic reactor column in CO_2 cycloaddition to epoxide;* ***d)*** *Yield vs. time on stream obtained for the continuous flow reaction between different epoxides and CO2 (65 bar). Conversion calculated by ^{1}H-NMR. Selectivity > 99%. Adapted from reference [187] with permission from the Royal Society of Chemistry.*

The introduction of 3DP in catalysis is a growing field, although ILs and PILs are not widely employed yet. Nevertheless, the use of IL-based materials in catalysis has been extensively studied.[188] The most common ionic moieties employed in this field are imidazolium cations although they are quite sensitive to basic conditions. Phosphonium ionic liquids have intermediate base stability,[189] while triazolium,[190] pyrazolium,[191] and cyclic ammonium (such as pyrrolidinium)[192] cations are often more stable to basic conditions, and are therefore more appropriate for the preparation of basic ionic liquids.

ILs and PILs, mainly imidazolium-based, have also been widely used for electronic, energy storage, supercapacitors and conductive applications. Soft somatosensitive actuators were constructed by directly ink writing with ILs via multi-material embedded which enables the formation of soft robotic actuators mimicking the human somatosensory system. The sensor ink consisted in a conductive shear-thinning ionogel formed with an IL and fumed silica as a rheology modifier, and exhibited long-term stability and hysteresis-free performance.[111b] Long and co-workers prepared a PIL-based 3D printable resin much more conductive, stable and environmentally friendly than using styrene, a common neutral polymer.[193] Extensive research has been devoted to PIL-based electrolytes,[21a, 194] however, their ionic conductivities have resulted too low for practical applications. Into this context, as above-mentioned, mixing PILs with ILs can enhance drastically the polymeric conductivity. Recently, Darren and co-workers have demonstrated that imidazolium PIL/IL-based polyelectrolytes are up to six times more conductive as well as more thermally and electrochemically stable than the analogous neutral polymer. The resulting PIL/IL mixture formed a photopolymerisable resin capable to be printed by SLA methodology.[163b]

Another important consideration is the possibility to manufacture all-printed devices. Liquids and colloid gels have been used for this purpose, however some serious issues appeared using a strong-acid or a strong-alkaline electrolyte, as it caused damages to the deposition nozzles. Electrolytes based on ILs are therefore very favourable for fully-printed devices, because ILs contribute much less to corrosion and they can work at higher voltages than traditional electrolytes.[26a] Also, PIL materials have been mixed with carbon-based nanocomposites for preparing 3D-printable resins, resulting very interesting works. In this regard, flexible and wearable conductive polymers were manufactured by VP using imidazolium-based PILs for dispersing carbon properly, represented in *Figure 18*.[23a]

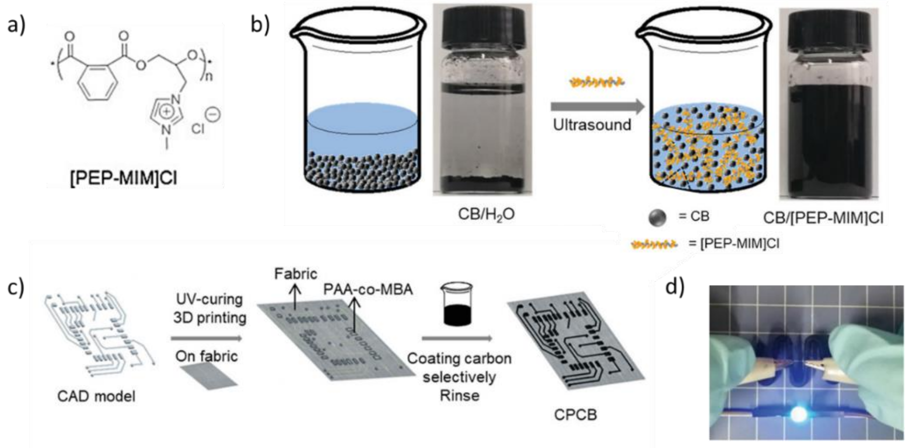

Figure 18. ***a)*** *Structure of the PIL used;* ***b)*** *Dispersion mechanism of carbon black by PIL;* ***c)*** *The preparation process starting from the CAD model;* ***d)*** *Image of the final device coated with carbon, showing its conductivity. Adapted from reference [23a] with permission.*

Carbon nanotubes (CNTs) have also been 3D-printed with a mixture of ILs and PILs for developing soft electronics, finding significant increasement of the composites conductivities (up to 520 S/m adding 15 wt% MWCNT).[30, 195] Graphene aerogels that can be employed for energy storage applications, such as batteries or supercapacitors, were fabricated by a freeze 3D printing technique, as shows *Figure 19*. Using an aqueous dispersion of graphene stabilised in imidazolium-based PILs it was possible to achieve an electrical conductivity of 149 S/m.[196]

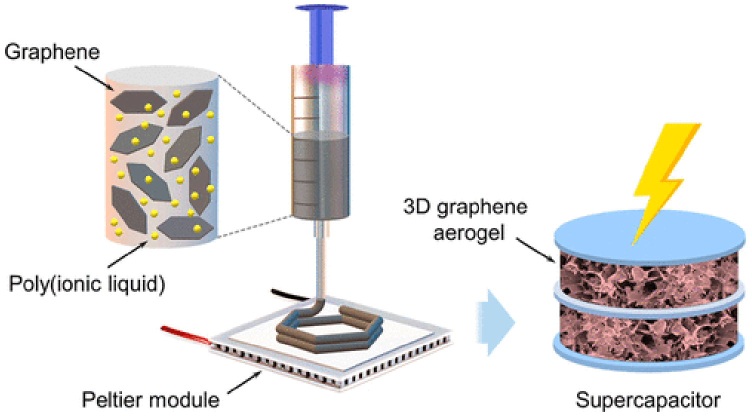

Figure 19. *Schematic representation of the PIL-based formulation, the 3D printing process and the final graphene aerogel. Reprinted with permission from reference [196]. Copyright 2020 American Chemical Society.*

Printable energetic materials based on vinylimidazolium monomers were also photopolymerised by a DLP printer, manufacturing complex geometries at high resolution while also providing a great control over the mechanical and energetic characteristics of the produced objects. The 3D printed polymers allowed to reduce the amount of filler without compromising the final performance of the device.[197]

Generally, much progress has been made in printing functional and smart materials as well as improving the printing technologies. For example, hybrid 3D printing processes that combine different manufacturing processes (multiprocess), have been implemented resulting in an advanced way to prepare intelligent materials with new and complex functionalities.[198] Even so, there is still a need to find new and more efficient printable materials and, simultaneously to engineer a printing process capable to introduce multiple materials in a single print in order to get the most from the additive manufacturing.

Chapter 2:

Polymeric Ionic Liquids with Antimicrobial Activity

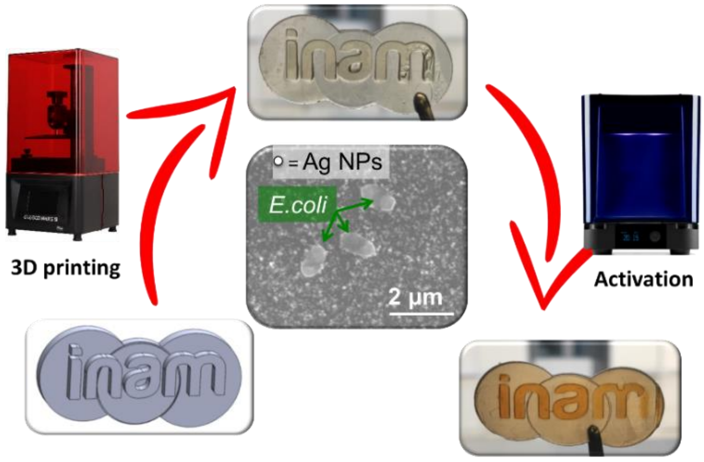

2.1 Summary

The development of antibiotic-resistance by microbes is becoming common and spreading rapidly across continents. The preparation of advanced antimicrobial materials is therefore an emerging concern. Antimicrobial materials can inhibit the growth or kill bacteria on their surface or in their surroundings with high effectiveness, low toxicity and minimal environmental impact.

Here, novel 3D printable materials based on polymeric ionic liquids (PILs) with antimicrobial activity were prepared. The combination of potential antimicrobial properties from PILs and their ability to stabilise nanomaterials with antimicrobial properties was studied. More concretely, nanomaterials based on silver and copper were studied, with the aim of conjugating antimicrobial properties, biocompatibility and 3D printability.

Initially, different formulations using a variety of monomeric ionic liquids and cross-linkers were evaluated to encapsulate a silver precursor ($AgSbF_6$). The interaction of the ionic liquid moieties with the silver precursor enabled the controlled *in situ* formation and stabilisation of silver nanoparticles *via* extended UV photoreduction after the printing process. An effective decoupling of the device manufacturing from the on-demand generation of nanomaterials was demonstrated, avoiding the potential aging of the nanomaterials through oxidation. The printed devices showed a multi-functional and tuneable microbicidal activity against Gram positive (*Bacillus subtilis - B. subtilis*) and Gram negative (*Escherichia coli - E. coli*) bacteria and against the fungus *Aspergillus niger* (*A. niger*). The polymeric material alone was found to be bacteriostatic, while the AgNPs conferred bactericidal properties to the material. Additionally, PIL-based formulations were optimised to be 3D-printed by DLP and MSLA technologies with desired geometries at high resolution. Moreover, the biocompatibility of different monomeric ionic liquids (mILs) and photoinitiators (PI) was evaluated, reporting enhanced viabilities depending on the mIL and PI chosen. It was found that Ag presented a considerable toxicity towards kidney tissue cells, which motivated to look for different antimicrobial materials.

In this way, the optimum non-toxic PIL-based formulations were used for encapsulating a copper precursor ($Cu(NO_3)_2$) in order to obtain antimicrobial and biocompatible devices. The stability of the copper particles in the polymer matrix was enhanced after applying a post-

treatment to the films by heating them at 160 °C. The treated copper-based films exhibited outstanding antibacterial activity against *S. epidermidis*. This is a bacterium found in the human epithelial microflora; however, its ability to form biofilms on indwelling medical devices can lead to infections. The biofilm protects the bacteria from antimicrobial agents. One approach to solve that problem is to fabricate medical devices with inherent antimicrobial properties. Herein, a simulated stent as a demonstrator of a medical device was successfully manufactured with a **Cu@PIL** formulation.

The biocompatibility and the antimicrobial properties of our PIL-based formulations were analysed by the *Instituto de Ciencia de Materiales de Aragón* (INMA). All the antimicrobial, fungicidal and cell viability tests reported here were done by Dr. Isabel Franco and Dr. Scott Mitchell. The experimental results generated in this Chapter have been published in *Biomaterials science* **2021,** *9* (16), 5397-5406, and there is another publication in preparation.

2.2 Introduction

In the last decade, antibiotic resistance has emerged as a worldwide concern.[199] This refers to the ability of microorganisms to resist the effects of antibiotics. Antibiotics are a class of antimicrobial agents that are specifically designed to target bacteria. When bacteria are exposed to antibiotics, some may survive and reproduce, passing on their resistance to their offspring. Over time, the population of bacteria may become entirely resistant to the antibiotic, making it ineffective for treatment. This is a serious problem because it can lead to the spread of infections that are difficult or impossible to treat. Antibiotic resistance can occur naturally, but it is also accelerated by the overuse and misuse of antibiotics. To overcome this issue, new materials with inherent antimicrobial activity are being developed.[200] Antimicrobial activity is the ability of a substance, such as a chemical or a metal, to inhibit the growth or kill microorganisms, such as bacteria, viruses, fungi, and parasites. This activity can be broad-spectrum, meaning it targets a wide range of microorganisms, or it can be specific to a particular type of microorganism. Examples of antimicrobial agents include antibiotics, disinfectants, and antifungals. This activity can be bacteriostatic or bactericidal, depending on the way the antibacterial agent acts.

Bacteriostatic agents are substances that inhibit the growth and reproduction of bacteria, but do not necessarily kill them.[201] These agents work by disrupting the normal metabolic processes of the bacteria, making it difficult for them to reproduce and spread. Bacteriostatic agents are useful in controlling bacterial infections, and can be used in combination with other treatments to help prevent the development of antibiotic resistance. Bactericidal agents, on the other hand, are substances that kill bacteria directly. They do this by damaging the cell membrane, interfering with the bacterial DNA, or inhibiting vital enzymes.[202] Bactericidal agents are typically more effective than bacteriostatic agents at eliminating bacterial infections, but they may not be as effective at preventing the development of antibiotic resistance. Some antimicrobial agents can be both bacteriostatic and bactericidal depending on the concentration, some others may only have one of the properties. Also, the same agent may have different action on different types of microorganisms, for example, a chemical that is bactericidal against Gram-negative bacteria, may be only bacteriostatic against Gram-positive.[203]

Gram-positive and Gram-negative bacteria are two groups of microorganisms that are characterized by their different cell wall structures and staining properties. Gram positive bacteria (such as *Bacillus subtilis*) have a thick peptidoglycan layer and no outer lipid membrane whilst Gram negative bacteria (such as *Escherichia coli*) have a thin peptidoglycan layer and have a complex outer lipid membrane that makes them more resistant to some antibiotics and other antimicrobial agents.[204] The thick peptidoglycan layer gives Gram-positive bacteria a characteristic blue-purple colour when stained with the Gram stain. Some bacteria can be both Gram-positive and Gram-negative depending on the culture conditions. Both types of bacteria can cause a wide range of infections, but some types of infections are more commonly associated with one group or the other. For example, Gram-positive bacteria are more commonly associated with skin and soft tissue infections, while Gram-negative bacteria are more commonly associated with urinary tract infections and food poisoning.[205]

Polymeric matrices have recently attracted a lot of interest in the antimicrobial field due to their higher efficiency, lower toxicity, minimisation of environmental problems, resistance and extended lifetime compared to their small molecular counterparts.[206] Additionally, polymers can be designed to be manufactured by 3D techniques. The unprecedent flexibility in design allows to fabricate medical devices with high resolution.[1, 195a, 197]

There are many antimicrobial agents that can be added as fillers into the polymeric matrices. Silver nanoparticles (AgNPs) exhibit a broad antimicrobial potential.[207] Indeed, several examples of AgNPs-polymeric materials and hydrogels formulated for being additively manufactured have been reported.[208] The nanoparticles are either dispersed in the resin before 3D printing or synthesised during the 3D printing process, thus generating ready-to-use printed devices. A limitation of this strategy is that the metal reduction takes place at the same time that the printing, what does not allow for tuneable fabrication of nanoparticles. A potential solution to this issue is to decouple the manufacturing process from the reduction of the metal. The polymeric matrices need to keep the metal precursor in the oxidised form to enable a controlled reduction of the NPs at the point of need. In this way, optimal antimicrobial efficacy is preserved while allowing the design freedom given by 3D printing and the fabrication of parts with the required mechanical properties. Some papers report the possibility to do this, however they often need post-printing treatments such as energy-intensive heating steps[65c] or immersion of the printed piece in a reducing solution.[209]

Another challenge that might arise when working with nanoparticles is their effective stabilisation.[107a] Different strategies employing 3D printable polymers have been proven effective to offset this issue.[65b] In this regard, the ability of ionic liquids and PILs to stabilise and support metal nanoparticle precursor salts and nanoparticles has been also employed.[150a, 210] Ionic liquids are gaining prominence in the clinical use as they present some desirable characteristics highly relevant, such as improved bacterial resistance, antibiofilm properties, and the possibility of being designed and 3D-printed to possess inherently broad antimicrobial properties against bacteria and fungi.[211] Over the last five years, the use of PILs for antimicrobial applications have increased considerably, but it is still in its early stages. Generally, imidazolium based PILs are the most widespread investigated due to their outstanding thermal stability, low Tg values and easy synthesis.[178] Antimicrobial activity of imidazolium salts and their polymer derivatives has been extensively demonstrated,[31b, 212] and in contrast to the cytotoxic ILs, PILs have shown to be biocompatible.[213] Brushes based on imidazolium PIL with high antibacterial activity have been successfully printed.[214] Apart from imidazolium groups, cholinium-based PILs have showed some antimicrobial activity as well.[51a]

On the other hand, the substitution of silver salts by copper salts is of great interest for improving the sustainability and biocompatibility of the process and the devices, since Cu nanoparticles are slightly less toxic than silver.[215] Copper and copper-based materials have been studied for their antimicrobial properties and have been used in a variety of applications such as medical devices, food packaging, and textiles.[216] The antimicrobial properties of copper are due to its ability to disrupt the membrane potential of microorganisms, leading to a loss of vital ions and enzymes, and ultimately cell death. Muwaffak *et al*. incorporated metallic copper into an FDA-approved polymer (polycaprolactone) to produce filaments for 3D printing. In that way, customised wound dressings were prepared. However, high temperatures are required in the printing process.[217] In the literature, there are few examples of antibacterial materials mixing PILs with copper as antimicrobial agent. Zheng *et al*. reported the antibacterial performance of three different metals (Cu, Fe and Zn) incorporated into PIL-membranes. PIL-Cu membrane and PIL-Zn membrane had an enhanced antibacterial activity and all the membranes presented a low haemolysis toward human red blood cell.[218] Further research is necessary for developing innovative bioactive polymeric materials.

The analyses carried out in this Chapter to study the biocompatibility and antimicrobial activity are described here.

A cell viability test is a method used to determine the number of live cells in a culture or sample. These tests are used in cell biology and biotechnology to measure the health and growth of cells in culture, and are also used in toxicology to assess the effects of drugs, chemicals, or other agents on cells. There is a variety of cell viability tests used depending on the type of cells, the samples and the goals of the experiment. MTT assay is one of the most common methods, in which live cells convert a yellow tetrazolium salt, MTT, into a purple formazan product that is quantified by spectrophotometry.[219]

On the other hand, the antimicrobial activity of a material in solution in direct contact with bacteria is determined using a positive and a negative control. The positive control contains microbes and culture medium, while the negative control is the culture medium without any microorganism, such as water. The antimicrobial activity of the tested material can be determined by comparing the bacterial growth in the test culture to the bacterial growth in the positive control culture. The negative control serves as a baseline. Both tests are used to ensure that the inhibitory effect observed is due to the material, and not to other factors. After incubating the cultures for a specified period of time at the appropriate conditions, the growth of the bacteria can be calculated by counting the number of colonies or by measuring the absorbance (optical density) of the cultures. The material with higher inhibitory effect on bacterial growth is considered to have more antimicrobial activity. Additionally, the minimum inhibitory concentration (MIC) and the minimum bactericidal concentration (MBC) of the tested material can be determined by performing serial dilutions of the tested material and analysing the growth of the bacteria.[220]

Finally, zone of inhibition and halo inhibition tests are another type of test used to measure the antibacterial activity of a compound or substance. It consists of placing a small amount of a bacterium on an agar plate, and then applying a disc or circle impregnated with the substance to be tested. The disc is placed on the agar plate and incubated for certain period of time. After incubation, the diameter of the area around the disc where there is no bacterial growth is measured. This area is known as the 'zone of inhibition' or 'inhibition halo' and its size indicates the effectiveness of the substance in controlling bacterial growth. The larger the zone of inhibition, the greater the antibacterial activity of the substance. In this test, a negative control containing only bacteria and a positive control containing bacteria together with a reference antibiotic are used.[221]

2.3 Objectives

Here, the main goal is to prepare non-toxic antibacterial materials based on polymeric ionic liquids to be manufactured by DLP and MSLA.

Firstly, 3D printable PILs will be formulated to fabricate multifunctional materials that feature four key properties:

- Decoupling the synthesis of silver nanoparticles from the 3D printing step
- On-demand photoreductive formation of AgNPs within the material

- An antimicrobial effect of the PIL backbone
- A broad antimicrobial action afforded by AgNPs

Further objectives are:

- To optimise the formulations in order to obtain high-resolution tailor-made devices
- To investigate the biocompatible properties of the 3D-printed materials
- To stabilise copper salts to prepare environmentally friendly copper-based compounds
- To evaluate the antimicrobial activity of a variety of copper samples
- To manufacture a medical device using non-toxic and antimicrobial 3D printable formulations

As a proof-of-concept, a model resembling a medical stent was 3D printed at high resolution to demonstrate the viability of employing this technology to fabricate biocompatible and bacterial resistant devices.

2.4 Results and Discussion

2.4.1 Summary of the Nomenclature found in Chapter 2

Table 2. *Nomenclature used for naming the films prepared with different mILs (mIL1, mIL2 and mIL3).*

Entry	***Film***	***mILX (mol%)***	***Cross-linker (mol%)***	***Additive (wt%)***
1	PILX	80	BDA (20)	-
2	Ag@PILX	80	BDA (20)	$AgSbF_6$ (1)
3	PILX.1	60	PEGDA 575 (40)	-
4	PILX.2	80	PEGDA 575 (20)	-
5	PILX.3	90	PEGDA 575 (10)	-
6	PILX.4	100	-	-
7	PILX.5	80	PEGDA 250 (20)	-
8	PILX.6	80	PEGDA 700 (20)	-
9	Ag@PILX.2	80	PEGDA 575 (20)	$AgSbF_6$ (1)
10	Cu@PILX.2	80	PEGDA 575 (20)	$Cu(NO_3)_2·3H_2O$ (2)

Where X = 1, 2, or 3 depending on the mIL used (mIL1, mIL2 or mIL3, respectively):

Monomeric Ionic Liquids

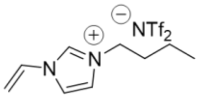

1-butyl-3-vinylimidazolium
bis(trifluoromethane)sulfonimide
(mIL1)

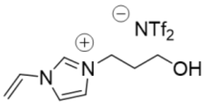

1-(3-hydroxypropyl)-3-vinylimidazolium
bis(trifluoromethane)sulfonimide
(mIL2)

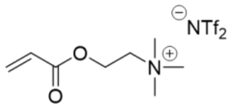

[2-(acryloyloxy)ethyl]trimethyl-ammonium
bis(trifluoromethane)sulfonimide
(mIL3)

2.4.2 PIL Formulations Containing Silver

Several photopolymers based on mixtures of monomeric ionic liquids (mILs), cross-linkers and photoinitiator (PI) were developed to obtain printable antimicrobial materials. The components used are represented in *Figure 20*a.

The first tuneable 3D printing ink formulation was based on the polymerisable ionic liquid 1-butyl-3-vinylimidazolium bis(trifluoromethane)sulfonimide (mIL1) since it had previously demonstrated to be a suitable PIL for stabilising and solubilising hybrid organic–inorganic polyoxometalates, and formed mechanically resistant polymers when 3D printed.[31a] Based on the group experience, the initial formulation (**PIL1**) consisted of mIL1 (80 mol%), the cross-linker 1,4-butanediol diacrylate (BDA, 20 mol%) and the organic PI diphenyl(2,4,6-trimethylbenzoyl)phosphine oxide (TPO, 1 wt%), obtaining a clear, pale yellow viscous liquid. The photopolymerisation of **PIL1** resulted in well-defined clear and yellow films (*Figure 20*b). To this baseline formulation silver hexafluoroantimonate ($AgSbF_6$, ~1 wt%) salt was solubilised and stabilised. After 3D-printing, the resulting **Ag@PIL1** pieces presented also a yellow colour which was attributed to the polymer (*Figure 20*c). Therefore, we could suggest that the encapsulated silver was still in the Ag^+ state, despite exposure to the light during the 3D printing step.

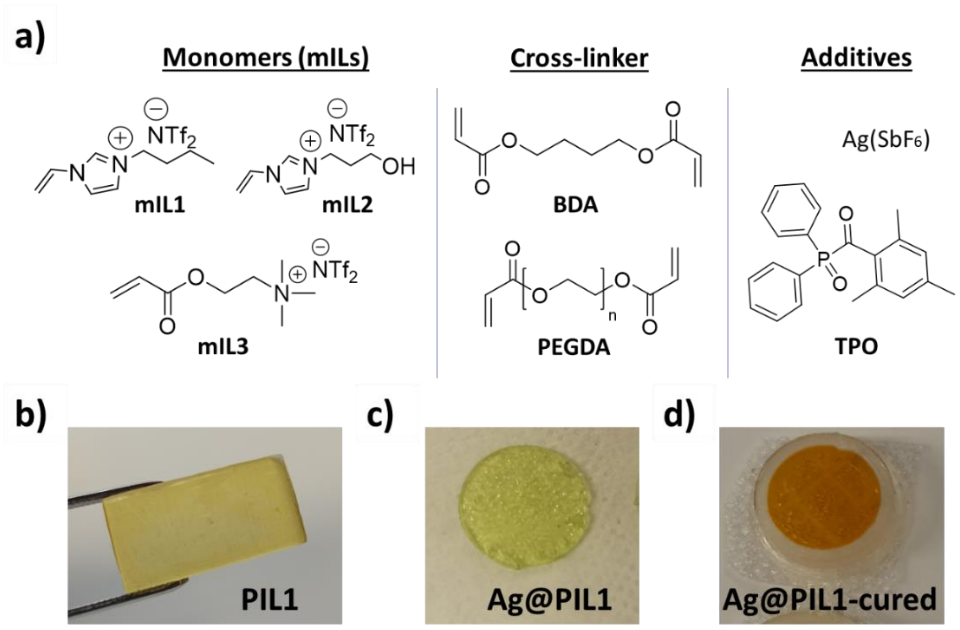

Figure 20. ***a)** The components employed for the development of 3D printable PIL-based formulations; **b) PIL1** after printing; **c)** Printed **Ag@PIL1** film without post-curing; **d)** Printed **Ag@PIL1** film exposed to UV light during 20 minutes.*

Furthermore, the UV-Visible spectra of the as printed pieces confirmed the absence of an absorption peak in the region λ ≈ 375-475 nm, attributable to the localised surface plasmon resonance (LSPR) band of the AgNPs.[222] As it can be seen in *Figure 21*a (red line), the UV-Visible spectra only shows the expected absorption peak features for the photoinitiator TPO.[223] Then, upon exposure to UV light, the photo-reduction of Ag^+ to Ag(0) was initiated and the colour of the printed parts changed over time to increasingly darker shades of amber (*Figure 20*d). UV-Vis transmission spectroscopy experiments with UV post-curing treatment further confirmed the formation of AgNPs due to the presence of a shoulder peak centred at λ ≈ 450 nm increasing in absorbance, which is attributed to the AgNPs plasmon. Meanwhile, the absorbance of the peak features attributed to the PI (λmax = 380 nm) decreased with increasing exposure time (*Figure 21*a). The presence of Ag(0) was further confirmed by characterisation with XPS, which revealed the expected peaks in the spectrum for $Ag3d_{3/2}$ and $Ag3d_{5/2}$ (*Figure 21*b).[224] Indeed, the slight asymmetry of the $Ag3d_{5/2}$ peak toward higher binding energies could be due to a convoluted peak that corresponds to aggregated Ag nanoparticles, which further corroborates the presence of AgNPs.[225]

Additionally, Ag3d bands corresponding to the **Ag@PIL1** before post-curing (red spectrum) are broad signals, while the cured film (black spectrum) presented narrow bands that can be attributed to Ag(0) species.

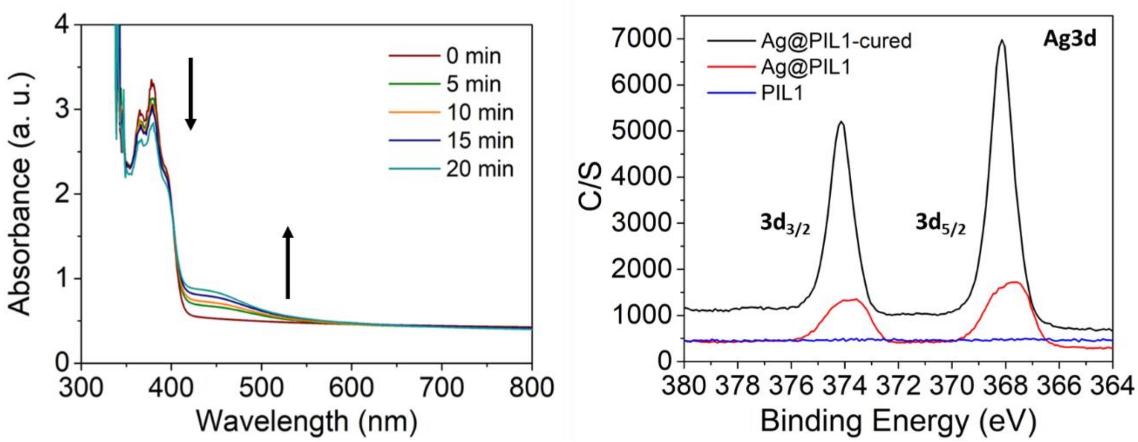

Figure 21. ***a)*** *UV-Vis spectra of a 3D printed* ***Ag@PIL1*** *film at different post-curing times;* ***b)*** *XPS spectra of a photo-reduced* ***Ag@PIL1*** *film revealing the expected Ag3d$_{3/2}$ and Ag3d$_{5/}$2 peaks, compared with an Ag-based film without curing and a bare* ***PIL1*** *film.*

Mechanical analysis of parts exposed to UV photoreduction for different times indicated an increase in tensile stiffness with increasing UV exposure time. The samples were individually analysed and single experiment results are shown. Interestingly, the mechanical properties (stress-strain curves) showed a dependence on irradiation times. The increase in irradiation time led to a more mechanically resistant materials (*Figure 22*a). However, an excessive curing time led to a more brittle material, presumably due to an overcuring of the polymers. Moreover, the corresponding tanδ vs temperature curves revealed that the Tg values also increased with increasing UV exposure time (*Figure 22*b). Two maxima were observed, which was attributed to the presence of small aggregates or nanoparticles. Nevertheless, FT-IR studies during post-curing revealed only a small decrease in the intensity of the C=C stretch peak at ~1650 cm^{-1} after 5 minutes of photocuring, and no further changes (*Figure 22*c). Therefore, it is proposed that the increase in tensile stiffness and Tg upon increased UV exposure time is due to the continued formation of AgNPs and/or aggregation of AgNPs, both of which contribute to modifying the mechanical properties of polymer matrices.[226]

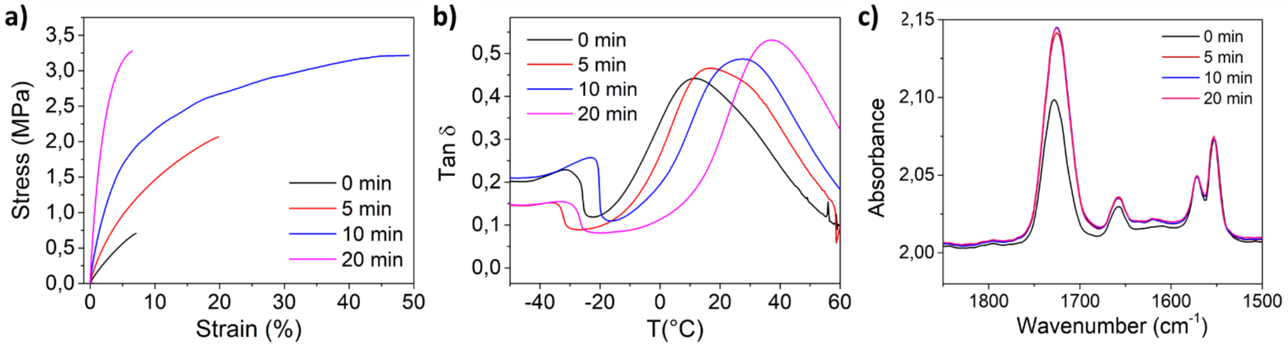

Figure 22. ***a)** Stress-Strain curves for **Ag@PIL1** 3D printed parts demonstrating an increase in tensile stiffness with increasing UV exposure time; **b)** The tanδ vs temperature curves, where the Tg values (defined as the x-axis values at each curve maximum) increase with increasing post-curing time, and **c)** FT-IR spectra demonstrating little to no change in the C=C peak upon increasing UV exposure time. This suggests that further polymerisation of unpolymerised C=C bonds in the materials is not contributing to the increases in tensile stiffness and Tg upon UV exposure.*

After analysing **mIL1**-based formulations, we studied the ability of another imidazolium monomer with a terminal OH in the aliphatic side chain (1-(3-hydroxypropyl)-3-vinylimidazolium bis(trifluoromethane)sulfonimide, mIL2) to stabilise AgNPs. Interestingly, changing the monomer in the formulation (**PIL2**) whilst keeping the rest of the formulation constant (20 mol% BDA and 1 wt% TPO), led to better resolved plasmons after curing, showing a well-defined plasmon with a maximum at λ = 422 nm (*Figure 23*a). Similar to **Ag@PIL1**, the colour of the films changed upon UV exposure time. However, the printed **Ag@PIL2** parts resulted in excessively rigid samples, which deformed and cracked during the polymerisation process (*Figure 23*b). It was hypothesised that the presence of the hydroxyl group of the cation, combined with the use of BDA as cross-linking agent, had an influence on the mechanical properties of the resulting material, which in turn affected the printability. Instead, when poly(ethyleneglycol) diacrylate (PEGDA, M_n = 575 g/mol) was employed as a cross-linking agent in same percentage (20 mol%) (**PIL2.2**), much more flexible films with enhanced mechanical properties were obtained (*Figure 23*c). The new formulation with PEGDA was able to 3D-print tailored geometries with an error <15 % (calculated from the difference in the main dimensions set in the CAD file compared to the actual printed part) (*Figure 23*d-f). Accuracy was not the key parameter at this point of the study, and the optimisation of the formulations to achieve optimal printing resolution is shown in **Section 2.4.3**.

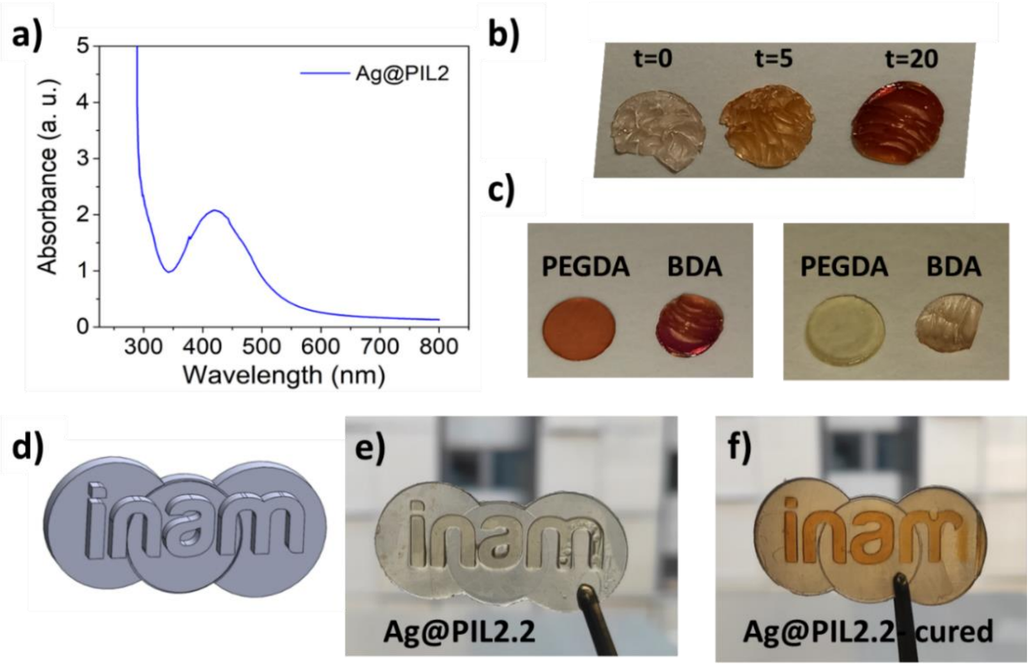

Figure 23. ***a)*** *The UV-Visible peak feature attributed to the AgNPs plasmon of resonance in 3D-printed and photocured* ***Ag@PIL2****;* ***b)*** ***Ag@PIL2*** *films exhibited different colours depending on the post-curing time (in minutes);* ***c)*** *(Left) 3D-printed parts of* ***Ag@PIL2****-based formulation with PEGDA and BDA after 20 mins of UV exposure, and (right) before photocuring, highlighting how the formulation with BDA deformed during 3D printing, whereas with PEGDA the printing presented good resolution;* ***d)*** *Example CAD design that was employed as a benchmark for 3D-printing;* ***e)*** *3D-printed part of* ***Ag@PIL2.2*** *before Ag reduction;* ***f)*** *3D-printed part of* ***Ag@PIL2.2*** *after generating AgNPs by UV irradiation.*

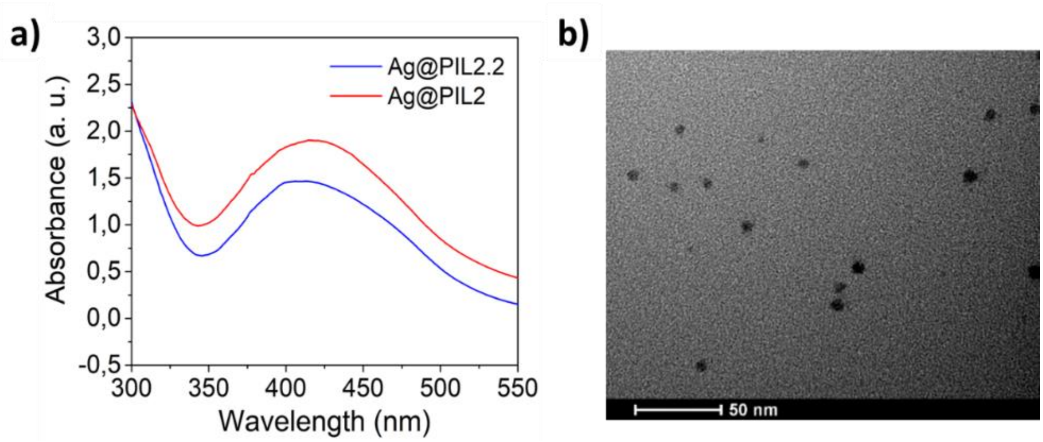

Figure 24. ***a)*** *UV-Vis spectra of* ***Ag@PIL2*** *film (using BDA, red curve) and* ***Ag@PIL2.2*** *film (using PEGDA, blue curve);* ***b)*** *Transmission electron micrograph of a 3D printed* ***Ag@PIL2.2*** *film post-cured, showing the presence of AgNPs dispersed within the PIL matrix.*

The **Ag@PIL2.2** film presented a well-defined UV-Visible peak attributable to the LSPR characteristic of AgNPs centred at 413 nm (*Figure 24*a, blue spectrum). TEM microscopy confirmed the presence of spherical AgNPs within the PIL matrix (*Figure 24*b). A similar ability to stabilise AgNPs upon extended photoreduction under same conditions was observed with both cross-linkers.

Likewise, a cholinium-based monomeric ionic liquid containing an acrylate group, [2-(acryloyloxy)ethyl]trimethyl-ammonium bis(trifluoromethane)sulfonimide (mIL3), was tested, resulting in faster polymerisation than the vinyl group from mIL1 and mIL2 due to the acrylate group. A formulation containing PEGDA (20 mol%) was selected for the improved mechanical properties. Once again, the UV-Visible spectrum of the printed **Ag@PIL3.2** film confirmed the absence of an absorption peak in the region λ ≈ 375-475 nm, attributable to the AgNPs (*Figure 25*, blue curve). Whereas, the UV-Vis spectrum of the same film after UV curing treatment showed the formation of AgNPs by the presence of its characteristic plasmon of resonance centred at λ = 435 nm (*Figure 25*, black curve).[222]

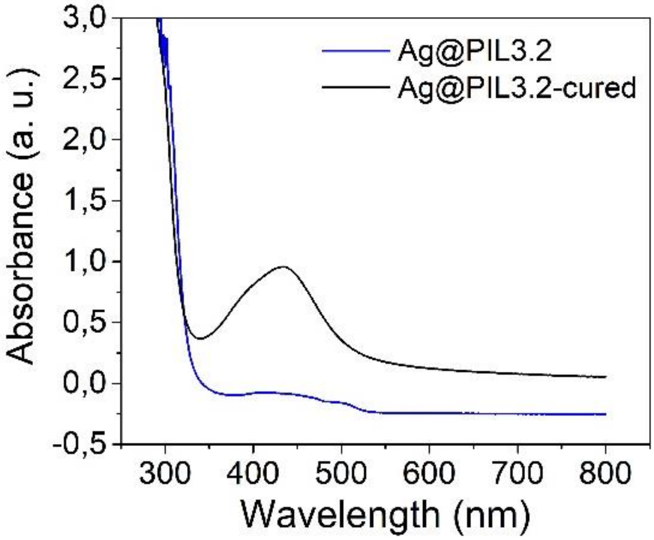

Figure 25. *UV-Vis spectra of* ***Ag@PIL3.2*** *film cross-linked with PEGDA (20 mol%) before curing (blue) and after curing it (black) under UV light during 20 minutes at 40 °C.*

On the contrary, when using a commercial resin or lower mIL:PEGDA ratios, the silver was photoreduced during the printing step.

Aging experiments were performed to determine the stability of the **Ag@PIL** parts over time. To examine the photostability, **Ag@PIL2.2** films were stored either under ambient lighting or under dark conditions. We observed that the films that had been photoreduced by post-curing exhibited an increase in the magnitude of the absorbance peak attributed to AgNPs when exposed to ambient light conditions, suggesting the continuous photoreduction of AgNPs (*Figure 26*).

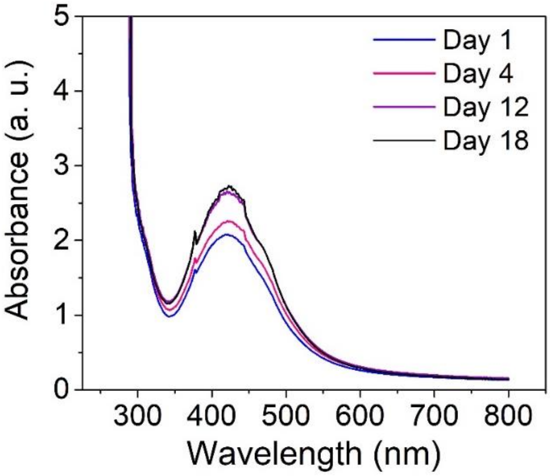

Figure 26. *Ag@PIL2.2 film generated by post-curing photoreduction and aged under ambient light over a period of 18 days, causing an increase in the absorbance of the peak attributed to the AgNPs plasmon.*

When non-photoreduced **Ag@PIL2.2** pieces were stored for three weeks under ambient irradiation, a peak (centred at ~450 nm) in the UV-Visible transmission spectra developed, suggesting the formation of AgNPs (*Figure 27*a). In contrast, non-photoreduced 3D printed **Ag@PIL2.2** films stored in the dark showed no LSPR related band (*Figure 27*b). Therefore, it was determined that storage in dark conditions was required to prevent photo-aging. Storage in dark conditions demonstrated the hypothesis that it is possible to decouple the manufacturing of devices by 3DP from the synthesis of the nanoparticles.

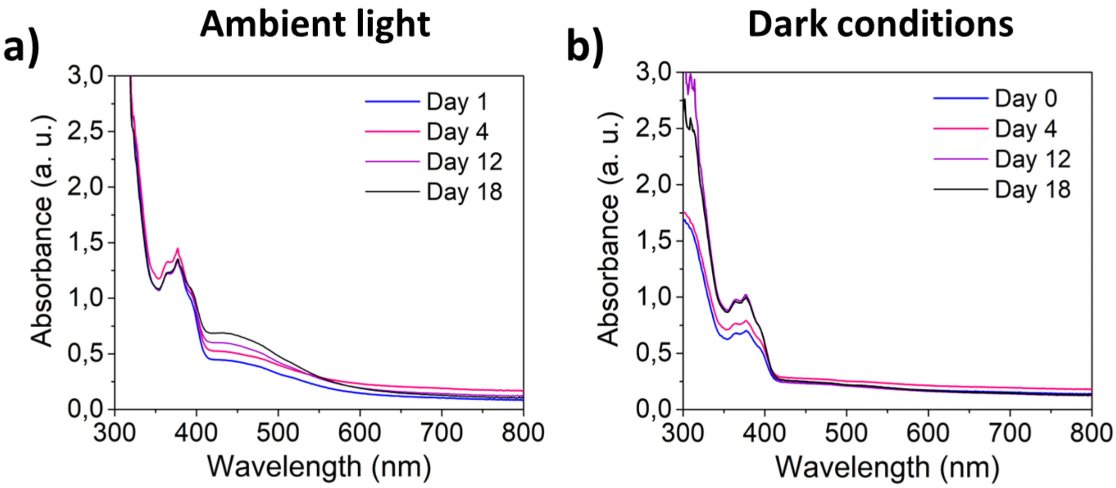

Figure 27. *a)* ***Ag@PIL2.2*** *film non-reduced and then aged under ambient light highlighting the development of a peak feature at ~450 nm suggesting the formation of AgNPs;* ***b) Ag@PIL2.2*** *film non-reduced and then aged under dark conditions, showing no sign of an AgNPs plasmon. In all cases the samples were exposed to ambient atmosphere.*

In summary, the formulations based on the three mILs were 3D-printed, decoupling the synthesis of the AgNPs from the additive manufacturing process. The reduction of the silver was well controlled after the printing process. According to the results, the most suitable formulations were prepared by mixing 80 mol% of mIL, 20 mol% of PEGDA 575 and 1 wt% of TPO. In some cases, the films were photopolymerised directly under a UV light lamp (20 min at 40 °C in aerobic atmosphere) without involving 3D printing.

Antimicrobial Studies

As mentioned above, the antimicrobial properties of our PIL-based formulations have been analysed in collaboration with the *Instituto de Ciencia de Materiales de Aragón* (INMA), by Dr. Isabel Franco and Dr. Scott Mitchell.

The combination of hydrophobic PILs with AgNPs make potential candidates for antimicrobial surface coatings to prevent biofilm formation. The antimicrobial activity of **Ag@PILs** were evaluated against non-pathogenic *E. coli* (*EC*) and *B. subtilis* (*BS*) and two fungi (*A. niger* (*AN*) and *C. cladosporioides* (*CC*)) *via* zone of inhibition tests and cell proliferation assays, combined with biofilm inhibition studies. The different antimicrobial tests are described in the *Experimental Part* (**Section 2.6.4**). In general, both **PIL** and **Ag@PIL** samples inhibited microbial growth, but Ag-containing PILs were more effective at reducing bacterial viability. In the first instance a Zone of Inhibition test of **PIL1** and **Ag@PIL1** revealed that only the **Ag@PIL1** displayed an inhibition halo against *EC* and *BS* (Figure 28a). This inhibition of bacterial growth around the sample is due to the diffusion of the Ag^+ ions into the agar, which is the most important factor in the antimicrobial activity of the AgNPs against bacteria.[211d] No inhibition halo was found with the **PIL1** samples due to the lack of silver. A delay halo -characterised for the mycelium growth- was found around **Ag@PIL1** incubated in the plate inoculated with *AN*. No inhibition nor delay halo was found with **PIL1** and neither **Ag@PIL1** sample incubated in the plate inoculated with *CC* (Figure 28b).

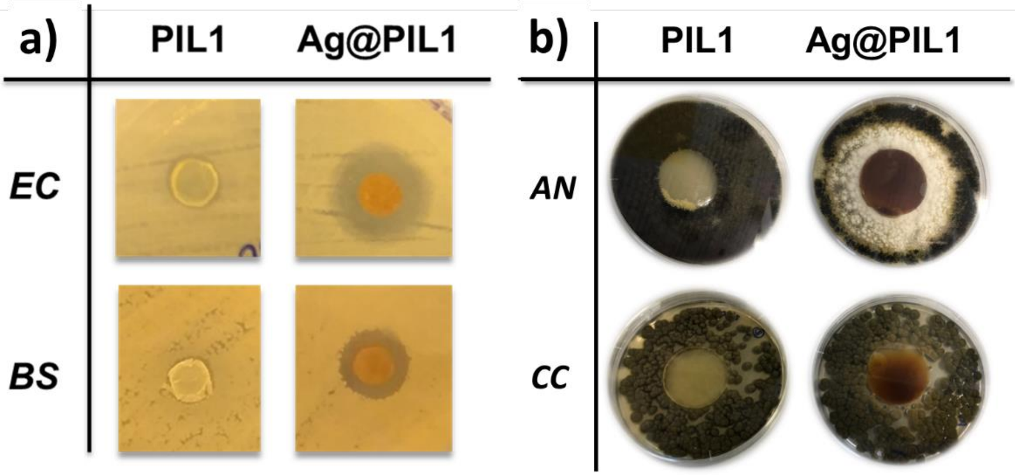

Figure 28. ***a)*** *Zone of Inhibition test of* ***PIL1*** *with BDA (20 mol%) and* ***Ag@PIL1*** *against two bacterial strains (E. coli and B. subtilis); and* ***b)*** *Inhibition halo against two fungi (A. niger and C. cladosporioides).*

In order to determine the antibacterial activity of the samples in solution, the bacterial growth in cell culture media in the presence of the samples was monitored by optical density. **PIL1** repressed the growth of *EC* and *BS* in liquid media over a 24-hour period but, interestingly, the corresponding reduction in bacterial cell viability was lower for the Gram-positive *BS* (Figure 29a). This was confirmed by Environmental Scanning Electron Microscopy (ESEM), which showed a high degree of sporulation in *B. subtilis* (Figure 29c). On the other hand, the **Ag@PIL1** variant was found to reduce bacterial cell growth of *EC* and *BS* by 86 % and 75 %, respectively, as expected due to the antimicrobial effect of silver. Evaluation of the antibacterial activity of the **PIL2.2** formulation yielded similar results, however, **Ag@PIL2.2** was found to possess the highest degree of inhibition after 24 hours of incubation, resulting in a reduction of around 95 % for both bacterial strains (*Figure 29*b).

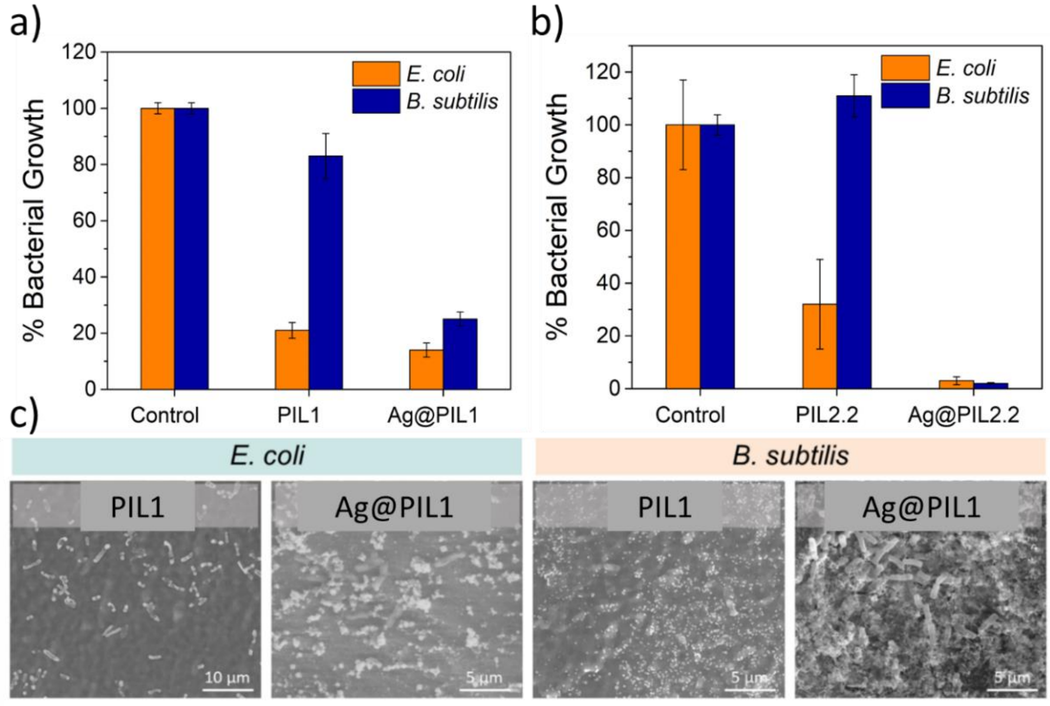

Figure 29. *Bacterial cell viability of E. coli and B. subtilis incubated with* ***a) PIL1*** *and* ***Ag@PIL1****;* ***b) PIL2.2*** *and* ***Ag@PIL2.2****;* ***c)*** *ESEM images of* ***PIL1*** *and* ***Ag@PIL1*** *inoculated with E. coli and B. subtilis. Both* ***PIL1*** *and* ***Ag@PIL1*** *affect E. coli morphology, disrupting the cell membrane. On the other hand,* ***PIL1*** *stimulates the B. subtilis sporulation, while* ***Ag@PIL1*** *prevents colonisation of the polymeric surface due to a higher bactericidal effect.*

Broth and agar dilution methods are standard methods used to determine the antimicrobial effect of the compounds, but these assays are standardised for soluble compounds. Hence, performing a surface antimicrobial assay is essential when using compounds which are meant to be applied as a coating or, like in this case, they are created directly as a 3D object. Here, a modified Japanese Industrial Standard (JIS) Z 2801 method, described in **Section 2.6.4** was used to determine the surface antimicrobial activity of **PIL1** and **Ag@PIL1**. **PIL1** displayed a bacterial reduction of 100 % and 89 % for *E. coli* and *B. subtilis*, respectively, while **Ag@PIL1** reduced 100 % of the bacterial cell count. Subcultures of the supernatants confirmed the bactericidal effect of the **Ag@PIL1**, while **PIL1** only displayed bactericidal effect against *E. coli*. These results are commensurate with the results in liquid medium and the ESEM images, where the samples containing Ag displayed a higher antimicrobial effect, with *BS* being the most resistant strain. The differences in antimicrobial activity between the solution and the surface activity tests show that the antimicrobial properties are based primarily on surface contact-killing rather than the release of an active component, such as Ag^+ ions, into the local environment.[211d]

On the contrary, the formulations based on mIL3 (**PIL3.2** and **Ag@PIL3.2**) did not report any antimicrobial effect as shows *Figure 30*. These results differ from the high antibacterial activity found for the imidazolium formulations (using mIL1 and mIL2). The chemical structure of the monomeric ionic liquid employed plays a major role in the final antimicrobial properties of the materials. The free electrons from the nitrogen of the imidazolium group are probably responsible for the antimicrobial action. In contrast, the cholinium used in this study consisted of a quaternary amine with no free electrons. In the literature, imidazolium PILs are commonly used for antimicrobial applications, while cholinium-based materials are rather rare.

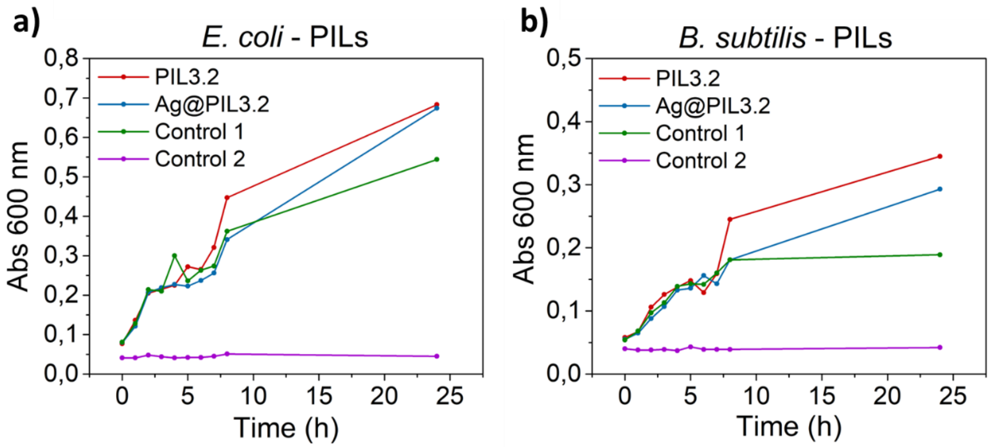

Figure 30. *Optical density graphs of **a)** E. coli and **b)** B. subtilis, incubated with **PIL3.2** and **Ag@PIL3.2** vs the control experiments (Control 1: positive and Control 2: negative).*

2.4.3 Optimisation of Printing Resolution

The polymer formulation was optimised in order to obtain printings with high resolution. A wide variety of photopolymers were prepared and characterised using the three monomeric ionic liquids (mIL1, mIL2 and mIL3) and PEGDA as cross-linker with different average molecular weights (250, 575, 700 g/mol). The molar percentage of mIL/PEGDA was varied, while TPO (1 wt%) was the selected PI in the whole study. The range of concentrations of mIL:PEGDA were varied from 100:0 to 60:40. All the tested formulations are summarised in *Table 3*. Additionally, a low concentration of a dye was added to improve the resolution. In this way, methyl red (MR) was added (0.1 wt%), giving a distinctive red colour on all the printings.

All the polymerisation reactions were followed by FT-IR spectroscopy. It was possible to calculate the polymeric conversions by assessing the disappearance of the double bond bands. To this end, the evolution of the FT-IR signals belonging to the acrylate and vinyl functional groups before and after 3D-printing irradiation were analysed. The polymeric conversion was calculated according to the literature.[227] The spectra were normalised using the area of the SO_2 band at 1350 cm^{-1}, belonging to the counter-anion bis(trifluoromethane)sulfonimide (NTf_2). The disappearance of the bands related to the C=C bond at 1640 cm^{-1} and 990 cm^{-1} verified the conversion of the double bonds after polymerisation. Dynamic mechanical thermal analysis (DMTA) was performed using printed flat films (30 mm × 10 mm × 0.5 mm). The glass transition temperature (Tg) was measured as the temperature corresponding to the maximum of the tanδ curve. Three replicates were tested for each formulation (*Figure 31*).

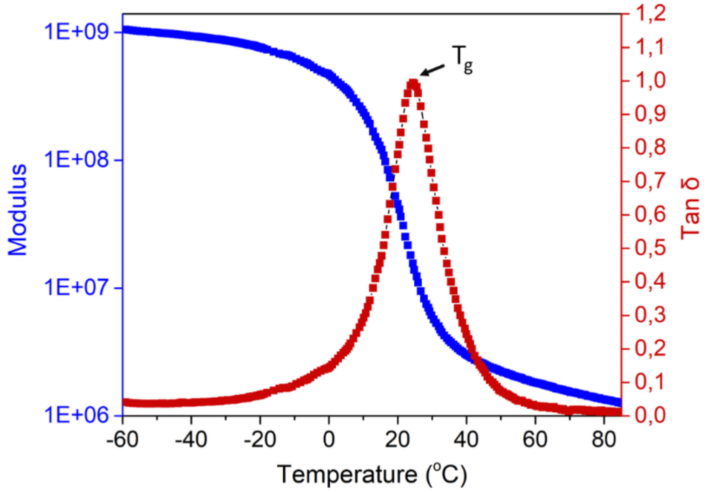

Figure 31. *The modulus and its respective tanδ vs temperature curves of* ***PIL3.2*** *films to exemplify the methodology followed for calculating the Tg of all the samples. The Tg values were defined as the x-axis values at the maximum of the tanδ curve.*

Additionally, thin films (0.3 - 0.6 mm) of each sample were printed and used to calculate the gel content (insoluble fraction). This test was performed using the standard method ASTM D2765-16.[228] The films were placed in a metal net, previously weighed, and then soaked in chloroform at room temperature for 24 hours to dissolve the non-crosslinked products. The samples were then dried overnight at 80 °C, and the gel content percentage was calculated as the weight change before and after the solvent extraction.

Table 3. *Summary of all the formulations prepared and a quantitative assessment of the properties of the materials developed.*

Entry	***Code***	***mIL (mol%)***	***PEGDA (MW)***	***PEGDA (mol%)***	***Polymeric Conversion (%)***	***Tg (ºC)***	***Gel Content (%)***
1	PEGDA	0	575	100	99	-20.2	99
2	mIL1.1	60	575	40	98	-10.1	81
3	mIL1.2	80	575	20	99	-13.9	71
4	mIL1.3	90	575	10	99	-14.1	57
5	mIL1.4	100	-	0	62	-16.3	50
6	mIL1.5	80	250	20	97	-3.7	68
7	mIL1.6	80	700	20	99	-27.1	74
8	mIL2.1	60	575	40	90	-9.9	90
9	mIL2.2	80	575	20	96	1.4	95
10	mIL2.3	90	575	10	35	7.5	93
11	mIL2.4	100	-	0	48	10.5	89
12	mIL2.5	80	250	20	75	-	67
13	mIL2.6	80	700	20	76	-2.9	82
14	mIL3.1	60	575	40	98	6.2	99
15	mIL3.2	80	575	20	93	23.7	99
16	mIL3.3	90	575	10	98	57	98
17	mIL3.4	100	-	0	73	64	90
18	mIL3.5	80	250	20	63	6.8	93
19	mIL3.6	80	700	20	99	2.5	95

The gel content and the polymeric conversion provided information on the reactivity and the degree of polymerisation of each formulation. From *Table 3* can be concluded that, in general, mIL3 formulations polymerised more efficiently due to its highest reactivity. In the *Figure 32*a, is possible to observe that the C=C peaks disappeared after polymerising, which explains the high conversions achieved in most mIL3-based formulations, > 90 %. As it was expected, a larger molar percentage of cross-linker led to higher degrees of polymerisation, with some exceptions. While pure mIL formulations (**mILx.4**, *Table 3*, entries 5, 11 and 17), reported the lowest gel content and polymeric conversion percentage. Simultaneously, the addition of PEGDA to mIL2 and mIL3 caused a decrease in the Tg, as expected since the Tg of PEGDA is lower than that of the mILs. Nevertheless, the behaviour of mIL1 is the opposite due to its low Tg. *Table 3* also reveals that formulations using PEGDA 250 were less reactive than those with PEGDA 575 and PEGDA 700.

Important parameters such as polymerisation kinetics were analysed to get good printing conditions. Polymerisation kinetics of all formulations were followed by photorheology. Once the storage modulus reached a plateau the polymerisation was completed. As it can be seen in *Figure 32*b, **mIL3.2** reactivity (black line) was faster than that of **mIL2.2** (red line) and **mIL1.2** (blue line) due to its acrylate double bond.

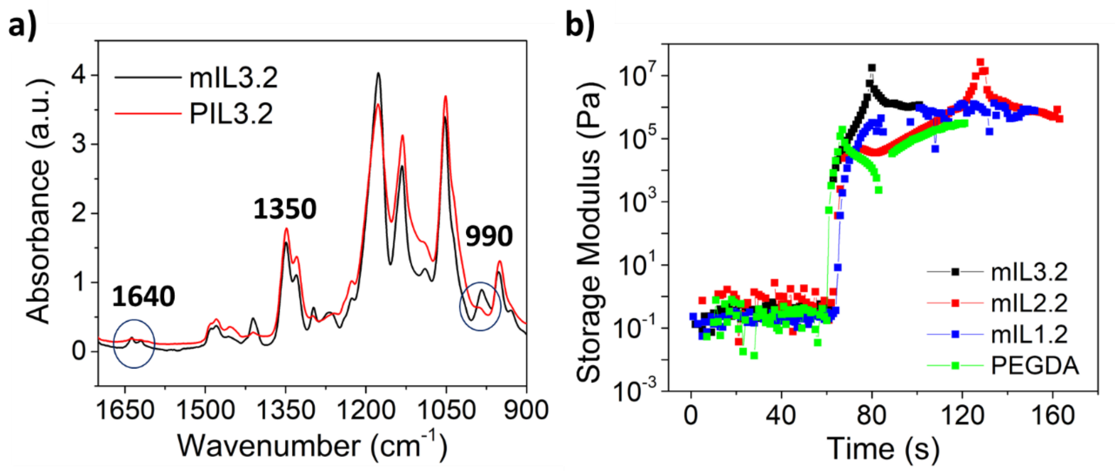

Figure 32. ***a)*** *FT-IR spectra before 3D-printing (**mIL3.2**) and after (**PIL3.2**), showing the disappearance of the C=C peaks (at 1640 cm^{-1} and 990 cm^{-1}) while the reference peak (1350 cm^{-1}) kept constant;* ***b)*** *Photorheology curves of the three monomers with PEGDA 575 (**mIL1.2, mIL2.2, mIL3.2**) compared with pure PEGDA 575 (**PEGDA**).*

The reactivity of **mIL3.2** was similar to that of the diacrylate groups of PEGDA (green line). In contrast imidazolium-based formulations, **mIL2.2** and **mIL1.2**, had a vinyl double bond which was slightly slower to initiate polymerisation as it can be seen from the delay time. The delay time before starting the photopolymerisation for **mIL3.2** was around 0.3 s while for **mIL2.2** and **mIL1.2** was more than 2 s. The storage modulus was similar between them, reaching a plateau around 10^5 Pascals which means that the polymerisation was completed at that point. However, great differences were found when measuring the monomeric formulations without cross-linker (**mIL1.4**, **mIL2.4**, **mIL3.4**), which presented higher delay times and much lower kinetics (related with the slope gradient) (*Figure 33*). This behaviour was expected since pure mIL formulations are less reactive, requiring longer time and more energy to polymerise. Indeed, the mILs without cross-linker were unable to manufacture solid 3D objects because the polymerisation was only partial as shows the polymeric conversion and the gel content of the films in *Table 3*.

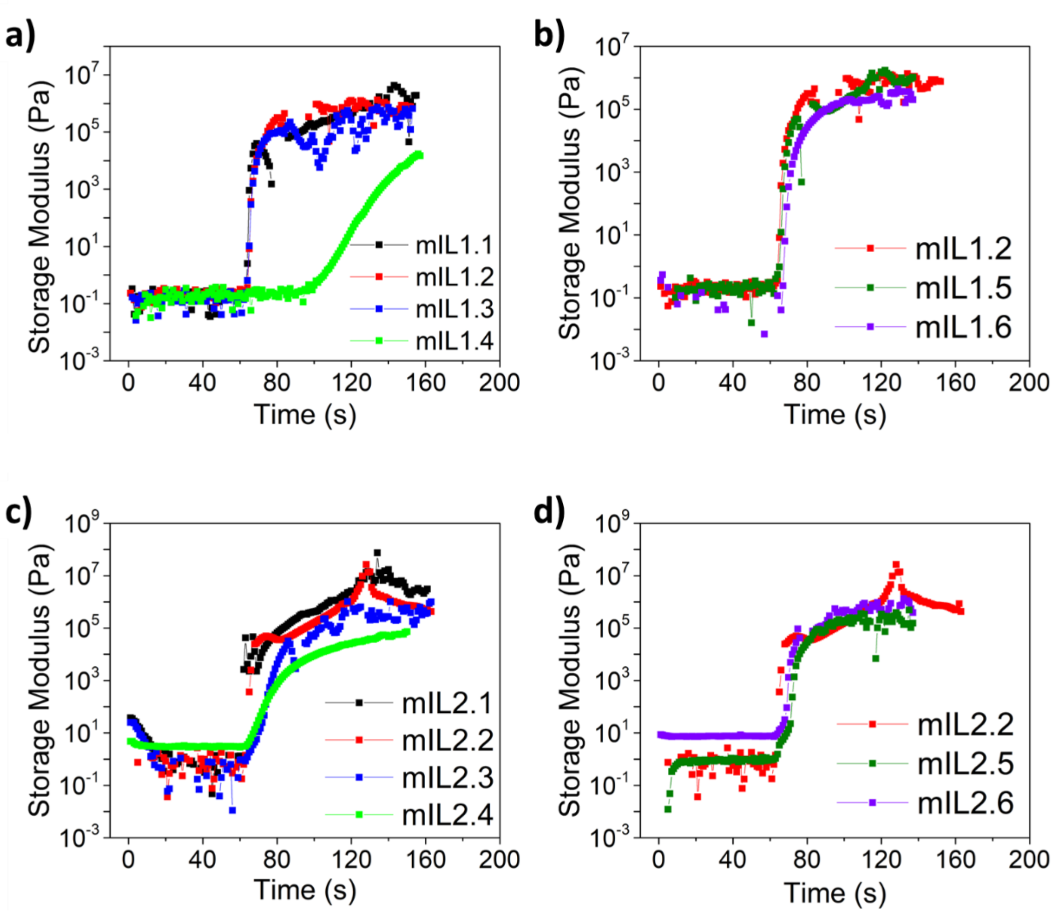

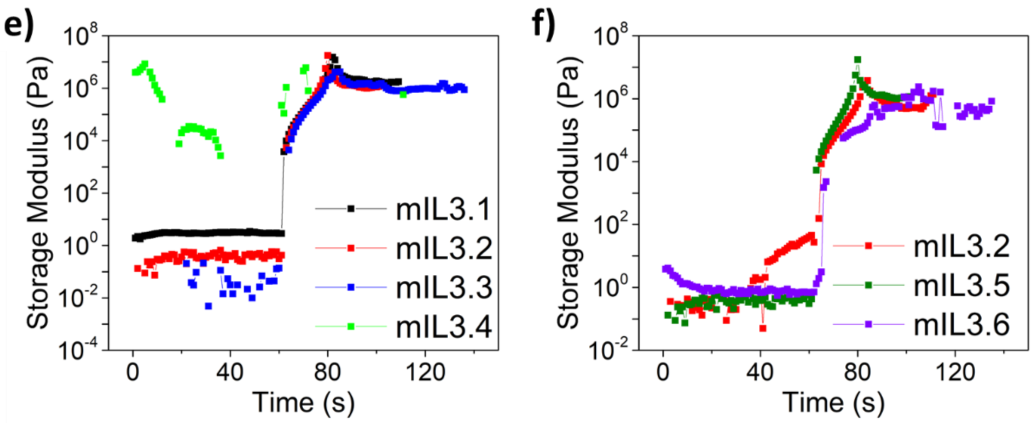

Figure 33. ***(a,c,e)*** *Photorheology spectra of different concentrations of mILX:PEGDA 575 and,* ***(b, d, f)*** *Formulations of 80 mol% of mILX with 20 mol% of PEGDA 575/250/700 . mIL1 corresponds to 1-butyl-3-vinylimidazolium bis(trifluoromethane)sulfonimide, mIL 2 to 1-(3-hydroxypropyl)-3-vinylimidazolium bis(trifluoromethane)sulfonimide and mIL3 is [2-(acryloyloxy)ethyl]trimethyl-ammonium bis(trifluoromethane)sulfonimide. Details about the formulations can be found in* Table 3.

The printing parameters were adjusted for each formulation to improve the resolutions of the printed parts (see *Table 4*). The main parameters modified were the exposure time of light per layer that depends on the reactivity of the formulations. All printings presented two different exposure times, one for the first layers and the other for the rest of the printing. Generally, the first printed layers need a longer light exposure time to ensure their attachment to the platform, for that reason those first layers are referred in the text as *burn-in* section. Other parameters like the light power which affects de kinetics, the separation and approach velocities, and the slides per layer are also remarkably important. The last one is a measure of vertical resolution and affects the quality and detail of the printed piece. A higher number of slides per layer usually results in better surface quality and more detail in the printed piece. The compositions were processed with an Asiga PICO2 DLP printer to manufacture complex and bespoke macroscopic devices, with tailored shapes and properties. By varying the ionic monomer concentration, the molecular weight of the cross-linker and the display images, precise 3D design and specific polymeric properties were achieved.

Table 4. *Printing parameters for each formulation.*

Entry	***PIL***	***Burn-in exposure time (s)***	***Exposure time (s)***	***Light power (mW/cm^2)***	***Velocity [1] (mm/s)***	***Slides per layer [2]***
1	PIL1.1	10	8	38	2	2
2	PIL1.2	14	12	38	2	2
3	PIL1.3	14	12	38	2	2
4	PIL1.5*	16	14	39	2	2
5	PIL1.6*	12	10	39	2	2
6	PIL2.1	5	3	35	4	1
7	PIL2.2	6	5	35	4	1
8	PIL2.3	7	5	39	4	1
9	PIL2.5*	6	3	38	4	1
10	PIL2.6*	8	6	38	4	1
11	PIL3.1	5	3	35	4	1
12	PIL3.2	5	4	35	4	1
13	PIL3.3	7	5	39	4	1
14	PIL3.5	6	3	38	4	1
15	PIL3.6	4	3	35	1	3

*Only small and flat pieces were 3D-printed. [1] "Velocity" includes separation and approach velocities of the build platform. [2] "Slides per layer" refers to the number of times that the sliding blade (located underneath the vat) moves to form a new layer in the printed piece. All samples were printed with *burn-in* thickness of 0.3 mm and layer thickness of 0.1 mm. All formulations prepared contained MR (0.1 wt%) to improve the printing accuracy.

All the printings were scanned by a 3D scanner to evaluate the fidelity of the printed part to the digital design. That equipment reported the resolution of the printings after comparing the scanned figures with the original CAD models (*Figure 34*).

Both mIL3 and mIL2 formulations could be printed with similar parameters, although their composition was quite different, since mIL3 was a cholinium monomer and mIL2 was an imidazolium. While the other imidazolium monomer mIL1 needed much more time and slides per layer in order to obtain good printings. Still, the resolution of both imidazole monomers was remarkably lower (with a standard deviation (σ) between the scan data and the reference model of 0.37 mm), probably due to the inferior reactivity of the vinyl groups from imidazolium in contrast to the acrylates from the cholinium ($\sigma = 0.20$ mm) (*Figure 35*).

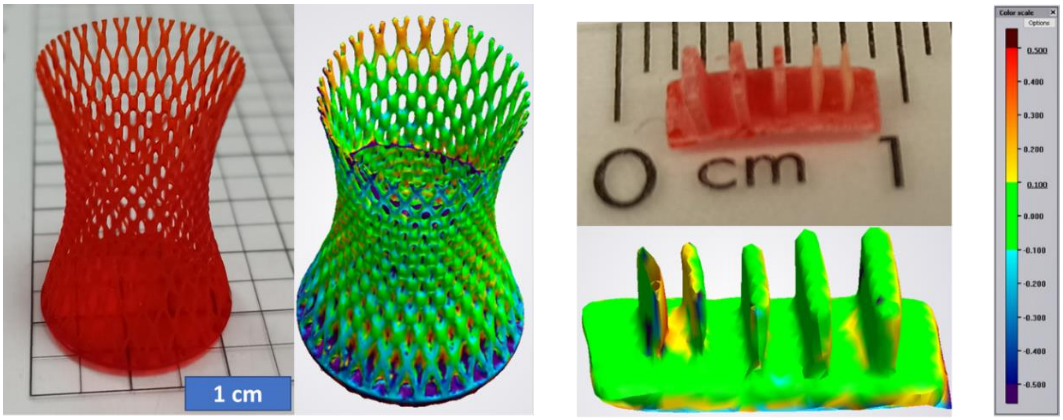

Figure 34. *3D-printed structures of **PIL3.2** and the evaluation of the printing resolution by comparing the STL file to the scanned image acquired from the printed parts. The part in the right shows columns with decreasing thickness from 500 to 50 µm. The printed part is accurately reproducing the original STL file, thus demonstrating a resolution of 50 µm in the printed parts.*

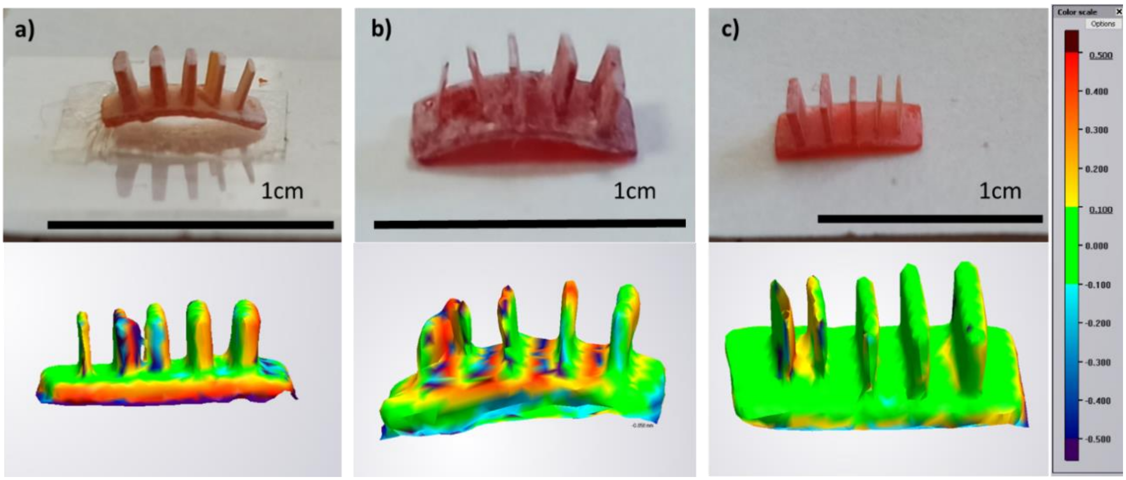

Figure 35. *Evaluation of 3D printing resolution with different formulations: **a) PIL1.2; b) PIL2.2; c) PIL3.2**.*

Likewise, formulations with PEGDA 250 and PEGDA 700 were not suitable for printing elaborated devices, only flat bases were properly printed. The parts were either too tightly cross-linked or not enough cross-linked, in both cases resulting in some deformation in the complex structures. For that reason, PEGDA 575 was chosen as the cross-linker in the future tests. Additionally, the printing resolution of formulations with 90 mol% of mIL was in general poor (σ ~0.45 mm). In contrast, formulations with 80 mol% of mIL presented really good printing resolutions (σ ~0.25 mm) (*Figure 36*).

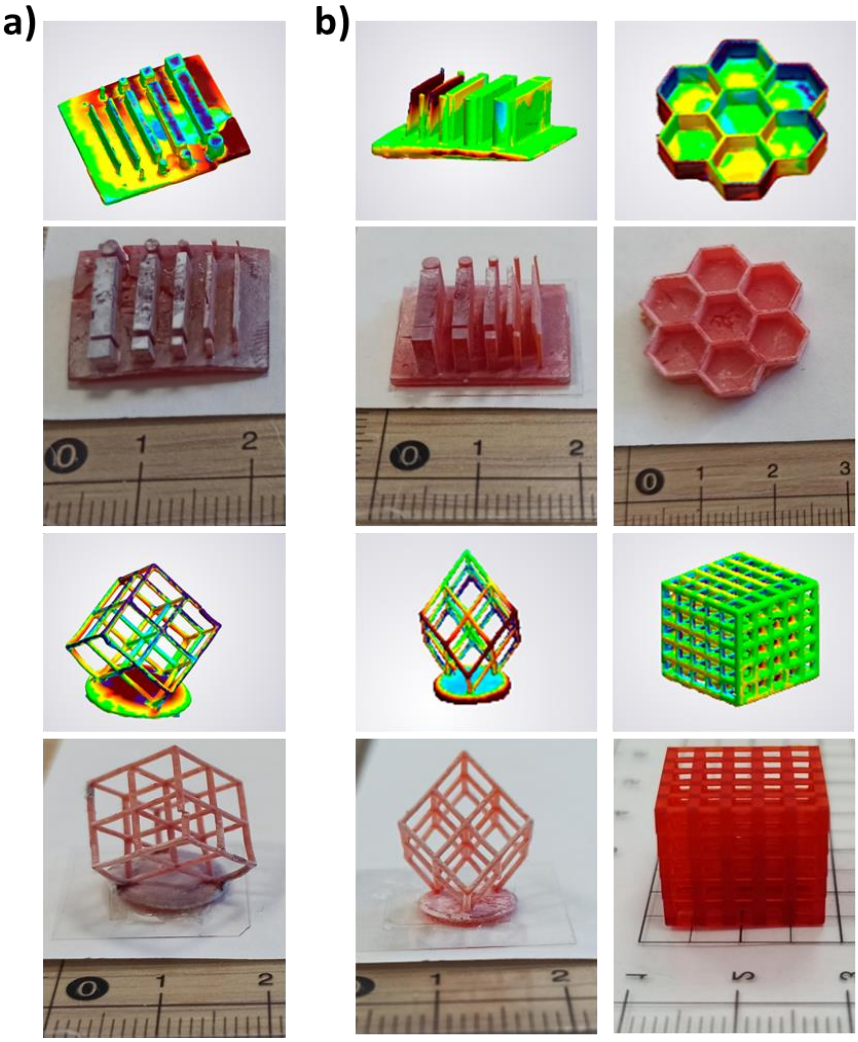

Figure 36. *3D-printed complex geometries and comparison of the scanned components to the original CAD model using* ***a) mIL2.2*** *formulation;* ***b) mIL3.2*** *formulation.*

2.4.4 Development of Biocompatible Formulations

The antimicrobial materials are a key point for developing medical devices, but for that purpose it is essential to prepare biocompatible materials.

In a preliminary test, we found that **PIL2.2**, which showed good antibacterial activity, also showed high toxicity (*Figure 37*). The incubation of Vero cells with **PIL2.2** resulted in an apoptotic state, a form of programmed cell death; while the cells with **Ag@PIL2.2** suffered necrosis, a form of traumatic cell death that results from acute cellular injury.

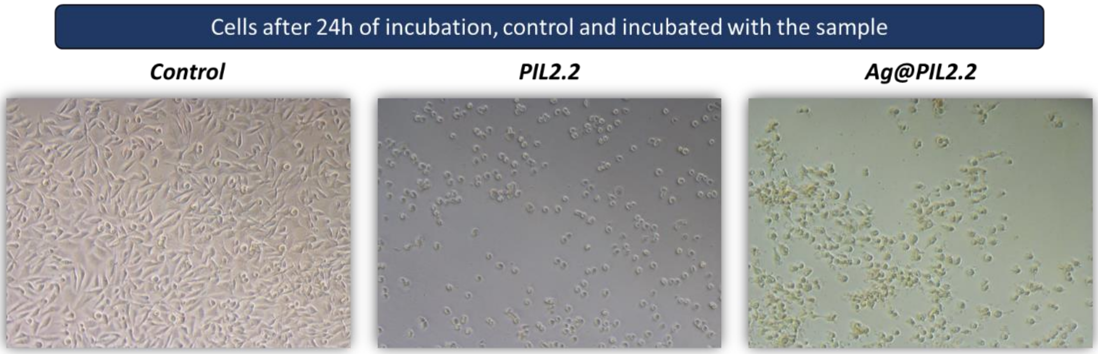

In the control wells (without sample) the **cells were live** and attached to the well surface

In the wells incubated with PIL films in the absence of Ag, the cells were in an **apoptotic** state, round-shaped and floating

In the wells incubated with the Ag-containing PIL films, the cells seem to have suffered **necrosis**

Figure 37. *Vero cells incubation without sample (control), with* ***PIL2.2*** *film and with* ***Ag@PIL2.2*** *film after 24 hours.*

A cell viability test was performed with different polymers using Vero cells (see the test description in **Section 2.6.5**). In contrast, **PIL1.2** and **PIL3.2** presented high viability. Therefore, the monomer employed was remarkably important in terms of biocompatibility. Additionally, the effect of the PI was also evaluated to find non-cytotoxic formulations. Three different PIs, -phenylbis(2,4,6-trimethylbenzoyl)phosphine oxide (BAPO), 2,2-dimethoxy-2-phenylacetophenone (DPAP) and 2-hydroxy-2-methylpropiophenone (HMPP)- were used and compared with TPO. The four photoinitiators were characterised by UV-Vis spectroscopy (*Figure 38*a). However, HMPP was unable to form robust films, even increasing the photopolymerising time to 40 minutes (*Figure 38*b).

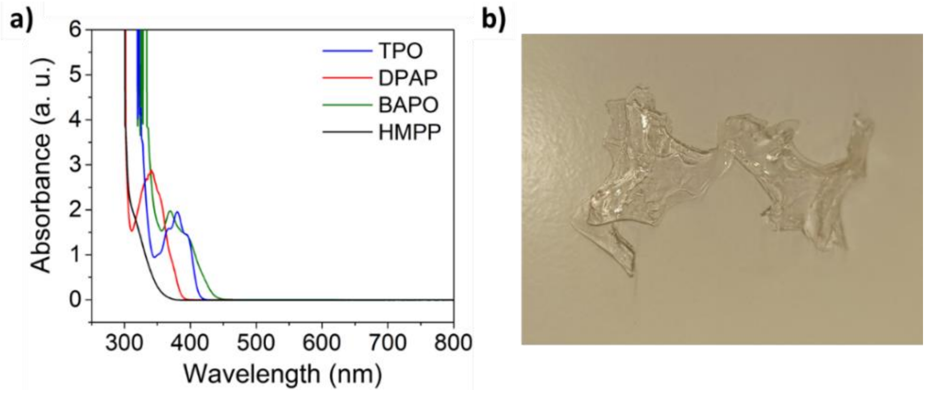

Figure 38. ***a)*** *UV-Vis spectra of the four PIs employed;* ***b) PIL3.2*** *film photopolymerised using HMPP as PI, under UV light at 40 ºC during 40 minutes. The resulting film was very fragile.*

The formulations containing BAPO reported the lowest viabilities. Meanwhile, the biocompatibility of DPAP and TPO formulations was notably superior. For instance, **PIL1.2** was photopolymerised using the three PIs, showing moderate and high viability with DPAP and TPO, respectively. Both components, mILs and PIs, played an important role for obtaining biocompatible PIL-based formulations, shown in *Figure 39*.

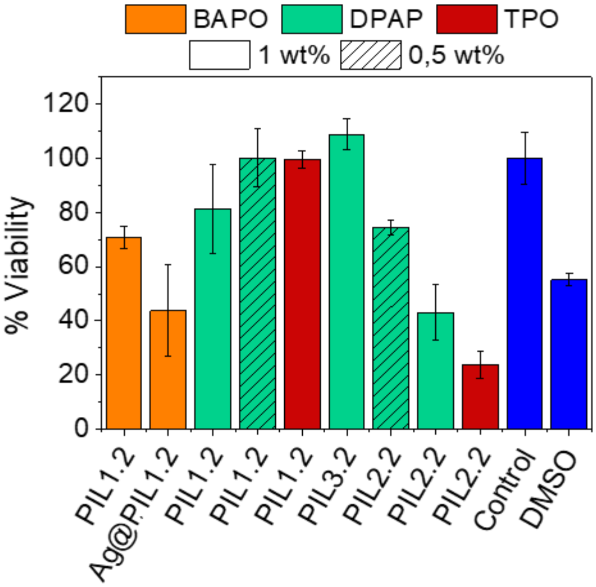

Figure 39. *Cell viability test using different formulations, changing the monomers (mIL1, mIL2, mIL3), the PI and the weight percentage of PIs. The control of the experiment was carried out using a highly biocompatible sample (Control) and dimethyl sulfoxide (DMSO) (blue) as a reference of a toxic environment for cells. All formulations were prepared using mIL (80 mol%) and PEGDA 575 (20 mol%).*

Likewise, the percentage of PI involved resulted to be another critical point. Different concentrations of PI were tested (0.5 wt%, 1 wt%), finding an enhanced viability using a lower concentration. For that reason, all films prepared in this and the following sections contained 0.5 wt% of PI, unless otherwise stated. Thereby, non-toxic films were obtained by choosing the adequate combination of monomeric ionic liquids, PI-type and concentration. In some cases, *e.g.* PIL3.2 shows a cell viability slightly larger than the control, which is not unusual in biocompatibility studies. This indicates that the cells are growing in a similar fashion to the control media.

Furthermore, a thorough washing protocol (WP) was developed to remove the unreactive and potential cytotoxic products (monomers and photoinitiator), thus it is another key factor for reducing material's toxicity. The protocol followed for washing all the bare films and **Ag@PIL** printings consisted in immersing them into a vial with ethanol (EtOH, 96 %), keep them in ultrasounds during 1 hour and then keeping them in EtOH one day. The washing was also performed with isopropanol (IPA), however ethanol removed better the excess of PI as it can be seen in *Figure 40*a-c. In the *Figure 40*d-f we can observe that the silver plasmon did not disappear after the washing step, hence the parts were not damaged.

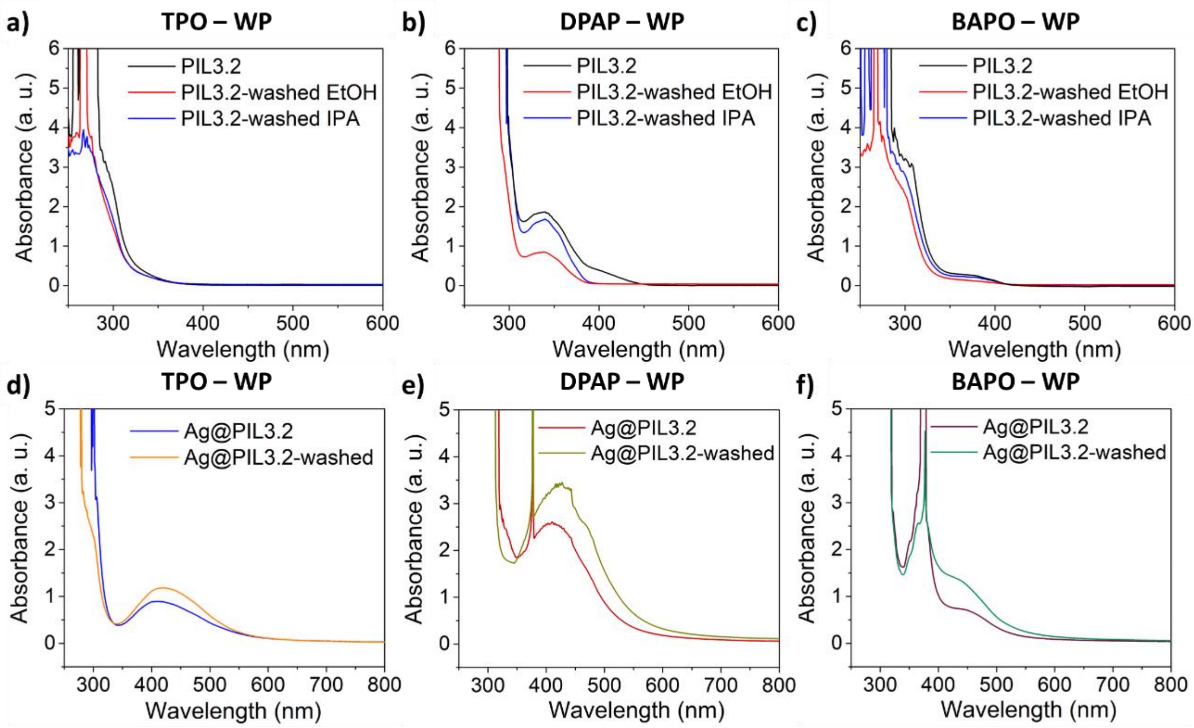

Figure 40. *UV-Vis spectra before and after washing bare* ***PIL3.2*** *using different PIs following same protocol with EtOH and IPA,* ***a)*** *TPO;* ***b)*** *DPAP;* ***c)*** *BAPO; and UV-Vis spectra before and after washing with EtOH* ***Ag@PIL3.2*** *films using different PIs,* ***d)*** *TPO;* ***e)*** *DPAP;* ***f)*** *BAPO.*

The washing was done for films using the three different PIs (TPO, DPAP and BAPO). Similar results were obtained for all of them, demonstrating that there was no leaching effect of mIL, PI or AgNPs, so all three PIs were able to encapsulate the silver. The thickness of the films was optimised as well, since too thick films saturated the signal in the UV-Vis spectra. According to *Figure 41*, the optimum thickness was set between 1 mm and 0.5 mm.

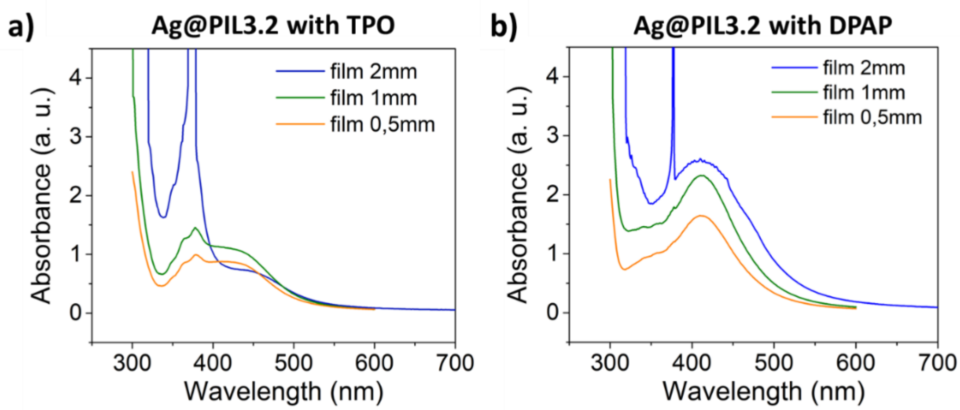

Figure 41. *UV-Vis spectra of* ***Ag@PIL3.2*** *films with different thickness,* ***a)*** *using TPO as PI;* ***b)*** *using DPAP as PI. In both cases, the samples with a thickness of 2 mm presented a saturated band that corresponds to the PI.*

2.4.5 PIL Formulations Containing Copper

Afterwards, the capacity of the monomeric ionic liquids to stabilise other metallic salts was evaluated. Silver nanoparticles are not very environmentally friendly, so we changed silver by another more sustainable metal.[215] The natural antimicrobial activity of copper, copper oxide (CuO) and copper alloys is well established.[229] Some studies demonstrated that the addition of copper nanoparticles to polymers used in AM was beneficial for developing medical devices, enhancing the antimicrobial properties and avoiding bacterial growth.[230] Polymers are widely used for medical device prototyping, so the improved antimicrobial performance after copper addition may provide an alternative to rapidly manufacture tailored medical devices and parts during a disaster or pandemic.[231]

The first step was to find a suitable copper salt that could be solubilised into our formulations without the use of any additional solvent or additive, taking advantage of the solvent properties of the PILs. Different copper-based salts were tested, finding that not all of them were properly solubilised in our formulations. The tested salts were: copper iodide, copper dichloride, copper thiocyanate, copper acetate and copper dinitrate. The latter one ($Cu(NO_3)_2 \cdot 3H_2O$) was the unique salt that was solubilised into the mIL:PEGDA mixture. The formulations were prepared using PEGDA 575, in a molar relation 80:20 mol/mol (mIL:PEGDA), which was found to be the formulation with the highest printing resolution, shown in **Section 2.4.3**. TPO was then added in an amount of 0.5 wt%, as this was the amount determined in **Section 2.4.4**. Curiously, we found that the delay times of imidazolium-based formulations were reduced after adding metallic salts as shows *Figure 42* (red and blue spectra).

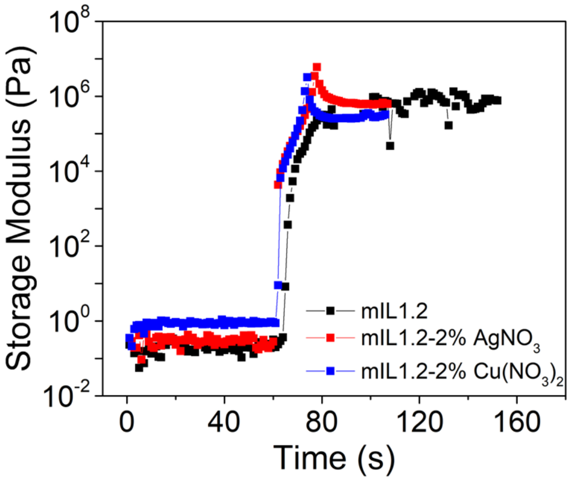

Figure 42. *Photorheology spectra of* ***mIL1.2*** *formulation (black) and same formulation with silver (red) and copper (blue).*

The blue colour from the copper salt changed during the film preparation, resulting a green photopolymer. That change in colour may be due to ambient conditions (moisture or oxygen), promoting a change in the copper salt formulation, from $Cu(NO_3)_2 \cdot 3H_2O$ to another specie. According to the literature, is possible to generate $Cu_2(OH)_3NO_3$, which is a green solid, by heating (> 160 °C) or submitting the $Cu(NO_3)_2 \cdot 3H_2O$ to basic conditions.[232] The resulting substance could be a mixture of the both species and it would explain the colour changes. The copper complex formed will be studied below. However, this change in the mixture colour did not always occur (*Figure 43*a). Despite the different colours of the film, no big changes in the UV-Vis spectrum were observed (*Figure 43*b).

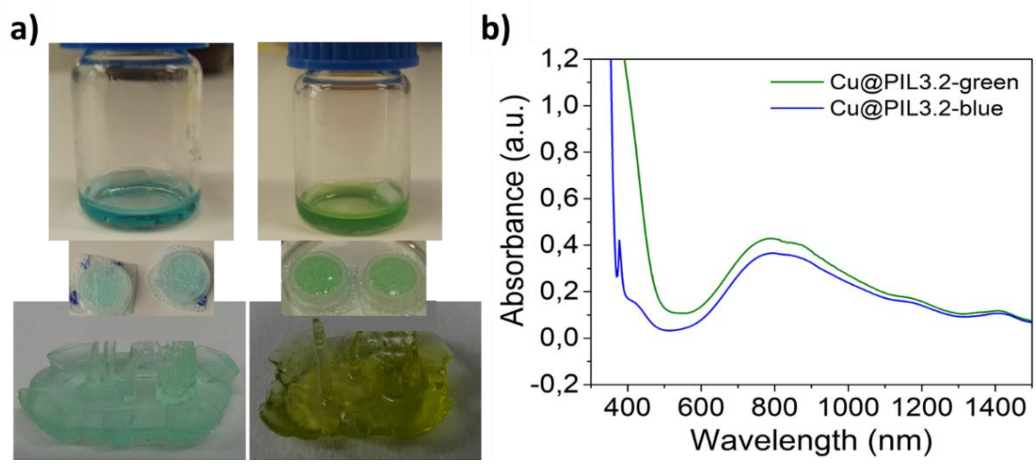

Figure 43. ***a)*** *(Left) Blue colour of* ***Cu@PIL3.2*** *formulation, (right) green colour of* ***Cu@PIL3.2*** *formulation;* ***b)*** *UV-Vis spectra of the blue and the green films.*

Both mIL1 and mIL3 were capable to encapsulate the copper species, since a characteristic band appeared in the UV-Vis spectra (*Figure 44*a). In both cases, the band had a maximum at 787 nm, which is in agreement with the absorption band of $Cu(NO_3)_2$ that appears in the range of 650-950 nm.[233] Moreover, the three photoinitiators (TPO, DPAP and BAPO) were capable to encapsulate copper during the photopolymerisation (*Figure 44*b).

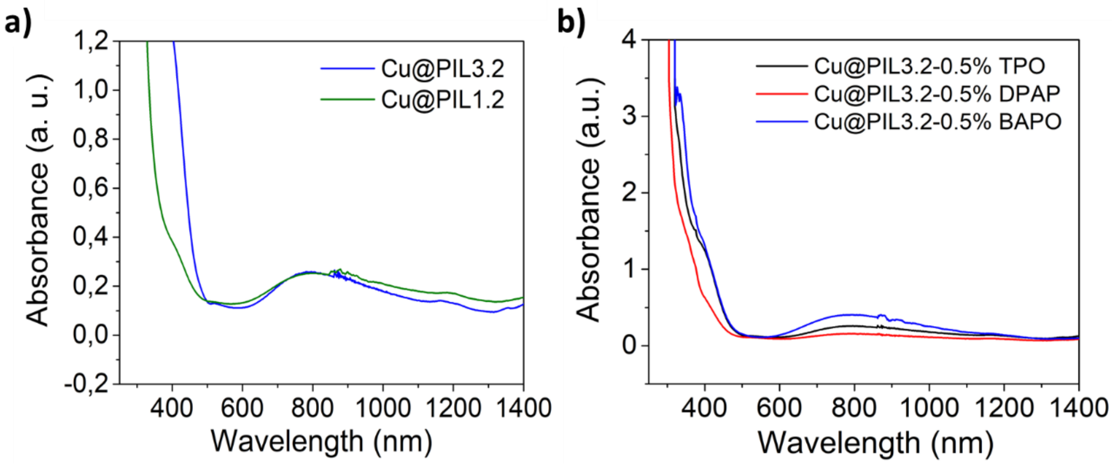

Figure 44. *UV-Vis spectra of* ***a)*** *different PIL films with 2 wt% of copper and TPO (0.5 wt%);* ***b) PIL3.2****-based films with 2 wt% of copper and different PIs (0.5 wt%).*

Different concentrations of copper salt (1 and 2 wt%) were tested using TPO (*Figure 45*a) and DPAP (*Figure 45*b). As expected, the copper band was significantly superior using 2 wt%. On the other hand, copper presents less bactericidal effect than silver,[229b] thus we decided to use 2 wt% of copper concentration in all our tests. An aging study of Cu-based films was also carried out. An experiment similar to that conducted with the silver compounds was performed for the copper samples, testing a **Cu@PIL3.2** film under ambient light (*Figure 45*c) and under dark conditions (*Figure 45*d). The copper band was not modified when the film was kept under dark conditions, however it changed under ambient light, meaning that the light had an impact in the copper particles.

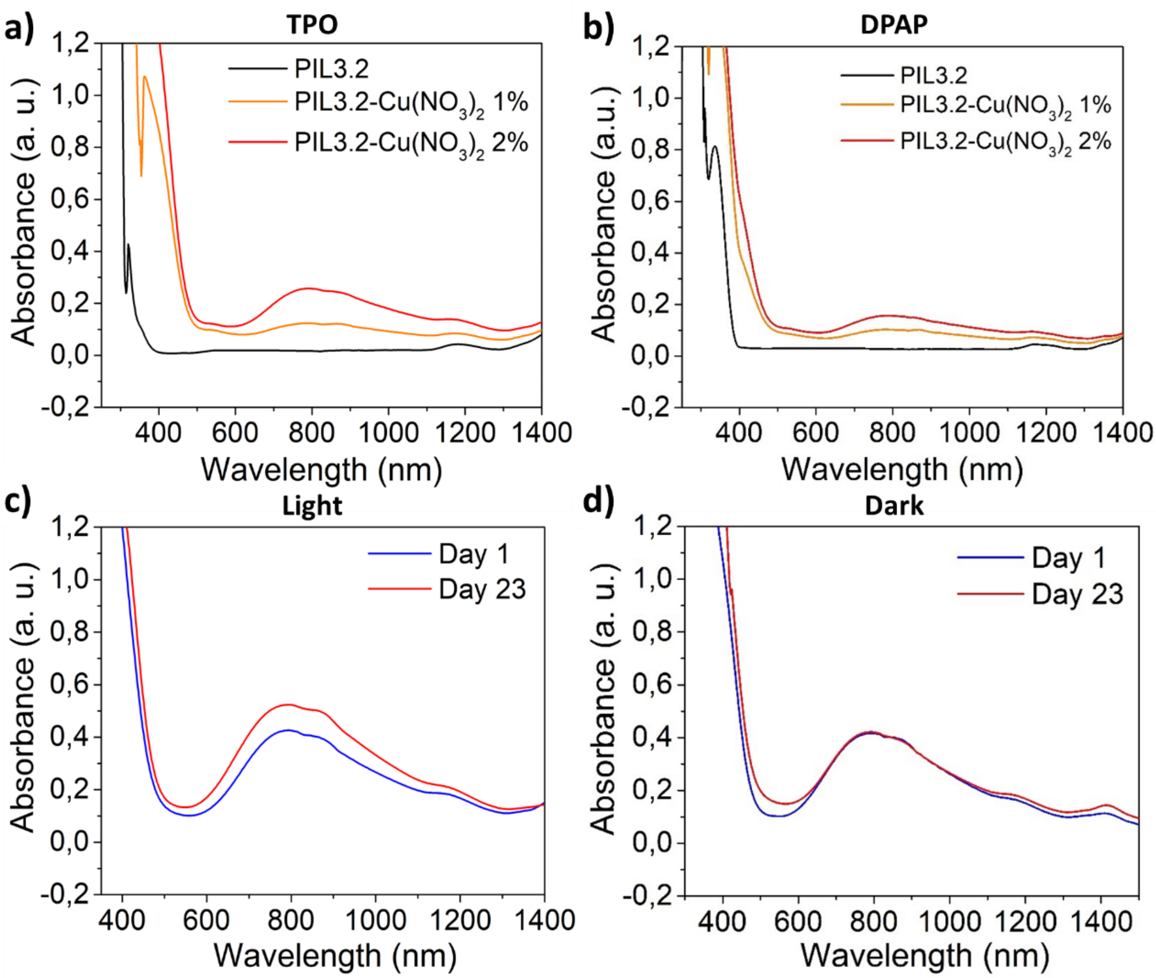

Figure 45. *UV-Vis spectra of* ***a)*** *TPO-based* ***PIL3.2*** *films with different concentrations of Cu(NO$_3$)$_2$ (1 wt% and 2 wt%);* ***b)*** *DPAP-based* ***PIL3.2*** *films with different concentrations of Cu(NO$_3$)$_2$ (1 wt% and 2 wt%), and* ***PIL3.2*** *film with copper (2 wt%) stored* ***c)*** *under ambient light during 23 days, and* ***d)*** *under dark conditions during 23 days, showing no change in the copper band.*

Moreover, after 3D-printing, the films already presented a signal belonging to the copper (black spectrum). It could be that the printing process photoreduced the copper simultaneously. In order to analyse this effect in detail, we compared the copper salt signal (blue spectrum) with the one of our samples, before and after 3D-printing, finding insignificant changes (*Figure 46*). Therefore, we can suggest that the copper was not reduced to Cu (0) nanoparticles as it happened with silver.

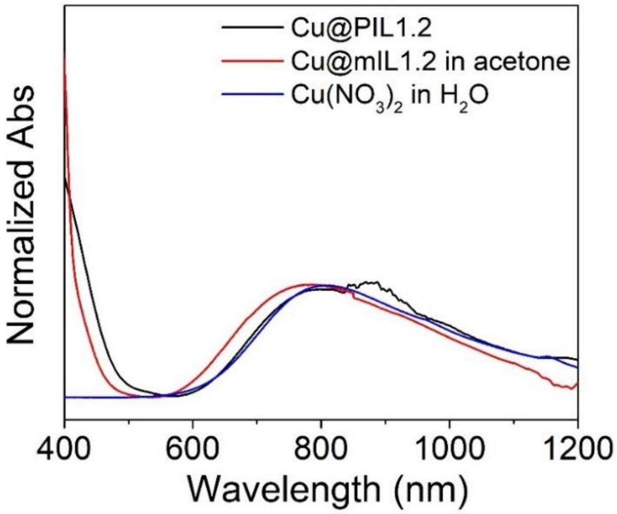

Figure 46. *Normalised UV-Vis spectra of* ***Cu@PIL1.2*** *film (black), the photopolymer (red) and pure copper salt (blue).*

In order to improve the biocompatibility of the copper-based films, the above-mentioned washing protocol (WP) with EtOH was performed. Nevertheless, **Cu@PIL** samples needed a less aggressive WP, otherwise the films presented significantly leaching of copper from the film. This effect was confirmed by UV-Vis transmission spectroscopy, showing the disappearance of the copper characteristic signal, independently of the PI used (*Figure 47*a-c) as well as the mIL employed (*Figure 47*d). For that reason, the WP for **Cu@PIL** samples was changed and consisted in immersing them in ethanol during 1 hour to remove non-reactive monomers and excess PI. This new protocol did not damage the films prepared with TPO, since the copper band was not modified as shows *Figure 47*e. However, the films photopolymerised using DPAP still presented some leaching during the washing. In that case, a yellowish solution appeared after the WP due to the leaching of the copper, *Figure*

*47*f. This is indicative that the copper was not properly integrated into DPAP-based films. For this reason, this PI was not employed in subsequent studies.

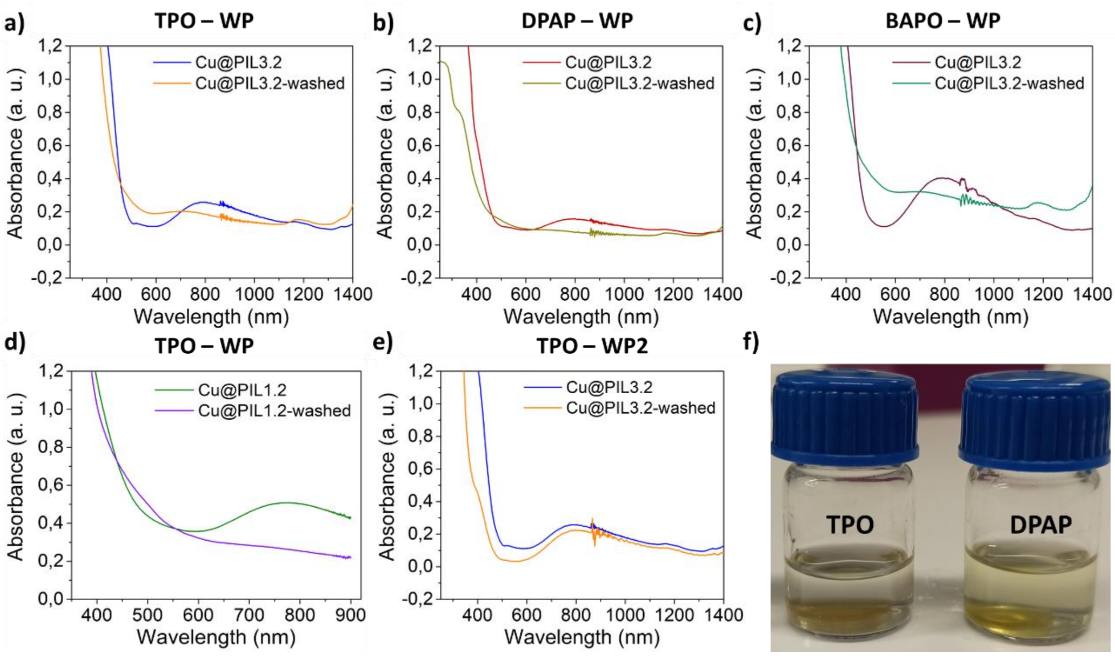

Figure 47. *UV-Vis spectra before and after washing **Cu@PIL3.2** films using different PIs following the first washing protocol (immersing films in EtOH 1 h in ultrasounds and then kept them in EtOH one day), **a)** TPO; **b)** DPAP; **c)** BAPO; **d)** UV-Vis spectra before and after washing **Cu@PIL1.2** with TPO following the first washing protocol; **e)** UV-Vis spectra before and after washing **Cu@PIL3.2** with TPO following the second washing protocol (immersing film in EtOH during 1 hour); **f)** Different films immersed in EtOH during 1 hour, (left) **Cu@PIL3.2** film with TPO and (right) **Cu@PIL3.2** film with DPAP.*

The presence of copper into the films was further confirmed by characterisation with XPS. *Figure 48* exhibits the high-resolution (HR) XPS Cu 2p and Cu LMM Auger spectra of the **Cu@PIL1.2** film, where a doublet located at ~932/952 eV was obtained. However, the typical satellite of Cu (II) was not identified. The doublet identified is characteristic of $Cu(OH)_3NO_3$ species,[234] while it does not appear in the XPS of $Cu(NO_3)_2$ found in the literature.[235] The spectra were calibrated using the energy reference of the C 1s (C-C) at 285 eV.

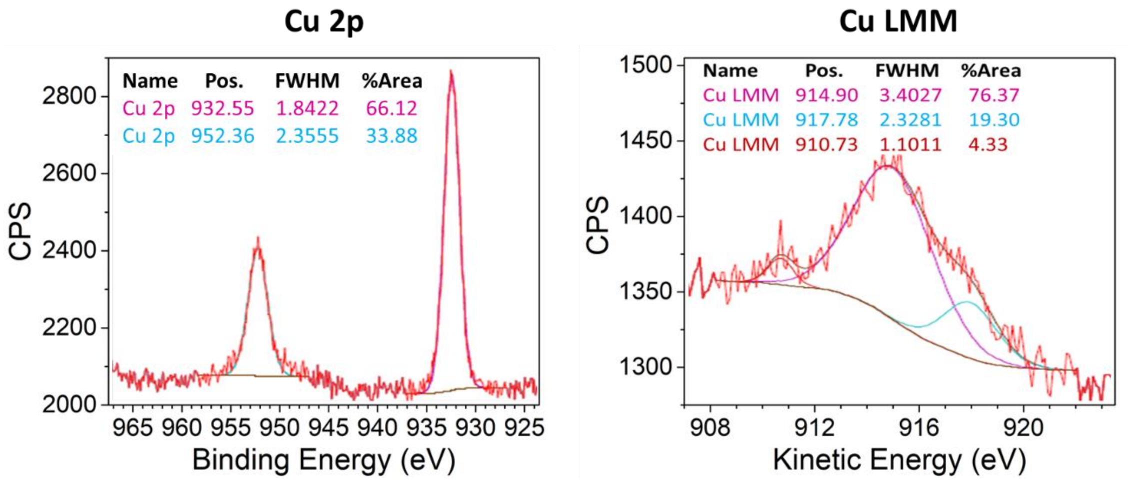

Figure 48. *HR-XPS of Cu 2p and Cu LMM Auger spectra for **Cu@PIL1.2** sample.*

The copper in **PIL1.2** film could be a mixture of Cu (I) and Cu (II), explaining the absence of Cu (II) satellites. According to similar XPS results found in the literature, copper (I) could form a complex with the C2 of the imidazolium group.[236] Still, the copper contained in our films seemed to be very reactive and unstable, so probably we had a mixture of copper species. This factor made difficult to identify the copper state by FT-IR and Raman spectroscopy, where we could not identify any characteristic band (*Figure 49*).

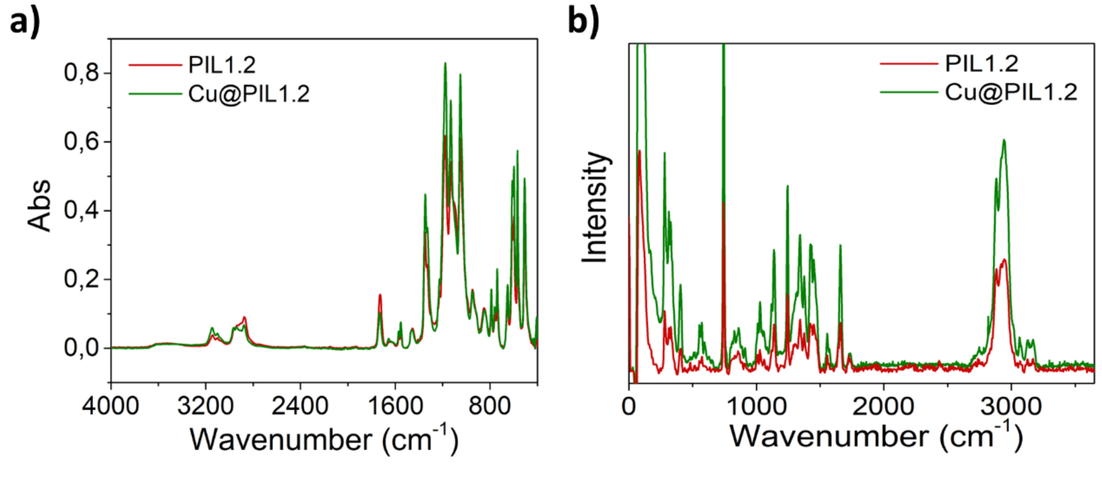

Figure 49. ***a)** FT-IR spectra, and **b)** Raman spectra of **PIL1.2** and **Cu@PIL1.2** films.*

The UV-Vis spectrum showed the expected absorption peak centred at λ ≈ 750 nm attributed to copper moieties ($Cu(NO_3)_2$ or $Cu(OH)_3NO_3$). PIL-based formulation may not be a strongly stabilising system for the copper species formed. This is consistent with the copper leaching observed during the washing of Cu-based films due to poor copper encapsulation. The conversion from $Cu(OH)_3NO_3$ to CuO after heating at 160 °C is well-reported.[232a, 237] Thus we treated our copper samples at 160 °C for 30 min (**Cu@PIL1.2-h**), finding that the colour of the films changed from green to a dark brownish appearance (*Figure 50*a). Whereas, neither our pristine formulation **PIL1.2** nor pure $Cu(NO_3)_2$ changed their colour to dark brown after heating. This indicates that a reaction of the copper species occurred in presence of PIL formulation. However, XPS analysis was inconclusive since copper signals were not detected after heating (*Table 5*). Copper species may have migrated from the surface to the core of the sample due to a possible encapsulation effect of the monomer after the thermal treatment, becoming undetectable by XPS.

Table 5. *Chemical atomic composition of **PIL1.2** with copper (2 wt%) and the film with copper heated at 160 °C (**Cu@PIL1.2-h**).*

Sample	C-(C,H) (at.%)	C-N, C-O (at.%)	(C=O)-O-C, C-S (at.%)	C=O (at.%)	(C=O)-O-C (at.%)	Cu^{2+} (at.%)	C-N (at.%)	C-F (at.%)
Cu@PIL1.2	14.83	8.10	18.13	1.10	1.08	0.18	2.87	17.74
Cu@PIL1.2-h	13.06	18.04	7.68	0.77	0.86	-	3.25	21.37

In both samples C 1s have the same chemical species, however the intensity of **C**-N / **C**-O and (C=O)-**O**-C / **C**-S species is evidently different, this could be due to the encapsulation after the thermal treatment.

UV-Vis analysis was performed after heating the simples at different temperatures. In *Figure 50*b, it can be seen the absorption peak features for the CuO (at 430 nm) in the sample heated at 100 °C (blue spectrum). In the rest of the samples, that band was not so visible, since the absorption of species in the UV region seems to saturate the signal observed. The more heated the films were, the more yellowish/brownish they appeared (*Figure 50*c). That must be the reason why the signal started to be saturated around 450 nm, where compounds with yellow colour absorbs. The film heated at 100 °C presented lower absorption and thus, the signal was less saturated. In this case, a convoluted band attributed to CuO was observed. Thinnest films could avoid saturation but it was not possible to prepare thinner films consistently. Furthermore, the characteristic signal of CuO is a band of low absorption.[238]

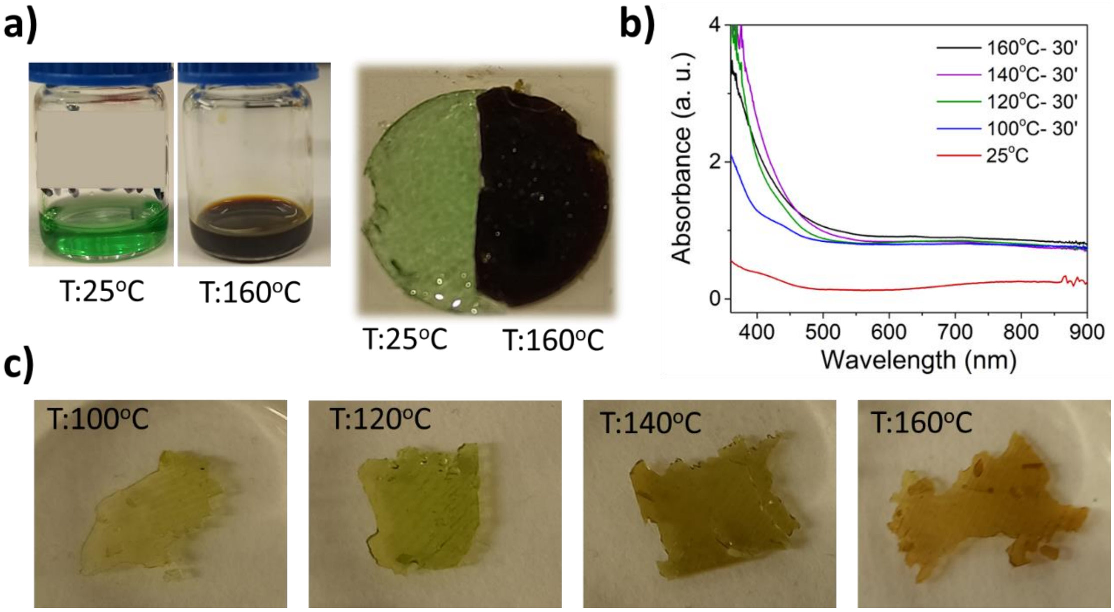

Figure 50. *a)* ***Cu@PIL1.2*** *formulation at 25 and 160 °C;* ***b)*** *UV-Vis spectra of* ***Cu@PIL1.2*** *film heated at different temperatures;* ***c)*** *Colour of the films after heating at different temperatures.*

After heating the samples for 30 min at 160 °C, the resulting copper species seemed better stabilised than untreated samples, probably due to the formation of copper nanoparticles, since no leaching was observed during the washing process. The formation of the nanoparticles was confirmed by TEM (*Figure 51*). As a result, the antimicrobial activity also changed after treating the samples, finding an enhanced antibacterial effect for the **Cu@PIL1.2-h** films (described below).

In addition, copper and silver-based films cured by heating them at 160 °C presented a higher Tg. **Ag@PIL3.2-h** film had a Tg more than 10 °C higher than the Tg of the bare film (it increased from 24 °C to 36 °C). While, the Tg of the film **PIL1.2** changed from -14 °C to 14 °C after adding copper and heating. The Tg of the bare polymers can be seen in **Section 2.4.3**, *Table 3*. Probably, those changes are attributed to the nanoparticles aggregation which contribute to modifying the mechanical properties of polymeric matrices.

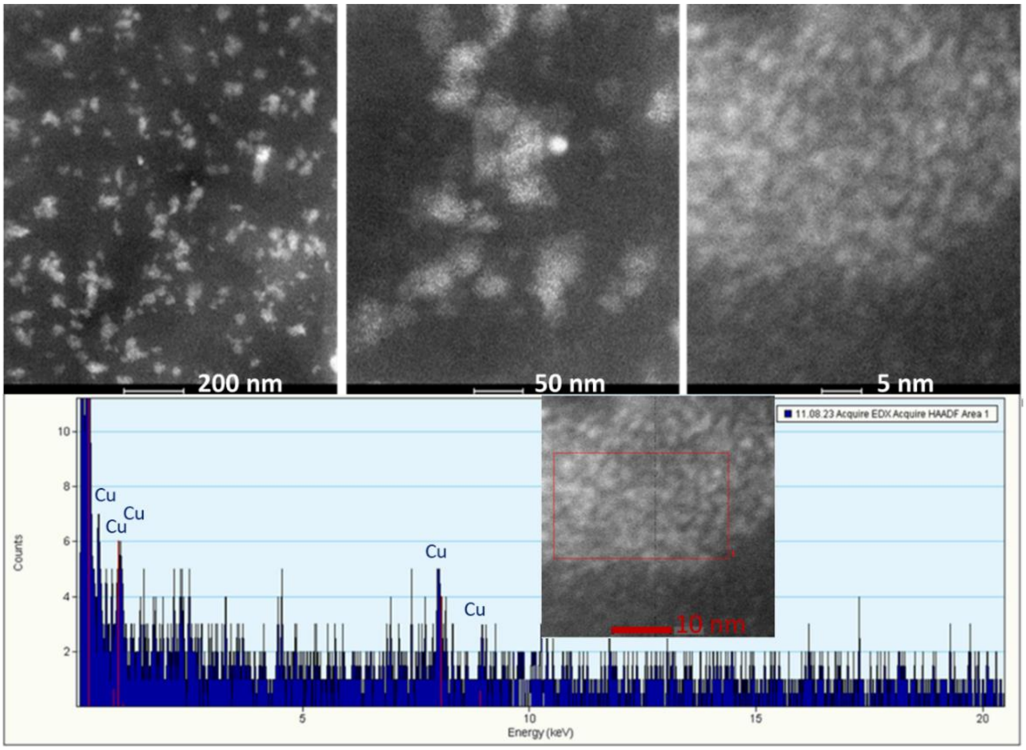

Figure 51. *TEM images of a* ***Cu@PIL1.2-h*** *sample.*

Antimicrobial Studies

The antimicrobial activity of **Cu@PIL** materials especially formulated for AM was evaluated by the *Instituto de Ciencia de Materiales de Aragón*, following the same procedure previously described in **Section 2.4.2**.

The antimicrobial analysis was mainly focused on **Cu@PIL1.2** films, since **PIL1.2** formulation had reported high biocompatibility and antimicrobial activity. Despite having high cell viability, **PIL3.2** films were found to have a poor antimicrobial activity, and **PIL2.2**-based films were fairly toxic. The bactericidal properties of the Cu based films before (**Cu@PIL1.2**) and after thermal treatment at 160 ºC (**Cu@PIL1.2-h**) were studied against non-pathogenic *E. coli* and *B. subtilis* in solution, using a positive and a negative control (*Figure 52*a). All the films were washed for 1 hour in a 24 well-plate with 1 mL of EtOH before being tested. After the washing step, the samples were dried in a clean well inside a laminar flow cabinet and then placed in a new 24-well plate. The bacterial growth in cell culture media in the presence of the films was monitored by optical density. **Cu@PIL1.2-h** presented the highest degree of inhibition after 24 hours of incubation due to the presence of copper nanoparticles. This effect was more remarkable for *E. coli* strains, although both samples, **Cu@PIL1.2** and **Cu@PIL1.2-h**, showed a very large variability in the results. The wide variation in performance makes it difficult to draw a definitive conclusion about the effect on this strain. On the other hand, highly reproducible results were obtained against *B. subtilis* with both samples. In this case, the antimicrobial performance was similar for the films **Cu@PIL1.2** and **Cu@PIL1.2-h**, both showing moderate activity, resulting in a reduction of around 70 %.

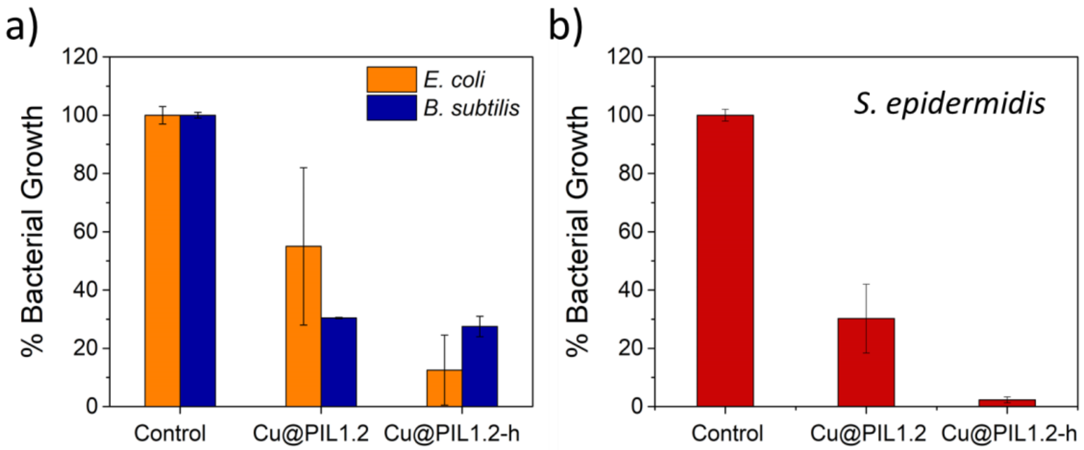

Figure 52. *Bacterial cell viability of* ***a)*** *E. coli and B. subtilis and* ***b)*** *S. epidermidis, incubated with* *Cu@PIL1.2* *and* *Cu@PIL1.2-h* *vs the control experiment.*

Additionally, in order to exploit the biocompatibility of the PIL materials for medical devices, a skin strain *Staphylococcus epidermidis* (*S. epidermidis*) was also evaluated (Figure 52b). *S. epidermidis* is a Gram-positive bacterium that is commonly found on the skin and in the nasal passages of humans, without causing harm.[239] However, in certain situations, this bacterium can cause infections that are acquired in a healthcare setting. These infections can include skin and soft tissue infections, wound infections, and bloodstream infections. It has been reported to be a frequent colonizer of indwelling medical devices, such as catheters, prosthetic joints and heart valves, where it can form biofilms. Still, *S. epidermidis* is considered to be less resistant to antibiotics than some other bacteria, owing to its structure.[240] In our study, **Cu@PIL1.2-h** samples repressed the growth of that strain in liquid media outstandingly (98 %). This is an extremely efficient outcome, with high reproducibility and reliability. In contrast, **Cu@PIL1.2** presented a degree of inhibition of around 70 % with higher variability in the results. The differences in the antimicrobial activity of the two copper samples can be explained by the rearrangement of the copper after being treated at 160 ºC. The proper stabilisation of the copper promotes the formation of nanoparticles what makes the film more antibacterially active.

In summary, **Cu@PIL1.2** only displayed bacteriostatic effect against *S. epidermidis*, meaning that the sample was able to partially inhibit the bacterial growth, but could not kill the bacteria; while **Cu@PIL1.2-h** PILs had a bactericide effect on *S. epidermidis*.

2.4.6 3D-Printed Medical Demonstrator

Finally, with the goal to fabricate a customised medical device with antimicrobial and biocompatible properties, a medical stent was 3D-printed as a proof-of-concept.

In a first study, the stent was manufactured using a formulation based on **PIL3.2** owing to its good printability shown in **Section 2.4.3**. **Cu@PIL3.2** stents were successfully 3D-printed at high resolution using a MSLA printer. The printing parameters needed to be optimised since the addition of copper modified the polymerisation time. As shows Figure 53, the exposure time was enhanced until obtaining the complete stent.

Figure 53. *Evolution of **Cu@PIL3.2** 3D-printed stent modifying the exposure time.*

The stent was properly printed with and without copper. The resolution of the stent based on **PIL3.2** without copper was quite low with a variance between the scan data and the reference model of 0.2 mm^2 and a standard deviation (σ) of 0.48 mm (Figure 54a). The printing resolution was notably enhanced after adding methyl red to the formulation, reporting a variance of 0.05 mm^2 and σ = 0.23 mm (Figure 54b). The addition of copper also helped to improve printing accuracy (σ = 0.21 mm) (Figure 54c). Nevertheless, adding MR to the copper-based formulation was counter-productive, since the resolution of the stent decreased (σ = 0.50 mm) (*Figure 54*d). We can suggest that this effect may be produced because both elements (MR and copper) reduce the reactivity of the mixture and the photopolymer colour was dark, hindering the focusing of light on the layer that was being printed. Therefore, that formulations needed more time to photopolymerise, and the light penetration was lower, which affected the printing quality.

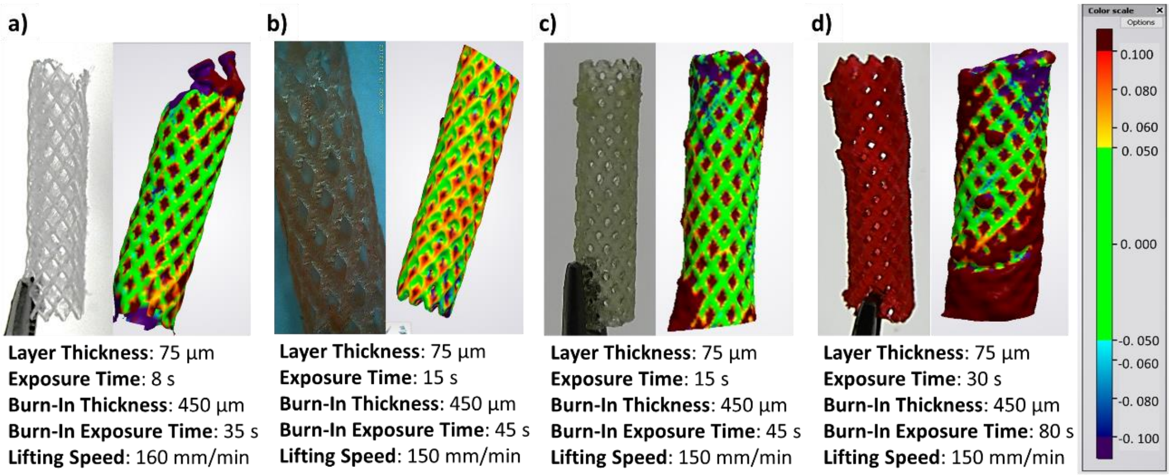

a)
Layer Thickness: 75 µm
Exposure Time: 8 s
Burn-In Thickness: 450 µm
Burn-In Exposure Time: 35 s
Lifting Speed: 160 mm/min

b)
Layer Thickness: 75 µm
Exposure Time: 15 s
Burn-In Thickness: 450 µm
Burn-In Exposure Time: 45 s
Lifting Speed: 150 mm/min

c)
Layer Thickness: 75 µm
Exposure Time: 15 s
Burn-In Thickness: 450 µm
Burn-In Exposure Time: 45 s
Lifting Speed: 150 mm/min

d)
Layer Thickness: 75 µm
Exposure Time: 30 s
Burn-In Thickness: 450 µm
Burn-In Exposure Time: 80 s
Lifting Speed: 150 mm/min

Figure 54. *Stents of 3 mm of diameter using different formulations,* ***a)*** *PIL3.2;* ***b)*** *Cu@PIL3.2;* ***c)*** *PIL3.2 with MR (0.1 wt%);* ***d) Cu@PIL3.2*** *with MR (0.1 wt%).*

The microscopic images obtained for the different stents show the impressive detail of the printings *Figure 55*a, b. Furthermore, it was possible to print a **Cu@PIL3.2** stent with the size halved at very high precision, with an error <5 % (calculated from the difference in the main dimensions set in the CAD file compared to optical microscopic images of the printed part) (*Figure 55*c-e).

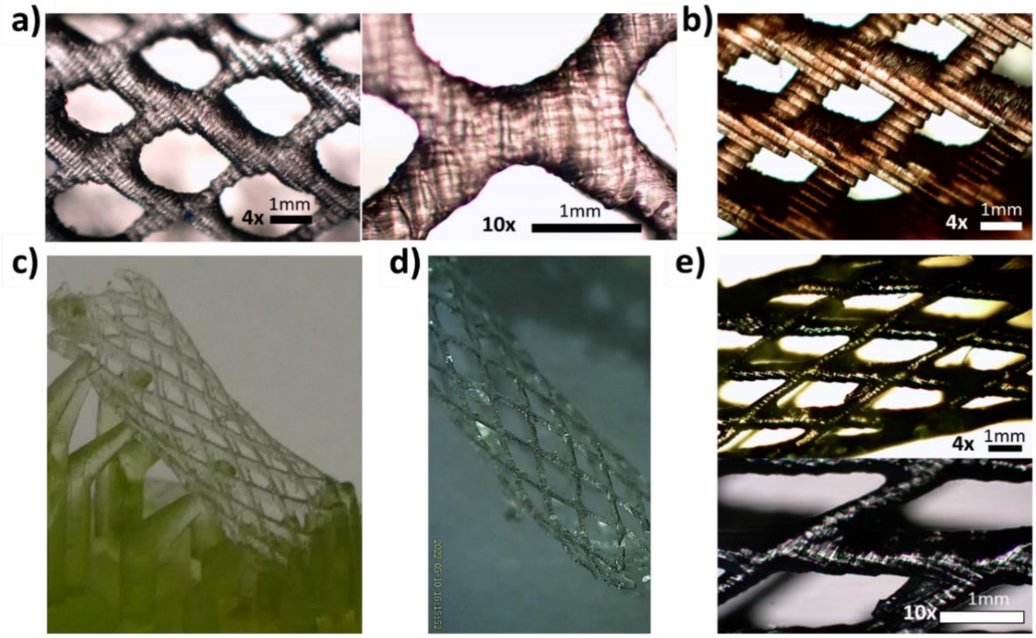

Figure 55. *Microscopic images of **a)** a **Cu@PIL3.2** stent; **b)** a **PIL3.2** stent with MR; **c)** a **Cu@PIL3.2** stent with the size reduced by half (1.5 mm of diameter); **d)** Reduced **Cu@PIL3.2** stent under magnifier glass; **e)** Optical microscopic images of a reduced **Cu@PIL3.2** stent.*

The heating treatment (30 min at 160 ºC) that was necessary to obtain copper nanoparticles did not affect the polymer matrix or the physical structure of the material, thus it was possible to obtain stents with NPs of copper without affecting the structure (*Figure 56*a).

In contrast, the antimicrobial formulation based on **mIL1.2** with copper was not able to build the complex stent structure. As it can be seen in *Figure 56*b, only the supporting base of the object was properly printed. The exposure time of light per layer was increased to ensure the photopolymerisation of each layer. However, after increasing the exposure time, no changes were found and from 60 seconds the layers were sticked on the bath.

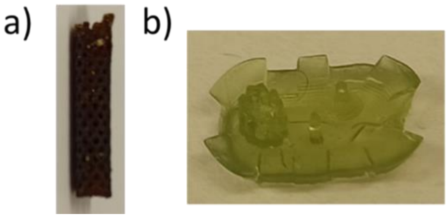

Layer Thickness: 50 µm
Exposure Time: 45 s
Burn-In Thickness: 300 µm
Burn-In Exposure Time: 100 s
Lifting Speed: 160 mm/min

Figure 56. *__a)__ __Cu@PIL3.2__ stent treated at 160 ºC for 30 minutes; __b)__ Picture of __Cu@PIL1.2__ 3D-printed base with the printing parameters.*

2.5 Conclusions

In this Chapter, a broad variety of novel antimicrobial formulations based on imidazolium and cholinium PILs were developed, fully characterised and optimised to be printed with high resolution by DLP and MSLA. In a first study, different formulations were functionalised with silver nanoparticles (AgNPs). The fabrication of low polydispersity AgNPs was effectively decoupled from the manufacturing process. Moreover, the studied photopolymers were capable of controlling the synthesis from the on-demand generation and stabilisation of AgNPs *via* photoreduction, and thus, their synergistic antimicrobial activity. Imidazolium-based formulations presented a bacteriostatic activity while those materials with silver exhibited bactericidal properties against Gram-positive *Bacillus subtilis* (*B. subtilis*) and Gram-negative *Escherichia coli* (*E. coli*) bacteria, and *Aspergillus niger* (*A. niger*) fungi. On the contrary, cholinium-based PILs, both with and without silver, did not show any antibacterial activity.

Afterwards, the 3D printable formulations were optimised in order to achieve desired geometries with high resolution. The photopolymer's composition as well as the printing parameters were modified to obtain 3D printed parts with high resolution ($\sigma \sim 0.20$ mm). And then, the biocompatibility of those formulations was evaluated. Non-cytotoxic materials were developed using appropriate combinations of mILs and PIs. The effect of the monomeric ionic liquid and the photoinitiator employed was tested finding that they both played an important role for obtaining biocompatible formulations. While mIL1 and mIL3 had low toxicity, mIL2 was highly toxic probably due to the hydroxyl group. Likewise, formulations using BAPO were very toxic compared to those using DPAP and TPO. The amount of PI added was also considerably important, finding slight improvements in cell viability when 0.5 wt% of PI was used. It is noteworthy to remark that not only the selection of suitable materials but also an adequate post-printing protocol was necessary for developing biocompatible materials.

Lastly, the stabilisation of copper salts was studied in order to improve the sustainability of the materials compared with silver composites. Only $Cu(NO_3)_2{\cdot}3H_2O$ salt (2 wt%) was properly solubilised into the formulation based on PIL1 (80 mol%) and PEGDA (20 mol%) without the addition of a solvent (**Cu@PIL1.2**). A treatment based on heating the photopolymerised samples at 160 °C was necessary to form copper nanoparticles and enhance the stabilisation of the metal in the films (**Cu@PIL1.2-h**). The antimicrobial activity of the Cu-based films was investigated for both the treated and non-treated samples, finding a higher activity for the former ones. In particular, **Cu@PIL1.2-h** films exhibited remarkable potential to inhibit the growth of *S. epidermidis* bacteria (98 %). These functional formulations with biocompatible and antimicrobial properties were evaluated to 3D-print a medical demonstrator, although only **Cu@PIL3.2** stents were successfully manufactured at high resolution (σ = 0.21 mm).

2.6 Experimental Part

2.6.1 Materials

Unless otherwise stated, all reagents in this PhD work were purchased from Sigma-Aldrich and used without further purification. Lithium bis(trifluoromethane) sulfonimide ($LiNTf_2$, 99 %) was purchased from IOLITEC GmbH and used as received.

2.6.2 Equipment

In this study, UV–vis spectra were collected using a Jasco V-780 UV–vis spectrophotometer and a Perkin Elmer UV–vis–NIR spectrophotometer. ^1H NMR spectra and ^{13}C NMR spectra were recorded on a Bruker ASCEND^{TM} 400 (400 MHz) spectrometer at ambient temperature. The mechanical analyses were performed using a Tritec 2000 dynamometer (Triton 6 Technology Ltd, London UK), varying the temperature from -70 °C to 80 °C. The moduli measurements as a function of temperature were measured using a strain amplitude of 0.1 % and frequency of 1 Hz. Two different FT-IR spectrometers were used. The first one was a Nicolet iS50 FT-IR from Thermo Fisher Scientific, equipped with an attenuated total reflection (ATR) accessory (Smart iTX, Thermo Fisher Scientific). The second one was a FT/IR-6200 from Jasco, equipped with an ATR accessory (ATR Pro One, Jasco). The spectra were recorded with a resolution of 4 cm^{-1} in the wavelength range between 650 and 4000 cm^{-1} averaging 16 scans for each spectrum. Raman Spectroscopy was performed with Raman Confocal Microscope apyron, from WITec. Real-time rheological measurements were performed using an Anton Paar rheometer (Physica MCR 302) in parallel plate mode with a Hamamatsu LC8 lamp with visible bulb and a cut-off filter below 400 nm equipped with 8 mm light guide. The distance between the two plates was fixed to 0.2 mm. The sample was kept at an established temperature (25 ^{o}C) and shear frequency (1 rad/s). In order to allow the system to stabilize, the visible light was switched on after 60 seconds. Concomitant changes in viscoelastic material moduli during polymerisation were measured as a function of exposure time. Thermal gravimetric analysis was performed on TGA-DSC3 analyser from Mettler Toledo. Samples for TGA analysis were heated in an inert atmosphere up to 800 ^{o}C with a heating rate of 10 ^{o}C/min. Then, the equipment used at INMA for microscopy analyses consisted in Environmental Scanning Electron Microscopy and Transmission Electron Microscopy. Environmental Scanning Electron Microscopy (ESEM) data was collected on a Quanta FEG-250 (FEI Company) field emission SEM for high-resolution imaging working in ESEM mode using a GSED detector under high relative humidity conditions. Transmission Electron Microscopy (TEM) measurements were performed using a JEOL 2000-FX operated with an accelerating voltage of 200 kV. The samples were prepared using ultramicrotomy process, where sample slices of few nanometers thickness were deposited on TEM grids. Surface chemical composition and electronic state of the materials were determined by X-ray Photoelectron Spectroscopy (XPS, ESCA-2R, Scienta-Omicron). Spectra were recorded using monochromatic Al Kα = 1486.6 eV. The following sequence of spectra were recorded: survey spectra, C 1s, Cs 3d, Pb 4f, Br 3d, O 1s, N 1s, F 1s, S 2p and C 1s again to verify the stability of the charge as the function of time. The survey and high-resolution spectra were recorded at a pass energy of 150 and 20 eV, respectively. Binding energy scale was referenced to adventitious carbon (284.8 eV). CasaXPS processing software (Casa software Ltd) was used to analyse the data and the quantitative analysis was made using sensitivity factors provided by the manufacturer.

A DLP printer (Asiga PICO2) and a MSLA printer (Elegoo mars 2 Pro), were the 3D printers employed. The DLP printing system was equipped with a LED light source operating at 405 nm. The Elegoo Mars 2 Pro printer was equipped with a 2560 × 1620 mono liquid crystal display (LCD), illuminating at 405 nm. The CAD files were designed and converted to STL-type files using SolidWorks CAD software. The digital light processing fabrication in both printers began by slicing the 3D CAD model into individual 2D images for projecting onto the photocurable liquid. For Asiga PICO2 printer, the additive manufacturing software used to create slices was Asiga Composer. For the Elegoo Mars 2 Pro 3D printer the slicer software employed was ChituBox.

2.6.3 Printing Process

The procedure for 3DP monomeric ionic liquids was the same for all formulations studied in this PhD thesis. The AM software allowed to specify a desired thickness, control the projection time of the images by the projector, and the velocity in the movement of the build plate. Then, the printer vat was filled with the different formulations and the build plate was lowered into the mixture at bottom of the vat. At this point, the software controlled the projector to display a black background with white images of each of the layers which were to be photocured. The UV light passed through the transparent bottom of the vat. Each layer was cured during the previously determined time. After that time, the printer showed a black background while the build plate was automatically lifted at a predetermined speed. This methodology was followed for each layer until the object was completed. After manufacturing, the device was removed and cleaned with isopropyl alcohol to eliminate any uncured ink. Finally, the part was photocured under UV light for 20 minutes at 40 ^{o}C.

The samples were scanned by a 3D optical scanner, 3Shape E3, to compare the printed parts with the CAD models. Then, 3Shape Convice Analyzer was used for performing the comparative analysis between them (accuracy 0.007 mm – ISO 12836). Before analysing deviations, the scan data and the reference model must be aligned. In this work, the alignment was done using the "Best Fit" approach, which employs the least squares principle, *i.e.*, the differences between the scan and the models are mathematically divided. The comparative analysis is frequently shown as a coloured 3D map.

2.6.4 Antimicrobial Studies

The antimicrobial studies were carried out in collaboration with the *Instituto de Ciencia de Materiales de Aragón* (INMA). All the data related with these tests are described in our published paper.[31b] All tested samples were 3D-printed with the same size (circles of 5 mm in diameter and 0.5 mm of thickness, and squares 2x2 cm and 0.5 mm of thickness) to improve the reproducibility of the tests.

Microorganisms and growth conditions: Three bacterial strains were tested in the antibacterial assays: *Escherichia coli* DH5α as a Gram-negative model and *Bacillus subtilis* 1904-E and *Staphylococcus epidermidis* as Gram-positive models. Two fungi from the "Colección Española de Cultivos Tipo (CECT)" were tested in the antifungal assays: Aspergillus niger CECT 2088 and Cladosporium cladosporioides CECT 2111. Fungal spore suspensions were stored in 0.1% Tween, 20% glycerol at -80 ^{o}C prior to use. The following culture media was used: Tryptone Soy Agar (TSA) (Thermo ScientificTM), Sabouraud Dextrose Agar supplemented with chloramphenicol (SDA) (Scharlab, S. L.), as solid media; Luria-Bertani (LB) and Nutrient Broth (NB) (Scharlab, S. L.) as liquid media. The microbial growth conditions are summarized in the Table 6.

Table 6. *Microorganisms and growth conditions.*

Microorganism		***Solid medium***	***Liquid medium***	***Incubation temperature (^{o}C)***	***Pre-inoculum incubation***
Bacteria	*E. coli*	TSA	LB	37	24 hours
	B. subtilis	TSA	NB	37	24 hours
	S. epidermidis	TSA	NB	37	24 hours
Fungi	*A. niger*	SDA	-	35	4 days
	C. cladosporioides	SDA	-	25	4 days

Bacterial cell proliferation assay: Bacterial growth was recorded measuring the optical density (OD) of the samples at 600 nm over a 24-hour period using a microplate reader (Thermo Scientific MULTISKAN GO). Results were compared with the OD variation of a control culture containing only *E. coli*, *B. subtilis* or *S. epidermidis*. The data for all control experiments and antibacterial assays are based on a total of six repeats to verify the reproducibility of the results and to calculate the mean values and the standard deviation; each experiment was repeated a minimum of three times to verify the results between different inoculations. The PIL samples, previously sterilised with ethanol 70 %, were placed in a 24-well plate inoculated with 1 mL of the inoculum ($1x10^{7}$ CFU (Colony Forming

Units)/mL of *E. coli*, *B. subtilis* or *S. epidermidis*), incubated at 37 ^{0}C with mild shaking, and the antiproliferative effects induced by the samples were observed by plotting optical density (OD) vs. time. Bacterial growth was recorded measuring the optical density (OD) of 100 µL collected from each well of the 24-well plate, in a 96-well plate. Measurements at 600 nm were performed using a microplate reader, each hour during the first 8 hours and at 24 hours as a final point. To maintain the final volume (1 mL) during the experiment, the 100 µL subtracted from the wells from the 24-well plate were replaced with 100 µL of medium. Results were compared with the OD variation of the positive control culture containing only bacteria (1 mL 10^{7} CFU/mL of *E. coli*, *B. subtilis* or *S. epidermidis*). The negative control contained 1 mL of liquid media and served as baseline. Statistical analysis was performed using unpaired t-test. P values <0.05 were considered significant. Single stars denote $0.01<P<0.05$.

Agar diffusion test: A modified Kirby Bauer disk diffusion technique was used. The 3D printed samples (3 mm-diameter circles of **PIL** and **Ag@PIL**) were first sterilised with ethanol 70 % and then they were placed in solid media previously inoculated with a bacterial lawn (10^{7} CFU/mL) of *E. coli* or *B. subtilis*. After 24 hours of incubation at 37 ^{0}C, the inhibition halo around the samples was observed.

For the antifungal assay, the 3D printed samples (20 mm-diameter circles of **PIL** and **Ag@PIL**) were sterilized with ethanol 70 % and then placed in solid media previously inoculated with a spore solution (10^{4} conidia mL^{-1}) of *A. niger* or *C. cladosporioides*. After 96 hours of incubation at the corresponding temperature (see *Table 6*), the inhibition halo around the samples was observed.

Surface antimicrobial activity: The surface antimicrobial activity was studied using a modified JIS Z 2801 standard. The protocol lasts three days. On the first day a bacterial suspension of 1×10^{7} CFU/mL is prepared and then 50 µL of this suspension is added over the surface of the samples of interest (2x2 cm) and over a reference sample with no antimicrobial activity (2x2 cm) after the sterilisation of these samples with ethanol 70 %. In order to even the contact surface, a coverslip was put above the 50 µL of bacterial suspension in all the samples. The samples were incubated into a humid chamber at 37 ^{0}C for 24h. After the 24h of incubation the bacteria over the samples were extracted into liquid medium by putting the samples into a 50 mL falcon with 15 mL of culture media and shaking them one minute with a vortex. The culture media with the extracted bacteria was then diluted and sown in agar plates, which were incubated at 37 ^{o}C during 24h. On the last day, the CFU of the cultivated agar plates were counted. The percentage of bacterial reduction was obtained using the following formula: Log Reduction = log (CFU reference sample) – log (CFU antimicrobial sample).

2.6.5 Biocompatible Studies

The cytotoxicity of the PIL-based materials was carried out by an MTT assay. Vero cell lines were used in the tests, which are a type of fibroblast-like cell extracted from the kidney tissue of the African green monkey. All films were 3D-printed with the same size (circles of 5 mm in diameter and 0.5 mm of thickness) to improve the reproducibility of the tests.

Day 1

1. Preparation of the samples

The samples were sterilized with ethanol 70 %, rinsed with sterile distilled water and dried inside the cabinet. Each sample was then incubated inside a 96-well plate well with 200 µL of DMEM (Dulbecco's Modified Eagle Medium) culture media with phenol red for 24 hours at 37 ^{o}C. The PILs were used in quadruplicates. Four replicates were performed for each sample.

2. Preparation of Vero cells

Another 96-well plate was incubated with 10000 cells/well (200 µL each well, cell solution 50000 cells/mL) for 24 hours at 37 ^{o}C.

Day 2

The medium of the cells was replaced with the DMEM incubated with the PILs. The medium of the positive controls was replaced with fresh DMEM. Then, the plate was incubated 24 hours at 37 ^{o}C.

Day 3

Before the MTT protocol, the cells were visualised in the optical microscope. The cells were washed twice with 100 µL of PBS (phosphate buffered saline) and then incubated with 200 µL of the MTT solution (0.5 mg/mL) for 1.5 hours. Afterwards, the plate was centrifuged for 25 min (2500 rpm, 25 °C) and the supernatant was discarded. The MTT crystals were resuspended in 200 µL DMSO and the plate was read at 570 nm after 10 minutes of stirring. Each well was diluted 1/5 (50 µL of each well plus 200 µL DMSO (V_{tot} = 250 µL) to avoid absorbances >1. The viability of the cells was calculated using the absorbance data of each sample in comparison with the control samples (100 % viability).

2.6.6 Synthesis and Characterisation of Monomeric Ionic Liquids

The main monomers evaluated in this Chapter and, in general, in this PhD work were 1-butyl-3-vinylimidazolium bis(trifluoromethane)sulfonimide (mIL1), 1-(3-hydroxypropyl)-3-vinylimidazolium bis(trifluoromethane)sulfonimide (mIL2) and [2-(acryloyloxy)ethyl]trimethyl-ammonium bis(trifluoromethane)sulfonimide (mIL3). The three monomers were synthesised from their halide salts by anion exchange as described in the literature.[31a] All the characterising spectra referred in this Section can be found in **Chapter 6: Annex, Section 6.1**.

1-butyl-3-vinylimidazolium bromide (BVI.Br)

1-bromobutane (33 g, 240 mmol) dissolved in acetonitrile (10 mL) was added dropwise to a solution of 1-vinylimidazole (15 g, 160 mmol) in acetonitrile (15 mL). The resulting reaction mixture was left to react for 18 h at 40 °C. After evaporating the solvent, the crude product was then washed with diethyl ether (40 mL) four times. During the last wash the product crystallised becoming a white solid. The solid was re-dissolved in dichloromethane (5 mL) and slowly added to rapidly stirred diethyl ether (50 mL) to form a purer white solid. The solid product was dried under reduced pressure at room temperature for 6 h to afford 1-butyl-3- vinylimidazolium bromide (23.26 g, Yield: 63 %).

The resulting mIL was characterised by ^{1}H NMR, ^{13}C NMR, ESI-MS and elemental analysis. ^{1}H NMR (400 MHz, $CDCl_3$): δ / ppm = 10.85 (s, 1H), 7.94 (t, *J* = 2.0 Hz, 1H), 7.66 (t, *J* = 2.0 Hz, 1H), 7.45 (dd, *J* = 15.8, 8.4 Hz, 1H), 6.02 (dd, *J* = 15.8, 3.2 Hz, 1H), 5.36 (dd, *J* = 8.8, 3.2 Hz, 1H), 4.39 (t, *J* = 7.2 Hz, 2H), 1.95-1.87 (m, 2H), 1.41-1.31 (m, 2H), 0.93 (t, *J* = 7.2 Hz, 3H). ^{13}C

NMR (400 MHz, $CDCl_3$): δ / ppm = 135.9, 128.3, 122.9, 119.5, 109.9, 50.2, 32.1, 19.5, 13.5. ESI-MS in positive mode: Calculated: 151.12 m/z; Found: 151.1 m/z. ESI-MS in negative mode: Calculated: 78.92 m/z; Found: 79.1 m/z. Elemental Analysis: Calculated: C, 46.77; H, 6.54; N, 12.12; Found: C, 46.02; H, 6.13; N, 11.98 (*Figure A1* and *Figure A2*).

1-butyl-3-vinylimidazolium bis(trifluoromethane)sulfonimide (mIL1)

$LiNTf_2$ (22.35 g, 78 mmol) was dissolved in water (15 mL) and it was added dropwise to an aqueous solution (20 mL) of 1-butyl-3-vinylimidazolium bromide (15 g, 65 mmol), forming two liquid phases. The mixture was stirred rapidly for 18 h at room temperature. The phases were then separated and the aqueous phase was extracted three times with dichloromethane (50 mL). The combined organic phases were washed four times with water (75 mL) and dried over $MgSO_4$ anhydride. The product was further dried under reduced pressure at 45 °C for 3 h (24.40 g, Yield: 87 %).

The resulting mIL was characterised by ^1H NMR, ^{13}C NMR, ESI-MS, elemental analysis, FT-IR and TGA-DSC. ^1H NMR (400 MHz, $CDCl_3$): δ / ppm = 8.97 (s, 1H), 7.63 (t, J = 1.6 Hz, 1H), 7.45 (t, J = 2.0 Hz, 1H), 7.12 (dd, J = 15.6, 8.4 Hz, 1H), 5.80 (dd, J = 15.2, 2.8 Hz, 1H), 5.40 (dd, J = 8.4, 2.8 Hz, 1H), 4.21 (t, J = 7.6 Hz, 2H), 1.90-1.82 (m, 2H), 1.41-1.32 (m, 2H), 0.95 (t, J = 7.6 Hz, 3H). ^{13}C NMR (400 MHz, $CDCl_3$): δ / ppm = 134.4, 128.1, 123.3, 121.5, (q, CF_3), 119.5, 110.4, 50.4, 31.9, 19.4, 13.3. ESI-MS in positive mode: Calculated: 151.12 m/z; Found: 151.1 m/z. ESI-MS in negative mode: Calculated: 279.92 m/z; Found: 280.1 m/z. Elemental Analysis: Calculated: C, 30.63; H, 3.50; N, 9.74; Found: C, 31.47; H, 3.75; N, 9.92. FT-IR bands: 3144 cm^{-1} (C=C), 2955 cm^{-1} (C-H), 1656 cm^{-1} (C=N), 1551 cm^{-1} (C=C), 1340 cm^{-1} (SO_2), 1178 cm^{-1} (C-C), 1133 cm^{-1} (CF_3), 789 cm^{-1} (C-S), 738 cm^{-1} (S-N). T_{onset}: 430.39 °C (*Figure A3* - *Figure A5*).

1-(3-hydroxypropyl)-3-vinylimidazolium bromide (HVI.Br)

1-bromopropanol (66.5 g, 480 mmol) dissolved in acetonitrile (20 mL) was added dropwise to a solution of 1-vinylimidazole (30 g, 320 mmol) in acetonitrile (20 mL). The resulting reaction mixture was left to react for 20 h at 40 °C. After evaporating the solvent, the crude product was then washed with diethyl ether (100 mL) three times. The crude product was re-dissolved in dichloromethane (10 mL) and slowly added to rapidly stirred diethyl ether (80 mL) to form a white solid. The solid product was dried under reduced pressure at room temperature for 6 h to afford 1-(3-hydroxypropyl)-3-vinylimidazolium bromide (60.6 g, Yield: 82 %).

The resulting mIL was characterised by ^{1}H NMR, ^{13}C NMR, ESI-MS and elemental analysis. ^{1}H NMR (400 MHz, CD_3OD): δ / ppm = 9.35 (s, 1H), 8.01 (t, *J* = 1.6 Hz, 1H), 7.78 (t, *J* = 2.0 Hz, 1H), 7.36 (dd, *J* = 15.6, 8.8 Hz, 1H), 5.96 (dd, *J* = 15.6, 2.4 Hz, 1H), 5.47 (dd, *J* = 8.8, 2.8 Hz, 1H), 4.40 (t, *J* = 6.8 Hz, 2H), 3.63 (t, *J* = 5.6 Hz, 2H), 2.18-2.08 (m, 2H). ^{13}C NMR (400 MHz, CD_3OD): δ / ppm = 136.7, 129.8, 124.6, 120.7, 109.9, 58.9, 48.5, 33.3. ESI-MS in positive mode: Calculated: 153.10 m/z; Found: 153.0 m/z. ESI-MS in negative mode: Calculated: 78.92 m/z; Found: 79.1 m/z. Elemental Analysis: Calculated: C, 41.22; H, 5.62; N, 12.02; Found: C, 41,65; H, 5.95; N, 12.17 (*Figure A6* and *Figure A7*).

1-(3-hydroxypropyl)-3-vinylimidazolium bis(trifluoromethane)sulfonimide (mIL2)

$LiNTf_2$ (105.87 g, 370 mmol) was dissolved in water (50 mL) and it was added dropwise to an aqueous solution (150 mL) of 1-(3-hydroxypropyl)-3-vinylimidazolium bromide (57.31 g, 250 mmol). The mixture formed two liquid phases and it was stirred rapidly for 18 h at room temperature. The phases were then separated and the aqueous phase was extracted three times with ethyl acetate (160 mL). The combined organic phases were washed three times with water (300 mL) and dried over $MgSO_4$ anhydride. The product was further dried under reduced pressure at 45 °C for 3 h (96 g, Yield: 90 %).

The resulting mIL was characterised by ^{1}H NMR, ^{13}C NMR, ESI-MS, elemental analysis, FT-IR and TGA-DSC. ^{1}H NMR (400 MHz, CD_3OD): δ / ppm = 9.24 (s, 1H), 7.97 (t, *J* = 1.6 Hz, 1H), 7.74 (t, *J* = 2.0 Hz, 1H), 7.19 (dd, *J* = 15.6, 8.8 Hz, 1H), 5.92 (dd, *J* = 15.6, 2.8 Hz, 1H), 5.46 (dd, *J* = 8.4, 2.4 Hz, 1H), 4.38 (t, *J* = 7.2 Hz, 2H), 3.62 (t, *J* = 6 Hz, 2H), 2.16-2.06 (m, 2H). ^{13}C NMR (400 MHz, CD_3OD): δ / ppm = 136.6, 129.7, 124.6, 122.8, (q, CF_3), 120.7, 109.9, 58.9, 48.5, 33.2. ESI-MS in positive mode: Calculated: 153.10 m/z; Found: 153.1 m/z. ESI-MS in negative mode: Calculated: 279.92 m/z; Found: 280.3 m/z. Elemental Analysis: Calculated: C, 27.72; H, 3.02; N, 9.7; Found: C, 24.5; H, 2.67; N, 8.73. FT-IR bands: 3538 cm^{-1} (-OH), 3142 cm^{-1} (C=C), 2961 cm^{-1} (C-H), 1652 cm^{-1} (C=N), 1550 cm^{-1} (C=C), 1336 cm^{-1} (SO_2), 1179 cm^{-1} (C-C), 1130 cm^{-1} (CF_3), 790 cm^{-1} (C-S), 741 cm^{-1} (S-N). T_{onset}: 414.24 °C (*Figure A8* - *Figure A10*).

[2-(acryloyloxy)ethyl]trimethyl-ammonium bis(trifluoromethane)sulfonimide (mIL3)

[2-(acryloyloxy)ethyl]trimethyl-ammonium bis(trifluoromethylsulfonyl)imide was synthesised directly from the commercial halide salt, [2-(acryloyloxy)ethyl]trimethyl-ammonium chloride. $LiNTf_2$ (42.7g, 148 mmol) was dissolved in water (40 mL) and it was added dropwise to an aqueous solution (40 mL) of [2-(acryloyloxy)ethyl]trimethyl-ammonium chloride (24 g, 124 mmol). The mixture formed two liquid phases and it was stirred rapidly for 18 h at room temperature. The phases were then separated and the aqueous phase was extracted three times with dichloromethane (100 mL). The combined organic phases were washed three times with water (125 mL) and dried over $MgSO_4$ anhydride. The product was further dried under reduced pressure at 45 ^oC for 3 h (49.5 g, Yield: 91 %).

The resulting mIL was characterised by ^1H NMR, ^{13}C NMR, ESI-MS, elemental analysis, FT-IR and TGA-DSC. ^1H NMR (400 MHz, $(CD_3)_2CO$): δ / ppm = 6.40 (dd, *J* = 16, 1.2 Hz, 1H), 6.22 (dd, *J* = 10.4, 7.2 Hz, 1H), 5.99 (dd, *J* = 9.2, 1.2 Hz, 1H), 4.75 (m, 2H), 4.03 (m, 2H), 3.50 (s, 9H). ^{13}C NMR (400 MHz, $(CD_3)_2CO$): δ / ppm = 165.7, 132.5, 128.7, 122.8, (q, CF_3), 66.0, 58.9, 54.7. ESI-MS in positive mode: Calculated: 158.12 m/z; Found: 158.3 m/z. ESI-MS in negative mode: Calculated: 279.92 m/z; Found: 280.1 m/z. Elemental Analysis: Calculated: C, 27.40; H, 3.68; N, 6.39; S, 14,63; Found: C, 26.53; H, 3.68; N, 6.66; S, 14.70. FT-IR bands: 3054 cm^{-1} (C=C), 2976 cm^{-1} (C-H), 1727 cm^{-1} (C=O), 1628 cm^{-1} (C=C), 1340 cm^{-1} (SO_2), 1174 cm^{-1} (C-C), 1131 cm^{-1} (CF_3), 788 cm^{-1} (C-S), 740 cm^{-1} (S-N). T_{onset}: 361.22 ^oC (*Figure A11* - *Figure A13*).

Chapter 3:

Stabilisation of Perovskites with Polymeric Ionic Liquids

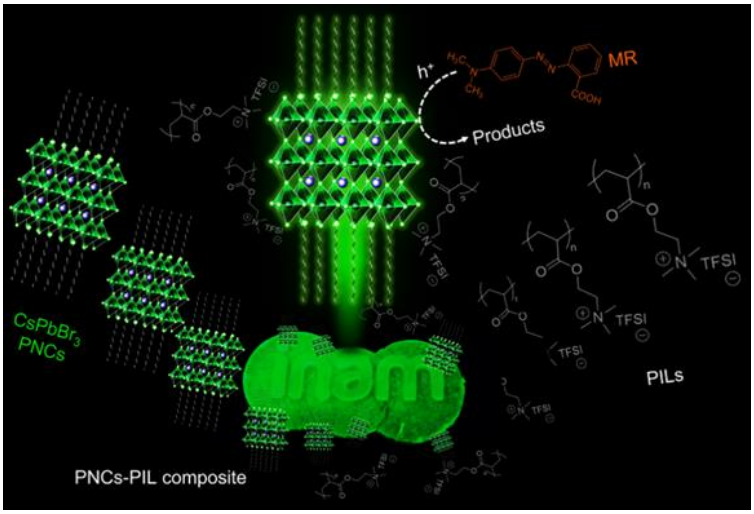

3.1 Summary

In this Chapter, metal halide-based perovskite nanocrystals (PNCs) were embedded into polymerisable ionic liquids (**PILs@PS**) to enhance the stability of the nanocrystals. Perovskites have emerged as potential candidates for photonic and optoelectronic applications because of their outstanding optical properties with controllable size, composition, morphologies and orientation. However, their sensitivity to humidity, heat and water represents a great challenge that limits their applications. On the other side, polymeric ionic liquids (PILs) stand out above other materials for their tuneable properties and their ability to stabilise molecular and nanostructured materials.

Herein, we demonstrate the synergistic potential of encapsulating caesium perovskites into PILs. The stability of the nanocrystals after encapsulation was enhanced, showing better light, moisture, water and thermal stability compared to pure PNCs. Several halide perovskites nanocrystals based on $CsPbX_3$ structure (X = Cl, Br, I and combinations) were tested. Moreover, a lead-free perovskite (Sn (II)-doped CsBr) was also analysed.

The photoluminescence (PL) and photoluminescence quantum yield (PLQY) was maintained for several months under different harsh conditions, while that of pristine PNCs was fully quenched along with structure degradation in few days or even hours. Furthermore, the possibility to exchange the ions of the perovskite for those of the medium was studied. More importantly, the formulations were 3D printed into complex geometries, enabling the direct translation of the optical properties of the perovskites to the macrosystems.

Since PNCs are promising candidates as visible-light photocatalysts, a PIL film containing perovskite nanocrystals was used as photocatalyst in the degradation of methyl red (MR) using solar energy, and it remained active even after recycles. The experimental results generated in this Chapter have been published in *Nanoscale* **2023**, *15*, 4962-4971.

3.2 Introduction

The chemical industry is responsible for the production of the chemicals and materials underpinning modern societies. Nevertheless, it is also a major polluter, which needs to be addressed to become a sustainable manufacturing industry. Within this remit, organic dye emissions are a major cause of pollution in the environment.[241] In this regard, photocatalytic degradation is a promising route to convert organic waste into harmless substances. Photocatalytic degradation is a specific type of photodegradation in which a photocatalyst material is used to breakdown pollutants or other harmful compounds, altering their chemical and physical properties by exposure to light. It is a process where the photocatalyst absorbs light and generates electron-hole pairs that form reactive species, which then react with the pollutants transforming them into less harmful products. The formation of reactive species is determined by the energy and wavelength of the absorbed light and the material's electronic structure. The interactions between the reactive species and the material are governed by chemical kinetics and thermodynamics.[242] The photocatalytic (PC) activity is typically measured by the rate at which a specific reaction occurs under defined conditions. The activity depends on the properties of the photocatalyst, the light source and the reaction conditions, which can be optimized to improve the performance. It is a sustainable and cost-effective method for pollution control and remediation, which can be powered by solar energy. The use of solar energy is particularly attractive because it is a powerful, abundant and renewable energy source. Additionally, by using solar energy to drive photocatalytic reactions, it reduces the consumption of fossil fuels, being a way of resolving the associated energy and environmental issues.[243] Furthermore, it can also lead to cost savings and greater scalability compared to other forms of energy.

Therefore, to maximise the utilisation of sunlight, it is critical to employ a photocatalyst capable of absorbing the whole spectrum of visible light in order to improve solar conversion efficiency. Most investigations have focused on the use of TiO_2 as photocatalyst, but it can only absorb UV light ($\lambda < 387$ nm) due to its wide band gap (3.2 eV) and high recombination of electron–hole pairs.[244] Several visible-light catalysts have been used such as organic conjugated polymers,[245] inorganic semiconductors,[246] and transition metal complexes.[247] However, those materials are complicated to prepare and expensive. Perovskite nanocrystals (PNCs) have appeared as highly effective photocatalysts in the entire UV-visible-NIR region.

In the past few years, all-inorganic perovskite nanocrystals have been in the spotlight due to them intrinsic properties including highly oxidizing/reducing power coming from their tuneable band structure, high absorption coefficient, good light-trapping ability, tolerance to defects and narrowband emission.[248] These materials can be synthesised by facile and low-cost methods with precise control over their size and composition, offering high photoluminescence quantum yield (PLQY) up to 100%.[249] All these advantages make them excellent materials to boost the performance of optoelectronic devices including light emitting diodes (LED), lasers, solar cells, photodetectors, and display backlights.[250] Moreover, their PC activity, which is determined by their capacity to form electron–hole pairs for undergoing secondary reactions, combined with solar energy open a new sustainable pathway into the photocatalysis field.[251] The PC efficiency of the PNCs can be enhanced by preventing the recombination of photogenerated electrons and holes, boosting the carrier separation efficiency and lengthening their diffusion distance and lifetime.

In particular, metal halide perovskites have attracted extensive attention as photocatalysts.[252] The PC activity of these perovskites cover a broad range of applications: CO_2 reduction,[253] hydrogen production,[254] organic chemical reactions[255] or pollutant degradation.[256] Gao *et al*. used $CsPbX_3$ perovskite crystals as photocatalysts for dye degradation for first time. In this study, the perovskites were able to photodegrade methyl orange, showing the outstanding photocatalytic activity of $CsPbCl_3$ and $CsPbBr_3$. Methyl orange solution turned colourless within 100 min.[257]

Nevertheless, the low resistance of $CsPbX_3$ (X = Cl, Br and I) to light, heat, oxygen, and water limits its use in large-scale applications.[258] Currently, extensive research has been conducted to overcome the stability limitations of perovskites, mostly due to their ionic nature and low melting temperatures. For example, embedding them into glass by the melt-quenching method and subsequent crystallisation process has been a solution, but some aggregation and clustering issues appeared.[259] Another way to enhance the stability of PNCs is encapsulating them with stable sol or polymer.[260] Incorporating nanoparticles into macroscopic polymeric matrices to form thin films has been demonstrated to be an efficient methodology for protecting semiconductor devices against environmental degradation.[261] Some recent reports show the benefits of encapsulating hydrophobic lead-halide NCs into water-repelling hydrophobic bulk polymers enhancing light stability and retention of optical properties upon water exposure by preventing access of water to the NCs surface.[262] The polymeric matrix employed plays a key role to get a good encapsulation. Still, some issues including easy leakage of PNCs from the polymeric microspheres or uneven distribution can arise because PNCs are only physically bounded to the polymer.[263] In this regard, the encapsulation of PNCs by polymerisation of the monomeric formulation with the nanocrystals dispersed in it can be a fast and effective way to prepare microspheres in the presence of NCs, thus solving the above-mentioned problems. The in-situ encapsulation can be carried out by functionalising and polymerising the PNCs ligands,[264] the perovskite itself[265] or by adding a co-monomer.[249a, 266] This is still an underexplored field since most of the methods involve polar reaction medium and relatively high polymerisation temperature (above 60 °C).[267] Additionally, it is interesting to find polymeric matrices with tailored hydrophobicity and with improved ligand−polymer interactions.[262b] Recently, our group has published the implementation of non-toxic and low-cost vitamins for enhancing the photophysical properties and stability of perovskite nanocrystals into a 3D printable formulation.[268]

As it has been previously described in **Chapter 1**, polymerisable ionic liquids are ideal materials to stabilise molecular and nanostructured materials as a result of their ionic and supramolecular interactions.[23b] Several articles introduce the use of PILs/ILs together with PNCs in order to improve the applicability of their systems, for instance as gating material for electronic applications,[269] as hole/electron transport material in perovskite solar cells,[270] as candidate for absorbing CO_2,[271] as perovskite/ionic liquid interfaces for transient opto-electronic conversion in AC photovoltaic devices.[272] However, in those examples PILs are not used as a perovskite stabiliser. Xia *et al.* has recently published a report showing the advantages of protecting hybrid perovskites from decomposition in humid environments with in situ ionic liquid polymerisation. The sensitivity to moisture during the cell fabrication was effectively reduced, improving quality and long-term stability.[177] Likewise, PILs and ILs have been used as perovskite passivation agents, improving the solar cell performance and reducing the degradation rate.[273] Furthermore, these polymers can be especially designed to be printed by 3D techniques, which is of huge interest since traditional polymerisation techniques limit the geometries that can be potentially generated.[31a] Although organic room-temperature phosphorescent luminogens[274] and fluorescent quantum dots[275] have been added as additives into 3D printing materials, perovskites are not as common yet because they are sensitive to environments such as polar solvents, humidity and heat.[274] To date, the thermoplastics capable to encapsulate PNCs for 3D printing have not been fully explored. Tai *et al.* studied different polymers and found that only polycaprolactone (PCL) could effectively encapsulate PNCs, transferring them optical properties to the printed objects. This was possible thanks to the low melting point of PCL.[276]

For these reasons, combinations based on PILs can represent a great chance for designing photoactive 3D printed devices for photocatalysis, optoelectronic, conductive, electrochemical and redox applications among others. To the best of our knowledge, the development of advanced formulations stabilising photoluminescence (PL) all-inorganic perovskites with polymerisable ionic liquid especially designed for additive manufacturing has not been widely exploited yet.

The theoretical underpinnings of the fluorescence techniques used in this Chapter are described here. A fluorometer and a PLQY instrument are both used to measure the fluorescence of a sample, although they have different features and applications.

A fluorometer is an instrument that measures the intensity of light emitted by a sample when it is excited by light of a specific wavelength. The excited molecule then returns to its ground state by releasing the absorbed energy in the form of light (fluorescence). This light is usually in the form of a photon, and is emitted at a longer wavelength than the excitation light. This technique is mainly used to measure the concentration of specific molecules in a sample, such as DNA, RNA, proteins, and small molecules like ions or metabolites.[277] The sample is placed in the sample holder, and the light source is turned on to excite the molecules in the sample. The emitted light is then passed through the filter or monochromator (to select the specific wavelength of light and separate the excitation light from the emitted light) and detected by the detector. The intensity of the emitted light is then measured and is proportional to the concentration of the specific molecules in the sample. This data is analysed and processed by a computer to determine the concentration of the specific molecules in the sample and the fluorescence of the material.[278]

A Photoluminescence Quantum Yield (PLQY) instrument measures the efficiency with which a sample converts absorbed light energy into emitted light energy. It is used to evaluate the quantum efficiency of a sample, such as semiconductors, organic materials, and biological samples. An integrating sphere, also known as an Ulbricht sphere, is an important component of a PLQY instrument. It is used to collect and redistribute the emitted light from the sample so that the detector inside the sphere can measure light coming from all directions, thus integrating all the light from the source. The integrating sphere ensures that all the emitted light is collected, regardless of the emission pattern of the sample, which is important for accurate PLQY measurements. The detector can be a simple photometer, a spectrophotometer or a radiometer.[279]

By measuring the total emitted light intensity inside the sphere, and knowing the energy of the excitation light, the PLQY of the sample can be calculated as the ratio of the emitted light (photon emission rate) to the absorbed light (photon absorption rate). PLQY is an intrinsic property of the sample and not dependent on the excitation light intensity, therefore, it is usually normalized by the absorbed energy. It is a dimensionless parameter between 0 and 1, where 1 means that 100% of the excitation energy is converted into photoluminescence. There are different ways to measure the photon emission rate and the photon absorption rate, depending on the type of sample and the experimental setup. One way to measure the photon emission rate is by using a detector to measure the intensity of the emitted light, and then calculating the photon emission rate based on the detector sensitivity and the light intensity. To measure the photon absorption rate, the sample can be exposed to light of a specific wavelength and the intensity of the absorbed light can be measured using a technique such as absorption spectroscopy.[280]

3.3 Objectives

The main objective of the work performed in this Chapter is to develop for first-time novel 3D printable PIL materials capable to effectively stabilise all-inorganic halide perovskite nanocrystals.

To meet this goal, different specific objectives are devised:

- To evaluate different mILs and cross-linkers to encapsulate PNCs in order to prepare fluorescent formulations
- To transfer the optical properties of the PNCs to the photopolymerised solids
- To improve the stabilisation of the PNCs optimising the photopolymer composition

- To embed a variety of lead perovskites based on $CsPbX_3$ structure (X = Cl, Br, I and combinations) into the optimised formulations
- To embed lead-free perovskites into the optimised formulations

Then, to demonstrate the ability of PIL materials to stabilise PNCs, different studies will be performed:

- Characterisation of the PL and PLQY of the polymer composites for over 700 days under different conditions (closed in the dark at 25 ^{o}C, exposed to atmospheric air, closed in liquid water at 25 ^{o}C and opened in an oven at 70 ^{o}C) using a variety of formulations, which allows the analysis of structure-activity relationships.
- Analysis of the ionic exchange of the ions from the PNCs embedded in the PILs by those in solution.
- 3D printing the photopolymer in order to obtain optically active devices with tailored geometries.
- Evaluation of the photocatalytic activity of a PIL-based film with perovskite nanocrystals (**PIL@PS**) for the photodegradation of organic dyes.

3.4 Results and Discussion

3.4.1 Summary of the Nomenclature found in Chapter 3

Table 7. *Summary of the nomenclature used for naming the mIL3-based films depending on the formulation employed.*

Entry	*Film*	*mIL3 (mol%)*	*BA (mol%)*	*BDA (mol%)*
1	PIL3a	100	-	-
2	PIL3b	95	-	5
3	PIL3c	90	5	5
4	PIL3d	80	15	5
5	PIL3e	75	20	5
6	PIL3f	65	30	5
7	PIL3g	20	75	5
8	PIL3h	-	95	5

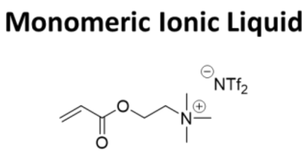

[2-(acryloyloxy)ethyl]trimethyl-ammonium bis(trifluoromethane)sulfonimide

(mIL3)

Table 8. *Nomenclature of mIL3-based films embedding different perovskite nanocrystals.*

Entry	**Film**	**Perovskite Structure (2 wt%)**
1	PIL3a@PS	$CsPbBr_3$
2	PIL3a@PS1	$CsPbCl_3$-Sr
3	PIL3a@PS2	$CsPbCl_{2.25}Br_{0.75}$
4	PIL3a@PS3	$CsPbCl_{1.5}Br_{1.5}$
5	PIL3a@PS4	$CsPbBr_{0.75}I_{2.25}$
6	PIL3a@PS5	$CsPbI_3$
7	PIL3a@PS6	Sn (II)-doped CsBr

3.4.2 Preparation of Photoluminescent Films

Caesium lead halide nanocrystals based on $CsPbX_3$ structure (X = Cl, Br, I and combinations) were prepared at the Group for Advanced Semiconductors (GAS) from the Institute of Advanced Materials (INAM). The nanocrystals were received in a hexane dispersion (50 mg/mL).

A family of monomers were tested for stabilising $CsPbBr_3$ NCs (1 wt%), showing that not all the monomers were capable to encapsulate and stabilise the nanocrystals. The monomers synthesised and evaluated were: 1-butyl-3-vinylimidazolium bis(trifluoromethane)sulfonimide (mIL1), [2-(acryloyloxy)ethyl]trimethyl-ammonium bis(trifluoromethane)sulfonimide (mIL3), 1-butyl-3-vinylimidazolium dicyanamide (BVI.N(CN)$_2$), 1-butyl-3-vinylimidazolium iodide (BVI.I), [2-(acryloyloxy)ethyl]trimethyl-ammonium chloride (AcrEMA.Cl), [2-(acryloyloxy)ethyl]trimethyl-ammonium dicyanamide (AcrEMA.N(CN)$_2$), [2-(acryloyloxy)ethyl]trimethyl-ammonium iodide (AcrEMA.I) and [2-(acryloyloxy)ethyl]trimethyl-ammonium tetrafluoroborate (AcrEMA.BF$_4$), as well as the neutral monomer vinyl imidazolium (VIm). In a first stage, it was studied their capacity to form films, finding that only some of them were able to polymerise forming robust solid parts. In the case of AcrEMA.Cl, AcrEMA.I and AcrEMA.BF$_4$, they were solid compounds, so different strategies were tried to generate liquid formulations. They were mixed with mIL1, mIL3, butyl acrylate (BA), PEGDA and BDA but it was not possible to dissolve them at room temperature or at 40 ^oC. BVI.I, BVI.N(CN)$_2$ and AcrEMA.N(CN)$_2$ were very viscous and sticky. For this reason, it was necessary to use a cross-linker to reduce the viscosity of the mixture and to photopolymerise them. After that, rigid films were formed. On the other hand, mIL1 and mIL3 were polymerised without further issues as we have reported in **Chapter 2**. The neutral monomer, VIm, was also easily photopolymerised. Therefore, the monomers considered for encapsulating PNCs were VIm, mIL1 and mIL3 and their analogous with iodide (BVI.I) and dicyanamide (BVI.N(CN)$_2$ and AcrEMA.N(CN)$_2$). However, only mIL1 and mIL3 were able to stabilise the perovskite into the liquid precursor and after polymerisation without quenching the PNCs photoluminiscence. The neutral monomer (VIm) was totally unable to stabilise the PNCs, as evidenced by a complete degradation of their PL after 10 minutes of stirring. BVI.N(CN)$_2$, even with a cross-linker, was too sticky, and it was impossible to mix it with CsPbBr$_3$. AcrEMA.N(CN)$_2$ and BVI.I derived photopolymers were able to stabilise partially the PNCs but after polymerisation, the CsPbBr$_3$ was totally deactivated (*Figure 57*). Similarly, the PNCs were quenched after a while being simply in contact with the discarded solid monomers (AcrEMA.Cl, AcrEMA.I and AcrEMA.BF$_4$). All the results are summarised in *Table 9*.

Figure 57. *(Left) AcrEMA.N(CN)$_2$-based photopolymer with 5 mol% of cross-linker (BDA) and CsPbBr$_3$; (right) the film formed after polymerisation. The absence of the green colour under UV illumination indicates that the PNCs are completely degraded.*

The monomer mIL1 was miscible with hexane, so, in the first studies, the perovskite was mixed directly with mIL1 without further treatment. However, those films exhibited some bubbles and, after evaporating the hexane (70 °C, 30 min), the films were visually observed to be more photoactive (*Figure 58*a), as indicated by an increased photoluminiscence. In addition, since mIL3 was immiscible with hexane, the methodology followed for the rest of the mixtures using CsPbX$_3$ NCs was to evaporate the hexane under reduced pressure at 45 °C after adding the mIL.

Following the methodology implemented to stabilise metallic nanoparticles in **Chapter 2**, PEGDA 575 was used as cross-linker in a concentration 80:20 mol/mol (mIL:PEGDA).

Nevertheless, PEGDA contributed to the deactivation of the PNCs (*Figure 58*b, left). Both, mIL1 and mIL3 formulated with PEGDA were unable to stabilise the PNCs. The reduction of the amount of cross-linker to 95:5 mol/mol (mIL:PEGDA) did not solve the problem. Hence, the cross-linker was changed to BDA in a percentage 95:5 mol/mol (mIL:BDA). With the new cross-linker, mIL1 and mIL3 offered a good encapsulation of $CsPbBr_3$, specially mIL3 (*Figure 58*b, right). The films obtained using BDA were much more rigid than with PEGDA. From now, the films containing BDA (95:5 mol/mol, mIL:BDA) are referred as **PILXb** and **PILXb@PS** when adding $CsPbBr_3$, which was the main PNCs studied in this work.

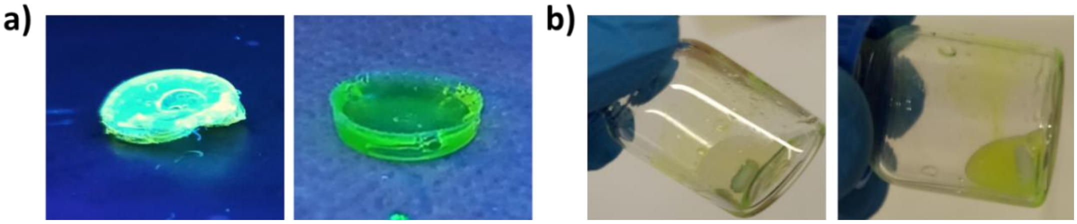

Figure 58. ***a)*** *(Left)* ***PIL1b@PS*** *film prepared without removing the hexane, and (right) after evaporating the hexane from the PNCs;* ***b)*** *(left) mIL3 with PEGDA (80:20 mol/mol) and* $CsPbBr_3$*, showing a white mixture due to the deactivation of the perovskite, and (right) mIL3 with BDA (95:5 mol/mol) and* $CsPbBr_3$ *(1 wt%), showing a greenish mixture corresponding to the emission colour of the perovskite.*

The films were analysed by fluorescence techniques, using a fluorometer to confirm the presence of the PNCs. Nevertheless, an important issue appeared for mIL1-based films, since the imidazolium group had the emission signal from 450 to 600 nm, in the range where appears the emission band of $CsPbBr_3$, as we can see in *Figure 59*a. Thus, the signal corresponding to the perovskite was overlapped by the imidazolium. Moreover, in *Figure 59*b it can be appreciated that 3D-printed **PIL1b@PS** films presented a partial blue emission attributed to the imidazolium.

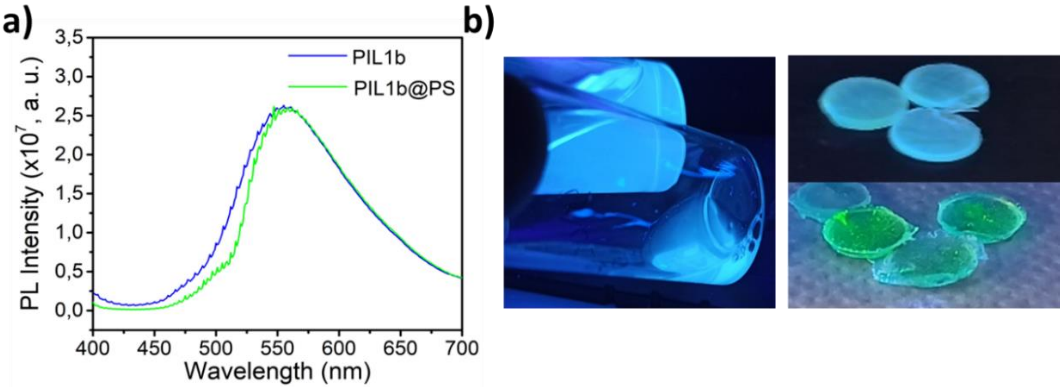

Figure 59. *a) PL spectra of **PIL1b** film and **PIL1b@PS** film (λ_{ex}= 365 nm); **b)** (left) the intrinsic photoluminiscence of mIL1, (right, up) **PIL1b** printed films and (right, down) **PIL1b@PS** printed films.*

Additionally, as shows *Table 9*, the PLQY achieved by mIL1 was extremely low for being used in future applications, while PLQY of mIL3 was remarkably good. Therefore, the monomer employed for the following experiments was mIL3.

Table 9. *Summary of the monomers employed, specifying their capacity to form a film, to stabilise $CsPbBr_3$ after polymerisation and the PLQY reached.*

Entry	***mILs***	***Monomer phase***	***Polymerisation***	***PL Activity***	***PLQY***
1	BVI.I	**Liquid**	V	X	-
2	BVI.N(CN)$_2$	**Liquid**	V	X	-
3	mIL1	**Liquid**	V	V	**6**
4	AcrEMA.Cl	Solid	X	X	-
5	AcrEMA.I	Solid	X	X	-
6	AcrEMA.N(CN)$_2$	**Liquid**	V	X	-
7	AcrEMA.BF$_4$	Solid	X	X	-
8	mIL3	**Liquid**	V	V	**45**
9	ViIm	**Liquid**	V	X	-

The photopolymer matrices were prepared mixing mIL3 with BDA (5 mol%) as cross-linker and TPO (1 wt%) as photoinitiator. The liquid mixture was 3D-printed or photopolymerised following standard conditions (illuminating upon UV light for 20 minutes at 40 °C under aerobic atmosphere). Afterwards, solid photoluminescence films were obtained with a tailored geometry.

XPS analysis was performed to elucidate the influence of **PIL3b** on the composition and chemical environment of PNCs. The presence of Cs, Pb, Br, N, in addition to the co-existence of F and S from the mIL3 was observed in the XPS spectra (*Figure 60*a).

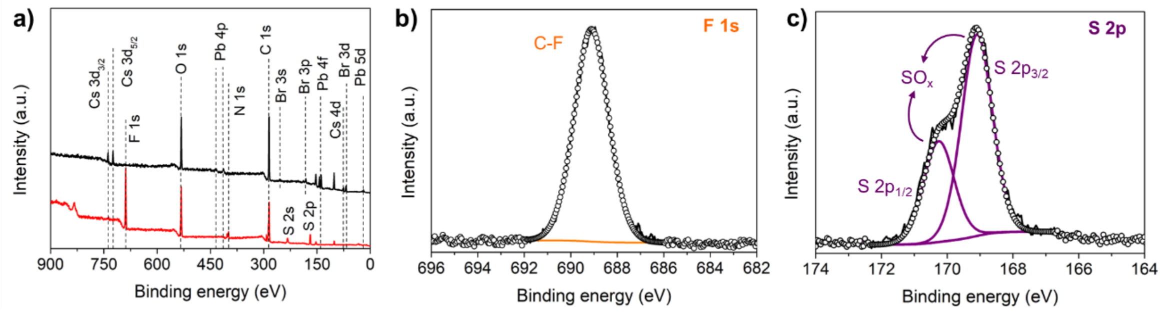

Figure 60. ***a)*** *XPS survey and HR-XPS;* ***b)*** *F 1s; and* ***c)*** *S 2p spectra for pristine* $CsPbBr_3$ *and* ***PIL3b@PS*** *samples.*

The corresponding chemical composition of the PNCs in absence and presence of **PIL3b** is summarised in *Table 10*. *Figure 61*a exhibits the high-resolution (HR) XPS Cs 3d spectra of the samples, where a characteristic doublet located ~725/738 eV was obtained. This doublet represents the Cd$_{5/2}$ and Cd$_{3/2}$ core levels, indicating the presence of Cs$^+$ into the $CsPbBr_3$ lattice.[281] Then, we acquired the typical HR-XPS Br 3d spectra of PNCs with and without the monomer, achieving a doublet located ~68/69 eV (*Figure 61*b). These peaks attributed to the Br$_{5/2}$ and Br$_{3/2}$ core levels, are representative of the formation of Pb-Br bonds coming from the [$PbBr_6$] octahedra contained into the nanocrystals.[282] Last, *Figure 61*c shows the HR-XPS Pb 4f spectra of the samples, observing the characteristic Pb 4f$_{7/2}$ and Pb 4f$_{5/2}$ core levels ~138/143 eV, respectively.[283] These signals correspond to the presence of Pb^{2+} contained into the nanocrystal lattice. On the other hand, *Figure 61*d displays the HR-XPS N 1s spectra of the pristine and modified PNCs with monomer, noting some differences in the chemical contributions from the main N 1s signal. In the case of pristine PNCs, two signals are evidenced ~400 and 402 eV, ascribed to C-NH_2 and C-NH_3^+ species, respectively. These species are attributed to the attached oleyl ammonium cations covering the PNCs surface.[284] Interestingly, after the addition of the polymeric formulation, the abovementioned signals were displaced to 399 and 403 eV, respectively. We attributed these peaks to the emergence of C-N and S-N coming from the AcrEMA cation and NTf_2 anion, respectively. At this stage, it is deductible that PNCs are entirely covered by the monomer.

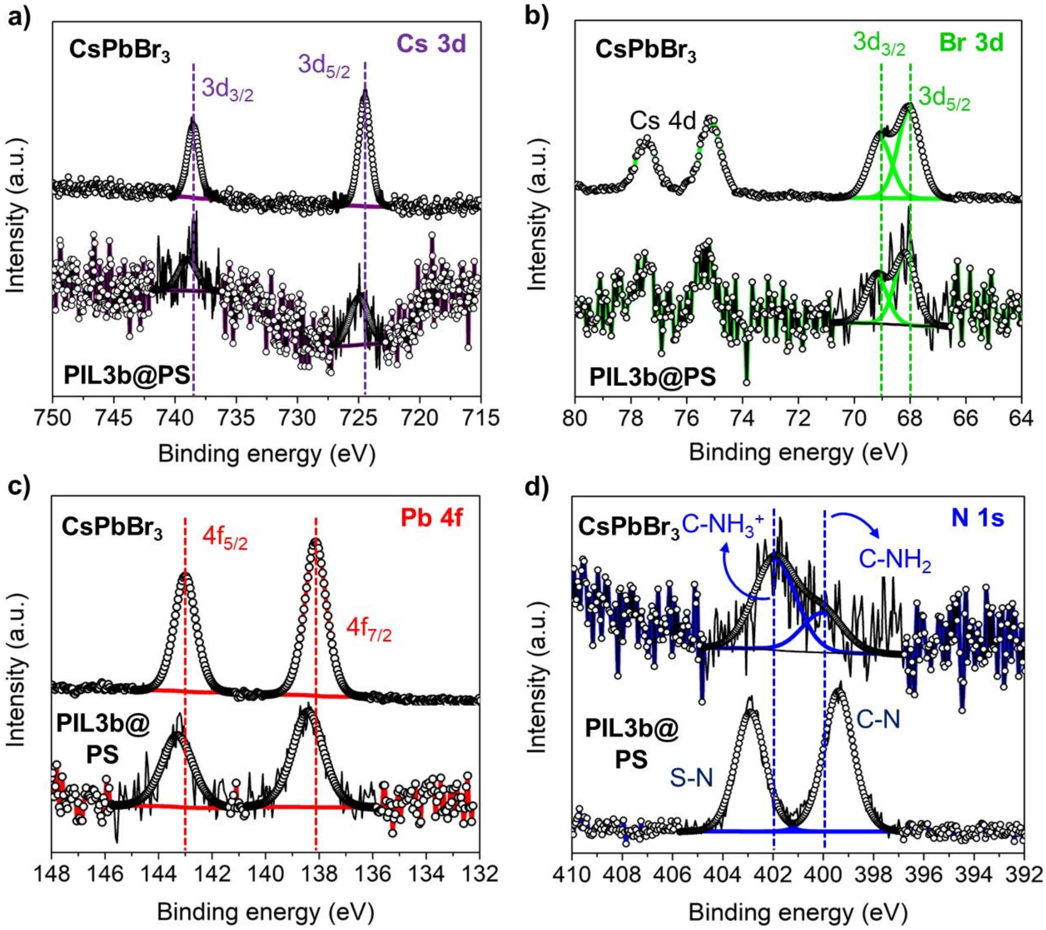

Figure 61. *HR-XPS* ***a)*** *Cs 3d;* ***b)*** *Br 3d;* ***c)*** *Pb 4f; and* ***d)*** *N 1s spectra for pristine* $CsPbBr_3$ *PNCs and* ***PIL3b@PS*** *samples.*

The stoichiometry of the pristine PNCs (*Table 10*) are far from the typical Cs:Pb:Br molar ratio = 1:1:3, suggesting that the material shows a high density of surface defects. This is probably due to the PNCs synthesis and purification methodologies.[285] However, after encapsulating the PNCs with the PIL formulation, the Cs^+ deficiency is compensated, while the Br content is lower. We attributed this improvement to the incorporation of fluorine and sulfur species coming from the monomeric ionic liquid, replacing/filling halide sites in the nanocrystals. Through HR-XPS F 1s and S 2p spectra obtained from the **PIL3b@PS** combination (*Figure 60*b, c), we identified the presence of C-F (689 eV), and SO_x bonds (doublet at 169/170 eV), respectively, from the bis(trifluoromethanesulfonyl)imide ion.[286] In this context, this species could mediate the PNCs surface complexation through the sulfonyl/fluoride-metal surface interaction.

This hypothesis is reinforced by the shift of BEs of the Cs 3d, Br 3d and Pb 4f doublets to higher values (*Figure 61*). This indicates the introduction of a more electronegative element into the perovskite structure, as the case of F or O atoms from NTf_2. Therefore, we can conclude that PILs can favour the surface defect passivation of PNCs, which is a key factor to promote a long-term stability and good optical properties such as PLQY, into the PIL matrix.

Table 10. *Chemical atomic composition of pristine $CsPbBr_3$ PNCs and **PIL3b@PS** samples.*

Samples	**C (at.%)**	**O (at.%)**	**Pb (at.%)**	**Br (at.%)**	**Cs (at.%)**	**N (at.%)**	**F (at.%)**	**S (at.%)**	**Cs/Pb**	**Br/Pb**
Pristine PNCs	73.85	20.34	1.03	2.69	0.64	1.45	-	-	0.62	2.61
PIL3b@PS	57.61	18.67	0.03	0.06	0.03	5.55	12.84	5.21	1.00	2.00

3.4.3 Optimisation of the Formulation

According to the literature, butyl acrylate (BA) is commonly used to increase the flexibility of polymeric matrices, since it reduces the glass transition temperature (Tg) of the material.[287] Thus, different formulations using mIL3 (100-0 mol%) and butyl acrylate (BA, 0-95 mol%) were prepared in order to obtain adequate mechanical and optical properties, following the polymerisation reaction shown in *Figure 62*a. Nevertheless, not all the combinations were efficient matrices for stabilising the $CsPbBr_3$, as the PNCs were totally deactivated after their encapsulation in some of the formulations. The complete list of formulations evaluated and their PL activity after embedding $CsPbBr_3$ is shown in *Figure 62*b.

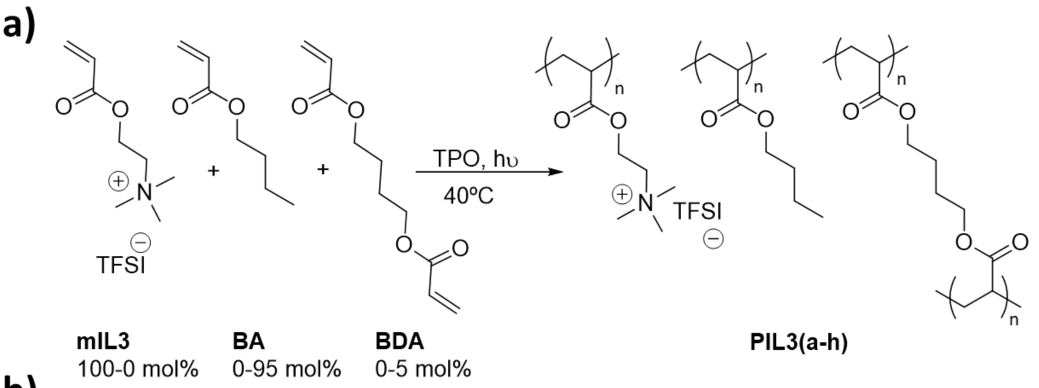

b)

Formulation	mIL3 (mol%)	BA (mol%)	BDA (mol%)	PL
PIL3a@PS	100	0	0	✓
PIL3b@PS	95	0	5	✓
PIL3c@PS	90	5	5	✓
PIL3d@PS	80	15	5	✓
PIL3e@PS	75	20	5	✗
PIL3f@PS	65	30	5	✗
PIL3g@PS	20	75	5	✗
PIL3h@PS	0	95	5	✓

Figure 62. a) *Components used in the polymerisation reaction;* **b)** *Different formulations prepared for encapsulating CsPbBr$_3$ NCs and their PL activity.*

PIL3a@PS was sticky and fragile, which demonstrated that the cross-linker (BDA) was necessary to obtain robust films. On the other hand, the neutral polymer butyl acrylate (**PIL3h@PS**) needed 5 mol% of cross-linker to form a film, and still that formulation had the poorest mechanical properties, because really fragile films were obtained. The fluorescence of the films decreased with increasing the mole percent of butyl acrylate, and above 15 mol% of additive (BA) the films were not fluorescent anymore (**PIL3e@PS**, **PIL3f@PS**, **PIL3g@PS**) as it can be seen in *Figure 63*. The combination of high concentrations of BA with mIL3 generated an unstable matrix for CsPbBr$_3$, promoting its quenching.

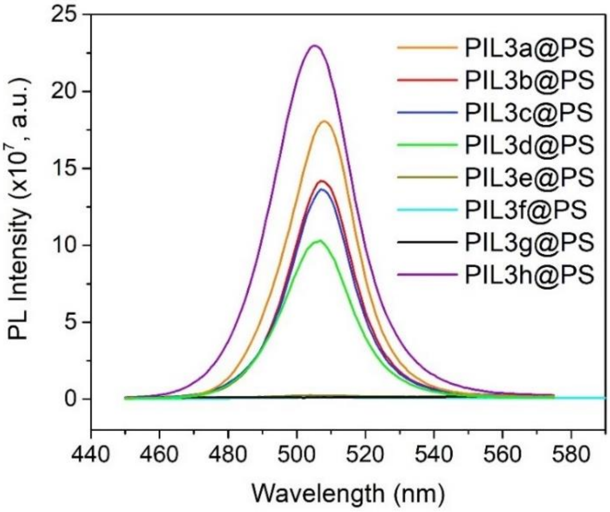

Figure 63. *Photoluminescence spectra of all the formulations using $CsPbBr_3$.*

Additionally, PNCs concentration was varied and the optimal concentration was 2 wt% with respect to the weight of the formulation, since it presented a PLQY around 45 %. Lower concentrations reported poorer PL (*Figure 64*) while using higher concentrations (5 wt%), the PLQY was notably decreased to 26 %. Hence, in following experiments a concentration of 2 wt% was employed.

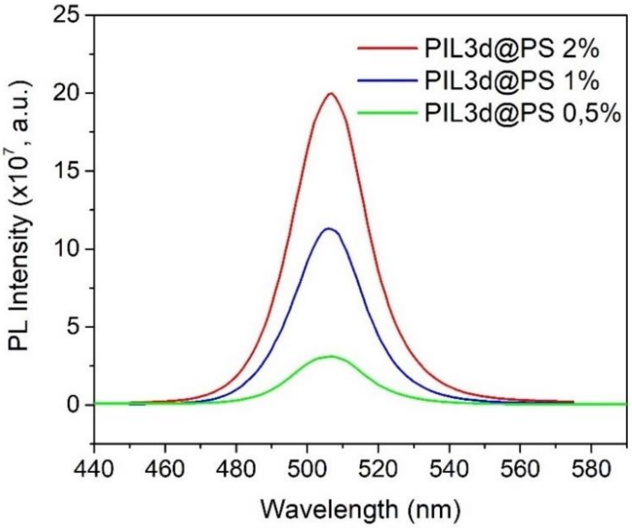

Figure 64. *PL spectra of **PIL3d@PS** films using different perovskite concentrations (2 wt%, 1 wt%, 0.5 wt%).*

3.4.4 Stability Studies

$CsPbBr_3$ stability was evaluated using different PIL formulations. The specific conditions for performing the stability tests are described in the *Experimental Part*, in **Section 3.6.3**. The first study was done storing the films in the dark within more than 2 years (see Figure 65). The samples were covered with aluminium and kept in a drawer. According to the results, **PIL3a@PS, PIL3b@PS** and **PIL3c@PS** were the best formulations for stabilising PNCs (2 wt%), keeping the PLQY of the films around 50 and 60 % (stored under aerobic atmosphere in the dark, at room temperature with a relative humidity of 60 %). The PL was notably increased during that time. This can be attributed to the dynamic rearrangement of the PNCs, since surface defects can be passivated with active materials,[288] in this case PILs. On the contrary, the PLQY of not embedded $CsPbBr_3$ decreased 70% in less than 200 days. However, not all the polymeric matrices were good for stabilising PNCs since **PIL3d@PS** and **PIL3h@PS** loose partially and even totally their photoluminescence after less than 300 days.

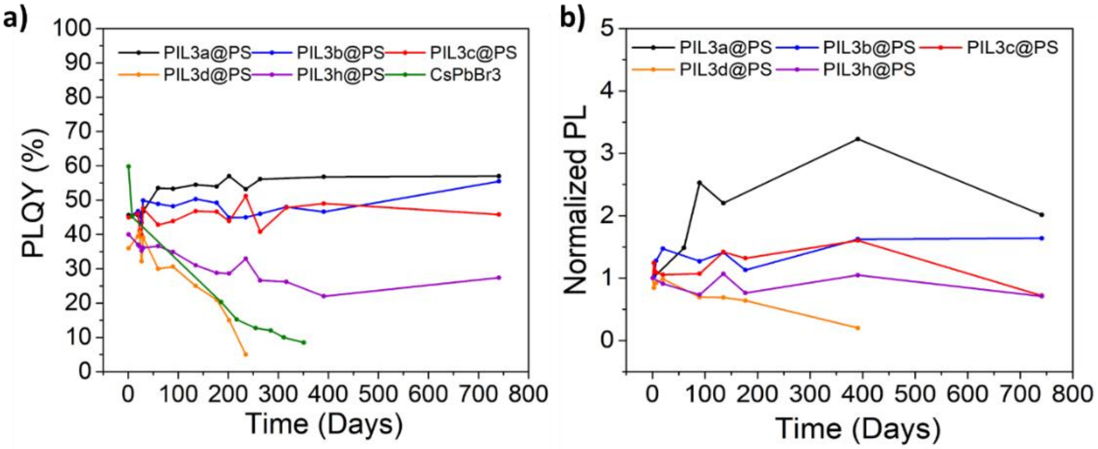

Figure 65. *Stability study in the dark at 25 °C performed along more than 700 days, measuring* ***a)*** *PLQY;* ***b)*** *Normalised photoluminescence of all* ***PIL3x@PS*** *formulations capable to stabilise* $CsPbBr_3$.

Although the stability and PL activity of **PIL3a@PS** was remarkably high, that formulation was not used in further tests since the film was very brittle and sticky as mentioned in **Section 3.4.3**. Only **PIL3b@PS** and **PIL3c@PS** films were employed to study the stability of the $CsPbBr_3$ at different conditions: exposed to air and light at 25 °C (*Figure 66*a), at 70 °C without light irradiation (*Figure 66*b) and immersed in liquid water under day light conditions at 25 °C (*Figure 66*c, d).

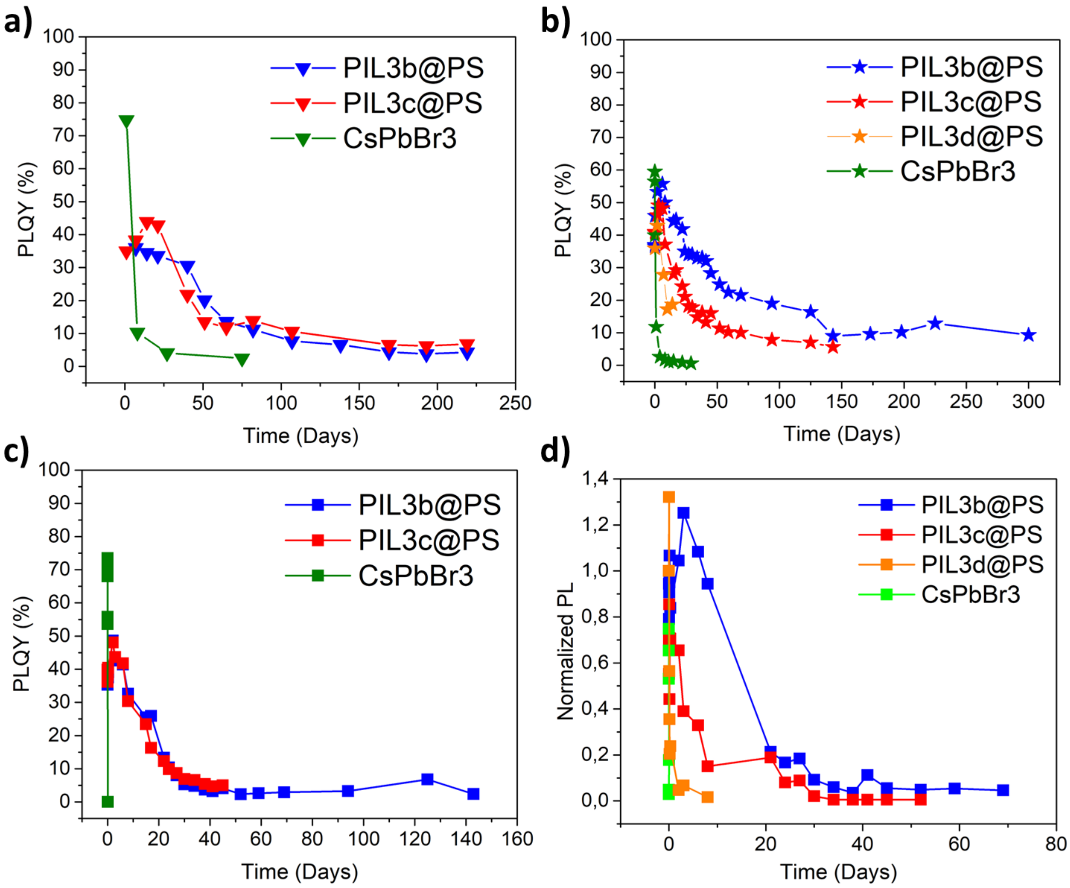

Figure 66. ***a)*** *PLQY of* ***PIL3b@PS*** *and* ***PIL3c@PS*** *films compared with pure* $CsPbBr_3$ *being opened to air and light;* ***b)*** *PLQY of* ***PIL3b@PS, PIL3c@PS*** *and* ***PIL3d@PS*** *films compared with pure* $CsPbBr_3$ *at 70 ºC;* ***c)*** *PLQY of* ***PIL3b@PS*** *and* ***PIL3c@PS*** *films compared with pure* $CsPbBr_3$ *in water at 25 ºC;* ***d)*** *Normalised PL of* ***PIL3b@PS, PIL3c@PS*** *and* ***PIL3d@PS*** *films compared with pure* $CsPbBr_3$ *in water at 25 ºC. Details about the formulations can be found in* Figure 62*.*

Under challenging conditions, pristine PNCs lost more than 90% of their photoluminescence in less than 5 days, specially upon immersion in water where PNCs degrade within minutes. Encapsulated PNCs in **PIL3b**, however, stored under ambient conditions (oxygen, light and humidity) and exposed at 70 ºC only exhibited a decrease of the PLQY around 15% after the first 40 days. In both cases, the PLQY was measured for more than 200 days, reporting still some PL. In water conditions, **PIL3b** formulation was able to stabilise $CsPbBr_3$, maintaining the PLQY for almost 150 days. On the other hand, **PIL3d** formulation was totally unable to stabilise PNCs in thermal and in water conditions. The high stabilization observed with **PIL3b** formulation (95 mol% of mIL3 and 5 mol% of BDA) was obtained due to the material's hydrophobicity as the NTf_2 anion from the PIL is a hydrophobic anion.[83, 146a] While **PIL3d** contained a lower amount of mIL3 (80 mol%) combined with a neutral polymer (BA, 15 mol%). In addition, the films were not hygroscopic and did not present porosity, as shown by SEM and profilometry analyses (*Figure 67*). These results, in combination with the data obtained from the XPS analysis shown in **Section 3.4.2**, demonstrate a high stabilisation capacity for the **PIL3b** formulation.

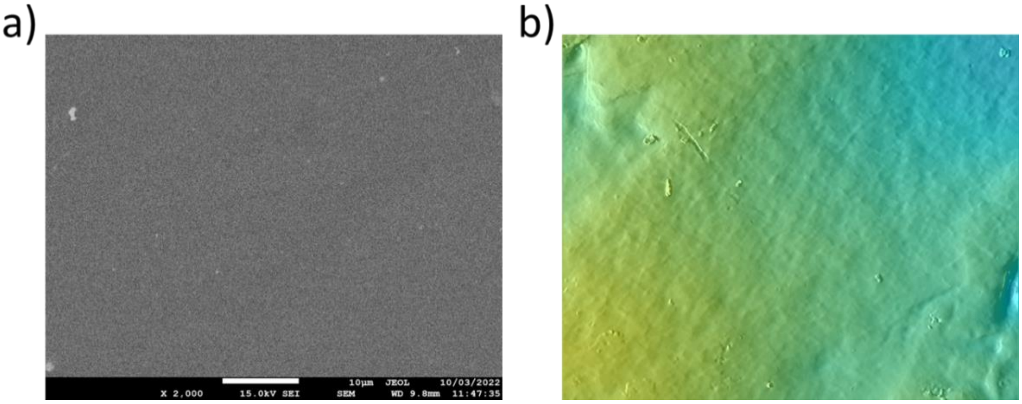

Figure 67. *Images of a* ***PIL3b@PS*** *film obtained by* ***a)*** *SEM, and* ***b)*** *profilometry.*

For the air stability test, the samples were left opened on the laboratory bench. The aqueous stability tests were done immersing the photomaterials in water and stored under day light conditions. In the thermal stability experiment, we found that the PNCs composites were degraded after being some hours at 115 °C as shown in *Figure 68*. Then, we decided to conduct the test in an oven at 70 °C without light irradiation.

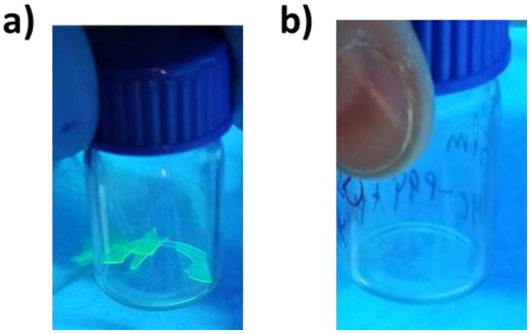

Figure 68. ***a)*** *Initial PL of* ***PIL3b@PS*** *film under UV light;* ***b) PIL3b@PS*** *film under UV light after being several hours at 115 °C. The colour disappearance means that the PNCs were degraded.*

3.4.5 Stabilisation of Different Perovskites

Apart from studying the stabilisation of $CsPbBr_3$ nanocrystals, we also analysed the stability of a variety of PNCs based on $CsPbX_3$ structure where X = Br, Cl, I, and Cl:Br, Br:I combinations: $CsPbCl_3$-Sr (PS1), $CsPbCl_{2.25}Br_{0.75}$ (PS2), $CsPbCl_{1.5}Br_{1.5}$ (PS3), $CsPbBr_{0.75}I_{2.25}$ (PS4), $CsPbI_3$ (PS5). The different perovskites (2 wt%) were encapsulated using **PIL3a** and **PIL3b** formulations, reporting the PLQY in *Table 11*. Unfortunately, the PNCs with iodide (PS4 and PS5) were unstable into both polymeric matrices. The set of formulations prepared in this regard are named **PIL3x@PSy**, where y is referred to the perovskite used (1-5). By changing the halides, the absorption wavelength of the perovskite was modified obtaining films with different colours (see *Figure 69*).

Table 11. *Summary of the PLQY and wavelength (in nm) of different PNCs structures and they embedded in two different formulations (**PIL3a** and **PIL3b**).*

Entry	*Sample*	*Perovskite Structure*	*PLQY (%)*	*Wavelength (nm)*
1	PS1	$CsPbCl_3$-Sr	7	408
2	PIL3a@PS1	$CsPbCl_3$-Sr	2.4	407
3	PIL3b@PS1	$CsPbCl_3$-Sr	3.3	407
4	PS2	$CsPbCl_{2.25}Br_{0.75}$	6	418
5	PIL3a@PS2	$CsPbCl_{2.25}Br_{0.75}$	1.2	413
6	PIL3b@PS2	$CsPbCl_{2.25}Br_{0.75}$	1.4	413
7	PS3	$CsPbCl_{1.5}Br_{1.5}$	4	458
8	PIL3a@PS3	$CsPbCl_{1.5}Br_{1.5}$	1.5	448
9	PIL3b@PS3	$CsPbCl_{1.5}Br_{1.5}$	1.2	450

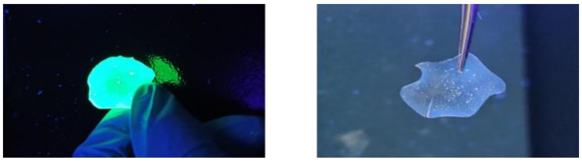
PIL3a@PS PIL3a@PS1

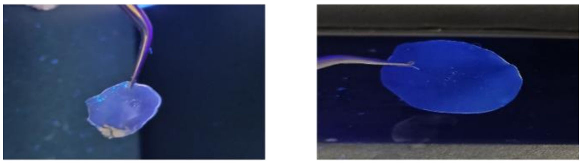
PIL3a@PS2 PIL3a@PS3

Figure 69. *Pictures of the films obtained using **PIL3a** formulation with the tested PNCs.*

The encapsulation of these different PNCs was also evaluated using mIL1, but this monomer could not stabilise them. And, the combination of $CsPbBrX_3$ with mIL3:PEGDA 575 (95:5 mol/mol) formulation did not report any photoactivity, similar to what happened with $CsPbBr_3$ (reported in **Section 3.4.2**).

Although the toxicity of lead perovskites limits their commercial use and scalability, yet the most common all-inorganic perovskite photocatalysts are lead-based. Recently, lead-free perovskites are gaining popularity but still suffer from poor efficiency and instability. Herein, a non-lead-perovskite has also been tested and properly stabilised: Sn (II)-doped CsBr (PS6). *Figure 70* shows the normalised photoluminescence of all the PNCs stabilised and properly photopolymerised into **PIL3a** formulation.

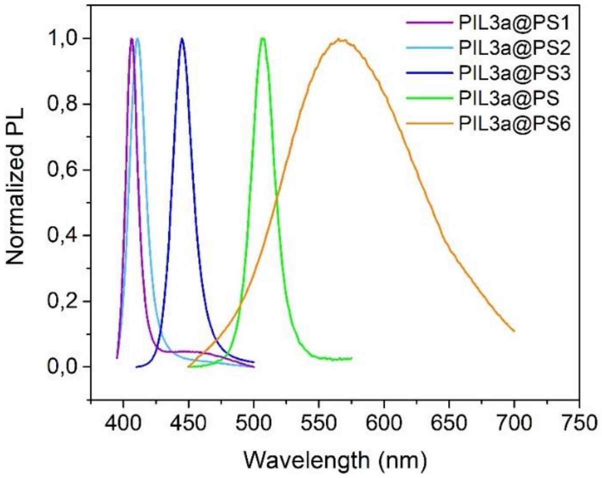

Figure 70. *Normalised photoluminescence spectra using different PNCs: PS1 ($CsPbCl_3$-Sr), PS2 ($CsPbCl_{2.25}Br_{0.75}$), PS3 ($CsPbCl_{1.5}Br_{1.5}$), PS ($CsPbBr_3$) and PS6 (Sn-doped CsBr).*

Lead-free composites were prepared using previously synthesised Sn-doped CsBr NCs dispersed in toluene. In one attempt to use the solid nanocrystals without solvent, the photopolymer was not homogeneous and, for instance, the addition of BA quenched the nanocrystals. It was tried to follow the same procedure implemented for encapsulating $CsPbBrX_3$: evaporating the toluene at 60 °C. Nevertheless, the solvent was not totally removed and the films were not well-formed. Afterwards, we decided to centrifugate toluene from a mixture of mIL3 with Sn-doped CsBr. In this way, the resulting mixture was completely homogeneous. Then, cross-linker and PI were added to the dried mixture, obtaining a homogeneous photoluminescence polymer (*Figure 71*). The centrifugation process was performed at 1500 rpm during 5 min, and was repeated several times to ensure the complete absence of toluene. The results obtained were very promising since the PLQY achieved (22 %) were remarkably similar to the one of the pure Sn-doped CsBr NCs (24 %).

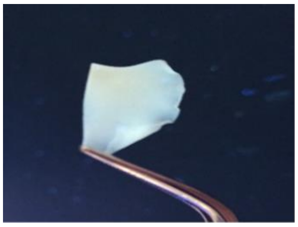

Figure 71. *Optical image of the photoluminescence observed in* ***PIL3a@PS6****.*

The stability in the dark of all these perovskite materials was tested as well. Into this context, films using **PIL3a** and **PIL3b** formulations with the different PNCs were kept wrapped in aluminium foil for more than 2 years. The PLQY and the photoluminescence of the films were measured over this period, revealing good retention of the optical properties and even an improvement in the PL activity, as well as the PLQY, after several months (*Figure 72*). Although the photoluminescence values achieved with these PNCs were not very impressive, a clear enhancement over time was observed with most of the samples. This effect may be due to a rearrangement of the structure of the perovskite nanocrystals as a result of their good stabilisation in the PIL matrix.

The polymerisation reaction of all the films was performed using the standard conditions (under UV light for 20 min at 40 ^{o}C in aerobic atmosphere).

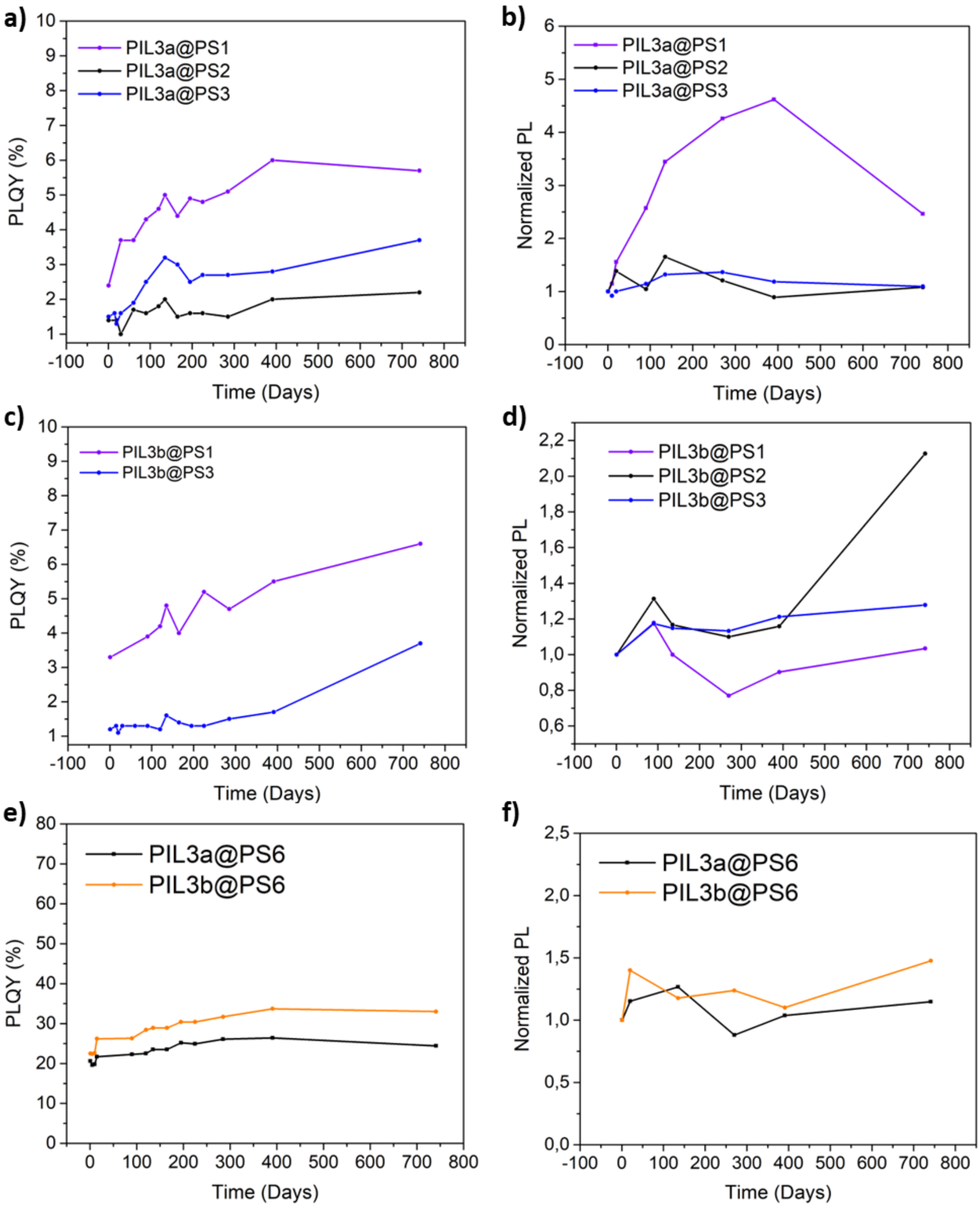

Figure 72. ***a)*** *PLQY and* ***b)*** *Normalised PL of PS1, PS2 and PS3 NCs embedded in* ***PIL3a*** *formulation;* ***c)*** *PLQY of PS1 and PS3 NCs embedded in* ***PIL3b*** *formulation;* ***d)*** *Normalised PL of PS1, PS2 and PS3 NCs embedded in* ***PIL3b*** *formulation;* ***e)*** *PLQY and* ***f)*** *Normalised PL of non-lead perovskite, PS6, encapsulated into* ***PIL3a*** *and* ***PIL3b*** *formulations. All samples were measured along more than 700 days.*

3.4.6 Ionic Exchange Study

The possibility of changing the halides from the perovskite is a really exciting approach, since it makes possible to tailor the absorption wavelength of the material by a simple anion exchange.

For this purpose, it was studied the possibility of mixing halide-based mILs with different perovskites in order to see the exchange between the anionic halides. Unfortunately, AcrEMA.Cl and AcrEMA.I could not form films, only BVI.I was capable to form films. A miscible mixture of mIL1:BVI.I (1.5:1 mol/mol) with $CsPbBr_3$ reported a green colour that was slowly becoming orange on the walls of the vial while the green colour went disappearing until PNCs were deactivated (*Figure 73*). The introduction of mIL1 was necessary to act as an intermediate between BVI.I and the perovskite; otherwise, they kept immiscible without mixing. Before adding mIL1, the perovskite kept its fluorescence and did not change its colour. However, after adding mIL1, all the components were properly mixed turning to orange and ending deactivating the PNCs.

Figure 73. *A mixture based on mIL1:BVI.I (1.5:1 mol/mol) with $CsPbBr_3$.*

Another interesting field is the possibility to exchange the halides from the PNCs embedded in solid materials, changing the colour of the films. This phenomenon was studied in different films: **PIL3b@PS**, **PIL3c@PS** (the two formulations that stabilised more efficiently PNCs, shown in **Section 3.4.4**) and the neutral formulation based on butyl acrylate (**PIL3h@PS**). The test consisted in immersing the films into a solution of potassium iodide (KI) in methanol (MeOH, 10 mg/mL) to substitute the bromide anions from $CsPbBr_3$ with the iodide from KI. When that substitution took place, the wavelength of the $CsPbBr_3$ shifted from the green to the red (the iodine emission range). We found that **PIL3h@PS** was the only tested film that modified its emission wavelength from 510 nm to 651 nm within few minutes (*Figure 74*). The film was totally red in less than 10 minutes.

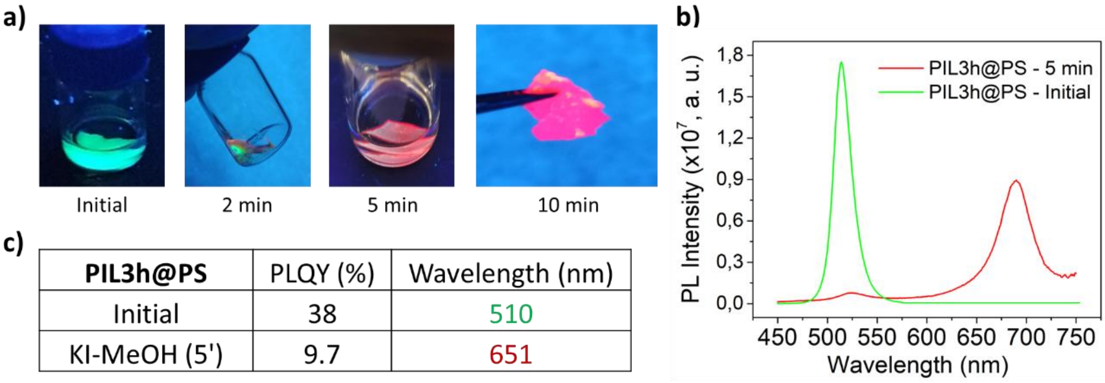

PIL3h@PS	PLQY (%)	Wavelength (nm)
Initial	38	510
KI-MeOH (5')	9.7	651

Figure 74. ***a)*** *Images showing the evolution in the colour change of* ***PIL3h@PS*** *film within less than 10 minutes in KI solution;* ***b)*** *PL spectra of the film's initial emission wavelength (green) and the film emission wavelength after 5 minutes immersed in a solution of KI (red);* ***c)*** *Initial PLQY of the film and after 5 minutes immersed in a solution of KI, with its corresponding wavelength.*

Meanwhile, PIL-based formulations probably encapsulated PNCs more strongly, preventing the passage of iodide through the polymer matrix. The films kept the green colour until its degradation due to the effect of the methanol. The PLQY of the samples was reduced from 40 % to 1 % after 30 minutes into the solvent, however the emission wavelength remained unaltered at 512 nm.

Previously, we tried to do the test in water instead of using MeOH as the embedded PNCs were relatively stable in that medium (see **Section 3.4.4**), however no changes in colour were detected for any tested film (*Figure 75*).

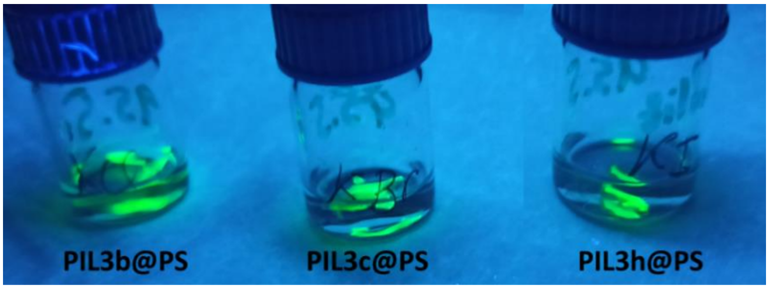

Figure 75. *(Left)* ***PIL3b@PS*** *film, (centre)* ***PIL3c@PS*** *film, (right)* ***PIL3h@PS*** *film, immersed in a solution of potassium iodide (KI) in H_2O (10 mg/mL) during more than 2 hours.*

Therefore, MeOH was the solvent chosen for carrying out these experiments. Since it was possible to exchange the bromide anions of **PIL3h@PS** film by iodide anions, it was tried using that formulation to do the reverse process, turning the modified film (**PIL3h@mPS**) back to green. In this study, firstly, as above explained, a **PIL3h@PS** film (green) was introduced into a solution of KI in MeOH (10 mg/mL) during 15 minutes, so the colour of the film changed to red. And then, after drying the **PIL3h@mPS** film in vacuum during 2 hours, it was immersed into a solution of potassium bromide (KBr) in MeOH (10 mg/mL). As we expected, the iodide anions were replaced by the bromides from the solution, returning the green colour of the perovskite as it can be seen in *Figure 76*. The film was totally green in less than 20 minutes.

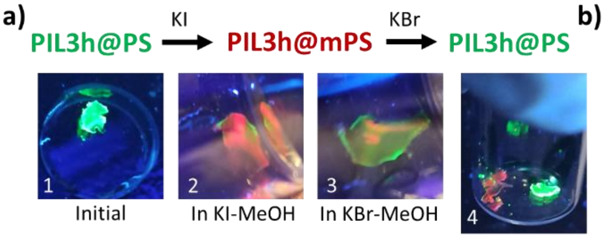

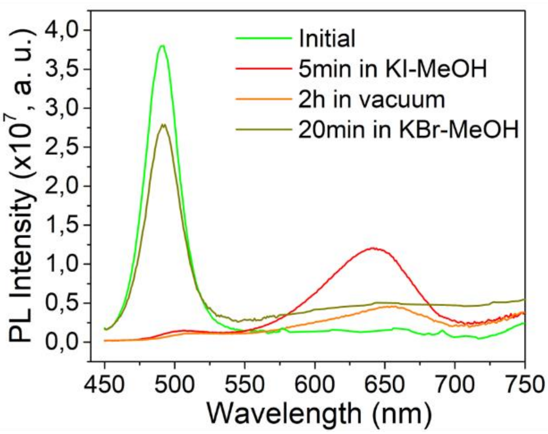

c)

PIL3h@PS	PLQY (%)	Wavelength (nm)
Initial	46	521
KI-MeOH (5')	8.5	664
KI-MeOH (2h)	7.1	662
KBr-MeOH (20')	6	521

Figure 76. ***a)*** *Images showing (1) the initial* ***PIL3h@PS*** *film, (2) after put it in KI-MeOH (turning red), (3) then, the modified* ***PIL3h@mPS*** *film was introduced in KBr-MeOH (turning green again) and (4) pieces of both films (green and red) together, keeping their PL for several days;* ***b)*** *PL spectra of* ***PIL3h@PS*** *film measured at different moments during the anion exchange reaction;* ***c)*** *PLQY of the film measured at different moments during the anion exchange reaction.*

Another interesting approach would be to shift the wavelength of $CsPbBr_3$ towards the blue emission colour. For this study it was used **PIL3h@PS** film that was introduced into a sodium chloride (NaCl) solution (5 mg/mL) in MeOH. NaCl was used because KCl was totally insoluble in MeOH, chlorobenzene, tetrahydrofuran, dichloromethane and chloroform. However, the wavelength emission slightly changed, from 520 nm to 495 nm. Further studies were performed using the precursor of the perovskite methylammonium chloride (MACl), which was soluble in butanol. But still, no changes in colour were detected. Also, MAI dissolved in butanol was used for repeating the iodide exchange, finding that the PLQY of the films did not decay as fast as with MeOH.

Also, it was possible to demonstrate that the exchange reaction can occur even directly on the surface of the films without immersing the sample into a solution. In this regard, the liquid precursor of **PIL3h@PS** was photopolymerised on the surface of a glass and, after adding some drops of a KI solution, the film turned red immediately as shows *Figure 77*a. On the other hand, the formulation used was modified to evaluate the effect of the different components. For example, when the content of cross-linker was increased to 10 mol% BDA, the exchange reaction with iodide was much slower (more than 30 minutes to observe some red colour) and only part of the film was modified as it can be seen in *Figure 77*b. Therefore, it was concluded that the more cross-linked the film was, the less exchange took place.

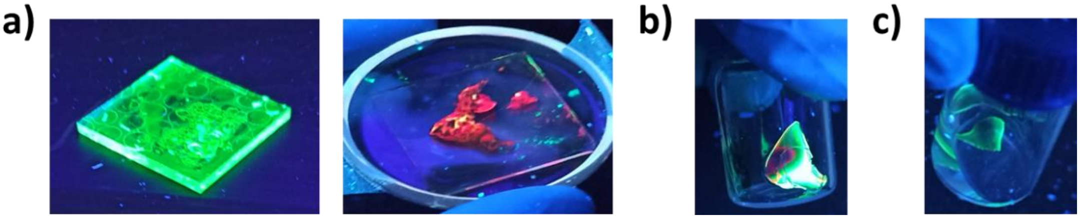

Figure 77. ***a)*** *PIL3h@PS film on the surface of a glass, before and after dropping KI solution;* ***b)*** *Film prepared with 90 mol% of BA and 10 mol% of BDA after being 30 minutes into KI solution;* ***c)*** *Film prepared with 60 mol% of BA, 20 mol% of PEGDA and 20 mol% of BDA after being 10 minutes into KI solution.*

Since the non-ionic material was favourable for the exchange reaction, a completely different neutral formulation based on a mixture of BA, PEGDA and BDA (60:20:20 mol/mol/mol) was tested. Nevertheless, this formulation was totally unable to stabilise properly $CsPbBr_3$. At 70 ^{o}C, the PNCs were completely quenched in less than 5 days, while in water PLQY decayed in less than 5 hours. For that reason, the exchange reaction carried out in MeOH medium deactivated the PNCs in few minutes, shown in *Figure 77*c.

3.4.7 3D-Printable Formulation

The most efficient formulations for the stabilisation of PNCs (**PIL3b** and **PIL3c**) were successfully 3D printed. The photopolymers were able to stabilise $CsPbBr_3$ nanocrystals (2 wt%) during the printing process and transfer their intrinsic PL properties to the printed parts, as shown in *Figure 78*. In this example, the manufacturing was performed by a masked stereolithography printer (MSLA, Elegoo Mars 2 Pro) using a LED light (405 nm) to drive the photopolymerisations. Then, the parts were washed in hexane during 5 minutes to remove any excess of unreacted monomers and post-cured using an UV light for 20 min at 40 °C.

Figure 78. *Logo of INAM 3D-printed with* ***PIL3b*** *formulation (up) with* $CsPbBr_3$ *NCs (2 wt%) (down) without PNCs. Picture taken under UV light.*

The printing parameters were adjusted for the formulation regardless of the presence of perovskite nanocrystals, as their aggregation did not significantly affect the printing conditions. The exposure time of light for the layers were 6 seconds, and 8 seconds for the *burn-in* layers (*i. e.,* the first six layers attached to the platform), and all layers had 0.1 mm of thickness. The light power was fixed at 40 W. This light power refers to the power of the UV lamp that is used to cure the resin during the 3D printing process.

3.4.8 Application in Dye Photodegradation

Organic dye emissions from industry are a major cause of pollution in the environment. Herein, photocatalytic degradation is a promising route to convert organic waste into harmless substances. Perovskite nanocrystals are very efficient photocatalysts in the visible region, allowing them to fully utilize solar energy.[251]

Within this context, the resultant **PIL3b@PS** film was tested as photocatalyst for the degradation of methyl red (MR). In this study, PILs were not only acting as good stabilizers of the perovskites, but also as good adsorbent materials. The experiment consisted in introducing the photocatalyst, a **PIL3b@PS** film, into a 30 µM solution of MR in hexane, illuminating the sample with 1 sun of visible light, using an UV filter (for further details see the *Experimental Part*, **Section 3.6.4**). In a first attempt, we tried to carry out the test in aqueous media but the dye degradation did not take place in water. Instead a wavelength shift was observed as previously reported.[289] The solution colour changed from yellow to red after 22 hours illuminating the sample with 1 sun due to a shift in the MR structure, which may be caused by a change in the pH of the medium (Figure 79).[289b]

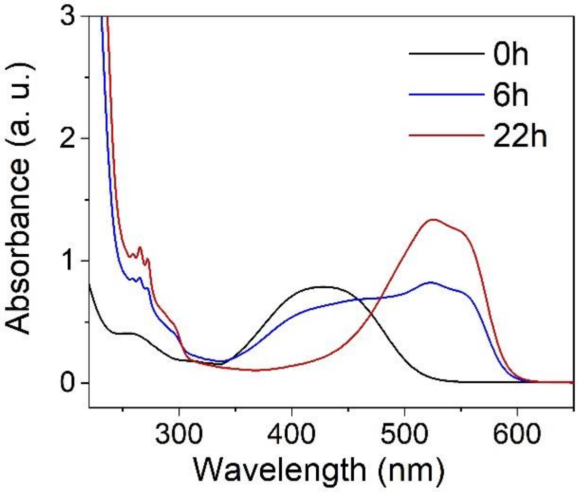

Figure 79. *Absorption spectra of methyl red in water using a* ***PIL3b@PS*** *film as photocatalyst under visible light irradiation for 22 h.*

MR dye solution in hexane showed two absorption bands with a λ_{max} at 450 nm, responsible for the yellowish colour. According to the literature, the visible absorption bands are attributed to the n → π* transition associated to the chromophoric -N=N- group found in azo dyes, while the UV bands are attributed to the benzene rings.[290] During the photodegradation, both bands decreased, indicating that the decomposition of MR involved the cleavage of benzene rings and the chromophore groups. After 22 h of reaction, the decolourisation was nearly completed, obtaining 95 % of MR degradation (Figure 80a). The control experiment (blank) was performed under same conditions without introducing any photocatalyst (*Figure 80*b), and the effect of the bare film without PNCs (**PIL3b**) was evaluated as well (*Figure 80*c), resulting in a MR degradation of 50 % and 70 %, respectively. Moreover, insignificant change in the absorption peak intensity was observed in dark and under laboratory light after 22 h (in the presence or absence of **PIL3b@PS** film).

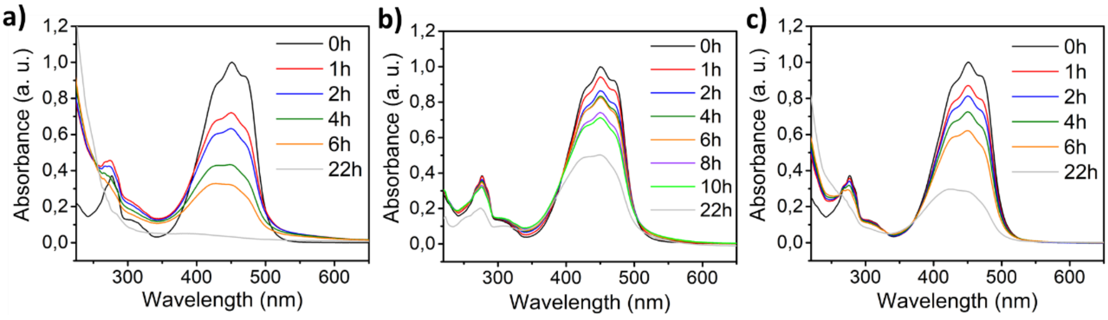

Figure 80. *Absorption spectra of methyl red during photocatalytic degradation along 22 h under visible light irradiation **a)** using **PIL3b@PS** film; **b)** for the blank experiment; **c)** using **PIL3b** film.*

Differences between the MR concentration using **PIL3b** and the blank can be attributed to the adsorption of MR on the surface of the film. Likewise, the light had also an effect on the MR degradation, as it can be seen from the blank sample, although it was almost negligible compared with the high kinetics promoted by the PNCs (*Figure 81*a). The kinetics of the three samples fits well with a pseudo-first order equation, demonstrating that the rate of decay related to the **PIL3b@PS** experiment is the greatest one in absolute value (K_s = 0.06 h^{-1}) compared to **PIL3b** (K_s = 0.02 h^{-1}) and blank (K_s = 0.01 h^{-1}). Additionally, the decolourisation of MR is notable after comparing the solution initial colour (dark yellow, *Figure 81*b-1) and the final colour after 22 h of reaction by using **PIL3b@PS** film (almost transparent, *Figure 81*b-2). On the other hand, while using **PIL3b** film the solution remained yellowish (*Figure 81*b-3). The colour of the films also changed after the experiments. The PNCs composite (**PIL3b@PS**) depicted a dark yellow colour after 22 h of MR degradation (*Figure 81*c-2), similar to the initial colour of the film (*Figure 81*c-1). Whereas the film without PNCs (**PIL3b**) ended reddish due to the adsorption of MR in the film (*Figure 81*c-3). This confirms that the photodegradation in case of **PIL3b@PS** was nearly completed.

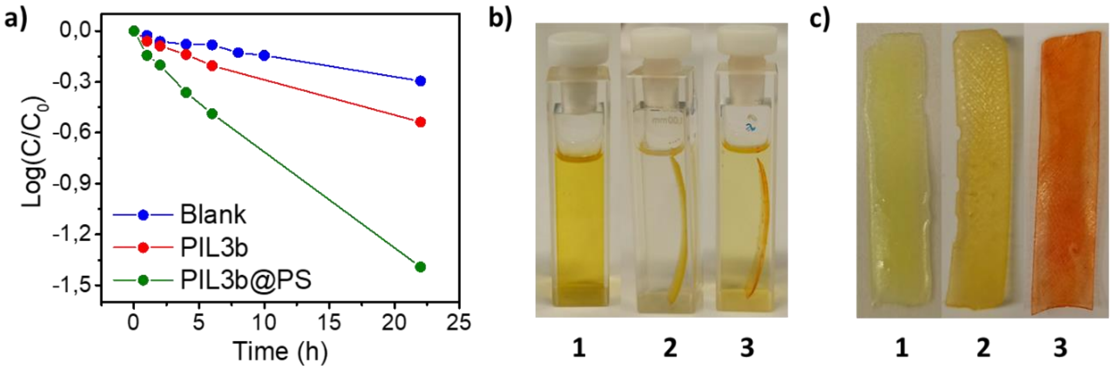

Figure 81. ***a)*** *The logarithm of the ratio between the concentration after photocatalytic degradation and the initial concentration of dye showing the kinetics of the blank, using a* ***PIL3b*** *film and a* ***PIL3b@PS*** *film;* ***b)*** *(1) Initial colour of MR solution; (2) MR solution colour after 22 h with a* ***PIL3b@PS*** *film; (3) MR solution colour after 22 h with a* ***PIL3b*** *film;* ***c)*** *(1) Initial colour of* ***PIL3b@PS*** *film; (2)* ***PIL3b@PS*** *film after 22 h into MR solution; (3)* ***PIL3b*** *film after 22 h into MR solution.*

The total degradation of MR was also confirmed by ESI-MS, where the representative peaks related to MR completely disappeared after the photodegradation reaction (*Figure 82*). Instead, new peaks that could not be identified appeared.

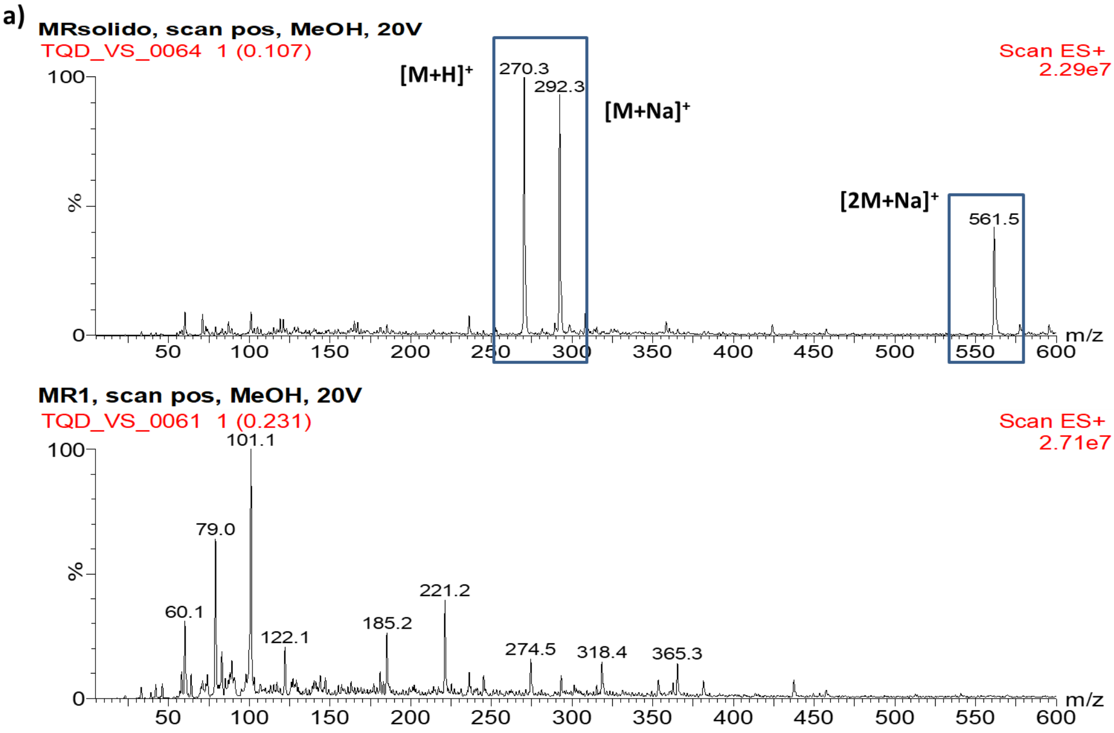

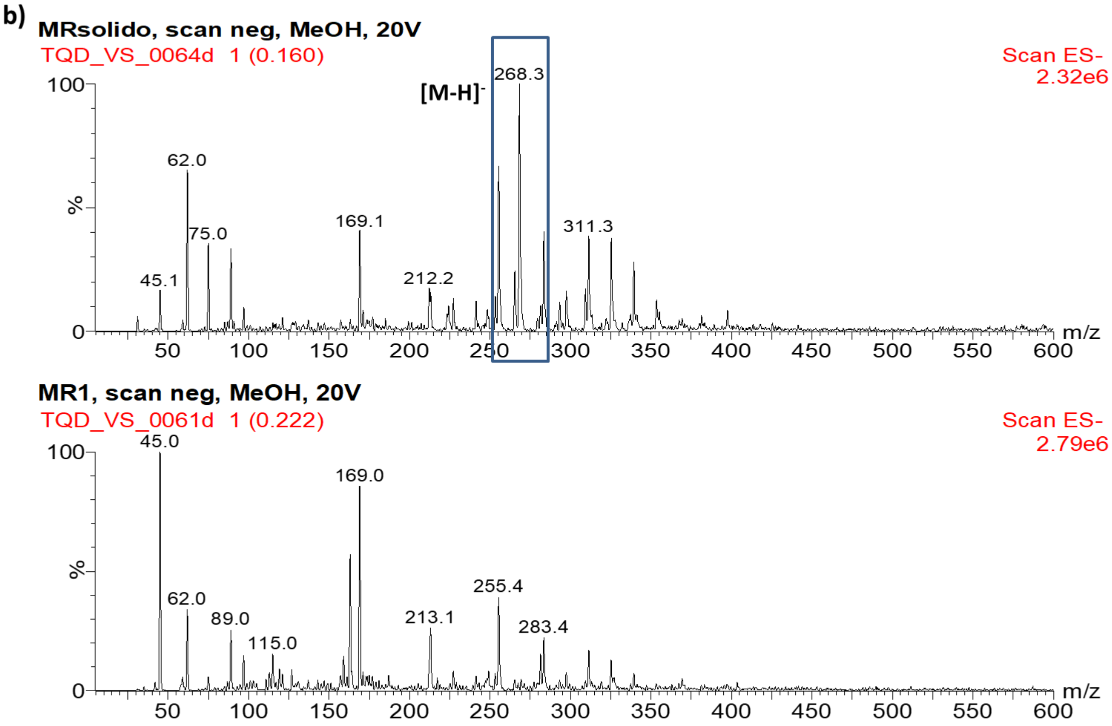

Figure 82. *ESI-MS spectra of pure methyl red (MRsolido) and MR after photodegradation (MR1) using* ***PIL3b@PS*** *film as photocatalyst,* ***a)*** *in positive mode;* ***b)*** *in negative mode.*

Nevertheless, the polymer matrix of **PIL3b** and **PIL3b@PS** was not degraded during the photocatalysis reaction, as no differences were observed in the FT-IR spectra (*Figure 83*).

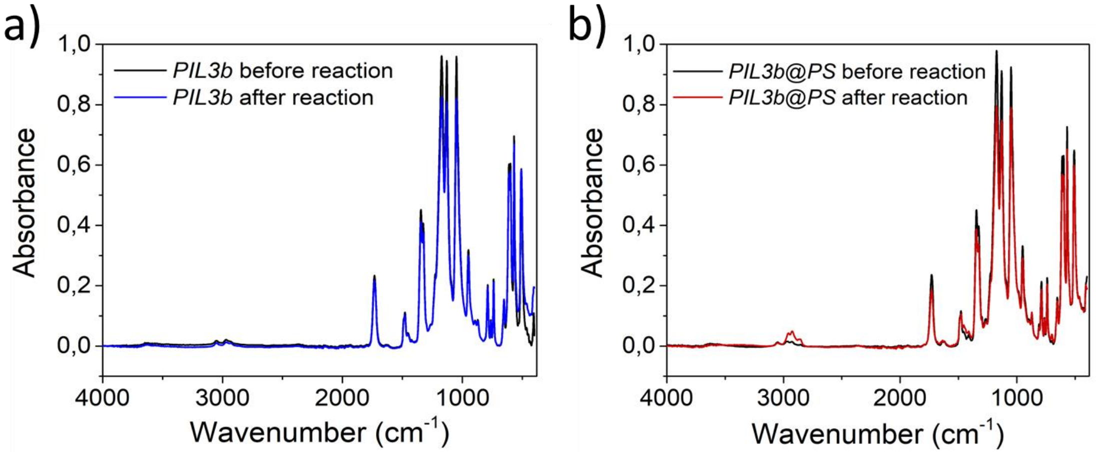

Figure 83. *FT-IR spectra before and after photocatalysis reaction of* ***a)*** *a* ***PIL3b*** *film and,* ***b)*** *a* ***PIL3b@PS*** *film.*

The films were recycled, without any further treatment, three times with new MR solution (*Figure 84*). Clearly, the experiment with **PIL3b@PS** (green one) was over the three cycles the most effective system.

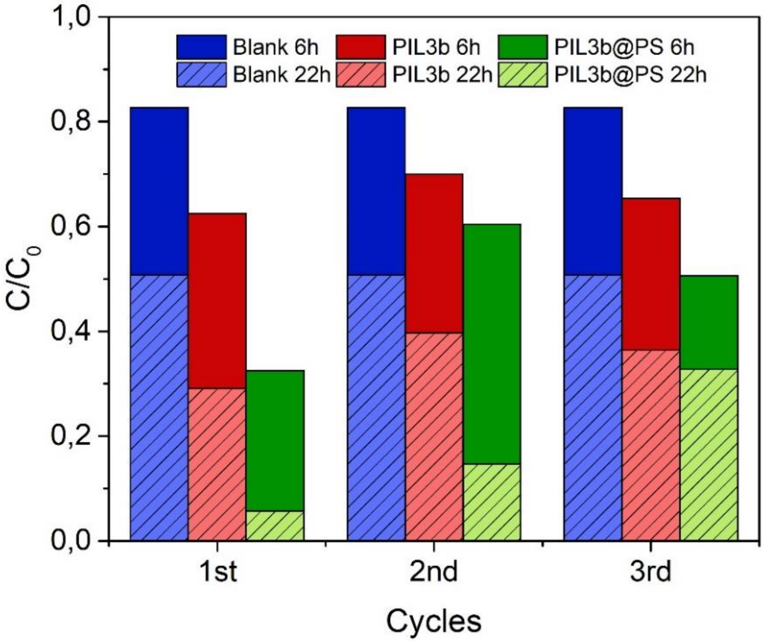

Figure 84. *Concentration lost at 6h and 22 h for the blank, using a **PIL3b** film and using a **PIL3b@PS** film as photocatalyst within 3 cycles.*

In the third cycle, after 22 h, the degradation is far from complete, only 68 % of MR is degraded. For that reason, **PIL3b@PS** film presented a reddish appearance (*Figure 85*a, left), similar to **PIL3b** film (*Figure 85*a, right). At this point, we can suggest that there are no more active PNCs on the surface of the film since the PLQY was not detectable. However, some fluorescence was observed by the fluorometer, thus indicating that there was still PNCs remaining in the core of the film as shows *Figure 85*b, c.

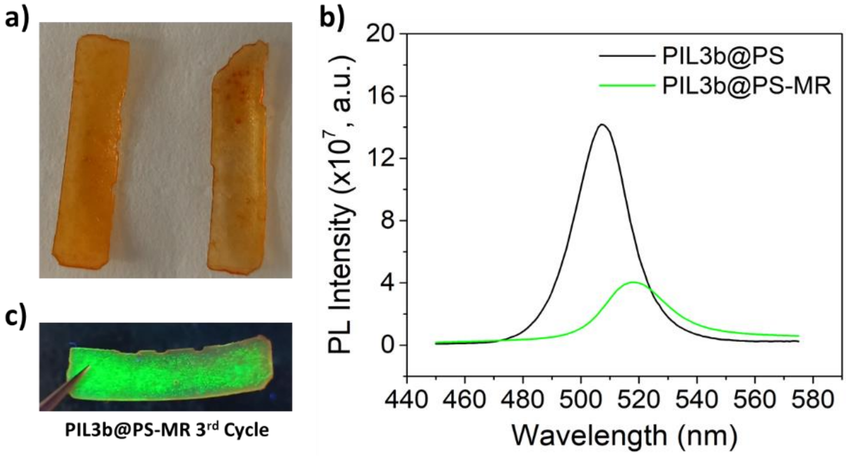

Figure 85. *Analysis of the film* ***PIL3b@PS*** *after three cycles of dye degradation experiments.* ***a)*** *Colour of the films* ***PIL3b@PS*** *(left) and* ***PIL3b*** *(right) after the third cycle illuminating the films immersed in MR solution with 1 sun;* ***b)*** *PL spectra of initial* ***PIL3b@PS*** *film and after 3 cycles immersed 22 h each cycle into a solution of MR and illuminated with visible light;* ***c)*** *Film* ***PIL3b@PS*** *after the third cycle, under UV light.*

Therefore, embedding the perovskite into a polymeric matrix allows to recycle it for several reaction cycles. The material without encapsulation was deactivated after the first cycle (*Figure 86*).

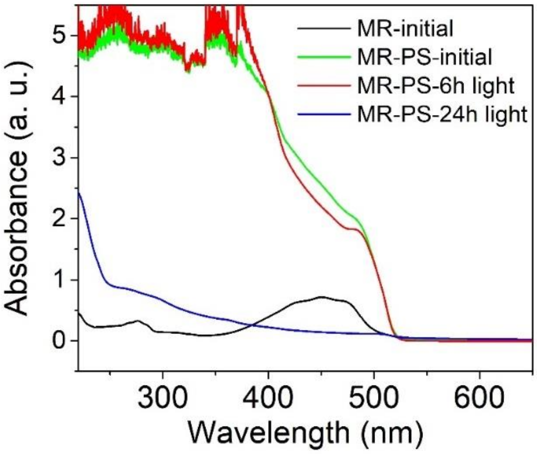

Figure 86. *Absorption spectra during MR photodegradation employing pristine $CsPbBr_3$ dissolved in hexane as photocatalyst illuminated with visible light for 24 h. The methyl red solution was measured before adding PNCs (MR-initial) and after adding the PNCs (MR-PS-initial). After 22 h, not only MR but also the PNCs signal disappeared.*

Similar as well-known semiconductor based-photocatalysts, PNCs can absorb visible-light photons to promote the generation of electron-hole pairs, which are the key factor to trigger oxidation-reduction reactions, respectively.[256d, 291] In order to precisely determine if the photodegradation in our system took place by the electrons or the holes, a hole scavenger (MeOH, 1 mM) was introduced. In presence of this alcohol (0.1 µL in 3 mL of hexane), the kinetics of MR photodegradation slowed down, becoming very similar to that of the film without PNCs (*Figure 87*). It is evident that the film **PIL3b@PS** with a hole scavenger was acting only as an adsorbent material with lower PC activity. The graphic shows that using a hole scavenger, **PIL3b@PS** film had same behaviour as **PIL3b** film. Hence, in this case the PNCs are not involved in the degradation process, since the holes are being blocked by MeOH. Therefore, the experiment confirms that the photoexcited holes generated in $CsPbBr_3$ NCs upon illumination are responsible for the decomposition of the dye.

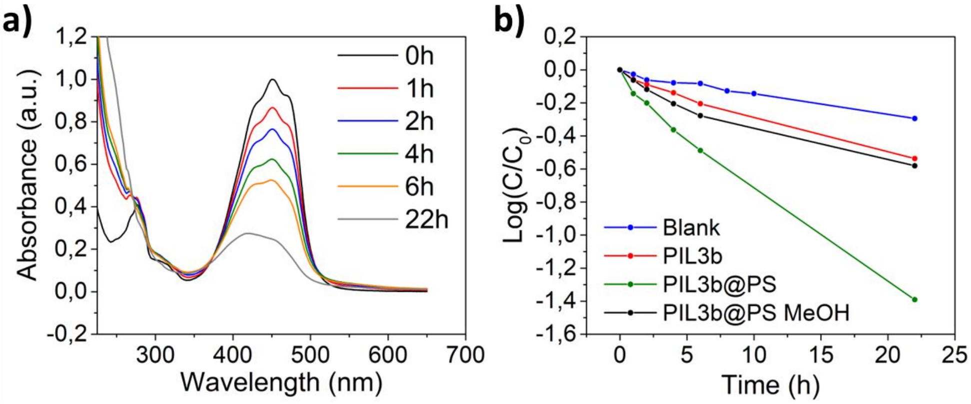

Figure 87. ***a)*** *UV-Vis spectra showing the MR photodegradation using **PIL3b@PS** film and a hole scavenger (MeOH) during 22 h illuminated with visible light;* ***b)*** *Comparison of the kinetics of the blank, **PIL3b**, **PIL3b@PS** and **PIL3b@PS** with a hole scavenger (MeOH).*

We can suggest that the holes photogenerated in the PNCs may migrate to the surface of the film to be in contact with MR and carry out the oxidation of the dye (*Figure 88*). After the first cycle, the number of PNCs in the surface of the film decreased as demonstrated the PLQY (fell from 40 % to 15 %), since the electrons were not efficiently removed from the medium, which eventually caused the degradation of the perovskite in the surface. However, the film was still photoluminescent, so the photoexcited holes may come from the PNCs remaining in the core of the film. This explains why the efficiency of the system was reduced and needed longer times for degrading MR, but still **PIL3b@PS** film presented a photodegradation effect after the third cycle. In conclusion, the advanced material **PIL3b@PS** is acting as a bifunctional advanced film capable to adsorb and, simultaneously, photodegrade organic dyes.

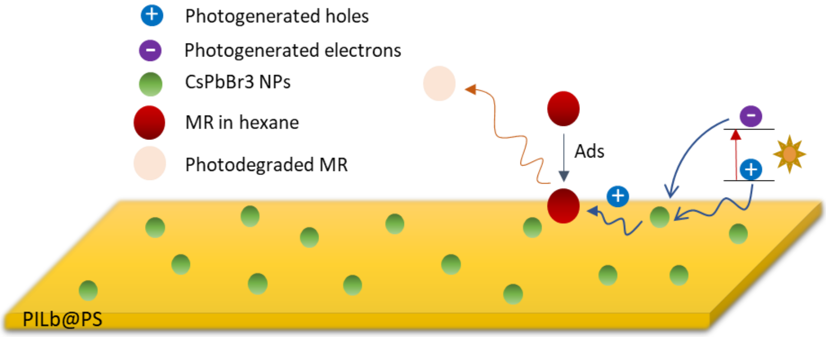

Figure 88. *Proposed mechanistic description for the adsorption and photocatalytic degradation of methyl red over the surface of **PIL3b@PS** film under sunlight. Our results suggest that the holes are responsible for the photodegradation of the dye.*

Apart from methyl red, other dyes and pollutants were tested such as benzyl alcohol and indigo. In the case of benzyl alcohol, the absorbance wavelength was around 250 nm, which overlapped with other signals and therefore the results were not reliable. The indigo was tested both in water and hexane, obtaining better results in the former one. Still, the photodegradation was not completed after 22 h, as it can be seen in *Figure 89*.

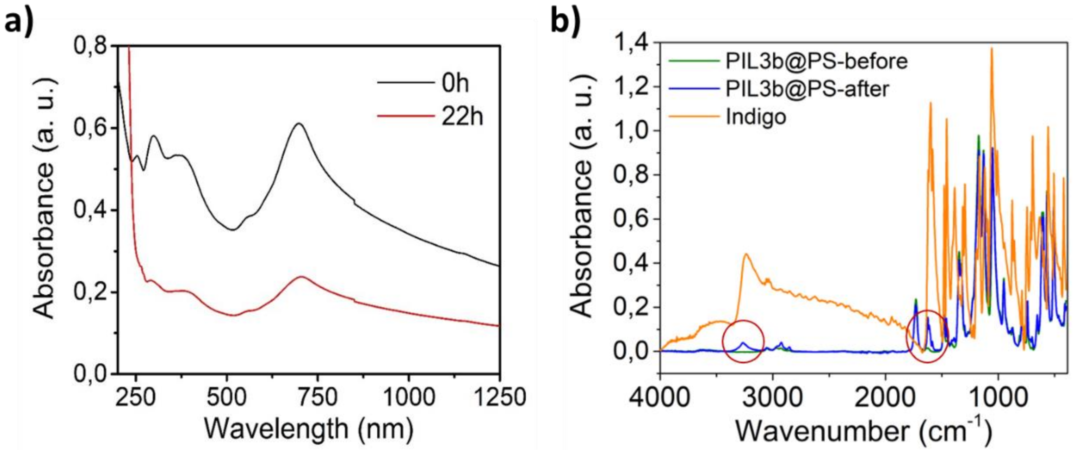

Figure 89. *a) Absorption spectra of indigo in water using **PIL3b@PS** photocatalyst along 22 h under visible light irradiation; **b)** FT-IR spectra of **PIL3b@PS** photocatalyst before and after the photocatalysis, showing some characteristic indigo bands after the photocatalysis.*

3.5 Conclusions

In this Chapter, perovskite nanocrystals have been embedded in polymeric ionic liquid matrices exploiting their well-established ability to stabilise molecular and nanostructured materials. The ionic and supramolecular interactions of PILs with the PNCs ions stabilise the nanocrystals before and after the polymerisation. The incorporation of fluorine and sulfur species coming from the monomeric ionic liquid, replaced/filled bromide vacancies formed during the synthesis of the PNCs.

Different formulations were prepared and characterised in order to find the most suitable encapsulating materials. The monomeric ionic liquid [2-(acryloyloxy)ethyl]trimethyl-ammonium bis(trifluoromethylsulfonyl)imide (mIL3) was able to effectively stabilise $CsPbBr_3$ NCs by in-situ photopolymerisation forming insoluble and hydrophobic cross-linked films. Then, the formulation was optimised by modifying mIL3 content. The photopolymer that reported best optical and mechanical performance was the mixture of mIL3 (95 mol%) with 5 mol% of BDA and 2 wt% of $CsPbBr_3$ (**PIL3b@PS**).

A variety of PNCs based on $CsPbX_3$ structure (X = Cl, Br and combinations) and lead-free perovskites were also properly encapsulated, reporting a stable PL and PLQY along more than 700 days. In particular, **PIL3b@PS** films exhibited impressive quantum yields (~50 %) and photoluminescence with enhanced water, air, light, oxygen, humidity and heat resistance. Moreover, these PNCs were specially formulated to be 3D-printed in tailored geometries, directly translating the perovskite properties to the additive manufactured objects.

On the other hand, PILs are good adsorbent materials, meanwhile the PNCs are well-known for their photocatalyst activity. In this regard, it was demonstrated the possibility to embed PNCs into PILs to form solid photocatalysts capable to adsorb and degrade organic dyes. A **PIL3b@PS** film was used as photocatalyst for increasing the rate of methyl red decomposition (95 %) under visible light. In all the studies conducted, the kinetics of the photocatalysis reactions were calculated. The film was recycled finding that after the third cycle there was still moderate activity (68 %) compared to control experiment. The mechanism of photodegradation was proposed through photoexcited holes.

3.6 Experimental Part

3.6.1 Materials

As mentioned in **Chapter 2**, all reagents were purchased from Sigma-Aldrich and used without further purification, unless otherwise stated. Lithium bis(trifluoromethane) sulfonimide ($LiNTf_2$, 99 %) was purchased from IOLITEC GmbH and used as received.

3.6.2 Equipment

In this Chapter, same equipment described in **Chapter 2** have been employed.

Additionally, a fluorometer and an absolute-PLQY were used to measure the photoluminescence of the samples. Photoluminescence (PL) spectra of the films containing $CsPbBr_3$ and Sn (II)-doped CsBr NCs were recorded on a HORIBA photoluminescence spectrometer from 450 to 750 nm with an integration time of 1 nm/s under an excitation wavelength of 420 nm. While PL spectra of the materials containing $CsPbX_3$ structure with X = Cl:Br combinations were recorded from 395 to 500 nm with an integration time of 1 nm/s under an excitation wavelength of 380 nm.

The absolute photoluminescence quantum yield of the PNCs was estimated through a Hamamatsu PLQY Absolute QY Measurement System C9920-02, equipped with an integrating sphere, at an excitation wavelength of 385 or 420 nm depending on the perovskite tested. Before conducting the measurements, absorbance was fixed in an interval range around 0.4 - 0.5, being these values adequate to achieve the maximum PLQY in the samples.

3.6.3 Stability Tests of the Perovskite Nanocrystals Composites

Four different studies were performed to compare the stability of pristine $CsPbBr_3$ with PNCs encapsulated in polymeric ionic liquids using different formulations. For the test in the dark the samples were covered with aluminium and kept in a drawer at room temperature with a relative humidity of 60 % under aerobic atmosphere. Simultaneously, for the air stability test, the samples were left on the laboratory bench open to atmospheric conditions (air, light and humidity) at room temperature. The aqueous stability tests were done immersing the samples in deionised water in a closed 5 mL vial and stored under day light conditions at room temperature. The temperature stability experiments were conducted in open 5 mL vials placed in an oven at 70 °C without light irradiation.

3.6.4 Set-up for the Photodegradation Experiments

A 30 µM solution of methyl red (MR) in hexane was prepared and introduced into fluorescent cuvettes together with the corresponding film. All the solution were prepared under aerobic conditions. The system was properly closed to avoid the evaporation of hexane. Then, the cuvettes were kept under visible light for 22 hours using a xenon lamp of 300 V at 100 mV/cm^2 (*Figure 90*). An UV filter was employed to avoid the effect of UV light for degrading the dyes.

Figure 90. *Experimental set-up used for photodegrading methyl red.*

The UV-Vis absorbance of the methyl red was measured at different times to study the kinetics of the degradation reaction. All the experiments were repeated at least twice. For the recycle test, the films were removed from the solution and used in the next cycle with new MR solution without any additional treatment.

3.6.5 Synthesis and Characterisation of Monomeric Ionic Liquids

The synthesised monomers were: mIL1, mIL3, BVI.N(CN)$_2$, BVI.I, AcrEMA.N(CN)$_2$, AcrEMA.I, AcrEMA.BF$_4$. The synthetic procedure of the first two (mIL1 and mIL3) was previously explained in **Chapter 2, Section 2.6.6**. In this section, we will describe the synthesis of the other monomers.

The monomer VIm was used directly from the commercial bottle (1-vinylimidazole), while [2-(acryloyloxy)ethyl]trimethyl-ammonium chloride (AcrEMA.Cl) was obtained after evaporating the water from the commercial reagent, [2-(acryloyloxy)ethyl]trimethyl-ammonium chloride (80 wt%, in H_2O). All the characterising spectra referred in this Section can be found in **Chapter 6: Annex, Section 6.2**.

1-butyl-3-vinylimidazolium dicyanamide (BVI.N(CN)$_2$)

1-butyl-3-vinylimidazolium dicyanamide was prepared following a procedure found in the literature.[31a] Firstly, Ag[N(CN)$_2$] was synthesised by mixing sodium dicyanamide with silver nitrate. Sodium dicyanamide (7.8 g, 84 mmol) was dissolved in mili-Q water (50 mL) and the solution was added dropwise to a saturated aqueous solution of silver nitrate (14.31 g, 84 mmol) in a 100 mL round-bottom flask with a Teflon coated magnetic stir bar. Immediately, a white solid precipitated. The reaction mixture was stirred overnight in darkness at room temperature. The resulting white solid was filtered and washed with mili-Q water and methanol. Then, the Ag[N(CN)$_2$] solid product was dried in a vacuum oven at 70 ^oC for 24 h (14.32 g, Yield: 98 %). 1-butyl-3-vinylimidazolium dicyanamide was prepared mixing Ag[N(CN)$_2$] (2.07 g, 12 mmol), in slight molar excess, with 1-butyl-3-vinylimidazolium bromide (2.56 g, 11 mmol) dissolved in mili-Q water (12 mL). The resulting suspension was stirred overnight in the dark at room temperature and then filtered to remove any trace of AgBr and unreacted Ag[N(CN)$_2$]. Evaporation of the filtrate was performed under reduced pressure at 40 ^oC to give a white viscous liquid (2.32 g, Yield: 97 %).

The resulting mIL was characterised by ^1H NMR, ^{13}C NMR, ESI-MS and elemental analysis. ^1H NMR (400 MHz, $CDCl_3$): δ / ppm = 9.49 (s, 1H), 8.11 (t, *J* = 2 Hz, 1H), 7.87 (t, *J* = 1.9 Hz, 1H), 7.34 (dd, *J* = 24, 8.4 Hz, 1H), 6.10 (dd, *J* = 18.4, 2.8 Hz, 1H), 5.66 (dd, *J* = 11.2, 2 Hz, 1H), 4.44 (t, *J* = 7.2 Hz, 2H), 2.10 (m, 2H), 1.61 (m, 2H), 1.19 (t, *J* = 7.6 Hz, 3H). ^{13}C NMR (400 MHz, $CDCl_3$): δ / ppm: 127.7, 122.7, 119.2, 118.9, 109.9, 49.4, 31.2, 18.8, 12.3. ESI-MS in positive mode: Calculated: 151.12 m/z; Found: 151.1 m/z. ESI-MS in negative mode: Calculated: 66.01 m/z; Found: 66.1 m/z. Elemental Analysis: Calculated: C, 60.81; H, 6.96; N, 32.23; Found: C, 58.90; H, 6.39; N, 31.06 (*Figure A14* and *Figure A15*).

1-butyl-3-vinylimidazolium iodide (BVI.I)

1-butyl-3-vinylimidazolium iodide was prepared using the method developed by Salamone and co-workers.[292] Vinyl imidazole (5 g, 53 mmol) was dissolved in acetonitrile (5 mL). Then, butane iodide (14.66 g, 80 mmol) dissolved in acetonitrile (5 mL) was added dropwise. The resulting mixture was stirred during 6 hours at 40 °C. Afterwards, the solvent was evaporated under vacuum at 45 °C to give viscous liquid. The liquid was washed five times with ether (20 mL) and then, it was re-dissolved in dichloromethane (minimum amount) and slowly added to rapidly stirred ethyl acetate (20 mL) to form a purer solid. This procedure was also repeated five times. The liquid was dried in an oven at 45 °C for 24 h to give a dark red viscous liquid (8.95 g, Yield: 61 %).

The resulting mIL was characterised by ^{1}H NMR, ^{13}C NMR, ESI-MS, elemental analysis, FT-IR and TGA-DSC. ^{1}H NMR (400 MHz, $CDCl_3$): δ / ppm = 10.49 (s, 1H), 7.87 (t, *J* = 1.9 Hz, 1H), 7.66 (t, *J* = 1.9 Hz, 1H), 7.41 (dd, *J* = 15.6, 8.7 Hz, 1H), 6.02 (dd, *J* = 15.6, 3.1 Hz, 1H), 5.41 (dd, *J* = 8.7, 3.1 Hz, 1H), 4.41 (t, *J* = 7.4 Hz, 2H), 1.93 (m, 2H), 1.38 (m, 2H), 0.94 (t, *J* = 7.4 Hz, 3H). ^{13}C NMR (400 MHz, $CDCl_3$): δ / ppm: 135.1, 128.1, 123.1, 119.7, 110.5, 50.3, 32.1, 19.5, 13.5. ESI-MS in positive mode: Calculated: 151.12 m/z; Found: 151.3 m/z. ESI-MS in negative mode: Calculated: 126.91 m/z; Found: 126.9 m/z. Elemental Analysis: Calculated: C, 38.87; H, 5.44; N, 10.07; Found: C, 38.81; H, 5.52; N, 9.96. FT-IR bands of the compound hydrated: 3447 cm^{-1} (H_2O), 3060 cm^{-1} (C=C), 2948 cm^{-1} (C-H), 1656 cm^{-1} (C=N), 1544 cm^{-1} (C=C), 1165 cm^{-1} (C-C). T_{onset}: 286.00 °C (*Figure A16* - *Figure A18*).

[2-(acryloyloxy)ethyl]trimethyl-ammonium dicyanamide (AcrEMA.N(CN)$_2$)

[2-(acryloyloxy)ethyl]trimethyl-ammonium dicyanamide was prepared following same procedure used for synthesising BVI.N(CN)$_2$.[31a] Silver dicyanamide (1.9 g, 11 mmol) was mixed with [2-(acryloyloxy)ethyl]trimethyl-ammonium chloride (2 g, 10 mmol) dissolved in mili-Q water (10 mL) in a 50 mL round-bottom flask with a Teflon coated magnetic stir bar. An emulsion appeared, changing the solution colour from transparent to reddish. The resulting suspension was stirred overnight in the dark at room temperature and then filtered and washed with mili-Q water to remove any trace of AgCl and unreacted Ag[N(CN)$_2$]. Evaporation of the filtrate was performed under vacuum at 45 °C to give viscous liquid. Then, the product was re-dissolved in methanol (15 mL) and dried over $MgSO_4$ anhydride to remove the remaining water. The white product was decanted and dried under reduced pressure at 37 °C (1.8 g, Yield: 77 %).

The resulting mIL was characterised by ^{1}H NMR, ^{13}C NMR, ESI-MS, elemental analysis, FT-IR and TGA-DSC. ^{1}H NMR (400 MHz, MeOD): δ / ppm = 6.44 (dd, *J* = 16, 1.2 Hz, 1H), 6.24 (dd, *J* = 11.2, 6.8 Hz, 1H), 6.00 (dd, *J* = 9.2, 1.6 Hz, 1H), 4.65 (m, 2H), 3.77 (m, 2H), 3.24 (s, 9H). ^{13}C NMR (400 MHz, MeOD): δ / ppm: 166.5, 132.8, 128.7, 120.5, 66.1, 59.0, 54.5. ESI-MS in positive mode: Calculated: 158.12 m/z; Found: 157.9 m/z. ESI-MS in negative mode: Calculated: 66.01 m/z; Found: 65.9 m/z. Elemental Analysis: Calculated: C, 53.56; H, 7.19; N, 24.98; Found: C, 51.58; H, 7.83; N, 23.44. FT-IR bands: 3454 cm^{-1} (N-C≡N), 3032 cm^{-1} (C=C), 2969 cm^{-1} (C-H), 2234-2133 cm^{-1} (C≡N), 1726 cm^{-1} (C=O), 1628 cm^{-1} (C=C), 1263 cm^{-1} (C-N), 1179 cm^{-1} (C-C), 951 cm^{-1} (C-N), 521 cm^{-1} (N-C≡N). T_{onset}: 237.81 °C (*Figure A19* - *Figure A21*).

[2-(acryloyloxy)ethyl]trimethyl-ammonium iodide (AcrEMA.I)

[2-(acryloyloxy)ethyl]trimethyl-ammonium iodide was prepared by the same procedure used for BVI.I.[292] [2-(acryloyloxy)ethyl]trimethyl-ammonium choline (2 g, 14 mmol) was dissolved in dry tetrahydrofuran (5 mL). Then, methyl iodide (2.3 g, 16 mmol) dissolved in dry tetrahydrofuran (4 mL) was added dropwise. Immediately, a solid precipitate and more dry tetrahydrofuran (2 mL) were added. The resulting mixture was stirred during 18 hours at RT. Afterwards, the solid was washed with cold hexane and evaporated under vacuum at 45 °C to give a very hydrophilic white solid (3.4 g, Yield: 88 %).

The resulting mIL was characterised by ^{1}H NMR, ^{13}C NMR, ESI-MS, elemental analysis, FT-IR and TGA-DSC. ^{1}H NMR (400 MHz, D_2O): δ / ppm = 6.50 (dd, *J* = 16.6, 8.4 Hz, 1H), 6.29 (dd, *J* = 15.1, 2.1 Hz, 1H), 6.11 (dd, *J* = 10.7, 1.8 Hz, 1H), 4.71 (m, 2H), 3.84 (m, 2H), 3.29 (s, 9H). ^{13}C NMR (400 MHz, D_2O): δ / ppm: 167.3, 133.3, 127.0, 64.6, 58.5, 53.9. ESI-MS in positive mode: Calculated: 158.12 m/z; Found: 158.4 m/z. ESI-MS in negative mode: Calculated: 126.91 m/z; Found: 127.3 m/z. Elemental Analysis: Calculated: C, 33.70; H, 5.66; N, 4.91; Found: C, 32.13; H, 5.92; N, 4.17. FT-IR bands: 3012 cm^{-1} (C=C), 2948 cm^{-1} (C-H), 1727 cm^{-1} (C=O), 1628 cm^{-1} (C=C), 1265 cm^{-1} (C-C). T_{onset}: 234.46 °C (*Figure A22* and *Figure A23*).

[2-(acryloyloxy)ethyl]trimethyl-ammonium tetrafluoroborate (AcrEMA.BF_4)

[2-(acryloyloxy)ethyl]trimethyl-ammonium tetrafluoroborate was synthesised by an anion exchange with sodium tetrafluoroborate according to a similar protocol reported.[293] Sodium tetrafluoroborate (1.4 g, 13 mmol) was dissolved in mili-Q water (10 mL) and it was added dropwise to an aqueous solution (10 mL) of [2-(acryloyloxy)ethyl]trimethyl-ammonium chloride (2 g, 10 mmol). The mixture was stirred for 20 h at RT. Afterwards, the product was totally dissolved in the water. The mixture was put at 0 °C and after a while some product precipitated. It was redissolved in acetonitrile and evaporated under vacuum at 45 °C to give a white solid (0.7 g, Yield: 35 %).

The resulting mIL was characterised by ^{1}H NMR, ^{13}C NMR, ESI-MS, elemental analysis, FT-IR and TGA-DSC. ^{1}H NMR (400 MHz, D_2O): δ / ppm = 6.49 (dd, *J* = 15.8, 7.7 Hz, 1H), 6.28 (dd, *J* = 16.1, 2.3 Hz, 1H), 6.10 (dd, *J* = 10.7, 1.9 Hz, 1H), 4.69 (m, 2H), 3.82 (m, 2H), 3.27 (s, 9H). ^{13}C NMR (400 MHz, D_2O): δ / ppm: 167.3, 133.2, 127.0, 64.6, 58.4, 53.8. ^{19}F NMR (400 MHz, D_2O): δ / ppm: -150. ESI-MS in positive mode: Calculated: 158.12 m/z; Found: 158.2 m/z. ESI-MS in negative mode: Calculated: 87.00 m/z; Found: 87.2 m/z. Elemental Analysis: Calculated: C, 39.22; H, 6.58; N, 5.72; Found: C, 34.28; H, 6.27; N, 4.81. FT-IR bands: 3046 cm^{-1} (C=C), 2984 cm^{-1} (C-H), 1733 cm^{-1} (C=O), 1635 cm^{-1} (C=C), 1200 cm^{-1} (C-C), 526 cm^{-1} (B-F). T_{onset}: 331.35 °C (*Figure A24* - *Figure A26*).

Synthesis of $CsPbX_3$ (X = Cl, Br, I and Cl:Br, Br:I combinations)

All the $CsPbX_3$ PNCs used in this work were prepared in collaboration with Mora's group (INAM) by Andres Gualdrón-Reyes and Alexis Villanueva-Antolí. The $CsPbX_3$ PNCs were prepared using hot injection method previously described in literature with some modifications.[282] To prepare the Cs-oleate solution, 0.407 g Cs_2CO_3, 1.5 mL oleic acid (OA, 90 %) and 20 mL of 1-octadecene (1-ODE, 90 %) were mixed into a 50 mL-three neck flask, under vacuum for 30 min at 80 °C under vigorous stirring. The temperature was increased to 120 °C and kept under vacuum for 30 min. The mixture was heated at 150 °C under N_2 atmosphere, until complete Cs_2CO_3 dissolution. The resultant transparent solution was kept at 120 °C before use.

For the synthesis of $CsPbCl_3$-Sr, $CsPbBr_3$, $CsPbBrI_3$ and the combinations, $CsPbCl_{3-x}Br_x$, $CsPbBr_{3-x}I_x$, 0.8 g PbX_2 and the corresponding Cl:Br, Br:I molar ratios (3:1 and 1:1) (using $PbCl_2$ and PbI_2, respectively) were mixed with 50 mL 1-ODE into a 100 mL-three neck flask and degasified at 120 °C for 1 h under stirring. Then, 5.0 mL of each preheated OA and oleylamine (HT-OA, 98 %) were added to the flask to promote the PbX_2 dissolution. Then, the temperature of PbX_2 mixture was rapidly increased to reach 180 °C and 4 mL of preheated Cs-oleate was swiftly injected, obtaining a green precipitate in the colloidal solution. The flask was immediately added into an ice bath for 5 s to quench the reaction mixture. To isolate the final product, PNCs are centrifuged at 5000 for 5 min with methyl acetate (MeOAc, 99.5 %) (30 mL of PNCs liquor washed with 60 mL MeOAc). The supernatant is discarded, the PNCs pellets are redispersed in hexane at a concentration ~50 mg/mL and stored in the fridge for 24 h.

Synthesis of Sn(II)-doped CsBr

Lead-free perovskites were also prepared in collaboration with Mora's group (INAM) by Samrat Das Adhikari. 212 mg (1 mmol) of CsBr and 278 mg (1 mmol) of $SnBr_2$ were added to 25 mL of DMF and stirred for 30 min to obtain a clear solution. Finally, this solution was used as the precursor solution. Two different flow pumps were used and connected with a "T" junction. Herein, toluene was used as the antisolvent. Toluene was pumped using one of the pumps connected parallel to the product-side capillary, and precursor solution was pumped using another pump, which was connected perpendicular to the product-side capillary. The flow-rate of toluene was fixed to 1 mL/min and the flow-rate of precursor solution was changed from 0.1 to 0.5 mL/min.[294]

Viscosity Studies

Additionally, we studied specific properties, such as viscosity, surface tension (ST) and density, of some formulations using **mIL3**. The rheological analysis reported very high viscosities. For that reason, some solvents were added in very low concentrations to reduce the viscosity of the material. The selected solvents were tert-butanol (t-BOH), acetylacetone (Ac), chloride benzene (Clbz) and 2,4-pentanodione (Pne) taking into account some of their features like high boiling point, low viscosity, low density and slightly high surface tension, as well as their ability for stabilising PNCs. Different concentrations of the solvents were evaluated. In the case of the tert-butanol, we found that at low concentrations, both the monomer and PNCs were well dissolved and stabilised, however at concentrations higher than 100 mol% the mixture was miscible but the PNCs were quenched. Otherwise, using huge amounts of solvent (1 mL) the monomer was not solubilised and the PNCs precipitated without quenching.

The rheological as well as the surface tension measurements of **mIL3b** formulation were realised at 35, 40 and 45 ºC, while the density was measured at 30, 35 and 40 ºC (being 1.46, 1.45 and 1.42 g/mL, respectively). The results obtained for rheological and ST measurements are summarised in the following Table 12.

Table 12. *All the formulations prepared specifying the solvent and the percentage used and their respective viscosity and surface tension.*

		35 ºC		***40 ºC***		***45 ºC***	
Entry	***Formulation***	***Viscosity (cP)***	***ST (dyne/cm)***	***Viscosity (cP)***	***ST (dyne/cm)***	***Viscosity (cP)***	***ST (dyne/cm)***
1	mIL3b	190.33	37.15	101.40	36.37	61.78	33.42
2	mIL3b-10% t-BOH	154.23	36.10	86.96	35.96	52.19	34.40
3	mIL3b-20% t-BOH	145.03	-	81.07	35.93	50.22	34.30
4	mIL3b-30% t-BOH	127.32	-	72.13	35.27	45.63	32.03
5	mIL3b-40% t-BOH	106.30	-	61.68	33.57	39.93	31.95
6	mIL3b-50% t-BOH	109.56	-	61.48	32.93	38.02	32.02
7	mIL3b-60% t-BOH	100.64	32.91	59.49	32.25	38.14	32.20
8	mIL3d-40% t-BOH	83.50	33.23	50.10	32.79	32.38	33.81
9	mIL3d-5% Ac	64.73	-	50.60	-	40.61	-
10	mIL3d-10% Ac	52.24	-	41.54	-	33.78	-
11	mIL3d-20% Ac	33.90	34.54	28.48	34.10	24.17	34.13
12	mIL3d@PS-20% Ac*	42.42	28.57	34.62	28.05	27.09	30.40
13	mIL3d@PS-20% Ac	39.88	21.96	34.22	21.10	32.82	21.10
14	mIL3d-5% Clbz	65.10	-	51.12	32.74	41.50	31.66
15	mIL3d-10% Clbz	59.41	-	46.44	-	36.82	-
16	mIL3d-5% Pne	61.83	-	48.66	-	39.33	-
17	mIL3d-10% Pne	57.58	-	45.18	-	35.98	-

The percentage of solvents referred in the table were calculated in molar %. *In this sample the amount of $CsPbBr_3$ was 1 wt% instead of the usual 2 wt%. The solvents used were tert-butanol (t-BOH), acetylacetone (Ac), chloride benzene (Clbz) and 2,4-pentanodione (Pne).

3.6.6 Characterisation of the Films

On the other hand, the photopolymerised films were characterised by FT-IR, Raman, TGA-DSC, UV-Vis, SEM, optical microscopy and profilometry (see *Figure 91*-*Figure 95*).

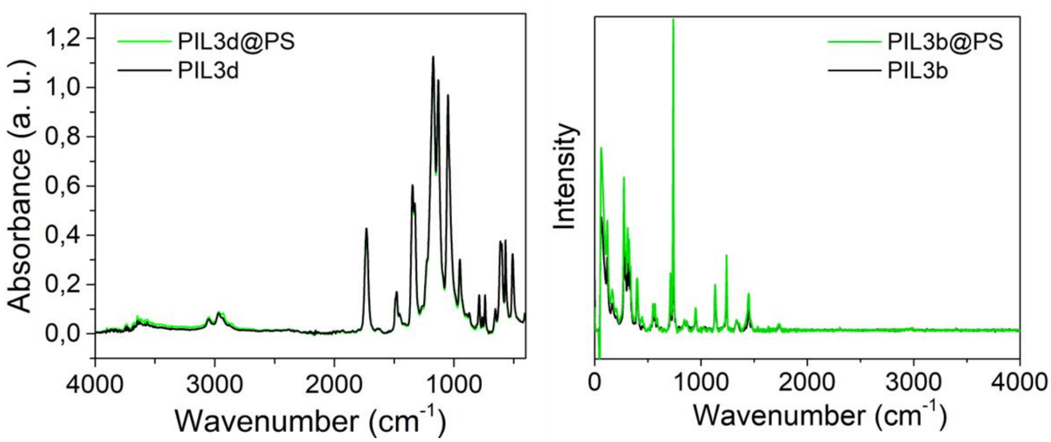

Figure 91. *(Left) FT-IR spectra and (right) Raman spectra of* ***PIL3****-based film (black) and PIL with perovskite nanocrystals (2 wt%) (green).*

As it can be seen in *Figure 91*, the presence of PNCs is imperceptible in these measurements. Likewise, the differences in the bands from the polymer matrix of the studied formulations were insignificant.

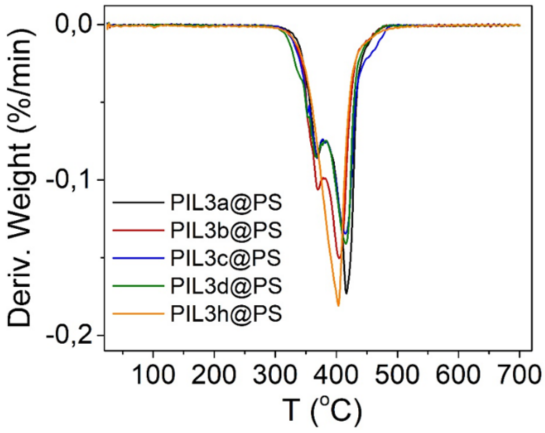

Entry	*Formulation*	*T_{onset} (°C)*
1	PIL3a@PS	385
2	PIL3b@PS	369
3	PIL3c@PS	373
4	PIL3d@PS	372
5	PIL3d	387
6	PIL3h@PS	375
7	mIL3	361
8	BDA	151

Figure 92. *DTG spectra of different* ***PIL3x@PS*** *formulations capable to stabilise $CsPbBr_3$, and a summary of the T_{onset} values obtained from the TGA spectra of the formulations and the monomeric ionic liquid (mIL3). The addition of cross-linker (BDA) reduces the thermal decomposition temperature (T_{onset}) due to its low T_{onset}, and the presence of PNCs also has a negative influence.*

Films with a higher BA percentage (like **PIL3d**) were less transparent than films without BA (**PIL3b**) as it can be seen in *Figure 93* (left).

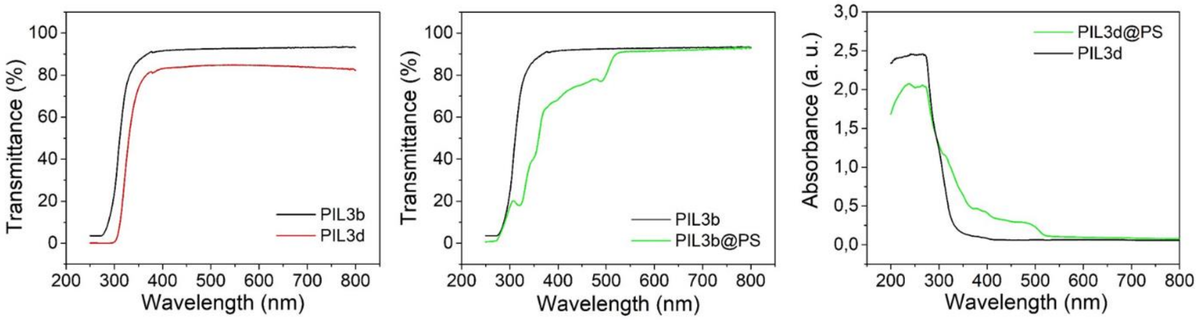

Figure 93. *(Left) Transmittance spectra of* ***PIL3b*** *(black) and* ***PIL3d*** *(red); (centre) Transmittance spectra of* ***PIL3b*** *(black) and* ***PIL3b@PS*** *(green), showing a remarkable influence of* $CsPbBr_3$ *in the range where the green perovskite absorbs (from 400 nm to 500 nm); (right) Absorbance spectra of* ***PIL3d*** *(black) and* ***PIL3d@PS*** *(green), showing the characteristic absorption band of* $CsPbBr_3$*.*

Also, the presence of the nanocrystals was observed in the film by scanning electron microscopy (SEM) (*Figure 94*) and optical microscopy (*Figure 95*). Aggregates of 1 µm were formed inside the film.

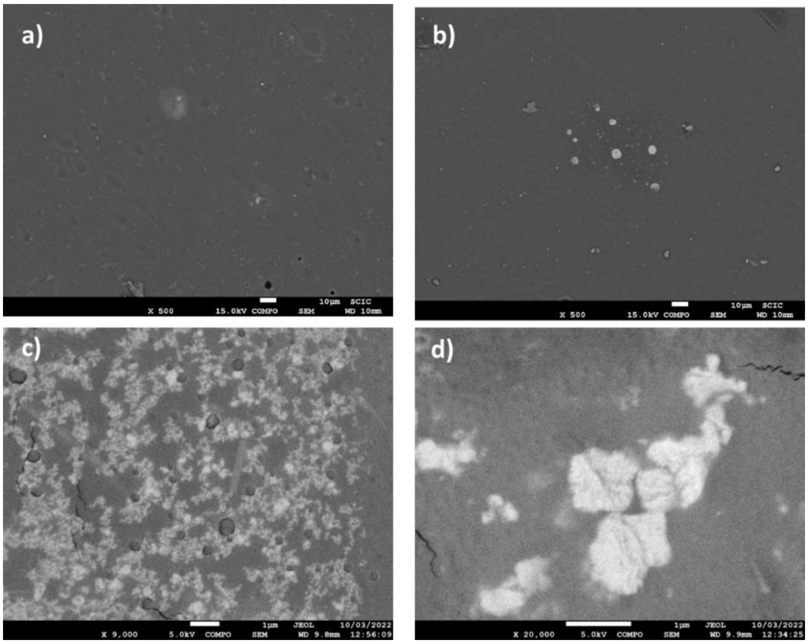

Figure 94. *SEM images of,* ***a) PIL3b*** *film at zoom 500;* ***b) PIL3b@PS*** *film at zoom 500;* ***c) PIL3b@PS*** *film at zoom 9000;* ***d) PIL3b@PS*** *film at zoom 20000.*

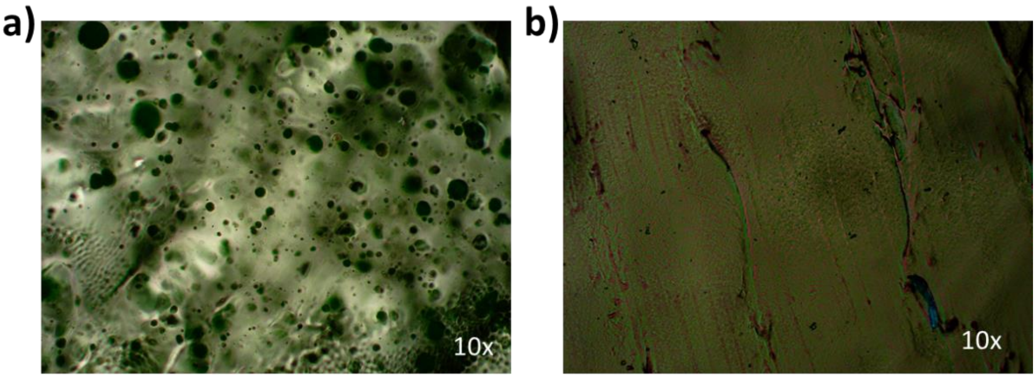

Figure 95. *Optical microscopy images of* ***a) PIL3b@PS*** *film;* ***b) PIL3b*** *film measured with zoom 10x.*

Porosity Studies

The porosity of film **PIL3b** and **PIL3b@PS** was analysed. A minimum amount of solvent was added to increase the porosity of the material. The solvents involved were tert-butanol, hexane and combinations of both of them, since those solvents do not damage the PNCs. We prepared **PIL3b@PS** films with hexane (14 % v/v), with tert-butanol (10 % v/v) and hexane : tert-butanol (7 % : 10 % v/v). And, similarly, we prepared three **PIL3b** films with same solvents at a concentration of 17.5 % v/v. The resulting films were characterised by SEM, optical microscopy and by profilometric laser. The addition of hexane had almost no effect in the formation of porous (*Figure 96*b), while some porosity was achieved in the films containing tert-butanol as can be observed in *Figure 96*c, d.

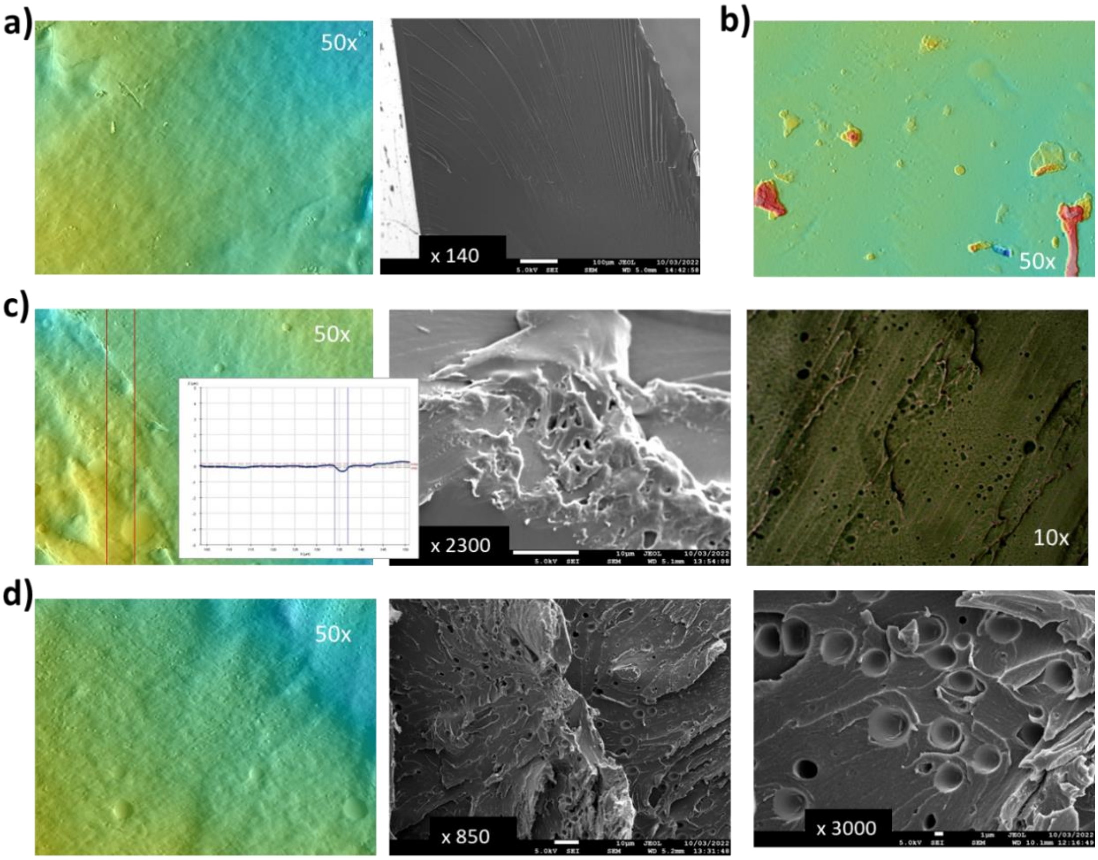

Figure 96. ***a)*** *Profilometric and SEM images from* ***PIL3b*** *film without solvent;* ***b)*** *Profilometric image of* ***PIL3b*** *film with 17.5 % v/v of hexane;* ***c)*** *Profilometric, SEM and optical microscopy images of* ***PIL3b*** *film with 17.5 % v/v of tert-butanol, showing porous of 3.65 µm of diameter;* ***d)*** *Profilometric and SEM images of* ***PIL3b*** *film with 17.5 % v/v of hexane and 17.5 % v/v of tert-butanol, showing big porous as well.*

Chapter 4:

Electric Properties of Advanced Composite Materials

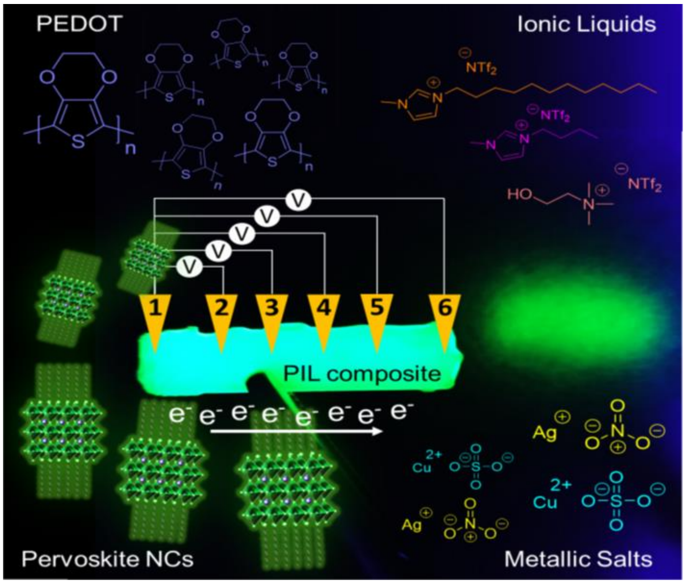

4.1 Summary

In the preceding chapters, some unique features of PILs have been demonstrated, such as their high tuneability, biocompatibility, ionic transport and their ability to stabilise different nanomaterials. Furthermore, it was possible to 3D-print the PIL-based formulations with different geometries at high resolution. In this Chapter, conductive materials were added as additives into the formulations to modify their electric properties.

On the one hand, a conductive polymer was added either in the polymeric phase or as a monomer for further polymerisation. The conductive polymer involved was poly(3,4-ethylenedioxythiophene) (PEDOT). Different concentrations of both PEDOT and its monomer EDOT were analysed. Two different procedures were considered when using EDOT, since the polymerisation of EDOT could be performed before or after polymerising the PIL formulation. Likewise, the EDOT oxidation was done using an oxidative atmosphere and using an oxidative chemical. A variety of samples was obtained following the different methodologies.

Moreover, the introduction of homogeneous ionic liquids (ILs) into PEDOT:PIL systems has been also evaluated for enhancing the conductivity of the materials. Herein, we prepared PIL-based films using either EDOT or PEDOT mixed with ILs (**E/P$_x$IL$_y$PIL**). The conductivities of those materials were compared to their analogous **IL$_y$PIL** films. On the other hand, it was investigated the possibility to obtain optoelectronic devices mixing the optical properties of perovskite nanocrystals (PNCs) with conductive polymers. While EDOT systems (**E$_x$PIL**) were not capable to stabilise $CsPbBr_3$ NCs; PEDOT-based films with perovskite (**P$_x$PIL@PS**) reported high photoluminescence (PLQY, ~40 %). The stabilisation of the PNCs in IL-based systems (**IL$_y$PIL@PS**) was also evaluated.

Furthermore, the conductive properties of bare PIL films with PNCs (**PIL@PS**) as well as **P$_x$PIL@PS** and **IL$_y$PIL@PS** systems were studied to see the influence of $CsPbBr_3$ in the electrical behaviour of the material. Finally, metallic compounds were formulated by adding different metallic salts at different concentrations, as metal salts and metallic nanoparticles can increase the conductivity of polymer composites by introducing free electrons into the polymer matrix.

The complex impedances and conductivities of all the materials prepared were analysed. These measurements were performed in collaboration with Agustin Álvarez Ojeda and Prof. Fabregat from GAME group (INAM) and in collaboration with Pietro Zaccagnini from Politecnico of Torino. At present, studies in this area are still ongoing and further research is needed to draw good conclusions from the results obtained.

4.2 Introduction

In the field of electrochemical device applications there is a continuous need for new and improved electrical materials with advanced properties. The recent emergence of hybrid organic/inorganic polymer systems have allowed a rapid development of organic electronic technology, presenting several advantages such as cost, flexibility or functionality compared to conventional devices.[295] Electrically conductive polymers (ECPs) represent a class of π-electron conjugated polymers widely studied since 1970's due to their unique features like high ionic and electronic conductivity and excellent mechanical properties. They can store charge and also exhibit high redox capacitance switching between p-type and n-type doped forms, which makes them very attractive for electrochromic applications,[296] rechargeable batteries,[297] supercapacitors,[298] sensors,[299] etc. Polythiophene, polyaniline and polypyrrole and their derivatives have attracted a great deal of attention in electroanalysis due to their good electrical conductivity and electrochemical stability. In particular, the family of polymers of poly(3,4-alkylenedioxythiophenes) (PXDOTs) have an electron-rich character that yields especially low switching potentials and long switching lifetimes.[300]

One of the most applied π-conjugated polymers is poly(3,4-ethylenedioxythiophene) (PEDOT) due to its several advantageous properties such as excellent thermal and electrochemical stability, high conductivity (300 S/cm), biocompatibility, low band gap, as well as the possibility to utilize eco-friendly aqueous electrolytes without instant degradation of the polymer.[301] Besides, EDOT can be easily polymerised by standard oxidative chemical[154b, 171b] or electrochemical polymerisation[302] because it has one of the lowest oxidation potentials among thiophene derivatives, a well-defined polymer backbone structure with a small amount of possible defects, and changes its colour from almost transparent or light blue in oxidised (p-doped) state to dark blue in its undoped state.[303] For all these exceptional properties, in the early 2000s, PEDOT was developed to the point of commercialisation (Baytron P, Bayer AG and AGFA),[300] and nowadays it is thoroughly studied in multiple applications including supercapacitors,[304] electrochromic devices,[305] organic solar cells[306] and sensors,[307] to mention a few.

Despite their good performance, conductive polymers are difficult to process because their insolubility in common solvents. PEDOT itself does not dissolve in either aqueous or organic solvents because of its extended π-conjugation, thus it needs some stabilizer (such as an electrolyte) to enable the dispersion. A common methodology was to use a liquid containing electrolyte (a salt solution in an organic solvent) or high-boiling plasticizer polymer gel electrolyte as poly(methylmethacrylate), and lithium bis(trifluoromethylsulfonyl)imide. Although those polyelectrolytes worked properly, the speed of the electroactive device was limited by the ability of the ions to move in and out of the polymer layers and the low conductivity of the medium.[300] Moreover, liquid electrolytes do present some drawbacks difficult to overcome, such as leakage and evaporation. An all solid-state polymer electrolyte has important advantages including mechanical stability, safety and simple processing.[164] In this regard, poly(3,4-ethylenedioxythiophene)-poly(styrenesulfonate) (PEDOT:PSS) complexes have been widely used as electrode material for electroanalysis due to its high conductivity, thermal stability and low redox potential.[308] In optoelectronic devices like organic light emitting diodes (OLEDs) it is also common to find PEDOT:PSS as a thin hole-transporting layer.[309] However, the hydrophilic nature of PEDOT:PSS complexes often limits its commercial use. Furthermore, the presence of residual water and the acidic PSS stabilizer can detrimentally affect the lifetime, the stability and often compromises the electrical performance of the final devices.[170] Doping PEDOT:PSS with ionic liquids, organic solvents, acids or salts can improve the conductivity, sensitivity to water and air and the acidity of the materials. The incorporation of some additives reduces the interaction between PEDOT and PSS, and promotes the phase separation of PEDOT and PSS, avoiding corrosion. Along these years, it has been shown that PEDOT films cycled in ionic liquids do not present a memory effect,[310] enhance the switching lifetimes of the devices,[171b, 300] and have higher electroactivity compared to films fabricated in common organic electrolytes (acetonitrile or propylene carbonate).[311] Moreover, the synergistic combination of PEDOT:PSS with a suitable ionic liquid can increase up to 5000-fold the electronic conductivity of the resulting composites. This phenomenon occurs because the IL ions are intercalated between PEDOT and PSS, resulting in a facilitated charge transport via conjugation in the PEDOT chains.[136] On the other hand, the combination of ILs with PEDOT has reported conductivities as high as 30000 S/m, two orders of magnitude larger than pure PEDOT:PSS.[312] Likewise, the introduction of PILs to create a PEDOT:PIL system have been also successfully tested. The hydrophobic PEDOT:PIL dispersions represents an alternative material for electrochemical applications due to its organic nature, its large electrochemical window and thermal stability (up to 300 ^{o}C).[21a, 143, 154b] Fluorescent OLED devices prepared using a PEDOT:PIL hole-injection layer presented a longer lifetime than conventional PEDOT:PSS based OLEDs.[171]

Additionally, the incorporation of ionic liquids in PIL formulations have been widely used to enhance the conductivity of the materials.[135-136] While ILs have their free charges moving freely, PILs are quasi-single-ion conductors, which leads to a decrease in the conductivity from ~10^{-2} to 10^{-6} S/cm after polymerisation.[313] For that reason, mixtures of ILs with PILs are very desirable and can be successfully prepared avoiding segregation into two phases due to the similarity in the chemical structure.[21a, 148, 162, 164] Perovskite nanocrystals have been also explored as a means to enhance the conductivity of a variety of materials, including polymer composites.[314] Perovskite materials are a class of compounds with a specific crystal structure, which have shown to have high electrical conductivity apart from optical properties.[315] In general, PNCs can effectively transfer charges to the polymer, resulting in a substantial increase in conductivity.

Another strategy to increase the conductivity of polymers is the addition of metal salts and metallic nanoparticles.[65b, 316] The free electrons introduced by the metals can move freely through the polymer, allowing for the flow of electrical current. The metal salts or nanoparticles can also increase the mobility of the polymer's own electrons, further enhancing conductivity. The specific mechanism and degree of enhancement will depend on the type and concentration of the metal salt or nanoparticle used, as well as the specific polymer being modified.

In this Chapter, the main property evaluated was conductivity. Conductivity is the ability of a material to conduct electric current. The control system involved for performing the conductive measurements include sensors to measure current and voltage, a measurement circuit to process the signals, a signal processing system to perform calculations and a user interface to display the results.

In the case of solid ionic liquids, the ionic conductivity is typically the dominant form of conductivity, although it is a complex measurement. For that reason, in this work we mainly studied the electrical behaviour of our systems. The theoretical underpinnings of the techniques used for measuring the conductivities are described here. The samples must be homogeneous, isotropic and linear in order to obtain reliable results.

Cyclic voltammetry (CV) is a powerful electroanalytical technique used to study the electrochemical behaviour of materials, such as redox processes, the capacitance and the total resistance. It involves the application of a controlled potential sweep to a working electrode in contact with an electrolyte solution or solid. The resulting current density is measured as a function of the applied potential, and this measurement is repeated multiple times to define a cyclic voltammogram. Therefore, the resistance of a material can be calculated using the inverse of the slope of a cyclic voltammetry curve. Similarly, the capacitance can be determined by the hysteresis of the j-V curve as a function of scan rate. CV is particularly useful for studying the electrochemical properties of materials such as redox reactions, adsorption, and electrocatalysis. The resulting voltammograms can provide information about the kinetics and thermodynamics of electrochemical processes, as well as the surface area, porosity, and electronic properties of the material.[317]

Impedance is a measure of the total opposition to current flow in an alternating current circuit. It is a complex quantity that can be represented as a vector in the complex plane. It consists of the combination of resistance and reactance, measured both in ohms (Ω). And it can be expressed as $Z = Z' + Z''$ where Z' is resistance and Z'' is reactance. Resistance is a measure of the opposition to current flow in a circuit that is caused solely by the movement of electrons through a material. Meanwhile, reactance is a measure of the opposition to current flow in a circuit that is caused by the presence of inductors and capacitors, which cause the current and voltage to be out of phase with each other. The value of the reactance is normally negligible. The impedance of a circuit can be affected by a variety of factors, including the frequency of the alternating current (AC), the type and value of the components in the circuit and the overall design of the circuit.[318]

A Nyquist plot is a graphical representation of the impedance of a material, where the real part of the impedance (Z') is plotted on the x-axis and the negative of the imaginary part of the impedance (-Z'') is plotted on the y-axis. The real and imaginary parts of the transfer function can be read off the plot to determine the resistance and reactance of the system, respectively. Therefore, this plot can be also used to study the electrochemical properties of a sample and its behaviour as a function of the frequency. From a Nyquist plot, it is possible to calculate both ionic and electrical conductivity. The method to calculate the conductivity will depend on the type of material being studied and the type of conductivity being measured.[319] Electrical conductivity is related to transport resistance of the system. In general, a Nyquist plot of a material with high electrical conductivity will have a crossing point near the origin of the x-axis, while a Nyquist plot of a material with low conductivity will have a crossing point far from the origin of the x-axis.

4.3 Objectives

The aim of this Chapter is to improve the conductive performance of the PIL-based formulations. The addition of different additives, including conducting polymers, ILs, PNCs and metallic salts, is evaluated to reduce the resistivity of the materials. Firstly, to prepare the samples, specific objectives are considered:

- To analyse a variety of mILs and formulations to get good matrices for stabilising the different additives
- To study three different strategies to prepare PEDOT:PIL systems
- To follow various methodologies to polymerise EDOT in order to obtain PEDOT
- To introduce synthesised ionic liquids into the PEDOT:PIL systems
- To encapsulate $CsPbBr_3$ NCs into the PIL-based formulations in order to obtain optoelectronic active materials
- To add silver and copper salts ($AgNO_3$ and $Cu(NO_3)_2$) in the PILs

In addition, different concentrations of the employed additives are investigated in order to have a wide range of samples. Then, once the samples are prepared and characterised the objectives are:

- To evaluate the photoluminescence and the stability of the embedded PNCs in the different formulations
- To measure the electrical properties of all the samples using cyclic voltammetry and impedance spectroscopy
- To demonstrate that PIL-based materials are more electrically conductive than non-ionic films

An in house-made 3D printed setup based on two-probe methodology has been designed and fabricated to measure the conductive performance of the films in a reproducible and reliable way.

4.4 Results and Discussion

4.4.1 Summary of the Nomenclature found in Chapter 4

Table 13. *Summary of the nomenclature used for naming the EDOT and PEDOT-based films.*

Entry	***Film***	***Polymerising Order***	***Conductive Additive***	***Additive Content***
1	E_{100}PIL3b	-	EDOT	100 mol% (1:1)
2	P_{100}PIL3b-1a	1st mIL - 2nd EDOT	Pol. EDOT by O_2	100 mol% (1:1)
3	P_{50}PIL3b-1b	1st mIL - 2nd EDOT	Pol. EDOT by APS	50 mol% (0.5:1)
4	P_{50}PIL3b-2a	1st EDOT - 2nd mIL	Pol. EDOT by APS and H_2O	50 mol% (0.5:1)
5	P_{50}PIL1-2b	1st EDOT - 2nd mIL	Pol. EDOT by APS and mIL1	50 mol% (0.5:1)
6	P_{50}PIL1-2c	1st EDOT - 2nd mIL	Pol. EDOT by APS and PEGDA	50 mol% (0.5:1)
7	$P_{0.5}$PIL3b-3	-	PEDOT	0.5 wt%

The abbreviation "Pol." means polymerised.

Table 14. *Nomenclature used for naming IL3-based films.*

Entry	***Film***	***IL3 (mol%)***	***Polymerising Order***	***Conductive Additive***
1	E_{50}PIL3b	-	-	EDOT
2	E_{50}IL3$_{75}$PIL3b	75	-	EDOT
3	P_{50}IL3$_{75}$PIL3b	75	1st mIL - 2nd EDOT	Polymerised EDOT by IL3
4	P_{50}PIL3b-1a	-	1st mIL - 2nd EDOT	Polymerised EDOT by O_2
5	P_{50}IL3$_5$PIL3b-1a	5	1st mIL - 2nd EDOT	Polymerised EDOT by O_2 and IL3
6	P_{50}IL3$_{95}$PIL1	95	1st EDOT - 2nd mIL	Polymerised EDOT by APS

Table 15. *Nomenclature used for naming the films containing $CsPbBr_3$ NCs (2 wt%).*

Entry	***Film***	***Conductive Additve***	***Additive Content***
1	E_{50}PIL3b@PS	EDOT	50 mol%
2	$P_{0.5}$PIL3b@PS	PEDOT	0.5 wt%
3	P_{50}PIL3b@PS	Polymerised EDOT by O_2	50 mol%
4	ILX$_y$PIL3b	ILs	y = 5 – 10 mol%
5	ILX$_y$PIL3b@PS	ILs	y = 5 – 10 mol%

Where ILX = IL1, IL2 or IL3:

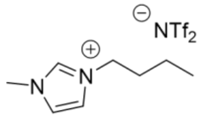

1-butyl-3-methylimidazolium bis(trifluoromethane) sulfonimide **(IL1)**

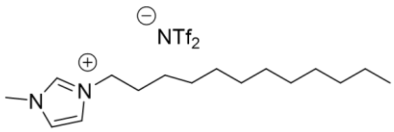

1-dodecane-3-methylimidazolium bis(trifluoromethane) sulfonimide **(IL2)**

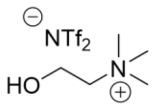

Choline bis(trifluoromethane)sulfonimide **(IL3)**

4.4.2 Preparation of PEDOT-based Systems

Several PEDOT-based systems were synthesised following different strategies, taking advantage of the excellent features of PILs as stabilisers. PEDOT:PIL organic dispersions could be prepared by introducing the two monomers (EDOT and mIL), polymerising first one and then the other one, or by adding already polymerised PEDOT. In all the films prepared, the percentage of EDOT and PEDOT added was calculated based on the amount of the mIL. Both products (EDOT and PEDOT) are commercially available. Three different approaches were evaluated: **P$_x$PIL-1**, **P$_x$PIL-2** and **P$_x$PIL-3**, where x refers to the amount of EDOT or PEDOT added. The details of each procedure are described in Scheme 2.

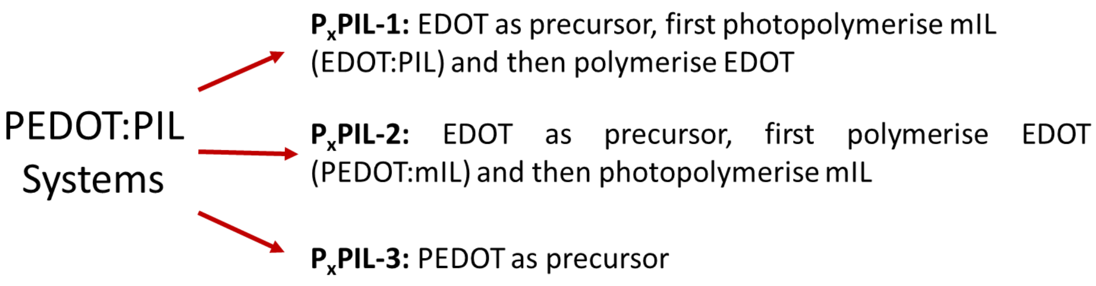

PEDOT:PIL Systems

P$_x$PIL-1: EDOT as precursor, first photopolymerise mIL (EDOT:PIL) and then polymerise EDOT

P$_x$PIL-2: EDOT as precursor, first polymerise EDOT (PEDOT:mIL) and then photopolymerise mIL

P$_x$PIL-3: PEDOT as precursor

Scheme 2. *Three methodologies considered for preparing PEDOT:PIL systems.*

1. **P$_x$PIL-1:** EDOT as precursor, first photopolymerise mIL (EDOT:PIL) and then polymerise EDOT.

Monomeric EDOT (50 mol% and 100 mol%) was mixed with monomeric ILs (mIL1 and mIL3) in a molar ratio of 0.5:1 and 1:1. Then, a cross-linker (PEGDA, 20 mol% or BDA, 5 mol%) and TPO (1 wt%) were added and the mixture was photopolymerised by UV light during 30 min at 40 °C. Afterwards, transparent, flexible and sticky films were formed (**E$_{50}$PIL1.2**, **E$_{50}$PIL3b**). The name of the formulations follows the structure defined in **Chapter 2** and **3**, **Section 2.4.3** and **3.4.3**. According to the literature, EDOT can be polymerised by an electrochemical reaction or by oxidative reaction.[303] The electrochemical polymerisation was tested here without success. On the contrary, two different ways to oxidise EDOT were successfully implemented. The first approach was to oxidise the transparent film under an O_2 atmosphere at 65 °C, represented in *Figure 97*a. After several hours the film became completely black (**P$_{50}$PIL1.2-1a, P$_{50}$PIL3b-1a**) (*Figure 97*b). This oxidation process was carried out on a hot plate, as EDOT was hardly oxidised at room temperature (*Figure 97*c).

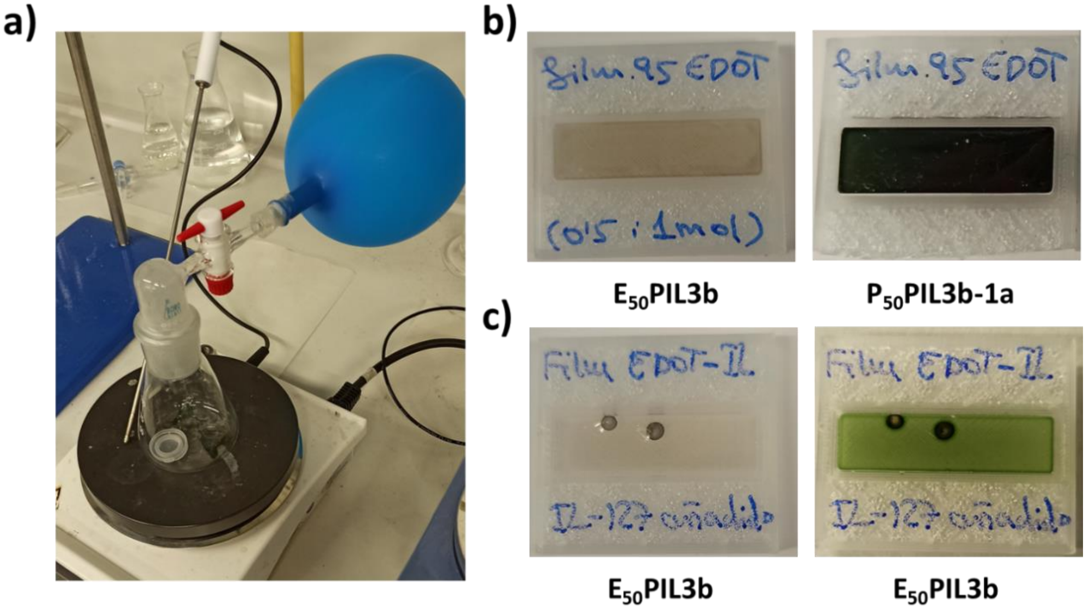

E$_{50}$PIL3b **P$_{50}$PIL3b-1a**

E$_{50}$PIL3b **E$_{50}$PIL3b**

Figure 97. ***a)*** *Set-up for oxidising the samples under an oxidative atmosphere at 65 °C;* ***b)*** *(Left) An EDOT-based film before and, (right) after 1 day oxidising EDOT under an O_2 atmosphere at 65 °C;* ***c)*** *(Left) An EDOT-based film before and, (right) after 10 days oxidising EDOT under an O_2 atmosphere at room temperature, showing a greenish colour, indicating that EDOT was not properly oxidised.*

The second approach was to chemically oxidise EDOT using ammonium persulfate (APS). In a quick test, we observed that EDOT rapidly oxidised by adding dropwise an aqueous solution of APS (EDOT:APS, 1:1.2 mol/mol). After few minutes stirring vigorously, the mixture colour started changing from transparent to greenish, dark blue and in 1 hour it was totally black. In this regard, a film was immersed into an aqueous solution of APS in excess (EDOT:APS, 1:3 mol/mol). The colour of both the solution and the film changed from transparent to blueish, and after 1.5 hours both were blackish (*Figure 98*).

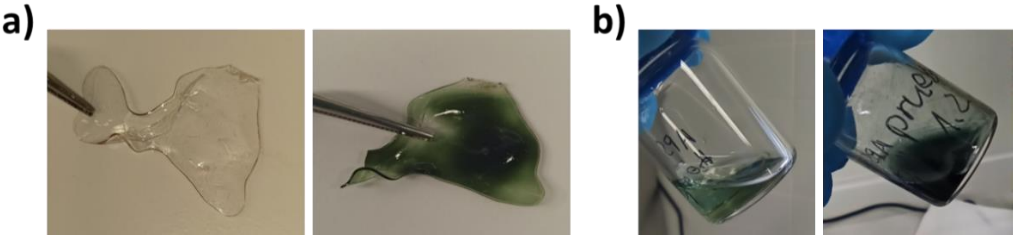

Figure 98. ***a)*** *E_{50}PIL1.2 film, (left) before, and (right) after introducing it into an aqueous solution of APS in excess (EDOT:APS, 1:3 mol/mol);* ***b)*** *APS solution, (left) in the beginning when* ***E_{50}PIL1.2*** *film was introduced, and (right) after 1.5 hours with the EDOT-based film.*

Thus, it can be concluded that some EDOT was leaching from the film and being oxidised in the aqueous solution. Then, the film was washed with water, ethanol and acetone to dry it, but the organic solvents also removed some PEDOT from the film, since it lost 5 % of weight during the washing. All these means that the film was not immobilising EDOT properly. In order to avoid these issues, an aqueous solution of APS was added dropwise directly over the film. After 7 hours at 60 °C, the solution was completely absorbed by the film and it became black (**P_{50}PIL3b-1b**) (*Figure 99*a). On the contrary, at room temperature the oxidation and colour changing did not occur (*Figure 99*b).

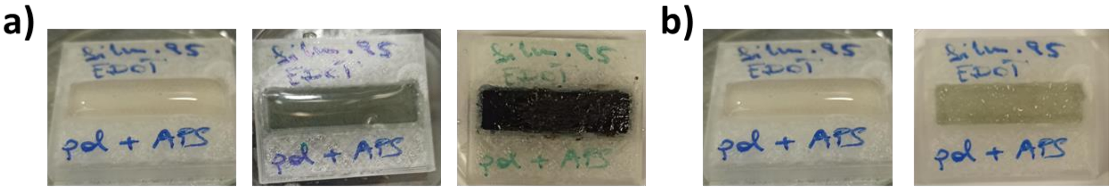

Initial 5 hours at 60°C 7 hours at 60°C Initial 1 day at RT

Figure 99. *E_{50}PIL3b films:* ***a)*** *Oxidative evolution of EDOT-based film with APS solution above the film under atmosphere conditions at 60 °C;* ***b)*** *Same oxidation procedure at room temperature.*

The resulting films obtained from the oxidation with APS (**P$_{50}$PIL3b-1b**) presented a different appearance than the previous films oxidised with molecular oxygen (**P$_{50}$PIL3b-1a**) as can be seen in *Figure 100*a. The opacity of the films was remarkably different; thus, the change was measured by UV-Vis spectroscopy to confirm this feature (*Figure 100*b). Since **E$_{50}$PIL3b** sample was highly transparent, its spectrum (black) was cut to better appreciate the variations found between **P$_{50}$PIL3b-1a** and **P$_{50}$PIL3b-1b** spectra (blue and red, respectively). A hypothesis could be that EDOT from **P$_{50}$PIL3b-1a** film was not fully oxidised. In order to enhance its opacity, a film was left more than three weeks into an oven at 60 °C, however no significant changes were found.

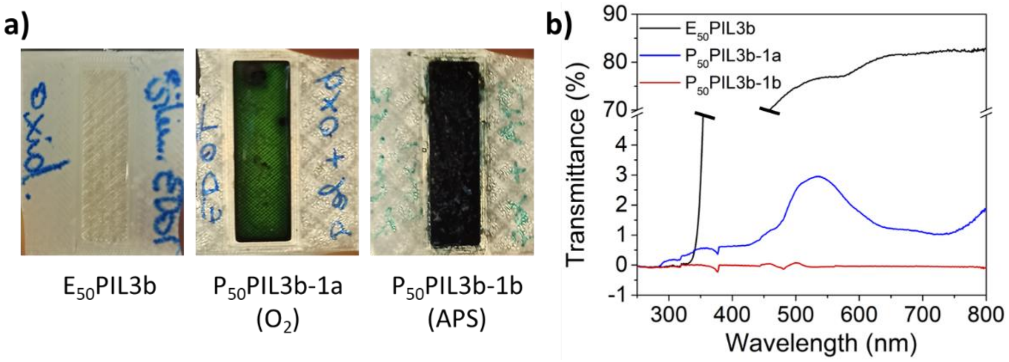

E$_{50}$PIL3b

P$_{50}$PIL3b-1a (O$_2$)

P$_{50}$PIL3b-1b (APS)

Figure 100. ***a)*** *Differences on the films after reacting with different oxidants;* ***b)*** *UV-Vis spectra of the films oxidated by different methods vs the non-oxidated film (**E$_{50}$PIL3b**) cut from 5 to 70 %.*

2. **P$_x$PIL-2:** EDOT as precursor, first polymerise EDOT (PEDOT:mIL) and then photopolymerise mIL

Another possibility considered was to oxidise EDOT in the first place, using an O$_2$ atmosphere, while keeping the mIL formulation in liquid state. At this point, we found that pristine EDOT (liquid) at 65 °C under oxidative atmosphere was not oxidised at all, neither EDOT:mIL mixture (*Figure 101*).

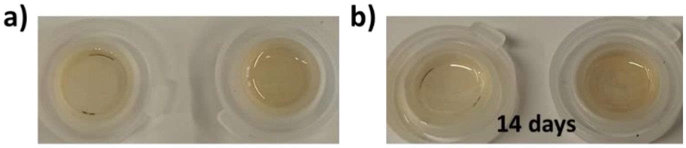

Figure 101. ***a)*** *(Left) Pristine EDOT, (right) EDOT:mIL mixture;* ***b)*** *(Left) Pristine EDOT, (right) EDOT:mIL mixture, after 14 days exposed to an oxidative atmosphere at 65 °C.*

This suggests that probably EDOT needs to be encapsulated into PILs to get oxidised by oxygen. On the other hand, APS could oxidise EDOT very easily, being a possible way to oxidise EDOT before photopolymerising the sample. An aqueous solution of EDOT (50 mol%) and APS in excess was prepared and became black rapidly, resulting in a PEDOT polymer. Then, the water was evaporated and **mIL3b** formulation (95 mol% mIL3 and 5 mol% BDA) was added. The mixture was photopolymerised under UV irradiation for 30 min at 40 ^{o}C. Even though the water had been removed prior to polymerisation, the black film was smooth and very fragile (**P$_{50}$PIL3b-2a**). Some water could remain within the mixture, thus affecting the photopolymerisation process. Hence, in order to remove water, solubility tests of APS and EDOT in mIL1, PEGDA and ViIm were attempted. The resulting mixtures of those substances with EDOT and APS were left one day stirring at 45 ^{o}C. The mixture of mIL1+EDOT+APS was totally black, but not homogenously liquid (with some solid parts). To this mixture, PEGDA (100 mol%) and TPO were added forming a really fragile film (**P$_{50}$PIL1-2b**). The mixture of PEGDA+EDOT+APS resulted also in a completely black, and more homogeneously distributed material. In this case, mIL1 and TPO were added forming a bit more robust film (**P$_{50}$PIL1-2c**). Thus, we could find some differences on the resulting film depending on the order that the components were added. Even though, the polymerisation of these samples was not optimal, probably because the dark environment reduced light penetration and radiation efficiency. Likewise, the presence of macromolecules (*e.g.*, PEDOT) could hinder the reaction and the cross-linking, both due to steric and mobility issues. Finally, the mixture of ViIm+EDOT+APS was dark orange and partially solid, so it was not considered for making a film (*Figure 102*).

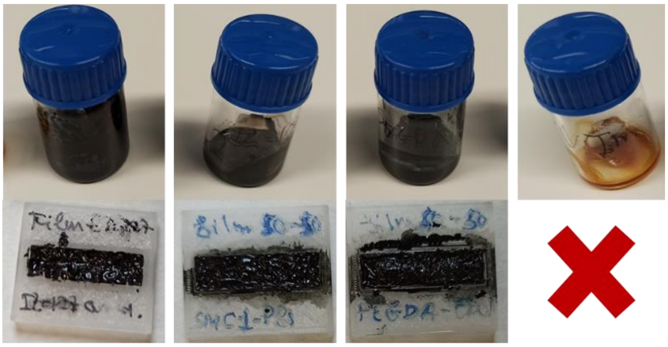

P$_{50}$PIL3b-2a **P$_{50}$PIL1-2b** **P$_{50}$PIL1-2c**

Figure 102. *The different mixtures and the films formed after photopolymerising the previously oxidised EDOT with APS.*

Another approach was to prepare a film using the hydrophilic monomer BVI.Br. Herein, a mixture of EDOT with BVI.Br (2:1 mol/mol) was dissolved in mili-Q water (10 mL) and added to an aqueous solution of APS (EDOT:APS 1:1.2 mol/mol, 1.7 mL). After several hours stirring, some black points appeared (*Figure 103*). Then, the black particles in suspension were recovered by filtration and dried at room temperature under vacuum to constant weight. Initially, after filtering, the solution was transparent and greenish, but after some time it got darker until becoming opaque black, probably some remaining EDOT and APS were reacting on the solution with the time.

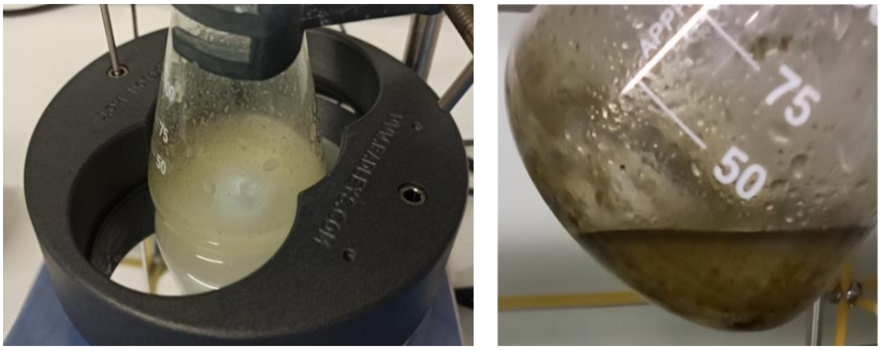

Figure 103. *(Left) APS solution with EDOT:BVI.Br in 10 mL of water, (right) the same solution after 2 hours. The solution and the solid particles became darker over time due to the oxidation of EDOT.*

The solid particles were well-dispersed into an organic solvent, MeOH, and after evaporating the solvent, dried black particles composed by PEDOT:BVI.Br were obtained (yield: 80 %). These particles were then used for preparing a film, mixing them with mIL1, PEGDA (20 mol%) and TPO (1 wt%). The mixture was properly dispersed and a black film was obtained, although it was not well polymerised.

3. **P_xPIL-3:** PEDOT as precursor

Some films were prepared using a commercial solution of PEDOT (nanoparticles <500 nm dispersed in H_2O, 10 mg of PEDOT per 1 g of solution) with different mILs. In a first study, **mIL1.2** (80 mol% mIL1 and 20 mol% PEGDA) was mixed with 57.7 mg (equivalents to 0.2 wt%) of PEDOT and stirred for 72 hours at room temperature. A well-dispersed mixture was obtained. Afterwards, TPO (1 wt%) was added and it was photopolymerised under UV light, 30 min at 40 °C. A blackish robust film was obtained, but it presented some bubbles, probably due to the water (**$P_{0.2}$PIL1.2-3**) (*Figure 104*a). In a second test, **mIL3b** was mixed with a higher content of PEDOT (0.5 wt%) and the water was evaporated under vacuum at 45 °C. A blacker film without bubbles was obtained (**$P_{0.5}$PIL3b-3**) (*Figure 104*b).

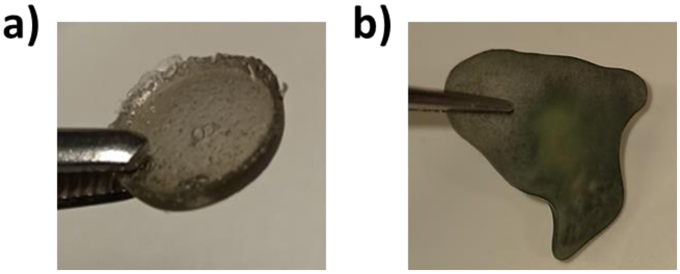

Figure 104. ***a)*** *Imidazolium* ***$P_{0.2}$PIL1.2-3*** *film;* ***b)*** *Cholinium* ***$P_{0.5}$PIL3b-3*** *film.*

Lastly, the hydrophilic monomer BVI.Br was tested. This time, a higher amount of PEDOT was used (5 wt%) and the mixture was stirred for 24 hours. Then, it was mixed with PEGDA (20 mol%) and TPO (1 wt%) and photopolymerised under UV light for 1 hour at 40 °C. A very small, sticky and soft black film was formed, probably because it was very hygroscopic and became soft at open atmosphere. In contrast, the hydrophobic films did not suffer any softening even after weeks. This hygroscopic effect has also been reported in the literature.[154a]

Table 16. *Summary of the films prepared in the* ***Section 4.4.2****.*

Entry	***Film***	***Polymerising Order***	***Conductive Additive***
1	E_{50}PIL3b	-	EDOT
2	P_{50}PIL3b-1a	1st mIL - 2nd EDOT	Polymerised EDOT by O_2
3	P_{50}PIL3b-1b	1st mIL - 2nd EDOT	Polymerised EDOT by APS
4	P_{50}PIL3b-2a	1st EDOT - 2nd mIL	Polymerised EDOT by APS and water
5	P_{50}PIL1-2b	1st EDOT - 2nd mIL	Polymerised EDOT by APS and mIL1
6	P_{50}PIL1-2c	1st EDOT - 2nd mIL	Polymerised EDOT by APS and PEGDA
7	$P_{0.5}$PIL3b-3	-	PEDOT

4.4.3 (P)EDOT-based Systems with Ionic Liquids

Homogenous ionic liquids (ILs) have very interesting properties, which have been briefly described in **Chapter 1**. Their use as additives for increasing the conductivity of the materials owing to their free charges moving freely has been widely reported.[135-136]

In this PhD thesis, three ionic liquids were synthesised and evaluated for enhancing the conductivity of our formulations: 1-butyl-3-methylimidazolium bis(trifluoromethane) sulfonimide (IL1), 1-dodecane-3-methylimidazolium bis(trifluoromethane) sulfonimide (IL2), choline bis(trifluoromethane)sulfonimide (IL3). We focused our study on ionic liquids based on sulfonimide anions because they are effective dopants for conducting polymers.[320] Additionally, it has been reported that NTf_2^- anion containing polymers presented a higher conductivity compared to other counter-anions, since the larger the anion the lower the Tg, although it is more localized than small anions.[146a]

In this regard, ILs were added to the EDOT/PEDOT:PIL systems. Firstly, the miscibility of the different components was previously evaluated, finding that EDOT:IL3 (1:0.2 mol/mol) was not miscible, while EDOT:IL1 and IL2 (1:0.2 mol/mol) were miscible. Meanwhile, the three ILs were miscible with the mILs and the cross-linker BDA. However, the mixture continued being immiscible after adding those components to EDOT:IL3. On the other hand, it was not possible to form consistent films with EDOT:IL1 and IL2 mixtures.

In order to avoid the miscibility issue with IL3, the possibility to add IL3 dropwise over the film after photopolymerising (EDOT:PIL-based film) was studied. The film was able to absorb IL3, allowing the formation of new IL systems (**E_xIL3$_y$PIL3b**, where x and y refers to the amount of EDOT and IL3 respectively). The film **E_{50}PIL3b** with IL3 absorbed led to increased film volume and flexibility. Different concentrations of IL3 in relation to mIL3 were tested: 5, 75 and 100 mol% (**E_{50}IL3$_5$PIL3b**, **E_{50}IL3$_{75}$PIL3b** and **E_{50}IL3$_{100}$PIL3b**). The addition of 75 mol% increased 20.5 % the volume of the film, whereas 100 mol% of IL3 increased 27 % the film volume, ending both samples completely dried. An excess of IL3 (200 mol%) was also tested (**E_{50}IL3$_{200}$PIL3b**) to have an idea about the maximum amount that could be absorbed by the film. Similar to **E_{50}IL3$_{100}$PIL3b** film, the **E_{50}IL3$_{200}$PIL3b** increased its volume by 27 % and ended wet, thus 100 mol% of IL3 was considered the maximum amount absorbed. In the four cases, the EDOT from the film was rapidly oxidised under atmospheric conditions at 65 °C obtaining PEDOT-based films in less than 1 hour (**P_{50}IL3$_5$PIL3b**, **P_{50}IL3$_{75}$PIL3b**, **P_{50}IL3$_{100}$PIL3b** and **P_{50}IL3$_{200}$PIL3b**) (*Figure 105*a).

These films presented a different appearance compared to the oxidised EDOT-films under oxidative atmosphere without ILs (**P_{50}PIL3b-1a**) (*Figure 105*b-1 to 4). The opacity of the films after adding IL3 was superior to **P$_{50}$PIL3b-1a**, similar to what happened when APS was used for oxidising EDOT, and this fact was further confirmed by UV-Vis spectroscopy (*Figure 105*c). **E$_{50}$PIL3b** spectrum (black) is cut to observe in more detail the differences among the rest of the spectra. Likewise, IL3 (5 mol%) was added dropwise to a film containing pre-polymerised EDOT by oxygen (**P$_{50}$IL3$_{5}$PIL3b-1a**, *Figure 105*b-5), finding a great improvement in its conductivity as we will see below in **Section 4.4.5**, *Table 22*, entry 6. After observing that the addition of IL3 increased the oxidation kinetics of EDOT by oxygen, a mixture of pristine EDOT with the different ILs was placed under oxygen atmosphere at 65 °C. Nevertheless, two days later nothing happened and the colour of EDOT did not change.

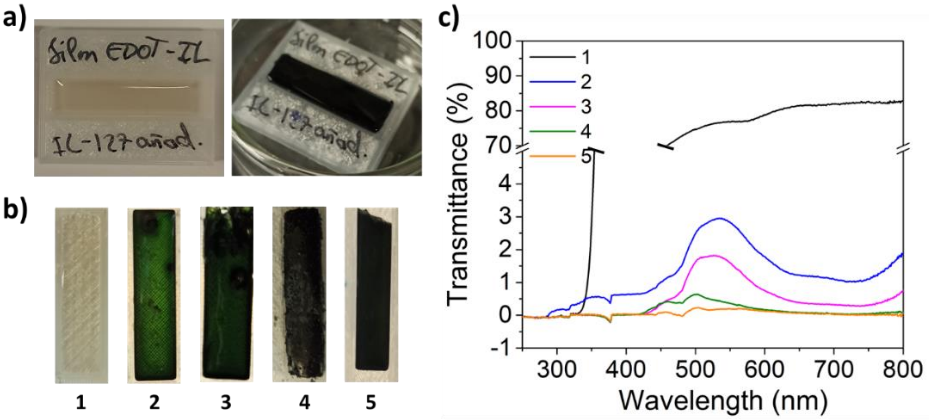

Figure 105. ***a)*** *(Left)* ***E$_{50}$PIL3b*** *film with IL3 (75 mol%) above, (right)* ***P$_{50}$IL3$_{75}$PIL3b*** *film showing the EDOT from the film completely oxidised (black) after 1 hour;* ***b)*** *(1)* ***E$_{50}$PIL3b*** *film, (2)* ***P$_{50}$PIL3b-1a*** *film (oxidised by O$_2$), (3)* ***P$_{50}$IL3$_{5}$PIL3b*** *film, (4)* ***P$_{50}$IL3$_{75}$PIL3b*** *film, (5)* ***P$_{50}$IL3$_{5}$PIL3b-1a*** *film, showing differences in their opacity;* ***c)*** *UV-Vis transmittance spectra of the films oxidated by different methods and different amounts of IL3 vs* ***E$_{50}$PIL3b*** *spectrum cut from 5 to 70 %.*

The combination of IL3:EDOT with an imidazolium monomer (mIL1) was also evaluated, obtaining a miscible solution. The monomer was mixed with IL3 (5 mol%), EDOT (50 mol%), PEGDA (20 mol%) and TPO (1 wt%), resulting a really fragile and flexible film after polymerising. The same procedure was repeated changing the ionic liquid IL3 by IL1, being miscible as well, but again a really fragile film was obtained. The neutral monomer, vinyl imidazole, was also photopolymerised with IL3 (5 mol%), EDOT (50 mol%), PEGDA (20 mol%) and TPO (1 wt%). All the components were miscible; however, the final film was too brittle. These films resulted to be excessively fragile for being further analysed.

Finally, the possibility to dissolve APS and EDOT in IL3 was evaluated. After one day stirring at 45 °C, the mixture was totally black with some solids remaining. Then, mIL1 and PEGDA (100 mol%) were added and after photopolymerising for 30 min at 40 °C a black and soft film was obtained (**$P_{50}IL3_{95}PIL1$**).

Table 17. *Summary of the films prepared in the* **Section 4.4.3***.*

Entry	***Film***	***IL3 (mol%)***	***Polymerising Order***	***Conductive Additive***
1	$E_{50}PIL3b$	0	-	EDOT
2	$E_{50}IL3_{75}PIL3b$	75	-	EDOT
3	$P_{50}IL3_{75}PIL3b$	75	1st mIL - 2nd EDOT	Polymerised EDOT by IL3
4	$P_{50}PIL3b$-1a	0	1st mIL - 2nd EDOT	Polymerised EDOT by O_2
5	$P_{50}IL3_5PIL3b$-1a	5	1st mIL - 2nd EDOT	Polymerised EDOT by O_2 and IL3
6	$P_{50}IL3_{95}PIL1$	95	1st EDOT - 2nd mIL	Polymerised EDOT by APS

4.4.4 Optoelectronic Systems with Perovskite Nanocrystals

PIL@PS Systems Containing EDOT/PEDOT

The introduction of perovskite nanocrystals (PNCs) combined with EDOT and PEDOT in PIL systems is a novel approach for obtaining optoelectronic devices. The aim of this system was to obtain a synergistic effect between the conductive polymers and the PNCs in order to improve the electronic properties of the material while exhibiting some optical features. Additionally, PNCs can present high electrical conductivity.[315] Indeed, the addition of PNCs in polymers as a way to improve their conductivity have been investigated.[314]

Films combining mIL, PNCs and EDOT were prepared and evaluated. The formulation **PIL3b** was the only one tested for the study with PNCs, since it had showed a great ability for stabilizing PNCs, reported in **Chapter 3**, **Section 3.4.4**. The concentrations of both EDOT and PEDOT were calculated always in relation to the mIL3 amount, while the PNCs concentration was based on the amount of mIL3 plus BDA and EDOT or PEDOT. Firstly, following the procedure detailed in **Section 3.4.2**, mIL3 was mixed with $CsPbBr_3$ (2 wt%, evaporating the hexane at 45 °C) and then, different concentrations of EDOT (50 and 100 mol%) were added. Finally, BDA (5 mol%) and TPO (1 wt%) were introduced and, after photopolymerising following the standard conditions (illuminating with UV light for 20 min at 40 °C under aerobic atmosphere), sticky and yellowish films were obtained (**$E_{50}PIL3b@PS$**,

E_{100}PIL3b@PS) (*Figure 106*a). The lower the amount of EDOT, the less fragile, flexible and sticky was the film, since EDOT was a liquid monomer inside a solid. Similarly, some films were prepared using the same formulation but changing EDOT by PEDOT at 0.5 wt% and 1 wt% concentrations. Water from the commercial PEDOT was removed by evaporation under reduced pressure, obtaining dried PEDOT dispersed in mIL3. Then, $CsPbBr_3$ dispersed in hexane was added. After removing the solvent, BDA (5 mol%) and TPO (1 wt%) were added and the mixture was photopolymerised following standard conditions. Depending on the amount of PEDOT incorporated, the resulting film was yellowish (**$P_{0.5}$PIL3b@PS**) or blackish (**P_1PIL3b@PS**) (*Figure 106*b).

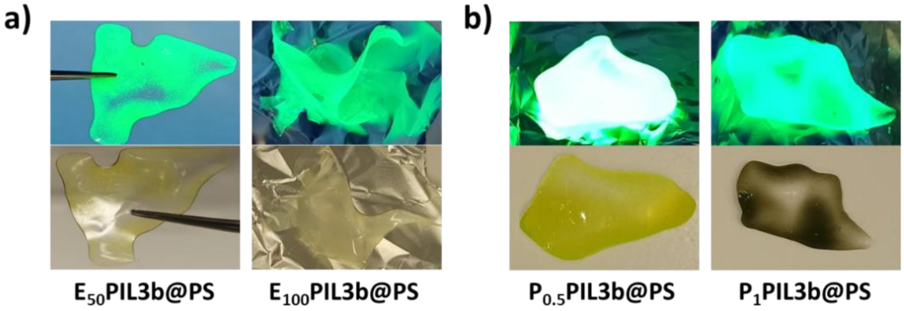

Figure 106. *Picture of* ***a)*** *EDOT-based films with $CsPbBr_3$;* ***b)*** *PEDOT-based films with $CsPbBr_3$, taken (up) under UV light, (down) under ambient light.*

The amount of PEDOT affected the photoluminescence of the films. PLQY of **$P_{0.5}$PIL3b@PS** was similar to the original **PIL3b@PS** film, whereas films with higher concentration of PEDOT (**P_1PIL3b@PS**) presented a PLQY notably inferior. A high amount of PEDOT had a negative influence on the photoluminescent properties of the material, as its dark colour hindered the fluorescence from the PNCs. But, the PLQY remained constant, demonstrating that PEDOT did not deactivated $CsPbBr_3$. In contrast, the introduction of EDOT quenched the PNCs within few days, regardless of the concentration used as it can be seen in *Figure 107*. In this case, the additive was a liquid monomer, so the PNCs were not properly stabilised into a solid matrix. The stability test was performed in the dark during several months following the conditions described in **Section 3.6.3**.

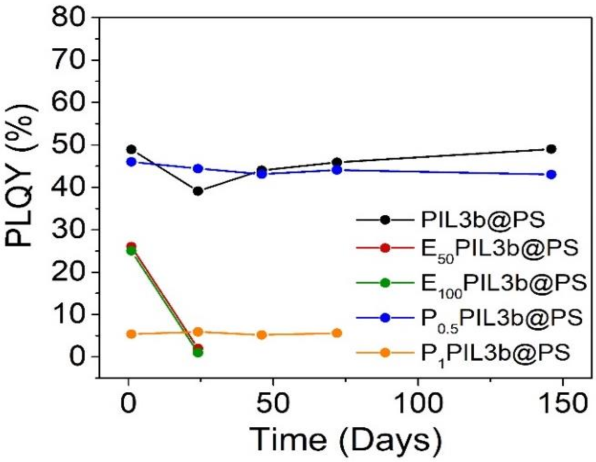

Figure 107. *Evaluation of the PLQY of different films containing perovskite nanocrystals.*

Furthermore, the possibility that PNCs could catalyse the oxidative reaction of EDOT was considered. Nevertheless, EDOT contained in a film with perovskite nanocrystals (**E_{50}PIL3b@PS**) did not oxidise faster or different than **E_{50}PIL3b** films. Thus, perovskite nanoparticles did not help in the EDOT oxidation under O_2 atmosphere (*Figure 108*a). Additionally, once the EDOT was oxidised (**P_{50}PIL3b@PS**), the PNCs were fully quenched, showing no photoluminescent at all (PLQY decreased from 25.7 to 0.3) (*Figure 108*b).

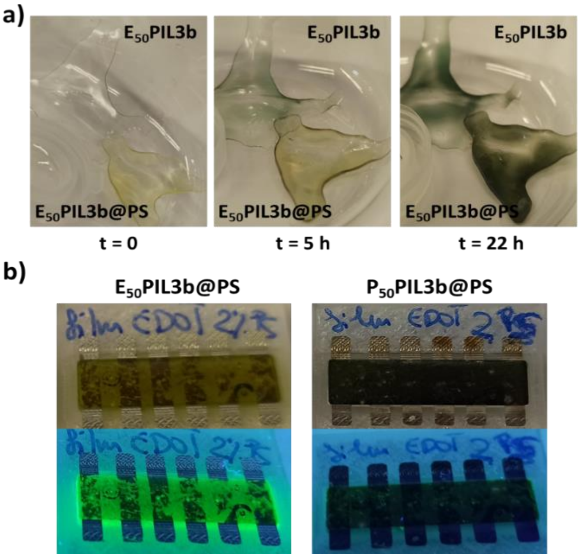

Figure 108. ***a)*** *Oxidative evolution along 22 hours, (up)* ***E_{50}PIL3b*** *film, (down)* ***E_{50}PIL3b@PS*** *film. Films kept under oxidative atmosphere at 65 °C;* ***b)*** *(left)* ***E_{50}PIL3b@PS*** *film showing a yellowish appearance and some PL activity, (right) same film after EDOT oxidation (black,* ***P_{50}PIL3b@PS****), showing none photoluminescence; pictures taken (up) under ambient light, (down) under UV light.*

PIL@PS Systems Containing Homogeneous Ionic Liquids

Firstly, IL-based films without PNCs were prepared. The formulations contained mIL3 (95 mol%), BDA as cross-linker (5 mol%), TPO as photoinitiator (1 wt%) and the corresponding IL (IL1, IL2, IL3) at different concentrations (**ILX$_y$PIL3b**, where X refers to the corresponding IL and y to the IL concentration added). The films obtained were light yellow and more flexible than the analogous without IL (**PIL3b**). Then, following the methodology described in **Section 3.4.2**, PNCs have been introduced into the IL-PIL system. The monomer mIL3 was mixed with $CsPbBr_3$ NCs dispersed in hexane (2 wt% in relation to mIL3 + IL weight). The solvent was removed and then BDA, IL and TPO were added. After the photopolymerisation, solid films were obtained (**ILX$_y$PIL3b@PS**). In a preliminary test we observed that films with an IL concentration higher than 20 mol% did not polymerise properly and the PNCs were totally deactivated. For this reason, a range of concentrations were evaluated in order to find the optimum molar concentration of IL (in relation to mIL3) for stabilising PNCs efficiently (*Figure 109*).

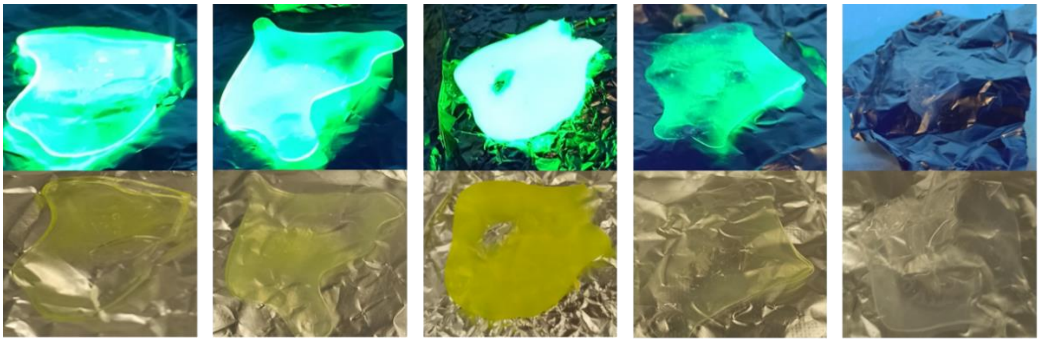
PIL3b@PS **IL3$_5$PIL3b@PS** **IL3$_8$PIL3b@PS** **IL3$_{10}$PIL3b@PS** **IL3$_{20}$PIL3b@PS**

Figure 109. *Pictures of **PIL3b@PS**-based films introducing different concentrations of IL3, (up) under UV light, (down) under ambient light.*

The PLQY of the IL:PIL films with different concentrations of IL3 (**IL3$_{10}$PIL3b@PS**, **IL3$_8$PIL3b@PS** and **IL3$_5$PIL3b@PS**) were analysed as a function of time for two years and compared to the analogous **PIL3b@PS** film. The samples were kept in the dark, further details are described in **Section 3.6.3**. As it can be seen in *Figure 110*, the film with 8 mol% of IL3 (**IL3$_8$PIL3b@PS**) was not only capable to stabilise $CsPbBr_3$ along more than 600 days, but the PL within that time overcame the photoluminescence of **PIL3b@PS**. Therefore, IL3 had a clear influence on the PL activity of the PNCs. After photopolymerising the film, the PLQY was quite low (25 %), and then it was increasing until the point to surpass the PL of **PIL3b@PS**, the formulation that showed better stabilising results in **Chapter 3**. The longer the time, the more evident this trend became. The addition of a higher concentrations of IL3, such as 10 mol% (**$IL3_{10}$PIL3b@PS**), presented a similar PLQY (27 %) than **$IL3_8$PIL3b@PS** the first day, but it decreased sharply after the fourth day. This effect was also observed in a film using IL2 (12 mol%). In contrast, the film with 5 mol% IL3 showed a high PLQY after the film preparation (43 %), comparable to the PLQY of **PIL3b@PS** (40 %). The initial PL of this film was less influenced by IL3 due to the low concentration. However, in few days the $CsPbBr_3$ started to be quenched. We can hypothesise that by using an appropriate amount of IL3, homogeneous matrices can be obtained, leading to an outstanding stabilisation of the PNCs.

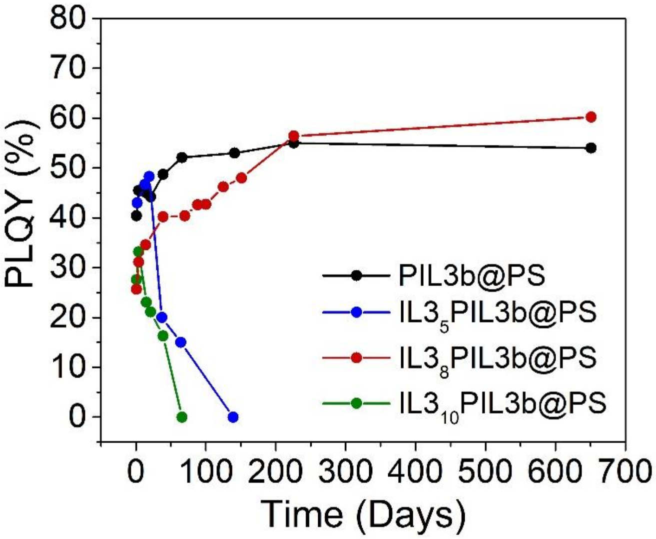

Figure 110. *PLQY stability study of IL-based films of choline bis(trifluoromethane)sulfonimide (IL3) with different concentrations (5, 8 and 10 mol%), performed along 651 days stored in the dark.*

Thus, the best optical properties were achieved using an IL concentration of 8 mol%. Higher concentrations of ILs (>10 mol%) reported low PLQY, the material was too plasticised and the PNCs were not properly embedded, although the films presented a higher thermal stability (*Figure 111*a). Nevertheless, the addition of low concentrations of ILs (<5 mol%) also had a negative influence on the resulting photoluminescence, deactivating in few days the perovskite nanocrystals.

At this point, the molar percentage chosen for ILs was 8 mol%. Films with the three different ILs were prepared to evaluate their capacity to encapsulate and enhance the PL of the $CsPbBr_3$. In this respect, a stability test was performed by measuring the PLQY for two years of three different films: **$IL1_8$PIL3b@PS, $IL2_8$PIL3b@PS** and **$IL3_8$PIL3b@PS**.

From *Figure 111*b it is concluded that IL3 achieved the highest PLQY and stabilised $CsPbBr_3$ much better than the imidazolium-based ILs (IL1 and IL2). This is in agreement with the stabilising behaviour found for the monomeric ionic liquids tested in **Chapter 3**, where cholinium mILs could stabilise the PNCs better than imidazolium monomers. This enhancement of PL activity using IL3 was probably due to ionic interactions between the $CsPbBr_3$ ions and the quaternary amine of IL choline. The samples were stored in the dark (see **Section 3.6.3**).

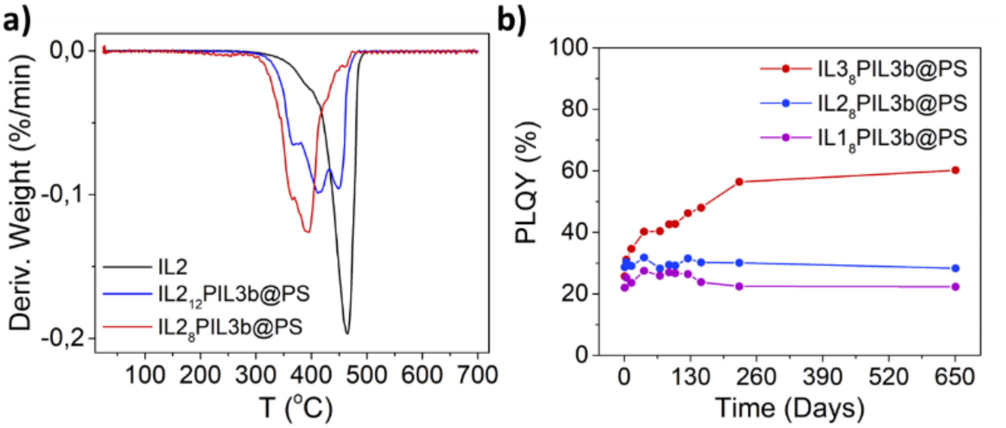

Figure 111. ***a)*** *DTG spectra of IL2-based materials (T_{onset} of IL2: 433 °C, T_{onset} of **$IL2_{12}$PIL3b@PS**: 371 °C and T_{onset} of **$IL2_8$PIL3b@PS**: 355 °C). The higher the IL content, the higher the stability;* ***b)*** *PLQY stability test of IL-based **PIL3b@PS** films using IL1, IL2 and IL3 performed along 651 days stored in the dark.*

Table 18. *Summary of the films prepared in the **Section 4.4.4**. All the samples contained 2 wt% of $CsPbBr_3$.*

Entry	*Film*	*Conductive Additve*	*Additive Content*
1	E_{50}PIL3b@PS	EDOT	50 mol%
2	$P_{0.5}$PIL3b@PS	PEDOT	0.5 wt%
3	P_{50}PIL3b@PS	Polymerised EDOT by O_2	50 mol%
4	$IL3_y$PIL3b	ILs	y = 5 – 12 mol%
5	$IL3_y$PIL3b@PS	ILs	y = 5 – 12 mol%

4.4.5 Conductivity of PIL Composites Containing Conductive Polymers, Ionic Liquids and Perovskite Nanocrystals

The conductivity of PILs depends on several factors including chemical nature of the polymer backbone, nature of the counter-ion, glass transition temperature, pressure, temperature, as well as other external factors such as contaminants, presence of water in the polymers, external humidity or the measurement technique. This makes difficult to compare the different conductivity values reported in the literature. Even though, our bare PILs presented a conductivity of the order of $10^{-6} – 10^{-5}$ S/m (analysed below), which is in good agreement with the values found for PILs in the literature.[21a, 321] These conductivities are usually too low for application in devices. Therefore, in order to increase the intrinsic conductivity of the PIL-based films, a variety of additives were evaluated, and their conductive properties were deeply studied.

For this purpose, an in-house developed 3D printed system was designed and fabricated to measure conductivity and impedance of the different materials in a reproducible and reliable way. All these measurements were performed in collaboration with Agustin Álvarez Ojeda from Prof. Fabregat's group (INAM). Our setup consisted of six electrical probes in a line, with equal spacing between each of the inner probes while the outer ones where a bit more separated as shown in (*Figure 112*a). The six probes were fixed to measure all the samples at the same contact distance, as shown in *Figure 112*b. The films were prepared using a 3D-printed mould; thus, the geometric dimensions were the same for all the samples (measured with a digital calliper): 26.6 x 7.3 x 2.1 mm.

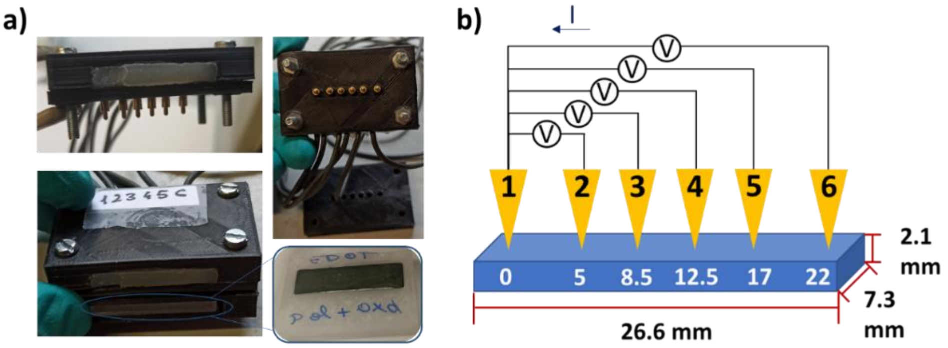

Figure 112. ***a)*** *Home-made set-up for measuring the conductivities and impedances of the prepared films;* ***b)*** *Schematic representation of the six probes system in contact with a film.*

In the first attempts, metallic gold was evaporated and deposited on the surface of the film to have a better contact with the measurement probes. A mask was used during the coating in order to define the geometrical area of the electrode during the charge transfer. After some preliminary tests, gold was replaced by silver, which showed higher stability with our samples. Still, when no metal was used, the reproducibility and conductivity results were improved. Probably, the metal contacts reacted with our polymers since we could appreciate that, in some cases, the colour of the metal changed, especially when PNCs were embedded into the films, as it can be seen in *Figure 113*.

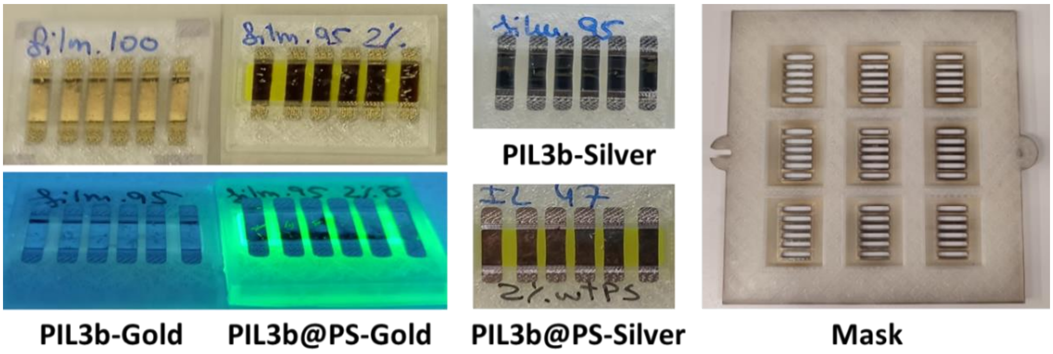

Figure 113. ***PIL3b** films coated with gold and silver; pictures taken under visible and UV light showing the PL activity of the $CsPbBr_3$; and the mask used for depositing the metal with 9 slots to put the samples in.*

The resistance (R) of the films was determined by the two-point probe method at room temperature, having the working and the sensing electrodes in one probe and the counter and reference electrodes in the other probe. The system was prepared to have our samples directly in contact with the six probes, hence the cyclic voltammetry (CV) and impedance spectroscopy (IS) were measured changing the contact distance between two probes (1-2, 1-3, 1-4, 1-5, 1-6) for each sample. The applied voltage was the same for the different distances, so the current intensity varied. The longer the distance, the bigger the resistance and therefore, following Ohm's law, the lower the intensity. This effect was clearly observed through the CV and Nyquist plots performed at each distance (*Figure 114*a and *Figure 115*a, respectively). All the measurements were made inside a Faraday cage to minimize the electromagnetic noise.

Since the resistance is not a material property, it is more appropriate to refer to resistivity (ρ). The corresponding resistivity and conductivity of each sample were calculated from both the IS and CV measurements, and then the average from both values was considered as the final result, represented in the following tables. The cyclic voltammetry measurement was repeated three times for each distance (1-2, 1-3, 1-4, 1-5, 1-6) in order to define a cyclic voltammogram. Since the third measurement provided more stable and less noisy plots, those plots were used for calculating the linear fitting of the curves (red lines, *Figure 114*a). In the cyclic voltammogram trace, the current at the working electrode is plotted versus the applied voltage. Therefore, considering Ohm's law (I = V/R), the resistance of each section was directly calculated as the inverse of the slope (s) reported by the linear fitting. These values were represented versus their respective contact distances (*Figure 114*b). Ideally, the plotted points had a linear trend. The slope of the linear fit of the different points was used for calculating the resistivity, taking into consideration the geometry of our films. According to the definition of Resistance (shown in *Figure 114*b), where R is the resistance (represented in the Y-axis) and L is the contact distance (represented in the X-axis), the slope is defined as ρ/(t·W). The thickness (t) and the width (W) of the samples were well-defined since a same mould model was used for preparing all the films. The units used for representing the resistivity were kΩ·m. At this point, the surface electric conductivity was simply given by the inverse of the resistivity, which is calculated from the equation: $\sigma = \rho^{-1}$ (S/m). This allowed to electrically characterize the materials by measuring surface resistivity.

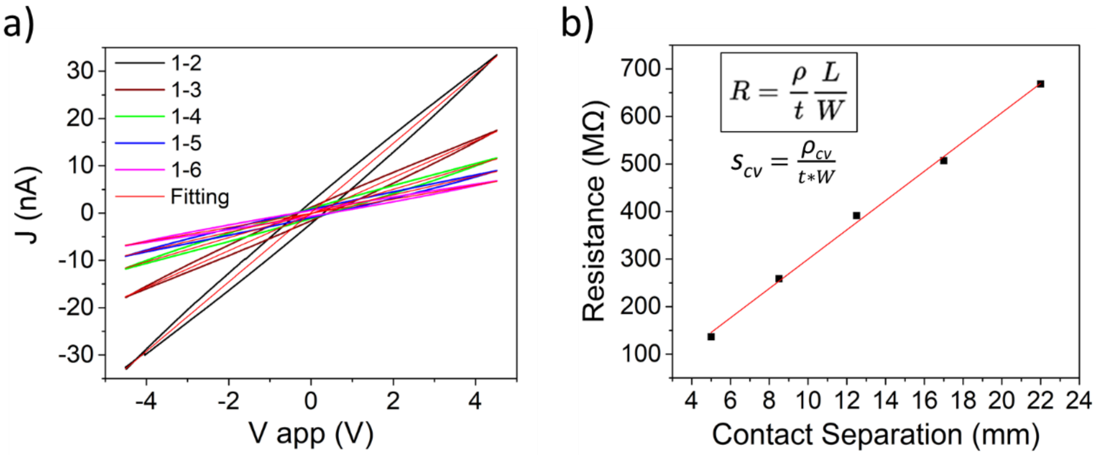

s (1-2) = $7.3 \cdot 10^{-9}$ A/V; R = 136 MΩ
s (1-3) = $3.9 \cdot 10^{-9}$ A/V; R = 258 MΩ
s (1-4) = $2.6 \cdot 10^{-9}$ A/V; R = 391 MΩ
s (1-5) = $2.0 \cdot 10^{-9}$ A/V; R = 507 MΩ
s (1-6) = $1.5 \cdot 10^{-9}$ A/V; R = 668 MΩ

s_{cv} = 30.8 MΩ/mm
ρ_{cv} = 472 kΩ·m
σ_{cv} = $2.12 \cdot 10^{-6}$ S/m

Figure 114. ***a)*** *Cyclic voltammetry plots measured at different contact distances for the sample* ***PIL3b*** *and their respective linear fitting (from the resulting slopes it was possible to calculate the resistance measured at each contact distance);* ***b)*** *Linear fit of the obtained resistance values versus the contact distance (the resistivity was calculated from the slope).*

The results obtained following this methodology were compared with the ones determined by the IS study. The Nyquist plots obtained at each distance were fitted by the Zview software (red lines), using the equivalent circuit represented in *Figure 115*a. In equivalent circuit models of electrochemical systems, the capacitor and resistor are often modelled in parallel because they represent different physical phenomena that occur simultaneously at the polymeric interface: the charge transfer (a Faradaic process) and the double layer charge (a non-Faradaic process). The capacitor (C_1) represents the capacitive behaviour of the system, while the resistor (R_1) represents the resistance to charge transport. In our system, R_1 was the only resistance considered for calculating the conductivity, since the contact resistance (R_s) was the same independently of the contact distance and insignificant compared to R_1. Therefore, R_1 values were represented versus their respective contact distances, and the resulting slope was used for calculating the resistivity (*Figure 115*b). The same procedure above-mentioned was followed to calculate the resistivity and the conductivity of each sample.

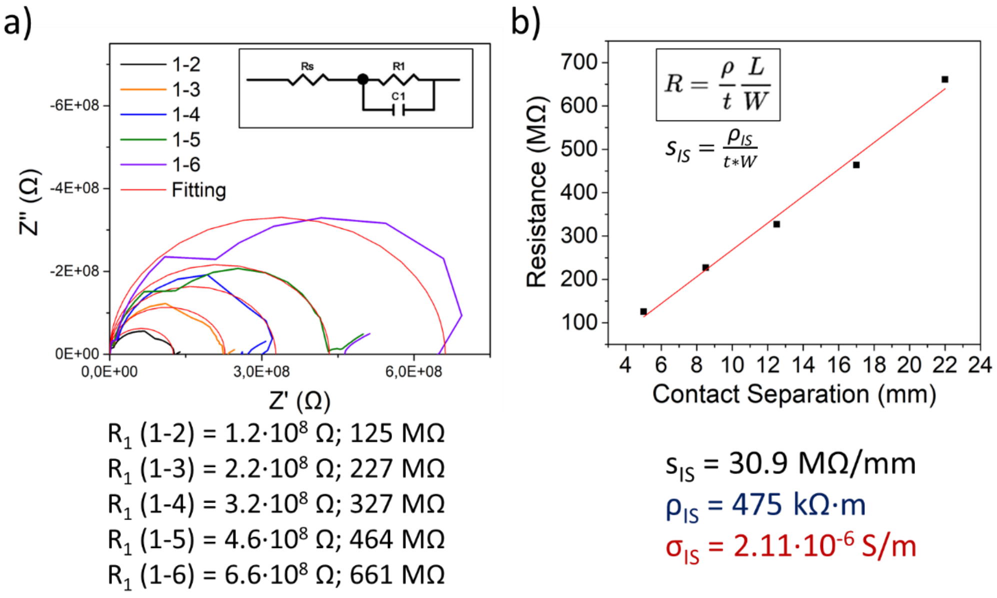

Figure 115. ***a)*** *Nyquist plots measured at different contact distances for the sample* ***PIL3b*** *and their respective fitting (the resistance was considered the R_1 value obtained from the fitting);* ***b)*** *Linear fit of the resistance values versus the contact distance (the resistivity was calculated from the slope).*

Generally, the results obtained by both methods were very similar as it can be seen in *Figure 116*, thus demonstrating the reliability of the method. In order to get a more precise result, the average of the two resistivity values (ρ_{cv} and ρ_{IS}) was calculated, and then that value was used for calculating the conductivities shown in the below tables. To simplify the results, we will represent only the linear regression plots of the CV and IS results for each sample.

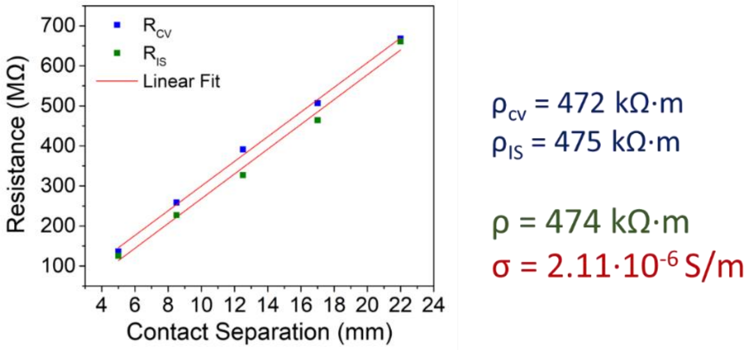

Figure 116. *Linear fit of the resistance values obtained from CV and IS studies versus the contact distance for* ***PIL3b*** *film, with the resistivity values calculated from each technique and the final resistivity and conductivity.*

Conductivity Results

First, the electronic properties of the bare PIL3x formulations were studied, reaching conductivities of 2 x 10^{-6} S/m. The electrons in PILs are localized within the individual molecules, so their mobility is limited by the crystal structure, which reduces conductivity. Still, the ionic nature of the polymeric ionic liquids improves the electrical charge transfer and thus PILs exhibit a higher conductivity than neutral polymers. This was well demonstrated in our study, since the conductivities of totally neutral films such as **PIL3h** (95 mol% butyl acrylate and 5 mol% BDA) and **VIm** (80 mol% vinyl imidazolium and 20 mol% BDA) (*Table 19*, entry 4 and 5) were several orders of magnitude lower compared to PIL-based films. The differences found between the non-cross-linked (**PIL3a**) and cross-linked (**PIL3b**) films were negligible due to the low amount of cross-linker employed (5 mol%) (*Table 19*, entry 1 and 2). Nevertheless, remarkable differences were noticed after the addition of another neutral polymer (**PIL3d**, containing 15 mol% BA) (*Figure 117*).

Table 19. *Resistivity and conductivity values of different **PIL3** formulations based on [2-(acryloyloxy)ethyl]trimethyl-ammonium bis(trifluoromethane)sulfonimide monomer.*

Entry	*Film*	*mIL (mol%)*	*Neutral polymer (mol%)*	*BDA (mol%)*	*Resistivity (kΩ·m)*	*Conductivity (S/m)*
1	PIL3a	100	-	-	503	2.00 x 10^{-6}
2	PIL3b	95	-	5	474	2.11 x 10^{-6}
3	PIL3d	80	BA (15)	5	939	1.07 x 10^{-6}
4	PIL3h	-	BA (95)	5	12737	7.85 x 10^{-8}
5	VIm	-	VIm (80)	20	4017	2.49 x 10^{-7}

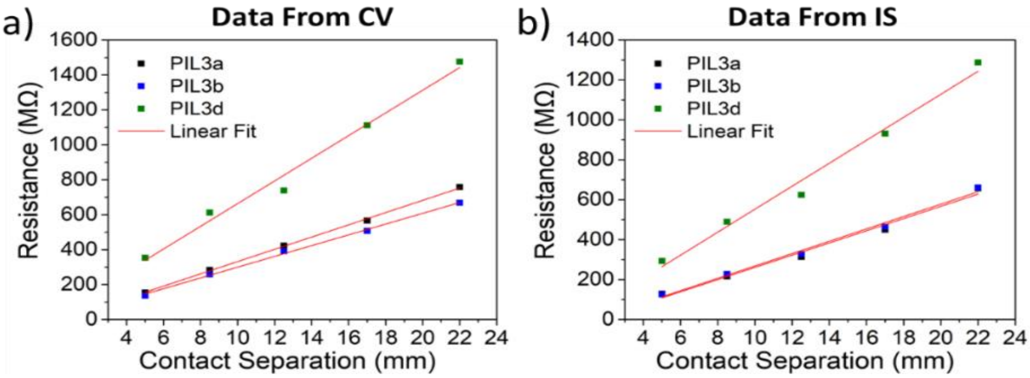

Figure 117. *Linear fit of the resistance values obtained by **a)** CV and, **b)** IS measurements, versus the contact distance for **PIL3a, PIL3b** and **PIL3d** films. **PIL3h** is not represented here since their resistance values are two orders of magnitude higher.*

After adding EDOT and PEDOT the conductivities of the PIL materials enhanced several orders of magnitude. The obtained values are quite similar to those found in the literature for PEDOT/PIL films, which are of the order of 10^{-5} – 10^{-1} S/cm.[154b, 171] The conductivities of the films containing EDOT increased by over one order (**PIL3b** vs **E_{50}PIL3b**, *Table 20*, entries 1 and 2, respectively). When we oxidised the film with oxygen to get PEDOT films (**P_{50}PIL3b-1a**), the conductivity decreased, becoming similar to that of **PIL3b**. The more oxidised the film, the lower the conductivity (*Table 20*, entries 3-6). Probably EDOT after polymerising was not homogeneously distributed, hindering electron mobility. Hence, this pathway to get conductive films was discarded. On the contrary, the addition of APS for oxidising the films (**P_{50}PIL3b-1b**) showed improved results since the conductivity increased one order of magnitude, although the films were much more fragile.

Table 20. *Resistivity and conductivity values of PIL-based films with EDOT and PEDOT.*

Entry	***Film***	***Conductive additive***	***Polymerising order***	***Resistivity (kΩ·m)***	***Conductivity (S/m)***
1	PIL3b	-	-	474	2.11×10^{-6}
2	E_{50}PIL3b	EDOT	-	30	3.38×10^{-5}
3	P_{50}PIL3b-1a[a]	Pol. EDOT by O_2	1st mIL - 2nd EDOT	294	3.41×10^{-6}
4	P_{50}PIL3b-1a[b]	Pol. EDOT by O_2	1st mIL - 2nd EDOT	417	2.40×10^{-6}
5	P_{50}PIL3b-1a[c]	Pol. EDOT by O_2	1st mIL - 2nd EDOT	798	1.25×10^{-6}
6	P_{50}PIL3b-1a[d]	Pol. EDOT by O_2	1st mIL - 2nd EDOT	1007	9.93×10^{-7}
7	P_{50}PIL3b-1b	Pol. EDOT by APS	1st mIL - 2nd EDOT	17	5.75×10^{-5}
8	P_{50}PIL3b-2a	Pol. EDOT by APS	1st EDOT - 2nd mIL	0.12	8.23×10^{-3}
9	P_{50}PIL1-2c	Pol. EDOT by APS	1st EDOT - 2nd mIL	0.16	6.13×10^{-3}
10	$P_{0.5}$PIL3b-3	PEDOT	-	79	1.26×10^{-5}

P_{50}PIL3b-1a film was oxidised during several days, [a]1 day, [b]12 days, [c]14 days and [d]21 days. The commercial EDOT content was 50 mol% and the commercial PEDOT content was 0.5 wt%. The abbreviation "Pol." means polymerised.

The films containing a pre-polymerised EDOT (**P_{50}PIL3b-2a** and **P_{50}PIL1-2c**, entries 8 and 9) reported promising conductivity values, but they were also soft and fragile. The obtained conductivities were more than three orders higher compared to **PIL3b** (*Figure 118*). Probably, the soft condition of the films facilitated the passage of the electrons. On the other hand, the films prepared using commercial PEDOT were slightly less conductive than EDOT-based films. It is noteworthy to remark that EDOT amount was higher than PEDOT amount, and EDOT was a liquid monomer. After photopolymerizing, the resulting **$P_{0.5}$PIL3b-3** films were solid and robust with a conductivity of 1×10^{-5} S/m (*Table 20*, entry 10).

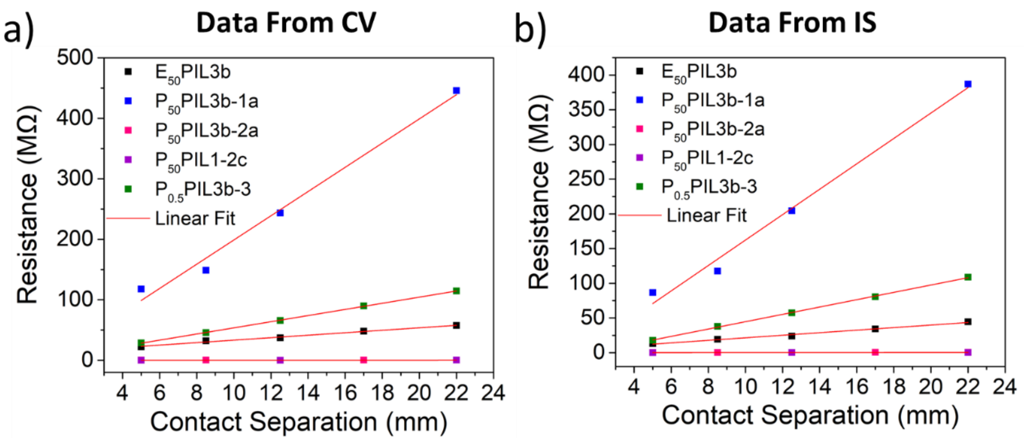

Figure 118. *Linear fit of the resistance values obtained by* ***a)*** *CV and,* ***b)*** *IS measurements, versus the contact distance for PIL-based films with EDOT, polymerised EDOT and PEDOT.*

The ionic liquids are broadly used as electrical conductivity enhancers and their conductivities are usually in the order of 10^{-2} S/cm.[21a] For IL:PIL systems, the conductivities can vary from 10^{-5} to 10^{-2} S/cm at room temperature with increasing ionic liquid content.[164] As expected, significant conductivity enhancement was observed when a higher amount of IL was added to the PIL-based material, but the films were more brittle. This is in good agreement with other studies where it was observed that the physical appearance of the polymer electrolytes changed from a transparent film (0:100 PIL) to a very viscous and sticky gel (75:25, IL:PIL) with some intermediate stages where the polymer electrolytes formed were rubbery and transparent.[164, 312a] A slight improvement in the conductivity was obtained for the films containing 8 mol% of the three different ILs (**IL1$_8$PIL3b**, **IL2$_8$PIL3b** and **IL3$_8$PIL3b**, *Table 21*, entries 2-4) compared to the bare film **PIL3b**. Nevertheless, higher concentrations of ILs sharply increased the conductivities. For example, a film with 75 mol% of IL3 (**IL3$_{75}$PIL3b**) enhanced the conductivity in three orders of magnitude (*Table 21*, entry 5).

A similar film was prepared adding IL3 after the polymerisation (**PIL3b+IL3$_{75}$**), for testing the differences between both methods of adding ILs (*Figure 119*). We observed that the film **IL3$_{75}$PIL3b** was more conductive compared to **PIL3b+IL3$_{75}$**, probably because in the latter film, the ionic liquid was not homogeneously distributed. As previously described, at high IL concentrations, the conductivity of our PIL systems reached values close to those for pure ILs, although the mechanical stability was compromised since the films presented a rubber-like and fragile appearance, as it has been reported in the literature.[164]

Table 21. *Resistivity and conductivity values of **PIL3b**-based films with ILs at different concentrations.*

Entry	*Film*	*IL (mol%)*	*Resistivity (kΩ·m)*	*Conductivity (S/m)*
1	PIL3b	-	474	2.11×10^{-6}
2	IL1$_{8}$PIL3b	8	191	5.32×10^{-6}
3	IL2$_{8}$PIL3b	8	95	1.06×10^{-5}
4	IL3$_{8}$PIL3b	8	203	4.99×10^{-6}
5	IL3$_{75}$PIL3b	75	0.56	2.00×10^{-3}
6	PIL3b+IL3$_{75}$	75	1.42	7.02×10^{-4}

IL1: 1-butyl-3-methylimidazolium bis(trifluoromethane) sulfonimide, IL2: 1-dodecane-3-methylimidazolium bis(trifluoromethane) sulfonimide, IL3: choline bis(trifluoromethane)sulfonimide.

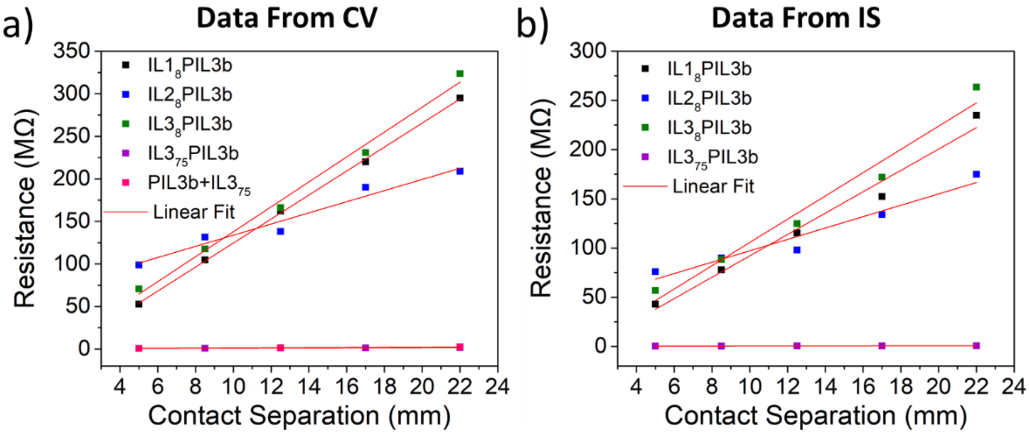

Figure 119. *Linear fit of the resistance values obtained by **a)** CV and, **b)** IS measurements, versus the contact distance for **PIL3b**-based films with ILs at different concentrations.*

The combination of EDOT and PEDOT with ILs gave some interesting results, especially when a low amount of IL3 (5 mol%) was added. The addition of ILs at high concentrations in the EDOT:PIL systems reported a small increase in conductivity compared to the IL:PIL systems, as ILs were the main reason for increasing the conductivity, suppressing the role of EDOT. Still, EDOT (50 mol%) was polymerised during the process and had some synergistic effect with the IL, reflected on the slight conductive increase found for **P$_{50}$IL3$_{75}$PIL3b**, **P$_{50}$IL3$_{100}$PIL3b** and **P$_{50}$IL3$_{200}$PIL3b** (*Table 22*, entries 2-4). The differences between **P$_{50}$IL3$_{100}$PIL3b** and **P$_{50}$IL3$_{200}$PIL3b** were minimal. This fact confirmed that the maximum amount of IL3 absorbed was 100 mol% as discussed in **Section 4.4.3**.

Table 22. *Resistivity and conductivity values of PIL-based films with ILs and PEDOT (commercial or polymerised from EDOT).*

Entry	***Films***	***Conductive additive***	***IL (mol%)***	***Resistivity (kΩ·m)***	***Conductivity (S/m)***
1	IL3$_{75}$PIL3b	-	75	0.56	2.00 x 10^{-3}
2	P$_{50}$IL3$_{75}$PIL3b	Pol. EDOT by IL3	75	0.33	3.06 x 10^{-3}
3	P$_{50}$IL3$_{100}$PIL3b	Pol. EDOT by IL3	100	0.11	9.27 x 10^{-3}
4	P$_{50}$IL3$_{200}$PIL3b	Pol. EDOT by IL3	200	0.10	1.01 x 10^{-2}
5	P$_{50}$IL3$_{5}$PIL3b-1a	Pol. EDOT by O$_2$	5	0.38	2.69 x 10^{-3}
6	P$_{0.5}$IL3$_{5}$PIL3b-3	PEDOT	5	0.25	3.92 x 10^{-3}
7	P$_{50}$IL3$_{95}$PIL1	Pol. EDOT by APS	95	0.08	1.21 x 10^{-2}

IL3: choline bis(trifluoromethane)sulfonimide. The commercial EDOT content was 50 mol% and the commercial PEDOT content was 0.5 wt%. The abbreviation "Pol." means polymerised.

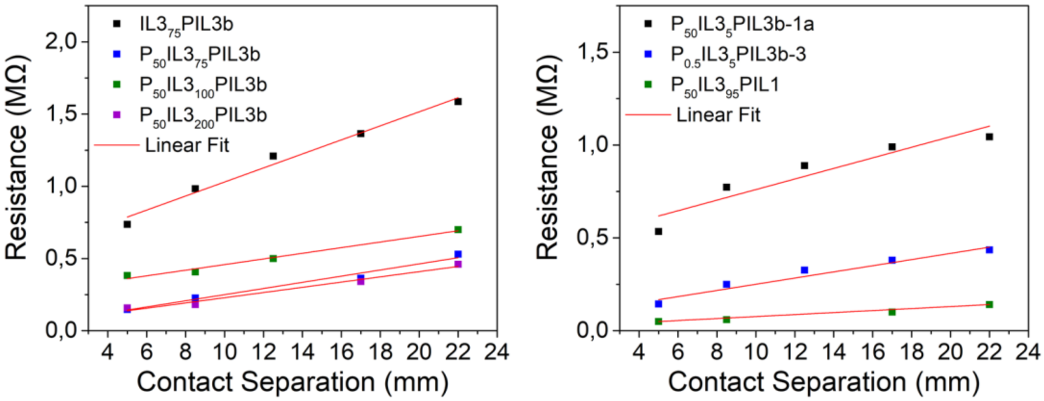

Figure 120. *Linear fit of the resistance values obtained by the CV measurement versus the contact distance for PIL-based films with ILs and PEDOT (commercial or polymerised from EDOT).*

The most notable improvement in terms of conductivity was found after adding IL3 to an already oxidised EDOT film under oxygen atmosphere. The oxidised film (**P$_{50}$PIL3b-1a**) had reported a conductivity of 3 x 10^{-6} S/m (*Table 20*, entry 3), and after adding a low concentration of IL3 (5 mol%) (**P$_{50}$IL3$_{5}$PIL3b-1a**), the conductivity increased three orders of magnitude (*Table 22*, entry 5). We had seen that low concentrations of ILs barely changed the conductivities, however, by mixing polymerised EDOT and IL3 at low concentrations, a notable synergistic effect was appreciated (*Figure 120*). This test was also carried out on a film containing commercial PEDOT (**P$_{0.5}$PIL3b-3**). Herein, IL3 (5 mol%) was added over the film (**P$_{0.5}$IL3$_{5}$PIL3b-3**) and its conductivity also presented a remarkable improvement (increasing from 1 x 10^{-5} to 4 x 10^{-3} S/m).

Then, we measured the conductivity of the film containing a mixture of IL3:APS:EDOT into a mIL1-based photopolymer (**$P_{50}IL3_{95}PIL1$**). In this sample, IL3 was used to solubilise APS and EDOT, and then it was mixed with mIL1, PEGDA and TPO. This film showed a high conductivity (1 x 10^{-2} S/m) probably due to its soft and flexible structure. As general trend, ILs not only acted as dopants for enhancing the conductivity but also as a plasticizer for PEDOT and PIL structures, modifying the materials robustness. Those changes are consistent with literature reports.[322]

Finally, the influence on the electrical properties of the addition of PNCs in the formulations, was evaluated. **PIL3b**-based films were prepared using different concentrations of $CsPbBr_3$ (1 wt%, 2 wt%, 5 wt% and 10 wt%). The addition of PNCs increased the conductivity of the material following the expected trend, the greater the amount of PNCs, the higher the resulting conductivity. In this regard, the highest conductive value was obtained with 10 wt% PNCs (*Table 23*, entry 4), which was the maximum amount capable to be stabilized into the film. Even though, the conductivities increased very slightly after adding perovskite nanocrystals, probably due to a low charge transfer from PNCs to the polymer.

Table 23. *Resistivity and conductivity values of $CsPbBr_3$-based films (**PIL@PS**).*

Entry	***Film***	***$CsPbBr_3$ (wt%)***	***IL (mol%)/ PEDOT (wt%)***	***Resistivity (kΩ·m)***	***Conductivity (S/m)***
1	$PIL3b@PS_1$	1	-	304	3.33 x 10^{-6}
2	$PIL3b@PS_2$	2	-	293	3.44 x 10^{-6}
3	$PIL3b@PS_5$	5	-	190	5.33 x 10^{-6}
4	$PIL3b@PS_{10}$	10	-	138	7.27 x 10^{-6}
5	$P_{0.5}PIL3b@PS$	2	0 / 0.5	36	2.80 x 10^{-5}
6	$IL1_8PIL3b@PS$	2	8 / 0	182	5.57 x 10^{-6}
7	$IL2_8PIL3b@PS$	2	8 / 0	138	7.39 x 10^{-6}
8	$IL3_8PIL3b@PS$	2	8 / 0	165	6.24 x 10^{-6}

The rest of the samples were prepared using 2 wt% of PNCs, since that was the optimum concentration, in terms of stability, determined in **Chapter 3**. After adding 2 wt% of PNCs, the conductivity of PEDOT-based films was doubled (**$P_{0.5}PIL3b@PS$**, *Table 23*, entry 5). On the other hand, the addition of PNCs into IL:PIL systems (**$IL1_8PIL3b@PS$**, **$IL2_8PIL3b@PS$** and **$IL3_8PIL3b@PS$**, entries 6-8) barely improved the conductive results compared to the systems without PNCs reported in *Table 21*, entries 2-4. In particular, the conductivity of **IL2$_8$PIL3b@PS** was decreased after adding $CsPbBr_3$; the electron transfer may be affected negatively by the combination of the long chain of IL2 (1-dodecyl-3-methylimidazolium) with PNCs. Consequently, in general, the PNCs had a very small impact on the conductivity results (*Figure 121*).

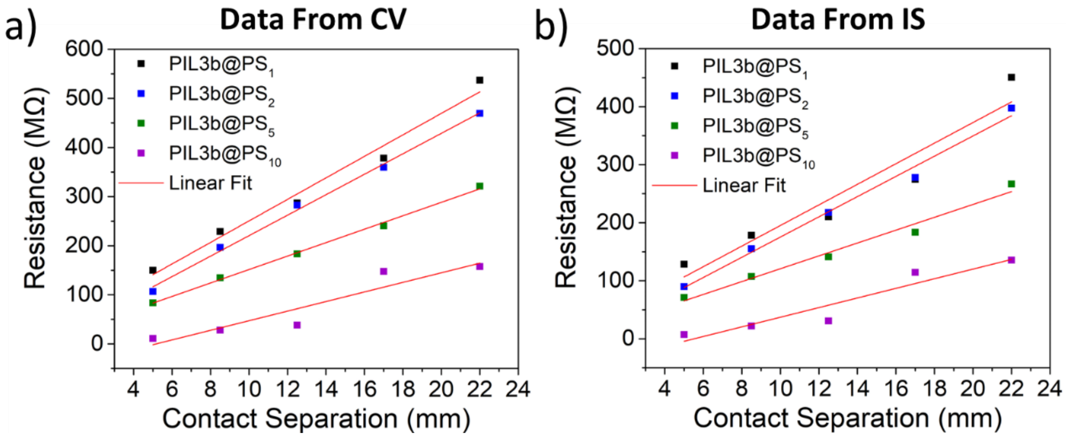

Figure 121. *Linear fit of the resistance values obtained by* ***a)*** *CV and,* ***b)*** *IS measurements, versus the contact distance for* ***PIL3b****-based films with different concentrations of $CsPbBr_3$ (1, 2, 5, 10 wt%).*

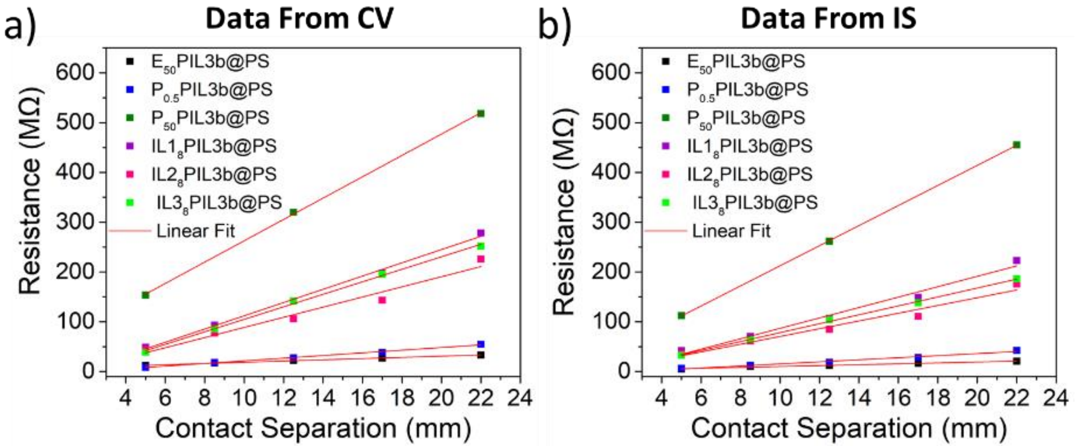

Figure 122. *Linear fit of the resistance values obtained by* ***a)*** *CV and,* ***b)*** *IS measurements, versus the contact distance for* ***PIL3b@PS****-based films with EDOT, polymerised EDOT, PEDOT and different ILs (IL1, IL2 and IL3).*

4.4.6 Conductivity of PIL Composites Containing Metallic Nanoparticles

Metallic salts and nanoparticles have been widely employed for enhancing the conductivity of both PIL-based and non-ionic materials.[65b, 303]

The impedances of some of our formulations were studied before and after adding different metallic salts. The impedance measurements of the metallic-based films were performed in collaboration with Pietro Zaccagnini from Politecnico of Torino. An in-house method of the group was implemented for doing the measurements. The setup consisted of a two-probe system, in which the film was sandwiched between both probes (*Figure 123*a). Since the probes were circular with a diameter of 10 mm, circular thin films (~200 µm of thickness) with that geometrical area were prepared for these measurements. In this study, only one contact distance was measured (fixed by the thickness of the film). Therefore, the charge transport resistance that was obtained after fitting Nyquist plots with the Zview software using a Randles circuit (represented in *Figure 123*b), was employed for calculating the resistivity. In this study, a Warburg element (Ws_1) was added in the circuit to represent the diffusion process of the ions across the film at high frequencies presented in our systems. Then, the capacitor (Cdl) and the resistor (R_1) were represented in parallel to describe the frequency-dependent behaviour of the system and to better understand the relationship between the capacitive and resistive elements in the circuit. In this way, the electrochemical properties of the films were evaluated (*i. e.*, charge transfer and double layer capacitance). Finally, R_s referred to the contact resistance.

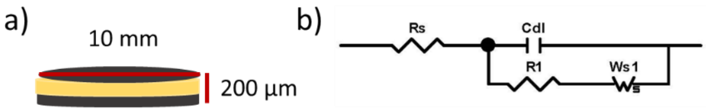

Figure 123. ***a)*** *Set-up for measuring the conductivities and impedances of the metallic films;* ***b)*** *Randles circuit employed for doing the fitting in Zview software.*

The resistivity was calculated using the equation showed in *Figure 124*a, where *R* was the charge transport resistance R_1, *A* was the geometrical area of the circular films (r = 5 mm) and *L* was the thickness of the films (~200 µm). Since the resistivity of the samples was high, the R_s did not alter the resistance we read out from our samples, thus we only considered the transport resistance for calculating the impedances.

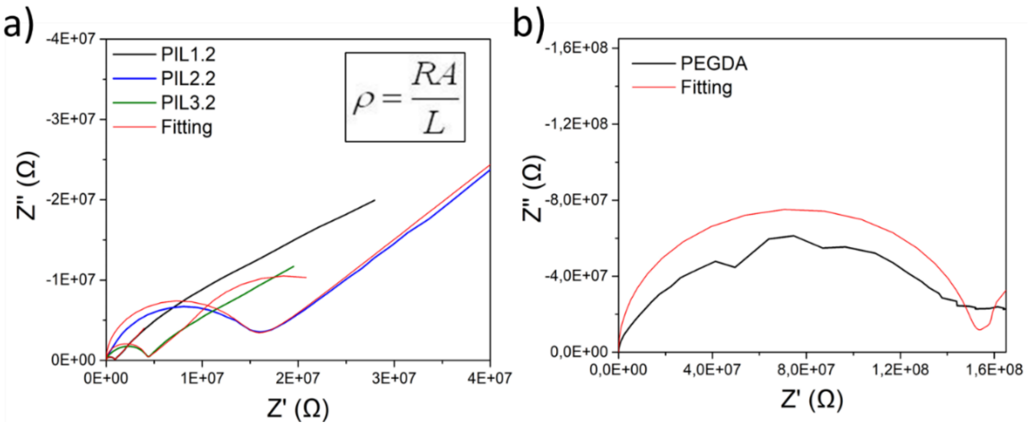

Figure 124. *Nyquist plots of **a)** PIL-based films; **b)** PEGDA film.*

In the first place, the conductivities of the bare PIL-based films with PEGDA 575 (20 mol%) (**PIL1.2**, **PIL2.2** and **PIL3.2**) were evaluated and compared with pure PEGDA 575 conductivity (*Table 24*). The imidazolium films based on mIL1 resulted to be the most conductive materials, while, as expected, the non-ionic film composed purely of PEGDA showed a huge resistance (*Figure 124*).

Table 24. *Resistivity and conductivity values of **PIL**-based films. Details about the formulation nomenclature can be found in **Section 2.4.3** (*Table 3*).*

Entry	***Film***	***PIL:PEGDA (mol/mol)***	***Resistivity (kΩ·m)***	***Conductivity (S/m)***
1	PIL1.2	80:20	479	2.09×10^{-6}
2	PIL2.2	80:20	6898	1.45×10^{-7}
3	PIL3.2	80:20	1790	5.59×10^{-7}
4	PEGDA	0:100	84150	1.19×10^{-8}

PIL1 based on 1-butyl-3-vinylimidazolium bis(trifluoromethane)sulfonimide (mIL1), PIL2 based on 1-(3-hydroxypropyl)-3-vinylimidazolium bis(trifluoromethane)sulfonimide (mIL2) and PIL3 based on [2-(acryloyloxy)ethyl]trimethyl-ammonium bis(trifluoromethane)sulfonimide (mIL3).

PIL1.2 presented the highest conductivity, since its Tg was the lowest one (-13.9 ºC), reported in **Section 2.4.3** (*Table 3*, entry 3). On the contrary **PIL2.2** reported the lowest conductivity although its Tg value (1.4 ºC) was lower compared to **PIL3.2**'s Tg (23.7 ºC) (*Table 3*, entries 9 and 15). These conductivity results were remarkably lower compared to those obtained for the PIL-based formulations using BDA (5 mol%) as cross-linker. The more cross-linked the film was, the lower its conductivity was, as the charges had less mobility. Additionally, the increase in the neutral polymer proportion by reducing the percentage of PIL also had a negative effect on the resulting conductivities. These results are interesting, since it could be assumed that the ether groups in PEGDA would improve ion stabilisation reporting higher conductivity than the apolar cross-linker BDA. However, BDA was employed in lower amounts, which reinforces that the conductivity properties are due to the IL moieties in the polymer. Moreover, the methods and equipment used to measure the samples were different, which could influence the final result.

To the polymer baseline, a silver nitrate salt ($AgNO_3$) was added in a range of concentrations from 1 wt% to 9 wt%, and their impedances were tested. To obtain metal nanoparticles, the samples were exposed to UV light for 30 minutes at 40 °C. An addition of more than 9 wt% of $AgNO_3$ resulted in the precipitation of the salt, as it could not be stabilised properly in the photopolymer. The addition of 1 wt% of the silver salt increased the resistivity of the material, (*Table 25*, entry 1), while 2 wt% and especially 5 wt% of $AgNO_3$ exhibited an enhanced conductivity compared to the bare polymer **PIL3.2** (*Figure 125*a). According to the literature, the resistivity decreases increasing the silver content in the formulation.[65b] This trend fitted well up to the sample containing 5 wt% $AgNO_3$, which was the optimum concentration; thereafter, higher amounts of silver registered lower conductivity (*Figure 125*b).

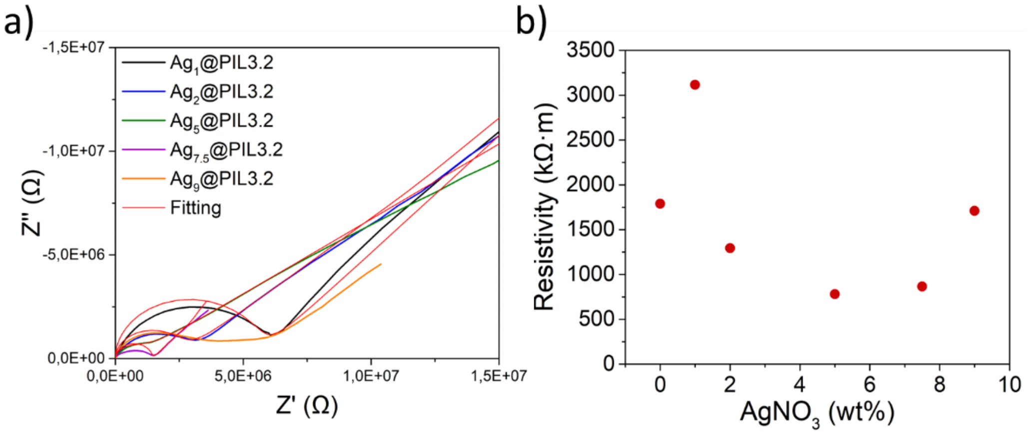

Figure 125. ***a)*** *Nyquist plots of* ***PIL3.2****-based films with different concentrations of* $AgNO_3$ *(1, 2, 5, 7.5 and 9 wt%);* ***b)*** *Resistivity values versus the silver concentration.*

Hence, we can suggest that in our formulations, a high weigh percentage of silver led to large agglomerations of the nanoparticles due to a bad distribution of the salt, forming bulks and reducing the contact between them. For that reason, the addition of high concentrations of silver limited the conductive improvements, and thus the conductivity of the film with 9 wt% $AgNO_3$ (**Ag_9@PIL3.2**, *Table 25*, entry 6) was very similar to that of the bare PIL film without silver (**PIL3.2**).

Table 25. *Resistivity and conductivity values of* ***PIL3.2*** *films with different concentrations of $AgNO_3$.*

Entry	***Film***	***$AgNO_3$ (wt%)***	***Resistivity (kΩ·m)***	***Conductivity (S/m)***
1	PIL3.2	-	1790	5.59×10^{-7}
2	Ag_1@PIL3.2	1	3116	3.21×10^{-7}
3	Ag_2@PIL3.2	2	1294	7.73×10^{-7}
4	Ag_5@PIL3.2	5	780	1.28×10^{-6}
5	$Ag_{7.5}$@PIL3.2	7.5	866	1.16×10^{-6}
6	Ag_9@PIL3.2	9	1710	5.85×10^{-7}

This test was also performed for **PIL1.2**-based materials, and in a preliminary study it was observed that copper-based films exhibited increasing conductivity with the amount of metal salt added. For that reason, this phenomenon was further studied, evaluating samples with different concentrations of copper nitrate salt ($Cu(NO_3)_2$, 1, 2, 5 and 10 wt%). The samples were heated for 30 min at 160 °C to get nanoparticles. Once again, the addition of 1 wt% of salt reported a higher resistivity (*Table 26*, entry 2) than **PIL1.2**, while the sample with 2 wt% of salt was almost one order of magnitude more conductive than **PIL1.2** (*Figure 126*). This trend was followed by the samples with 5 wt% and 10 wt% of copper, showing an enhanced conductivity with the increase of metal nanoparticles. The highest conductivity was achieved with the film **Cu_{10}@PIL1.2** (*Table 26*, entry 5), as it was not possible to solubilise a larger amount of copper salt in the formulation without adding a solvent. This improvement in conductivity with increasing the percentage of copper is due to the higher number of free electrons introduced by the metal, which can move freely through the polymer. It can be concluded that the NPs were well distributed. Nevertheless, in both studies, the sample with 1 wt% of metallic nanoparticles exhibited a higher resistivity than the bare polymer. Probably, that amount of salt was too low for having a good contact between the particles, making it difficult the passage of electrons. In addition, the samples must be homogeneous and isotropic to get good conductivities. It could be possible that the salt in those samples was not homogenously distributed due to the low amount dissolved.

Table 26. *Resistivity and conductivity of* ***PIL1.2*** *films with different concentrations of copper nitrate.*

Entry	***Film***	***$Cu(NO_3)_2$ (wt%)***	***Resistivity (kΩ·m)***	***Conductivity (S/m)***
1	PIL1.2	-	479	2.09×10^{-6}
2	Cu_1@PIL1.2	1	557	1.80×10^{-6}
3	Cu_2@PIL1.2	2	82	1.21×10^{-5}
4	Cu_5@PIL1.2	5	23	4.35×10^{-5}
5	Cu_{10}@PIL1.2	10	5	2.00×10^{-4}

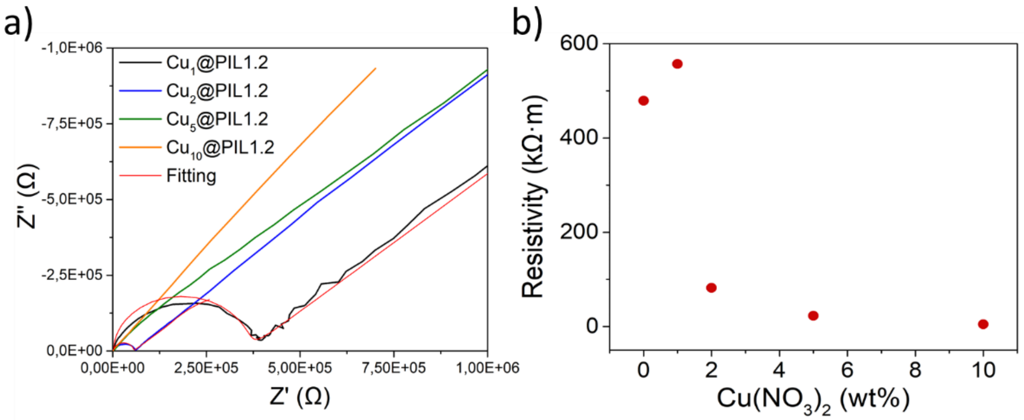

Figure 126. ***a)*** *Nyquist plots of* ***PIL1.2****-based films with different concentrations of* $Cu(NO_3)_2{\cdot}3H_2O$ *(1, 2, 5, 10 wt%);* ***b)*** *Resistivity values versus the copper concentration.*

4.5 Conclusions

In this Chapter, the conductivity of PIL-based materials was enhanced by adding different additives. In a first place, a variety of samples were prepared introducing PEDOT or by polymerising the corresponding monomer. Three different strategies were followed to prepare the films. And, moreover, two different approaches were considered for polymerising EDOT monomers, by an oxidative atmosphere or using an oxidative chemical (ammonium persulfate, APS). We found that EDOT-based films were robust and presented an improved conductivity (10^{-5} S/m) compared to the bare PIL polymer (10^{-6} S/m), although after oxidising them under oxidative atmosphere for obtaining PEDOT, the resistivity increased. In contrast, EDOT-based films oxidised with APS reported a similar conductivity than EDOT films but the films were not robust. On the other hand, the pre-polymerisation of EDOT before photopolymerising the films, led to brittle and inconsistent films with high conductivities (10^{-3} S/m). Finally, the films prepared using commercial PEDOT were robust and presented a similar conductivity than EDOT-based films (10^{-5} S/m).

In the second place, several homogeneous ionic liquids at different concentrations were introduced into the PEDOT:PIL systems, finding some remarkable improvements in terms of conductivity (10^{-3} - 10^{-2} S/m) due to their free charges moving freely. The addition of ILs on EDOT-based films conducted to a rapid polymerisation of EDOT. A synergistic effect between PEDOT and IL3 (choline bis(trifluoromethane)sulfonimide) was observed after adding 5 mol% IL3 on a PEDOT film. The conductivity increased in two orders of magnitude. This work has shown that the use of ionic liquids as a secondary doping gives much better results in terms of electric conductivity, but in return the materials were less robust.

In the third place, it was evaluated the capacity to encapsulate $CsPbBr_3$ in PIL-based formulations to obtain optoelectronic materials. EDOT:PIL, PEDOT:PIL and IL:PIL systems, as well as bare PILs were combined with PNCs to improve both optical and electrical properties of the films. The capability of these systems to stabilise PNCs was evaluated. In particular, PEDOT-based films (**$P_{0.5}$PIL3b@PS**) and PILs containing 8 mol% of IL3 (**$IL3_8$PIL3b@PS**) reported a high photoluminescence (~45 % and 65 %, respectively), demonstrating a good ability for stabilising $CsPbBr_3$. Also, the influence of PNCs to improve the conductive performance was investigated, resulting in improvements of at most one order of magnitude after adding PNCs.

Lastly, metallic salts ($AgNO_3$ and $Cu(NO_3)_2$) were added to the PIL-based materials in a range of concentrations (0 – 10 wt%). In these studies, an enhancement of the electrical properties was observed in both cases, with a maximum using a concentration of 5 wt% for Ag (10^{-6} S/m) and 10 wt% for the copper-based samples (10^{-4} S/m), observing a direct relationship between conductivity improvement and copper content. Another remarkable observation was that the degree of cross-linking showed a negative influence on conductivity. This indicates that the rigidity of the polymer limits ion mobility and the IL moieties are probably responsible for the electrical conductivity. The addition of higher amounts of cross-linker increases the percentage of neutral polymer, reducing the amount of ionic polymer in the formulation. This may also influence the final conductivity of the films, since it has been confirmed that neutral polymers exhibited the lowest conductivity (10^{-8} S/m), regardless the cross-linker content.

In general, it can be concluded that mechanical properties have to be sacrificed in order to improve conductive properties. And, the conductivity decreases as the amount of neutral polymer increases and as the polymer becomes more cross-linked.

4.6 Experimental Part

4.6.1 Materials

As mentioned in **Chapter 2**, all reagents were purchased from Sigma-Aldrich and used without further purification, unless otherwise stated. Lithium bis(trifluoromethane) sulfonimide ($LiNTf_2$, 99 %) was purchased from IOLITEC GmbH and used as received.

4.6.2 Equipment

In this Chapter, same equipment described in **Chapter 2** and **Chapter 3** have been employed.

In addition, the impedance spectroscopy (IS) and the cyclic voltammetry (CV) were measured with a potentiostat/galvanostat Autolab PGSTAT30 (Eco Chemie) equipped with a FRA2, keeping the samples inside a Faraday cage to reduce the noise measured. The CV was performed at a constant rate of 0.2 V/s, from -4.5 V to 4.5 V. For the IS measurement, a 20 mV AC perturbation was applied. The low-frequency and high-frequency limits were 0.1 Hz and 1 MHz, respectively. The measurements were performed at short-circuit, an applied voltage of cero. Analysis of all Nyquist spectra was done using Zview software.

4.6.3 Synthesis and Characterisation of Ionic Liquids

The ionic liquids evaluated in this Chapter were 1-butyl-3-methylimidazolium bis(trifluoromethane) sulfonimide (IL1), 1-dodecane-3-methylimidazolium bis(trifluoromethane) sulfonimide (IL2) and choline bis(trifluoromethane)sulfonimide (IL3). The three ILs were synthesised from their halide salts by anion exchange as described in the literature.[31a] All the characterising spectra referred in this Section can be found in **Chapter 6: Annex, Section 6.3**.

1-butyl-3-methylimidazolium bromide (BMI.Br)

1-bromobutane (4.2 g, 30 mmol) dissolved in dichloromethane (14 mL) was added dropwise to a solution of 1-methylimidazole (2 g, 24 mmol) in dichloromethane (20 mL). The resulting reaction mixture was left to react for 20 h at 60 °C. After evaporating the solvent, the crude product was then washed with diethyl ether (20 mL) five times. Then, it was re-dissolved in acetonitrile (5 mL) and slowly added to rapidly stirred toluene (20 mL) to form a purer solid. This procedure was repeated two times. During the last wash the product crystallised becoming a white solid. The solid product was dried under reduced pressure at room temperature for 3 h (1.16 g, 22 %).

The resulting IL was characterised by ^{1}H NMR, ^{13}C NMR and ESI-MS. ^{1}H NMR (400 MHz, MeOD): δ / ppm = 8.98 (s, 1H), 7.65 (d, *J* = 2.0 Hz, 1H), 7.58 (d, *J* = 2.0 Hz, 1H), 4.23 (t, *J* = 7.2 Hz, 2H), 3.94 (s, 3H), 1.88 (m, 2H), 1.38 (m, 2H), 0.99 (t, *J* = 7.5 Hz, 3H). ^{13}C NMR (400 MHz, MeOD): δ / ppm = 124.9, 123.6, 50.6, 36.5, 33.1, 20.4, 13.7. ESI-MS in positive mode: Calculated: 139.12 m/z; Found: 140.4 m/z. ESI-MS in negative mode: Calculated: 78.92 m/z; Found: 78.9 m/z (*Figure A27* and *Figure A28*).

1-butyl-3-methylimidazolium bis(trifluoromethane) sulfonimide (IL1)

Lithium bis(trifluoromethane) sulfonimide ($LiNTf_2$) (1.6 g, 5 mmol) was dissolved in water (2 mL) and it was added dropwise to an aqueous solution (2.5 mL) of 1-butyl-3-methylimidazolium bromide (1 g, 4 mmol), forming two liquid phases. The mixture was stirred rapidly for 18 h at room temperature. The phases were then separated and the aqueous phase was extracted three times with dichloromethane (15 mL). The combined organic phases were washed three times with water (20 mL) and dried over $MgSO_4$ anhydride. The product was further dried under reduced pressure at 50 °C for 8 h (2.03 g, Yield: 63 %).

The resulting IL was characterised by ^{1}H NMR, ^{13}C NMR, ESI-MS, elemental analysis, FT-IR, Raman and TGA-DSC. ^{1}H NMR (400 MHz, $CDCl_3$): δ / ppm = 8.76 (s, 1H), 7.26 (d, *J* = 1.8, 2H), 7.2 (d, *J* = 1.6 Hz, 2H), 4.17 (t, *J* = 7.6 Hz, 2H), 3.94 (s, 3H), 1.85 (m, 2H), 1.38 (m, 2H), 0.96 (t, *J* = 8.8 Hz, 3H). ^{13}C NMR (400 MHz, $CDCl_3$): δ / ppm = 136.2, 123.8, 122.4, (q, CF_3), 50.1, 36.4, 32.0, 19.4, 13.3. ESI-MS in positive mode: Calculated: 139.12 m/z; Found: 139.4 m/z. ESI-MS in negative mode: Calculated: 279.92 m/z; Found: 280.1 m/z. Elemental Analysis: Calculated: C, 28.64; H, 3.61; N, 10.02; S, 15.29; Found: C, 28.26; H, 3.64; N, 9.71; S, 14.14. FT-IR bands: 3157 cm^{-1} (C=C), 2968 cm^{-1} (C-H), 1572 cm^{-1} (C=C), 1341 cm^{-1} (SO_2), 1177 cm^{-1} (C-C), 1132 cm^{-1} (CF_3), 789 cm^{-1} (C-S), 739 cm^{-1} (S-N). T_{onset}: 453.37 °C (*Figure A29* - *Figure A31*).

1-dodecane-3-methylimidazolium bromide (DMI.Br)

1-bromododecane (7.8 g, 31 mmol) dissolved in dichloromethane (16 mL) was added dropwise to a solution of 1-methylimidazole (2 g, 24 mmol) in dichloromethane (20 mL). The resulting reaction mixture was left to react for 20 h at 60 °C. After evaporating the solvent, the crude product was then washed with diethyl ether (20 mL) three times. Then, it was re-dissolved in acetonitrile (5 mL) and slowly added to rapidly stirred toluene (20 mL) to form a purer solid. During the last wash the product crystallised, and then the white solid was filtrated. The solid product was dried under reduced pressure at room temperature for 6 h (3.6 g, 44 %).

The resulting IL was characterised by ^{1}H NMR, ^{13}C NMR and ESI-MS. ^{1}H NMR (400 MHz, MeOD): δ / ppm = 7.64 (d, *J* = 2.0 Hz, 1H), 7.58 (d, *J* = 2.0 Hz, 1H), 4.22 (t, *J* = 7.4 Hz, 2H), 3.94 (s, 3H), 1.90 (m, 2H), 1.36-1.29 (m, 18H), 0.90 (t, *J* = 7.4 Hz, 3H). ^{13}C NMR (400 MHz, MeOD): δ / ppm = 124.9, 123.6, 50.9, 36.5, 33.0, 30.7-29, 27.3, 14.4. ESI-MS in positive mode: Calculated: 251.25 m/z; Found: 252.5 m/z. ESI-MS in negative mode: Calculated: 78.92 m/z; Found: 79.0 m/z (*Figure A32* and *Figure A33*).

1-dodecane-3-methylimidazolium bis(trifluoromethane) sulfonimide (IL2)

Lithium bis(trifluoromethane) sulfonimide ($LiNTf_2$) (2.1 g, 7 mmol) was dissolved in water (2 mL) and it was added dropwise to an aqueous solution (7 mL) of 1-dodecane-3-methylimidazolium bromide (2 g, 6 mmol), forming two liquid phases. The mixture was stirred rapidly for 18 h at room temperature. The phases were then separated and the aqueous phase was extracted three times with dichloromethane (15 mL). The combined organic phases were washed three times with water (30 mL) and dried over $MgSO_4$ anhydride. The product was further dried under reduced pressure at 50 °C for 8 h (2.03 g, Yield: 63 %).

The resulting IL was characterised by ^{1}H NMR, ^{13}C NMR, ESI-MS, elemental analysis, FT-IR, Raman and TGA-DSC. ^{1}H NMR (400 MHz, $CDCl_3$): δ / ppm = 8.81 (s, 1H), 7.28 (t, *J* = 1.8 Hz, 2H), 7.25 (t, *J* = 1.8 Hz, 2H), 4.17 (t, *J* = 7.6 Hz, 2H), 3.96 (s, 3H), 1.87 (m, 2H), 1.33-1.25 (m, 18H), 0.88 (t, *J* = 7.2 Hz, 3H). ^{13}C NMR (400 MHz, $CDCl_3$): δ / ppm = 136.4, 123.8, 122.3, (q, CF_3), 50.4, 36.5, 32.0, 30.2-29.0, 26.3, 22.9, 14.2. ESI-MS in positive mode: Calculated: 251.25 m/z; Found: 251.6 m/z. ESI-MS in negative mode: Calculated: 279.92 m/z; Found: 279.9 m/z. Elemental Analysis: Calculated: C, 40.67; H, 5.88; N, 7.91; S, 12.06; Found: C, 39.57; H, 5.86; N, 7.60; S, 12.72. FT-IR bands: 3157 cm^{-1} (C=C), 2923-2856 cm^{-1} (C-H), 1572 cm^{-1} (C=C), 1348 cm^{-1} (SO_2), 1180 cm^{-1} (C-C), 1133 cm^{-1} (CF_3), 787 cm^{-1} (C-S), 740 cm^{-1} (S-N). T_{onset}: 433.21 °C (*Figure A34* - *Figure A36*).

Choline bis(trifluoromethane)sulfonimide (IL3)

Choline bis(trifluoromethane)sulfonimide was synthesised from commercial choline chloride (Ch.Cl) by an anion exchange reaction with lithium bis(trifluoromethane)sulfonimide, following Wales *et al.* protocol.[31a] $LiNTf_2$ (23.5 g, 82 mmol) was dissolved in mili-Q water (70 mL) and it was added dropwise to an aqueous solution (30 mL) of choline chloride (24 g, 124 mmol). The mixture formed two liquid phases and it was stirred rapidly for 20 h at room temperature. The phases were then separated and the aqueous phase was extracted three times with ethyl acetate (100 mL). The combined organic phases were washed three times with mili-Q water (100 mL) and dried over Na_2SO_4 anhydride. The yellowish liquid product was further dried under reduced pressure at 45 °C for 4 h (22.4 g, Yield: 80 %).

The resulting IL was characterised by ^{1}H NMR, ^{13}C NMR, ESI-MS, elemental analysis, FT-IR, Raman and TGA-DSC. ^{1}H NMR (400 MHz, MeOD): δ / ppm = 4.04 (m, 2H), 3.52 (m, 2H), 3.25 (s, 9H). ^{13}C NMR (400 MHz, MeOD): δ / ppm: (q, CF_3), 69.0, 57.1, 54.7. ESI-MS in positive mode: Calculated: 104.11 m/z; Found: 104.3 m/z. ESI-MS in negative mode: Calculated: 279.92 m/z; Found: 280.1 m/z. Elemental Analysis: Calculated: C, 21.88; H, 3.67; N, 7.29; S, 16.68; Found: C, 18.79; H, 3.08; N, 6.47; S, 15.60. FT-IR bands: 3541 cm^{-1} (-OH), 3059 cm^{-1} (C=C), 2975 cm^{-1} (C-H), 1480 cm^{-1} (O-H), 1348 cm^{-1} (SO_2), 1178 cm^{-1} (C-C), 1130 cm^{-1} (CF_3), 792 cm^{-1} (C-S), 741 cm^{-1} (S-N). T_{onset}: 417.58 °C (*Figure A37* - *Figure A39*).

4.6.4 Characterisation of the Films

The resulting films were characterised by UV-Vis, FT-IR, Raman and TGA-DSC (see *Figure 127* - *Figure 134*).

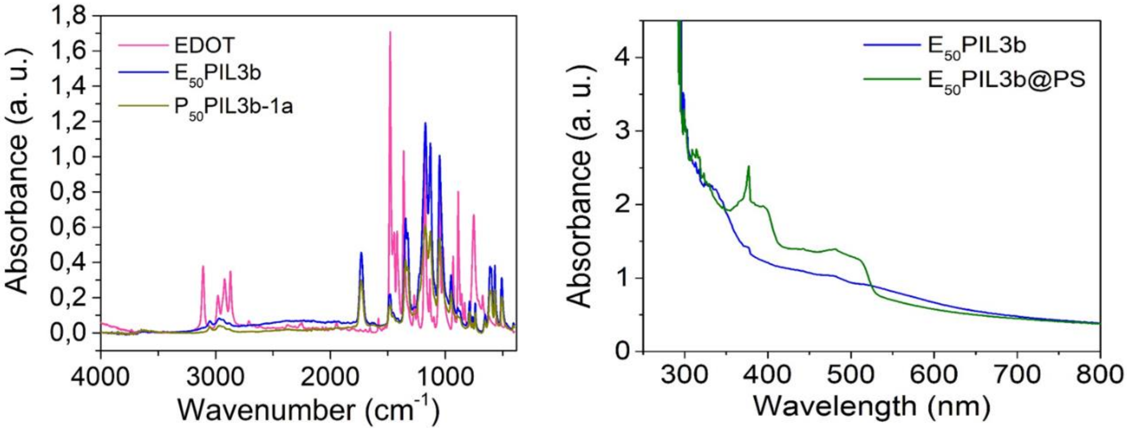

Figure 127. *(Left) FT-IR spectra of pure EDOT (pink), a film with EDOT (50 mol%) (blue) and the same film after oxidising EDOT under oxidative atmosphere (**P_{50}PIL3b -1a**, dark yellow); (right) UV-Vis spectra of EDOT-based film with $CsPbBr_3$ (2 wt%) (green line, showing the characteristic absorption band of $CsPbBr_3$) and without (blue).*

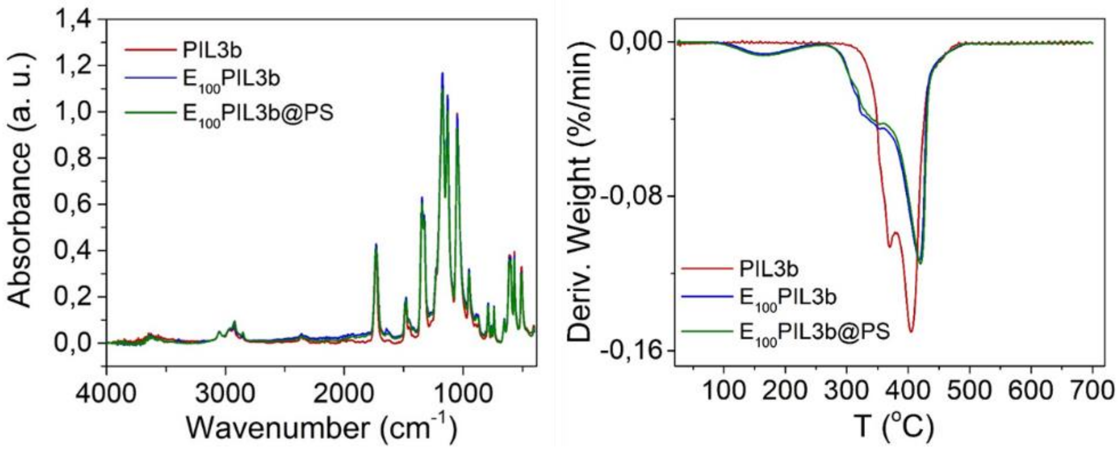

Figure 128. *(Left) FT-IR spectra and (right) DTG spectra of films with EDOT (100 mol%) and $CsPbBr_3$ (2 wt%) (green) and without (blue). The T_{onset} of EDOT-based films was notably lower than **PIL3b** films, decreasing from 390 °C to 343 °C after the addition of EDOT due to the low T_{onset} of EDOT (112 °C).*

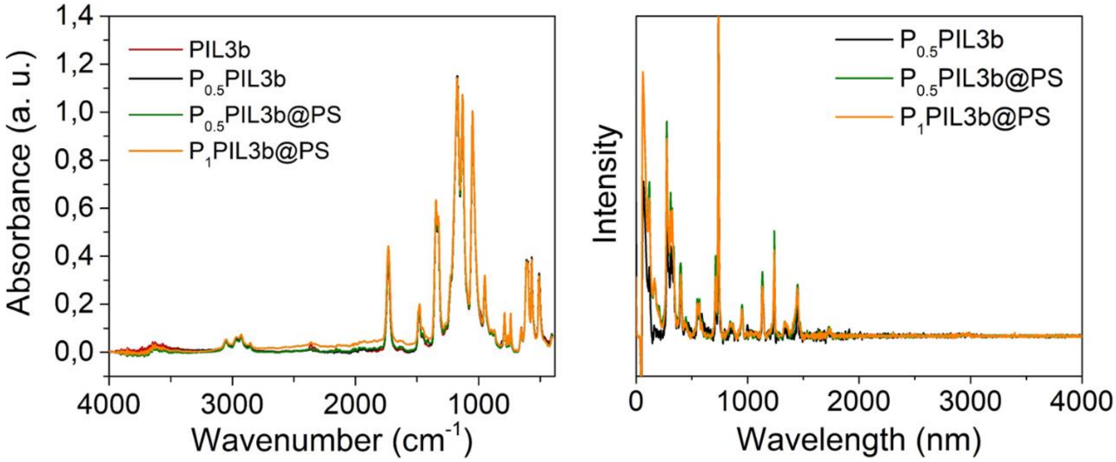

Figure 129. *(Left) FT-IR spectra of films with PEDOT at different concentrations (0.5 wt% and 1 wt%) with and without $CsPbBr_3$; (right) Raman spectra of the PEDOT-based films.*

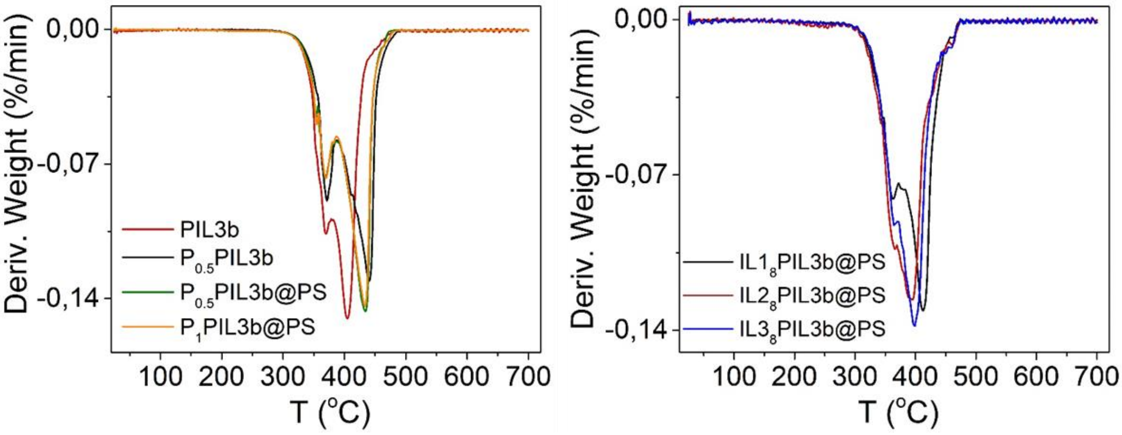

Figure 130. *(Left) DTG spectra of PEDOT-based films. The addition of PEDOT hardly modified the T_{onset} of the films (~388 °C); (right) DTG spectra of different IL-based films with $CsPbBr_3$. Similar T_{onset} were obtained for the three films (~365 °C).*

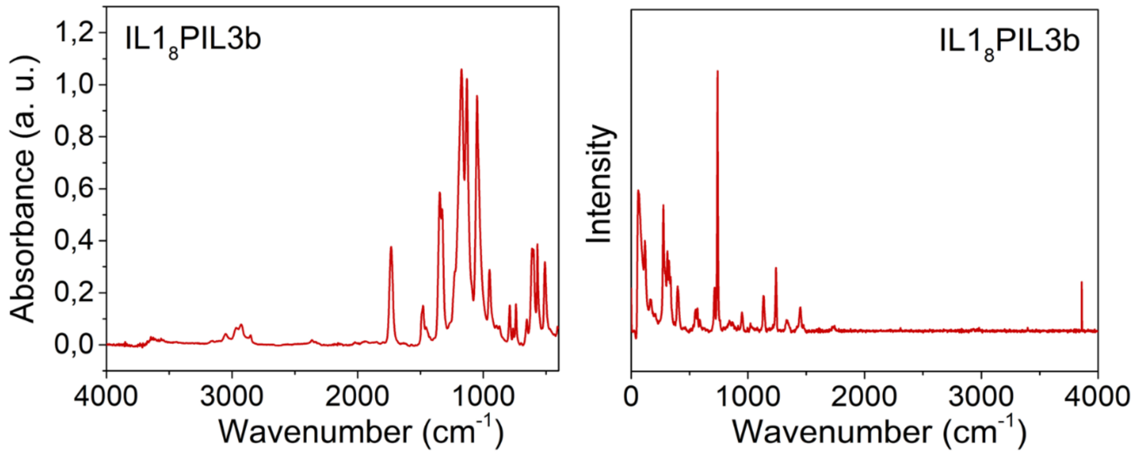

Figure 131. *(Left) FT-IR spectrum and (right) Raman spectrum of* ***PIL3b*** *film with 1-butyl-3-methylimidazolium bis(trifluoromethane) sulfonimide (IL1) at 8 mol% (****IL1$_8$PIL3b****).*

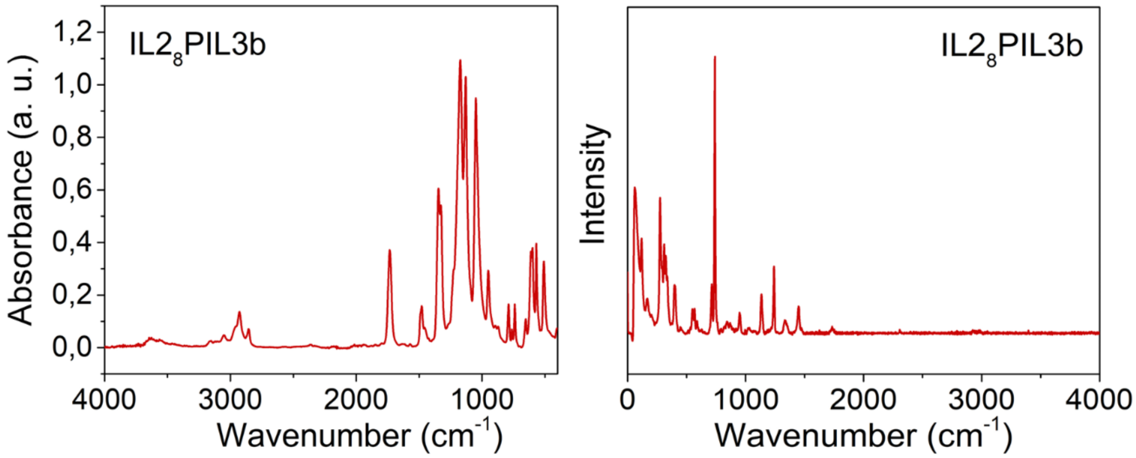

Figure 132. *(Left) FT-IR spectrum and (right) Raman spectrum of* ***PIL3b*** *film with 1-dodecane-3-methylimidazolium bis(trifluoromethane) sulfonimide (IL2) at 8 mol% (****IL2$_8$PIL3b****).*

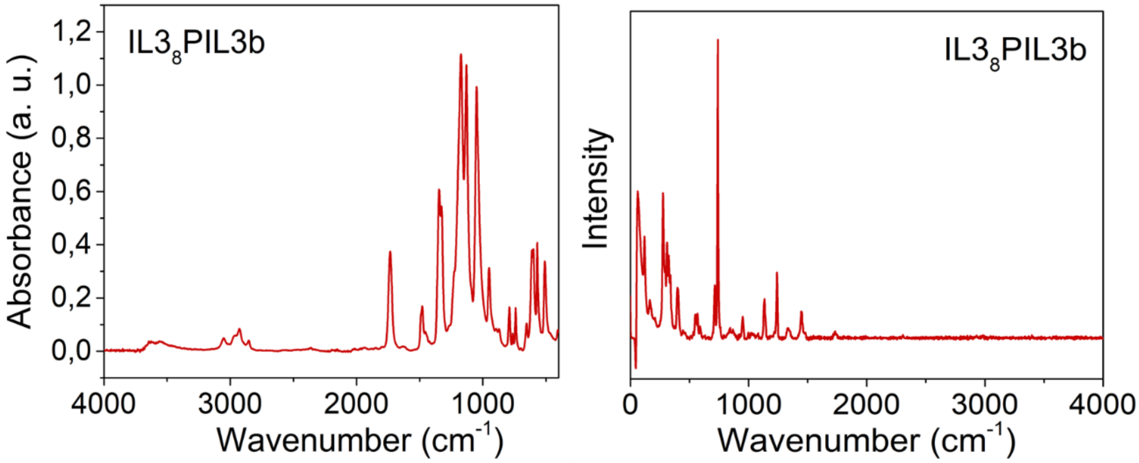

Figure 133. *(Left) FT-IR spectrum and (right) Raman spectrum of* ***PIL3b*** *film with choline bis(trifluoromethane)sulfonimide (IL3) at 8 mol% (****IL3$_8$PIL3b****).*

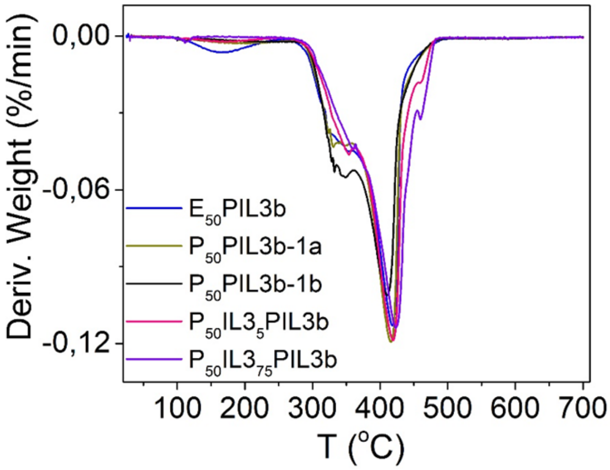

Entry	*Formulation*	*T$_{onset}$ (°C)*
1	E$_{50}$PIL3b	343
2	P$_{50}$PIL3b-1a	370
3	P$_{50}$PIL3b-1b	347
4	P$_{50}$IL3$_5$PIL3b	373
5	P$_{50}$IL3$_{75}$PIL3b	376
6	EDOT	112

Figure 134. *DTG spectra of different films containing EDOT before and after polymerising it by different methodologies (by oxygen (****P$_{50}$PIL3b-1a****), by APS (****P$_{50}$PIL3b-1b****), by the presence of ILs (****P$_{50}$IL3$_5$PIL3b****,* ***P$_{50}$IL3$_{75}$PIL3b****)). The presence of monomeric EDOT decreased the T$_{onset}$ of the film (entry 1), but after polymerising it the thermal stability enhanced, specially by adding ILs (entries 4 and 5). The samples polymerised with APS (entry 3) reported a similar T$_{onset}$ than EDOT films, suggesting than maybe the polymerisation of EDOT was not completed.*

Chapter 5:

General Conclusions

The evolution of additive manufacturing in recent years has been phenomenal. The increased funding, research and development worldwide will result in a fast transition from conventional fabrication to 3D printing technologies both in laboratory and large-scale industrial applications. This technology also allows to go a step further by enabling 4D printing, which is another emerging field, and it is a key factor for the success of the industry 4.0 paradigm. However, there are still several issues that need to be improved in order to compete with traditional methods in the bulk production. As discussed, many of the materials used in additive manufacturing are not yet optimized for the fabrication process. Polymeric ionic liquids (PILs) are appearing as a very desirable material, capable to properly stabilize nano and molecular structures. In a short period of time, printable PILs have had a notably impact across several sectors of 3DP, expanding the uses of this discipline and opening up alternative options in material design.

In this PhD thesis, a wide variety of PIL-based 3D printable materials has been developed. A big family of monomeric ionic liquids, mainly based on imidazole and choline monomers, was synthesised, changing both cation and anion, and thus, modifying their intrinsic features according to the desired application. The different formulations were characterised and optimised to generate high-resolution printed parts with vat polymerisation technologies. Moreover, different active materials were added into the photopolymers, and their functionalities were successfully transferred to the 3D-printed devices. Depending on the additives used, a variety of applications were developed. This has led to the realisation and completion of three different projects, the outcomes of which have been published or are in the process of publication.

In the first project, 3D-printable materials were functionalised with metallic nanoparticles to improve the antimicrobial activity of the polymers. The ability of PILs to stabilise active nanomaterials *via* UV exposure was demonstrated, and it was possible to decouple the fabrication of silver nanoparticles from the printing process. The imidazolium printed devices showed a multi-functional and tuneable microbicidal activity against Gram positive (*B. subtilis*) and Gram negative (*E. coli*) bacteria and against the fungus *A. niger*, while cholinium mIL did not exhibit antibacterial properties. Furthermore, the formulations and the printing parameters were optimised for the additive manufacturing, obtaining high resolutions with a standard deviation of 0.20 mm. Non-cytotoxic 3D-printed parts were obtained using appropriate combinations of mILs and PIs. Additionally, stable copper-based samples were developed and showed outstanding antibacterial activity against *S. epidermidis* bacteria. Finally, a copper-based model of a medical stent was 3D-printed at high resolution.

In the second project, photoluminescent films were prepared by the addition of perovskite nanocrystals (PNCs). A family of formulations based on [2-(acryloyloxy)ethyl]trimethyl-ammonium bis(trifluoromethane)sulfonimide (mIL3) was capable to encapsulate and stabilise all-inorganic PNCs based on $CsPbX_3$ structure (X = Cl, Br, I and combinations) before and during the printing process. Likewise, lead-free perovskites (Sn-doped CsBr) were also embedded and stabilised in PIL matrices. The insoluble and hydrophobic cross-linked solids presented high quantum yields (~50 %) and photoluminescence with enhanced water, light, oxygen, moisture and thermal resistance. Moreover, these photopolymers were specially formulated to be 3D-printed in customized geometries, transferring the perovskite characteristics to the printed structures. In particular, the polymer prepared with mIL3 (95 mol%), BDA (5 mol%) and $CsPbBr_3$ (2 wt%) (**PIL3b@PS**) was used as photocatalyst in the photodegradation of methyl red under visible light, obtaining 95 % of the dye degradation. The kinetics of the photocatalysis reaction using **PIL3b@PS** was three times higher than that of the film without perovskite. The film remained active even after recycles.

Lastly, in the third project, conductive fillers were added to improve the materials' conductivity. Several samples that included PEDOT and its corresponding monomer EDOT were developed. The films were prepared using three distinct strategies based on the order to polymerise the monomers (mIL and EDOT). Additionally, various methods for polymerising EDOT monomers were also taken into consideration (by an oxidative atmosphere or using an oxidative chemical). The electronic and the mechanical properties of the samples varied depending on the methodology followed. The conductivity range varied between 10^{-5} and 10^{-3} s/m. Furthermore, several ILs were synthesised, characterised and added into the PEDOT:PIL systems, finding remarkable improvements in terms of conductivity (10^{-2} S/m). Nevertheless, the enhancement in electrical properties significantly harmed the mechanical properties. The encapsulation of perovskite nanocrystals was also evaluated to obtain optoelectronic devices. The perovskite (2 wt%) was well stabilised in PEDOT-based films and PILs containing 8 mol% of choline bis(trifluoromethane)sulfonimide (IL3). Finally, PIL materials were functionalised with metallic salts ($AgNO_3$ and $Cu(NO_3)_2$) in a range of concentrations. The optimum concentration of silver salt was 5 wt% since that sample reached the highest conductive value (1.28×10^{-6} S/m). Meanwhile, copper-based samples showed conductivities of the order of 10^{-4} S/m. Additionally, the conductivity of copper samples increased in relation to the amount of salt, being 10 wt% the highest amount added.

In general, imidazolium-based formulations had a high antimicrobial activity, however the encapsulation of PNCs was totally inefficient. On the contrary, cholinium-based materials presented a poor antimicrobial activity and lower conductivity values than imidazole, but showed a remarkable ability to embed PNCs and stabilise them before and after manufacturing. Therefore, optimal formulations were successfully developed and tailored to each specific application. This evidences the tuneability of polymeric ionic liquid-based materials, which can efficiently and synergistically interact with a broad range of substrates and thus lead to cutting-edge applications in different fields. In all the studies, the counter-anion that yielded the best results was the bis(trifluoromethane) sulfonimide (NTf_2) due to its hydrophobicity, liquid state, higher thermal stability and high conductivity.

The main purpose of this thesis was successfully achieved since it was demonstrated the ability of PILs to stabilise and encapsulate different active materials during the printing process. Moreover, the properties of the functional materials were properly transferred to the additive manufactured objects. The benefits of stabilising smart compounds on PILs were noteworthy, finding potential antibacterial and photoactive applications for the composites. In addition, the possibility to obtain optoelectronic devices was investigated, although further experiments are necessary.

In conclusion, the combination of PIL-based materials with functionalities provides a synergistic performance that will pave the way for novel applications, especially when coupled to the freedom of design inherent in 3DP techniques. By now, several researchers in the 3DP world have used ILs and PILs, and we forecast that their use will continue to grow. However, in order to overcome the limitations imposed by AM, more sophisticated ionic liquids must be created taking advantage of their tunability. It is imperative to study the synergic interactions between the components to develop effective photopolymer resins. And, learning more about the factors that influence in the composites would aid in the design of more efficient synthesis routes, which would improve the performance of the final devices.

Conclusions Generals

La fabricació additiva ha evolucionat moltíssim en els darrers anys. L'augment del finançament, la investigació i el desenvolupament arreu del món donarà lloc a una ràpida transició de la fabricació convencional a les tecnologies d'impressió 3D tant en aplicacions de laboratori com industrials a gran escala. Aquesta tecnologia també permet anar un pas més enllà en permetre la impressió 4D, que és un altre camp emergent, i és un factor clau per a l'èxit del paradigma de la indústria 4.0. No obstant això, encara hi ha diverses qüestions que cal millorar per competir amb els mètodes tradicionals en la producció a granel. Com s'ha comentat, molts dels materials utilitzats en la fabricació additiva encara no estan optimitzats per al procés de fabricació. Els líquids iònics polimèrics (PILs) estan apareixent com un material molt desitjable, capaços d'estabilitzar adequadament estructures nano i moleculars. En un curt període de temps, els PIL imprimibles han tingut un impacte notable en diversos sectors del 3DP, ampliant els usos d'aquesta disciplina i obrint opcions alternatives en el disseny de materials.

En aquesta tesi doctoral, s'ha desenvolupat una gran varietat de materials imprimibles en 3D basats en PILs. Es van sintetitzar diversos líquids iònics monomèrics, basats principalment en monòmers d'imidazol i colina, canviant tant el catió com l'anió, i així, modificant les seves característiques intrínseques per tal d'aconseguir l'aplicació desitjada. Les diferents formulacions es van caracteritzar i optimitzar per generar peces impreses d'alta resolució amb tecnologies basades en la fotopolimerització. A més, es van afegir diferents materials actius als fotopolímers i les seves funcionalitats es van transferir amb èxit als dispositius impresos en 3D. En funció dels additius utilitzats, es van desenvolupar diverses aplicacions. Això ha portat a la realització i finalització de tres projectes diferents, els resultats dels quals s'han publicat o estan en procés de publicació.

En el primer projecte, es van funcionalitzar materials imprimibles en 3D amb nanopartícules metàl·liques per millorar l'activitat antimicrobiana dels polímers. Es va demostrar la capacitat dels PILs per estabilitzar nanomaterials actius mitjançant l'exposició UV i va ser possible desacoblar la fabricació de nanopartícules de plata del procés d'impressió. Els dispositius impresos amb imidazol van mostrar una activitat microbicida multifuncional contra bacteris (Gram positius (*B. subtilis*) i Gram negatius (*E. coli*)) i contra el fong *A. niger*, mentre que la colina no tenia propietats antibacterianes. A més, es van optimitzar les formulacions i els paràmetres d'impressió per a la fabricació 3D, obtenint altes resolucions amb una desviació estàndard de 0,20 mm. Es van obtenir peces impreses en 3D biocompatibles mitjançant combinacions adequades de mILs i PI. A més, es van desenvolupar mostres de coure estables que van mostrar una activitat antibacteriana excepcional contra els bacteris *S. epidermidis*. Finalment, es va imprimir en 3D a alta resolució un dispositiu mèdic basat en coure.

En el segon projecte, es van preparar pel·lícules fotoluminiscents mitjançant l'addició de nanocristalls de perovskita (PNCs). Una família de formulacions basades en [2-(acriloiloxi)etil]trimetil-amoni bis(trifluorometà)sulfonimida (mIL3) va ser capaç d'encapsular i estabilitzar PNCs inorgàniques d'estructura $CsPbX_3$ (X = Cl, Br, I i combinacions) abans i durant el procés d'impressió. De la mateixa manera, perovskites sense plom (CsBr dopat amb Sn) també es van incrustar i estabilitzar en matrius de PILs. Els sòlids reticulats insolubles i hidròfobs van presentar alts rendiments quàntics (~50%) i fotoluminescència amb una major resistència a l'aigua, la llum, l'oxigen, la humitat i a la calor que la PNCs pura. A més, aquests fotopolímers es van formular especialment per ser impresos en 3D en geometries personalitzades, transferint les característiques de la perovskita a les estructures impreses. En particular, el polímer preparat amb mIL3 (95 mol%), BDA (5 mol%) i $CsPbBr_3$ (2 wt%) (**PIL3b@PS**) es va utilitzar com a fotocatalitzador en la fotodegradació del vermell de metil sota llum visible, obtenint el 95% de la degradació del colorant. La cinètica de la reacció de fotocatàlisi mitjançant **PIL3b@PS** va ser tres vegades superior a la de la pel·lícula sense perovskita. La pel·lícula es va mantenir activa fins i tot després del reciclatge.

Finalment, en el tercer projecte s'han afegit additius conductors per millorar la conductivitat dels materials. Es van desenvolupar diverses mostres que incloïen PEDOT o el seu monòmer corresponent EDOT. Les pel·lícules es van preparar mitjançant tres estratègies diferents basades en l'ordre de polimerització dels monòmers (mIL i EDOT). A més, també es van tenir en compte diversos mètodes per polimeritzar els monòmers EDOT (mitjançant una atmosfera oxidativa o utilitzant una substància química oxidativa). Les propietats electròniques i mecàniques de les mostres variaven en funció de la metodologia seguida. El rang de conductivitat estava entre 10^{-5} i 10^{-3} S/m. A més, es van sintetitzar, caracteritzar i afegir diversos ILs als sistemes PEDOT:PIL, trobant millores notables en les conductivitats (10^{-2} S/m). No obstant això, la millora de les propietats elèctriques va perjudicar significativament les propietats mecàniques. També es va avaluar l'encapsulació de nanocristalls de perovskita per obtenir dispositius optoelectrònics. Les PNCs (2% en pes) es va estabilitzar bé en films de PEDOT i films amb un 8 mol% de colina bis (trifluorometà) sulfonimida (IL3). Finalment, els materials de PILs es van funcionalitzar amb sals metàl·liques ($AgNO_3$ i $Cu(NO_3)_2$). En el cas de la plata es va trobar que la concentració òptima era 5% en pes de sal ja que aquesta mostra va assolir el valor conductor més alt ($1,3 \times 10^{-6}$ S/m). D'altra banda, les mostres basades en coure van mostrar una conductivitat més alta que les mostres de plata, augmentant en general en més d'un ordre de magnitud. A mesura que s'augmentava la quantitat de coure, augmentava la conductivitat dels films.

En general, les formulacions a base d'imidazol tenien una alta activitat antimicrobiana, però l'encapsulació de PNCs va ser totalment ineficient. Per contra, els materials basats en colina presentaven una activitat antimicrobiana deficient i uns valors de conductivitat més baixos que l'imidazol, però mostraven una capacitat notable per incorporar PNCs i estabilitzar-los abans i després de la impressió. Per tant, es van desenvolupar amb èxit formulacions òptimes i adaptades a cada aplicació específica. Això evidencia la sintonització dels materials basats en líquids iònics polimèrics, que poden interactuar de manera eficient i sinèrgica amb una àmplia gamma de substrats i, per tant, conduir a aplicacions d'avantguarda en diferents camps. En tots els estudis, el contra-anió que va donar millors resultats va ser la bis(trifluorometà)sulfonimida (NTf_2) per la seva hidrofobicitat, estat líquid, major estabilitat tèrmica i alta conductivitat.

L'objectiu principal d'aquesta tesi es va aconseguir amb èxit ja que es va demostrar la capacitat dels PILs per estabilitzar i encapsular diferents materials actius durant el procés d'impressió. A més, les propietats dels materials funcionals es van transferir adequadament als objectes manufacturats. Els avantatges d'estabilitzar compostos intel·ligents en PILs van ser destacables, trobant possibles aplicacions antibacterianes i fotoactives. A més, es va investigar la possibilitat d'obtenir dispositius optoelectrònics, tot i que calen més proves.

En conclusió, la combinació de PILs amb funcionalitats proporciona un rendiment sinèrgic que obrirà el camí per a aplicacions noves, especialment quan s'acobla a la llibertat de disseny inherent a les tècniques d'impressió 3D. Per ara, diversos investigadors de 3DP han utilitzat ILs i PILs, i preveiem que el seu ús continuarà creixent. Tanmateix, per superar les limitacions imposades per la AM, s'han de crear líquids iònics més sofisticats aprofitant la seva sintonització. És imprescindible estudiar les interaccions sinèrgiques entre els components que formen els nous materials per desenvolupar resines foto-polimèriques efectives. I sens dubte, conèixer millor els factors que influeixen sobre els compostos polimèrics ajudaria a dissenyar vies de síntesi més eficients, que millorarien el rendiment dels dispositius finals.

Chapter 6:

Annex

All the characterisation spectra of the synthesised compounds mentioned throughout this PhD thesis are presented below. This Chapter is divided into three sections, each showing the spectra of the compounds synthesised in each main Chapter (described in **Section 2.6.6**, **3.6.5** and **4.6.3**, respectively).

6.1 Characterisation of the Compounds Synthesised in Chapter 2

Spectra mentioned in **Section 2.6.6**.

1-butyl-3-vinylimidazolium bromide (BVI.Br)

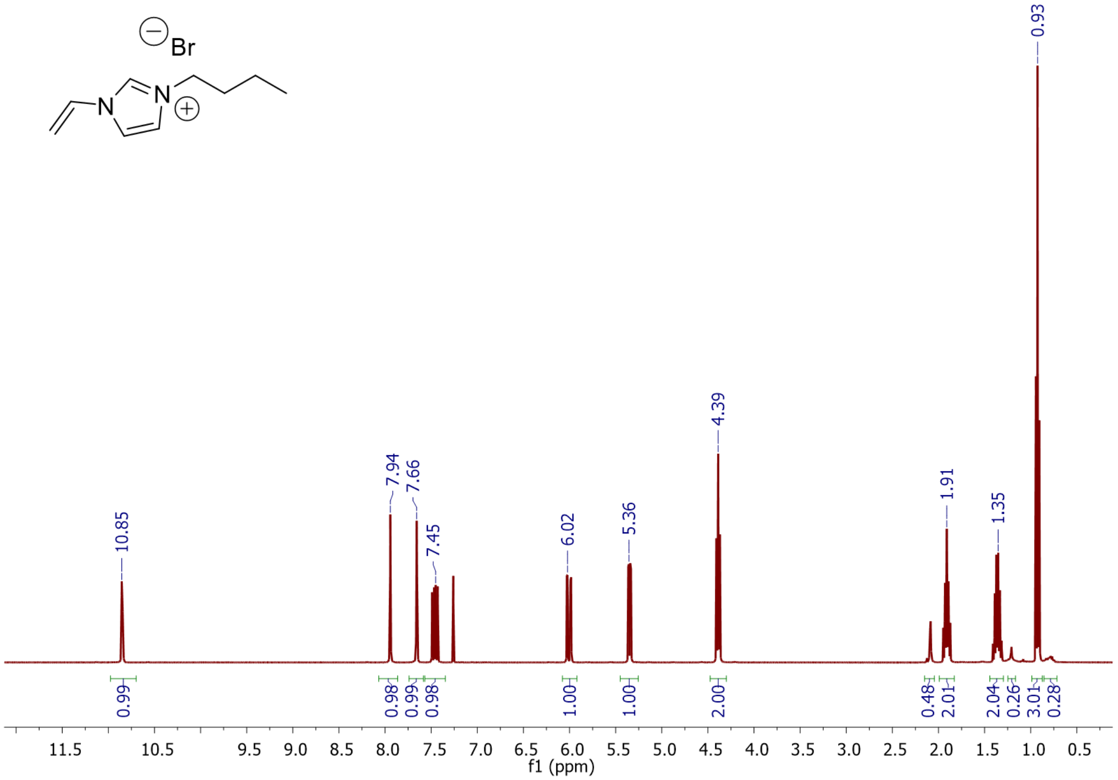

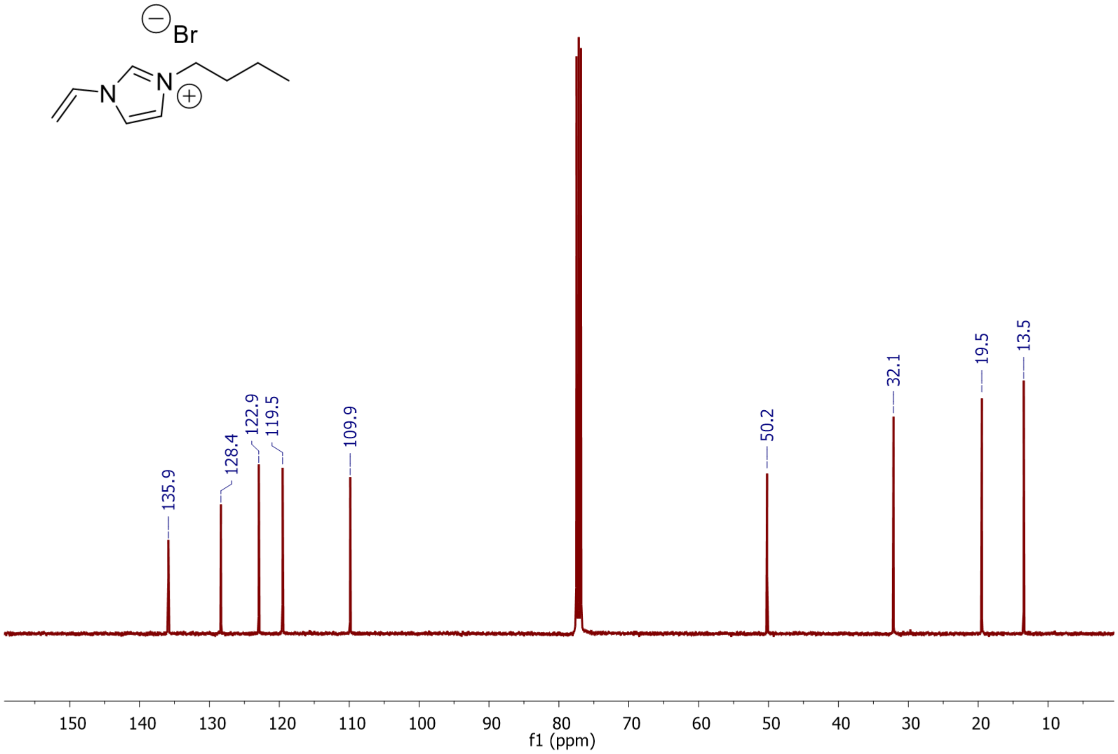

Figure A1. *^{1}H NMR and ^{13}C NMR spectra of BVI.Br.*

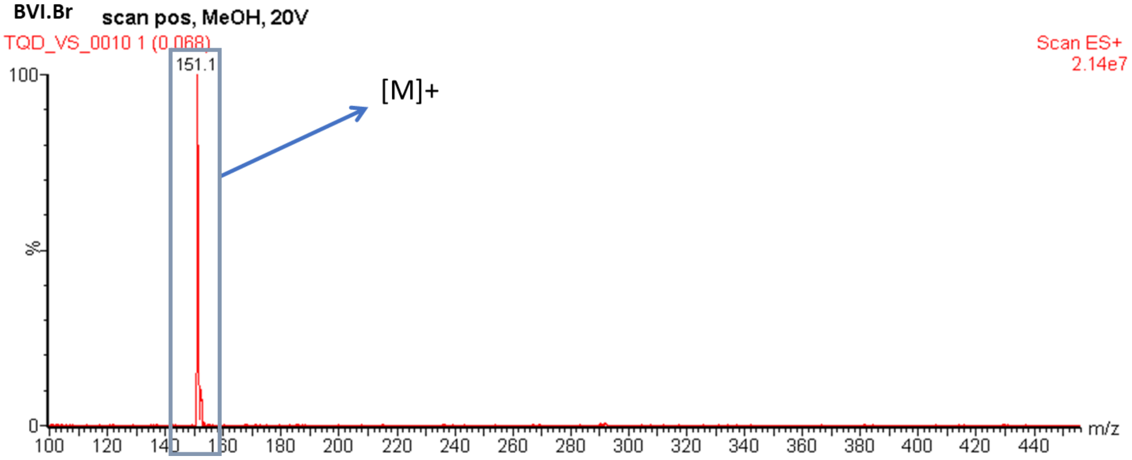

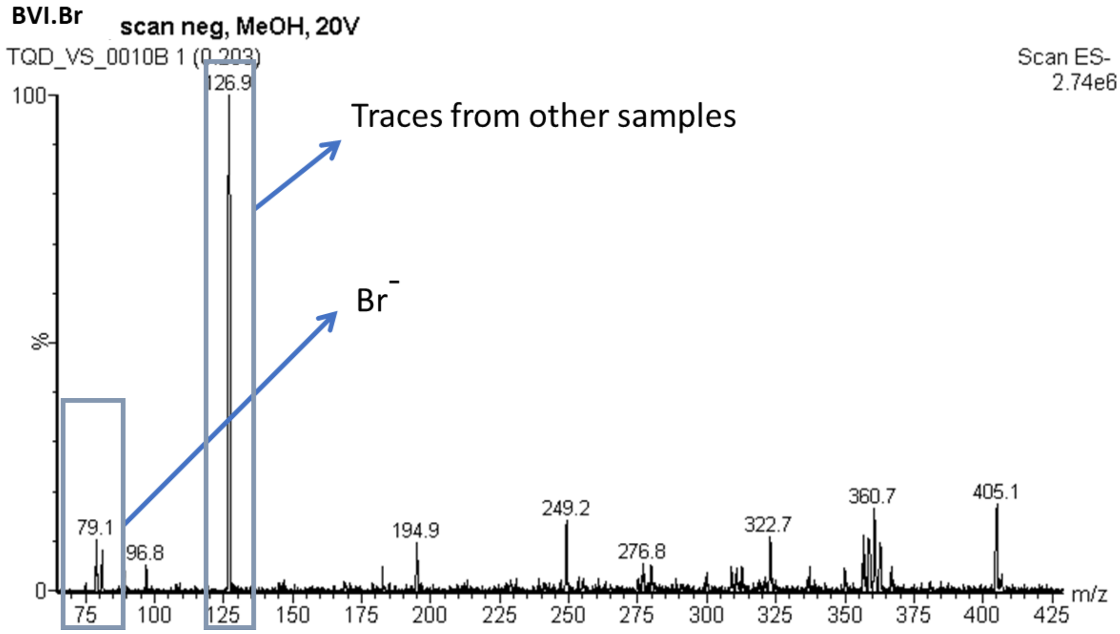

Figure A2. *ESI-MS spectra of BVI.Br in positive and negative mode.*

1-butyl-3-vinylimidazolium bis(trifluoromethane)sulfonimide (mIL1)

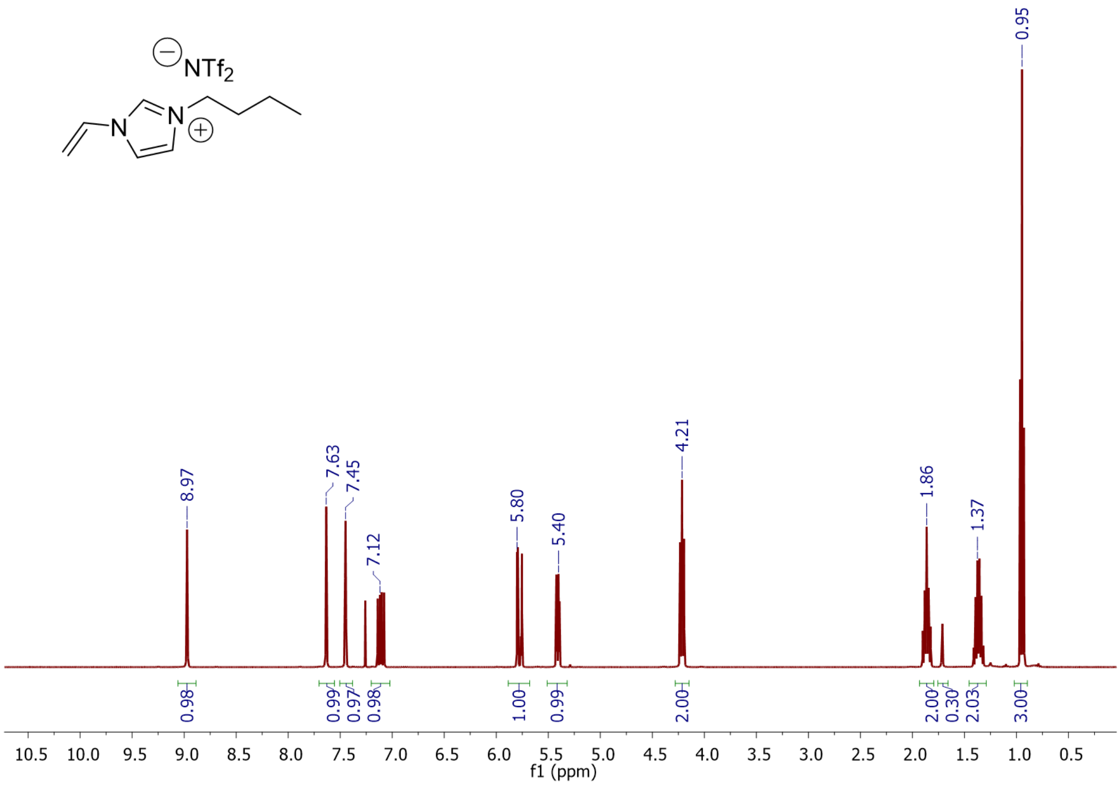

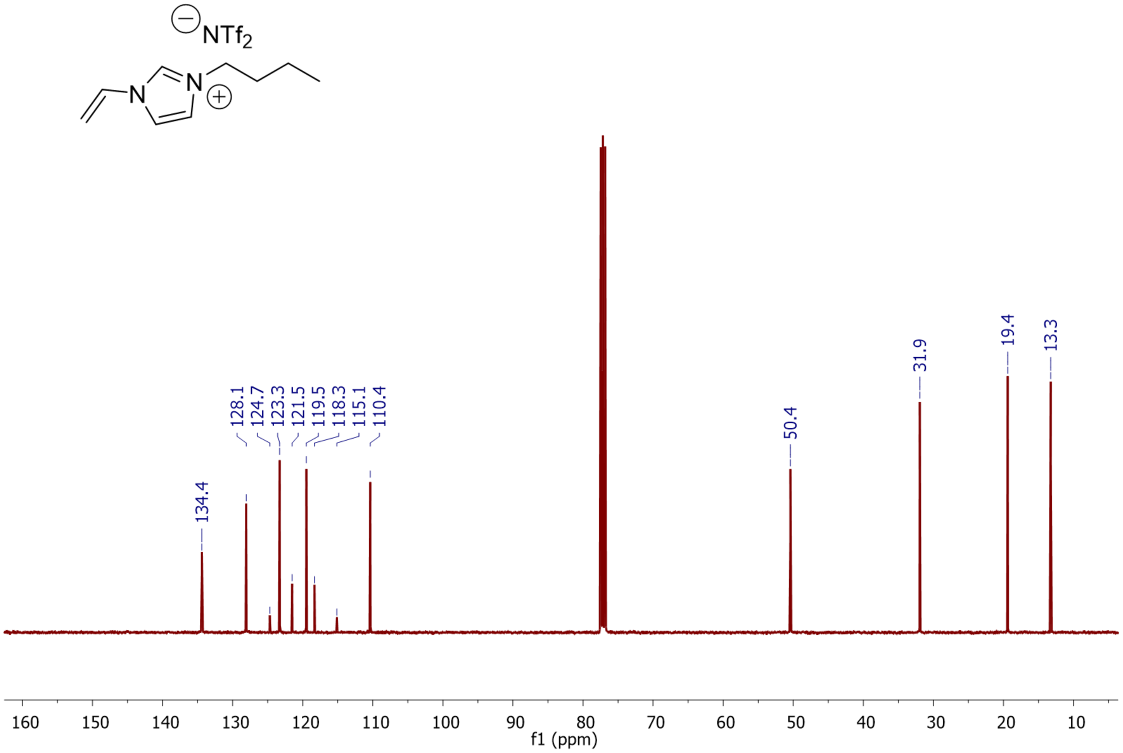

Figure A3. *^{1}H NMR and ^{13}C NMR spectra of mIL1.*

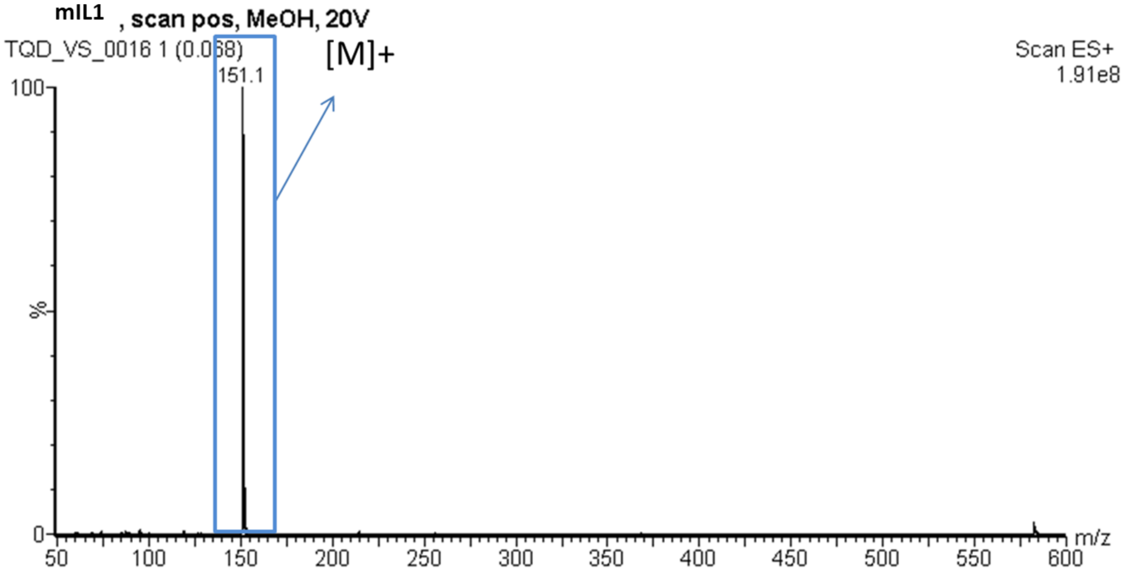

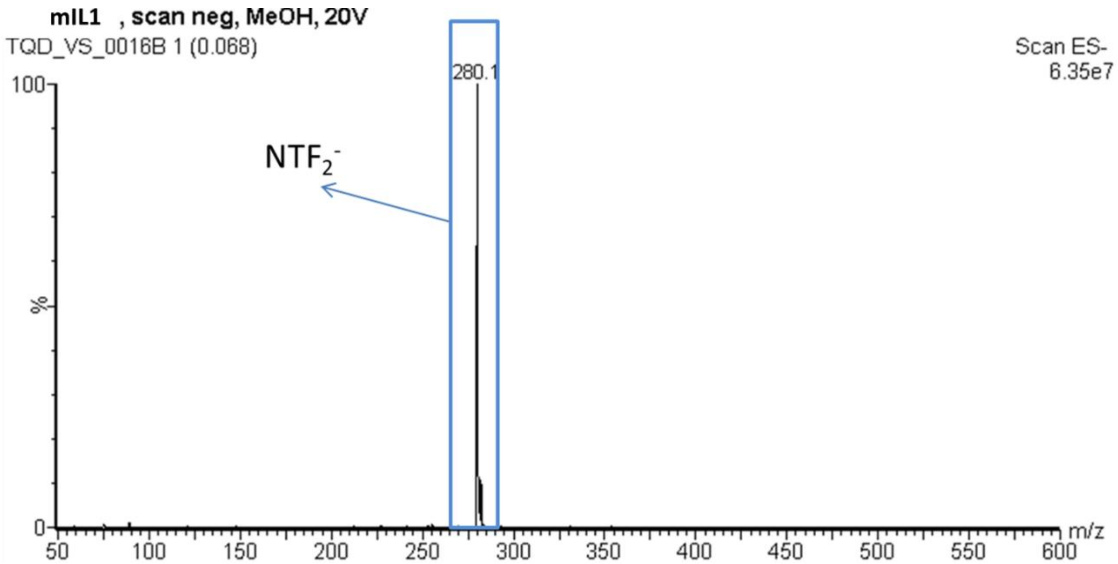

Figure A4. *ESI-MS spectra of mIL1 in positive and negative mode.*

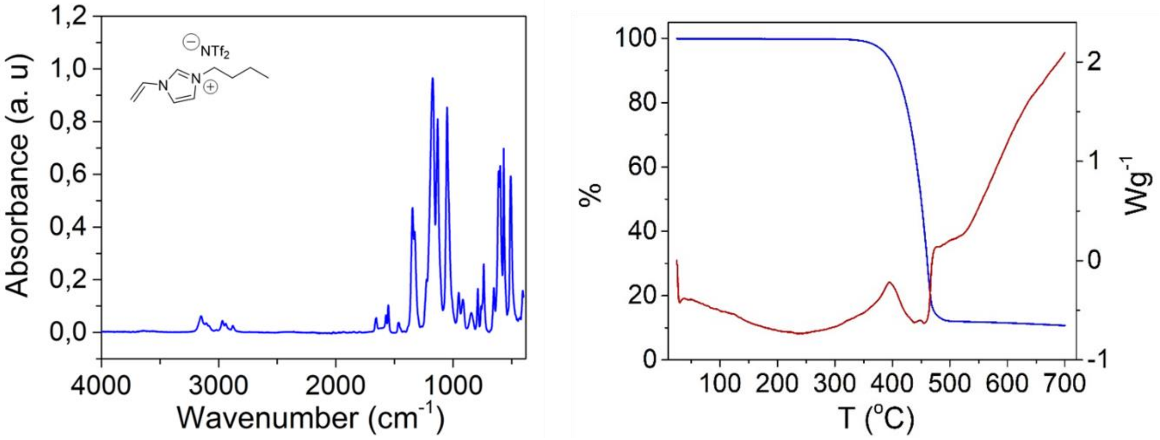

Figure A5. *(Left) FT-IR spectrum of mIL1; (right) TGA-DSC spectra of mIL1.*

1-(3-hydroxypropyl)-3-vinylimidazolium bromide (HVI.Br)

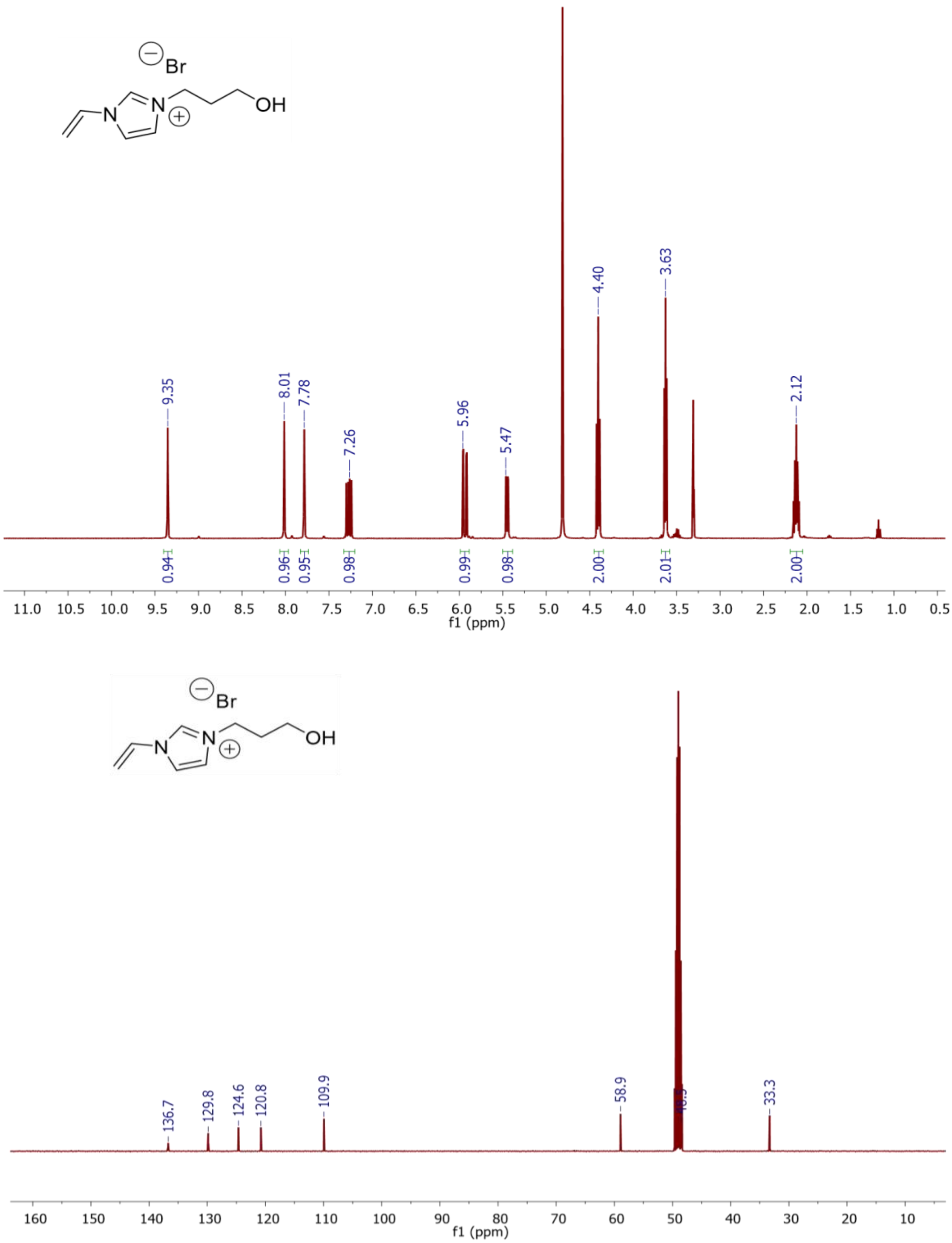

Figure A6. *^{1}H NMR and ^{13}C NMR spectra of HVI.Br.*

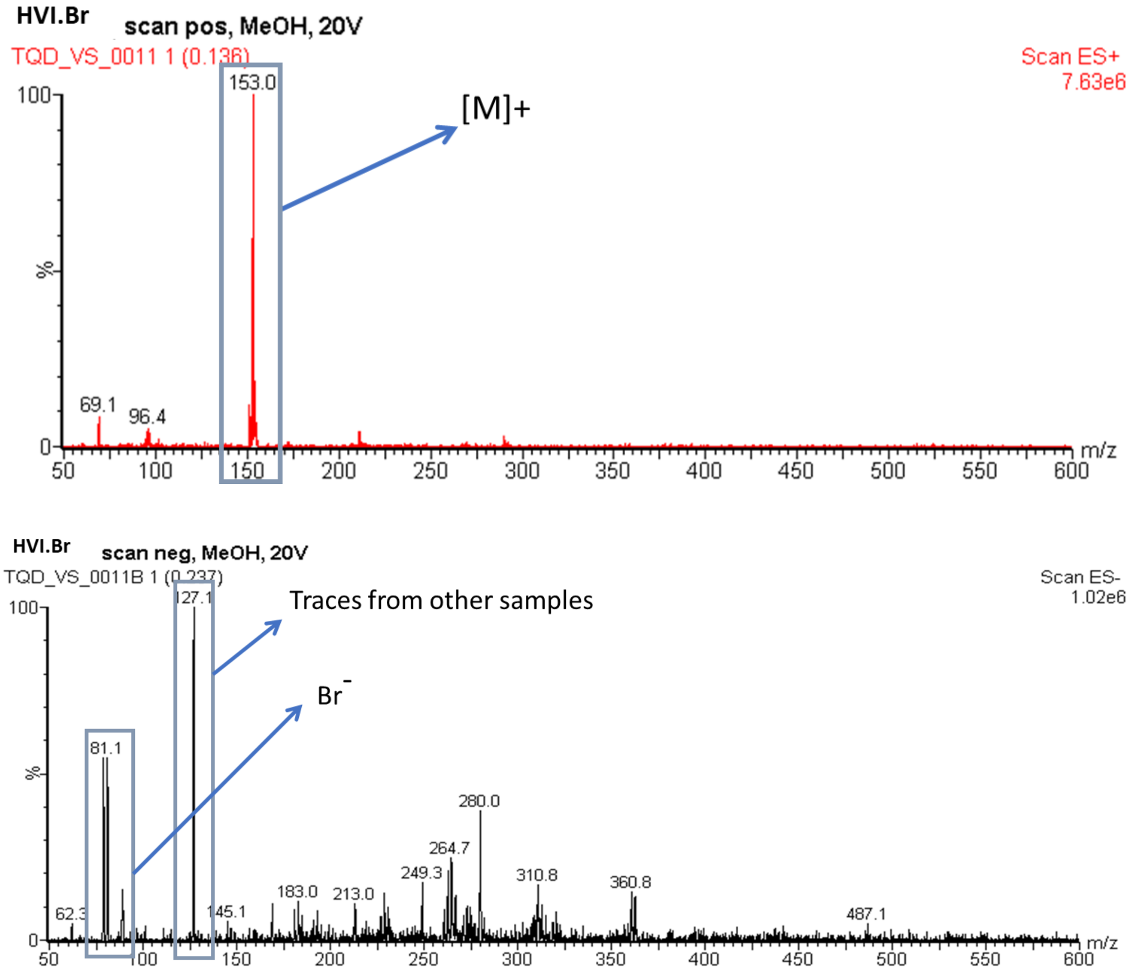

Figure A7. *ESI-MS spectra of HVI.Br in positive and negative mode.*

1-(3-hydroxypropyl)-3-vinylimidazolium bis(trifluoromethane)sulfonimide (mIL2)

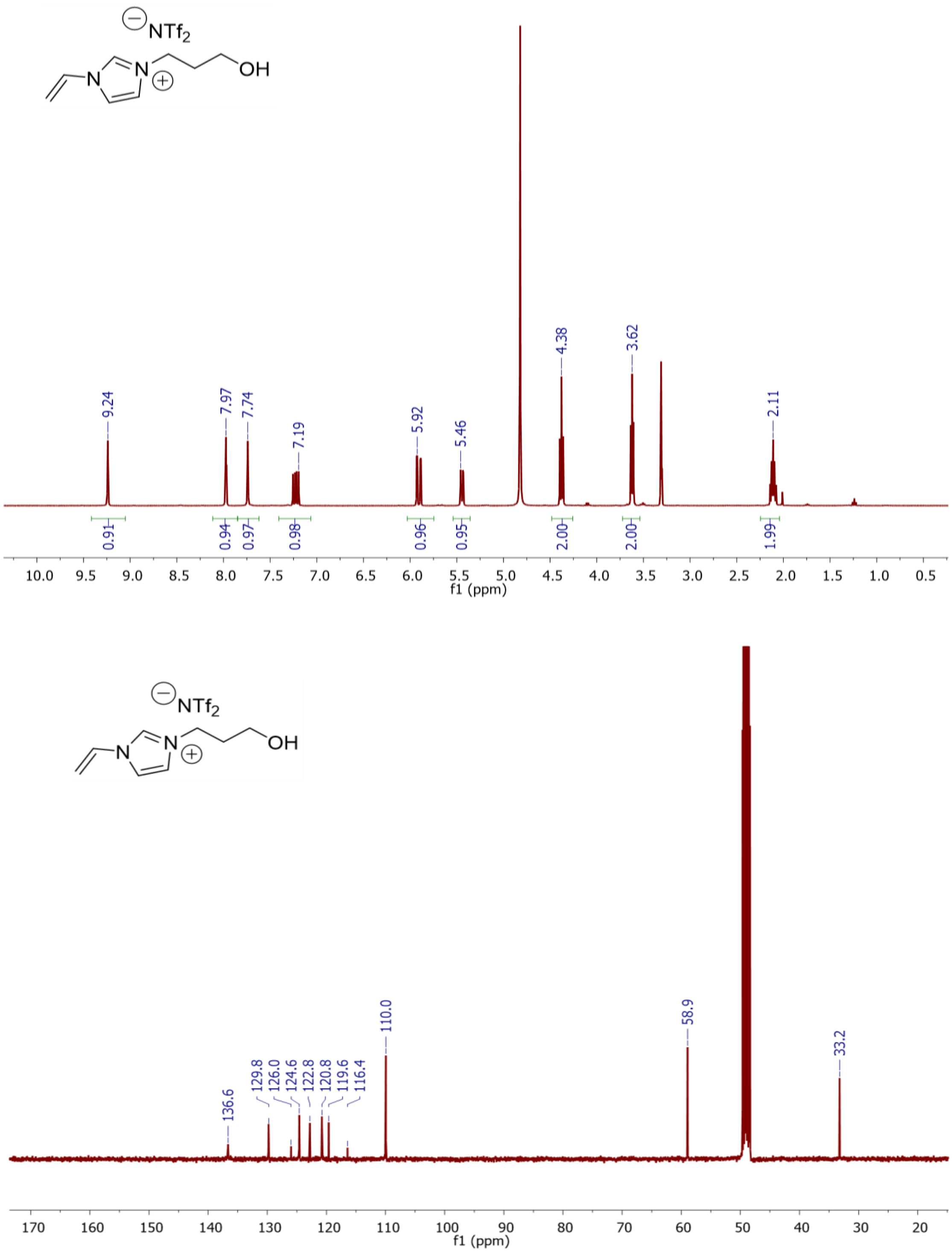

Figure A8. *^{1}H NMR and ^{13}C NMR spectra of mIL2.*

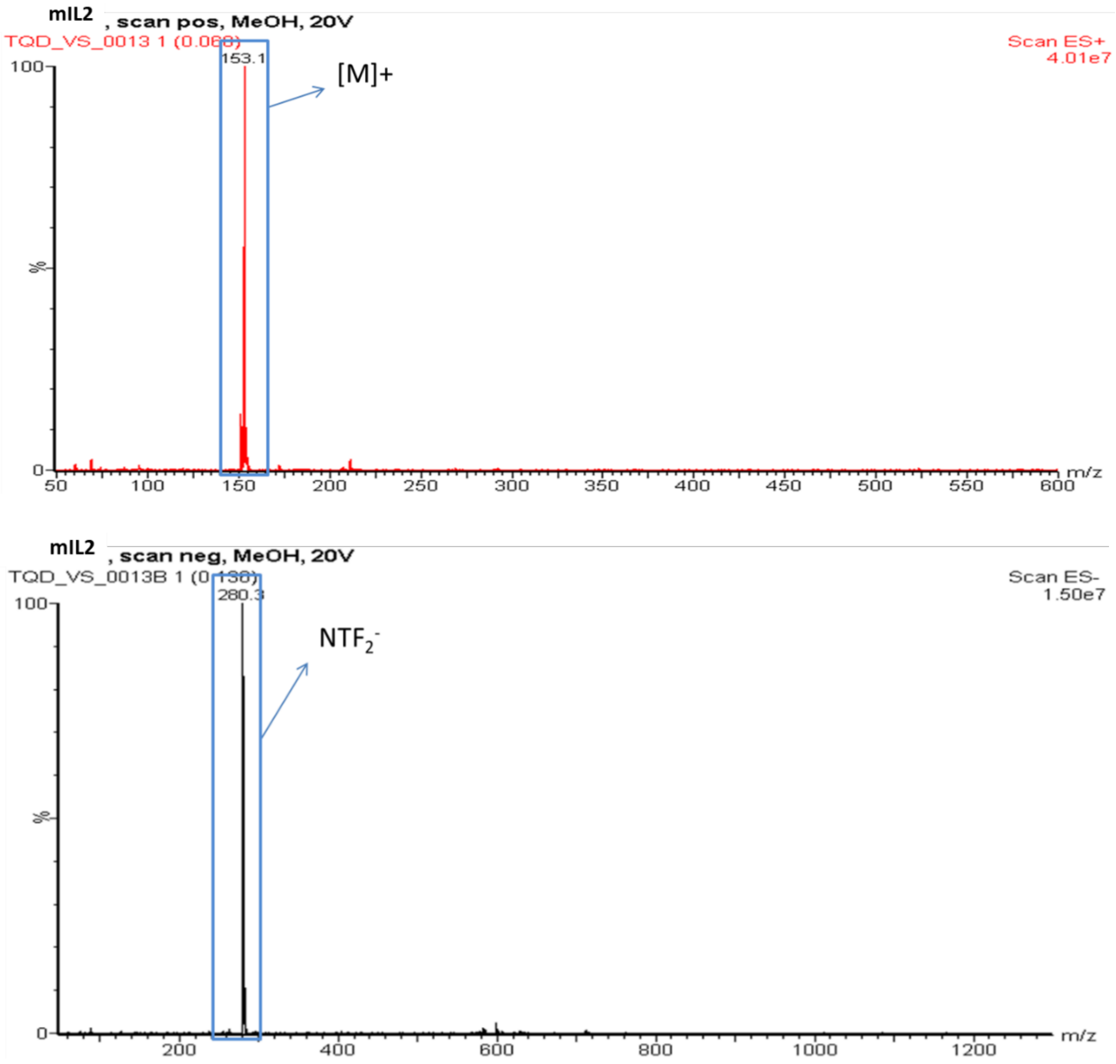

Figure A9. *ESI-MS spectra of mIL2 in positive and negative mode.*

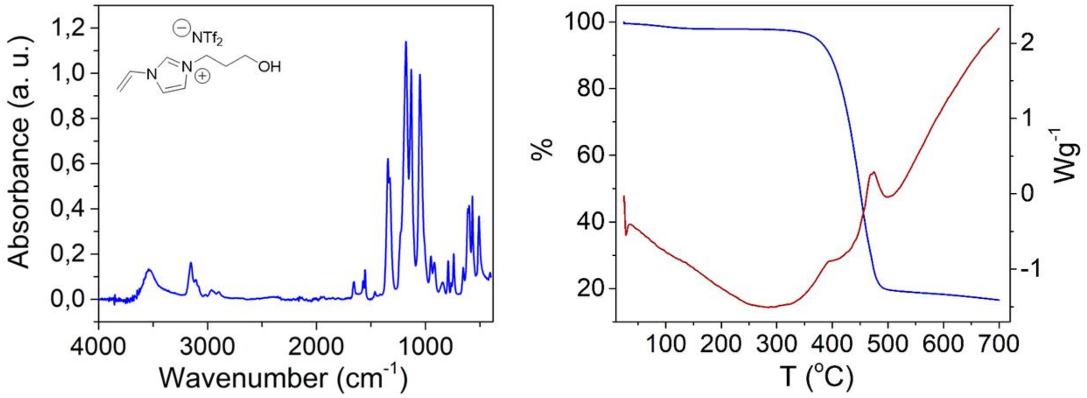

Figure A10. *(Left) FT-IR spectrum of mIL2; (right) TGA-DSC spectra of mIL2.*

[2-(acryloyloxy)ethyl]trimethyl-ammonium bis(trifluoromethane)sulfonimide (mIL3)

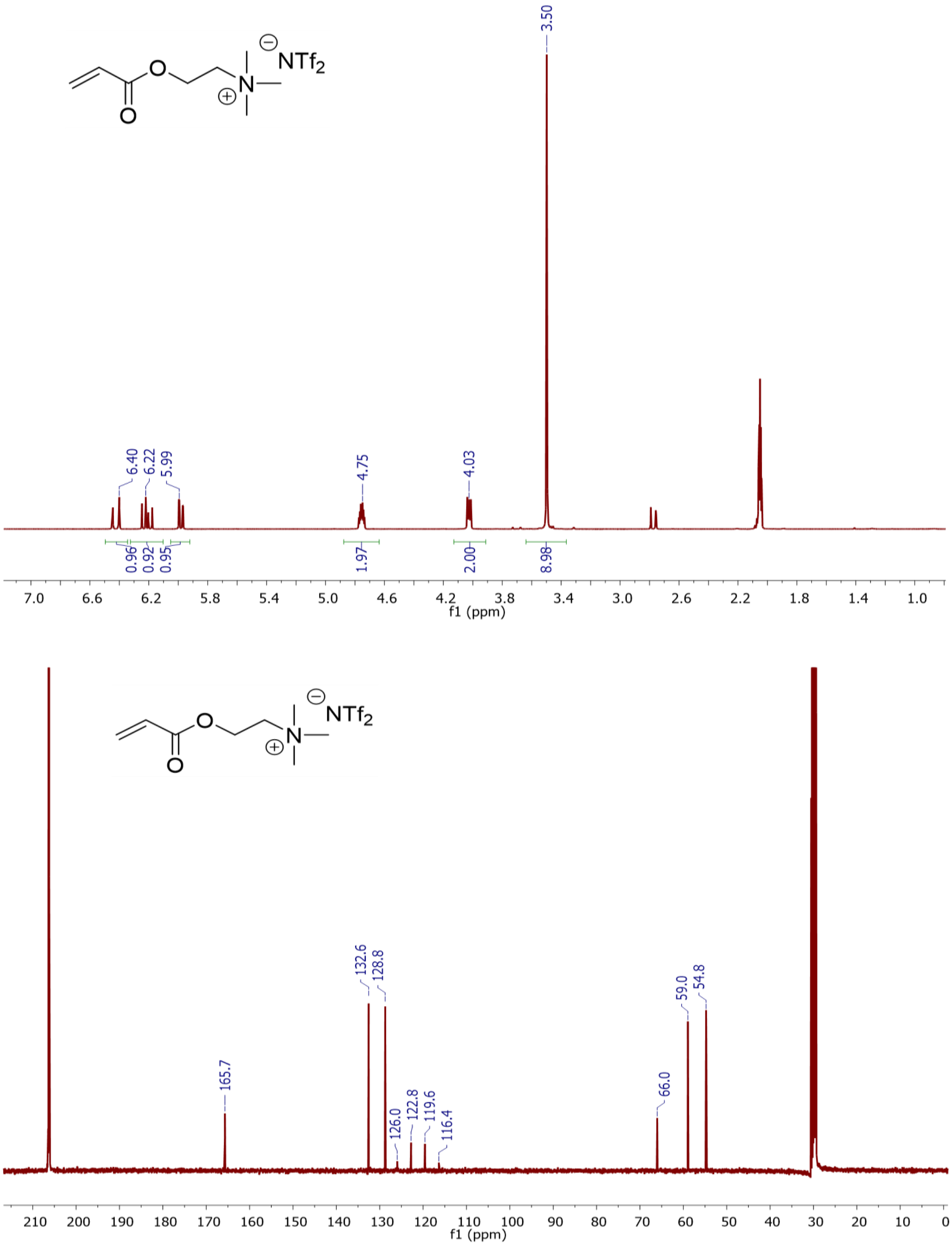

Figure A11. *^{1}H NMR and ^{13}C NMR spectra of mIL3.*

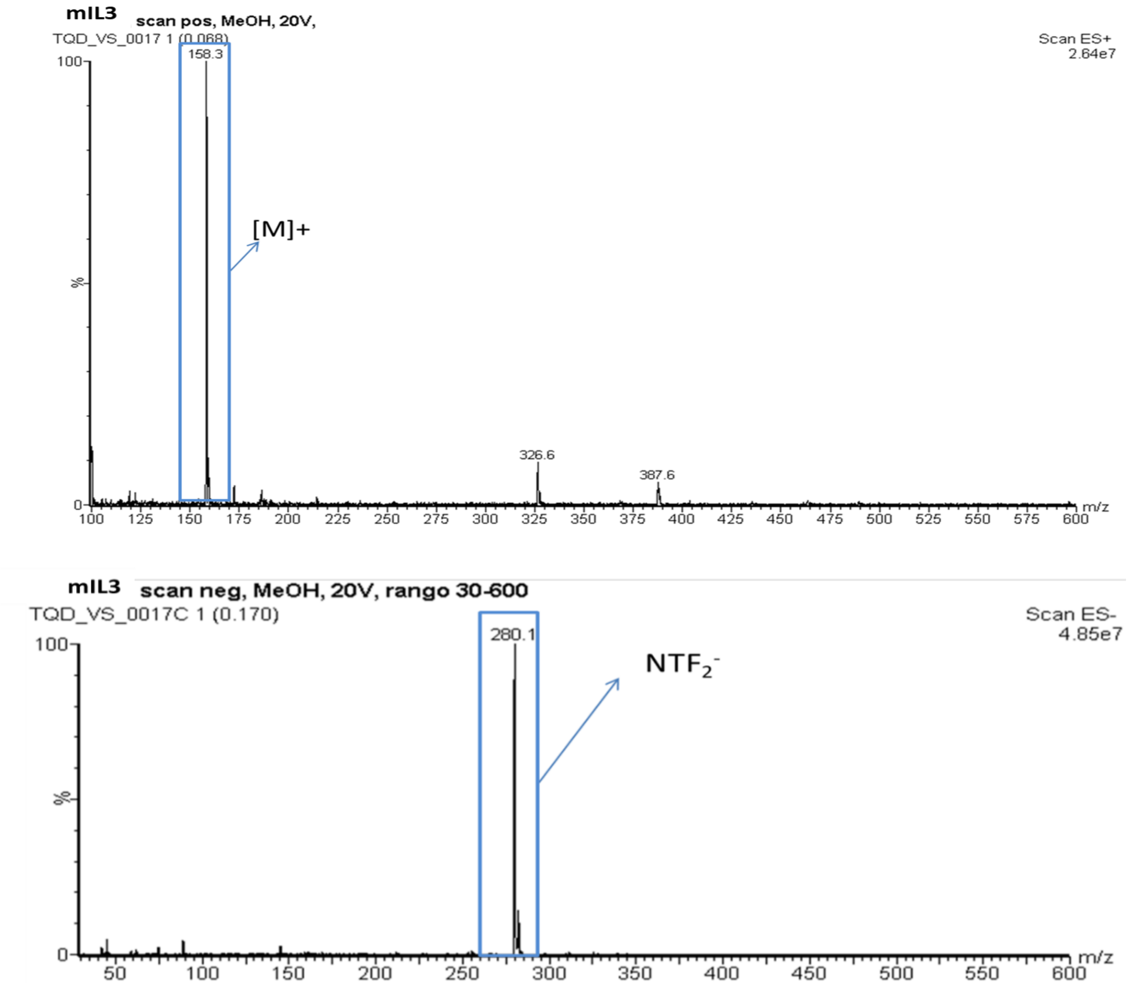

Figure A12. *ESI-MS spectra of mIL3 in positive and negative mode.*

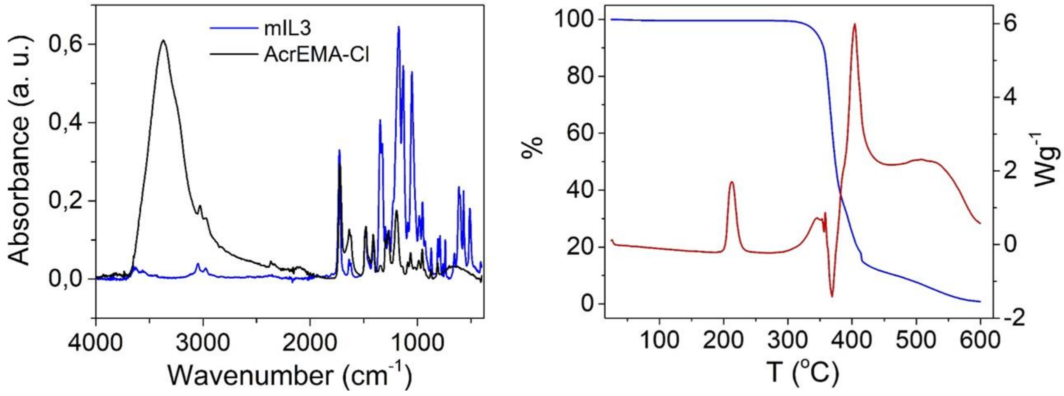

Figure A13. *(Left) FT-IR spectrum of mIL3 (blue) and the precursor AcrEMA.Cl (black); (right) TGA-DSC spectra of mIL3.*

6.2 Characterisation of the Compounds Synthesised in Chapter 3

Spectra mentioned in **Section 3.6.5**.

1-butyl-3-vinylimidazolium dicyanamide (BVI.N(CN)₂)

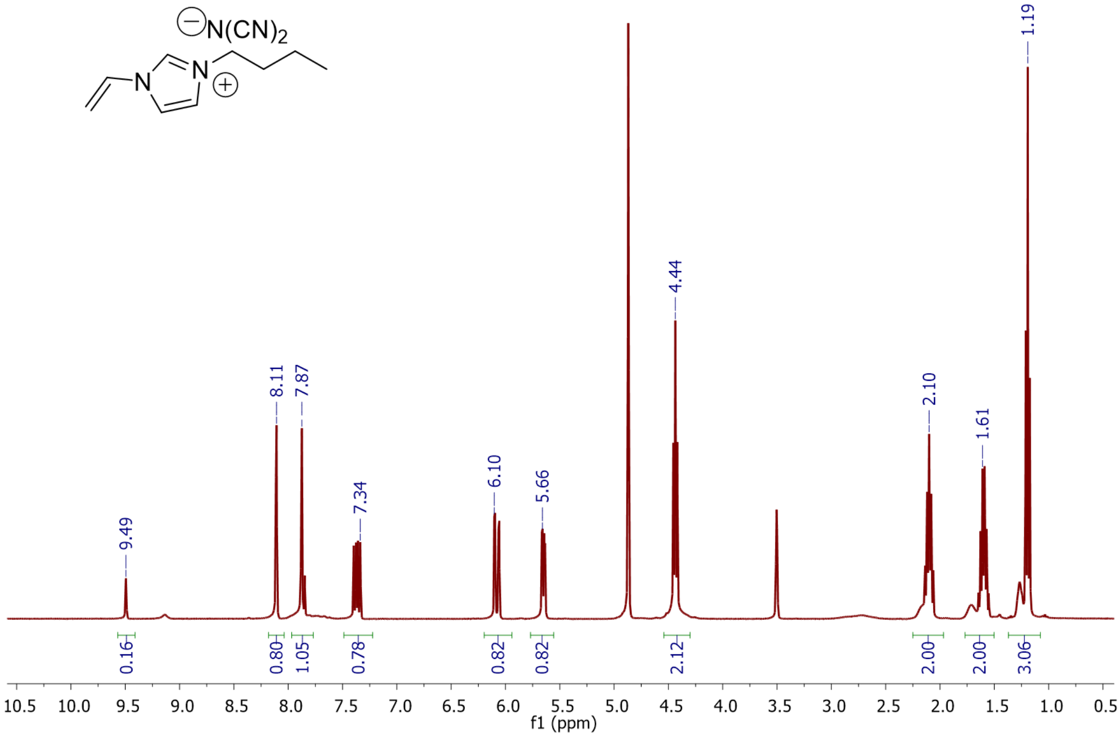

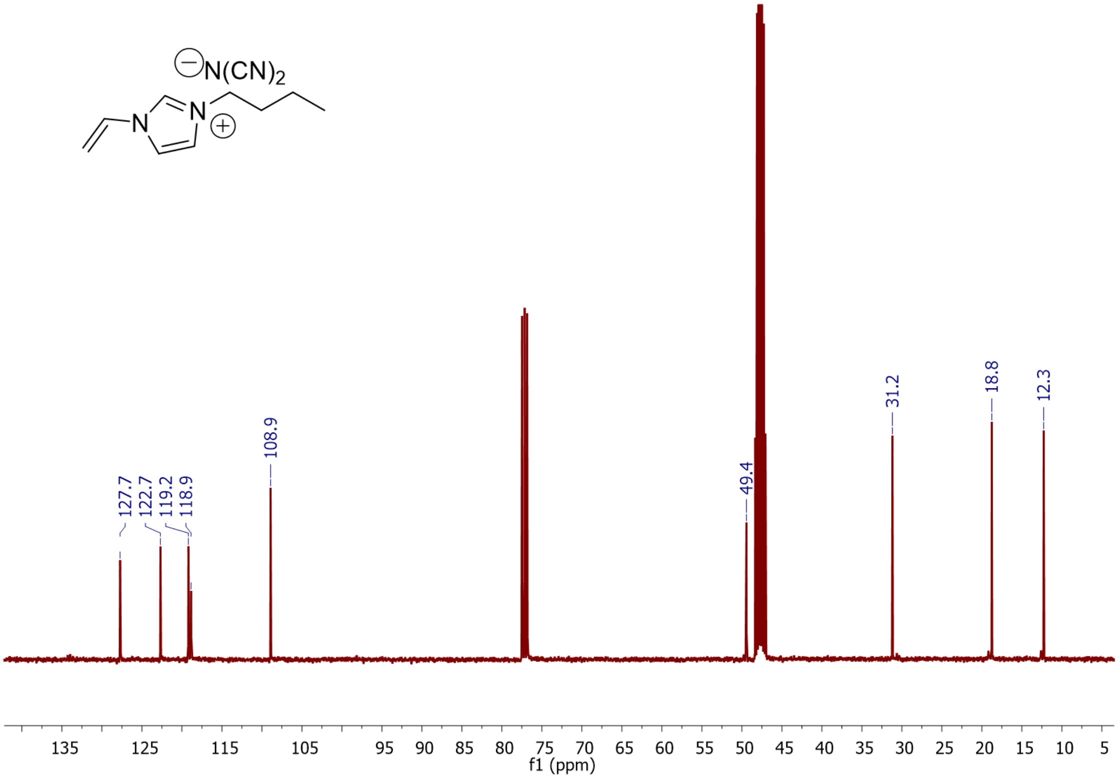

Figure A14. ${}^{1}H$ *NMR and* ${}^{13}C$ *NMR spectra of BVI.N(CN)*$_2$*.*

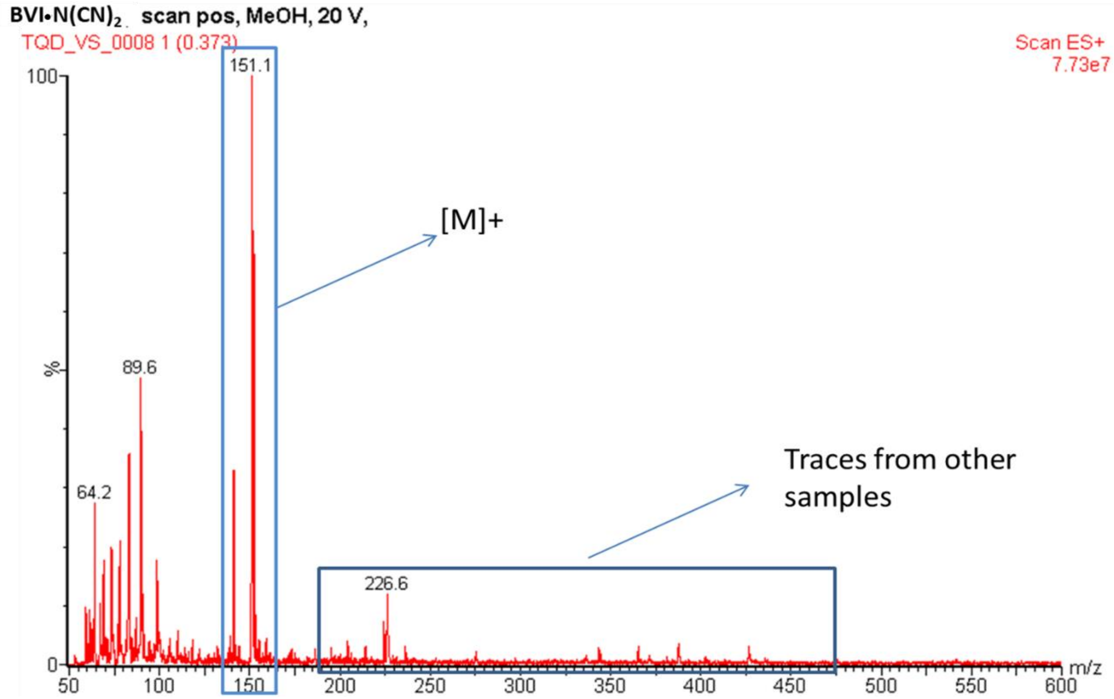

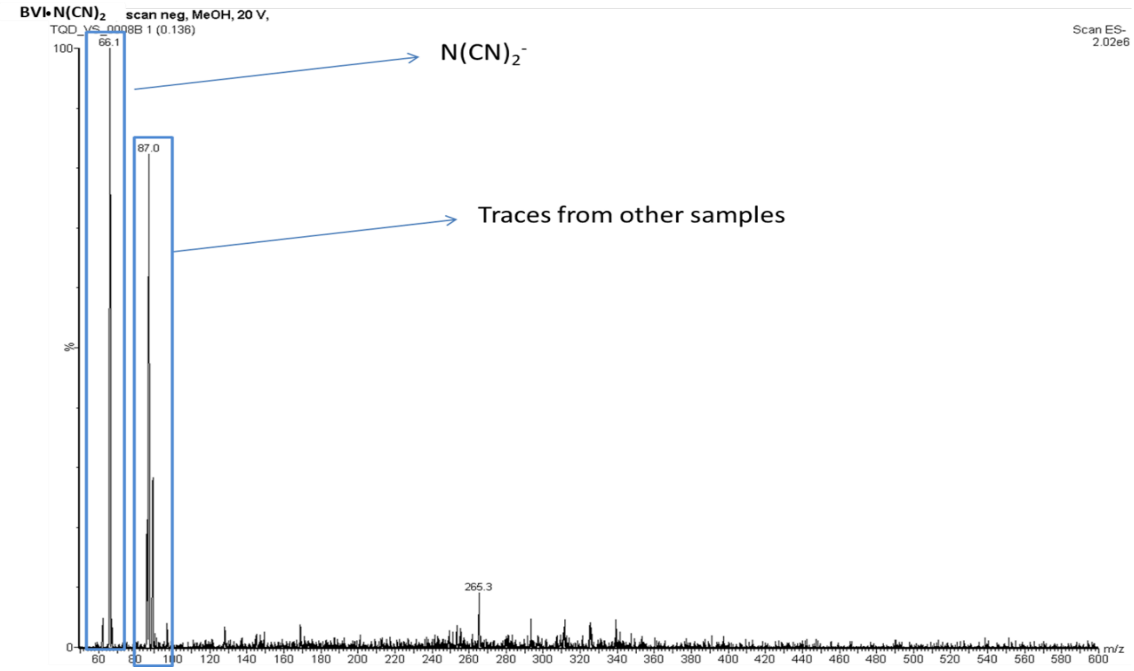

Figure A15. *ESI-MS spectra of BVI.N(CN)$_2$ in positive and negative mode.*

1-butyl-3-vinylimidazoliumiodide (BVI.I)

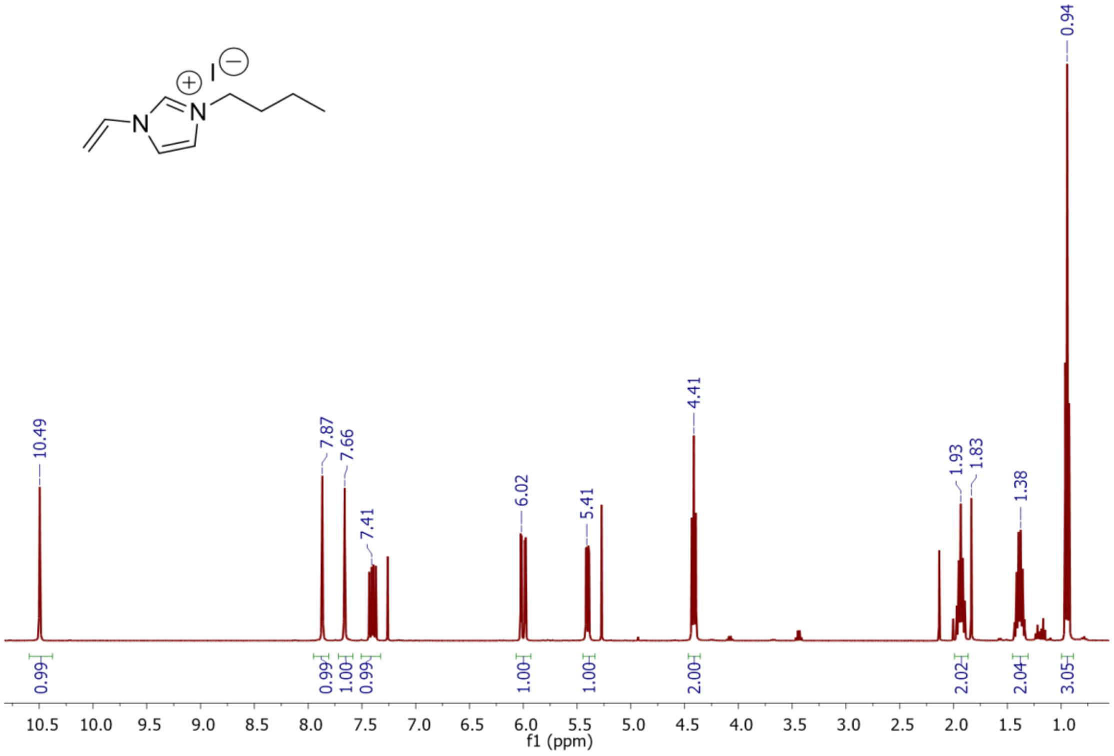

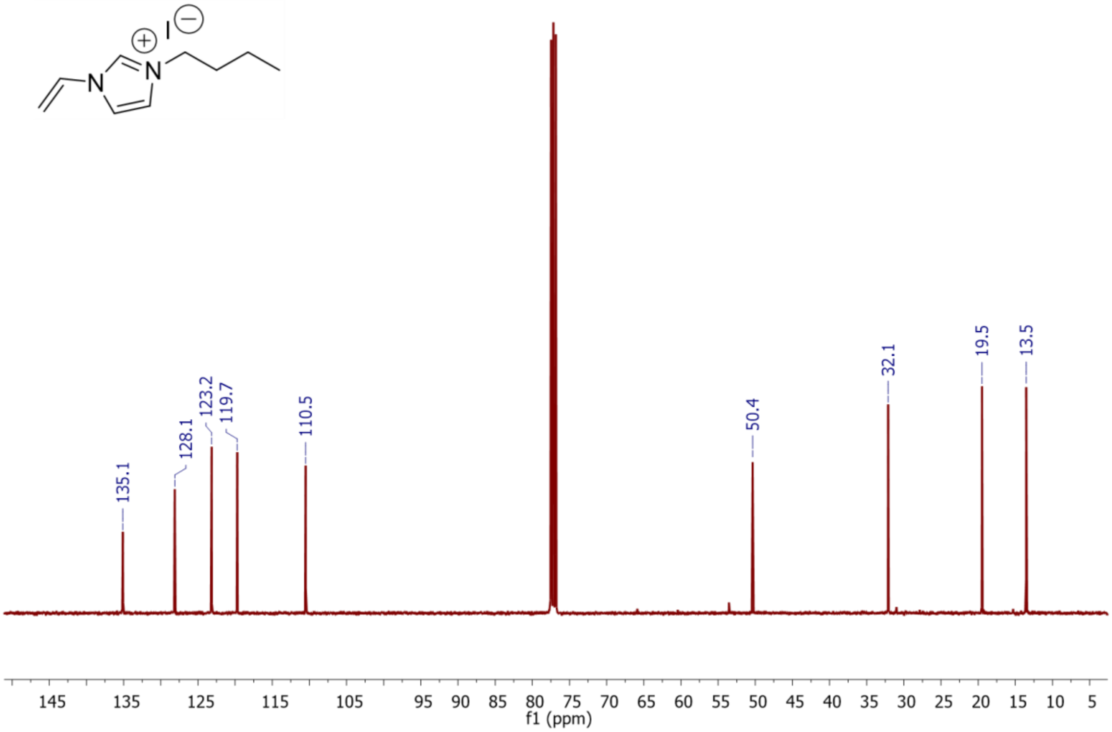

Figure A16. ** *^{1}H NMR and ^{13}C NMR spectra of BVI.I.*

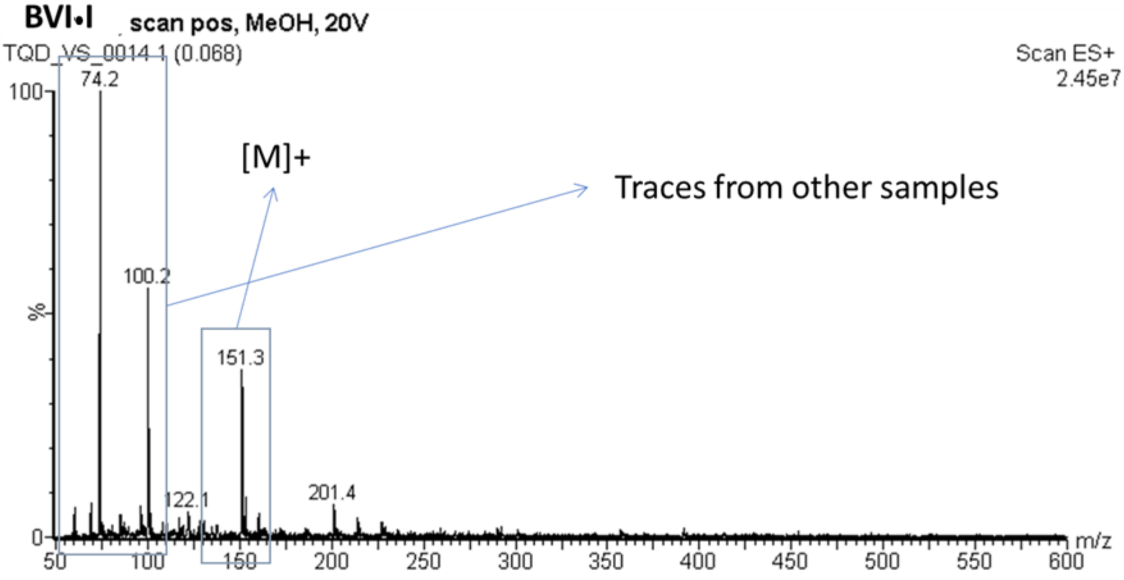

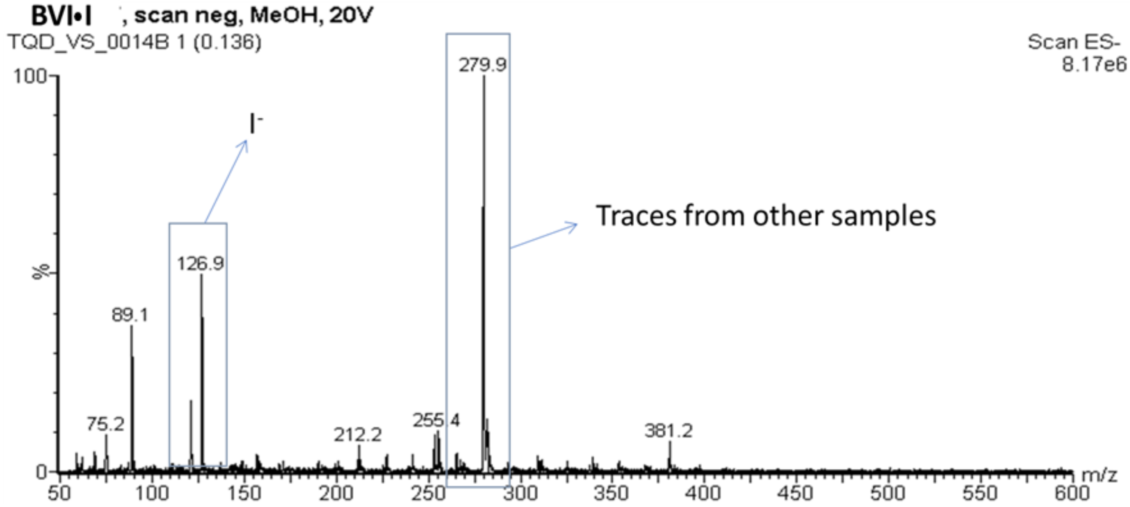

Figure A17. *ESI-MS spectra of BVI.I in positive and negative mode.*

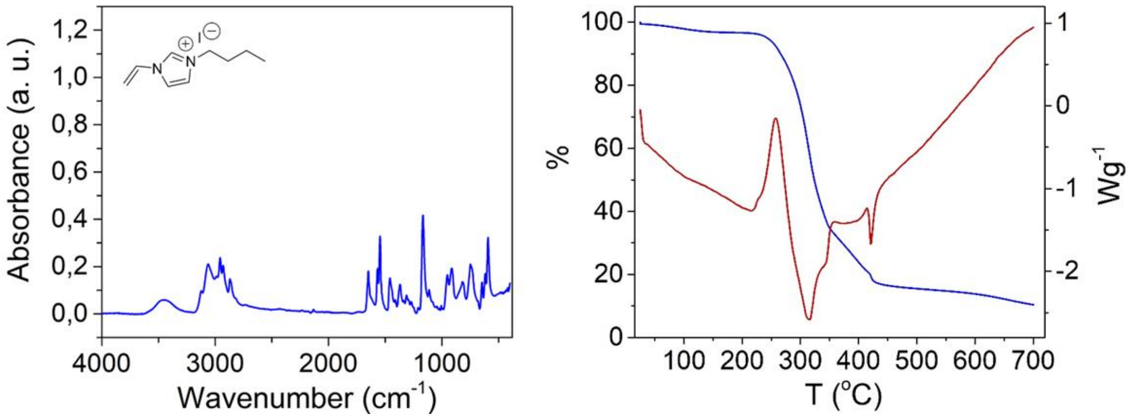

Figure A18. *(Left) FT-IR spectrum of BVI.I; (right) TGA-DSC spectra of BVI.I.*

[2-(acryloyloxy)ethyl]trimethyl-ammonium dicyanamide (AcrEMA.N(CN)$_2$)

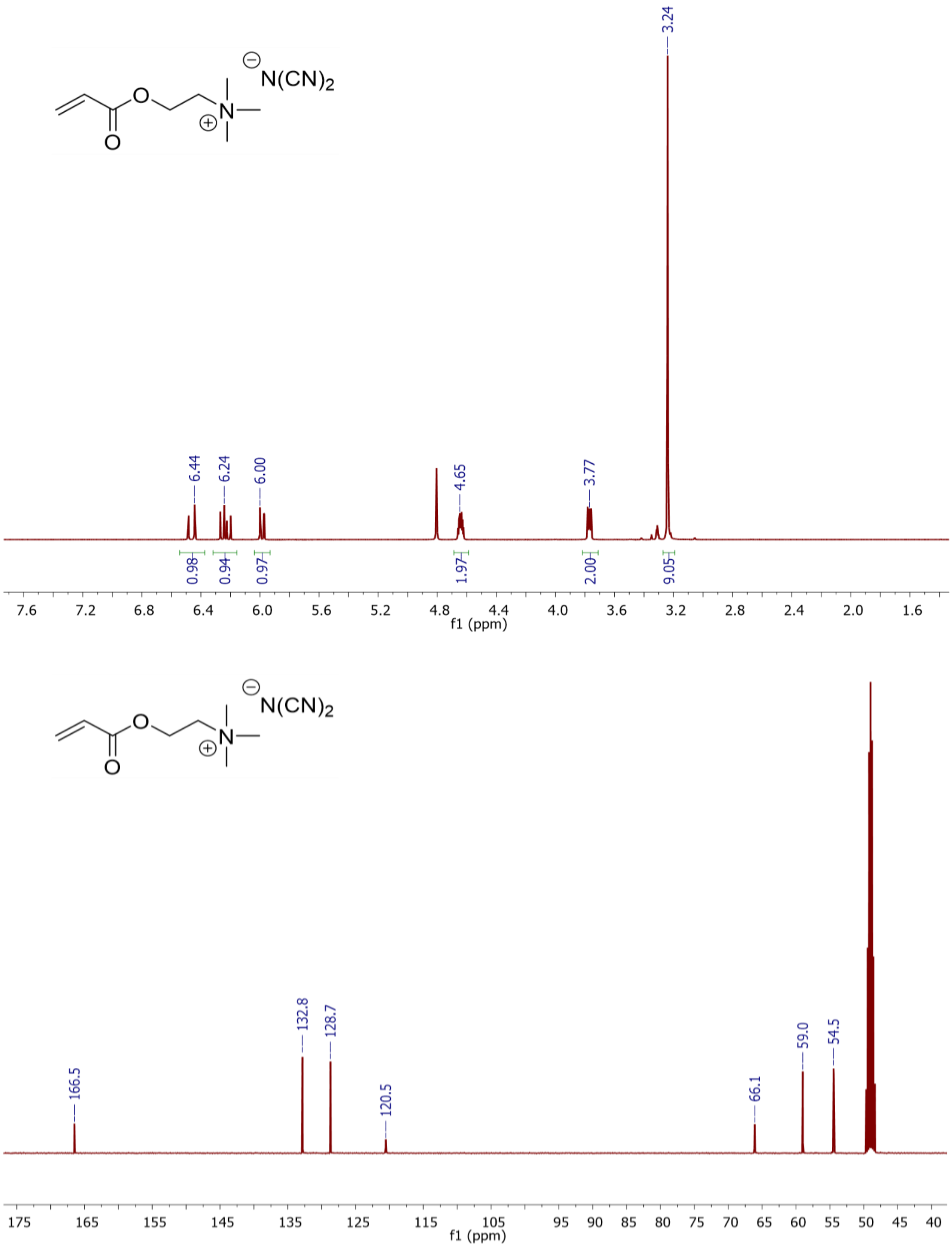

Figure A19. *^{1}H NMR and ^{13}C NMR spectra of AcrEMA.N(CN)$_2$.*

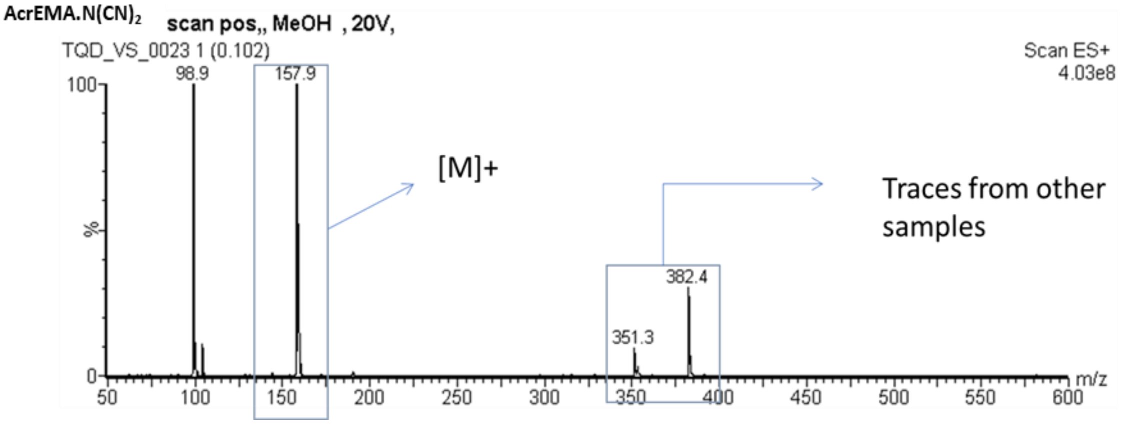

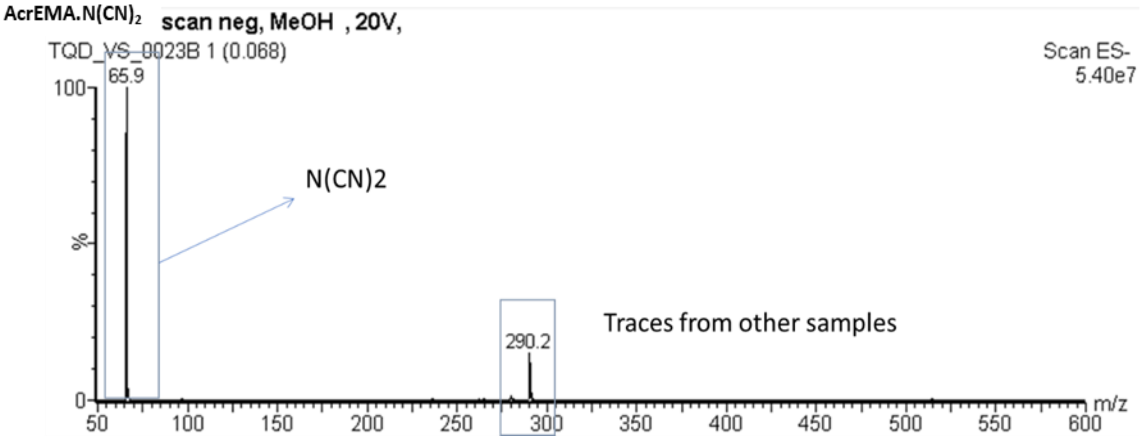

Figure A20. *ESI-MS spectra of AcrEMA.N(CN)$_2$ in positive and negative mode.*

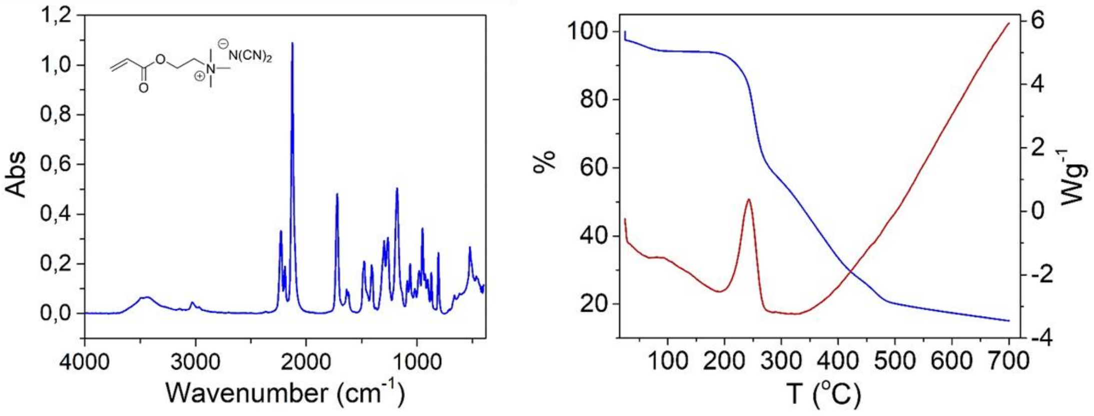

Figure A21. *(Left) FT-IR spectrum of AcrEMA.N(CN)$_2$; (right) TGA-DSC spectra of AcrEMA.N(CN)$_2$.*

[2-(acryloyloxy)ethyl]trimethyl-ammonium iodide (AcrEMA.I)

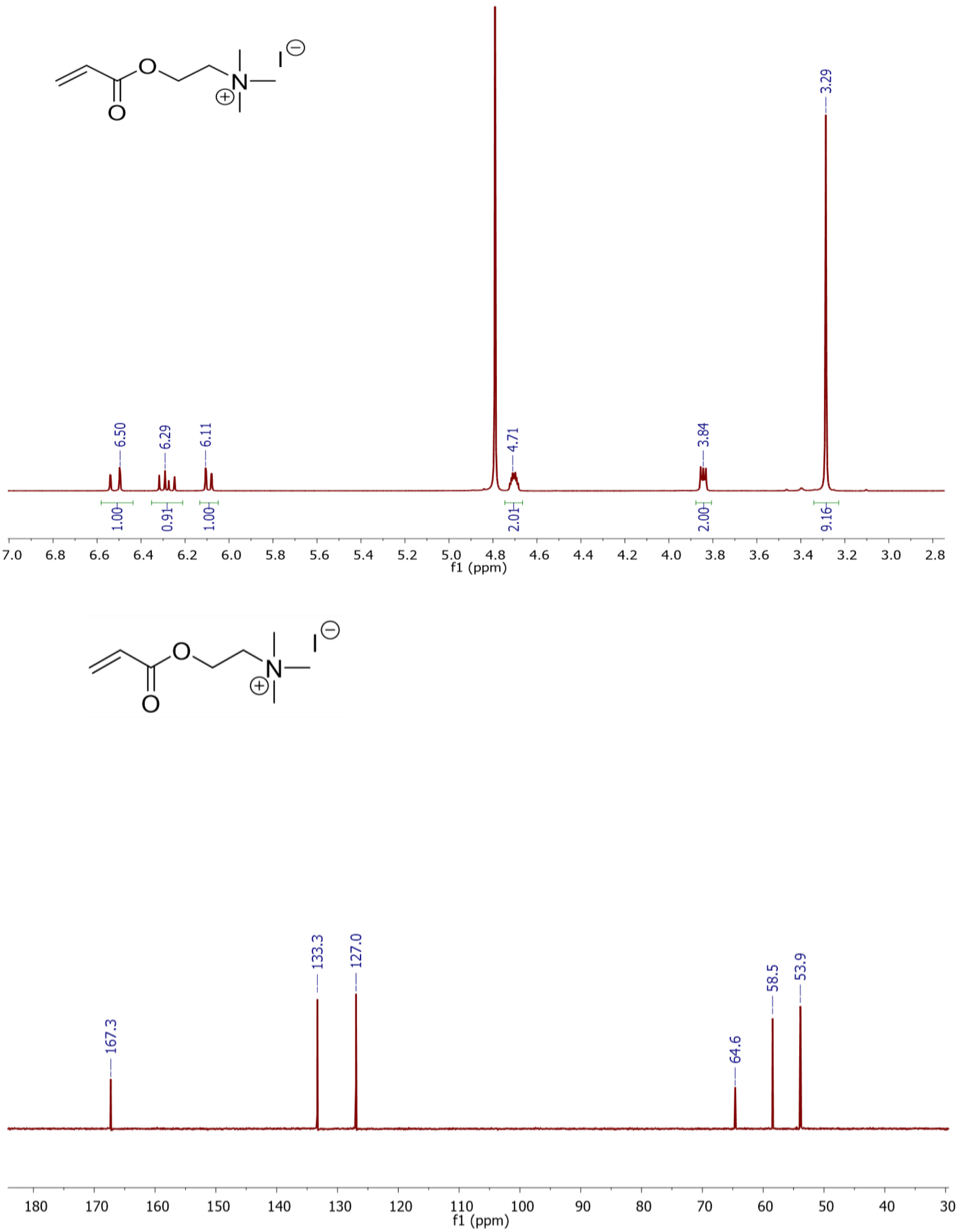

Figure A22. *^{1}H NMR and ^{13}C NMR spectra of AcrEMA.I.*

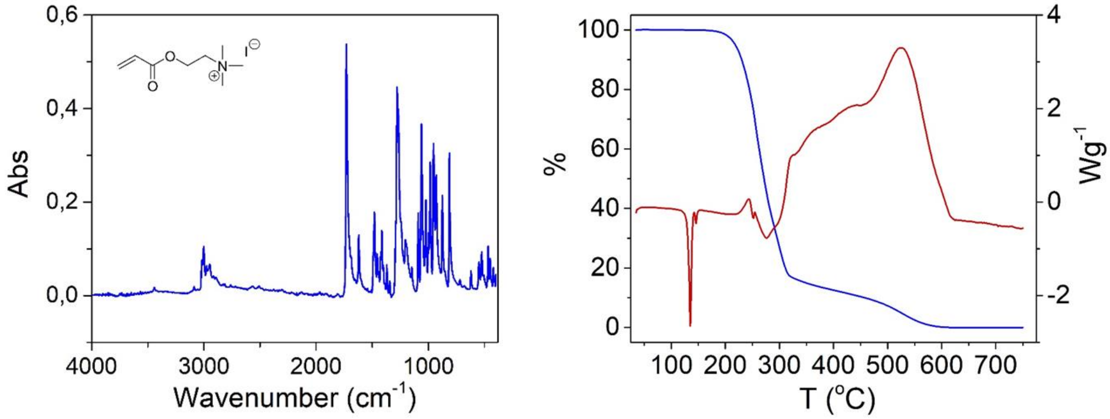

Figure A23. *(Left) FT-IR spectrum of AcrEMA.I; (right) TGA-DSC spectra of AcrEMA.I.*

[2-(acryloyloxy)ethyl]trimethyl-ammonium tetrafluoroborate (AcrEMA.BF$_4$)

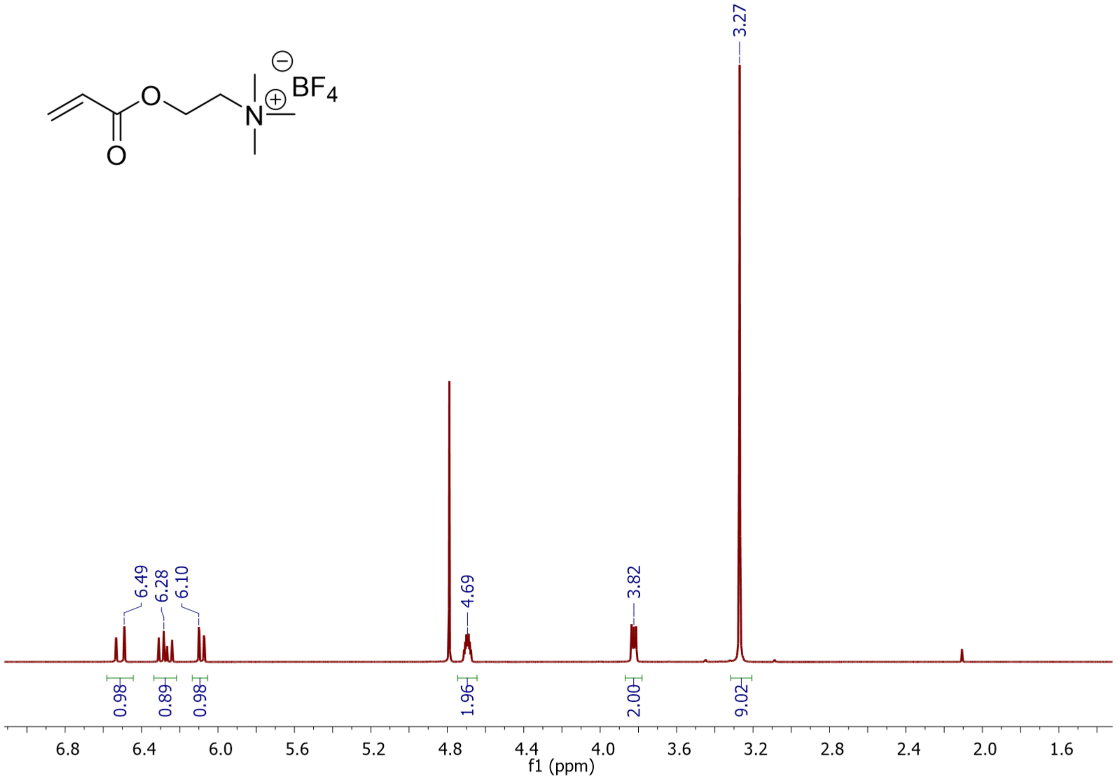

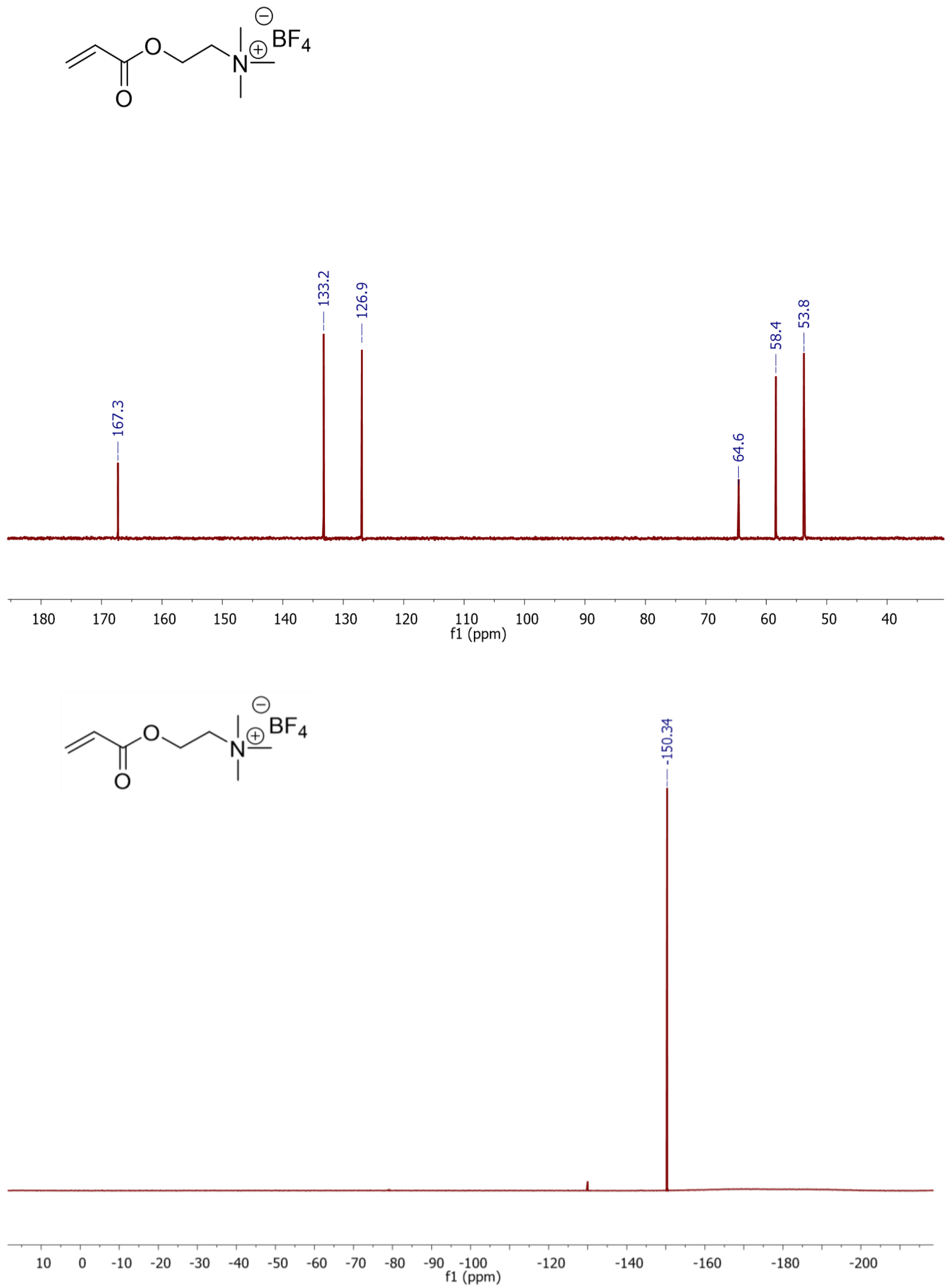

Figure A24. ^{1}H NMR, ^{13}C NMR and ^{19}F NMR spectra of AcrEMA.BF_4.

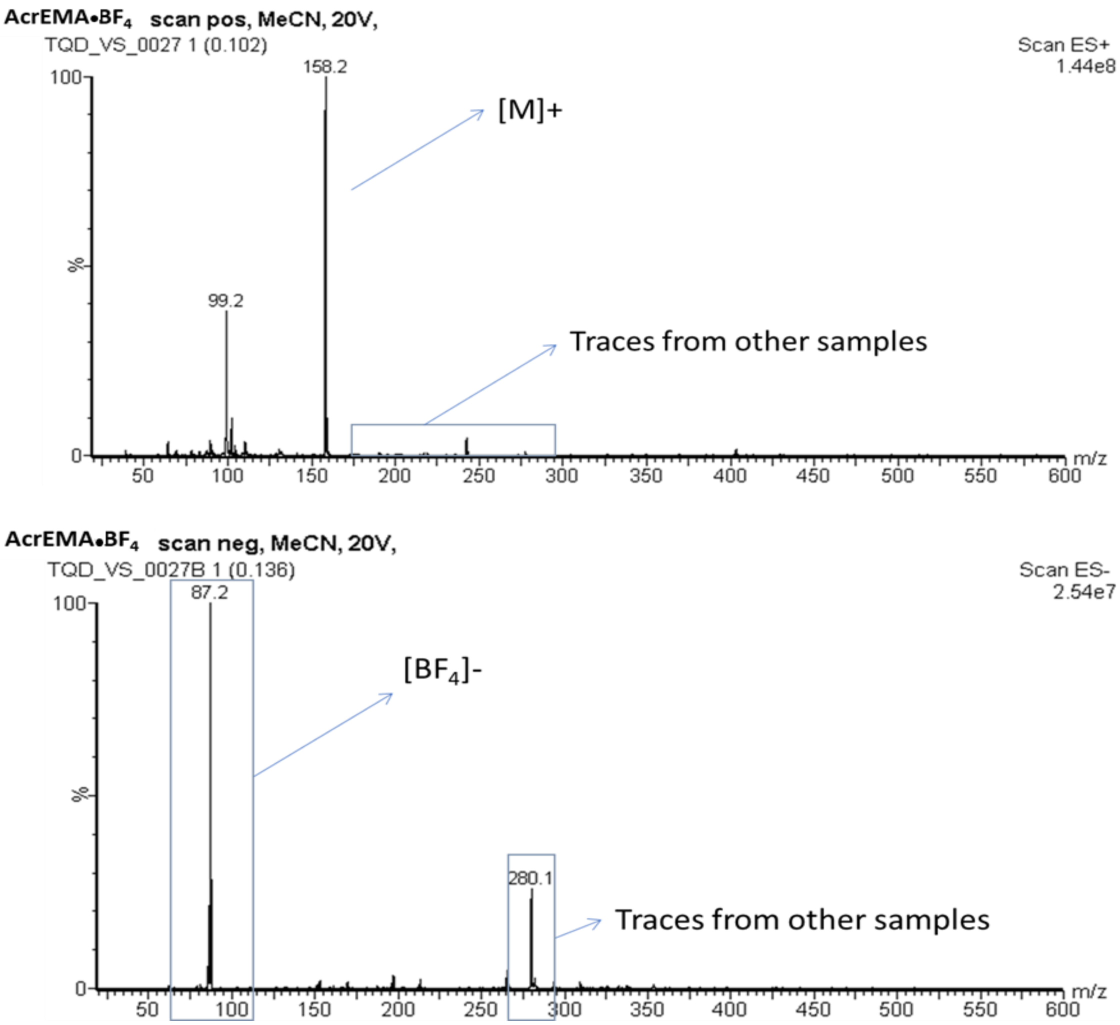

Figure A25. *ESI-MS spectra of AcrEMA.BF$_4$ in positive and negative mode.*

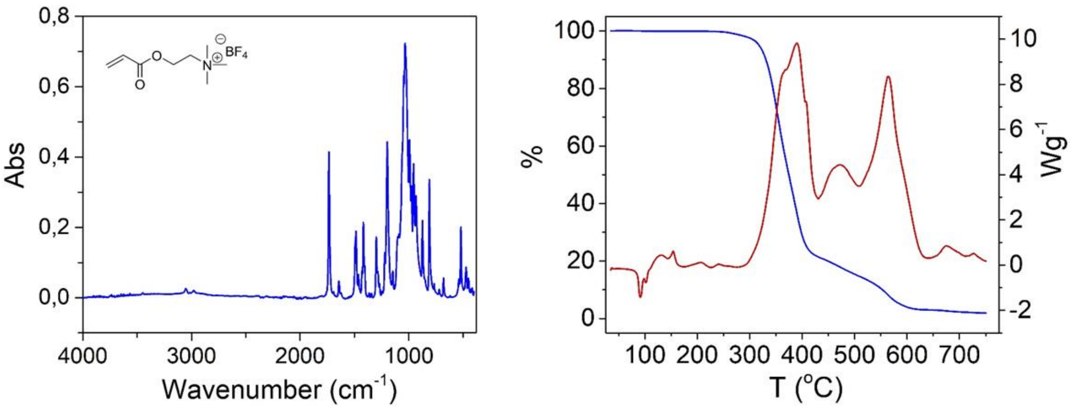

Figure A26. *(Left) FT-IR spectrum of AcrEMA.BF$_4$; (right) TGA-DSC spectra of AcrEMA.BF$_4$.*

6.3 Characterisation of the Compounds Synthesised in Chapter 4

Spectra mentioned in **Section 4.6.3**.

1-butyl-3-methylimidazolium bromide (BMI.Br)

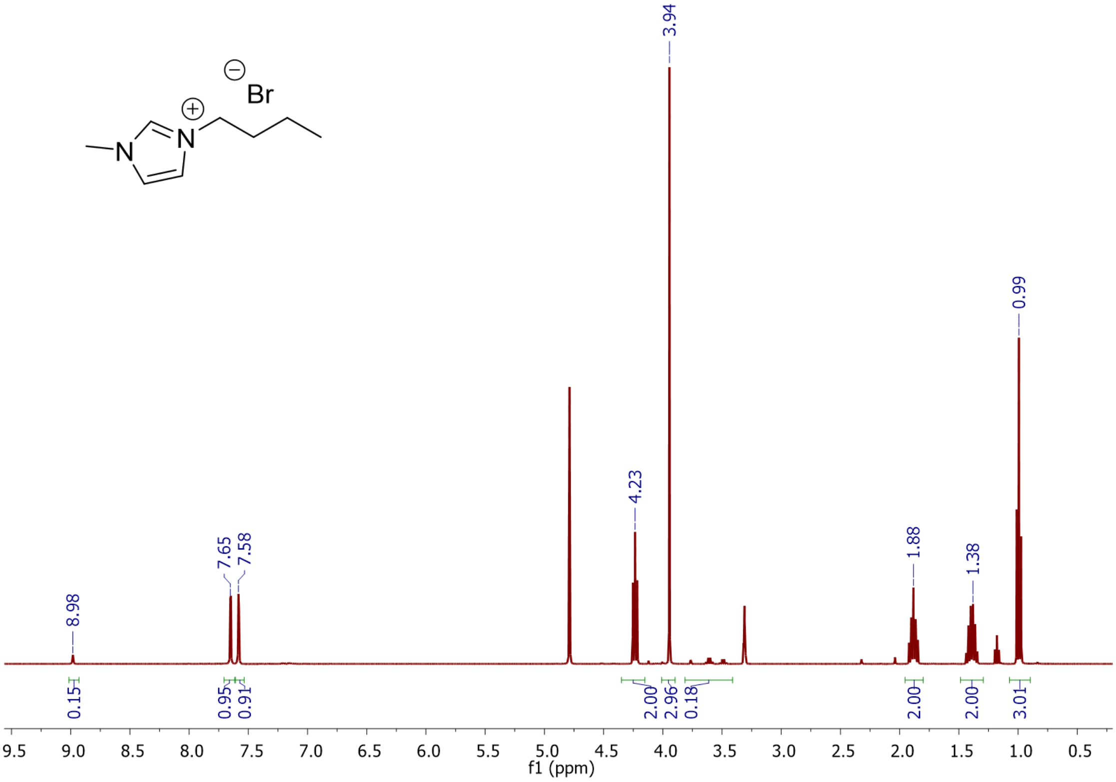

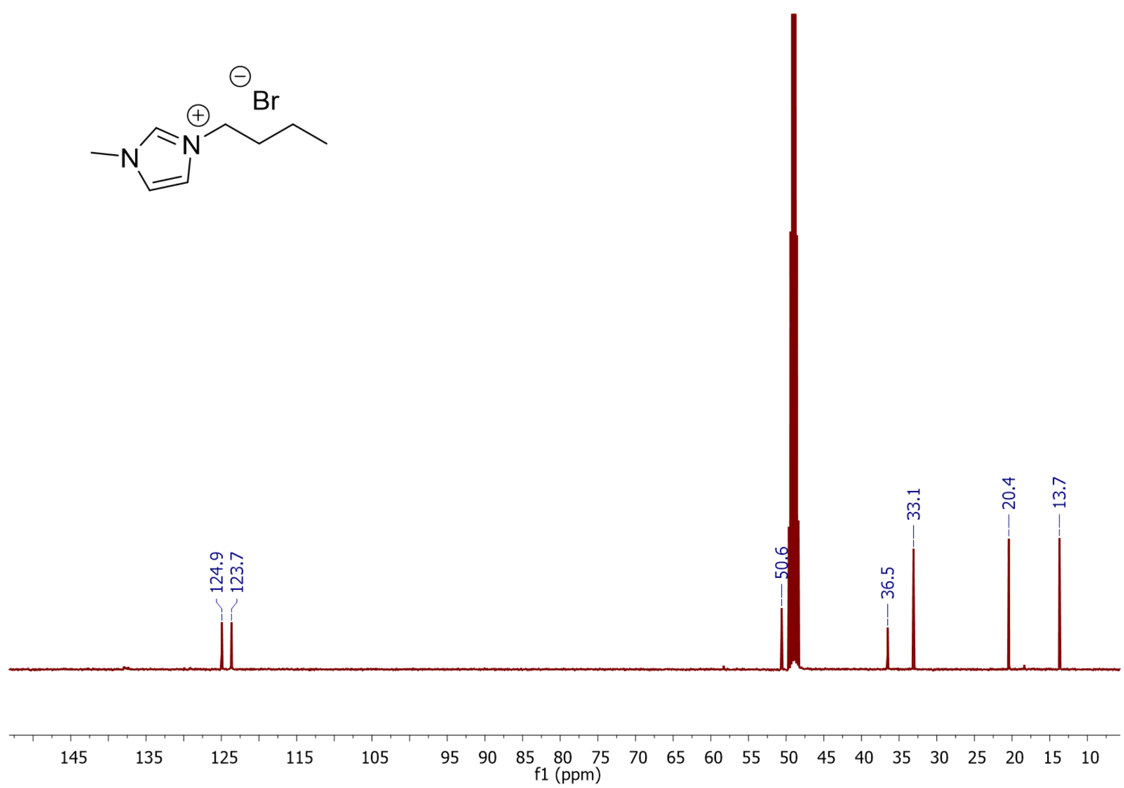

Figure A27. *^{1}H NMR and ^{13}C NMR spectra of BMI.Br.*

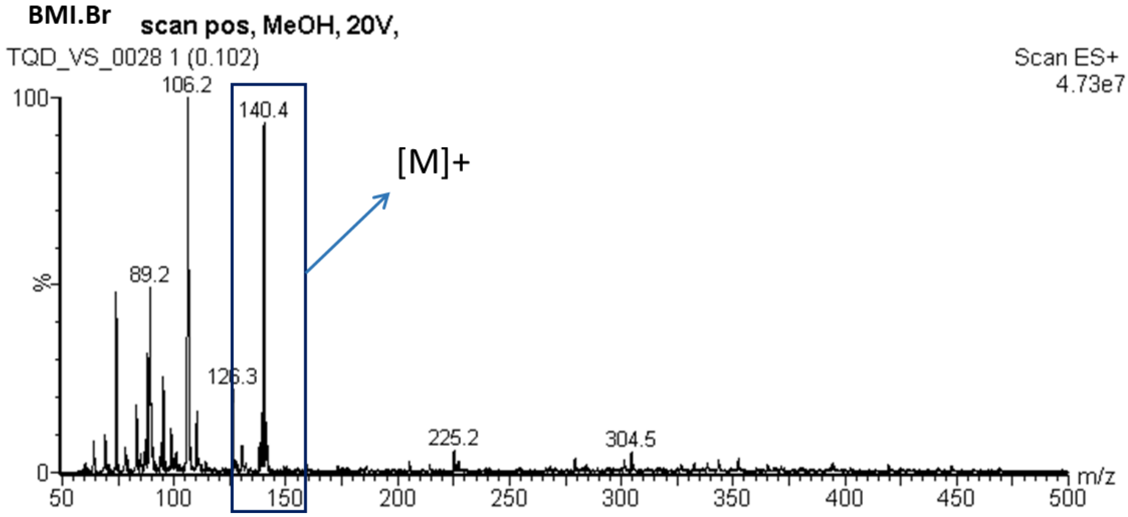

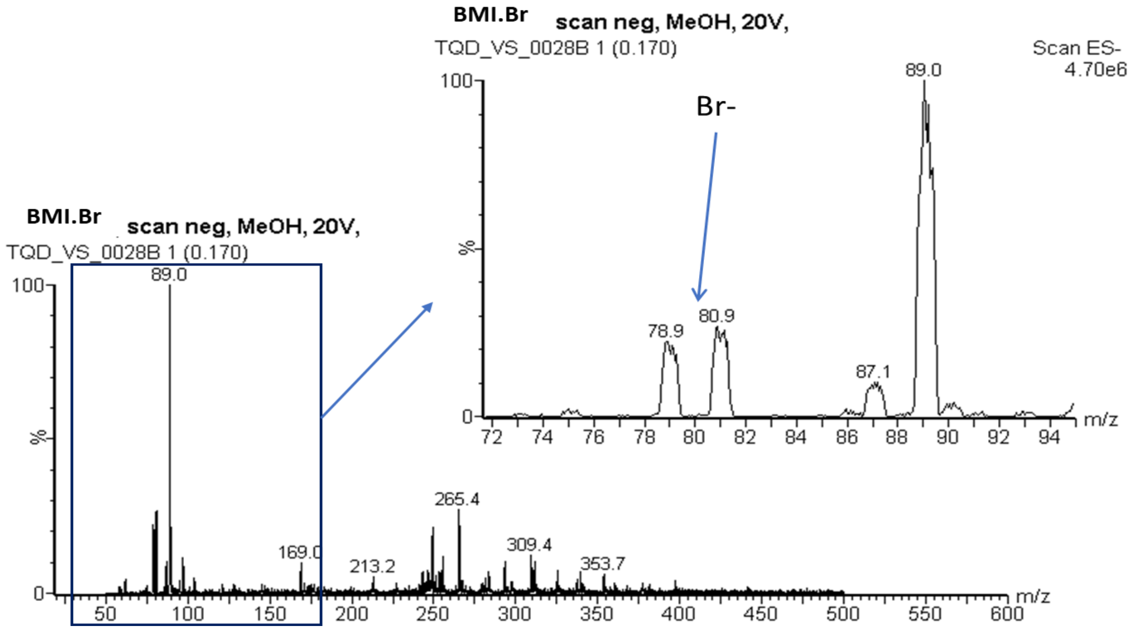

Figure A28. *ESI-MS spectra of BMI.Br in positive and negative mode.*

1-butyl-3-methylimidazolium bis(trifluoromethane) sulfonimide (IL1)

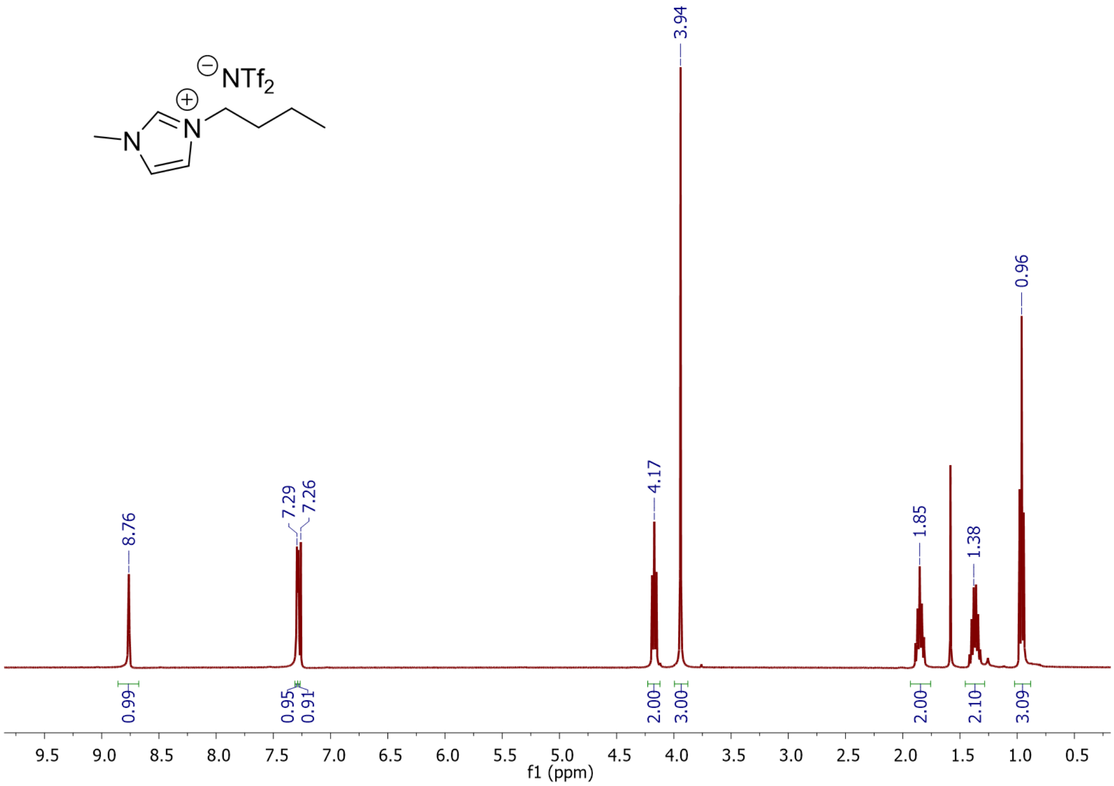

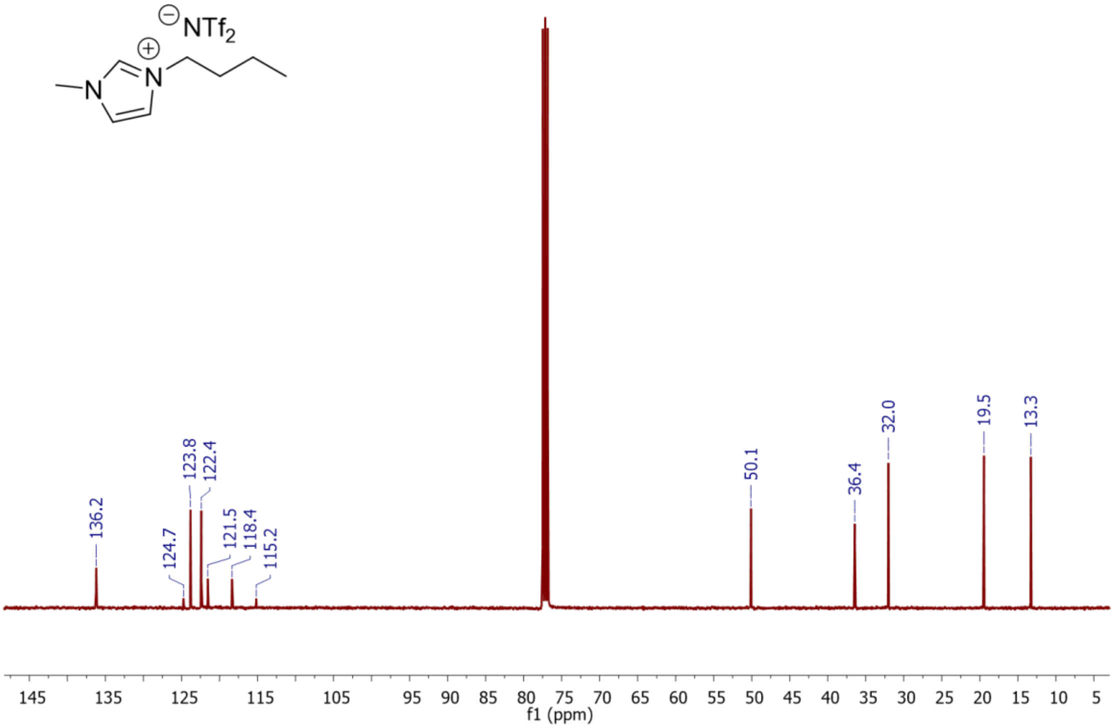

Figure A29. *^{1}H NMR and ^{13}C NMR spectra of IL1.*

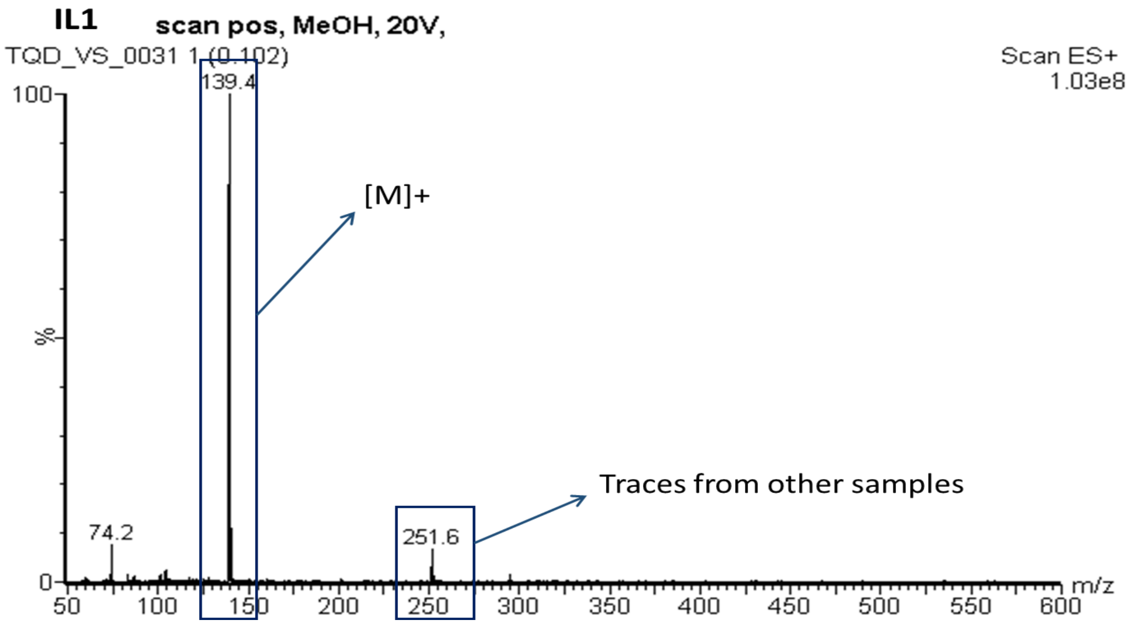

[M]+

Traces from other samples

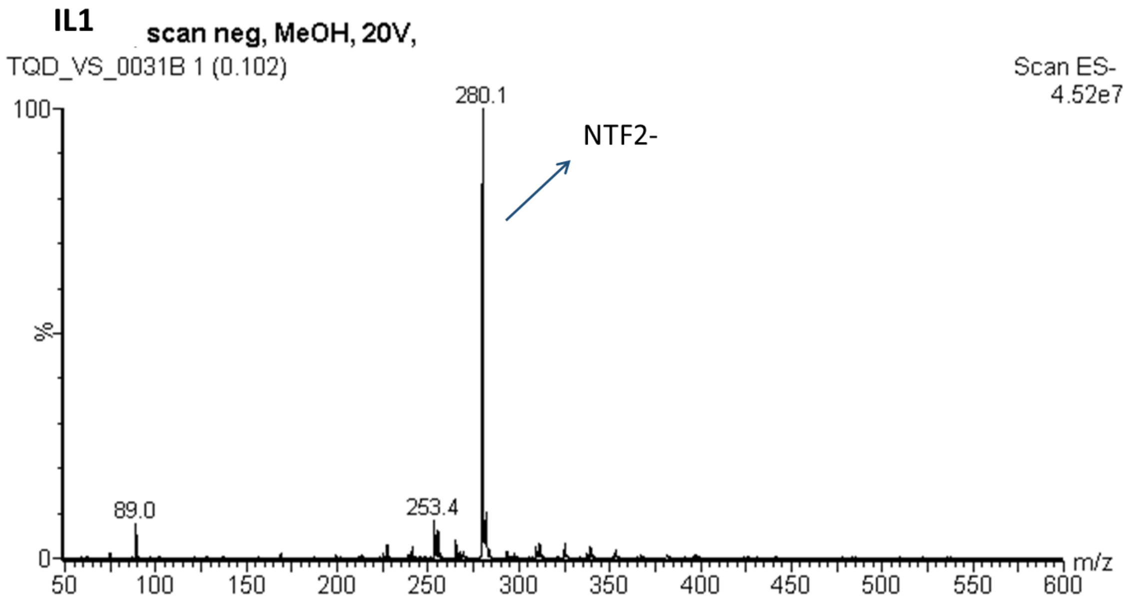

Figure A30. *ESI-MS spectra of IL1 in positive and negative mode.*

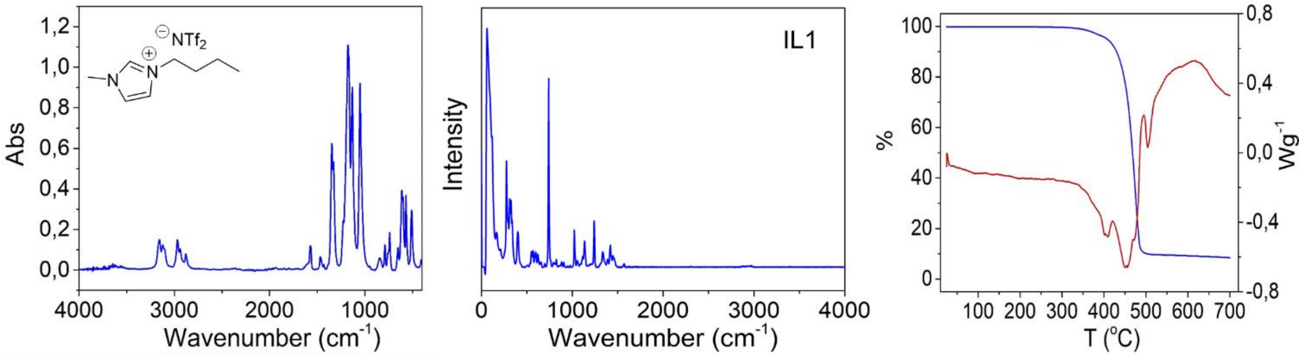

Figure A31. *(Left) FT-IR spectrum of IL1; (centre) Raman spectrum of IL1 (emission wavelength at 785 nm); (right) TGA-DSC spectra of IL1.*

1-dodecane-3-methylimidazolium bromide (DMI.Br)

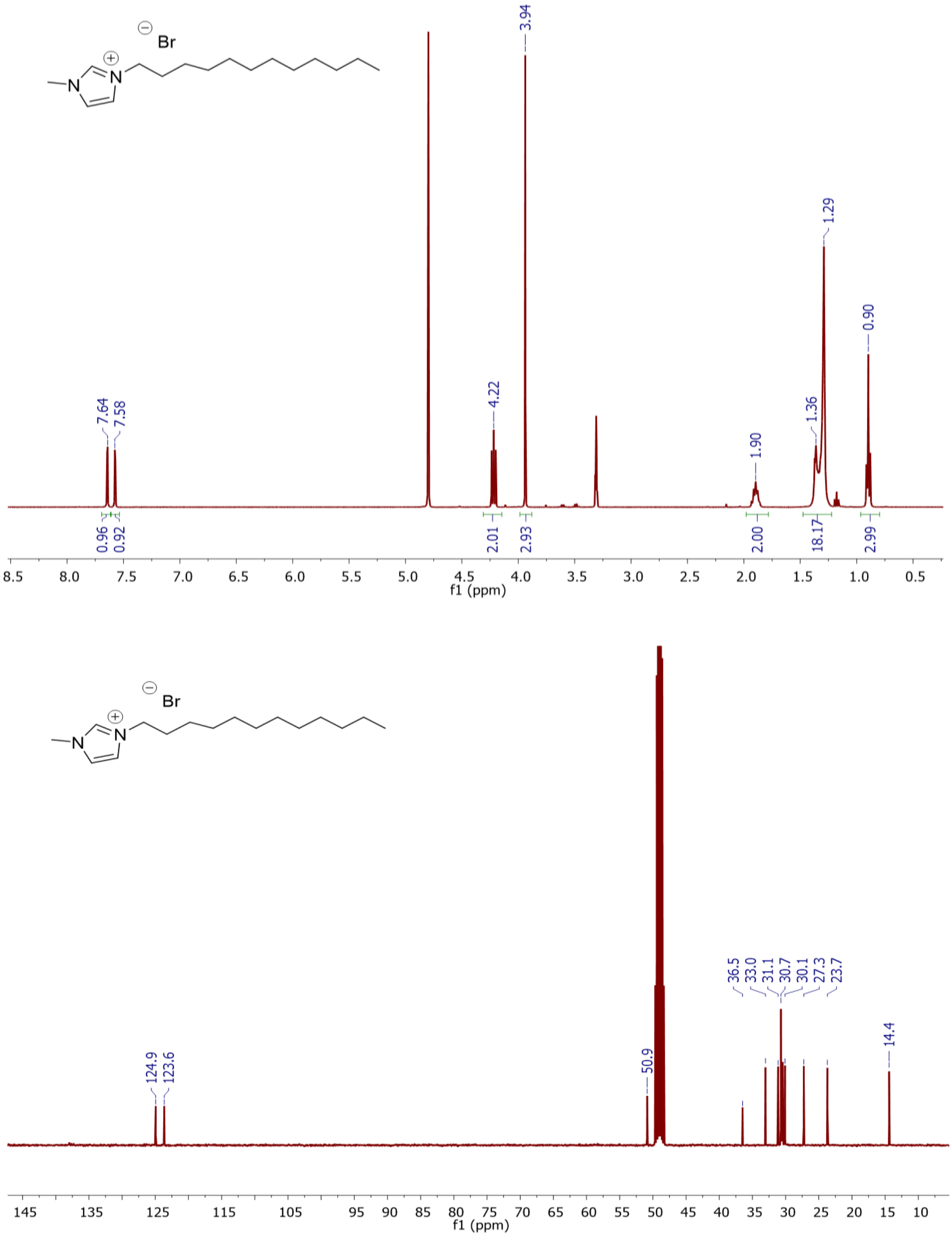

Figure A32. ^{1}H NMR and ^{13}C NMR spectra of DMI.Br.

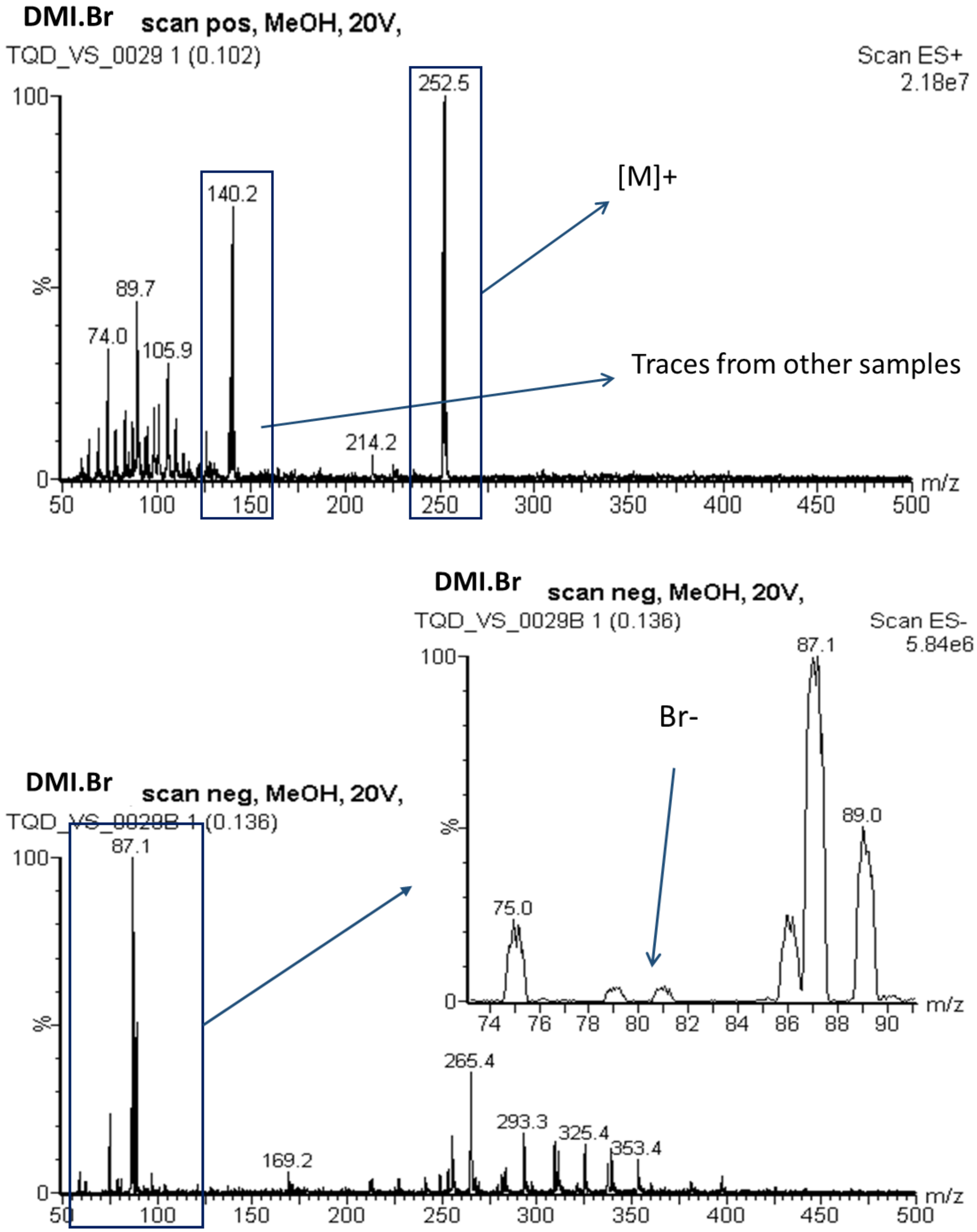

Figure A33. *ESI-MS spectra of DMI.Br in positive and negative mode.*

1-dodecane-3-methylimidazolium bis(trifluoromethane) sulfonimide (IL2)

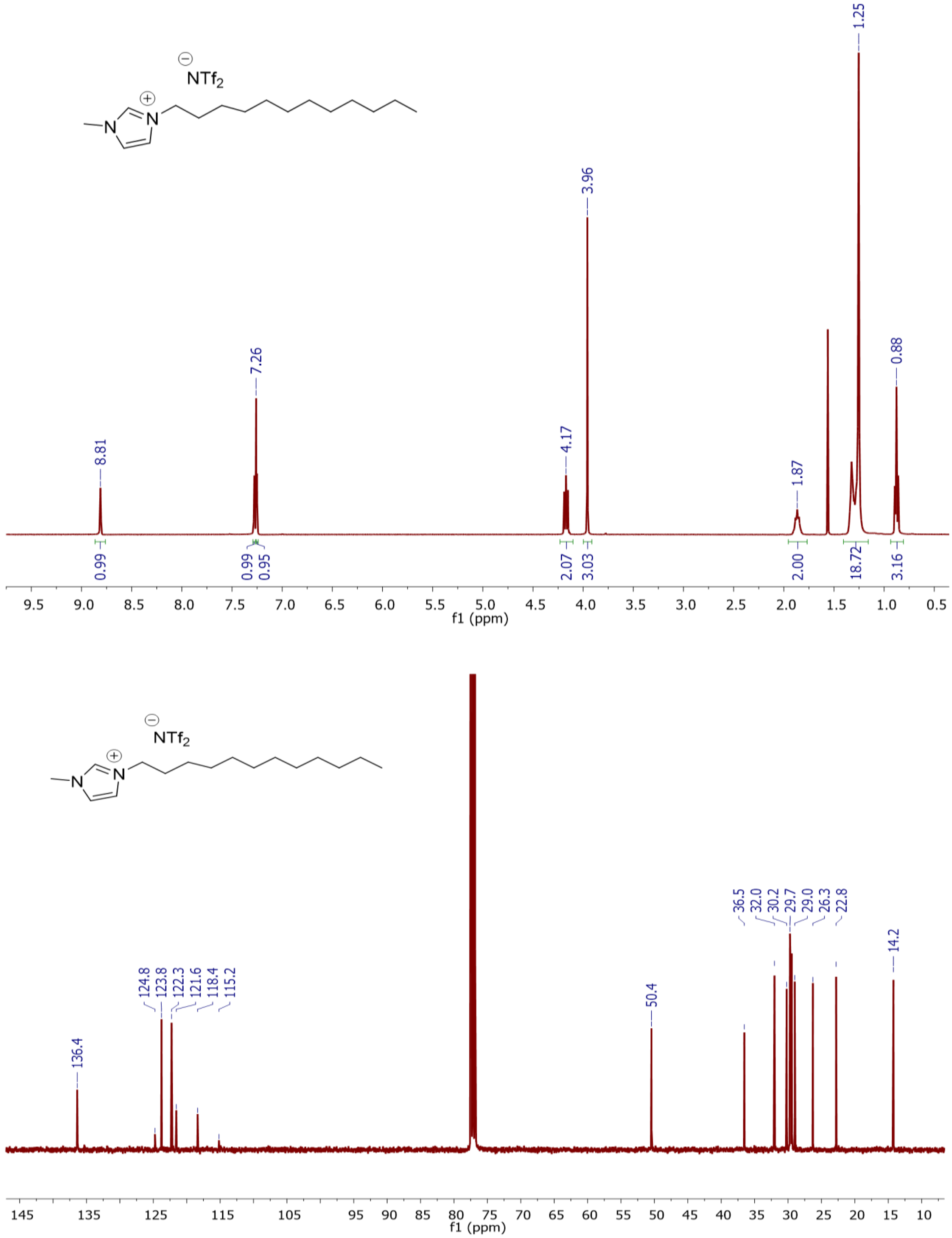

Figure A34. ^{1}H NMR and ^{13}C NMR spectra of IL2.

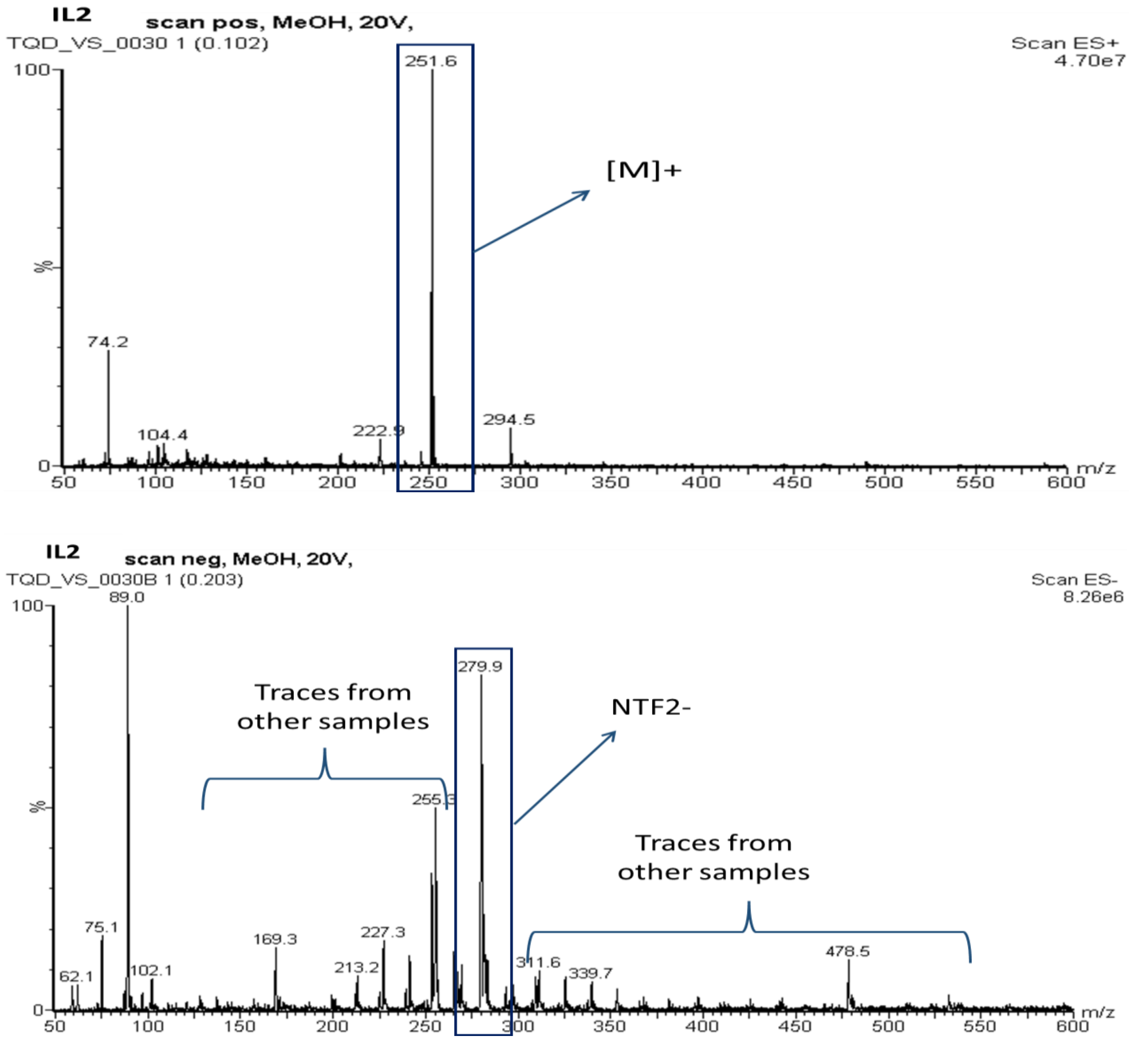

Figure A35. *ESI-MS spectra of IL2 in positive and negative mode.*

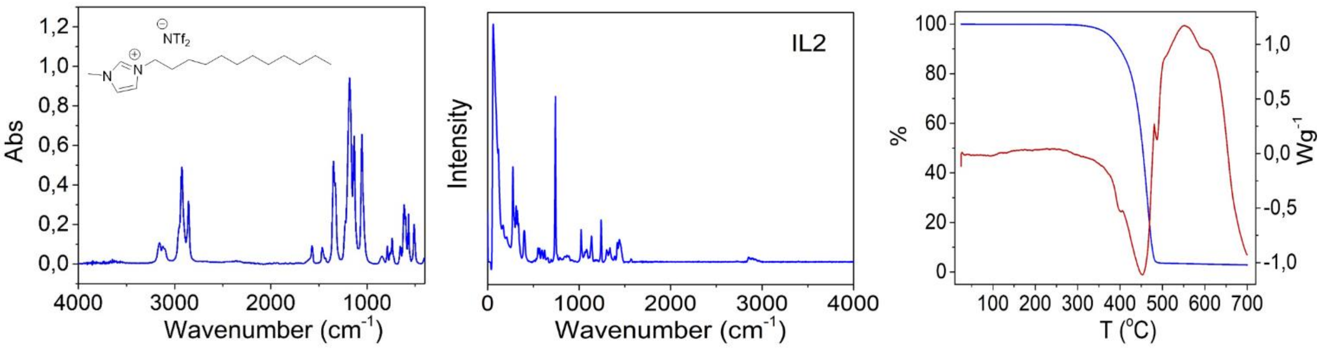

Figure A36. *(Left) FT-IR spectrum of IL2; (centre) Raman spectrum of IL2 (emission wavelength at 785 nm); (right) TGA-DSC spectra of IL2.*

Choline bis(trifluoromethane)sulfonimide (IL3)

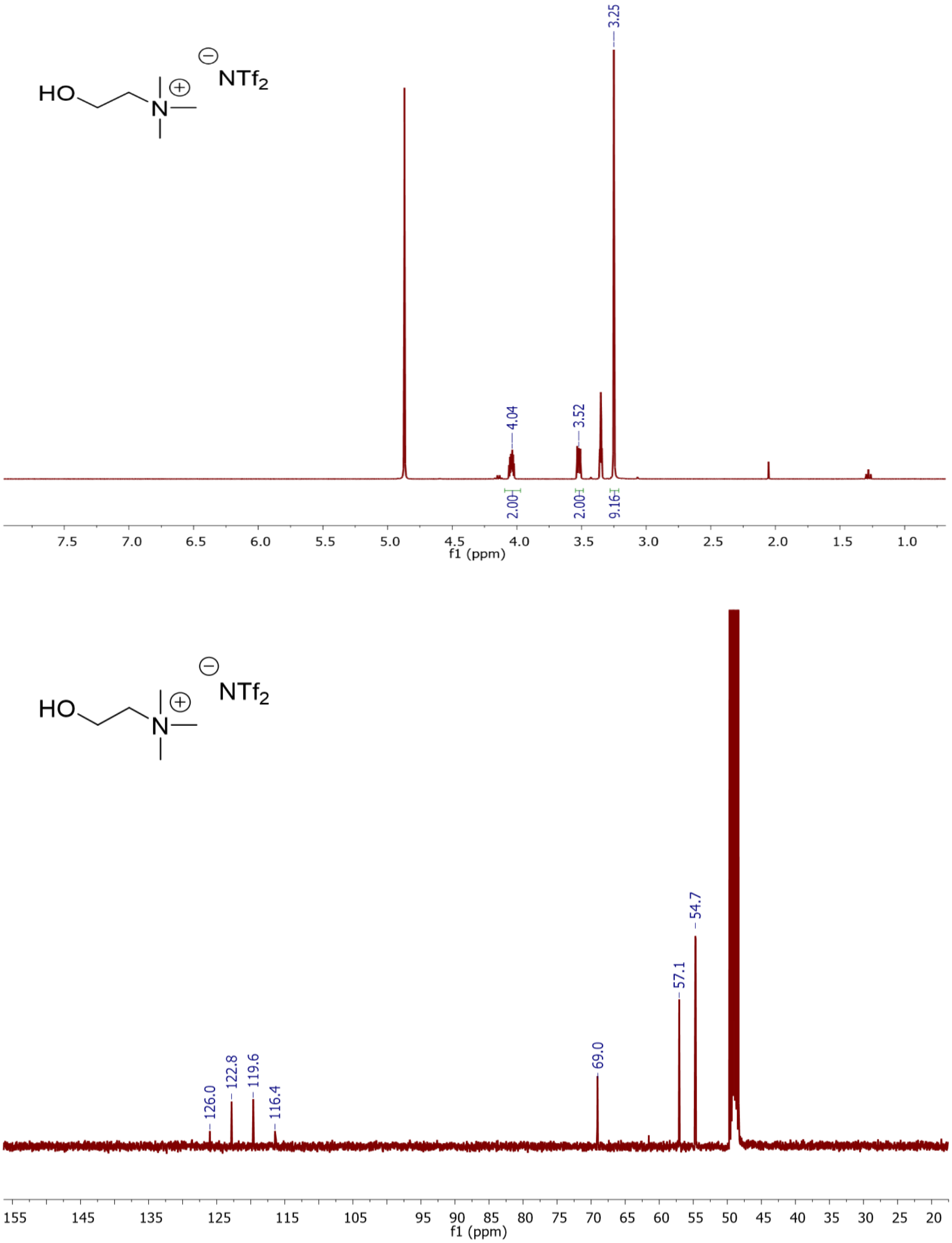

Figure A37. *^{1}H NMR and ^{13}C NMR spectra of IL3.*

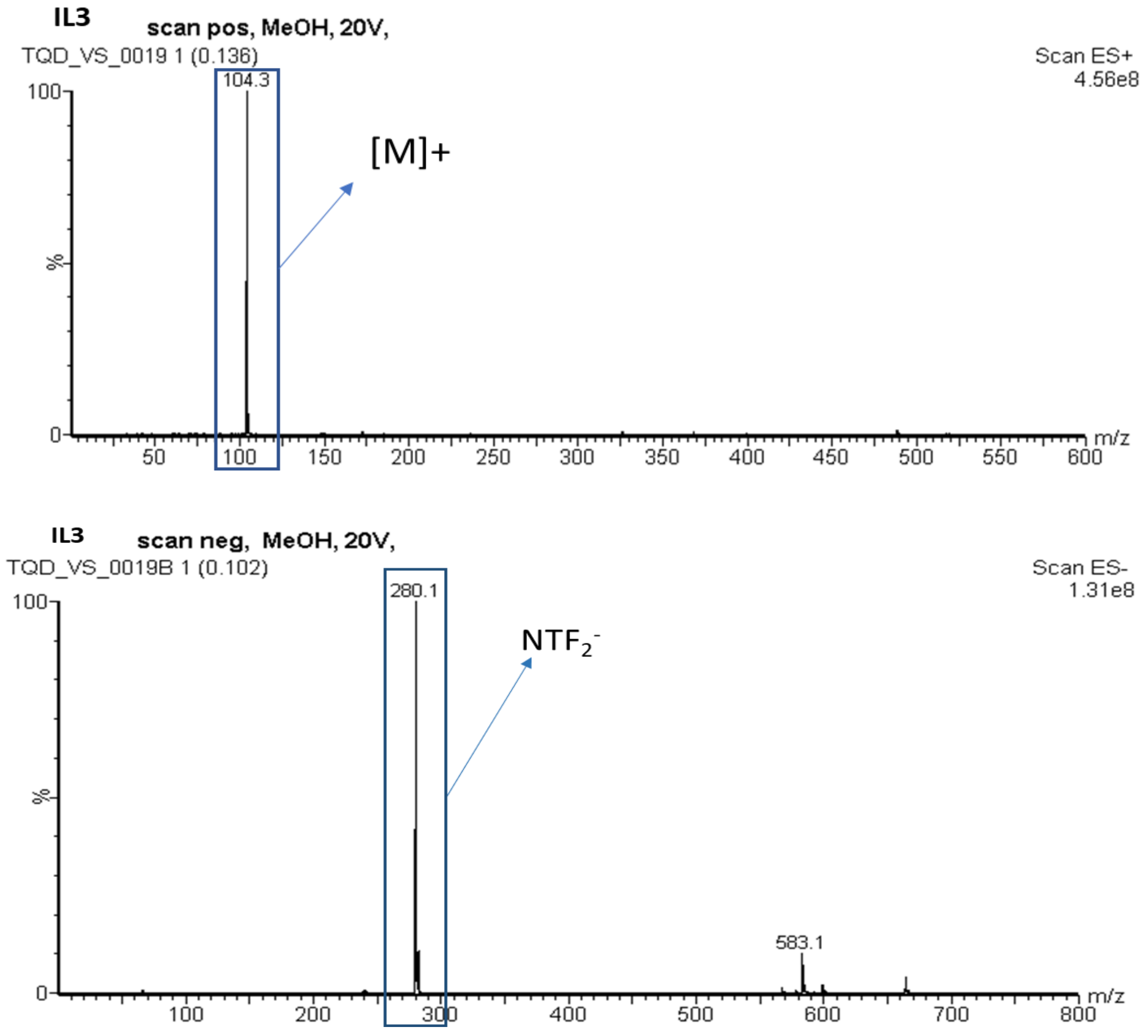

Figure A38. *ESI-MS spectra of IL3 in positive and negative mode.*

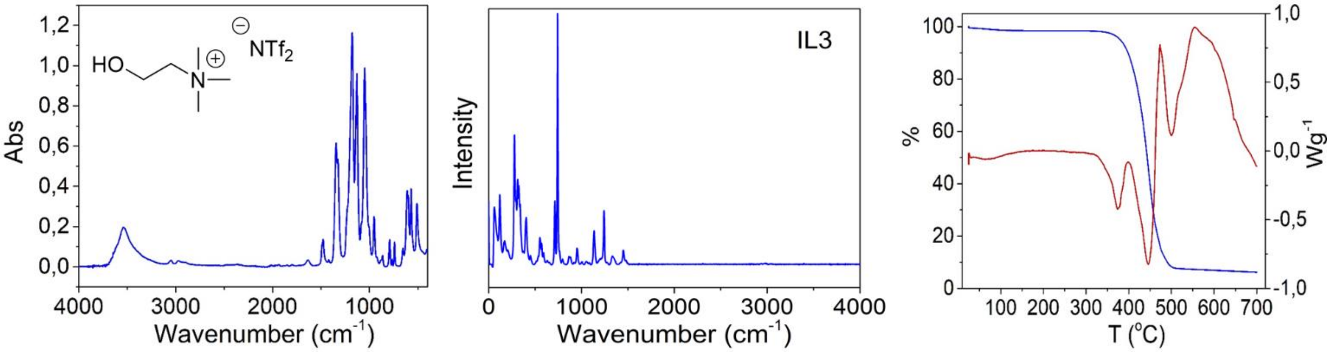

Figure A39. *(Left) FT-IR spectrum of IL3; (centre) Raman spectrum of IL3 (emission wavelength at 785 nm); (right) TGA-DSC spectra of IL3.*

References

1. Ngo, T. D.; Kashani, A.; Imbalzano, G.; Nguyen, K. T. Q.; Hui, D., Additive manufacturing (3D printing): A review of materials, methods, applications and challenges. *Composites Part B: Engineering* **2018,** *143*, 172-196.

2. Berman, B., 3-D printing: The new industrial revolution. *Business Horizons* **2012,** *55* (2), 155-162.

3. Wohlers, T. T.; Campbell, I.; Diegel, O.; Huff, R.; Kowen, J., *3D printing and Additive Manufacturing Global State of the Industry Annual Worldwide Progress*. Wohlers Associates.

4. Maciel, V. G.; Wales, D. J.; Seferin, M.; Sans, V., Environmental performance of 3D-Printing polymerisable ionic liquids. *Journal of Cleaner Production* **2019,** *214*, 29-40.

5. Dilberoglu, U. M.; Gharehpapagh, B.; Yaman, U.; Dolen, M., The Role of Additive Manufacturing in the Era of Industry 4.0. *Procedia Manufacturing* **2017,** *11*, 545-554.

6. (a) Oliveira, J.; Correia, V.; Castro, H.; Martins, P.; Lanceros-Mendez, S., Polymer-based smart materials by printing technologies: Improving application and integration. *Additive Manufacturing* **2018,** *21*, 269-283; (b) Qiu, X.; Hu, S., “Smart” Materials Based on Cellulose: A Review of the Preparations, Properties, and Applications. *Materials* **2013,** *6* (3), 738-781.

7. Narupai, B.; Nelson, A., 100th Anniversary of Macromolecular Science Viewpoint: Macromolecular Materials for Additive Manufacturing. *ACS Macro Letters* **2020,** *9*, 627-638.

8. Bogue, R., Smart materials: A review of capabilities and applications. *Assembly Automation* **2014,** *34* (1), 16-22.

9. (a) Shafranek, R. T.; Millik, S. C.; Smith, P. T.; Lee, C.-U.; Boydston, A. J.; Nelson, A., Stimuli-responsive materials in additive manufacturing. *Progress in Polymer Science* **2019,** *93*, 36-67; (b) Lin, Q.; Tang, M.; Ke, C., Thermo-responsive 3D-printed polyrotaxane monolith. *Polymer Chemistry* **2020,** *11* (2), 304-308; (c) Dharmarwardana, M.; Arimilli, B. S.; Luzuriaga, M. A.; Kwon, S.; Lee, H.; Appuhamillage, G. A.; McCandless, G. T.; Smaldone, R. A.; Gassensmith, J. J., The thermo-responsive behavior in molecular crystals of naphthalene diimides and their 3D printed thermochromic composites. *CrystEngComm* **2018,** *20* (39), 6054-6060.

10. (a) Berry, D. R.; Díaz, B. K.; Durand-Silva, A.; Smaldone, R. A., Radical free crosslinking of direct-write 3D printed hydrogels through a base catalyzed thiol-Michael reaction. *Polymer Chemistry* **2019,** *10* (44), 5979-5984; (b) Appuhamillage, G. A.; Berry, D. R.; Benjamin, C. E.; Luzuriaga, M. A.; Reagan, J. C.; Gassensmith, J. J.; Smaldone, R. A., A biopolymer-based 3D printable hydrogel for toxic metal adsorption from water. *Polymer International* **2019,** *68* (5), 964-971; (c) Smith, P. T.; Narupai, B.; Tsui, J. H.; Millik, S. C.; Shafranek, R. T.; Kim, D. H.; Nelson, A., Additive Manufacturing of Bovine Serum Albumin-Based Hydrogels and Bioplastics. *Biomacromolecules* **2020,** *21* (2), 484-492.

11. Zhang, M.; Li, L.; Lin, Q.; Tang, M.; Wu, Y.; Ke, C., Hierarchical-Coassembly-Enabled 3D-Printing of Homogeneous and Heterogeneous Covalent Organic Frameworks. *J Am Chem Soc* **2019,** *141* (13), 5154-5158.

12. Murphy, R. D.; Kimmins, S.; Hibbitts, A. J.; Heise, A., 3D-extrusion printing of stable constructs composed of photoresponsive polypeptide hydrogels. *Polymer Chemistry* **2019,** *10* (34), 4675-4682.

13. (a) Wong, J.; Gong, A. T.; Defnet, P. A.; Meabe, L.; Beauchamp, B.; Sweet, R. M.; Sardon, H.; Cobb, C. L.; Nelson, A., 3D Printing Ionogel Auxetic Frameworks for Stretchable Sensors. *Advanced Materials Technologies* **2019,** *4* (9), 1900452; (b) Wong, J.; Basu, A.; Wende, M.; Boechler, N.; Nelson, A., Mechano-Activated Objects with Multidirectional Shape Morphing Programmed via 3D Printing. *ACS Applied Polymer Materials* **2020,** *2* (7), 2504-2508; (c) Wang, Z.; Zhang, J.; Liu, J.; Hao, S.; Song, H.; Zhang, J., 3D Printable, Highly Stretchable, Superior Stable Ionogels Based on Poly(ionic liquid) with Hyperbranched Polymers as Macro-cross-linkers for High-Performance Strain Sensors. *ACS Applied Materials & Interfaces* **2021,** *13* (4), 5614-5624.

14. Boydston, A. J.; Nelson, A., Chemical advances in additive manufacturing. *Polymer Chemistry* **2019,** *10*, 5948.

15. Yin, J.; Lei, Q.; Dong, Y.; Zhao, X., Stimuli Responsive Smart Fluids Based on Ionic Liquids and Poly(ionic liquid)s. In *Polymerized Ionic Liquids*, The Royal Society of Chemistry: 2018; pp 180-201.

16. Tang, Y.; Tang, B.; Wu, P., A polymeric ionic liquid functionalized temperature-responsive composite membrane with tunable responsive behavior. *Journal of Materials Chemistry A* **2015,** *3* (15), 7919-7928.

17. Tudor, A.; Florea, L.; Gallagher, S.; Burns, J.; Diamond, D., Poly(Ionic Liquid) Semi-Interpenetrating Network Multi-Responsive Hydrogels. *Sensors* **2016,** *16* (2), 219.

18. Zhao, Q.; Heyda, J.; Dzubiella, J.; Täuber, K.; Dunlop, J. W. C.; Yuan, J., Sensing Solvents with Ultrasensitive Porous Poly(ionic liquid) Actuators. *Advanced Materials* **2015,** *27* (18), 2913-2917.

19. Zhao, Q.; Yin, M.; Zhang, A. P.; Prescher, S.; Antonietti, M.; Yuan, J., Hierarchically Structured Nanoporous Poly(Ionic Liquid) Membranes: Facile Preparation and Application in Fiber-Optic pH Sensing. *Journal of the American Chemical Society* **2013,** *135* (15), 5549-5552.

20. Darabi, A.; Jessop, P. G.; Cunningham, M. F., CO2-responsive polymeric materials: synthesis, self-assembly, and functional applications. *Chemical Society Reviews* **2016,** *45* (15), 4391-4436.

21. (a) Mecerreyes, D., Polymeric ionic liquids: Broadening the properties and applications of polyelectrolytes. *Progress in Polymer Science* **2011,** *36* (12), 1629-1648; (b) Marcilla, R.; Blazquez, J. A.; Rodriguez, J.; Pomposo, J. A.; Mecerreyes, D., Tuning the solubility of polymerized ionic liquids by simple anion-exchange reactions. *Journal of Polymer Science Part A: Polymer Chemistry* **2004,** *42* (1), 208-212.

22. Nulwala, H.; Mirjafari, A.; Zhou, X., Ionic liquids and poly(ionic liquid)s for 3D printing – A focused mini-review. *European Polymer Journal* **2018,** *108*, 390-398.

23. (a) Lv, X.; Wang, J.; Ding, D.; Liang, J.; Zhao, Z.; Liang, Y.; Zhang, Z.; Ye, C.; Chen, Y.; Wei, P.; Wang, Y.; He, Y.; Xia, Y., 3D Printing Conductive Composites with Poly(ionic liquid) as a Noncovalent Intermedia to Fabricate Carbon Circuits. *Macromolecular Materials and Engineering* **2021,** *306* (12), 2100560; (b) Qian, W.; Texter, J.; Yan, F., Frontiers in poly(ionic liquid)s: syntheses and applications. *Chem Soc Rev* **2017,** *46* (4), 1124-1159.

24. Hull, C. W. Apparatus for Production of Three-Dimensional Objects by Stereolithography. 1986.

25. Zhu, C.; Liu, T.; Qian, F.; Chen, W.; Chandrasekaran, S.; Yao, B.; Song, Y.; Duoss, E. B.; Kuntz, J. D.; Spadaccini, C. M.; Worsley, M. A.; Li, Y., 3D printed functional nanomaterials for electrochemical energy storage. *Nano Today* **2017,** *15*, 107-120.

26. (a) Zhang, F.; Wei, M.; Viswanathan, V. V.; Swart, B.; Shao, Y.; Wu, G.; Zhou, C., 3D printing technologies for electrochemical energy storage. *Nano Energy* **2017,** *40*, 418–431; (b) Pham, D. T.; Gault, R. S., A comparison of rapid prototyping technologies. *International Journal of Machine Tools and Manufacture* **1998,** *38* (10), 1257-1287; (c) Rajaguru, K.; Karthikeyan, T.; Vijayan, V., Additive manufacturing – State of art. *Materials Today: Proceedings* **2020,** *21*, 628-633; (d) Horn, T. J.; Harrysson, O. L. A., Overview of Current Additive Manufacturing Technologies and Selected Applications. *Science Progress* **2012,** *95* (3), 255-282.

27. Gardan, J., Additive Manufacturing Technologies: State of the Art and Trends. *International Journal of Production Research* **2015,** *54*.

28. Miralles-Comins, S.; Alvarez, E.; Lozano, P.; Sans, V., 9 Exothermic advanced manufacturing techniques in reactor engineering: 3D printing applications in flow chemistry. **2021**, 259-276.

29. Karjalainen, E.; Wales, D. J.; Gunasekera, D. H. A. T.; Dupont, J.; Licence, P.; Wildman, R. D.; Sans, V., Tunable Ionic Control of Polymeric Films for Inkjet Based 3D Printing. *ACS Sustainable Chemistry & Engineering* **2018,** *6* (3), 3984-3991.

30. Ahmed, K.; Kawakami, M.; Khosla, A.; Furukawa, H., Soft, conductive nanocomposites based on ionic liquids/carbon nanotubes for 3D printing of flexible electronic devices. *Polymer Journal* **2019,** *51* (5), 511-521.

31. (a) Wales, D. J.; Cao, Q.; Kastner, K.; Karjalainen, E.; Newton, G. N.; Sans, V., 3D-Printable Photochromic Molecular Materials for Reversible Information Storage. *Adv Mater* **2018,** *30* (26), 1800159; (b) Wales, D. J.; Miralles-Comins, S.; Franco-Castillo, I.; Cameron, J. M.; Cao, Q.; Karjalainen, E.; Alves Fernandes, J.; Newton, G. N.; Mitchell, S. G.; Sans, V., Decoupling manufacturing from application in additive manufactured antimicrobial materials. *Biomaterials science* **2021,** *9* (16), 5397-5406.

32. (a) Schultz, A. R.; Lambert, P. M.; Chartrain, N. A.; Ruohoniemi, D. M.; Zhang, Z.; Jangu, C.; Zhang, M.; Williams, C. B.; Long, T. E., 3D Printing Phosphonium Ionic Liquid Networks with Mask Projection Microstereolithography. *ACS Macro Letters* **2014,** *3* (11), 1205-1209; (b) Radchenko, A. V.; Duchet-Rumeau, J.; Gérard, J.-F.; Baudoux, J.; Livi, S., Cycloaliphatic epoxidized ionic liquids as new versatile monomers for the development of shape memory PIL networks by 3D printing. *Polymer Chemistry* **2020,** *11* (34), 5475-5483.

33. Stansbury, J. W.; Idacavage, M. J., 3D printing with polymers: Challenges among expanding options and opportunities. *Dental Materials* **2016,** *32* (1), 54-64.

34. Kannurpatti, A. R., Photochemistry of Polymers: Photopolymerization Fundamentals and Applications **1996,** *Vol. 10285*.

35. Pascault, J. P.; Sautereau, H.; Verdu, J.; Williams, R. J. J., *Thermosetting Polymers*

36. Mondschein, R. J.; Kanitkar, A.; Williams, C. B.; Verbridge, S. S.; Long, T. E., Polymer structure-property requirements for stereolithographic 3D printing of soft tissue engineering scaffolds. *Biomaterials* **2017,** *140*, 170-188.

37. Melchels, F. P. W.; Feijen, J.; Grijpma, D. W., A review on stereolithography and its applications in biomedical engineering. *Biomaterials* **2010,** *31* (24), 6121-6130.

38. Ikuta, K.; Hirowatari, K. In *Real three dimensional micro fabrication using stereo lithography and metal molding*, [1993] Proceedings IEEE Micro Electro Mechanical Systems, 10-10 Feb. 1993; 1993; pp 42-47.

39. Podgórski, M.; Huang, S.; Bowman, C. N., Additive Manufacture of Dynamic Thiol–ene Networks Incorporating Anhydride-Derived Reversible Thioester Links. *ACS Applied Materials & Interfaces* **2021,** *13* (11), 12789-12796.

40. Oesterreicher, A.; Wiener, J.; Roth, M.; Moser, A.; Gmeiner, R.; Edler, M.; Pinter, G.; Griesser, T., Tough and degradable photopolymers derived from alkyne monomers for 3D printing of biomedical materials. *Polymer Chemistry* **2016,** *7* (32), 5169-5180.

41. Gong, H.; Bickham, B. P.; Woolley, A. T.; Nordin, G. P., Custom 3D printer and resin for 18 µm × 20 µm microfluidic flow channels. *Lab on a Chip* **2017,** *17* (17), 2899-2909.

42. (a) Tumbleston, J. R.; Shirvanyants, D.; Ermoshkin, N.; Janusziewicz, R.; Johnson, A. R.; Kelly, D.; Chen, K.; Pinschmidt, R.; Rolland, J. P.; Ermoshkin, A.; Samulski, E. T.; DeSimone, J. M., Continuous liquid interface production of 3D objects. *Science* **2015,** *347* (6228), 1349-1352; (b) Balli, J.; Kumpaty, S.; Anewenter, V. In *Continuous Liquid Interface Production of 3D Objects: An Unconventional Technology and its Challenges and Opportunities*, ASME 2017 International Mechanical Engineering Congress and Exposition, 2017.

43. Quan, H.; Zhang, T.; Xu, H.; Luo, S.; Nie, J.; Zhu, X., Photo-curing 3D printing technique and its challenges. *Bioactive Materials* **2020,** *5* (1), 110-115.

44. Yu, C.; Schimelman, J.; Wang, P.; Miller, K. L.; Ma, X.; You, S.; Guan, J.; Sun, B.; Zhu, W.; Chen, S., Photopolymerizable Biomaterials and Light-Based 3D Printing Strategies for Biomedical Applications. *Chemical Reviews* **2020,** *120* (19), 10695-10743.

45. (a) Liu, Y.; Hu, Q.; Zhang, F.; Tuck, C.; Irvine, D.; Hague, R.; He, Y.; Simonelli, M.; Rance, G. A.; Smith, E. F.; Wildman, R. D., Additive Manufacture of Three Dimensional Nanocomposite Based Objects through Multiphoton Fabrication. *Polymers* **2016,** *8* (9); (b) Xing, J.-F.; Zheng, M.-L.; Duan, X.-M., Two-photon polymerization microfabrication of hydrogels: an advanced 3D printing technology for tissue engineering and drug delivery. *Chemical Society Reviews* **2015,** *44* (15), 5031-5039.

46. Zhou, X.; Hou, Y.; Lin, J., A review on the processing accuracy of two-photon polymerization. *AIP Advances* **2015,** *5* (3), 030701.

47. Indrasen, B.; Brett, K.; Maxim, S.; Christopher, S.; Hayden, T. In *Computed axial lithography: volumetric 3D printing of arbitrary geometries (Conference Presentation)*, SPIE Commercial + Scientific Sensing and Imaging, Orlando, United States, Orlando, United States, 2018.

48. Bernal, P. N.; Delrot, P.; Loterie, D.; Li, Y.; Malda, J.; Moser, C.; Levato, R., Biofabrication: Volumetric Bioprinting of Complex Living-Tissue Constructs within Seconds (Adv. Mater. 42/2019). *Advanced Materials* **2019,** *31* (42), 1970302.

49. (a) Felix, J. F.; Barros, R. A.; de Azevedo, W. M.; da Silva, E. F., X-ray irradiation: A non-conventional route for the synthesis of conducting polymers. *Synthetic Metals* **2011,** *161* (1), 173-176; (b) Chen, Z.; Wang, X.; Li, S.; Liu, S.; Miao, H.; Wu, S., Near-Infrared Light Driven Photopolymerization Based On Photon Upconversion. *ChemPhotoChem* **2019,** *3* (11), 1077-1083.

50. Li, L.; Zhang, P.; Zhang, Z.; Lin, Q.; Wu, Y.; Cheng, A.; Lin, Y.; Thompson, C. M.; Smaldone, R. A.; Ke, C., Hierarchical Co-Assembly Enhanced Direct Ink Writing. *Angewandte Chemie* **2018,** *130*, 5199 – 5203.

51. (a) Li, Z.; Wang, C.; Qiu, W.; Liu, R., Antimicrobial Thiol–ene–acrylate Photosensitive Resins for DLP 3D Printing. *Photochemistry and Photobiology* **2019,** *95* (5), 1219-1229; (b) Wu, J.; Yan, Y.; Zhang, L.; Qin, Z.; Tao, S., Enhanced Mass Transfer and Improved Catalyst Recovery in a Stirred Reactor by Polymeric Ionic Liquids Modified 3D Printed Devices. *Advanced Materials Technologies* **2018**.

52. Narupai, B.; Nelson, A., 100th Anniversary of Macromolecular Science Viewpoint: Macromolecular Materials for Additive Manufacturing. *ACS Macro Letters* **2020,** *9* (5), 627-638.

53. (a) Lammel-Lindemann, J.; Dourado, I. A.; Shanklin, J.; Rodriguez, C. A.; Catalani, L. H.; Dean, D., Photocrosslinking-based 3D printing of unsaturated polyesters from isosorbide: A new material for resorbable medical devices. *Bioprinting* **2020,** *18*, e00062; (b) Holger, L.; Sascha, E.; Andreas, H.; Ludwig, P.; Sascha, S.; Jana, B.; Martin, M. W.; Arnold, G. In *Advantages and drawbacks of Thiol-ene based resins for 3D-printing*, Proc.SPIE, 2015.

54. Andrzejewska, E., Photopolymerization kinetics of multifunctional monomers. *Progress in Polymer Science* **2001,** *26* (4), 605-665.

55. Yagci, Y.; Jockusch, S.; Turro, N. J., Photoinitiated Polymerization: Advances, Challenges, and Opportunities. *Macromolecules* **2010,** *43* (15), 6245-6260.

56. (a) Shanmugam, S.; Xu, J.; Boyer, C., Light-Regulated Polymerization under Near-Infrared/Far-Red Irradiation Catalyzed by Bacteriochlorophyll a. *Angewandte Chemie International Edition* **2016,** *55* (3), 1036-1040; (b) Al Mousawi, A.; Poriel, C.; Dumur, F.; Toufaily, J.; Hamieh, T.; Fouassier, J. P.; Lalevée, J., Zinc Tetraphenylporphyrin as High Performance Visible Light Photoinitiator of Cationic Photosensitive Resins for LED Projector 3D Printing Applications. *Macromolecules* **2017,** *50* (3), 746-753; (c) Zhang, J.; Lalevée, J.; Zhao, J.; Graff, B.; Stenzel, M. H.; Xiao, P., Dihydroxyanthraquinone derivatives: natural dyes as blue-light-sensitive versatile photoinitiators of photopolymerization. *Polymer Chemistry* **2016,** *7* (47), 7316-7324; (d) Xu, J.; Shanmugam, S.; Fu, C.; Aguey-Zinsou, K.-F.; Boyer, C., Selective Photoactivation: From a Single Unit Monomer Insertion Reaction to Controlled Polymer Architectures. *Journal of the American Chemical Society* **2016,** *138* (9), 3094-3106.

57. (a) Sangermano, M.; Roppolo, I.; Chiappone, A., New Horizons in Cationic Photopolymerization. *Polymers* **2018,** *10* (2), 136; (b) Kutal, C.; Grutsch, P. A.; Yang, D. B., A novel strategy for photoinitiated anionic polymerization. *Macromolecules* **1991,** *24* (26), 6872-6873; (c) Wang, Y.-H.; Wan, P., Ketoprofen as a photoinitiator for anionic polymerization. *Photochemical & Photobiological Sciences* **2015,** *14* (6), 1120-1126; (d) Ikemura, K.; Endo, T., A review of the development of radical photopolymerization initiators used for designing light-curing dental adhesives and resin composites. *Dental Materials Journal* **2010,** *29* (5), 481-501; (e) Sangermano, M.; Razza, N.; Crivello, J. V., Cationic UV-Curing: Technology and Applications. *Macromolecular Materials and Engineering* **2014,** *299* (7), 775-793.

58. (a) Tomal, W.; Ortyl, J., Water-Soluble Photoinitiators in Biomedical Applications. *Polymers* **2020,** *12* (5), 1073; (b) Liu, S.; Chen, H.; Zhang, Y.; Sun, K.; Xu, Y.; Morlet-Savary, F.; Graff, B.; Noirbent, G.; Pigot, C.; Brunel, D.; Nechab, M.; Gigmes, D.; Xiao, P.; Dumur, F.; Lalevée, J., Monocomponent Photoinitiators based on Benzophenone-Carbazole Structure for LED Photoinitiating Systems and Application on 3D Printing. *Polymers* **2020,** *12* (6), 1394.

59. (a) Falco, A.; Petrelli, M.; Bezzeccheri, E.; Abdelhalim, A.; Lugli, P., Towards 3D-printed organic electronics: Planarization and spray-deposition of functional layers onto 3D-printed objects. *Organic Electronics* **2016,** *39*, 340-347; (b) Fan, J.; Montemagno, C.; Gupta, M., 3D printed high transconductance organic electrochemical transistors on flexible substrates. *Organic Electronics* **2019,** *73*, 122-129.

60. Schuster, M.; Turecek, C.; Kaiser, B.; Stampfl, J.; Liska, R.; Varga, F., Evaluation of Biocompatible Photopolymers I: Photoreactivity and Mechanical Properties of Reactive Diluents. *Journal of Macromolecular Science, Part A* **2007,** *44* (5), 547-557.

61. Gonzalez, G.; Chiappone, A.; Roppolo, I.; Fantino, E.; Bertana, V.; Perrucci, F.; Scaltrito, L.; Pirri, F.; Sangermano, M., Development of 3D printable formulations containing CNT with enhanced electrical properties. *Polymer* **2017,** *109*, 246-253.

62. Roppolo, I.; Chiappone, A.; Angelini, A.; Stassi, S.; Frascella, F.; Pirri, C. F.; Ricciardi, C.; Descrovi, E., 3D printable light-responsive polymers. *Materials Horizons* **2017,** *4* (3), 396-401.

63. Wang, F.; Chong, Y.; Wang, F.; He, C., Photopolymer resins for luminescent three-dimensional printing. *Journal of Applied Polymer Science* **2017,** *134* (32), 44988.

64. (a) Lin, D.; Jin, S.; Zhang, F.; Wang, C.; Wang, Y.; Zhou, C.; Cheng, G. J., 3D stereolithography printing of graphene oxide reinforced complex architectures. *Nanotechnology* **2015,** *26* (43), 434003; (b) Down, M. P.; Martínez-Periñán, E.; Foster, C. W.; Lorenzo, E.; Smith, G. C.; Banks, C. E., Next-Generation Additive Manufacturing of Complete Standalone Sodium-Ion Energy Storage Architectures. *Advanced Energy Materials* **2019,** *9* (11); (c) Wu, Q.; Wei, J.; Xu, B.; Liu, X.; Wang, H.; Wang, W.; Wang, Q.; Liu, W., A robust, highly stretchable supramolecular polymer conductive hydrogel with self-healability and thermo-processability. *Sci Rep* **2017,** *7*, 41566.

65. (a) Nazar, R.; Sangermano, M.; Vitale, A.; Bongiovanni, R., Silver polymer nanocomposites by photoreduction of AgNO3 and simultaneous photocrosslinking of the acrylic matrix: effect of PVP on Ag particle formation. *Journal of Polymer Engineering* **2018,** *38* (8), 803-809; (b) Fantino, E.; Chiappone, A.; Roppolo, I.; Manfredi, D.; Bongiovanni, R.; Pirri, C. F.; Calignano, F., 3D Printing of Conductive Complex Structures with In Situ Generation of Silver Nanoparticles. *Advanced Materials* **2016,** *28* (19), 3712-3717; (c) Fantino, E.; Chiappone, A.; Calignano, F.; Fontana, M.; Pirri, F.; Roppolo, I., In Situ Thermal Generation of Silver Nanoparticles in 3D Printed Polymeric Structures. *Materials* **2016,** *9* (7), 589.

66. Scordo, G.; Bertana, V.; Scaltrito, L.; Ferrero, S.; Cocuzza, M.; Marasso, S. L.; Romano, S.; Sesana, R.; Catania, F.; Pirri, C. F., A novel highly electrically conductive composite resin for stereolithography. *Materials Today Communications* **2019,** *19*, 12-17.

67. Liu, R.; Wang, Z.; Sparks, T.; Liou, F.; Newkirk, J., 13 - Aerospace applications of laser additive manufacturing. In *Laser Additive Manufacturing*, Brandt, M., Ed. Woodhead Publishing: 2017; pp 351-371.

68. Yan, Q.; Dong, H.; Su, J.; Han, J.; Song, B.; Wei, Q.; Shi, Y., A Review of 3D Printing Technology for Medical Applications. *Engineering* **2018,** *4* (5), 729-742.

69. Garcia-Gonzalez, D.; Garzon-Hernandez, S.; Arias, A., A new constitutive model for polymeric matrices: Application to biomedical materials. *Composites Part B: Engineering* **2018,** *139*, 117-129.

70. Chen, R. K.; Jin, Y.-a.; Wensman, J.; Shih, A., Additive manufacturing of custom orthoses and prostheses—A review. *Additive Manufacturing* **2016,** *12*, 77-89.

71. Norman, J.; Madurawe, R. D.; Moore, C. M. V.; Khan, M. A.; Khairuzzaman, A., A new chapter in pharmaceutical manufacturing: 3D-printed drug products. *Advanced Drug Delivery Reviews* **2017,** *108*, 39-50.

72. NIH 3D Print Exchange | A collection of biomedical 3D printable files and 3D printing resources supported by the National Institutes of Health (NIH). https://www.ncbi.nlm.nih.gov/pubmed/.

73. Derakhshanfar, S.; Mbeleck, R.; Xu, K.; Zhang, X.; Zhong, W.; Xing, M., 3D bioprinting for biomedical devices and tissue engineering: A review of recent trends and advances. *Bioactive Materials* **2018,** *3* (2), 144-156.

74. Jia, W.; Gungor-Ozkerim, P. S.; Zhang, Y. S.; Yue, K.; Zhu, K.; Liu, W.; Pi, Q.; Byambaa, B.; Dokmeci, M. R.; Shin, S. R.; Khademhosseini, A., Direct 3D bioprinting of perfusable vascular constructs using a blend bioink. *Biomaterials* **2016,** *106*, 58-68.

75. Everett, H. HP partners with l'oréal for flexible cosmetics production, metal jet momentum continues. https://3dprintingindustry.com/news/hp-partners-with-loreal-for-flexible-cosmetics-production-metal-jet-momentum-continues-199703/.

76. Beamler, A. M. Business cases: 3D printing in the automotive industry. https://www.beamler.com/3d-printing-in-the-automotive-industry/.

77. Porsche Communication for journalists. Classic parts from a 3D printer. https://newsroom.porsche.com/en/company/porsche-classic-3d-printer-spare-parts-sls-printer-production-cars-innovative-14816.html.

78. (a) DebRoy, T.; Wei, H. L.; Zuback, J. S.; Mukherjee, T.; Elmer, J. W.; Milewski, J. O.; Beese, A. M.; Wilson-Heid, A.; De, A.; Zhang, W., Additive manufacturing of metallic components – Process, structure and properties. *Progress in Materials Science* **2018,** *92*, 112-224; (b) Uhlmann, E.; Kersting, R.; Klein, T. B.; Cruz, M. F.; Borille, A. V., Additive Manufacturing of Titanium Alloy for Aircraft Components. *Procedia CIRP* **2015,** *35*, 55-60.

79. 3D opportunity for aerospace and defense. Additive manufacturing takes flight. https://dupress.deloitte.com/dup-us-en/focus/3d-opportunity/additivemanufacturing-3d-opportunity-in-aerospace.html.

80. Capabilities & Services | SpaceX. http://www.spacex.com/about/capabilities.

81. Grady, J. E.; Halbig, M. C.; Singh, M., *A Fully Nonmetallic Gas Turbine Engine Enabled by Additive Manufacturing*. National Aeronautics and Space Administration, Glenn Research Center: 2015.

82. Zocca, A.; Colombo, P.; Gomes, C. M.; Günster, J., Additive Manufacturing of Ceramics: Issues, Potentialities, and Opportunities. *Journal of the American Ceramic Society* **2015,** *98* (7), 1983-2001.

83. Wu, P.; Wang, J.; Wang, X., A critical review of the use of 3-D printing in the construction industry. *Automation in Construction* **2016,** *68*, 21-31.

84. (a) Labeaga-Martínez, N.; Sanjurjo-Rivo, M.; Díaz-Álvarez, J.; Martínez-Frías, J., Additive manufacturing for a Moon village. *Procedia Manufacturing* **2017,** *13*, 794-801; (b) Khoshnevis, B., Automated construction by contour crafting—related robotics and information technologies. *Automation in Construction* **2004,** *13* (1), 5-19.

85. Hanaphy, P. COBOD clients 3D print three U.S. homes in bid to start tackling affordable housing crisis. https://3dprintingindustry.com/news/cobod-clients-3d-print-three-u-s-homes-in-bid-to-start-tackling-affordable-housing-crisis-198888/.

86. Everett, H. WASP 3D prints sustainable "the house of dust" liveable sculpture. https://3dprintingindustry.com/news/wasp-3d-prints-sustainable-the-house-of-dust-liveable-sculpture-193016/.

87. Mantihal, S.; Kobun, R.; Lee, B.-B., 3D food printing of as the new way of preparing food: A review. *International Journal of Gastronomy and Food Science* **2020,** *22*, 100260.

88. Sun, J.; Zhou, W.; Yan, L.; Huang, D.; Lin, L.-y., Extrusion-based food printing for digitalized food design and nutrition control. *Journal of Food Engineering* **2018,** *220*, 1-11.

89. (a) Lanaro, M.; Forrestal, D. P.; Scheurer, S.; Slinger, D. J.; Liao, S.; Powell, S. K.; Woodruff, M. A., 3D printing complex chocolate objects: Platform design, optimization and evaluation. *Journal of Food Engineering* **2017,** *215*, 13-22; (b) Liu, L.; Meng, Y.; Dai, X.; Chen, K.; Zhu, Y., 3D Printing Complex Egg White Protein Objects: Properties and Optimization. *Food and Bioprocess Technology* **2019,** *12* (2), 267-279.

90. He, C.; Zhang, M.; Fang, Z., 3D printing of food: pretreatment and post-treatment of materials. *Critical Reviews in Food Science and Nutrition* **2020,** *60* (14), 2379-2392.

91. Zhang, T.; Huang, Z.; Yang, T.; Kong, H.; Luan, J.; Wang, A.; Wang, D.; Kuo, W.; Wang, Y.; Liu, C.-T., In situ design of advanced titanium alloy with concentration modulations by additive manufacturing. *Science* **2021,** *374* (6566), 478-482.

92. Madeleine, P. University of Bristol is Recycling Surgical Masks into 3D Printing Materials. https://www.3dnatives.com/en/university-of-bristol-recycling-surgical-masks-3d-printing-materials-100220224/#!

93. (a) Chatterjee, K.; Ghosh, T. K., 3D Printing of Textiles: Potential Roadmap to Printing with Fibers. *Advanced Materials* **2020,** *32* (4), 1902086; (b) Korger, M.; Bergschneider, J.; Lutz, M.; Mahltig, B.; Finsterbusch, K.; Rabe, M., Possible Applications of 3D Printing Technology on Textile Substrates. *IOP Conference Series: Materials Science and Engineering* **2016,** *141*, 012011; (c) Mawale, M. B.; Kuthe, A. M.; Dahake, S. W., Additive layered manufacturing: State-of-the-art applications in product innovation. *Concurrent Engineering* **2016,** *24* (1), 94-102; (d) Cao, Y.; Zhang, G.; Zhang, Y.; Yue, M.; Chen, Y.; Cai, S.; Xie, T.; Feng, X., Direct Fabrication of Stretchable Electronics on a Polymer Substrate with Process-Integrated Programmable Rigidity. *Advanced Functional Materials* **2018,** *28* (50), 1804604.

94. Pérez, M.; Carou, D.; Rubio, E. M.; Teti, R., Current advances in additive manufacturing. *Procedia CIRP* **2020,** *88*, 439-444.

95. (a) Choi, J.; Kwon, O. C.; Jo, W.; Lee, H. J.; Moon, M.-W., 4D Printing Technology: A Review. *3D Printing and Additive Manufacturing* **2015,** *2* (4), 159-167; (b) Tibbits, S., 4D Printing: Multi-Material Shape Change. *Architectural Design* **2014,** *84* (1), 116-121.

96. (a) Cortés, A.; Cosola, A.; Sangermano, M.; Campo, M.; González Prolongo, S.; Pirri, C. F.; Jiménez-Suárez, A.; Chiappone, A., DLP 4D-Printing of Remotely, Modularly, and Selectively Controllable Shape Memory Polymer Nanocomposites Embedding Carbon Nanotubes. *Advanced Functional Materials* **2021,** *31* (50), 2106774; (b) Roselli, L.; Borges Carvalho, N.; Alimenti, F.; Mezzanotte, P.; Orecchini, G.; Virili, M.; Mariotti, C.; Goncalves, R.; Pinho, P., Smart surfaces: Large area electronics systems for internet of things enabled by energy harvesting. *Proceedings of the IEEE* **2014,** *102* (11), 1723-1746.

97. Oropallo, W.; Piegl, L. A., Ten challenges in 3D printing. *Engineering with Computers* **2016,** *32* (1), 135-148.

98. Street, R. A.; Ng, T. N.; Schwartz, D. E.; Whiting, G. L.; Lu, J. P.; Bringans, R. D.; Veres, J., From printed transistors to printed smart systems. *Proceedings of the IEEE* **2015,** *103* (4), 607-618.

99. Yang, J.; Vitale, A.; Bongiovanni, R.; Nie, J., Synthesis and characterization of siloxane photopolymers used for microfluidic devices. *New Journal of Chemistry* **2015,** *39* (4), 2532-2540.

100. Reichardt, C., Solvatochromic Dyes as Solvent Polarity Indicators. *Chemical Reviews* **1994,** *94* (8), 2319-2358.

101. Priimagi, A.; Kaivola, M.; Virkki, M.; Rodríguez, F. J.; Kauranen, M., Suppression Of Chromophore Aggregation In Amorphous Polymeric Materials: Towards More Efficient Photoresponsive Behavior. *Journal of Nonlinear Optical Physics & Materials* **2010,** *19* (01), 57-73.

102. Kausar, A., A review of high performance polymer nanocomposites for packaging applications in electronics and food industries. *Journal of Plastic Film & Sheeting* **2020,** *36* (1), 94-112.

103. Zhang, Y.; Li, H.; Yang, X.; Zhang, T.; Zhu, K.; Si, W.; Liu, Z.; Sun, H., Additive manufacturing of carbon nanotube-photopolymer composite radar absorbing materials. *Polymer Composites* **2018,** *39* (S2), E671-E676.

104. Song, S. Y.; Park, M. S.; Lee, D.; Lee, J. W.; Yun, J. S., Optimization and characterization of high-viscosity ZrO2 ceramic nanocomposite resins for supportless stereolithography. *Materials & Design* **2019,** *180*, 107960.

105. Kim, J. H.; Lee, S.; Wajahat, M.; Jeong, H.; Chang, W. S.; Jeong, H. J.; Yang, J.-R.; Kim, J. T.; Seol, S. K., Three-Dimensional Printing of Highly Conductive Carbon Nanotube Microarchitectures with Fluid Ink. *ACS Nano* **2016,** *10* (9), 8879-8887.

106. Varghese, G.; Moral, M.; Castro-García, M.; López-López, J. J.; Marín-Rueda, J. R.; Yagüe-Alcaraz, V.; Hernández-Afonso, L.; Ruiz-Morales, J. C.; Canales-Vázquez, J., Fabrication and characterisation of

ceramics via low-cost DLP 3D printing. *Boletín de la Sociedad Española de Cerámica y Vidrio* **2018,** *57* (1), 9-18.

107. (a) Weng, Z.; Zhou, Y.; Lin, W.; Senthil, T.; Wu, L., Structure-property relationship of nano enhanced stereolithography resin for desktop SLA 3D printer. *Composites Part A: Applied Science and Manufacturing* **2016,** *88*, 234-242; (b) Palaganas, J. O.; Palaganas, N. B.; Ramos, L. J. I.; David, C. P. C., 3D Printing of Covalent Functionalized Graphene Oxide Nanocomposite via Stereolithography. *ACS Applied Materials & Interfaces* **2019,** *11* (49), 46034-46043.

108. (a) Im, H.; Lee, Y.; Kim, D. H.; Inturu, O.; Liu, N.; Lee, S.; Kwon, S.-J.; Lee, H.-S.; Kim, S., A highly sensitive ultrathin-film iron corrosion sensor encapsulated by an anion exchange membrane embedded in mortar. *Construction and Building Materials* **2017,** *156*, 506-514; (b) Murphy, E. B.; Wudl, F., The world of smart healable materials. *Progress in Polymer Science* **2010,** *35* (1), 223-251.

109. Wang, W.; Srinivasan, V.; Chua, K. C., Extending the lifetime of wireless sensor networks through mobile relays. *IEEE/ACM Transactions on Networking* **2008,** *16* (5), 1108-1120.

110. (a) Wilson, S. A.; Jourdain, R. P. J.; Zhang, Q.; Dorey, R. A.; Bowen, C. R.; Willander, M.; Wahab, Q. U.; Willander, M.; Al-hilli, S. M.; Nur, O.; Quandt, E.; Johansson, C.; Pagounis, E.; Kohl, M.; Matovic, J.; Samel, B.; van der Wijngaart, W.; Jager, E. W. H.; Carlsson, D.; Djinovic, Z.; Wegener, M.; Moldovan, C.; Iosub, R.; Abad, E.; Wendlandt, M.; Rusu, C.; Persson, K., New materials for micro-scale sensors and actuators: An engineering review. *Materials Science and Engineering: R: Reports* **2007,** *56* (1), 1-129; (b) Khan, S.; Lorenzelli, L.; Dahiya, R. S., Technologies for printing sensors and electronics over large flexible substrates: A review. *IEEE Sensors Journal* **2015,** *15* (6), 3164-3185; (c) Dietze, M.; Es-Souni, M., Structural and functional properties of screen-printed PZT–PVDF-TrFE composites. *Sensors and Actuators A: Physical* **2008,** *143* (2), 329-334.

111. (a) Zhang, M.; Li, L.; Wang, M.; Li, T.; Song, K.; Nie, Y.; Ren, B., 3D Printing for Biological Scaffolds using Poly(Ionic Liquid)/Gelatin/Sodium Alginate Ink. *Macromolecular Materials and Engineering* **2021,** *306* (7), 2100084; (b) Truby, R. L.; Wehner, M.; Grosskopf, A. K.; Vogt, D. M.; Uzel, S. G. M.; Wood, R. J.; Lewis, J. A., Soft Somatosensitive Actuators via Embedded 3D Printing. *Advanced Materials* **2018,** *30* (15).

112. Du, Y.; Cai, K.; Chen, S.; Wang, H.; Shen, S. Z.; Donelson, R.; Lin, T., Thermoelectric Fabrics: Toward Power Generating Clothing. *Scientific Reports* **2015,** *5* (1), 6411.

113. Gabriel, S.; Weiner, J., Ueber einige Abkömmlinge des Propylamins. *Berichte der deutschen chemischen Gesellschaft* **1888,** *21* (2), 2669-2679.

114. (a) Welton, T., Ionic liquids: a brief history. *Biophysical Reviews* **2018,** *10* (3), 691-706; (b) Dubal, D. P.; Chodankar, N. R.; Kim, D.-H.; Gomez-Romero, P., Towards flexible solid-state supercapacitors for smart and wearable electronics. *Chemical Society Reviews* **2018,** *47* (6), 2065-2129; (c) Smiglak, M.; Pringle, J. M.; Lu, X.; Han, L.; Zhang, S.; Gao, H.; MacFarlane, D. R.; Rogers, R. D., Ionic liquids for energy, materials, and medicine. *Chemical Communications* **2014,** *50* (66), 9228-9250.

115. (a) Evans, D. F.; Chen, S. H.; Schriver, G. W.; Arnett, E. M., Thermodynamics of solution of nonpolar gases in a fused salt. "Hydrophobic bonding" behavior in a nonaqueous system. *J Am Chem Soc* **1981**, 481–482; (b) Fischer, T.; Sethi, A.; Welton, T.; Woolf, J., Diels-Alder reactions in room-temperature ionic liquids. *Tetrahedron Letters* **1999,** *40* (4), 793-796; (c) Badri, M.; Brunet, J.-J.; Perron, R., Ionic liquids as solvents for the regioselective O-alkylation of C/O ambident nucleophiles. *Tetrahedron Letters* **1992,** *33* (31), 4435-4438.

116. (a) Earle, M. J.; Seddon, K. R., Ionic liquids. Green solvents for the future. *Pure and Applied Chemistry* **2000,** *72* (7), 1391-1398; (b) Seddon, K. R., Ionic Liquids for Clean Technology. *Journal of Chemical Technology & Biotechnology* **1997,** *68* (4), 351-356.

117. (a) Swatloski, R. P.; Holbrey, J. D.; Rogers, R. D., Ionic liquids are not always green: Hydrolysis of 1-butyl-3- methylimidazolium hexafluorophosphate. *Green Chemistry* **2003,** *5* (4), 361-363; (b) Thuy Pham, T. P.; Cho, C. W.; Yun, Y. S., Environmental fate and toxicity of ionic liquids: A review. *Water Research* **2010,** *44* (2), 352-372; (c) Cevasco, G.; Chiappe, C., Are ionic liquids a proper solution to current environmental challenges? *Green Chemistry* **2014,** *16* (5), 2375-2385.

118. Welton, T., Solvents and sustainable chemistry. *Proceedings of the Royal Society A: Mathematical, Physical and Engineering Sciences* **2015,** *471* (2183), 20150502.

119. (a) Wasserscheid, P.; Keim, W., Ionic Liquids—New “Solutions” for Transition Metal Catalysis. *Angewandte Chemie International Edition* **2000,** *39* (21), 3772-3789; (b) Dupont, J.; de Souza, R. F.; Suarez, P. A. Z., Ionic Liquid (Molten Salt) Phase Organometallic Catalysis. *Chemical Reviews* **2002,** *102* (10), 3667-3692.

120. Poole, C. F.; Furton, K. G.; Kersten, B. R., Liquid Organic Salt Phases for Gas Chromatography. *Journal of Chromatographic Science* **1986,** *24* (9), 400-409.

121. Zeng, S.; Zhang, X.; Bai, L.; Zhang, X.; Wang, H.; Wang, J.; Bao, D.; Li, M.; Liu, X.; Zhang, S., Ionic-Liquid-Based CO2 Capture Systems: Structure, Interaction and Process. *Chemical Reviews* **2017,** *117* (14), 9625-9673.

122. (a) Liu, H.; Liu, Y.; Li, J., Ionic liquids in surface electrochemistry. *Physical Chemistry Chemical Physics* **2010,** *12* (8), 1685-1697; (b) Medetalibeyoğlu, H.; Manap, S.; Yokuş, Ö. A.; Beytur, M.; Kardaş, F.; Akyıldırım, O.; Özkan, V.; Yüksek, H.; Yola, M. L.; Atar, N., Fabrication of Pt/Pd Nanoparticles/Polyoxometalate/Ionic Liquid Nanohybrid for Electrocatalytic Oxidation of Methanol. *Journal of The Electrochemical Society* **2018,** *165* (5), F338-F341; (c) Majidi, L.; Yasaei, P.; Warburton, R. E.; Fuladi, S.; Cavin, J.; Hu, X.; Hemmat, Z.; Cho, S. B.; Abbasi, P.; Vörös, M.; Cheng, L.; Sayahpour, B.; Bolotin, I. L.; Zapol, P.; Greeley, J.; Klie, R. F.; Mishra, R.; Khalili-Araghi, F.; Curtiss, L. A.; Salehi-Khojin, A., New Class of Electrocatalysts Based on 2D Transition Metal Dichalcogenides in Ionic Liquid. *Advanced Materials* **2019,** *31* (4), 1804453; (d) Lim, H.-K.; Kwon, Y.; Kim, H. S.; Jeon, J.; Kim, Y.-H.; Lim, J.-A.; Kim, B.-S.; Choi, J.; Kim, H., Insight into the Microenvironments of the Metal–Ionic Liquid Interface during Electrochemical CO2 Reduction. *ACS Catalysis* **2018,** *8* (3), 2420-2427.

123. Egorova, K. S.; Gordeev, E. G.; Ananikov, V. P., Biological Activity of Ionic Liquids and Their Application in Pharmaceutics and Medicine. *Chemical Reviews* **2017,** *117* (10), 7132-7189.

124. Nancarrow, P.; Mohammed, H., Ionic Liquids in Space Technology – Current and Future Trends. *ChemBioEng Reviews* **2017,** *4* (2), 106-119.

125. Radai, Z.; Kiss, N. Z.; Keglevich, G., An Overview of the Applications of Ionic Liquids as Catalysts and Additives in Organic Chemical Reactions. *Curr. Org. Chem.* **2018,** *22* (6), 533-556.

126. (a) Lee, J. W.; Shin, J. Y.; Chun, Y. S.; Jang, H. B.; Song, C. E.; Lee, S.-g., Toward Understanding the Origin of Positive Effects of Ionic Liquids on Catalysis: Formation of More Reactive Catalysts and Stabilization of Reactive Intermediates and Transition States in Ionic Liquids. *Accounts of Chemical Research* **2010,** *43* (7), 985-994; (b) Zhang, Q.; Zhang, S.; Deng, Y., Recent advances in ionic liquid catalysis. *Green Chemistry* **2011,** *13* (10), 2619-2637.

127. (a) Wang, D.; Zhao, F.; Zhu, G.; Xia, C., Production of eco-friendly poly(oxymethylene) dimethyl ethers catalyzed by acidic ionic liquid: A kinetic investigation. *Chemical Engineering Journal* **2018,** *334*, 2616-2624; (b) Roman, F. F.; Ribeiro, A. E.; Queiroz, A.; Lenzi, G. G.; Chaves, E. S.; Brito, P., Optimization and kinetic study of biodiesel production through esterification of oleic acid applying ionic liquids as catalysts. *Fuel* **2019,** *239*, 1231-1239; (c) Vieira, M. O.; Monteiro, W. F.; Neto, B. S.; Ligabue, R.; Chaban, V. V.; Einloft, S., Surface Active Ionic Liquids as Catalyst for CO2 Conversion to Propylene Carbonate. *Catalysis Letters* **2018,** *148* (1), 108-118.

128. Dai, J.; Patti, A. F.; Longé, L.; Garnier, G.; Saito, K., Oxidized Lignin Depolymerization using Formate Ionic Liquid as Catalyst and Solvent. *ChemCatChem* **2017,** *9* (14), 2684-2690.

129. (a) Tiago, G. A. O.; Matias, I. A. S.; Ribeiro, A. P. C.; Martins, L. M. D. R. S., Application of Ionic Liquids in Electrochemistry—Recent Advances. *Molecules* **2020,** *25* (24), 5812; (b) Armand, M.; Endres, F.; MacFarlane, D. R.; Ohno, H.; Scrosati, B., Ionic-liquid materials for the electrochemical challenges of the future. *Nature Materials* **2009,** *8* (8), 621-629.

130. (a) Galiński, M.; Lewandowski, A.; Stępniak, I., Ionic liquids as electrolytes. *Electrochimica Acta* **2006,** *51* (26), 5567-5580; (b) Watanabe, M.; Thomas, M. L.; Zhang, S.; Ueno, K.; Yasuda, T.; Dokko, K., Application of Ionic Liquids to Energy Storage and Conversion Materials and Devices. *Chemical Reviews*

2017, *117* (10), 7190-7239; (c) Jónsson, E., Ionic liquids as electrolytes for energy storage applications – A modelling perspective. *Energy Storage Materials* **2020,** *25*, 827-835; (d) Stettner, T.; Huang, P.; Goktas, M.; Adelhelm, P.; Balducci, A., Mixtures of glyme and aprotic-protic ionic liquids as electrolytes for energy storage devices. *The Journal of Chemical Physics* **2018,** *148* (19), 193825; (e) Sevilla, M.; Ferrero, G. A.; Diez, N.; Fuertes, A. B., One-step synthesis of ultra-high surface area nanoporous carbons and their application for electrochemical energy storage. *Carbon* **2018,** *131*, 193-200.

131. (a) Chapman Varela, J.; Sankar, K.; Hino, A.; Lin, X.; Chang, W.-s.; Coker, D.; Grinstaff, M., Piperidinium ionic liquids as electrolyte solvents for sustained high temperature supercapacitor operation. *Chemical Communications* **2018,** *54* (44), 5590-5593; (b) Zaccagnini, P.; di Giovanni, D.; Gomez, M. G.; Passerini, S.; Varzi, A.; Lamberti, A., Flexible and high temperature supercapacitor based on laser-induced graphene electrodes and ionic liquid electrolyte, a de-rated voltage analysis. *Electrochimica Acta* **2020,** *357*, 136838; (c) Suominen, M.; Lehtimäki, S.; Yewale, R.; Damlin, P.; Tuukkanen, S.; Kvarnström, C., Electropolymerized polyazulene as active material in flexible supercapacitors. *Journal of Power Sources* **2017,** *356*, 181-190.

132. (a) Navarra, M. A.; Fujimura, K.; Sgambetterra, M.; Tsurumaki, A.; Panero, S.; Nakamura, N.; Ohno, H.; Scrosati, B., New Ether-functionalized Morpholinium- and Piperidinium-based Ionic Liquids as Electrolyte Components in Lithium and Lithium–Ion Batteries. *ChemSusChem* **2017,** *10* (11), 2496-2504; (b) Kerner, M.; Johansson, P., Pyrrolidinium FSI and TFSI-Based Polymerized Ionic Liquids as Electrolytes for High-Temperature Lithium-Ion Batteries. *Batteries* **2018,** *4* (1), 10.

133. (a) Yang, D.; Zhu, Q.; Han, B., Electroreduction of CO2 in Ionic Liquid-Based Electrolytes. *The Innovation* **2020,** *1* (1), 100016; (b) Pardal, T.; Messias, S.; Sousa, M.; Machado, A. S. R.; Rangel, C. M.; Nunes, D.; Pinto, J. V.; Martins, R.; da Ponte, M. N., Syngas production by electrochemical CO2 reduction in an ionic liquid based-electrolyte. *Journal of CO2 Utilization* **2017,** *18*, 62-72.

134. (a) Sharma, T.; Gultekin, B.; Dhapola, P. S.; Sahoo, N. G.; Kumar, S.; Agarwal, D.; Jun, H. K.; Singh, D.; Nath, G.; Singh, P. K.; Singh, A., Ionic liquid doped Poly (methyl methacrylate) for energy applications. *Journal of Molecular Liquids* **2022,** *352*, 118494; (b) Hao, X.; Wenren, H.; Wang, X.; Xia, X.; Tu, J., A gel polymer electrolyte based on PVDF-HFP modified double polymer matrices via ultraviolet polymerization for lithium-sulfur batteries. *Journal of Colloid and Interface Science* **2019,** *558*, 145-154.

135. (a) Gao, G.; Wang, J.; Zhang, X.; Li, H.; Wang, L.; Liu, T., An ionic liquid enhanced gel polymer electrolyte for high performance lithium-metal batteries based on sulfurized polyacrylonitrile cathode. *Composites Communications* **2022,** *31*, 101100; (b) Ding, Y.; Zhang, J.; Chang, L.; Zhang, X.; Liu, H.; Jiang, L., Preparation of High-Performance Ionogels with Excellent Transparency, Good Mechanical Strength, and High Conductivity. *Advanced Materials* **2017,** *29* (47), 1704253.

136. (a) Kee, S.; Kim, N.; Kim, B. S.; Park, S.; Jang, Y. H.; Lee, S. H.; Kim, J.; Kim, J.; Kwon, S.; Lee, K., Controlling Molecular Ordering in Aqueous Conducting Polymers Using Ionic Liquids. *Adv Mater* **2016,** *28* (39), 8625-8631; (b) de Izarra, A.; Park, S.; Lee, J.; Lansac, Y.; Jang, Y. H., Ionic Liquid Designed for PEDOT:PSS Conductivity Enhancement. *J Am Chem Soc* **2018,** *140* (16), 5375-5384.

137. Plechkova, N. V.; Seddon, K. R., Applications of ionic liquids in the chemical industry. *Chemical Society Reviews* **2008,** *37* (1), 123-150.

138. (a) Mehnert, C. P., Supported Ionic Liquid Catalysis. *Chemistry – A European Journal* **2005,** *11* (1), 50-56; (b) Karbass, N.; Sans, V.; Garcia-Verdugo, E.; Burguete, M. I.; Luis, S. V., Pd(0) supported onto monolithic polymers containing IL-like moieties. Continuous flow catalysis for the Heck reaction in near-critical EtOH. *Chemical Communications* **2006,** (29), 3095-3097; (c) Burguete, M. I.; Galindo, F.; Garcia-Verdugo, E.; Karbass, N.; Luis, S. V., Polymer supported ionic liquid phases (SILPs) versus ionic liquids (ILs): how much do they look alike. *Chem Commun (Camb)* **2007,** (29), 3086-8.

139. (a) Patil, R. V.; Chavan, J. U.; Dalal, D. S.; Shinde, V. S.; Beldar, A. G., Biginelli Reaction: Polymer Supported Catalytic Approaches. *ACS Combinatorial Science* **2019,** *21* (3), 105-148; (b) Osada, I.; de Vries, H.; Scrosati, B.; Passerini, S., Ionic-Liquid-Based Polymer Electrolytes for Battery Applications. *Angewandte Chemie International Edition* **2016,** *55* (2), 500-513.

140. (a) Hirao, M.; Ito, K.; Ohno, H., Preparation and polymerization of new organic molten salts; N-alkylimidazolium salt derivatives. *Electrochimica Acta* **2000,** *45* (8), 1291-1294; (b) Yoshizawa, M.; Ogihara, W.; Ohno, H., Novel polymer electrolytes prepared by copolymerization of ionic liquid monomers. *Polymers for Advanced Technologies* **2002,** *13* (8), 589-594; (c) Ogihara, W.; Washiro, S.; Nakajima, H.; Ohno, H., Effect of cation structure on the electrochemical and thermal properties of ion conductive polymers obtained from polymerizable ionic liquids. *Electrochimica Acta* **2006,** *51* (13), 2614-2619; (d) Yoshizawa, M.; Hirao, M.; Ito-Akita, K.; Ohno, H., Ion conduction in zwitterionic-type molten salts and their polymers. *Journal of Materials Chemistry* **2001,** *11* (4), 1057-1062.

141. He, X.; Yang, Y.; Song, H.; Wang, S.; Zhao, H.; Wei, D., Polyanionic Composite Membranes Based on Bacterial Cellulose and Amino Acid for Antimicrobial Application. *ACS Applied Materials & Interfaces* **2020,** *12* (13), 14784-14796.

142. Nishimura, N.; Ohno, H., 15th anniversary of polymerised ionic liquids. *Polymer* **2014,** *55* (16), 3289-3297.

143. Yuan, J.; Mecerreyes, D.; Antonietti, M., Poly(ionic liquid)s: An update. *Progress in Polymer Science* **2013,** *38* (7), 1009-1036.

144. (a) Kausar, A., Research Progress in Frontiers of Poly(Ionic Liquid)s: A Review. *Polymer-Plastics Technology and Engineering* **2017,** *56* (17), 1823-1838; (b) Eftekhari, A.; Saito, T., Synthesis and properties of polymerized ionic liquids. *European Polymer Journal* **2017,** *90*, 245-272.

145. Lu, W.; Fadeev, A. G.; Qi, B.; Smela, E.; Mattes, B. R.; Ding, J.; Spinks, G. M.; Mazurkiewicz, J.; Zhou, D.; Wallace, G. G.; MacFarlane, D. R.; Forsyth, S. A.; Forsyth, M., Use of ionic liquids for π-conjugated polymer electrochemical devices. *Science* **2002,** *297* (5583), 983-987.

146. (a) Green, O.; Grubjesic, S.; Lee, S.; Firestone, M. A., The Design of Polymeric Ionic Liquids for the Preparation of Functional Materials. *Polymer Reviews* **2009,** *49* (4), 339-360; (b) Lu, J.; Yan, F.; Texter, J., Advanced applications of ionic liquids in polymer science. *Progress in Polymer Science* **2009,** *34* (5), 431-448.

147. (a) Qiu, B.; Lin, B.; Si, Z.; Qiu, L.; Chu, F.; Zhao, J.; Yan, F., Bis-imidazolium-based anion-exchange membranes for alkaline fuel cells. *Journal of Power Sources* **2012,** *217*, 329-335; (b) Qiu, B.; Lin, B.; Qiu, L.; Yan, F., Alkaline imidazolium- and quaternary ammonium-functionalized anion exchange membranes for alkaline fuel cell applications. *Journal of Materials Chemistry* **2012,** *22* (3), 1040-1045; (c) Lin, B.; Qiu, L.; Lu, J.; Yan, F., Cross-Linked Alkaline Ionic Liquid-Based Polymer Electrolytes for Alkaline Fuel Cell Applications. *Chemistry of Materials* **2010,** *22* (24), 6718-6725.

148. (a) Trigueiro, J. P. C.; Lavall, R. L.; Silva, G. G., Supercapacitors based on modified graphene electrodes with poly(ionic liquid). *Journal of Power Sources* **2014,** *256*, 264-273; (b) Ayalneh Tiruye, G.; Muñoz-Torrero, D.; Palma, J.; Anderson, M.; Marcilla, R., All-solid state supercapacitors operating at 3.5 V by using ionic liquid based polymer electrolytes. *Journal of Power Sources* **2015,** *279*, 472-480.

149. Shaplov, A. S.; Ponkratov, D. O.; Vygodskii, Y. S., Poly(ionic liquid)s: Synthesis, properties, and application. *Polymer Science Series B* **2016,** *58* (2), 73-142.

150. (a) Prabhu Charan, K. T.; Pothanagandhi, N.; Vijayakrishna, K.; Sivaramakrishna, A.; Mecerreyes, D.; Sreedhar, B., Poly(ionic liquids) as “smart” stabilizers for metal nanoparticles. *European Polymer Journal* **2014,** *60*, 114-122; (b) Sun, J.-K.; Kochovski, Z.; Zhang, W.-Y.; Kirmse, H.; Lu, Y.; Antonietti, M.; Yuan, J., General Synthetic Route toward Highly Dispersed Metal Clusters Enabled by Poly(ionic liquid)s. *Journal of the American Chemical Society* **2017,** *139* (26), 8971-8976.

151. (a) Liu, W.; Wang, D.; Duan, Y.; Zhang, Y.; Bian, F., Palladium supported on poly (ionic liquid) entrapped magnetic nanoparticles as a highly efficient and reusable catalyst for the solvent-free Heck reaction. *Tetrahedron Letters* **2015,** *56* (14), 1784-1789; (b) Pourjavadi, A.; Hosseini, S. H.; AghayeeMeibody, S. A.; Hosseini, S. T., Poly(basic ionic liquid) coated magnetic nanoparticles: High-loaded supported basic ionic liquid catalyst. *Comptes Rendus Chimie* **2013,** *16* (10), 906-911; (c) Vijayakrishna, K.; Charan, K. T. P.; Manojkumar, K.; Venkatesh, S.; Pothanagandhi, N.; Sivaramakrishna, A.; Mayuri, P.; Kumar, A. S.; Sreedhar, B., Ni Nanoparticles Stabilized by Poly(Ionic Liquids) as Chemoselective and

Magnetically Recoverable Catalysts for Transfer Hydrogenation Reactions of Carbonyl Compounds. *ChemCatChem* **2016,** *8* (6), 1139-1145.

152. Li, M.; Liu, Y.; Ding, S.; Zhu, A.; Shi, G., In situ synthesis of poly(ionic liquid)–Pt nanoparticle composite in glass capillary for the electrocatalytic reduction of oxygen. *Analyst* **2014,** *139* (22), 5964-5969.

153. (a) Isik, M.; Fernandes, A. M.; Vijayakrishna, K.; Paulis, M.; Mecerreyes, D., Preparation of poly(ionic liquid) nanoparticles and their novel application as flocculants for water purification. *Polymer Chemistry* **2016,** *7* (8), 1668-1674; (b) Yu, L.; Zhang, Y.; Wang, Y.; Zhang, H.; Liu, J., High flux, positively charged loose nanofiltration membrane by blending with poly (ionic liquid) brushes grafted silica spheres. *Journal of Hazardous Materials* **2015,** *287*, 373-383; (c) Chatterjee, P.; Nofen, E. M.; Xu, W.; Hom, C.; Jiang, H.; Dai, L. L., Pyrrole-based poly(ionic liquids) as efficient stabilizers for formation of hollow multi-walled carbon nanotubes particles. *Journal of Colloid and Interface Science* **2017,** *504*, 140-148; (d) Chen, S.; Xiang, Y.; Banks, M. K.; Peng, C.; Xu, W.; Wu, R., Polyoxometalate-coupled MXene nanohybrid via poly(ionic liquid) linkers and its electrode for enhanced supercapacitive performance. *Nanoscale* **2018,** *10* (42), 20043-20052.

154. (a) Marcilla, R.; Ochoteco, E.; Pozo-Gonzalo, C.; Grande, H.; Pomposo, J. A.; Mecerreyes, D., New Organic Dispersions of Conducting Polymers Using Polymeric Ionic Liquids as Stabilizers. *Macromolecular Rapid Communications* **2005,** *26* (14), 1122-1126; (b) Kim, T. Y.; Lee, T. H.; Kim, J. E.; Kasi, R. M.; Sung, C. S. P.; Suh, K. S., Organic solvent dispersion of poly(3,4-ethylenedioxythiophene) with the use of polymeric ionic liquid. *Journal of Polymer Science Part A: Polymer Chemistry* **2008,** *46* (20), 6872-6879; (c) Kim, T.; Tung, T. T.; Lee, T.; Kim, J.; Suh, K. S., Poly(ionic liquid)-mediated hybridization of single-walled carbon nanotubes and conducting polymers. *Chem Asian J* **2010,** *5* (2), 256-60; (d) Tung, T. T.; Kim, T. Y.; Shim, J. P.; Yang, W. S.; Kim, H.; Suh, K. S., Poly(ionic liquid)-stabilized graphene sheets and their hybrid with poly(3,4-ethylenedioxythiophene). *Organic Electronics* **2011,** *12*, 2215–2224.

155. (a) Hong, S. H.; Tung, T. T.; Huyen Trang, L. K.; Kim, T. Y.; Suh, K. S., Preparation of single-walled carbon nanotube (SWNT) gel composites using poly(ionic liquids). *Colloid and Polymer Science* **2010,** *288* (9), 1013-1018; (b) Fukushima, T.; Kosaka, A.; Ishimura, Y.; Yamamoto, T.; Takigawa, T.; Ishii, N.; Aida, T., Molecular Ordering of Organic Molten Salts Triggered by Single-Walled Carbon Nanotubes. *Science* **2003,** *300* (5628), 2072.

156. (a) Grollmisch, A.; Kragl, U.; Großeheilmann, J., Enzyme Immobilization in Polymerized Ionic Liquids-based Hydrogels for Active and Reusable Biocatalysts. *SynOpen* **2018,** *02* (02), 0192-0199; (b) Hosseini, S. H.; Hosseini, S. A.; Zohreh, N.; Yaghoubi, M.; Pourjavadi, A., Covalent Immobilization of Cellulase Using Magnetic Poly(ionic liquid) Support: Improvement of the Enzyme Activity and Stability. *Journal of Agricultural and Food Chemistry* **2018,** *66* (4), 789-798; (c) Santana, J. L.; Oliveira, J. M.; Nascimento, J. S.; Mattedi, S.; Krause, L. C.; Freitas, L. S.; Cavalcanti, E. B.; Pereira, M. M.; Lima, Á. S.; Soares, C. M. F., Continuous flow reactor based with an immobilized biocatalyst for the continuous enzymatic transesterification of crude coconut oil. *Biotechnology and Applied Biochemistry* **2020,** *67* (3), 404-413.

157. Texter, J., Anion Responsive Imidazolium-Based Polymers. *Macromolecular Rapid Communications* **2012,** *33* (23), 1996-2014.

158. Gupta, N.; Liang, Y. N.; Hu, X., Thermally responsive ionic liquids and polymeric ionic liquids: emerging trends and possibilities *Current opinion in Chemical Engineering* **2019,** *25*, 43-50.

159. Green, M. D.; Long, T. E., Designing Imidazole-Based Ionic Liquids and Ionic Liquid Monomers for Emerging Technologies. *Polym. Rev.* **2009,** *49* (4), 291-314.

160. Xiang, S.; He, X.; Zheng, F.; Lu, Q., Multifunctional flexible sensors based on ionogel composed entirely of ionic liquid with long alkyl chains for enhancing mechanical properties. *Chemical Engineering Journal* **2022,** *439*, 135644.

161. Döbbelin, M.; Arias, G.; Loinaz, I.; Llarena, I.; Mecerreyes, D.; Moya, S., Tuning Surface Wettability of Poly(3-sulfopropyl methacrylate) Brushes by Cationic Surfactant-Driven Interactions. *Macromolecular Rapid Communications* **2008,** *29* (11), 871-875.

162. (a) Tiruye, G. A.; Muñoz-Torrero, D.; Palma, J.; Anderson, M.; Marcilla, R., Performance of solid state supercapacitors based on polymer electrolytes containing different ionic liquids. *Journal of Power Sources* **2016,** *326*, 560-568; (b) Ponkratov, D. O.; Lozinskaya, E. I.; Vlasov, P. S.; Aubert, P.-H.; Plesse, C.; Vidal, F.; Vygodskii, Y. S.; Shaplov, A. S., Synthesis of novel families of conductive cationic poly(ionic liquid)s and their application in all-polymer flexible pseudo-supercapacitors. *Electrochimica Acta* **2018,** *281*, 777-788; (c) Teodoro, R. M.; Tomé, L. C.; Mantione, D.; Mecerreyes, D.; Marrucho, I. M., Mixing poly(ionic liquid)s and ionic liquids with different cyano anions: Membrane forming ability and CO 2 /N 2 separation properties. *Journal of Membrane Science* **2018,** *552*, 341-348.

163. (a) Fdz De Anastro, A.; Casado, N.; Wang, X.; Rehmen, J.; Evans, D.; Mecerreyes, D.; Forsyth, M.; Pozo-Gonzalo, C., Poly(ionic liquid) iongels for all-solid rechargeable zinc/PEDOT batteries. *Electrochimica Acta* **2018,** *278*, 271-278; (b) Sen, S.; Goodwin, S. E.; Barbará, P. V.; Rance, G. A.; Wales, D.; Cameron, J. M.; Sans, V.; Mamlouk, M.; Scott, K.; Walsh, D. A., Gel–Polymer Electrolytes Based on Poly(Ionic Liquid)/Ionic Liquid Networks. *ACS Applied Polymer Materials* **2021,** *3* (1), 200-208.

164. Marcilla, R.; Alcaide, F.; Sardon, H.; Pomposo, J. A.; Pozo-Gonzalo, C.; Mecerreyes, D., Tailor-made polymer electrolytes based upon ionic liquids and their application in all-plastic electrochromic devices. *Electrochemistry Communications* **2006,** *8* (3), 482-488.

165. Jeon, N.; Hwang, D. K.; Kang, Y. S.; Im, S. S.; Kim, D.-W., Quasi-solid-state dye-sensitized solar cells assembled with polymeric ionic liquid and poly(3,4-ethylenedioxythiophene) counter electrode. *Electrochemistry Communications* **2013,** *34*, 1-4.

166. Vidal, F.; Plesse, C.; Teyssie, D.; Chevrot, C., Long-life air working conducting semi-IPN/ionic liquid based actuator. *Synth Met* **2004,** *182*, 247.

167. Sans, V.; Karbass, N.; Burguete, M. I.; Compan, V.; Garcia-Verdugo, E.; Luis, S. V.; Pawlak, M., Polymer-supported ionic-liquid-like phases (SILLPs): transferring ionic liquid properties to polymeric matrices. *Chemistry* **2011,** *17* (6), 1894-906.

168. Appetecchi, G. B.; Kim, G. T.; Montanino, M.; Carewska, M.; Marcilla, R.; Mecerreyes, D.; De Meatza, I., Ternary polymer electrolytes containing pyrrolidinium-based polymeric ionic liquids for lithium batteries. *Journal of Power Sources* **2010,** *195* (11), 3668-3675.

169. Balli, B.; Şavk, A.; Şen, F., Graphene and polymer composites for supercapacitor applications. **2019**, 123-151.

170. de Jong, M. P.; van Ijzendoorn, L. J.; de Voigt, M. J. A., Stability of the interface between indium-tin-oxide and poly(3,4-ethylenedioxythiophene)/poly(styrenesulfonate) in polymer light-emitting diodes. *Appl. Phys. Lett.* **2000,** *77* (14), 2255-2257.

171. (a) Pozo-Gonzalo, C.; Marcilla, R.; Salsamendi, M.; Mecerreyes, D.; Pomposo, J. A.; Rodríguez, J.; Bolink, H. J., PEDOT:Poly(1-vinyl-3-ethylimidazolium) dispersions as alternative materials for optoelectronic devices. *Journal of Polymer Science Part A: Polymer Chemistry* **2008,** *46* (9), 3150-3154; (b) Kim, T.; Suh, M.; Kwon, S. J.; Lee, T. H.; Kim, J. E.; Lee, Y. J.; Kim, J. H.; Hong, M.; Suh, K. S., Poly(3,4-ethylenedioxythiophene) Derived from Poly(ionic liquid) for the Use as Hole-Injecting Material in Organic Light-Emitting Diodes. *Macromol Rapid Commun* **2009,** *30* (17), 1477-82.

172. Yella, A.; Lee, H.-W.; Tsao, H. N.; Yi, C.; Chandiran, A. K.; Nazeeruddin, M. K.; Diau, E. W.-G.; Yeh, C.-Y.; Zakeeruddin, S. M.; Grätzel, M., Porphyrin-Sensitized Solar Cells with Cobalt (II/III)–Based Redox Electrolyte Exceed 12 Percent Efficiency. *Science* **2011,** *334* (6056), 629.

173. Gracia, R.; Vijayakrishna, K.; Mecerreyes, D., Poly(ionic liquid)s with redox active counter-anions: All-in-one reactants and stabilizers for the synthesis of functional colloids. *Reactive and Functional Polymers* **2014,** *79*, 54-58.

174. Tung, T. T.; Kim, T. Y.; Suh, K. S., Nanocomposites of single-walled carbon nanotubes and poly(3,4-ethylenedioxythiophene) for transparent and conductive film. *Organic Electronics* **2011,** *12*, 22-28.

175. Tung, T. T.; Losic, D.; Park, S. J.; Feller, J. F.; Kim, T., Core-shell nanostructured hybrid composites for volatile organic compound detection. *Int J Nanomedicine* **2015,** *10 Spec Iss*, 203-14.

176. Kwona, S. J.; Kima, T. Y.; Leeb, B. S.; Leec, T. H.; Kimb, J. E.; Suh, K. S., Elastomeric conducting polymer nano-composites derived from ionic liquid polymer stabilized-poly(3,4-ethylenedioxythiophene). *Synthetic Metals* **2010,** *160*, 1092–1096.

177. Xia, R.; Gao, X. X.; Zhang, Y.; Drigo, N.; Queloz, V. I. E.; Tirani, F. F.; Scopelliti, R.; Huang, Z.; Fang, X.; Kinge, S.; Fei, Z.; Roldan-Carmona, C.; Nazeeruddin, M. K.; Dyson, P. J., An Efficient Approach to Fabricate Air-Stable Perovskite Solar Cells via Addition of a Self-Polymerizing Ionic Liquid. *Adv Mater* **2020,** *32* (40), e2003801.

178. Muñoz-Bonilla, A.; Fernández-García, M., Poly(ionic liquid)s as antimicrobial materials. *European Polymer Journal* **2018,** *105*, 135-149.

179. Jose, R. R.; Rodriguez, M. J.; Dixon, T. A.; Omenetto, F.; Kaplan, D. L., Evolution of Bioinks and Additive Manufacturing Technologies for 3D Bioprinting. *ACS Biomaterials Science & Engineering* **2016,** *2* (10), 1662-1678.

180. Elliott, G.; Kemp, R.; MacFarlane, D., The Development of Ionic Liquids for Biomedical Applications — Prospects and Challenges. *ACS Symposium Series* **2009,** *1030*, 95-105.

181. Noshadi, I.; Walker, B. W.; Portillo-Lara, R.; Shirzaei Sani, E.; Gomes, N.; Aziziyan, M. R.; Annabi, N., Engineering Biodegradable and Biocompatible Bio-ionic Liquid Conjugated Hydrogels with Tunable Conductivity and Mechanical Properties. *Scientific Reports* **2017,** *7* (1).

182. Parra-Cabrera, C.; Achille, C.; Kuhn, S.; Ameloot, R., 3D printing in chemical engineering and catalytic technology: structured catalysts, mixers and reactors. *Chemical Society Reviews* **2018,** *47* (1), 209-230.

183. (a) Penny, M. R.; Rao, Z. X.; Thavarajah, R.; Ishaq, A.; Bowles, B. J.; Hilton, S. T., 3D printed tetrakis(triphenylphosphine)palladium (0) impregnated stirrer devices for Suzuki–Miyaura cross-coupling reactions. *Reaction Chemistry & Engineering* **2022**; (b) Penny, M. R.; Hilton, S. T., Design and development of 3D printed catalytically-active stirrers for chemical synthesis. *Reaction Chemistry & Engineering* **2020,** *5* (5), 853-858.

184. Tubío, C. R.; Azuaje, J.; Escalante, L.; Coelho, A.; Guitián, F.; Sotelo, E.; Gil, A., 3D printing of a heterogeneous copper-based catalyst. *Journal of Catalysis* **2016,** *334*, 110-115.

185. Oliveira, L. V. F.; Limousy, L.; Bennici, S.; Josien, L.; Hajjar-Garreau, S.; Goddard, M.-L.; Bizeto, M. A.; Camilo, F. F., Facile Elaboration of Wet Cellulose Film as Catalyst Support of MnOx Nanoparticles for the Catalytic Oxidation of Dyes in Absence of Light. *Clean Technologies* **2021,** *3* (2), 288-298.

186. Sans, V., Emerging trends in flow chemistry enabled by 3D printing: Robust reactors, biocatalysis and electrochemistry. *Current Opinion in Green and Sustainable Chemistry* **2020,** *25*, 100367.

187. Valverde, D.; Porcar, R.; Zanatta, M.; Alcalde, S.; Altava, B.; Sans, V.; García-Verdugo, E., Towards highly efficient continuous-flow catalytic carbon dioxide cycloadditions with additively manufactured reactors. *Green Chemistry* **2022,** *24* (8), 3300-3308.

188. (a) McNeice, P.; Marr, P. C.; Marr, A. C., Basic ionic liquids for catalysis: the road to greater stability. *Catalysis Science & Technology* **2021,** *11* (3), 726-741; (b) Pârvulescu, V. I.; Hardacre, C., Catalysis in Ionic Liquids. *Chemical Reviews* **2007,** *107* (6), 2615-2665; (c) Welton, T., Ionic liquids in catalysis. *Coordination Chemistry Reviews* **2004,** *248* (21), 2459-2477.

189. (a) Ramnial, T.; Taylor, S. A.; Bender, M. L.; Gorodetsky, B.; Lee, P. T. K.; Dickie, D. A.; McCollum, B. M.; Pye, C. C.; Walsby, C. J.; Clyburne, J. A. C., Carbon-Centered Strong Bases in Phosphonium Ionic Liquids. *The Journal of Organic Chemistry* **2008,** *73* (3), 801-812; (b) Zanger, M.; Vander Werf, C. A.; McEwen, W. E., Kinetic Study Of The Decomposition Of Quaternary Phosphonium Hydroxides. *Journal of the American Chemical Society* **1959,** *81* (14), 3806-3807.

190. Raiguel, S.; Thomas, J.; Binnemans, K.; Dehaen, W., Multi-Gram Scale Synthesis of 1,2,3-Triazolium Ionic Liquids and Assay of Their Resistance towards Bases. *European Journal of Organic Chemistry* **2018,** *2018* (35), 4850-4856.

191. Vasilyev, D.; Shirzadi, E.; Rudnev, A. V.; Broekmann, P.; Dyson, P. J., Pyrazolium Ionic Liquid Co-catalysts for the Electroreduction of CO2. *ACS Applied Energy Materials* **2018,** *1* (10), 5124-5128.

192. Marino, M. G.; Kreuer, K. D., Alkaline Stability of Quaternary Ammonium Cations for Alkaline Fuel Cell Membranes and Ionic Liquids. *ChemSusChem* **2015,** *8* (3), 513-523.

193. White, B. T.; Meenakshisundaram, V.; Feller, K. D.; Williams, C. B.; Long, T. E., Vat photopolymerization of unsaturated polyesters utilizing a polymerizable ionic liquid as a non-volatile reactive diluent. *Polymer* **2021,** *223*, 123727.

194. (a) Chi, W. S.; Koh, J. K.; Ahn, S. H.; Shin, J. S.; Ahn, H.; Ryu, D. Y.; Kim, J. H., Highly efficient I2-free solid-state dye-sensitized solar cells fabricated with polymerized ionic liquid and graft copolymer-directed mesoporous film. *Electrochemistry Communications* **2011,** *13* (12), 1349-1352; (b) Kawano, R.; Katakabe, T.; Shimosawa, H.; Khaja Nazeeruddin, M.; Grätzel, M.; Matsui, H.; Kitamura, T.; Tanabe, N.; Watanabe, M., Solid-state dye-sensitized solar cells using polymerized ionic liquid electrolyte with platinum-free counter electrode. *Physical Chemistry Chemical Physics* **2010,** *12* (8), 1916-1921.

195. (a) Emon, M. O. F.; Alkadi, F.; Philip, D. G.; Kim, D.-H.; Lee, K.-C.; Choi, J.-W., Multi-material 3D printing of a soft pressure sensor. *Additive Manufacturing* **2019,** *28*, 629-638; (b) Emon, M. O. F.; Lee, J.; Choi, U. H.; Kim, D.-H.; Lee, K.-C.; Choi, J.-W., Characterization of a Soft Pressure Sensor on the Basis of Ionic Liquid Concentration and Thickness of the Piezoresistive Layer. *IEEE Sensors Journal* **2019,** *19* (15), 6076-6084.

196. Tran, T. S.; Dutta, N. K.; Choudhury, N. R., Poly(ionic liquid)-Stabilized Graphene Nanoinks for Scalable 3D Printing of Graphene Aerogels. *ACS Applied Nano Materials* **2020,** *3* (11), 11608-11619.

197. Sevilia, S.; Yong, M.; Grinstein, D.; Gottlieb, L.; Eichen, Y., Novel, Printable Energetic Polymers. *Macromolecular Materials and Engineering* **2019,** *304* (6).

198. MacDonald, E.; Wicker, R., Multiprocess 3D printing for increasing component functionality. *Science* **2016,** *353* (6307), aaf2093.

199. (a) Wright, G. D., Molecular mechanisms of antibiotic resistance. *Chemical Communications* **2011,** *47* (14), 4055; (b) Blair, J. M. A.; Webber, M. A.; Baylay, A. J.; Ogbolu, D. O.; Piddock, L. J. V., Molecular mechanisms of antibiotic resistance. *Nature Reviews Microbiology* **2015,** *13* (1), 42-51.

200. (a) Jones, A.; Mandal, A.; Sharma, S., Protein-based bioplastics and their antibacterial potential. *Journal of Applied Polymer Science* **2015,** *132* (18); (b) Mahira, S.; Jain, A.; Khan, W.; Domb, A. J., Chapter 1: Antimicrobial Materials—An Overview. In *Antimicrobial Materials for Biomedical Applications*, Royal Society of Chemistry: 2019; pp 1-37.

201. Webster, T. J.; Seil, I., Antimicrobial applications of nanotechnology: methods and literature. *International Journal of Nanomedicine* **2012**, 2767.

202. Finberg, R. W.; Moellering, R. C.; Tally, F. P.; Craig, W. A.; Pankey, G. A.; Dellinger, E. P.; West, M. A.; Joshi, M.; Linden, P. K.; Rolston, K. V.; Rotschafer, J. C.; Rybak, M. J., The Importance of Bactericidal Drugs: Future Directions in Infectious Disease. *Clinical Infectious Diseases* **2004,** *39* (9), 1314-1320.

203. French, G. L., Bactericidal agents in the treatment of MRSA infections—the potential role of daptomycin. *Journal of Antimicrobial Chemotherapy* **2006,** *58* (6), 1107-1117.

204. Kumariya, R.; Garsa, A. K.; Rajput, Y. S.; Sood, S. K.; Akhtar, N.; Patel, S., Bacteriocins: Classification, synthesis, mechanism of action and resistance development in food spoilage causing bacteria. *Microbial Pathogenesis* **2019,** *128*, 171-177.

205. Tariq, S.; Wani, S.; Rasool, W.; Shafi, K.; Bhat, M. A.; Prabhakar, A.; Shalla, A. H.; Rather, M. A., A comprehensive review of the antibacterial, antifungal and antiviral potential of essential oils and their chemical constituents against drug-resistant microbial pathogens. *Microbial Pathogenesis* **2019,** *134*, 103580.

206. Jain, A.; Duvvuri, L. S.; Farah, S.; Beyth, N.; Domb, A. J.; Khan, W., Antimicrobial Polymers. *Advanced Healthcare Materials* **2014,** *3* (12), 1969-1985.

207. (a) Dakal, T. C.; Kumar, A.; Majumdar, R. S.; Yadav, V., Mechanistic Basis of Antimicrobial Actions of Silver Nanoparticles. *Frontiers in Microbiology* **2016,** *7* (1831); (b) Estevez, M. B.; Raffaelli, S.; Mitchell,

S. G.; Faccio, R.; Alborés, S., Biofilm Eradication Using Biogenic Silver Nanoparticles. *Molecules* **2020,** *25* (9), 2023-2023.

208. (a) Taormina, G.; Sciancalepore, C.; Bondioli, F.; Messori, M., Special Resins for Stereolithography: In Situ Generation of Silver Nanoparticles. *Polymers* **2018,** *10*; (b) Podstawczyk, D.; Skrzypczak, D.; Połomska, X.; Stargała, A.; Witek-Krowiak, A.; Guiseppi-Elie, A.; Galewski, Z., Preparation of antimicrobial 3D printing filament: In situ thermal formation of silver nanoparticles during the material extrusion. *Polymer Composites* **2020,** *41* (11), 4692-4705; (c) Bergonzi, C.; Remaggi, G.; Graiff, C.; Bergamonti, L.; Potenza, M.; Ossiprandi, M. C.; Zanotti, I.; Bernini, F.; Bettini, R.; Elviri, L., Three-Dimensional (3D) Printed Silver Nanoparticles/Alginate/Nanocrystalline Cellulose Hydrogels: Study of the Antimicrobial and Cytotoxicity Efficacy. *Nanomaterials* **2020,** *10* (5), 844; (d) Vidakis, N.; Petousis, M.; Velidakis, E.; Liebscher, M.; Tzounis, L., Three-Dimensional Printed Antimicrobial Objects of Polylactic Acid (PLA)-Silver Nanoparticle Nanocomposite Filaments Produced by an In-Situ Reduction Reactive Melt Mixing Process. *Biomimetics* **2020,** *5* (3), 42.

209. Wu, Z.; Hong, Y., Combination of the Silver–Ethylene Interaction and 3D Printing To Develop Antibacterial Superporous Hydrogels for Wound Management. *ACS Applied Materials & Interfaces* **2019,** *11* (37), 33734-33747.

210. Dupont, J.; Scholten, J. D., On the structural and surface properties of transition-metal nanoparticles in ionic liquids. *Chemical Society Reviews* **2010,** *39* (5), 1780-1804.

211. (a) Guo, J.; Xu, Q.; Zheng, Z.; Zhou, S.; Mao, H.; Wang, B.; Yan, F., Intrinsically Antibacterial Poly(ionic liquid) Membranes: The Synergistic Effect of Anions. *ACS Macro Letters* **2015,** *4* (10), 1094-1098; (b) Misra, A.; Franco Castillo, I.; Müller, D. P.; González, C.; Eyssautier-Chuine, S.; Ziegler, A.; de la Fuente, J. M.; Mitchell, S. G.; Streb, C., Polyoxometalate-Ionic Liquids (POM-ILs) as Anticorrosion and Antibacterial Coatings for Natural Stones. *Angewandte Chemie International Edition* **2018,** *57* (45), 14926-14931; (c) Torres, M. D. T.; Voskian, S.; Brown, P.; Liu, A.; Lu, T. K.; Hatton, T. A.; de la Fuente-Nunez, C., Coatable and Resistance-Proof Ionic Liquid for Pathogen Eradication. *ACS Nano* **2021,** *15* (1), 966-978; (d) Yue, J.; Zhao, P.; Gerasimov, J. Y.; van de Lagemaat, M.; Grotenhuis, A.; Rustema-Abbing, M.; van der Mei, H. C.; Busscher, H. J.; Herrmann, A.; Ren, Y., 3D-Printable Antimicrobial Composite Resins. *Advanced Functional Materials* **2015,** *25* (43), 6756-6767.

212. (a) Zhang, T.; Guo, J.; Ding, Y.; Mao, H.; Yan, F., Redox-responsive ferrocene-containing poly(ionic liquid)s for antibacterial applications. *Science China Chemistry* **2019,** *62* (1), 95-104; (b) Zheng, Z.; Xu, Q.; Guo, J.; Qin, J.; Mao, H.; Wang, B.; Yan, F., Structure–Antibacterial Activity Relationships of Imidazolium-Type Ionic Liquid Monomers, Poly(ionic liquids) and Poly(ionic liquid) Membranes: Effect of Alkyl Chain Length and Cations. *ACS Applied Materials & Interfaces* **2016,** *8* (20), 12684-12692; (c) Fang, H.; Wang, J.; Li, L.; Xu, L.; Wu, Y.; Wang, Y.; Fei, X.; Tian, J.; Li, Y., A novel high-strength poly(ionic liquid)/PVA hydrogel dressing for antibacterial applications. *Chemical Engineering Journal* **2019,** *365*, 153-164.

213. (a) Bacon, S. L.; Ross, R. J.; Daugulis, A. J.; Parent, J. S., Imidazolium-based polyionic liquid absorbents for bioproduct recovery. *Green Chemistry* **2017,** *19* (21), 5203-5213; (b) Qian, L.; Hu, X.; Guan, P.; Gao, B.; Li, J.; Wang, C.; Tang, Y., Preparation of bovine serum albumin imprinting sensitive hydrogels using ionic liquid as co-monomer and stabilizer. *Talanta* **2014,** *121*, 56-64; (c) Isik, M.; Gracia, R.; Kollnus, L. C.; Tomé, L. C.; Marrucho, I. M.; Mecerreyes, D., Cholinium-Based Poly(ionic liquid)s: Synthesis, Characterization, and Application as Biocompatible Ion Gels and Cellulose Coatings. *ACS Macro Letters* **2013,** *2* (11), 975-979; (d) Claus, J.; Brietzke, A.; Lehnert, C.; Oschatz, S.; Grabow, N.; Kragl, U., Swelling characteristics and biocompatibility of ionic liquid based hydrogels for biomedical applications. *PLOS ONE* **2020,** *15* (4), e0231421; (e) Qin, J.; Guo, J.; Xu, Q.; Zheng, Z.; Mao, H.; Yan, F., Synthesis of Pyrrolidinium-Type Poly(ionic liquid) Membranes for Antibacterial Applications. *ACS Applied Materials & Interfaces* **2017,** *9* (12), 10504-10511.

214. He, B.; Du, Y.; Wang, B.; Wang, X.; Ye, Q.; Liu, S., Grafting embedded poly(ionic liquid) brushes on biomimetic sharklet resin surface for anti-biofouling applications. *Progress in Organic Coatings* **2021,** *157*, 106298.

215. Bondarenko, O.; Juganson, K.; Ivask, A.; Kasemets, K.; Mortimer, M.; Kahru, A., Toxicity of Ag, CuO and ZnO nanoparticles to selected environmentally relevant test organisms and mammalian cells in vitro: a critical review. *Archives of Toxicology* **2013,** *87* (7), 1181-1200.

216. (a) Vincent, M.; Duval, R. E.; Hartemann, P.; Engels-Deutsch, M., Contact killing and antimicrobial properties of copper. *Journal of Applied Microbiology* **2018,** *124* (5), 1032-1046; (b) Ahamed, M.; Alhadlaq, H. A.; Khan, M. A. M.; Karuppiah, P.; Al-Dhabi, N. A., Synthesis, Characterization, and Antimicrobial Activity of Copper Oxide Nanoparticles. *Journal of Nanomaterials* **2014,** *2014*, 637858.

217. Muwaffak, Z.; Goyanes, A.; Clark, V.; Basit, A. W.; Hilton, S. T.; Gaisford, S., Patient-specific 3D scanned and 3D printed antimicrobial polycaprolactone wound dressings. *International Journal of Pharmaceutics* **2017,** *527* (1), 161-170.

218. Zheng, Z.; Guo, J.; Mao, H.; Xu, Q.; Qin, J.; Yan, F., Metal-Containing Poly(ionic liquid) Membranes for Antibacterial Applications. *ACS Biomaterials Science & Engineering* **2017,** *3* (6), 922-928.

219. Andrighetti-Fröhner, C.; Antonio, R.; Creczynski-Pasa, T.; Barardi, C.; Simões, C., Cytotoxicity and potential antiviral evaluation of violacein produced by Chromobacterium violaceum. *Memórias do Instituto Oswaldo Cruz* **2003,** *98* (6), 843-848.

220. (a) da Silva, B. R.; de Freitas, V. A. A.; Carneiro, V. A.; Arruda, F. V. S.; Lorenzón, E. N.; de Aguiar, A. S. W.; Cilli, E. M.; Cavada, B. S.; Teixeira, E. H., Antimicrobial activity of the synthetic peptide Lys-a1 against oral streptococci. *Peptides* **2013,** *42*, 78-83; (b) Panpaliya, N. P.; Dahake, P. T.; Kale, Y. J.; Dadpe, M. V.; Kendre, S. B.; Siddiqi, A. G.; Maggavi, U. R., In vitro evaluation of antimicrobial property of silver nanoparticles and chlorhexidine against five different oral pathogenic bacteria. *The Saudi Dental Journal* **2019,** *31* (1), 76-83.

221. Tambe, S. M.; Sampath, L.; Modak, S. M., In vitro evaluation of the risk of developing bacterial resistance to antiseptics and antibiotics used in medical devices. *Journal of Antimicrobial Chemotherapy* **2001,** *47* (5), 589-598.

222. Bhui, D. K.; Bar, H.; Sarkar, P.; Sahoo, G. P.; De, S. P.; Misra, A., Synthesis and UV–vis spectroscopic study of silver nanoparticles in aqueous SDS solution. *Journal of Molecular Liquids* **2009,** *145* (1), 33-37.

223. Ikemura, K.; Ichizawa, K.; Yoshida, M.; Ito, S.; Endo, T., UV-VIS spectra and photoinitiation behaviors of acylphosphine oxide and bisacylphosphine oxide derivatives in unfilled, light-cured dental resins. *Dental Materials Journal* **2008,** *27* (6), 765-774.

224. Heilmann, A., *Polymer Films with Embedded Metal Nanoparticles*. Springer-Verlag Berlin Heidelberg: Berlin, Germany, 2003; p 216.

225. V, S. C.; Galindo, R. E.; Benito, N.; Palacio, C.; Cavaleiro, A.; Carvalho, S., Ag+ release inhibition from ZrCN–Ag coatings by surface agglomeration mechanism: structural characterization. *J. Phys. D: Appl. Phys.* **2013,** *46*, 325303.

226. Jancar, J.; Douglas, J. F.; Starr, F. W.; Kumar, S. K.; Cassagnau, P.; Lesser, A. J.; Sternstein, S. S.; Buehler, M. J., Current issues in research on structure–property relationships in polymer nanocomposites. *Polymer* **2010,** *51* (15), 3321-3343.

227. Recalde, I. B.; Recalde, D.; García-Lopera, R.; Gómez, C. M., FTIR isothermal cure kinetics and morphology of dicyanate ester resin/polysulfone blends. *European Polymer Journal* **2005,** *41* (11), 2635-2643.

228. Standard Test Methods for Determination of Gel Content and Swell Ratio of Crosslinked Ethylene Plastics. https://www.astm.org/d2765-16.html.

229. (a) Grass, G.; Rensing, C.; Solioz, M., Metallic copper as an antimicrobial surface. *Applied and environmental microbiology* **2011,** *77* (5), 1541-7; (b) Ren, G.; Hu, D.; Cheng, E. W. C.; Vargas-Reus, M. A.; Reip, P.; Allaker, R. P., Characterisation of copper oxide nanoparticles for antimicrobial applications. *International Journal of Antimicrobial Agents* **2009,** *33* (6), 587-590; (c) Nassar, M. A. Y.; Eldien, H. M. S.; Tawab, H. S. A.; Saleem, T. H.; Omar, H. M.; Nassar, A. Y.; Hussein, M. R. A., Time-dependent Morphological and Biochemical Changes following Cutaneous Thermal Burn Injury and Their Modulation by Copper Nicotinate Complex: An Animal Model. *Ultrastructural Pathology* **2012,** *36* (5), 343-355.

230. (a) Palza, H., Antimicrobial Polymers with Metal Nanoparticles. *International Journal of Molecular Sciences* **2015,** *16* (1), 2099-2116; (b) Palza, H.; Quijada, R.; Delgado, K., Antimicrobial polymer composites with copper micro- and nanoparticles: Effect of particle size and polymer matrix. *Journal of Bioactive and Compatible Polymers* **2015,** *30* (4), 366-380; (c) Palza, H.; Nuñez, M.; Bastías, R.; Delgado, K., In situ antimicrobial behavior of materials with copper-based additives in a hospital environment. *International Journal of Antimicrobial Agents* **2018,** *51* (6), 912-917.

231. (a) Zuniga, J. M.; Cortes, A., The role of additive manufacturing and antimicrobial polymers in the COVID-19 pandemic. *Expert Review of Medical Devices* **2020,** *17* (6), 477-481; (b) Zuniga, J., 3D Printed Antibacterial Prostheses. *Applied Sciences* **2018,** *8* (9), 1651; (c) González-Henríquez, C.; Sarabia-Vallejos, M.; Rodríguez Hernandez, J., Antimicrobial Polymers for Additive Manufacturing. *International Journal of Molecular Sciences* **2019,** *20* (5), 1210.

232. (a) Schildermans, I.; Mullens, J.; Van der Veken, B. J.; Yperman, J.; Franco, D.; Van Poucke, L. C., Preparation and thermal decomposition of Cu2(OH)3NO3. *Thermochimica Acta* **1993,** *224*, 227-232; (b) Güner, E. K.; Özer, A. In *Synthesis And Characterization Of Copper Hydroxynitrate And Copper Oxide By Hydrothermal Method*, 2017.

233. Akitsu, T.; Yamaguchi, J.; Uchida, N.; Aritake, Y., The Studies of Conditions for Inducing Chirality to Cu(II) Complexes by Chiral Zn(II) and Ni(II) Complexes with Schiff Base. *Research Letters in Materials Science* **2009,** *2009*, 484172.

234. Wang, M.; Zhang, Q.; Xie, Q.; Wan, L.; Zhao, Y.; Zhang, X.; Luo, J., Selective electrochemical reduction of carbon dioxide to ethylene on a copper hydroxide nitrate nanostructure electrode. *Nanoscale* **2020,** *12* (32), 17013-17019.

235. Copper (Cu) Compounds. Copper (II) Nitrate (CuNO3). https://xpsdatabase.com/copper-spectra-cuno3/.

236. (a) Zhang, Z.; Gao, H.; Wu, H.; Qian, Y.-H.; Chen, L.; Chen, J., Chemical Fixation of CO2 by Using Carbon Material-Grafted N-Heterocyclic Carbene Silver and Copper Complexes. *ACS Applied Nano Materials* **2018**; (b) Bacchella, C.; Dell'Acqua, S.; Nicolis, S.; Monzani, E.; Casella, L., A Cu-bis(imidazole) Substrate Intermediate Is the Catalytically Competent Center for Catechol Oxidase Activity of Copper Amyloid-β. *Inorganic Chemistry* **2021,** *60* (2), 606-613; (c) Bete, S. C.; Würtele, C.; Otte, M., A bio-inspired imidazole-functionalised copper cage complex. *Chemical Communications* **2019,** *55* (30), 4427-4430.

237. Güner, E. K.; Özer, A. In *Synthesis And Characterization Of Copper Hydroxynitrate And Copper Oxide By Hydrothermal Method* 2017.

238. Dulta, K.; Koşarsoy Ağçeli, G.; Chauhan, P.; Jasrotia, R.; Chauhan, P. K.; Ighalo, J. O., Multifunctional CuO nanoparticles with enhanced photocatalytic dye degradation and antibacterial activity. *Sustainable Environment Research* **2022,** *32* (1), 2.

239. Otto, M., Staphylococcus epidermidis — the 'accidental' pathogen. *Nature Reviews Microbiology* **2009,** *7* (8), 555-567.

240. (a) Nowacka, N.; Nowak, R.; Drozd, M.; Olech, M.; Los, R.; Malm, A., Antibacterial, Antiradical Potential and Phenolic Compounds of Thirty-One Polish Mushrooms. *PLOS ONE* **2015,** *10* (10), e0140355; (b) Boyle, M.; Sichel, C.; Fernández-Ibáñez, P.; Arias-Quiroz, G. B.; Iriarte-Puña, M.; Mercado, A.; Ubomba-Jaswa, E.; McGuigan, K. G., Bactericidal Effect of Solar Water Disinfection under Real Sunlight Conditions. *Applied and Environmental Microbiology* **2008,** *74* (10), 2997-3001.

241. (a) Lu, F.; Astruc, D., Nanocatalysts and other nanomaterials for water remediation from organic pollutants. *Coordination Chemistry Reviews* **2020,** *408*, 213180; (b) Martínez-Huitle, C. A.; Brillas, E., Decontamination of wastewaters containing synthetic organic dyes by electrochemical methods: A general review. *Applied Catalysis B: Environmental* **2009,** *87* (3), 105-145.

242. Sakthivel, S.; Neppolian, B.; Shankar, M. V.; Arabindoo, B.; Palanichamy, M.; Murugesan, V., Solar photocatalytic degradation of azo dye: comparison of photocatalytic efficiency of ZnO and TiO2. *Solar Energy Materials and Solar Cells* **2003,** *77* (1), 65-82.

243. (a) Sadhishkumar, S.; Balusamy, T., Performance improvement in solar water heating systems—A review. *Renewable and Sustainable Energy Reviews* **2014,** *37*, 191-198; (b) Siva Reddy, V.; Kaushik, S. C.; Ranjan, K. R.; Tyagi, S. K., State-of-the-art of solar thermal power plants—A review. *Renewable and Sustainable Energy Reviews* **2013,** *27*, 258-273; (c) Chong, M. N.; Jin, B.; Chow, C. W. K.; Saint, C., Recent developments in photocatalytic water treatment technology: A review. *Water Research* **2010,** *44* (10), 2997-3027.

244. (a) Abdelaal, M. Y.; Mohamed, R. M., Novel Pd/TiO2 nanocomposite prepared by modified sol–gel method for photocatalytic degradation of methylene blue dye under visible light irradiation. *Journal of Alloys and Compounds* **2013,** *576*, 201-207; (b) Pu, X.; Zhang, D.; Gao, Y.; Shao, X.; Ding, G.; Li, S.; Zhao, S., One-pot microwave-assisted combustion synthesis of graphene oxide–TiO2 hybrids for photodegradation of methyl orange. *Journal of Alloys and Compounds* **2013,** *551*, 382-388; (c) Li, F.-t.; Liu, Y.; Liu, R.-h.; Sun, Z.-m.; Zhao, D.-s.; Kou, C.-g., Preparation of Ca-doped LaFeO3 nanopowders in a reverse microemulsion and their visible light photocatalytic activity. *Materials Letters* **2010,** *64* (2), 223-225; (d) Niu, X.; Li, H.; Liu, G., Preparation, characterization and photocatalytic properties of REFeO3 (RE=Sm, Eu, Gd). *Journal of Molecular Catalysis A: Chemical* **2005,** *232* (1), 89-93.

245. Xiao, J.; Liu, X.; Pan, L.; Shi, C.; Zhang, X.; Zou, J.-J., Heterogeneous Photocatalytic Organic Transformation Reactions Using Conjugated Polymers-Based Materials. *ACS Catalysis* **2020,** *10* (20), 12256-12283.

246. Subudhi, S.; Tripathy, S. P.; Parida, K., Highlights of the characterization techniques on inorganic, organic (COF) and hybrid (MOF) photocatalytic semiconductors. *Catalysis Science & Technology* **2021,** *11* (2), 392-415.

247. Grübel, M.; Bosque, I.; Altmann, P. J.; Bach, T.; Hess, C. R., Redox and photocatalytic properties of a NiII complex with a macrocyclic biquinazoline (Mabiq) ligand. *Chemical Science* **2018,** *9* (13), 3313-3317.

248. (a) Sutherland, B. R.; Sargent, E. H., Perovskite photonic sources. *Nature Photonics* **2016,** *10* (5), 295-302; (b) Akkerman, Q. A.; Rainò, G.; Kovalenko, M. V.; Manna, L., Genesis, challenges and opportunities for colloidal lead halide perovskite nanocrystals. *Nature Materials* **2018,** *17* (5), 394-405; (c) Im, J.-H.; Lee, C.-R.; Lee, J.-W.; Park, S.-W.; Park, N.-G., 6.5% efficient perovskite quantum-dot-sensitized solar cell. *Nanoscale* **2011,** *3* (10), 4088; (d) Lee, M. M.; Teuscher, J.; Miyasaka, T.; Murakami, T. N.; Snaith, H. J., Efficient Hybrid Solar Cells Based on Meso-Superstructured Organometal Halide Perovskites. *Science* **2012,** *338* (6107), 643-647; (e) Zhou, H.; Chen, Q.; Li, G.; Luo, S.; Song, T. B.; Duan, H. S.; Hong, Z.; You, J.; Liu, Y.; Yang, Y., Interface engineering of highly efficient perovskite solar cells. *Science* **2014,** *345* (6196), 542-546.

249. (a) Protesescu, L.; Yakunin, S.; Bodnarchuk, M. I.; Krieg, F.; Caputo, R.; Hendon, C. H.; Yang, R. X.; Walsh, A.; Kovalenko, M. V., Nanocrystals of Cesium Lead Halide Perovskites (CsPbX3, X = Cl, Br, and I): Novel Optoelectronic Materials Showing Bright Emission with Wide Color Gamut. *Nano letters* **2015,** *15* (6), 3692-3696; (b) Dey, A.; Ye, J.; De, A.; Debroye, E.; Ha, S. K.; Bladt, E.; Kshirsagar, A. S.; Wang, Z.; Yin, J.; Wang, Y.; Quan, L. N.; Yan, F.; Gao, M.; Li, X.; Shamsi, J.; Debnath, T.; Cao, M.; Scheel, M. A.; Kumar, S.; Steele, J. A.; Gerhard, M.; Chouhan, L.; Xu, K.; Wu, X. G.; Li, Y.; Zhang, Y.; Dutta, A.; Han, C.; Vincon, I.; Rogach, A. L.; Nag, A.; Samanta, A.; Korgel, B. A.; Shih, C. J.; Gamelin, D. R.; Son, D. H.; Zeng, H.; Zhong, H.; Sun, H.; Demir, H. V.; Scheblykin, I. G.; Mora-Seró, I.; Stolarczyk, J. K.; Zhang, J. Z.; Feldmann, J.; Hofkens, J.; Luther, J. M.; Pérez-Prieto, J.; Li, L.; Manna, L.; Bodnarchuk, M. I.; Kovalenko, M. V.; Roeffaers, M. B. J.; Pradhan, N.; Mohammed, O. F.; Bakr, O. M.; Yang, P.; Müller-Buschbaum, P.; Kamat, P. V.; Bao, Q.; Zhang, Q.; Krahne, R.; Galian, R. E.; Stranks, S. D.; Bals, S.; Biju, V.; Tisdale, W. A.; Yan, Y.; Hoye, R. L. Z.; Polavarapu, L., State of the Art and Prospects for Halide Perovskite Nanocrystals. *ACS Nano* **2021,** *15* (7), 10775-10981.

250. (a) Kovalenko, M. V.; Protesescu, L.; Bodnarchuk, M. I., Properties and potential optoelectronic applications of lead halide perovskite nanocrystals. *Science* **2017,** *358* (6364), 745-750; (b) Wang, Y.; Li, X.; Song, J.; Xiao, L.; Zeng, H.; Sun, H., All-Inorganic Colloidal Perovskite Quantum Dots: A New Class of Lasing Materials with Favorable Characteristics. *Advanced Materials* **2015,** *27* (44), 7101-7108; (c) Song, J.; Li, J.;

Li, X.; Xu, L.; Dong, Y.; Zeng, H., Quantum Dot Light-Emitting Diodes Based on Inorganic Perovskite Cesium Lead Halides (CsPbX3). *Advanced Materials* **2015,** *27* (44), 7162-7167; (d) Nannen, E.; Frohleiks, J.; Gellner, S., Light-Emitting Electrochemical Cells Based on Color-Tunable Inorganic Colloidal Quantum Dots. *Advanced Functional Materials* **2020,** *30* (33), 1907349; (e) Li, X.; Wu, Y.; Zhang, S.; Cai, B.; Gu, Y.; Song, J.; Zeng, H., CsPbX3 Quantum Dots for Lighting and Displays: Room-Temperature Synthesis, Photoluminescence Superiorities, Underlying Origins and White Light-Emitting Diodes. *Advanced Functional Materials* **2016,** *26* (15), 2435-2445.

251. (a) Zhang, G.; Liu, G.; Wang, L.; Irvine, J. T. S., Inorganic perovskite photocatalysts for solar energy utilization. *Chemical Society Reviews* **2016,** *45* (21), 5951-5984; (b) Tang, P.; Tong, Y.; Chen, H.; Cao, F.; Pan, G., Microwave-assisted synthesis of nanoparticulate perovskite LaFeO3 as a high active visible-light photocatalyst. *Current Applied Physics* **2013,** *13* (2), 340-343; (c) Hu, J.; Ma, J.; Wang, L.; Huang, H., Synthesis and photocatalytic properties of LaMnO3–graphene nanocomposites. *Journal of Alloys and Compounds* **2014,** *583*, 539-545; (d) Zhang, H.; Lü, M.; Liu, S.; Wang, L.; Xiu, Z.; Zhou, Y.; Qiu, Z.; Zhang, A.; Ma, Q., Preparation and photocatalytic property of perovskite Bi4Ti3O12 films. *Materials Chemistry and Physics* **2009,** *114* (2), 716-721; (e) Wang, W.; Tadé, M. O.; Shao, Z., Research progress of perovskite materials in photocatalysis- and photovoltaics-related energy conversion and environmental treatment. *Chemical Society Reviews* **2015,** *44* (15), 5371-5408; (f) Ohno, T.; Tsubota, T.; Nakamura, Y.; Sayama, K., Preparation of S, C cation-codoped SrTiO3 and its photocatalytic activity under visible light. *Applied Catalysis A: General* **2005,** *288* (1), 74-79.

252. (a) Suresh, R.; Rajendran, S.; Kumar, P. S.; Hoang, T. K. A.; Soto-Moscoso, M., Halides and oxyhalides-based photocatalysts for abatement of organic water contaminants – An overview. *Environmental Research* **2022,** *212*, 113149; (b) Zhou, Y.; Lu, F.; Fang, T.; Gu, D.; Feng, X.; Song, T.; Liu, W., A brief review on metal halide perovskite photocatalysts: History, applications and prospects. *Journal of Alloys and Compounds* **2022,** *911*, 165062; (c) Schünemann, S.; van Gastel, M.; Tüysüz, H., A CsPbBr3/TiO2 Composite for Visible-Light-Driven Photocatalytic Benzyl Alcohol Oxidation. *ChemSusChem* **2018,** *11* (13), 2057-2061.

253. (a) Wang, J.; Li, H.; Gao, P.; Peng, Y.; Cao, S.; Antonietti, M., CsPbBr3 perovskite based tandem device for CO2 photoreduction. *Chemical Engineering Journal* **2022,** *443*, 136447; (b) Laishram, D.; Zeng, S.; Alam, K. M.; Kalra, A. P.; Cui, K.; Kumar, P.; Sharma, R. K.; Shankar, K., Air- and water-stable halide perovskite nanocrystals protected with nearly-monolayer carbon nitride for CO2 photoreduction and water splitting. *Applied Surface Science* **2022,** *592*, 153276.

254. Cai, C.; Teng, Y.; Wu, J.-H.; Li, J.-Y.; Chen, H.-Y.; Chen, J.-H.; Kuang, D.-B., In Situ Photosynthesis of an MAPbI3/CoP Hybrid Heterojunction for Efficient Photocatalytic Hydrogen Evolution. *Advanced Functional Materials* **2020,** *30* (35), 2001478.

255. (a) Shi, A.; Sun, K.; Chen, X.; Qu, L.; Zhao, Y.; Yu, B., Perovskite as Recyclable Photocatalyst for Annulation Reaction of N-Sulfonyl Ketimines. *Organic Letters* **2022,** *24* (1), 299-303; (b) Shi, T.; Sun, K.; Chen, X.-L.; Zhang, Z.-X.; Huang, X.-Q.; Peng, Y.-Y.; Qu, L.-B.; Yu, B., Recyclable Perovskite as Heterogeneous Photocatalyst for Aminomethylation of Imidazo-Fused Heterocycles. *Advanced Synthesis & Catalysis* **2020,** *362* (11), 2143-2149; (c) Fan, Q.; Zhu, L.; Li, X.; Ren, H.; Zhu, H.; Wu, G.; Ding, J., Visible-light photocatalytic selective oxidation of amine and sulfide with CsPbBr3 as photocatalyst. *New Journal of Chemistry* **2021,** *45* (30), 13317-13322; (d) Zhu, X.; Lin, Y.; Sun, Y.; Beard, M. C.; Yan, Y., Lead-Halide Perovskites for Photocatalytic α-Alkylation of Aldehydes. *Journal of the American Chemical Society* **2019,** *141* (2), 733-738; (e) Corti, M.; Chiara, R.; Romani, L.; Mannucci, B.; Malavasi, L.; Quadrelli, P., Nanocrystals perovskites photocatalyzed singlet oxygen generation for light-driven organic reactions. *Photochemical & Photobiological Sciences* **2022,** *21* (5), 613-624; (f) Liu, M.; Xia, P.; Zhao, G.; Nie, C.; Gao, K.; He, S.; Wang, L.; Wu, K., Energy-Transfer Photocatalysis Using Lead Halide Perovskite Nanocrystals: Sensitizing Molecular Isomerization and Cycloaddition. *Angewandte Chemie International Edition* **2022,** *61* (35), e202208241; (g) Zhang, Y.; Xia, M.; Li, M.; Ping, Q.; Yuan, Z.; Liu, X.; Yin, H.; Huang, S.; Rao, Y., Energy-

Transfer-Mediated Photocatalysis by a Bioinspired Organic Perylenephotosensitizer HiBRCP. *The Journal of Organic Chemistry* **2021,** *86* (21), 15284-15297.

256. (a) Karami, M.; Ghanbari, M.; Amiri, O.; Salavati-Niasari, M., Enhanced antibacterial activity and photocatalytic degradation of organic dyes under visible light using cesium lead iodide perovskite nanostructures prepared by hydrothermal method. *Separation and Purification Technology* **2020,** *253*, 117526; (b) Feng, X.; Ju, H.; Song, T.; Fang, T.; Liu, W.; Huang, W., Highly Efficient Photocatalytic Degradation Performance of CsPb(Br1–xClx)3-Au Nanoheterostructures. *ACS Sustainable Chemistry & Engineering* **2019,** *7* (5), 5152-5156; (c) Qian, X.; Chen, Z.; Yang, X.; Zhao, W.; Liu, C.; Sun, T.; Zhou, D.; Yang, Q.; Wei, G.; Fan, M., Perovskite cesium lead bromide quantum dots: A new efficient photocatalyst for degrading antibiotic residues in organic system. *Journal of Cleaner Production* **2020,** *249*, 119335; (d) Cardenas-Morcoso, D.; Gualdrón-Reyes, A. F.; Ferreira Vitoreti, A. B.; García-Tecedor, M.; Yoon, S. J.; Solis de la Fuente, M.; Mora-Seró, I.; Gimenez, S., Photocatalytic and Photoelectrochemical Degradation of Organic Compounds with All-Inorganic Metal Halide Perovskite Quantum Dots. *The Journal of Physical Chemistry Letters* **2019,** *10* (3), 630-636.

257. Gao, G.; Xi, Q.; Zhou, H.; Zhao, Y.; Wu, C.; Wang, L.; Guo, P.; Xu, J., Novel inorganic perovskite quantum dots for photocatalysis. *Nanoscale* **2017,** *9* (33), 12032-12038.

258. (a) Cho, H.; Kim, Y.-H.; Wolf, C.; Lee, H.-D.; Lee, T.-W., Improving the Stability of Metal Halide Perovskite Materials and Light-Emitting Diodes. *Advanced Materials* **2018,** *30* (42), 1704587; (b) Huang, S.; Li, Z.; Wang, B.; Zhu, N.; Zhang, C.; Kong, L.; Zhang, Q.; Shan, A.; Li, L., Morphology Evolution and Degradation of CsPbBr3 Nanocrystals under Blue Light-Emitting Diode Illumination. *ACS Applied Materials & Interfaces* **2017,** *9* (8), 7249-7258; (c) De Roo, J.; Ibáñez, M.; Geiregat, P.; Nedelcu, G.; Walravens, W.; Maes, J.; Martins, J. C.; Van Driessche, I.; Kovalenko, M. V.; Hens, Z., Highly Dynamic Ligand Binding and Light Absorption Coefficient of Cesium Lead Bromide Perovskite Nanocrystals. *ACS Nano* **2016,** *10* (2), 2071-2081.

259. (a) Li, P.; Lu, Y.; Duan, Y.; Xu, S.; Zhang, J., Potential Application of Perovskite Glass Material in Photocatalysis Field. *The Journal of Physical Chemistry C* **2021,** *125* (4), 2382-2392; (b) Li, S.; Pan, Y.; Wang, W.; Li, Y., CsPbX3 (X = Cl, Br, I) perovskite quantum dots embedded in glasses: Recent advances and perspectives. *Chemical Engineering Journal* **2022,** *434*, 134593.

260. (a) Song, T.; Feng, X.; Ju, H.; Fang, T.; Zhu, F.; Liu, W.; Huang, W., Enhancing acid, base and UV light resistance of halide perovskite CH3NH3PbBr3 quantum dots by encapsulation with ZrO2 sol. *Journal of Alloys and Compounds* **2020,** *816*; (b) Li, Z.-J.; Hofman, E.; Li, J.; Davis, A. H.; Tung, C.-H.; Wu, L.-Z.; Zheng, W., Photoelectrochemically Active and Environmentally Stable CsPbBr3/TiO2 Core/Shell Nanocrystals. *Advanced Functional Materials* **2018,** *28* (1), 1704288; (c) Chen, W.; Liu, H.; Fan, R.; Wang, P.; Sun, T.; Yang, Y., Formation and Encapsulation of Lead Halide Perovskites in Lanthanide Metal–Organic Frameworks for Tunable Emission. *ACS Applied Materials & Interfaces* **2020,** *12* (8), 9851-9857.

261. Kinjo, N., *Speciality Polymers-Polymer Physics*. Akademie Verlag: 1989.

262. (a) Raja, S. N.; Bekenstein, Y.; Koc, M. A.; Fischer, S.; Zhang, D.; Lin, L.; Ritchie, R. O.; Yang, P.; Alivisatos, A. P., Encapsulation of Perovskite Nanocrystals into Macroscale Polymer Matrices: Enhanced Stability and Polarization. *ACS Appl Mater Interfaces* **2016,** *8* (51), 35523-35533; (b) Raino, G.; Landuyt, A.; Krieg, F.; Bernasconi, C.; Ochsenbein, S. T.; Dirin, D. N.; Bodnarchuk, M. I.; Kovalenko, M. V., Underestimated Effect of a Polymer Matrix on the Light Emission of Single CsPbBr3 Nanocrystals. *Nano letters* **2019,** *19* (6), 3648-3653; (c) Wang, Y.; He, J.; Chen, H.; Chen, J.; Zhu, R.; Ma, P.; Towers, A.; Lin, Y.; Gesquiere, A. J.; Wu, S. T.; Dong, Y., Ultrastable, Highly Luminescent Organic-Inorganic Perovskite-Polymer Composite Films. *Adv Mater* **2016,** *28* (48), 10710-10717.

263. (a) Yang, X.; Xu, T.; Zhu, Y.; Cai, J.; Gu, K.; Zhu, J.; Wang, Y.; Shen, J.; Li, C., Preparation of CsPbBr3@PS composite microspheres with high stability by electrospraying. *Journal of Materials Chemistry C* **2018,** *6* (30), 7971-7975; (b) Zhang, C.; He, Z.; Chen, H.; Zhou, L.; Tan, G.; Wu, S.-T.; Dong, Y., Light diffusing, down-converting perovskite-on-polymer microspheres. *Journal of Materials Chemistry C* **2019,** *7* (22), 6527-6533.

264. Wang, L.; Zhu, Y.; Liu, H.; Gong, J.; Wang, W.; Guo, S.; Yu, Y.; Peng, H.; Liao, Y., Giant Stability Enhancement of CsPbX3 Nanocrystal Films by Plasma-Induced Ligand Polymerization. *ACS Appl Mater Interfaces* **2019,** *11* (38), 35270-35276.

265. (a) Cai, Y.; Li, Y.; Wang, L.; Xie, R. J., A Facile Synthesis of Water-Resistant CsPbBr3 Perovskite Quantum Dots Loaded Poly(methyl methacrylate)Composite Microspheres Based on In Situ Polymerization. *Advanced Optical Materials* **2019,** *7* (22), 1901075; (b) Pan, A.; Wang, J.; Jurow, M. J.; Jia, M.; Liu, Y.; Wu, Y.; Zhang, Y.; He, L.; Liu, Y., General Strategy for the Preparation of Stable Luminous Nanocomposite Inks Using Chemically Addressable CsPbX3 Peroskite Nanocrystals. *Chemistry of Materials* **2018,** *30* (8), 2771-2780.

266. Zhang, Z.; Li, L.; Liu, L.; Xiao, X.; Huang, H.; Xu, J., Water-Stable and Photoelectrochemically Active CsPbBr3/Polyaniline Composite by a Photocatalytic Polymerization Process. *The Journal of Physical Chemistry C* **2020,** *124* (40), 22228-22234.

267. (a) Yu, L.; Zhang, Y.; Dai, X.; Zhang, L.; Tan, J., Monodisperse poly(methyl methacrylate)microspheres with tunable carboxyl groupson the surface obtained by photoinitiated RAFTdispersion polymerization. *Chem. Commun.* **2019,** *55*, 7848; (b) Yuan, D.; Chen, L.; Xiong, X.; Yuan, L.; Liao, S.; Wang, Y., Removal of uranium (VI) from aqueous solution by amidoxime functionalized superparamagnetic polymer microspheres prepared by a controlled radical polymerization in the presence of DPE. *Chemical Engineering Journal* **2016,** *285*, 358-367.

268. Recalde, I.; Gualdrón-Reyes, A. F.; Echeverría-Arrondo, C.; Villanueva-Antolí, A.; Simancas, J.; Rodriguez-Pereira, J.; Zanatta, M.; Mora-Seró, I.; Sans, V., Vitamins as Active Agents for Highly Emissive and Stable Nanostructured Halide Perovskite Inks and 3D Composites Fabricated by Additive Manufacturing. *Advanced Functional Materials n/a* (n/a), 2210802.

269. Chen, S.; Frenzel, F.; Cui, B.; Gao, F.; Campanella, A.; Funtan, A.; Kremer, F.; Parkin, S. S. P.; Binder, W. H., Gating effects of conductive polymeric ionic liquids. *Journal of Materials Chemistry C* **2018,** *6* (30), 8242-8250.

270. (a) Geffroy, C.; Grana, E.; Bessho, T.; Almosni, S.; Tang, Z.; Sharma, A.; Kinoshita, T.; Awai, F.; Cloutet, E.; Toupance, T.; Segawa, H.; Hadziioannou, G., p-Doping of a Hole Transport Material via a Poly(ionic liquid) for over 20% Efficiency and Hysteresis-Free Perovskite Solar Cells. *ACS Applied Energy Materials* **2020,** *3* (2), 1393-1401; (b) Yang, D.; Zhou, X.; Yang, R.; Yang, Z.; Yu, W.; Wang, X.; Li, C.; Liu, S.; Chang, R. P. H., Surface optimization to eliminate hysteresis for record efficiency planar perovskite solar cells. *Energy & Environmental Science* **2016,** *9* (10), 3071-3078; (c) Zhou, X.; Hu, M.; Liu, C.; Zhang, L.; Zhong, X.; Li, X.; Tian, Y.; Cheng, C.; Xu, B., Synergistic effects of multiple functional ionic liquid-treated PEDOT:PSS and less-ion-defects S-acetylthiocholine chloride-passivated perovskite surface enabling stable and hysteresis-free inverted perovskite solar cells with conversion efficiency over 20%. *Nano Energy* **2019,** *63*, 103866.

271. (a) Tang, J.; Tang, H.; Sun, W.; Radosz, M.; Shen, Y., Poly(ionic liquid)s as new materials for CO2 absorption. *Journal of Polymer Science Part A: Polymer Chemistry* **2005,** *43* (22), 5477-5489; (b) Rebber, M.; Willa, C.; Koziej, D., Organic-inorganic hybrids for CO2 sensing, separation and conversion. *Nanoscale horizons* **2020,** *5* (3), 431-453.

272. Karak, S.; Nanjo, C.; Odaka, M.; Yuyama, K.; Masuda, G.; Matsushita, M. M.; Awaga, K., A perovskite based plug and play AC photovoltaic device with ionic liquid induced transient opto-electronic conversion. *Journal of Materials Chemistry A* **2016,** *4* (23), 9019-9028.

273. Mariotti, S.; Mantione, D.; Almosni, S.; Ivanović, M.; Bessho, T.; Furue, M.; Segawa, H.; Hadziioannou, G.; Cloutet, E.; Toupance, T., Ionic and poly(ionic liquid)s as perovskite passivating molecules for improved solar cell performances. *Journal of Materials Chemistry C* **2022,** *10* (43), 16583-16591.

274. Wang, J.; Gu, X.; Ma, H.; Peng, Q.; Huang, X.; Zheng, X.; Sung, S. H. P.; Shan, G.; Lam, J. W. Y.; Shuai, Z.; Tang, B. Z., A facile strategy for realizing room temperature phosphorescence and single molecule white light emission. *Nature communications* **2018,** *9* (1).

275. Brubaker, C. D.; Frecker, T. M.; McBride, J. R.; Reid, K. R.; Jennings, G. K.; Rosenthal, S. J.; Adams, D. E., Incorporation of fluorescent quantum dots for 3D printing and additive manufacturing applications. *Journal of Materials Chemistry C* **2018,** *6* (28), 7584-7593.

276. Tai, C. L.; Hong, W. L.; Kuo, Y. T.; Chang, C. Y.; Niu, M. C.; Karupathevar Ponnusamythevar Ochathevar, M.; Hsu, C. L.; Horng, S. F.; Chao, Y. C., Ultrastable, Deformable, and Stretchable Luminescent Organic-Inorganic Perovskite Nanocrystal-Polymer Composites for 3D Printing and White Light-Emitting Diodes. *ACS Appl Mater Interfaces* **2019,** *11* (33), 30176-30184.

277. Ririe, K. M.; Rasmussen, R. P.; Wittwer, C. T., Product Differentiation by Analysis of DNA Melting Curves during the Polymerase Chain Reaction. *Analytical Biochemistry* **1997,** *245* (2), 154-160.

278. Meech, S. R.; Phillips, D., Photophysics of some common fluorescence standards. *Journal of Photochemistry* **1983,** *23* (2), 193-217.

279. Porrès, L.; Holland, A.; Pålsson, L.-O.; Monkman, A. P.; Kemp, C.; Beeby, A., Absolute Measurements of Photoluminescence Quantum Yields of Solutions Using an Integrating Sphere. *Journal of Fluorescence* **2006,** *16* (2), 267-273.

280. Veldhuis, S. A.; Boix, P. P.; Yantara, N.; Li, M.; Sum, T. C.; Mathews, N.; Mhaisalkar, S. G., Perovskite Materials for Light-Emitting Diodes and Lasers. *Advanced Materials* **2016,** *28* (32), 6804-6834.

281. Deepa, M.; Salado, M.; Calio, L.; Kazim, S.; Shivaprasad, S. M.; Ahmad, S., Cesium power: low Cs+ levels impart stability to perovskite solar cells. *Physical Chemistry Chemical Physics* **2017,** *19* (5), 4069-4077.

282. Gualdrón-Reyes, A. F.; Rodríguez-Pereira, J.; Amado-González, E.; Rueda-P, J.; Ospina, R.; Masi, S.; Yoon, S. J.; Tirado, J.; Jaramillo, F.; Agouram, S.; Muñoz-Sanjosé, V.; Giménez, S.; Mora-Seró, I., Unravelling the Photocatalytic Behavior of All-Inorganic Mixed Halide Perovskites: The Role of Surface Chemical States. *ACS Applied Materials & Interfaces* **2020,** *12* (1), 914-924.

283. Lee, C.; Shin, Y.; Villanueva-Antolí, A.; Das Adhikari, S.; Rodriguez-Pereira, J.; Macak, J. M.; Mesa, C. A.; Giménez, S.; Yoon, S. J.; Gualdrón-Reyes, A. F.; Mora-Seró, I., Efficient and Stable Blue- and Red-Emitting Perovskite Nanocrystals through Defect Engineering: PbX2 Purification. *Chemistry of Materials* **2021,** *33* (22), 8745-8757.

284. Qiu, L.; Yang, H.; Dai, Z.; Sun, F.; Hao, J.; Guan, M.; Dang, P.; Yan, C.; Lin, J.; Li, G., Highly efficient and stable CsPbBr3 perovskite quantum dots by encapsulation in dual-shell hollow silica spheres for WLEDs. *Inorganic Chemistry Frontiers* **2020,** *7* (10), 2060-2071.

285. Zhang, Y.; Siegler, T. D.; Thomas, C. J.; Abney, M. K.; Shah, T.; De Gorostiza, A.; Greene, R. M.; Korgel, B. A., A “Tips and Tricks” Practical Guide to the Synthesis of Metal Halide Perovskite Nanocrystals. *Chemistry of Materials* **2020,** *32* (13), 5410-5423.

286. Wu, F.; Kim, G.-T.; Diemant, T.; Kuenzel, M.; Schür, A. R.; Gao, X.; Qin, B.; Alwast, D.; Jusys, Z.; Behm, R. J.; Geiger, D.; Kaiser, U.; Passerini, S., Reducing Capacity and Voltage Decay of Co-Free Li1.2Ni0.2Mn0.6O2 as Positive Electrode Material for Lithium Batteries Employing an Ionic Liquid-Based Electrolyte. *Advanced Energy Materials* **2020,** *10* (34), 2001830.

287. (a) Connal, L. A.; Vestberg, R.; Gurr, P. A.; Hawker, C. J.; Qiao, G. G., Patterning on Nonplanar Substrates: Flexible Honeycomb Films from a Range of Self-assembling Star Copolymers. *Langmuir* **2008,** *24* (2), 556-562; (b) Parod, R. J., Butyl Acrylate. In *Encyclopedia of Toxicology (Third Edition)*, Wexler, P., Ed. Academic Press: Oxford, 2014; pp 578-580; (c) Wu, Y.; Cao, R.; Wu, G.; Huang, W.; Chen, Z.; Yang, X.; Tu, Y., From ultratough artificial nacre to elastomer: Poly(n-butyl acrylate) grafted graphene oxide nanocomposites. *Composites Part A: Applied Science and Manufacturing* **2016,** *88*, 156-164; (d) Song, T.; Deng, J.; Deng, L.; Bai, L.; Zhang, X.; Zhang, S.; Szabo, P.; Daugaard, A. E., Poly(vinylimidazole-co-butyl acrylate) membranes for CO2 separation. *Polymer* **2019,** *160*, 223-230; (e) Kim, Y. M.; Lee, W. Y.; Choi, W. Y.; Moon, H. C., Impact of chain flexibility of copolymer gelators on performance of ion gel electrolytes for functional electrochemical devices. *Journal of Industrial and Engineering Chemistry* **2020,** *90*, 341-350.

288. Gualdrón-Reyes, A. F.; Fernández-Climent, R.; Masi, S.; Mesa, C. A.; Echeverría-Arrondo, C.; Aiello, F.; Balzano, F.; Uccello-Barretta, G.; Rodríguez-Pereira, J.; Giménez, S.; Mora-Seró, I., Efficient Ligand

Passivation Enables Ultrastable CsPbX3 Perovskite Nanocrystals in Fully Alcohol Environments. *Advanced Optical Materials n/a* (n/a), 2203096.

289. (a) Badr, Y.; Abd El-Wahed, M. G.; Mahmoud, M. A., Photocatalytic degradation of methyl red dye by silica nanoparticles. *Journal of Hazardous Materials* **2008,** *154* (1), 245-253; (b) Brooks, A.; Yeung, K.; Lewis, G.; Phillips, S., A Strategy for Minimizing Background Signal in Autoinductive Signal Amplification Reactions for Point-of-Need Assays. *Anal. Methods* **2015,** *7*.

290. (a) Plutino, M. R.; Guido, E.; Colleoni, C.; Rosace, G., Effect of GPTMS functionalization on the improvement of thepH-sensitive methyl red photostability. *Sensors and Actuators B* **2017,** *238*, 281–291; (b) Zhou, M.; Yu, Q.; Lei, L.; Barton, G., Electro-Fenton method for the removal of methyl red in an efficient electrochemical system. *Separation and Purification Technology* **2007,** *57* (2), 380-387.

291. Gupta, S. M.; Tripathi, M., An overview of commonly used semiconductor nanoparticles in photocatalysis. *High Energy Chemistry* **2012,** *46* (1), 1-9.

292. Salamone, J. C.; Israel, S. C.; Taylor, P.; Snider, B., Synthesis and homopolymerization studies of vinylimidazolium salts. *Polymer* **1973,** *14* (12), 639-644.

293. Park, M. J.; Lee, J. K.; Lee, B. S.; Lee, Y.-W.; Choi, I. S.; Lee, S.-g., Covalent Modification of Multiwalled Carbon Nanotubes with Imidazolium-Based Ionic Liquids: Effect of Anions on Solubility. *Chemistry of Materials* **2006,** *18* (6), 1546-1551.

294. Das Adhikari, S.; Masi, S.; Echeverría-Arrondo, C.; Miralles-Comins, S.; Sánchez, R. S.; Fernandes, J. A.; Chirvony, V.; Martínez-Pastor, J. P.; Sans, V.; Mora-Seró, I., Continuous-Flow Synthesis of Orange Emitting Sn(II)-Doped CsBr Materials. *Advanced Optical Materials* **2021,** *9* (21), 2101024.

295. (a) Santi, S.; Rossi, S., Molecular design of star-shaped benzotrithiophene materials for organic electronics. *Tetrahedron Letters* **2019,** *60* (36); (b) Oh, Y.-T.; Shin, D.-C., Purification and crystal growth of NPB via imidazolium based ionic liquids. *Journal of Crystal Growth* **2018,** *487*, 78-82.

296. (a) Sapp, S. A.; Sotzing, G. A.; Reynolds, J. R., High Contrast Ratio and Fast-Switching Dual Polymer Electrochromic Devices. *Chemistry of Materials* **1998,** *10* (8), 2101-2108; (b) Guven, N.; Camurlu, P.; Yucel, B., Multichromic polymers based on pyrene clicked thienylpyrrole. *Polymer International* **2015,** *64* (6), 758-765.

297. Novák, P.; Müller, K.; Santhanam, K. S. V.; Haas, O., Electrochemically Active Polymers for Rechargeable Batteries. *Chemical Reviews* **1997,** *97* (1), 207-282.

298. (a) Rudge, A.; Davey, J.; Raistrick, I.; Gottesfeld, S.; Ferraris, J. P., Conducting polymers as active materials in electrochemical capacitors. *Journal of Power Sources* **1994,** *47* (1), 89-107; (b) Rudge, A.; Raistrick, I.; Gottesfeld, S.; Ferraris, J. P., A study of the electrochemical properties of conducting polymers for application in electrochemical capacitors. *Electrochimica Acta* **1994,** *39* (2), 273-287.

299. Hofmann, A. I.; Smaal, W. T. T.; Mumtaz, M.; Katsigiannopoulos, D.; Brochon, C.; Schütze, F.; Hild, O. R.; Cloutet, E.; Hadziioannou, G., An Alternative Anionic Polyelectrolyte for Aqueous PEDOT Dispersions: Toward Printable Transparent Electrodes. *Angewandte Chemie* **2015,** *127* (29), 8626-8630.

300. Stenger-Smith, J. D.; Webber, C. K.; Anderson, N.; Chafin, A. P.; Zong, K.; Reynolds, J. R., Poly(3,4-alkylenedioxythiophene)-based supercapacitors using ionic liquids as supporting electrolytes. *Journal of the Electrochemical Society* **2002,** *149* (8), A973-A977.

301. Suominen, M.; Damlin, P.; Kvarnström, C., Electrolyte effects on formation and properties of PEDOT-graphene oxide composites. *Electrochimica Acta* **2019,** *307*, 214-223.

302. (a) Wu, M.; Zhang, H.; Zhao, F.; Zeng, B., A novel poly(3,4-ethylenedioxythiophene)-ionic liquid composite coating for the headspace solid-phase microextraction and gas chromatography determination of several alcohols in soft drinks. *Analytica Chimica Acta* **2014,** *850*, 41–48; (b) Shaplov, A. S.; Ponkratov, D. O.; Aubert, P. H.; Lozinskaya, E. I.; Plesse, C.; Vidal, F.; Vygodskii, Y. S., A first truly all-solid state organic electrochromic device based on polymeric ionic liquids. *Chem Commun (Camb)* **2014,** *50* (24), 3191-3.

303. (a) Heywang, G.; Jonas, F., Poly(alkylenedioxythiophene)s - New, very stable conducting polymers. *Advanced Materials* **1992,** *4* (2), 116-118; (b) Dietrich, M.; Heinze, J.; Heywang, G.; Jonas, F., Electrochemical and spectroscopic characterization of polyalkylenedioxythiophenes. *Journal of*

Electroanalytical Chemistry **1994,** *369* (1-2), 87-92; (c) Sotzing, G. A.; Reynolds, J. R.; Steel, P. J., Electrochromic conducting polymers via electrochemical polymerization of bis(2-(3,4-ethylenedioxy)thienyl) monomers. *Chemistry of Materials* **1996,** *8* (4), 882-889; (d) Groenendaal, L.; Zotti, G.; Aubert, P. H.; Waybright, S. M.; Reynolds, J. R., Electrochemistry of poly(3,4-alkylenedioxythiophene) derivatives. *Advanced Materials* **2003,** *15* (11), 855-879.

304. (a) Österholm, A. M.; Shen, D. E.; Dyer, A. L.; Reynolds, J. R., Optimization of PEDOT films in ionic liquid supercapacitors: Demonstration as a power source for polymer electrochromic devices. *ACS Applied Materials and Interfaces* **2013,** *5* (24), 13432-13440; (b) Karlsson, C.; Nicholas, J.; Evans, D.; Forsyth, M.; Stromme, M.; Sjodin, M.; Howlett, P. C.; Pozo-Gonzalo, C., Stable Deep Doping of Vapor-Phase Polymerized Poly(3,4-ethylenedioxythiophene)/Ionic Liquid Supercapacitors. *ChemSusChem* **2016,** *9* (16), 2112-21.

305. (a) Sapp, S. A.; Sotzing, G. A.; Reddinger, J. L.; Reynolds, J. R., Rapid switching solid state electrochromic devices based on complementary conducting polymer films. *Advanced Materials* **1996,** *8* (10), 808-811; (b) Gadgil, B.; Damlin, P.; Kvarnström, C., Graphene vs. reduced graphene oxide: A comparative study of graphene-based nanoplatforms on electrochromic switching kinetics. *Carbon* **2016,** *96*, 377-381.

306. Hong, W.; Xu, Y.; Lu, G.; Li, C.; Shi, G., Transparent graphene/PEDOT-PSS composite films as counter electrodes of dye-sensitized solar cells. *Electrochemistry Communications* **2008,** *10* (10), 1555-1558.

307. Määttänen, A.; Vanamo, U.; Ihalainen, P.; Pulkkinen, P.; Tenhu, H.; Bobacka, J.; Peltonen, J., A low-cost paper-based inkjet-printed platform for electrochemical analyses. *Sensors and Actuators, B: Chemical* **2013,** *177*, 153-162.

308. (a) Fan, X.; Nie, W.; Tsai, H.; Wang, N.; Huang, H.; Cheng, Y.; Wen, R.; Ma, L.; Yan, F.; Xia, Y., PEDOT:PSS for Flexible and Stretchable Electronics: Modifications, Strategies, and Applications. *Advanced Science* **2019,** *6* (19), 1900813; (b) Kim, Y. H.; Sachse, C.; Machala, M. L.; May, C.; Müller-Meskamp, L.; Leo, K., Highly Conductive PEDOT:PSS Electrode with Optimized Solvent and Thermal Post-Treatment for ITO-Free Organic Solar Cells. *Advanced Functional Materials* **2011,** *21* (6), 1076-1081.

309. (a) Zhou, Y.-f.; Yuan, Y.-b.; Cao, L.-f.; Zhang, J.; Pang, H.-q.; Lian, J.-r.; Zhou, X., Improved stability of OLEDs with mild oxygen plasma treated PEDOT:PSS. *Journal of Luminescence* **2007,** *122-123*, 602-604; (b) ZHANG Yichen, X. H., ZHAO Chunhui, Research Progress of PEDOT∶PSS Hole Transport Layer and Its Modification for Organic Solar Cells. *Materials Reports* **2021,** *35* (3), 3204-3208.

310. Randriamahazaka, H.; Plesse, C.; Teyssié, D.; Chevrot, C., Electrochemical behaviour of poly(3,4-ethylenedioxythiophene) in a room-temperature ionic liquid. *Electrochemistry Communications* **2003,** *5* (7), 613-617.

311. Wagner, K.; Pringle, J. M.; Hall, S. B.; Forsyth, M.; MacFarlane, D. R.; Officer, D. L., Investigation of the electropolymerisation of EDOT in ionic liquids. *Synthetic Metals* **2005,** *153* (1-3), 257-260.

312. (a) Döbbelin, M.; Marcilla, R.; Salsamendi, M.; Pozo-Gonzalo, C.; Carrasco, P. M.; Pomposo, J. A.; Mecerreyes, D., Influence of Ionic Liquids on the Electrical Conductivity and Morphology of PEDOT:PSS Films. *Chemistry of Materials* **2007,** *19* (9), 2147-2149; (b) Atoyo, J.; Burton, M. R.; McGettrick, J.; Carnie, M. J., Enhanced Electrical Conductivity and Seebeck Coefficient in PEDOT:PSS via a Two-Step Ionic liquid and NaBH4 Treatment for Organic Thermoelectrics. *Polymers (Basel)* **2020,** *12* (3); (c) Li, Q.; Zhou, Q.; Wen, L.; Liu, W., Enhanced thermoelectric performances of flexible PEDOT:PSS film by synergistically tuning the ordering structure and oxidation state. *Journal of Materiomics* **2020,** *6* (1), 119-127.

313. Ohno, H., Design of Ion Conductive Polymers Based on Ionic Liquids. *Macromolecular Symposia* **2007,** *249-250* (1), 551-556.

314. (a) Bkkar, M. A.; Olekhnovich, R. O.; Kremleva, A. V.; Kovach, Y. N.; Kalanchina, V.; Uspenskaya, M. V., Fabrication of electrospun polymer nanofibers modified with all-inorganic perovskite nanocrystals for flexible optoelectronic devices. *Applied Nanoscience* **2022,** *12* (10), 2961-2977; (b) Gomez, C. M.; Pan, S.; Braga, H. M.; de Oliveira, L. S.; Dalpian, G. M.; Biesold-McGee, G. V.; Lin, Z.; Santos, S. F.; Souza, J. A.,

Possible Charge-Transfer-Induced Conductivity Enhancement in TiO2 Microtubes Decorated with Perovskite CsPbBr3 Nanocrystals. *Langmuir* **2020,** *36* (19), 5408-5416.

315. (a) Park, J. H.; Lee, A.-y.; Yu, J. C.; Nam, Y. S.; Choi, Y.; Park, J.; Song, M. H., Surface Ligand Engineering for Efficient Perovskite Nanocrystal-Based Light-Emitting Diodes. *ACS Applied Materials & Interfaces* **2019,** *11* (8), 8428-8435; (b) Zhang, J.; Ji, S.; Ma, Y.; Guan, R.; Wu, X.; Qu, X.; Yan, B.; Zhang, D.; Zhao, J.; Yang, J., Tunable photoluminescence and an enhanced photoelectric response of Mn2+-doped CsPbCl3 perovskite nanocrystals via pressure-induced structure evolution. *Nanoscale* **2019,** *11* (24), 11660-11670.

316. (a) Del Castillo-Castro, T.; Larios-Rodriguez, E.; Molina-Arenas, Z.; Castillo-Ortega, M. M.; Tanori, J., Synthesis and characterization of metallic nanoparticles and their incorporation into electroconductive polymer composites. *Composites Part A: Applied Science and Manufacturing* **2007,** *38* (1), 107-113; (b) Iida, M.; Kawakami, S.; Syouno, E.; Er, H.; Taguchi, E., Properties of ionic liquids containing silver(I) or protic alkylethylenediamine cations with a bis(trifluoromethanesulfonyl)amide anion. *Journal of Colloid and Interface Science* **2011,** *356* (2), 630-638; (c) Zhan, Y.; Santillo, C.; Meng, Y.; Lavorgna, M., Recent advances and perspectives on silver-based polymer composites for electromagnetic interference shielding. *Journal of Materials Chemistry C* **2023,** *11* (3), 859-892.

317. Nicholson, R. S., Theory and Application of Cyclic Voltammetry for Measurement of Electrode Reaction Kinetics. *Analytical Chemistry* **1965,** *37* (11), 1351-1355.

318. (a) Bonanos, N.; Steele, B. C. H.; Butler, E. P., Applications of Impedance Spectroscopy. In *Impedance Spectroscopy*, 2005; pp 205-537; (b) Macdonald, J. R.; Johnson, W. B., Fundamentals of Impedance Spectroscopy. In *Impedance Spectroscopy*, 2005; pp 1-26.

319. Mei, B.-A.; Munteshari, O.; Lau, J.; Dunn, B.; Pilon, L., Physical Interpretations of Nyquist Plots for EDLC Electrodes and Devices. *The Journal of Physical Chemistry C* **2018,** *122* (1), 194-206.

320. Elschner, A.; Kirchmeyer, S.; Lövenich, W.; Merker, U.; Reuter, K. In *PEDOT: Principles and Applications of an Intrinsically Conductive Polymer*, 2010.

321. (a) Zhang, S. Y.; Zhuang, Q.; Zhang, M.; Wang, H.; Gao, Z.; Sun, J. K.; Yuan, J., Poly(ionic liquid) composites. *Chem Soc Rev* **2020,** *49* (6), 1726-1755; (b) Brinkkötter, M.; Lozinskaya, E. I.; Ponkratov, D. O.; Vlasov, P. S.; Rosenwinkel, M. P.; Malyshkina, I. A.; Vygodskii, Y.; Shaplov, A. S.; Schönhoff, M., Influence of anion structure on ion dynamics in polymer gel electrolytes composed of poly(ionic liquid), ionic liquid and Li salt. *Electrochimica Acta* **2017,** *237*, 237-247; (c) Brinkkötter, M.; Lozinskaya, E. I.; Ponkratov, D. O.; Vygodskii, Y.; Schmidt, D. F.; Shaplov, A. S.; Schönhoff, M., Influence of Cationic Poly(ionic liquid) Architecture on the Ion Dynamics in Polymer Gel Electrolytes. *The Journal of Physical Chemistry C* **2019,** *123* (21), 13225-13235.

322. (a) Teo, M. Y.; Kim, N.; Kee, S.; Kim, B. S.; Kim, G.; Hong, S.; Jung, S.; Lee, K., Highly Stretchable and Highly Conductive PEDOT:PSS/Ionic Liquid Composite Transparent Electrodes for Solution-Processed Stretchable Electronics. *ACS Applied Materials & Interfaces* **2017,** *9* (1), 819-826; (b) Wang, Y.; Zhu, C.; Pfattner, R.; Yan, H.; Jin, L.; Chen, S.; Molina-Lopez, F.; Lissel, F.; Liu, J.; Rabiah, N. I.; Chen, Z.; Chung, J. W.; Linder, C.; Toney, M. F.; Murmann, B.; Bao, Z., A highly stretchable, transparent, and conductive polymer. *Science Advances* **2017,** *3* (3), e1602076.